List of Contributors

M. Baldus, *Department for NMR-Based Structural Biology, Max-Planck-Institute for Biophysical Chemistry, Am Fassberg 11, 37077 Göttingen, Germany*

B. M. Goodson, *Department of Chemistry and Biochemistry, Southern Illinois University, 113 Neckers Hall, Carbondale, IL 62901, USA*

C. E. Hughes, *Department for NMR-Based Structural Biology, Max-Planck-Institute for Biophysical Chemistry, Am Fassberg 11, 37077 Göttingen, Germany*

R. E. Jacobs, *Biological Imaging Center, 139-74 Beckman Institute, California Institute of Technology, Pasadena, CA 91125, USA*

G. E. Martin, *Michigan Structure Elucidation Group, Pfizer Global Research and Development, Pfizer Corporation, Kalamazoo, MI 49001-0199, USA*

C. Mayer, *Institut für Chemie, Universität Duisburg-Essen, 47048 Duisburg, Germany*

P. T. Narasimhan, *Biological Imaging Center, 139-74 Beckman Institute, California Institute of Technology, Pasadena, CA 91125, USA*

D. Reichert, *Univ. Halle, FB Physik, Friedemann-Bach-Platz 6, 06108 Halle, Germany*

A. J. Williams, *Advanced Chemistry Development, 90 Adelaide St. W., Suite 600, Toronto, Ont., Canada M5H 3V9*

Preface

Volume 55 of Annual Reports on NMR consists of the usual eclectic combination of reports which represent advances in the various techniques and applications of NMR. It is dedicated to Professor Michal Witanowski of the Institute of Organic Chemistry of the Polish Academy of Sciences on the occasion of his 70th birthday. I have had the pleasure of knowing, and working with, Michal for almost 40 years on various areas of Nitrogen NMR. During this time he has been a frequent contributor to Annual Reports on NMR.

A very extensive account of Long-Range ^{1}H–^{15}N Heteronuclear Shift Correlation by G.E. Martin and A.J. Williams starts the volume, this is followed by a report on Magic-Angle-Spinning Solid State NMR Applied to Polypeptides and Proteins by C.E. Hughes and M. Baldus, D. Reichert covers NMR Studies of Dynamic Processes in Organic Solids, next is an account of NMR Studies of Nanoparticles by C. Mayer, Microscopy in Magnetic Resonance Imaging is reviewed by P.T. Narasimhan and R.E. Jacobs, finally Applications of Optical Pumping and Polarization Techniques in NMR, Part 1 Optical Nuclear Polarization in Molecular Crystals is reported on by B.M. Goodson.

It is a great pleasure for me to extend my thanks to all of the contributors for their extensive and valuable accounts and to the production staff at Elsevier for their assistance in the creation of this volume.

Royal Society of Chemistry   G. A. WEBB
Burlington House   October 2005
Piccadilly
London, *UK*

Contents

Long-Range ^{1}H–^{15}N Heteronuclear Shift Correlation
GARY E. MARTIN AND ANTONY J. WILLIAMS

Magic-Angle-Spinning Solid-State NMR Applied to Polypeptides and Proteins
COLAN E. HUGHES AND MARC BALDUS

NMR Studies of Dynamic Processes in Organic Solids
D. REICHERT

NMR Studies of Nanoparticles
CHRISTIAN MAYER

Microscopy in Magnetic Resonance Imaging
P.T. NARASIMHAN AND RUSSELL E. JACOBS

Applications of Optical Pumping and Polarization Techniques in NMR: I. Optical Nuclear Polarization in Molecular Crystals
BOYD M. GOODSON

Long-Range ^{1}H–^{15}N Heteronuclear Shift Correlation

GARY E. MARTIN[1] AND ANTONY J. WILLIAMS[2]

[1]*Michigan Structure Elucidation Group, Pfizer Global Research and Development, Pfizer Corporation, Kalamazoo, MI 49001-0199, USA*
[2]*Advanced Chemistry Development, 110 Yonge Street, 14th Floor, Toronto, Ont., Canada M5C 1T4*

The investigation of long-range ^{1}H–^{15}N heteronuclear shift correlation NMR experiments has gone from its inception in 1995 to a robust area of research with numerous studies now reported annually. The area has been reviewed twice, covering the literature through about mid-2000. The present report covers the period from where this author's previous review stopped in late-1999 through the present. New long-range heteronuclear shift correlation methods that are applicable to long-range ^{1}H–^{15}N 2D heteronuclear shift correlation are discussed followed by a discussion of

the impact of long-range ^{1}H–^{15}N data on Computer-Assisted Structure Elucidation methods and then a review of the applications of these techniques reported in the literature.

1. INTRODUCTION

The field of long-range ^{1}H–^{15}N 2D heteronuclear shift correlation spectroscopy at natural abundance began, arguably, with a pair of poster presentations from laboratories in Japan and the United States in 1993.[1,2] There is an earlier reported application of long-range ^{1}H–^{15}N 2D HMBC in the literature but these were non-gradient data acquired on a ^{15}N-enriched sample.[3] Efforts in one of the author's laboratories (GEM) in the early 1990s prior to the advent of gradient equipped NMR spectrometers were frustratingly difficult, giving sporadic results. The advent of NMR instruments equipped with gradient capabilities, however, moved this area of research forward substantially.[4,5]

In the interval from the first published reports in mid-1995[6–8] through the end of the century, more than 50 reports were published, and this field of investigation evolved from one of initial intellectual curiosity to a vigorous area of investigation that spawned a pair of reviews in 2000 and 2001.[9,10] Concurrent with the appearance of progressively more reports of studies utilizing long-range ^{1}H–^{15}N 2D heteronuclear shift correlation methods, a number of new long-range heteronuclear shift correlation methods have also been developed, only some of which have been applied to ^{1}H–^{15}N studies. Some of the new long-range heteronuclear shift correlation methods that have been devised were considered in a review devoted to that topic published in 2002.[11] More recent methods, and those with demonstrated applications to long-range ^{1}H–^{15}N studies will be considered in the present review. Following a brief survey of new long-range heteronuclear shift correlation experiments available to investigators, applications of these methods reported in the interval from mid-1999 through early 2004 will be reviewed.

2. NEW LONG-RANGE HETERONUCLEAR SHIFT CORRELATION METHODS

Long-range heteronuclear shift correlation experiments developed through 2002 have been reviewed.[11] Since then, the development of new methods has again slowed and there are only a few new reports in the literature to be described in this section of the review. Applications of some of the methods described previously, however, have begun to appear and it will be interesting to see whether one of the newer accordion-optimized methods such as IMPEACH-MBC[12,13] will eventually supplant the well-established GHMBC experiment for long-range ^{1}H–^{15}N applications.

2.1. Non-accordion long-range methods

Methods using fixed duration delays optimized for the presumed long-range heteronuclear coupling, typically GHMBC, continue to be heavily used for long-range ^{1}H–^{15}N heteronuclear chemical shift correlation studies. Congruence between the optimization and the actual coupling is reflected by the response intensity for a given long-range correlation. Using strychnine (**1**) as a model compound, this can be readily illustrated using a series of selective 1D ^{1}H–^{15}N shift correlation experiments in which the fixed duration delay is successively reoptimized from one experiment to the next, as shown in Fig. 1.

One means of circumventing a lack of knowledge of long-range couplings to a nuclide of interest is to sum the results from a series of variously optimized spectra. In a sense, this is what is being done in an accordion-optimized experiment, albeit with each increment of the evolution time optimized for a different long-range coupling within a predetermined range of possible coupling constants. Sørensen and co-workers have used what is essentially a combination of these approaches in a technique they refer to as broadband HMBC.[14] Their work compared conventional HMBC data acquired using a long-range delay, Δ, optimized for 65 ms (nt = 32 scans), with broadband HMBC data acquired as four subspectra with Δ = 440.7, 343.4, 290.3, and 242.2 ms (nt = 8 scans/Δ). A number of responses were seen with enhanced response intensity in the broadband
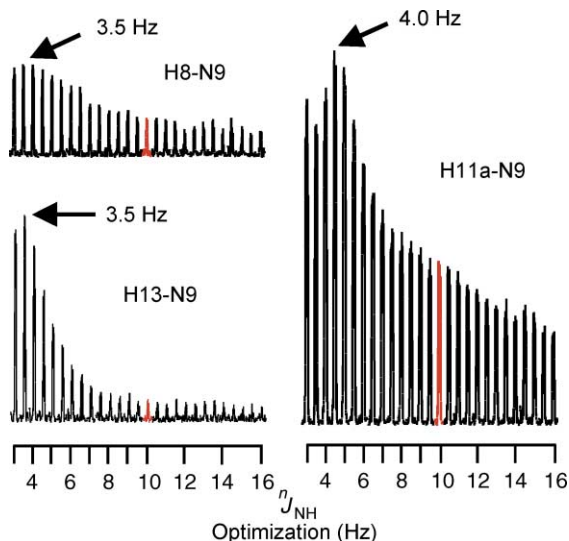
Fig. 1. Horizontal stack plots of a series of successively reoptimized selective 1D ^{1}H–^{15}N shift correlation experiments performed on the N9 amide nitrogen resonance of strychnine (**1**). The optimization of the long-range delay was varied in 0.5 Hz increments from 3 to 16 Hz. When strychnine was originally studied in the author's 1995 report, a 10 Hz optimization of the long-range delay was utilized.[6] As can be readily seen from these comparative plots, the agreement between the delay optimization of 10 Hz (red peaks) and the actual coupling constants was rather poor, leading to minimal response intensity for the H13–N9 long-range correlation that could have been missed if working with a dilute sample.

HMBC data as well as some responses not observed in the conventional HMBC spectrum. Because of the long duration of the Δ intervals in the broadband HMBC experiment reported, in the opinion of this author losses due to spin–spin relaxation during the long delays would be problematic when dealing with either very small samples or in the acquisition of long-range ^1H–^{15}N data where signals are quite weak because of the low abundance and gyromagnetic ratio of ^{15}N.

Another approach is to intentionally select a very small coupling optimization such that integer multiples of that coupling will be in phase and read out at the end of the experiment with maximal intensity. The author (GEM) and a co-worker reported this approach using a 1.75 Hz optimization in the acquisition of proton double quantum coherence of strychnine (**1**) many years ago with some degree of success.[15]
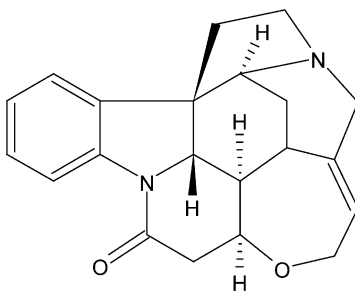
1

In a more recent report, Torres *et al.*[16] described two new long-range *J*-HSQMC pulse sequences that they labeled LR-*J*-HSMQC(80,27) and LR-*J*-HSMQC(27,80) that were developed using the $(3\beta_x)\beta_y$ composite 90° pulse sequence. They demonstrated that these experiments were effective for the observation of long-range couplings $^nJ_{CH} > 3$ Hz, although they report that the overall sensitivity of the experiments were slightly lower than the conventional decoupled HMBC experiment. Interestingly, they reported that the LR-*J*-HSMQC(27,80) experiment was very efficient in yielding two- and four-bond long-range correlations. In addition, using strychnine (**1**) as a model compound, they compared response intensity for all of the observed long-range ^1H–^{13}C correlation responses in a series of long-range experiments that included D-HMBC(80), D-HMBC(60), LR-*J*-HSMQC(80,27), LR-*J*-HSMQC(27,80), ACCORD-HMBC, J-IMPEACH-MBC, AND GSQMBC. Although reports of the application of these experiments to long-range ^1H–^{15}N have not been reported, it will be of interest to see if the utility of the LR-*J*-HSMQC(27,80) in observing ^2J and ^4J correlation responses applies to ^1H–^{15}N correlations.

Sprang and Bigler[17,18] have described non-accordion pulse sequences intended for the acquisition of separate subspectra for ^2J and ^nJ ($n > 2$) subspectra similar to the results obtained from the accordion-optimized CIGAR-HMBC experiment reported in 2000.[19] Their work is interesting in that the pulse sequences described segregate data in two files during the acquisition that can ultimately be processed to yield two subspectra, one containing only ^2J correlations and the other showing all ^nJ, $n > 1$, correlations. As described by the authors, these reports derive from the earlier HMSC experiment, which allowed
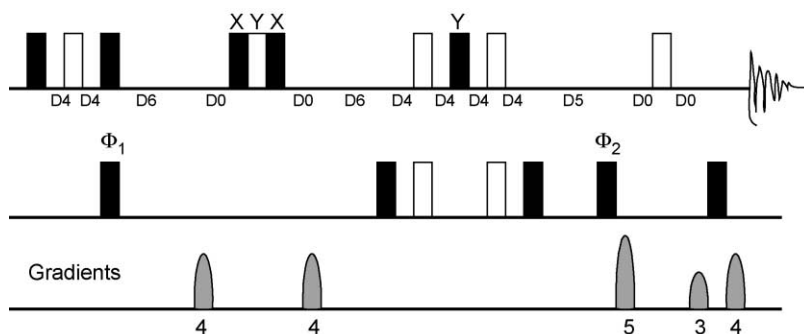
Fig. 2. Pulse sequence for the HMBC-RELAY experiment proposed by Sprang and Bigler to differentiate ^2J from ^nJ ($n=3, 4$) long-range heteronuclear correlations.[18] Pulses are represented as solid (90°) or open (180°) bars. All pulses are x except for the y pulse in the composite pulse and the last 90° proton pulse. A two step phase cycle, x, $-x$ is used for the pulse phases Φ_1, Φ_2, and the receiver phase. Two FIDs are recorded for each increment of the evolution time, t_1 with the phase Φ_1 set as x, $-x$ and $-x$, x, respectively (interleaved detection) with the data stored separately. Delays are set as: D4 $=1/[4^1J_{CH}]$, D6 $=1/[4^3J_{HH}]$, and D5 $=\frac{1}{2}[^nJ_{CH}]$. The evolution delay, D0, must remain equal for both evolution periods. The gradient ratio optimized for ^{1}H–^{13}C is 4, 4, 5, 3, 4. Shaped gradients are shown as described in the work of Sprang and Bigler but there is no reason why square gradients could not be used in this sequence.

the simultaneous measurement of direct and long-range heteronuclear correlations.[20] Being able to calculate a ^2J subspectrum vs. interpreting a data matrix containing skewed and non-skewed correlation responses as in a CIGAR-HMBC spectrum[19] affords a considerable simplification of the data interpretation. Moreover, having a ^2J subspectrum also offers a considerable advantage for restricting the interpretation of long-range correlation responses in Computer-Assisted Structure Elucidation (CASE) programs, thereby potentially shortening the overall elucidation calculation time.

In their discussion, Spang and Bigler highlight several fundamental problems associated with long-range heteronuclear couplings.[18] While they were referring to $^nJ_{CH}$ correlation responses, similar considerations will eventually derive for $^nJ_{NH}$ correlations, which are even less regular or predictable. The pulse sequence for the HMBC-RELAY experiment is shown in Fig. 2. For peptides in particular, $^2J_{NH}$ correlations to the amide nitrogen resonances could be readily identified using the HMBC-RELAY sequence. As there are numerous reports of long-range ^{1}H–^{15}N studies of cyclic peptide natural products appearing in the literature, these would be one viable application of the method. An example is discussed in Section 2.2 of this review for the oxazolidinone antibiotic Zyvox™ (**3**).

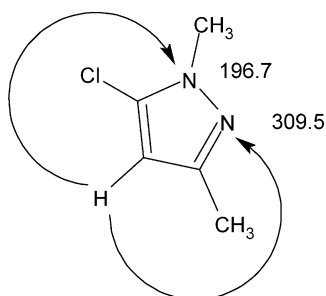## 2.2. Accordion-optimized long-range methods

The available accordion-optimized long-range heteronuclear shift correlation experiments were surveyed in a recent chapter.[11] No novel accordion-optimized methods have been reported, but following the author's initial report on the advantages of using the IMPEACH-MBC[12] sequence for long-range ^{1}H–^{15}N studies,[13] Kline and Cheatham have

initiated what may be the beginning of a systematic investigation of ^{15}N correlations in aliphatic, heteroalicyclic, and heteroaromatic small molecules through the use of a ^{15}N-optimized CIGAR-HMBC experiment.[21]

The ^{15}N-optimized CIGAR-HMBC experiment described by Kline and Cheatham[21] differs from the original CIGAR-HMBC experiment[19] only in that the low pass *J*-filter at the beginning of the pulse sequence and the attendant gradient pulses have been eliminated from the pulse sequence. Typically, even if investigators are using a conventional GHMBC experiment, it is advantageous to optimize the low-pass *J*-filter for a large potential one-bond correlation, e.g., 250–300 Hz (typical $^1J_{NH}$ correlations are normally in the range of 90–100 Hz) to allow the partially attenuated direct response correlation doublets to be observed in the experiment and thereby obviating the necessity of acquiring a separate ^{1}H–^{15}N HSQC spectrum. In the case of molecules where all of the nitrogen chemical shift data sought are associated with protonated ^{15}N resonances it is advantageous, from a sensitivity viewpoint, to acquire these data using a ^{1}H–^{15}N HSQC spectrum rather than any of the long-range optimized ^{1}H–^{15}N experiments.

One of the examples shown by Kline and Cheatham[21] compares the correlations observed in a GNHMBC[22] experiment with those from a ^{15}N-optimized CIGAR-HMBC experiment performed on 5-chloro-1,3-dimethylpyrazole (**2**). When conventional, statically optimized GNHMBC data were acquired, then only a correlation from the H4 resonance to the NMe N1 resonance at 196.7 ppm was observed. In contrast, when a 3–10 Hz optimized ^{15}N CIGAR-HMBC spectrum was recorded, a correlation was also observed to the N2 resonance at 309.5 ppm.

2

The work of Kline and Cheatham[21] just described, highlights one of the attractive features of accordion-optimized long-range methods when long-range ^{1}H–^{15}N heteronuclear shift correlation data are sought. By sampling a range of potential long-range ^{1}H–^{15}N couplings rather than a single or 'static' optimization as in a GHMBC experiment, responses can in some cases be observed which are completely missed in the GHMBC data, or more commonly, responses are observed with considerably greater signal-to-noise, allowing experiment times to be shortened somewhat. The initial comparison of the IMPEACH-MBC and GHMBC experiments (Fig. 3) showed an example of the latter case through a rather dramatic improvement
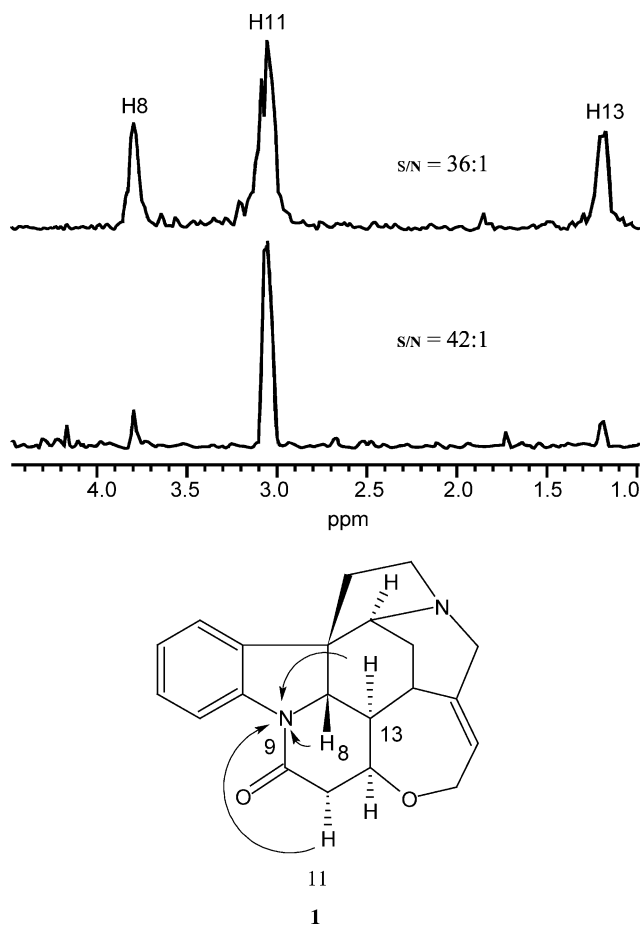
Fig. 3. Comparison traces for the N9 amide resonance of strychnine: (top) trace extracted from a 3–16 Hz optimized IMPEACH-HMBC experiment; (bottom) trace extracted from a conventional 8 Hz optimized GHMBC spectrum. Parameters were adjusted to give equivalent data matrices, the only difference being total acquisition time because of the difference between the statically optimized delay in the case of the GHMBC experiment and the accordion-optimized delay in the IMPEACH-MBC experiment.[12] While the overall *s/n* ratio of the IMPEACH-MBC spectrum is slightly lower than that of the GHMBC data (36:1 vs. 42:1), the response intensities for the H8 and H13 ^2J and ^3J correlations, respectively, are significantly improved in the IMPEACH-MBC data. The response intensity improvement can be attributed to the accordion-optimization range encompassing the actual long-range correlations of the H8–N9 and H13–N9 correlations (∼3.5 Hz).

for two of the long-range ^{1}H–^{15}N correlations of the N9 amide nitrogen of strychnine (**1**), albeit at the expense of the most intense of the three responses.

　　While it is too early to determine which of the available accordion-optimized long-range correlation experiments will provide the best means of observing long-range ^{1}H–^{15}N correlations, it is logical to suggest that these experiments will greatly facilitate

the observation of these correlations. In the longer term, the availability of these methods, particularly when coupled with cryogenic NMR probe technology, can be expected to greatly increase the amount of ^{15}N chemical shift and long-range correlation data being reported in the literature. This trend, in turn, should then facilitate the development of larger ^{15}N chemical shift databases, which can be of considerable value as the foundation data for development of algorithms to allow the prediction of ^{15}N shifts of proposed nitrogen-containing chemical structures before the data are acquired. ^{15}N chemical shift databases and long-range ^{1}H–^{15}N correlation data can also be employed in CASE studies, which have the potential to substantially reduce both the numbers of structures generated and the time required for a program to establish a structure.[23–28]

To date, the only application of one of the available experiments to differentiate between ^2J and ^nJ ($n=3,4$) correlation responses to long-range ^{1}H–^{15}N of which the authors are aware is in work from this laboratory.[29] Comparison contour plots showing the N7 amide correlations for the oxazolidinone antibiotic Zyvox™ (**3**) are shown in Fig. 4. In the ^2J, ^3J-HMBC data shown in the top panel, the correlation responses from the H6 methine and H9 methyl groups (both $^3J_{NH}$ correlation responses) are identical to those in the conventional GHMBC spectrum shown in the bottom panel of Fig. 4. In contrast, the $^2J_{NH}$ correlation response correlating the H6 methylene resonance to the N7 amide, shows the pronounced skew characteristic of a ^2J response in a ^2J, ^3J-HMBC experiment under favorable circumstances. The degree to which a given two-bond correlation response will be skewed is a function of the individual proton–proton couplings in question and the parameter choices made when the data are acquired. There have been no reported applications of either the $^2J/^nJ$ and HMBC-RELAY experiments described by Sprang and Bigler[17,18] for long-range ^{1}H–^{15}N experiments. In the opinion of the authors, the difference spectrum data from $^2J/^nJ$ and HMBC-RELAY experiments should be considerably easier to interpret since the $^2J_{NH}$ correlation responses would be contained in a difference plot.

2.3. 1D ^{1}H–^{15}N methods for the measurement of $^nJ_{NH}$ couplings at natural abundance

Parella and Bellow[30] have described both non-selective and selective versions of several proton-detected 1D NMR experiments that can be applied to ^{15}N. Using these methods, the authors reported the successful determination of both one-bond and long-range ^{1}H–^{15}N coupling constants using a model tripeptide at natural abundance. Their work was based, in part, on the 1D HSQC-TOCSY experiment. In general, the authors have utilized the Preservation of Enhanced Pathways (PEP) approach in the development of the sequences that they have described. The HSQC-TOCSY based experiments, of course, mandate a protonated ^{15}N resonance. The authors have, however, also proposed a ^{1}H–^{15}N HSQMBC experiment in which the heteronuclear coupling constants of both protonated and non-protonated ^{15}N resonances can be measured.
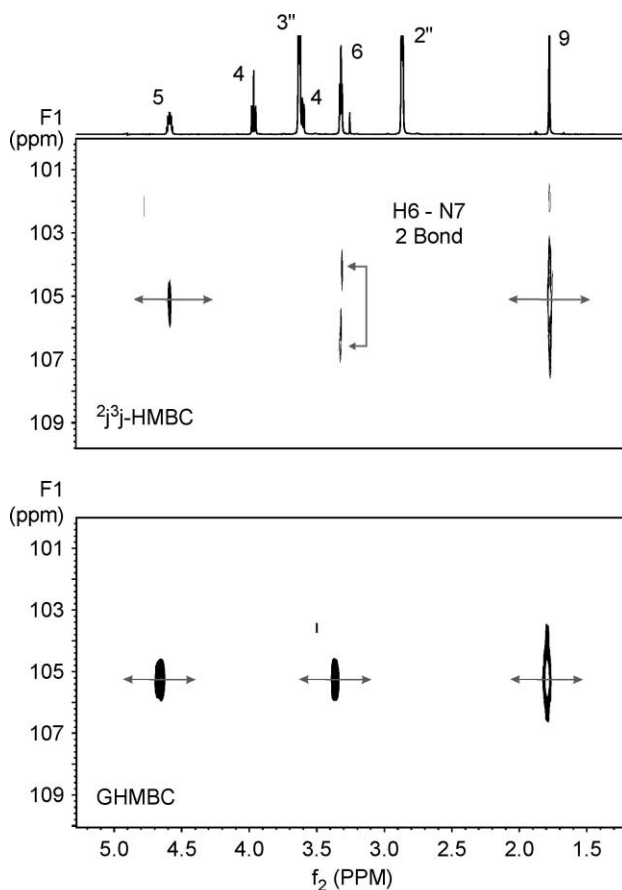
Fig. 4. Any of the long-range experiments designed to differentiate between ^2J and ^nJ ($n = 3, 4$), although developed for ^{1}H–^{13}C heteronuclear shift correlation applications, can also be applied to ^{1}H–^{15}N correlation. Experiments now available include CIGAR-HMBC[19], the earliest inverse-detected variant, and the $^2J/^nJ$[17] and HMBC-RELAY[18] experiments described by Sprang and Bigler. To date, only the CIGAR-HMBC experiment has been applied to ^{1}H–^{15}N heteronuclear shift correlation as shown above compared with conventional GHMBC data for the oxazolidinone antibiotic Zyvox™ (**3**).[29] It must be recalled that these experiments differentiate long-range heteronuclear couplings ^2J vs. ^nJ on the basis of homonuclear proton–proton couplings and require a protonated heteroatom if they are to work. In the case of Zyvox, only N7 is amenable to coupling constant differentiation, the H6–N7 correlation showing the skewed multiplet structure characteristic of a $^2J_{\text{NH}}$ correlation responsed in a ^{1}H–^{15}N CIGAR-HMBC experiment.

3. NMR PROBE TECHNOLOGY DEVELOPMENTS

3.1. Small volume conventional NMR probes

NMR probe technology was unvaried from one year to the next for many years. Investigators routinely used 5 mm NMR probes unless they had solubility problems, in which case, larger probes, ranging up to 22 mm commercially, were available. In the early 1990s, in an effort to obtain higher sensitivity, the first reports describing the development of 3 mm or 'micro' NMR probe technology appeared.[31,32] Pursuit of still greater facility for dealing with small samples led to the development of 1.7 mm submicro or SMIDG™ NMR probes in 1999[33,34] and still more recently by the development of a 1-mm probe.[35,36] Advances and applications of these probe technologies to the characterization of small samples, including long-range ^{1}H–^{15}N applications, have recently been reviewed.[37]

3.2. Cryogenic NMR probes

Cryogenically cooled NMR probes are not a new idea. It has been known for a considerable period of time that by cooling the probe of coils and associated electronics that considerable gains in sensitivity can be realized.[38–41] Work in this area through 2002 has been reviewed[42] and new applications are appearing with growing frequency as investigator access to instruments equipped with cryogenic NMR probe technology continues to improve. Examples of data acquired on instruments equipped with cryogenic NMR probes have been shown at ^{1}H observation frequencies ranging from 500 to 900 MHz. Because of the cost of this type of technology and the annual operating expenses, it is unlikely that this technology will migrate to lower field instruments in the near future.

Based on experience in one of the author's laboratories (GEM), cryogenic NMR probe technology may have the single biggest positive impact on increasing the facility with which long-range ^{1}H–^{15}N heteronuclear chemical shift correlation data may be acquired. To illustrate this point, a comparison of the results obtained with a conventional 3 mm gradient inverse triple resonance and 5 mm cryogenic gradient inverse probe technology for the acquisition of long-range ^{1}H–^{15}N data was performed. Using a 2 mg sample of the oxazolidinone antibiotic Eperezolid™ (**4**) dissolved in 150 μl d_3-acetonitrile, 5–10 Hz optimized ^{1}H–^{15}N CIGAR-HMBC[19] spectra were acquired using both probe technologies.[43] Comparison plots are shown in Fig. 5. In a conventional (warm) 500 MHz 3 mm gradient inverse triple resonance probe, good quality data were recorded in 4 h and showed correlations to all of the nitrogen resonances sufficient to assemble a structure if this had been an unknown. Projecting through the F_1 frequency domain, a signal-to-noise (s/n) ratio of 49:1 was obtained. These data are shown in Panels A and C of Fig. 5. The experiment was then repeated using the same sealed sample run coaxially in a 5 mm gradient inverse triple resonance cryogenic NMR probe, again at 500 MHz. The data acquisition was stopped after 26 min based on processing the interleaved data during acquisition. The 26 min 500 MHz 5 mm cryoprobe data are shown in Fig. 5, Panel B.
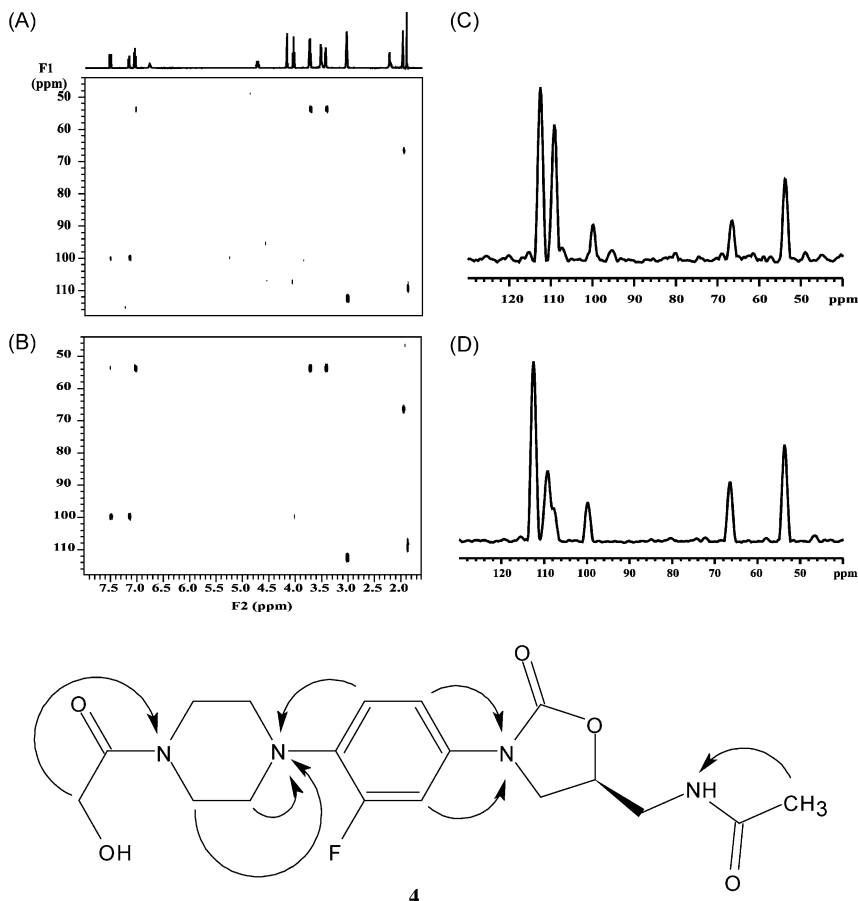
Fig. 5. Comparison of conventional 3 and 5 mm cryogenic gradient inverse triple resonance probe performance for long-range ^{1}H–^{15}N data acquisition using a 2 mg sample of the oxazolidinone antibiotic Eperezolid™ (**4**) dissolved in 150 μl of d_3-acetonitrile in a 3 mm NMR tube. (Panel A) ^{1}H–^{15}N CIGAR-HMBC[19] spectrum of **4**, optimized for 5–10 Hz, recorded at 500 MHz using a 3 mm gradient inverse triple resonance probe. The data were acquired in 4 h and afforded a signal-to-noise ratio on projection through the F_1 frequency domain of 49:1. (Panel B) Conventional ^{1}H–^{15}N GHMBC spectrum of **4** recorded at 500 MHz using a 5 mm gradient inverse triple resonance cryogenic NMR probe with the rf coil of the probe set to 25 K. The data acquisition time was 26 min and on projection through the F_1 frequency domain, gave a signal-to-noise ratio of 101:1. (Panel C) F_1 projection of the ^{1}H–^{15}N GHMBC spectrum shown in Panel A. (Panel D) F_1 projection of the ^{1}H–^{15}N GHMBC spectrum shown in Panel B.

When these data were projected through the F_1 frequency domain, despite the short acquisition time of 26 min, a *s/n* ratio of 101:1 was obtained, highlighting the considerable advantage of acquiring long-range ^{1}H–^{15}N heteronuclear shift correlation data using cryogenic NMR probe technology.

As more laboratories gain access to cryogenic NMR probe technology, the volume of and rate at which ^{15}N chemical shift data and information about long-range coupling

pathways appear in the literature should increase considerably. As these data continue to be reported, it is reasonable to expect that the use of ^{15}N as a chemical structure probe for unknowns, e.g., pharmaceuticals, $80+\%$ of which contain nitrogen, natural products, etc., will correspondingly increase. Another potential benefit of this trend, which is already beginning to be seen, will be the impact of being able to use ^{15}N chemical shift and long-range coupling pathway information in both NMR prediction, content databases and CASE software packages. Advanced Chemistry Development (ACD/Labs) of Toronto has a commercial ^{15}N NMR database that currently has ^{15}N shift data for >8300 compounds through early 2004, with >250 compounds added from the 2004 literature as of this writing. While this is a relatively small number of compounds relative to other available commercial heteronuclear content databases (ACD/Labs' v8.0 ^{13}C NMR database contains ^{13}C NMR shifts for $>165,000$ compounds), the size of the ^{15}N NMR database can, nevertheless, be expected to grow considerably as the rate at which ^{15}N shift data are reported correspondingly increases. The implications of this trend in the growth of ^{15}N NMR databases and their impact on CASE methods is considered in Section 4 of this chapter.

4. COMPUTER-ASSISTED STRUCTURE ELUCIDATION USING ^{15}N CHEMICAL SHIFT AND ^{1}H–^{15}N LONG-RANGE CORRELATION INFORMATION

Chemical structure characterization has undergone profound change with the advent of 2D-NMR spectroscopy. Homo- and heteronuclear shift direct correlation experiments make it possible to assemble chemical substructural fragments that can then be linked to one another via intervening quaternary carbons or through various heteroatoms (N, O, S, P, etc.) using a variety of long-range heteronuclear shift correlation experiments. In the case of the former, quaternary carbons can be linked via $^{n}J_{CH}$ ($n=2$–4, typically) long-range coupling pathways to protons or protonated carbons to assemble the substructural fragments into a complete chemical structure. However, as molecules become larger and progressively more complex, the number of permutations of how the various substructural fragments may be linked to intervening atoms increases in number quickly and assembling a structure can become a daunting task even for skilled spectroscopists.

CASE programs of varying degrees of sophistication have been developed that utilize NMR chemical shift and connectivity pathway information in concert to assemble all possible chemical structures from the substructural fragments, available quaternary carbons, and heteroatoms. These structures can then be sorted and rank ordered on the basis of many different criteria to reduce the number of possible structures that the spectroscopist has to consider to a manageable size. CASE programs capable of utilizing 2D NMR spectral data include Structure Elucidator,[27,28,44–47] SESAMI,[48,49] CHE-MICS,[50] CISOC-SES,[51–54] LSD,[55,56] LUCY,[57] and COCON.[58,59] The work extant in the literature in 1999 was reviewed by Jaspers.[60] Of the programs now available, those which have been used in conjunction with long-range ^{1}H–^{15}N NMR data include a report of Nuzillard and co-workers,[56] the work of Köck,[59] and the authors' research.[25,26,44,61]

CASE programs, in the simplest examples, can search 1D ^{1}H and ^{13}C NMR databases for spectra that match an unknown. At a more sophisticated level, 2D NMR homo- and heteronuclear direct connectivity data are utilized by the program to first assemble structural fragments. These fragments can then be assembled into a structure on the basis of long-range heteronuclear correlation data from an HMBC or similar experiment. In most cases, heteronuclear data are confined to direct and long-range ^{1}H–^{13}C shift correlation data. For some examples, however, these heteronuclear data are insufficient to establish the structure of an unknown and it becomes necessary to resort to ^{1}H–^{15}N shift correlation data. In many cases simply the use of connectivity information still fails to provide a solution to the problem and computer-based structure generation using a molecular formula as the defining input is utilized in order to create a set of output structures for consideration. Some examples are given below.

4.1. ^{15}N chemical shift prediction

4.1.1. Structure verification using a ^{15}N content database

For the chemist attempting to elucidate a chemical structure the ^{15}N chemical shift can offer direct information regarding the nitrogen environment. For the purpose of structure verification the common approach is to review the literature for related species and use their chemical shifts and couplings as models to allow estimates of these properties for the new species. While there are a number of texts, reviews, and publications available that have brought together the spectral properties of tens to hundreds of molecules these paper-based collections are cumbersome to use when it comes to searching for a particular chemical shift or a chemical structure or substructure. With both time and quality of the essence for such searches of data, the most obvious approach is to compile an appropriate collection of data into an electronic database and enable the appropriate types of searches.

When a content database of chemical structures and associated spectral parameters is made available, this can greatly speed up the process of identifying the nature of the compound. Electronic content databases are available from a number of sources. The largest and most up to date source of ^{15}N data is that supplied by ACD/Labs. The content database is delivered with their ACD/NNMR Predictor program.[62] It can be searched by chemical shift or range of chemical shifts as well as coupling constant. Add to this the ability to search through the databases by formula and mass (nominal, average, or exact) and an NMR spectroscopist has immediate access to a warehouse of valuable information.

The ACD/NNMR version 8 content database contains >8300 chemical structures ($>21,000$ ^{15}N chemical shifts). These data have been culled from the literature and checked for quality according to a number of stringent criteria prior to adding to the database. The chemical shift reference is homogenized during the process such that all shifts are relative to one reference. A record includes the chemical structure, the original literature reference, the ^{15}N chemical shift(s) and, where available, associated hetero-nuclear coupling constants. These data can be searched by structure, substructure,

similarity of structure, chemical shift and chemical shift range, coupling constant and coupling constant range, formula, and many other optional data fields.

The database is updated on an annual basis with new data extracted from the literature. This database is also the foundation of data supporting the prediction algorithms that are required to predict NMR spectral properties for chemical structures not contained within the database.

4.1.2. ^{15}N NMR prediction

The value of NMR prediction should be obvious as it brings the possibility of structure verification based on chemical shifts as well as offering the opportunity of using prediction to optimize experimental acquisition parameters and sweep widths for the acquisition of 2D spectra. ACD/Labs uses proprietary algorithms based on a modified form of HOSE-code technology[63] that allows NMR predictions, which has been applied to ^{15}N NMR prediction. In order to perform a prediction the user simply sketches the chemical structure of interest using a structure editor. The calculation of the chemical shifts and coupling constants is performed in a matter of seconds. A resulting table of chemical shifts displays the number of the atom in the structure that gives rise to the predicted shift; the value of the predicted shift; and the uncertainty of the predicted shift, based on 95% confidence limits for the structure fragment. The table also includes predicted coupling constants between pair of atoms.

It is possible to determine how the chemical shifts were predicted, and the type of structural fragments used to derive the parameters though a *Calculation Protocol* window which shows a series of points, each representing an individual chemical structure and associated chemical shift that was used to influence the chemical shift prediction. If the prediction was performed on a compound not in the database, then a variety of different structures is shown in the *Calculation Protocol* and displayed as a histogram plot containing structures which are only fragmentally similar to the input structure. The general applicability and success of ^{15}N NMR prediction will be examined in further detail below.

4.1.3. *Enhancing NMR prediction with user 'trained' databases*

Since chemical structure diversity continues to shift and new compounds are synthesized and characterized almost daily, it is a significant effort to ensure that the content of the database and the associated improvement in prediction accuracy is maintained. ACD/Labs culls data on an ongoing basis with sources including the published literature, academic laboratories, or from commercial projects where the compounds are now of non-commercial interest or have been protected by patenting. The value of proprietary data generated in-house is limited if these data cannot be collected and incorporated into a database for the reasons cited above. The idea of allowing these data to be searched together with the internal content database, as well as allowing them to contribute to the NMR predictions is possible by creating a *user database* of structures, associated shifts and other data. User databases can be built to contain 100s to 1000s of chemical structures that can then serve to enhance chemical shift prediction for a given laboratory and to provide a legacy resource for any organization.

4.1.4. *Validating ^{15}N NMR prediction*

The validation of ^{15}N NMR prediction is best performed by comparing the predicted shifts for compounds not in the database with the experimental shifts available in the literature or measured directly. ACD/Labs recently reported[64] a statistical analysis of their ^{15}N NMR prediction. Using a classical leave-one-out (LOO) approach they predicted the ^{15}N shifts for >8300 individual chemical structures contained within the ACD/NNMR v8.08 NNMR program database. The resulting analysis gave a correlation coefficient of $R^2=0.97$ over 21,244 points. The distribution in deviations between the experimental values and the predicted values using this LOO approach is shown in Fig. 6.

   Selecting 24 random compounds (none from tables of related structures) from different sections of the present review that are not in the ACD/NNMR v8.08 database, we calculated the ^{15}N shifts for the 71 nitrogen resonances contained in these structures. Plotting calculated vs. observed ^{15}N shifts for the 24 compounds used, we obtained the results shown in Fig. 7. Regression analysis of these data gave $R^2=0.97$, with a standard error of 14.8 ppm. Based on the structural diversity of the 24 compounds used in this analysis, a standard error of $<\pm15$ ppm is quite reasonable, and affords a basis for setting F_1 windows to acquire long-range ^{1}H–^{15}N data if one were dealing with an unknown molecule. This is discussed further below.

   Comparing human intuition relative to an electronic system provides another direct example of validation. In this case one of the authors (GEM) compared his intuitive estimates of the chemical shifts for model compound, **5**,[64,65] vs. those available from the NNMR v8.08 prediction program. The values are compared in Table 1.
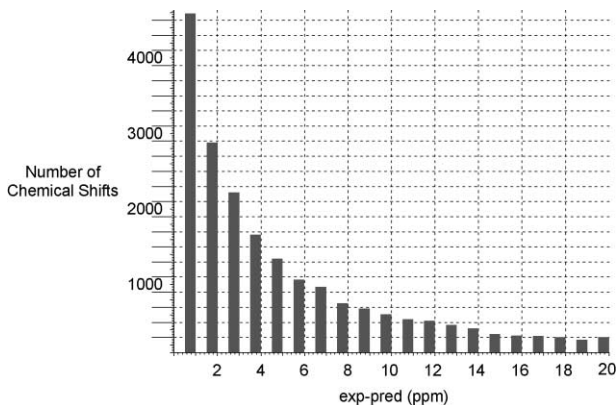
Fig. 6.   LOO (Leave-One-Out) analysis of the ^{15}N NMR database contained in ACD/Labs NNMR chemical shift and coupling constant prediction package. The calculation was performed by removing one ^{15}N shift and then calculating the ^{15}N shift in question using the remaining structures and data contained in the database. The resulting analysis gave a correlation coefficient of $R^2=0.97$ over 21,244 points. The presentation shows a plot of a number of chemical shifts vs. the difference between the experimental and predicted chemical shift values. Approximately 250 shifts out of $>21,000$ have a deviation of >20 ppm.
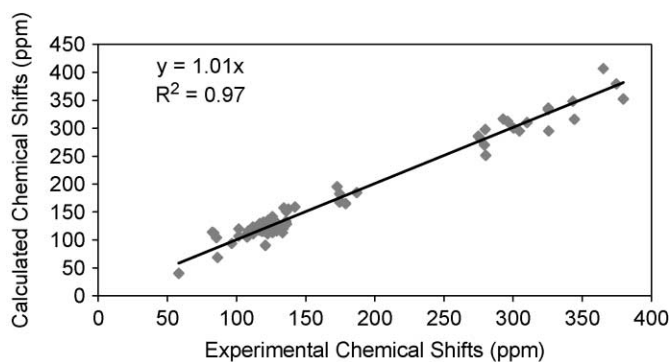
Fig. 7. Plot of observed vs. calculated ^{15}N chemical shifts for 24 compounds from this review (71 ^{15}N shifts). None of the 24 compounds selected were contained in the NNMR v8.08 database. When regression analysis was performed on these data the following results were obtained: $R^2 = 0.97$, standard error 14.8 ppm.
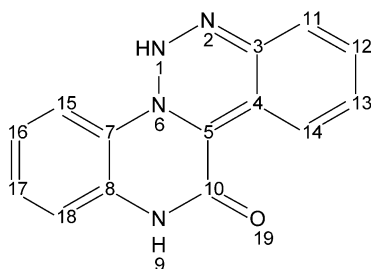
5

There are clearly disparities between the predicted values from both the scientist and the computer program; the largest differences are between the human-generated values with a difference of ~ 50 ppm for N2. Based on experience to date, and with the inherent limitations imposed by the present size of the nitrogen dataset used as a basis

Table 1. Comparison of author-estimated, v8.08 NNMR-predicted, and measured ^{15}N chemical shifts for a compound arbitrarily selected from the published literature[65]

Position	Author estimated ^{15}N shift	v8.0 NNMR predicted ^{15}N shift	Measured ^{15}N chemical shift
N1	130	167.3	177.8
N2	250	325.9	301.7
N6	125–140	148.6	126.9
N9	110	144.9	119.7

of the ^{15}N predictions, a guideline of setting the F_1 window to be $\sim \pm 40$ ppm around the extremes of the predicted ^{15}N shift data is appropriate. As shown by the data in Fig. 6, this should provide in excess of ± 2 standard deviations, which should be more than ample.

While the ^{15}N NMR database is still small relative to those available for other nuclei, and despite potential weaknesses in the ^{15}N shift prediction algorithms, variability of ^{15}N shifts as a function of solvent, temperature and pH, ^{15}N shift calculations nevertheless provide a useful means of double checking intuitive estimates of ^{15}N chemical shift behavior for even experienced spectroscopists and a vital starting point for less experienced investigators. With time the ACD/NNMR database will continue to grow as new data, are culled from the literature on an ongoing basis and new releases are issued annually. With a larger database and expansion of the associated structural diversity the predictions will likely improve as additional development of the algorithms will be feasible. Predicted long-range $^nJ_{NH}$ coupling constants from the NNMR prediction algorithm also provide a basis for long-range delay optimization when running long-range ^{1}H–^{15}N heteronuclear shift correlation experiments. Given the large variability of long-range $^nJ_{NH}$ coupling constants, using a 'favorite' optimization for the long-range delay, which is quite common among investigators acquiring long-range ^{1}H–^{13}C heteronuclear shift correlation data, is a less viable alternative for ^{1}H–^{15}N data than for ^{1}H–^{13}C experiments and has led to numerous reports in the literature where multiple optimizations of long-range ^{1}H–^{15}N heteronuclear shift correlation experiments are reported, and a number of those studies are cited in this review. It is also worth noting, that the range of predicted $^nJ_{NH}$ couplings from NNMR also provides a useful basis on which to set coupling constant ranges for accordion-optimized long-range experiments used for ^{1}H–^{15}N, e.g., IMPEACH-MBC[12,13] or ^{15}N-optimized CIGAR-HMBC.[21]

4.2. Application of ACD/Structure Elucidator to Known Alkaloid Structures

ACD/Structure Elucidator has matured over the past 6 years to become the most capable commercial CASE system available today. The expert system has been described in detail in previous works.[44] The first generation system was developed for the elucidation of molecular structures of intermediate-sized organic molecules with 20–25 skeletal atoms using simple 1D ^{13}C NMR spectra. The second publication[44] reported on developments allowing the elucidation of structures of large molecules, typical of those found in the world of natural products, and utilizing mainly 2D NMR data as the source datasets. The application and success of the system as a powerful and versatile tool for the structure elucidation of complex chemical structures has been demonstrated in numerous works and will not be discussed in more detail in this review.[25,26,28,45,46,66,67]

4.2.1. Determination of the structure of quindolinone (6) using structure elucidator

The simple indoloquinoline alkaloid quindoline (6), which contains two protonated NH resonances, readily afforded ^{1}H–^{13}C and ^{1}H–^{15}N direct heteronuclear shift correlation

data despite being available as only a 0.8 mg sample.[68] An NMR data ensemble consisting of 1D ^{1}H and ^{13}C chemical shift data, ^{15}N chemical shifts from a ^{1}H–^{15}N HMQC experiment, and ^{1}H–^{13}C HMQC and HMBC data were used as the input for ACD/Labs Structure Elucidator v7.0. In 42 min of computer time, the program output 296 structures that were sorted on the basis of the match between predicted ^{13}C shifts for each structure and the observed ^{13}C shift data. On this basis, the structure of quindoline, **6**, was first in the output list with a deviation $d = 3.36$ ppm. The next structure in the output list had a deviation of $d = 5.26$ ppm. Applications of the Structure Elucidator program to hundreds of examples have shown that only in rare cases does the actual structure have $d > 5$ ppm.
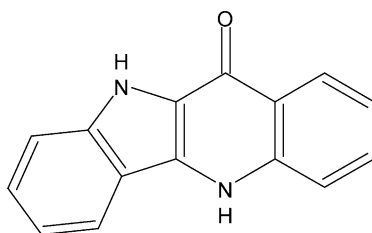

6

When the ^{1}H–^{15}N HMQC data were removed from the data input for Structure Elucidator v7.0, the program failed to give a result in 24 h, underscoring the criticality of ^{1}H–^{15}N data, even for some relatively simple molecules.

### 4.2.2. Attempted determination of the structure of cryptomisrine (**7**) using structure elucidator

Another member of the family of *Cryptolepus* indoloquinoline alkaloids is the dimeric structure cryptomisrine (**7**).[69] Data used as input for Structure Elucidator v7.0 included ^{1}H and ^{13}C shifts from 1D spectra, ^{1}H–^{1}H COSY, ^{1}H–^{13}C HMQC and HMBC, and ^{1}H–^{15}N HMQC correlation data. When the program was started, a total of five structures were generated within 1 min.[61] Sorting the structures on the basis of accurate ^{13}C shift calculation, the structure of cryptomisrine was rank ordered to first position with a deviation of $d = 5.45$, which is higher than normal for the correct structure. The next nearest match had a deviation of $d = 8.25$ ppm. When the ^{1}H–^{15}N HMQC data were removed from the data input, the program ran for 210 h, generating > 75 million structures without generating the correct structure. Of these 75 million structures, $> 22{,}000$ structures were stored after filtering, again underscoring the importance of ^{1}H–^{15}N heteronuclear shift correlation data in computer-assisted structure elucidation.
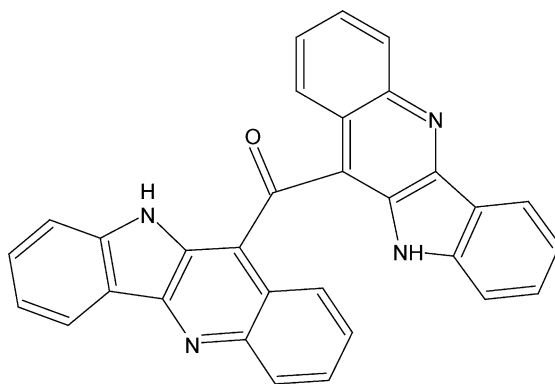
7

4.2.3. *Determination of the structure of cryptospirolepine (**8**) using structure elucidator with and without ^{1}H–^{15}N direct and long-range heteronuclear shift correlation data*

As a final example of the importance of ^{1}H–^{15}N direct and long-range heteronuclear shift correlation data on the elaboration of a complex alkaloid structure using CASE methods, we will consider the application of the Structure Elucidator v7.0 program package to the establishment of the structure of the complex spiro nonacyclic alkaloid cryptospirolepine (**8**).[70–72] In an initial attempt to solve the structure using Structure Elucidator, a data set for **8** consisting of ^{1}H, ^{13}C, and ^{15}N chemical shifts, ^{1}H–^{1}H COSY, ^{1}H–^{13}C HMQC and HMBC data, with three of the long-range C–H correlations marked as $^4J_{CH}$ correlations, and ^{1}H–^{15}N HMQC and HMBC data, the latter containing eight correlation responses, three of which were manually labeled as $^4J_{NH}$ was employed. Using these data, the program was unable to solve the structure directly. When a user fragment database was constructed using the other indoloquinoline alkaloids reported in the literature, the following results were obtained. Without providing any of the ^{1}H–^{15}N data to the program, 4384 structures were generated; 99 structures after filtering; and the correct structure of **8** was in the first position of the list sorted on the basis of predicted vs. observed ^{13}C shift data. With all of the ^{1}H–^{15}N data provided but none of the long-range correlations manually labeled as $^4J_{NH}$ correlations, a total of 792 structures were generated with only one structure remaining after the list was ordered and filtered. When all data were used and the $^4J_{NH}$ correlations manually labeled, the total number of structures generated was reduced to 368 structures with again only one structure after filtering. Once again, these results clearly underscore the importance of ^{1}H–^{15}N heteronuclear shift correlation data in computer-assisted structure elucidation efforts.[44,59,61]

8
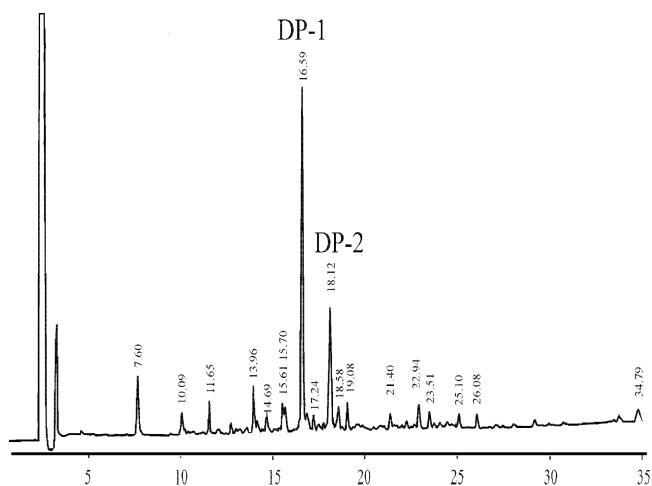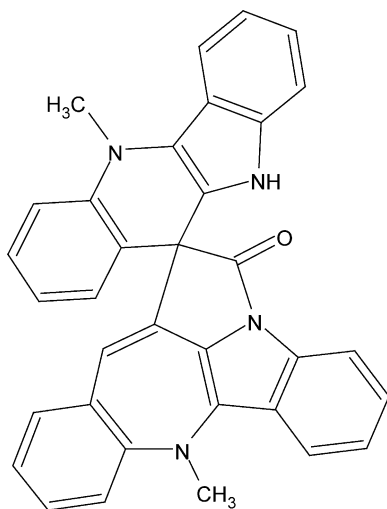
Fig. 8. HPLC trace of the d_6-DMSO solution of a 2.5 mg sample of cryptospirolepine (**7**) stored for 10 years. None of the starting alkaloid remains in the sample (LC/MS data). The two largest degradant species, DP-1 and DP-2 (35 and 16%, respectively) have been identified. The former, DP-1, was quickly identified by both spectroscopist data interpretation and by the Structure Elucidator v7.0 CASE program as cryptolepinone. The structure of the latter, DP-2, ultimately identified as cryptoquindoline (**8**), was determined in parallel, both by a competent spectroscopist with extensive experience with this class of alkaloid structures and using Structure Elucidator v7.0.

4.3. Using CASE methods in parallel to spectroscopist interpretation

Following long-term storage of a sample of 2.5 mg of cryptospirolepine (**8**) in d_6-DMSO in a sealed NMR tube, the sample was examined chromatographically and found to be a highly complex mixture of degradation products as shown in Fig. 8.[25] The larger of the two major degradants, DP-1 (35%) was readily identified as cryptolepinone, which can be envisioned to form via some form of oxidation at the spiro center of cryptospirolepine (**8**) giving the 11-one required in the structure. The next largest degradant peak, DP-2 (16%) was a more challenging structural problem. The molecule gave a molecular ion, MH$^+$ = 479 and HRMS data consistent with a molecular formula of $C_{34}H_{24}N_4O$. MS/MS fragment ions were observed at 464, 447, 435, 432, 247, 232, and 217 Da; the 232 daughter ion corresponds to a cryptolepine fragment minus a proton, suggesting that an 11-cryptolepinyl moiety, **9**, is a substructural component of the degradant structure.
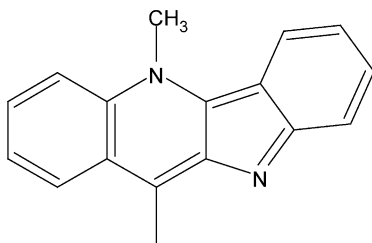

9

Cursory examination of the NMR sample, when dissolved in DMSO, allowed the deduction that an 11-cryptolepinyl moiety was contained in the structure based on the intense purple color, which is characteristic of the extended conjugation of cryptolepine.[25] Because of the relatively small size of the sample, ~100 μg, all of the NMR spectral data were recorded using a sealed sample of the degradant isolate in 150 μl of d_6-DMSO in a sealed 3 mm NMR tube using a 5 mm 500 MHz gradient inverse-detection triple resonance cryogenic NMR probe.

COSY, ROESY, ^{1}H–^{13}C HSQC and HMBC data allowed the assembly of a relatively large substructural component derived from the pentacyclic portion of the cryptospirolepine (**8**) structure as shown by **10**, the derived fragment denoted by bolded bonds. When all of the long-range ^{1}H–^{13}C correlations were factored in, the structural fragment shown by **10** allowed the incorporation of a carbonyl, as shown by **11**. From **11**, valence considerations, given that all of the atoms from the HRMS established empirical formula had been incorporated, allowed the deduction of a quindolinone fragment, **12**, which was also consistent with the MS fragmentation data. Given the quindolinonyl and 11-cryptolepinyl fragments, **12** and **9**, respectively, the final assembly of the structure of cryptoquindolinone (**13**) is completely straightforward.
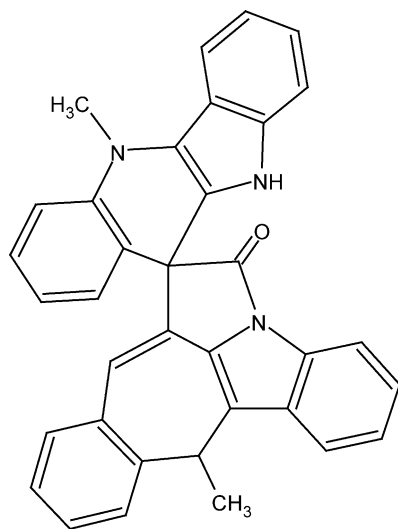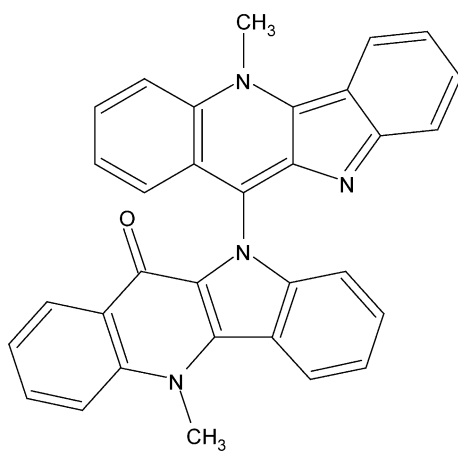
10
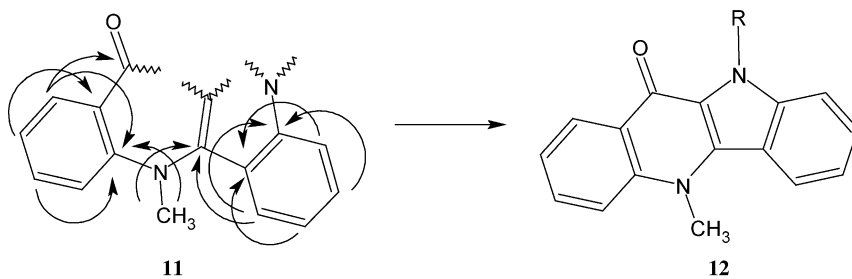
11

12

13

From the start of data interpretation to the completion of the structure elucidation, including the 'quantum leap' provided by the recognition that the structure contained an 11-cryptolepinyl moiety based on the observed color and then confirmed by the data assignment, a highly competent spectroscopist required 72 h to assemble the structure. Using the same data, including the ^{1}H–^{15}N CIGAR-HMBC data, which afforded correlations to three of the four annular nitrogens in the structure, Structure Elucidator v7.0 consumed $\sim$8 h of computer time, generating $\sim$3300 structures in the process. After filtering, the output reduced to 355 structures, which after sorting, left the cryptoquindoline structure in the second position, with a deviation, $d = 3.947$. The eight structures with the lowest deviation are shown in Fig. 9. The structure with the lowest deviation incorporates the 11-cryptolepinyl moiety and, instead of a quindolinoyl moiety that can be derived directly from the cryptospirolepine (**9**) skeletal framework, a cryptotackieinoyl moiety with both nitrogens on the same side of the indoloquinoline nucleus. While cryptotackieine, an indolo[2,3-*b*]-quinoline system, is known, there is no rational way to rearrange the indolobenzazepine-derived portion of the molecule to give anything other than the indolo[3,2-*b*]quinoline fragment represented by the quindolinoyl portion of the molecule. It should be noted that since the initial work regarding the application of Structure Elucidator to the elucidation of the structure of cryptoquindoline (**8**) was published[25] continued development has resulted in significant improvements in the ability of the Structure Elucidator program to resolve
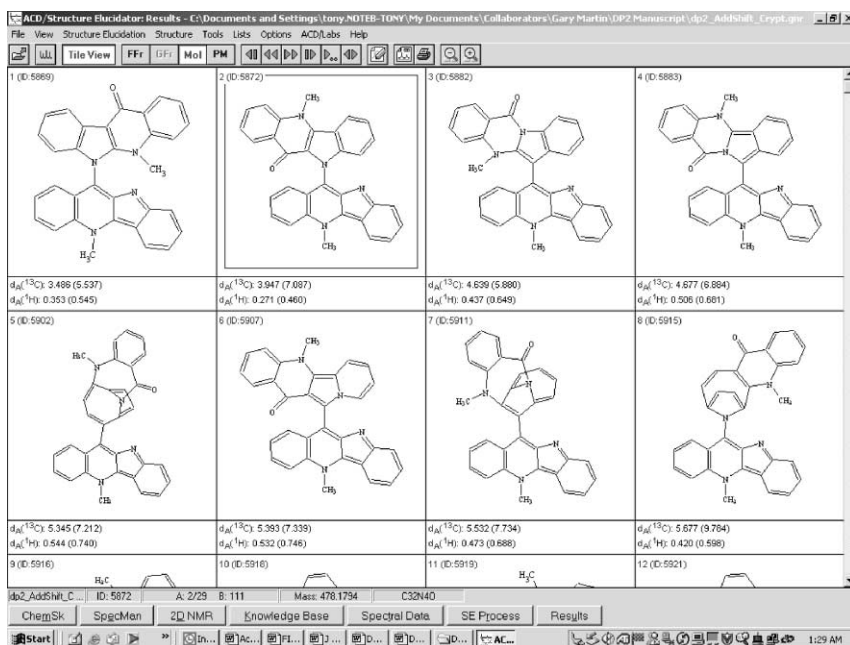
Fig. 9.   Structure Elucidator v7.0 output showing the structure of DP-2, cryptoquindolinone (**12**) in the second position of the sorted output table. Accurate ^{13}C chemical shift calculations ($d_A(^{13}$C)) were performed on the sorted list after which the structures were rank ordered on the basis of the deviation between the accurately calculated shift data and the observed ^{13}C data. It is on this basis that the structure of cryptoquindolinone was in the second position in the table.

ambiguities in data sets. In v8.0 of the program, the cryptoquindoline structure can now be solved without the input of any substructural fragments.

In comparing the time required to arrive at the final structure for both a highly trained spectroscopist and v7.0 of the Structure Elucidator program package, the program generated output containing the final structure considerably more quickly than the spectroscopist was able to arrive at the final structure. To keep this in perspective, however, a trained spectroscopist still has to examine the output of Structure Elucidator to determine which of the rank ordered structures is *most* consistent with the array of spectral information recorded for the molecule. Realistically, it is best to consider the relationship between a highly competent spectroscopist and a program package such as ACD/Labs' Structure Elucidator[62] as a symbiotic working relationship where each contributes to the structure elucidation process.[27] Structure Elucidator, for example, can never make the 'quantum leap' of recognition to suggest an 11-cryptolepinyl moiety in the structure that was possible for the spectroscopist based on a visual clue. Conversely, the spectroscopist can become hopelessly mired during the interpretation process on the basis of preformed suppositions or intuition, which the objectivity of the CASE program packages never suffer from.

5. LONG-RANGE CORRELATION STUDIES INVOLVING ^{15}N

The development of the HMBC experiment by Bax and Summers[73] has opened a wide range of investigation for many heteronuclei. In general terms a sensitive nuclide such as ^{1}H most commonly, or others such as ^{19}F or ^{31}P, is used to detect a less sensitive nuclide such as ^{13}C or ^{15}N to which the sensitive nuclide is long-range coupled. The reader interested in applications involving nuclides other than ^{15}N is referred to the recent chapter by Gudat.[74]

5.1. Long-range ^{15}N correlation studies of alkaloids and natural products

There are a myriad of different types of natural products reported in the literature, many classes of these natural products containing nitrogen. One of the most structurally diverse categories of natural products are the alkaloids, both terrestrial and marine, discussed in the following segments of this section. All the reports within a given section of the review are considered chronologically for the period late 1999 through early 2004 before moving on to the next section of the review. It should also be noted that ^{15}N shifts reported in this chapter are downfield relative to liquid ammonia, which is taken as 379.5 ppm upfield of nitromethane for chemical shift calculation purposes.

Some effort has been made to subgroup alkaloids into broad general categories such as the indole alkaloids with which this section begins. The categorization is arbitrary on the part of the authors and not intended to be rigorously systematic. In part, this approach was dictated by the occurrence of studies for various classes of alkaloids contained in the literature since mid-1999 when one of the authors' (GEM) last review of this active research area concluded.[9]

5.1.1. *Indole alkaloids*

The review of applications of long-range ^{1}H–^{15}N methods to alkaloids begins with the coverage of indole-derived alkaloids predominantly for historic reasons. Specifically this

author's (GEM) first efforts in this field of research were focused on the indole alkaloids strychnine (**1**), brucine, and holstiine and it hence seems appropriate to begin with the category of alkaloids with which this area of investigation was launched nearly a decade ago.[6]

Mesengricin. Seto and co-workers reported a study of the novel neuronal cell protecting substance mescengricin (**14**), a pyridoindole produced by *Streptomyces griseofulvis*.[75] There were only a few long-range correlations to the two nitrogen atoms as shown on the structure. No details of the optimization of the long-range delays used in determining the long-range correlations to nitrogen were reported. This study is also interesting in that it is one of a relatively few reports in the literature of the use of the D-HMBC experiment.[11,76] The ^{15}N shifts of the indole and pyridine nitrogen resonance were reported as 122 and 207 ppm, respectively; the former in the normal range for an indole nitrogen resonance while the pyridine nitrogen is shifted considerably upfield relative to the normal pyridine nitrogen shift range of ∼300–320 ppm.
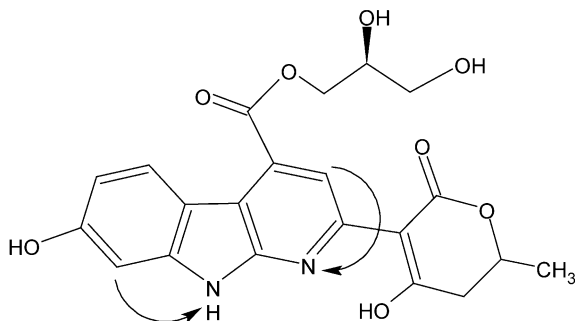
14

Harman. Yamaguchi and co-workers[76] next reported an extensive heteronuclear long-range correlation study of the pyridoindole alkaloid harman (**15**) involving both ^{13}C and ^{15}N. The authors employed and compared several pulse sequences in their study including *J*-HMBC, selective *J*-HMBC, and doubly selective *J*-HMBC experiments. Their study is also atypical in that they report the measurements of the various ^{n}J_{NH} coupling constants observed for harman.
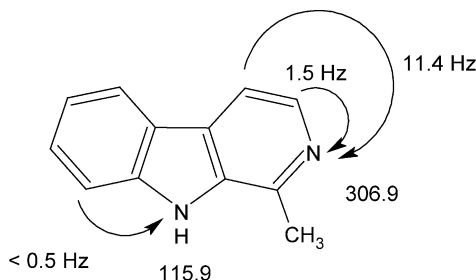
15

3-Hydroxyrutaecarpine. In the first report of a series involving various indole-derived alkaloids, Clark and co-workers[77] reported the structure of the indolopyrido-quinazoline alkaloid 3-hydroxyrutaecarpine (**16**) isolated from *Leptothyrsa sprucei*.

16
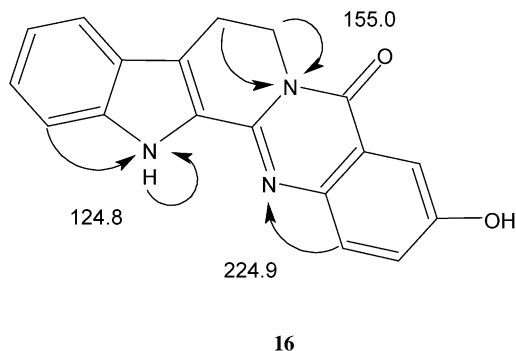
This study is both interesting and instructive in that the authors show how they integrated long-range ^1H–^{13}C (dashed arrows) and ^1H–^{15}N (solid arrows) correlation data to link the various substructures, **17–19**, into the finally determined structure.

17   **18**   **19**
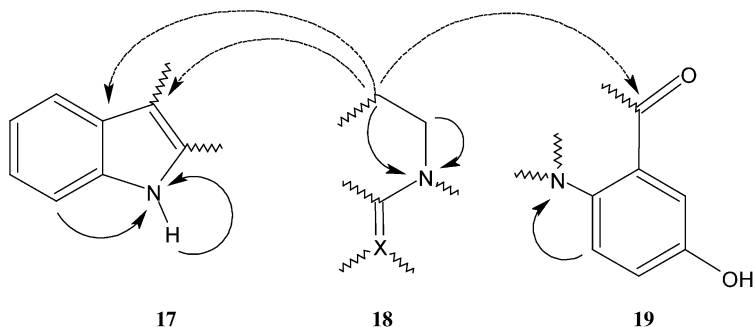
On first inspection, it appears that the ^{15}N shift of the N6 amide resonance at 155.0 ppm is somewhat anomalous. However, the ^{15}N shifts of oxoberberine (Section 5.1.3.1) and nauclealine-A (**20**, following section) assigned at 153.7 and 164.2 ppm, respectively, are consistent with the assigned shift of N6.

Nauclealines and naucleasides. In a study later in 2001, Clark and co-workers reported the application of long-range ^1H–^{15}N experiments during the isolation and structural characterization of another group of indole alkaloids, nauclealine-A (**20**), -B (**21**), and naucleaside-A and -B from the bark of *Nauclea orientalis*.[78] Long-range ^1H–^{15}N coupling pathways were reported for both nauclealine-A (**20**) and -B (**21**) but ^{15}N chemical shifts were reported only for the former, although it is likely that the ^{15}N shifts of the latter would be quite similar. ^{15}N experiments were not used in the elucidation of the structures of the naucleasides.

124.1 (left structure) 164.2 (right of left structure label)

20   **21**
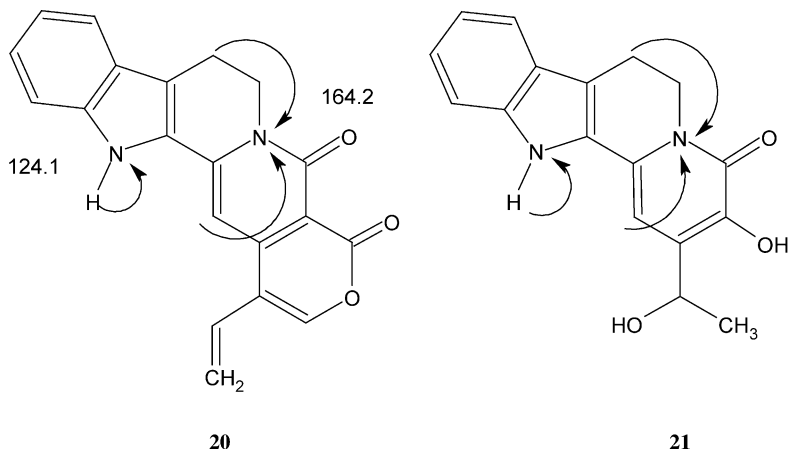
When looking at the reported ^{15}N shift data for nauclealine-A (**20**) it was of interest to calculate the shift of the N6 amide nitrogen resonance using the ACD/NNMR program package developed by ACD/Labs.[62] When this calculation was done, the indole ^{15}N chemical shift was calculated at 131.6 ± 6.8 ppm, which is in reasonable agreement with the reported shift for that nitrogen of 124.6 ppm. In stark contrast, the calculated shift for the N6 amide nitrogen resonance was 89.9 ± 39.1 ppm. When a calculated error this large is observed with the program, it is usually indicative of a relatively small number of example compounds used for the calculation and it is generally worth examining the model compounds used in the calculation, a feature which the program offers. When this was done, the calculated chemical shift was skewed low based on a number of bridgehead nitrogen shifts being averaged into the calculated shift. In addition, the shift of oxoberberine (153.7 ppm) was also used in the calculation. Clearly, given the structure of nauclealine-A (**20**) the calculation should be biased in the direction of the oxoberberine shift, which was an amide structure, rather than in the direction of simple bridgehead nitrogen shifts. As the ^{15}N chemical shift database grows, problems of this type will tend to diminish in frequency. The problem can also be circumvented by building a user database containing data for similar compounds from an investigator's own laboratory to optimize the utility of the program and its calculation routines.

Pentacyclic oxindole alkaloids. From the same laboratories at the University of Mississippi still later in 2001, a study of the 7-deoxyloganic acid and a series of pentacyclic oxindole alkaloids from the Peruvian plant *Uña de Gato* or Cat's Claw was reported.[79] This plant is indigenous to the Peruvian rainforest and used in traditional medicine by native people for a variety of ailments.

The general structure, stereochemistry at the five stereocenters, the N1 and N4 ^{15}N chemical shifts, and the observed long-range heteronuclear couplings of the series of oxindole alkaloids are shown in Table 2. The ^{15}N chemical shift range of the alkaloids described in this report was a useful reporter of stereochemical differences at the various stereocenters. The N1 ^{15}N shifts range from 136.9 to 135.1 ppm while in contrast, the N4 ^{15}N shifts ranged from 54.6 to 64.8 ppm. The *allo*-type isomers (3*S*, 20*S*) uncarine-C and E exhibited substantial ^{15}N shift differences at N4 (8–10 ppm) relative to the *epiallo*-type
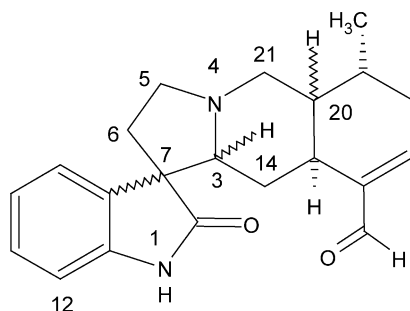
Table 2. Comparison of the stereochemical, N1 and N4 ^{15}N shifts and long-range couplings of a series of pentacyclic oxindole alkaloids isolated from the Peruvian plant *Uña de Gato* (Cat's Claw)[79]

		Stereochemistry	N1 ^{15}N shift and long-range coupled protons	N4 ^{15}N shift and long-range coupled protons
22	uncarine-C	3*S*, 7*R*, 15*S*, 19*S*, 20*S*	136.9 H1, H12	56.9 H5, H6, H14, H20, H21
23	uncarine-D	3*R*, 7*S*, 15*S*, 19*S*, 20*S*	135.1 H1, H12	64.8 H3, H6, H14
24	uncarine-E	3*S*, 7*S*, 15*S*, 19*S*, 20*S*	136.7 H1	54.6 H5, H6, H20, H21
25	mitraphylline	3*S*, 7*R*, 15*S*, 19*S*, 20*R*	135.1 H1, H12	64.7 H3, H5, H6, H14
26	isomitraphylline	3*S*, 7*S*, 15*S*, 19*S*, 20*R*	135.8 H1, H12	64.7 H5, H6, H21

(3*R*, 20*S*) uncarine-D and *normal*-type (3*S*, 20*R*) mitraphylline and isomitraphylline alkaloids. Differentiation of the alkaloids from one another was based on the combined use of optical rotation and ^{15}N data.

Porritoxin. Horiuchi and co-workers in 2002 reported a revision of the structure of the porritoxin (**28**), a phototoxin produced by the fungus *Alternaria porri*.[80] The structure of porritoxin was originally described as containing the 8-membered azoxocine ring as shown by **27**.
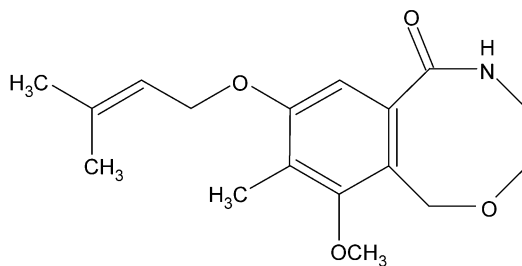

27

When the structure was originally determined in 1992 long-range ^{1}H–^{15}N methods, of course, were not available.[81] In their revision of the structure, Horiuchi and co-workers observed long-range correlations to a ^{15}N resonance at 120.0 ppm from all three methylene protons. For **27** to be the correct structure, one of the methylene to nitrogen correlations would have to be a $^5J_{NH}$ coupling, which is unlikely, although some correlations of that type have been reported (see Section 5.1.5). There was also no signal observed in a ^{1}H–^{15}N HSQC spectrum which also contradicted the originally proposed structure. On this basis, the authors revised the structure of porritoxin to the hydroxyethyl isoindolone as shown by **28**.

28
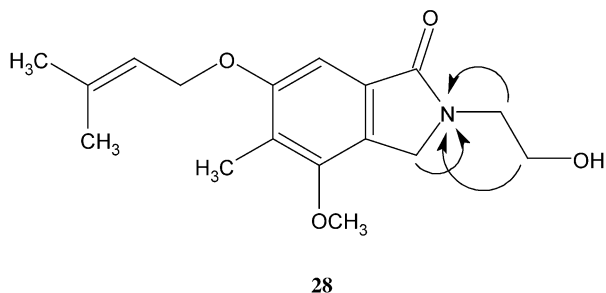
Kottamides A–D. Copp and co-workers[82] have made extensive use of long-range ^{1}H–^{15}N NMR methods in the characterization of a diverse assortment of marine natural products. One of their first reports using ^{1}H–^{15}N data were the isolation and characterization of a series of bioactive molecules they named kottamides A–D from
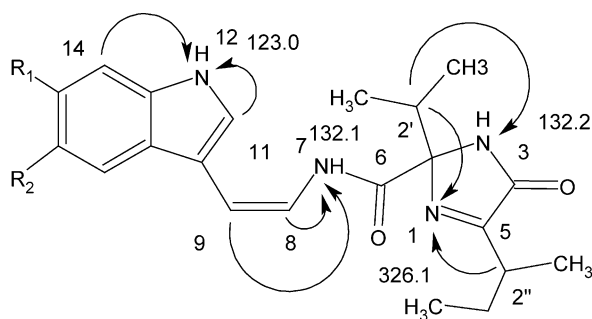

Table 3. Structural comparison of substituents and side chains for kottamides-A thru -D[82]

	R$_1$	R$_2$	C2 side chain	C5 side chain
29	–Br	–Br	Isopropyl (as shown above)	*Sec*-butyl (as shown above)
30	–Br	–H	Isopropyl	*Sec*-butyl
31	–H	–Br	Isopropyl	*Sec*-butyl
32	–Br	–Br	*Sec*-butyl	Methyl

the New Zealand ascidian *Pycnoclavella kottae*. Direct and long-range ^{1}H–^{15}N correlation data were only acquired for kottamide-A (**29**) and are shown in the structure accompanying Table 3. Key long-range ^{1}H–^{15}N coupling pathways measured for kottamide-A (**29**) are shown on the structure. The authors noted that the correlations from the 2′ and 2″ methine protons of the side chains to the nitrogen resonating at 326.1 were key observations in the assembly of the imidazolone portion of the structure. It is quite likely that had ^{15}N data been acquired for the other three analogues in the series that the ^{15}N chemical shifts and long-range coupling pathways would have been comparable to those of kottamide-A (**29**).

Kottamide-E. In a 2003 report, Appleton and Copp[83] reported the isolation and characterization of another analogue in this sequence, kottamide-E, **33**, which they described as the first example of a natural product bearing the amino acid 4-amino-1,2-dithiolane-4-carboxylic acid. All the nitrogens in the structure of **33** are protonated and were detected in a ^{1}H–^{15}N HSQC spectrum. The authors, however, also report the use of a 6 Hz optimized ^{1}H–^{15}N HMBC spectrum in the elucidation of the structure of the molecule.


33
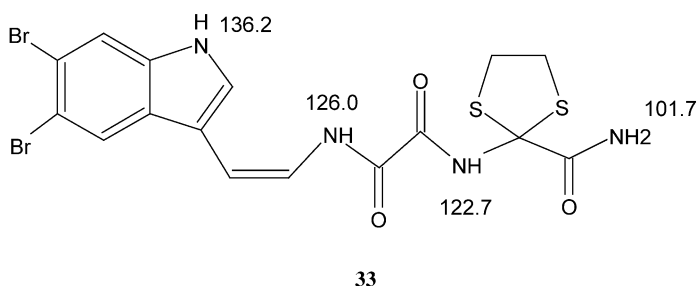
Novel imidazolidinone tetrahydropyrroloindole. During the attempted total synthesis of roquefortine C, a fungal metabolite of *Penicillium roqueforti*, an essential fungus in the production of Roquefort cheese, the copper catalyzed amidation of the vinyl bromide **34** in Scheme 1 was envisioned to lead to the requisite diketopiperazine ring contained in **35**.[84] Preliminary spectroscopic data, however, suggested that the amidation had not gone as anticipated and that an unknown cyclization product had instead formed.

Rather than amidation occurring to form the expected diketopiperazine, **35** instead it appears to have undergone a nucleophilic displacement of the vinyl bromide by the indole NH to form the novel imidazolidinone shown by **36**. The 90 Hz indole NH doublet was absent in the ^{1}H–^{15}N GHMBC spectrum recorded for **36** at the chemical shift of the indole nitrogen that resonated at 111.8 ppm. Correlations were observed to the bridgehead proton as well as to the vinyl proton, confirming the assignment. The balance of the long-range correlations to the five nitrogen atoms of **36** are shown in Scheme 1.

Biosynthesis of aspernomine. Nominine (**37**), an indole diterpenoid alkaloid, and the related alkaloid aspernomine (**38**) are known to arise from a common digerranylindole precursor, although the skeletal relationship of this pair of alkaloids was not well understood.

34

35

36

Scheme 1.

37

38

39   **40**
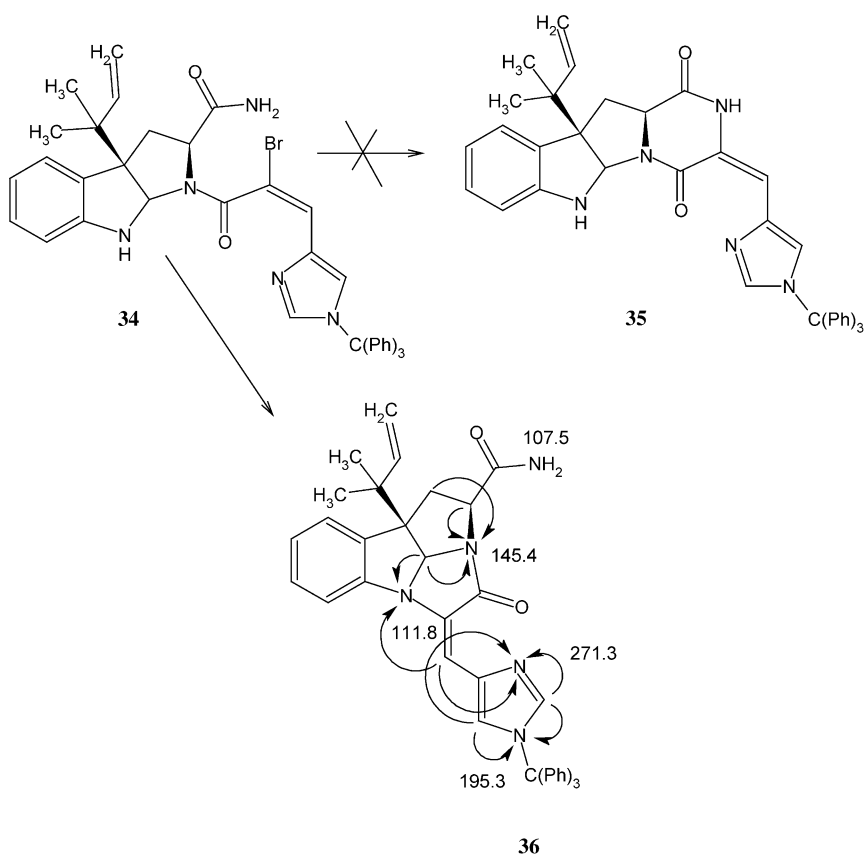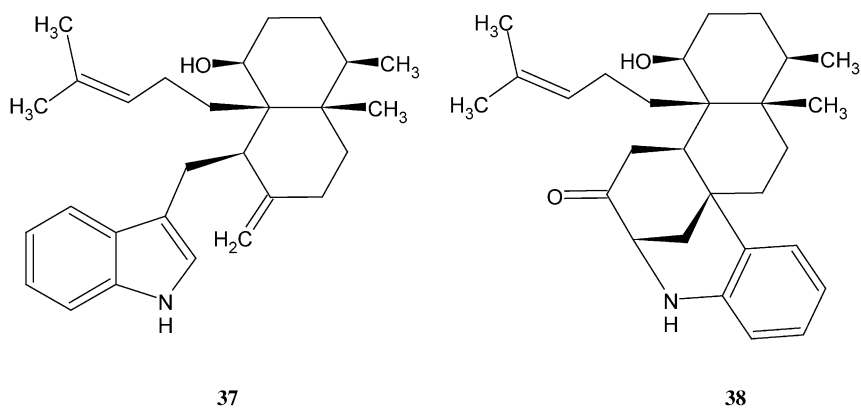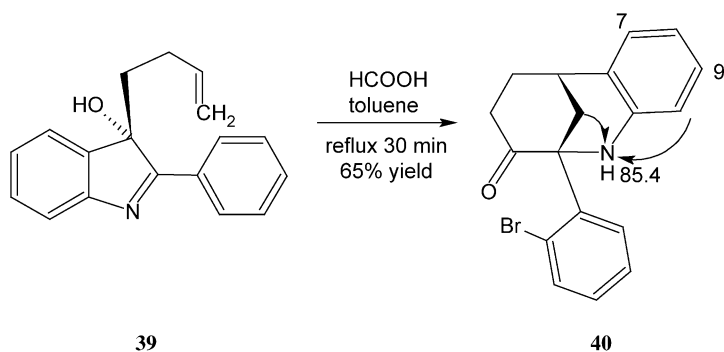
Scheme 2.

McWhorter and co-workers[85] observed a novel rearrangement of 2-(2-bromophenyl)-3-(3-butenyl)-3H-indol-3-ol (**39**, Scheme 2) to give a molecule with the uncommon 1,4,5,6-tetrahydro-2,6-methano-1-benzazocin-3(2H)one ring system contained in **40**. This rearrangement suggests that aspernomin (**38**) may arise biosynthetically from nominine (**37**) although this remains to be confirmed.

Long-range ^{1}H–^{15}N GHMBC data were used in the confirmation of the structure of **40**. The nitrogen in the benzazocine ring resonated at 85.4 ppm and was long-range coupled to the *peri* proton, H10, and to one of the H11 methylene protons. There was also a correlation observed to either the H7 or H9 proton although which of these could not be determined at the resolution in F_2 of the ^{1}H–^{15}N GHMBC data since they resonated at 7.15 and 7.16 ppm, respectively.

Speradine-A. Kobayashi and co-workers reported the isolation and structural characterization of speradine-A (**41**) using long-range ^{1}H–^{15}N data.[86] The novel pentacyclic oxindole alkaloid was isolated from the cultured broth of the marine fungus *Aspergillus tamarii* that was separated from driftwood at Okinawa. The only long-range correlations

41
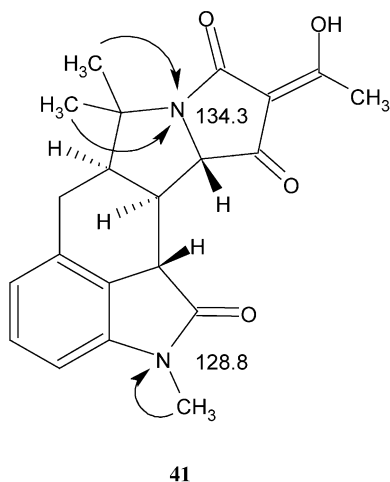
observed to the two nitrogen resonances in the molecule were from directly bound or nearby methyl groups, making the detection of these correlations a very simple task.

Bacillamide. Okada and co-workers[87] reported the isolation and characterization of a new algicide with activity against the harmful dinoflagellate *Cochlodinium polykiroides* from a marine bacterium *Bacillus* sp SY-1. The authors utilized long-range ^{1}H–^{15}N HMBC data in assembling the structure of the bacillamide (**42**).

42
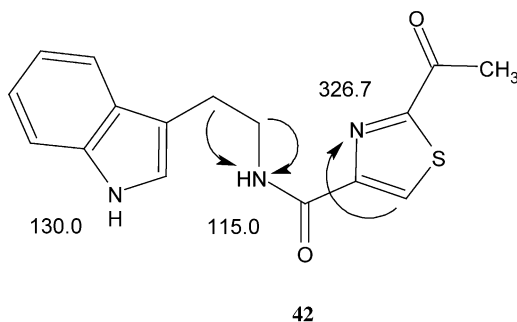
5.1.2. *Other five-membered ring-containing alkaloids and natural products, including fused ring systems*

An interesting study reported in 2001, although it did not utilize any inverse-detected 2D NMR data, did report a wealth of useful ^{15}N chemical shift data for parent azoles and benzazoles.[88] Solid-state ^{15}N chemical shift data were reported for several pyrazole analogues by Álvarez-Larena.[89] Trofimenko *et al.*[90] reported a study of the buttressing effects of the 4-*tert*-butyl group of a series of pyrazoles in the solid state, followed by a study by Claramunt and co-workers[91] of a series of halo triazoles. Martins and co-workers[92] reported ^{15}N data for a series of 5-trichloromethyl-1,2-dimethyl-1*H*-pyrazolium chlorides. Malpass and co-workers[93] reported direct observe ^{15}N chemical shift data for a series of bicyclic amines and lactams. Recently, a large body of ^{15}N chemical shift data for a series of 1,4-diazaspiro[4.5]decanes and 1,4-oxazaspiro[4.5]-decanes using direct observe ^{15}N methods were reported by Ariza-Castolo and co-workers.[94] Readers with an interest in the ^{15}N chemical shift behavior of these systems are directed to these references as a source of data.

5.1.2.1. Pyrroles and related systems

Discohabdin-R. Ford and Capon[95] utilized long-range ^{1}H–^{15}N 2D NMR data in the process of characterizing the complex pyrroloiminoquinone discohabdin-R (**43**) from two latrunculid marine sponges *Latrunculia* sp. and *Negombata* sp. Unfortunately, the authors did not report the ^{15}N chemical shifts of the three nitrogen resonances in the structure nor did they report any of the experimental details.

Isomalyngamides A and B. Two new compounds, isomalyngamides A and B, **44** and **45**, respectively, were isolated from the Hawaiian cyanobacterium *Lyngba majuscula*, which has amply been shown to be a rich source of bioactive secondary metabolites.[96] Long-range ^{1}H–^{15}N GHMBC data were used to assign the amide nitrogen resonances as
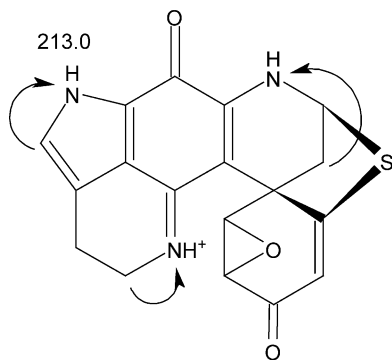
43

well as to locate the nitrogen within the molecular framework. It is also interesting to note that HETLOC was used to measure long-range heteronuclear coupling constants, allowing the assignment of the Z-configuration to the chloromethylene moieties of the structure.
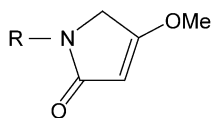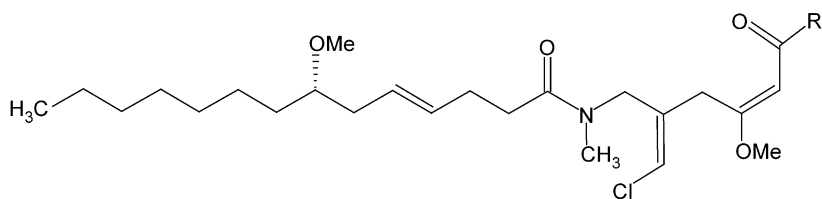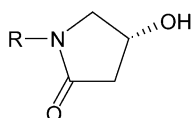
44   **45**

The *N*-methyl amide and pyrrolidinone amide nitrogens resonated at 107.4 and 159.5 ppm, respectively, for isomalyngamide A (**44**) and at 108.3 and 165.8 ppm for isomalyngamide B (**45**).

Palinurin. Hamann and co-workers[97] reported the results of an interesting biocatalytic transformation of the furan ring to the corresponding amide in the bioactive marine natural product palinurin (**46**, X=O). The authors utilized long-range ^{1}H–^{15}N data to establish the presence of the pyrrolidinone of palinurine A (**47**), the nitrogen resonating at 122.3 ppm, with the observed long-range correlations as shown. In addition to palinurine A, the authors also reported ^{15}N chemical shift data for palinurine B (**48**). The nitrogen resonance of palinurine B (**48**) resonated at 120.3 ppm.
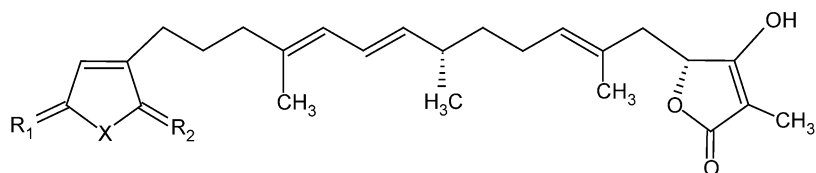
46
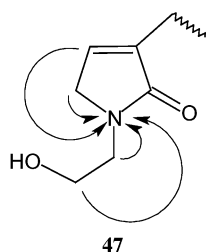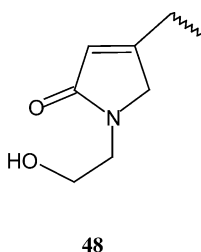
47   **48**

Kaitocephalin. During an effort to synthesize kaitocephalin (**49**) Loh *et al.*[98] reported the use of long-range ^{1}H–^{15}N data to confirm the structure that they had synthesized, by comparing ^{15}N shift assignments with those previously reported for this molecule by Seto and co-workers[99] when the molecule was first isolated in 1997. This is the first instance of which the authors are aware of the use of ^{15}N shift data for the confirmation of a synthesized natural product.
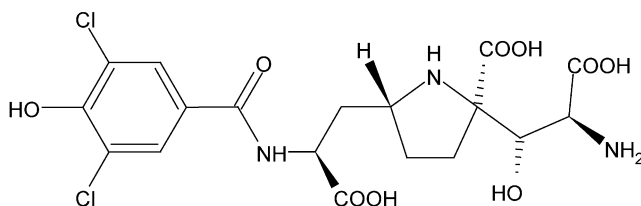
49

Palu'imide. Moore and co-workers[100] isolated a number of interesting and structurally diverse compounds from a collection of a Palauan, apratoxin-producing marine cyanobacterium *Lyngbya* sp. The authors utilized a combination of ^{1}H–^{15}N HSQC and HMBC data in the elucidation of the structure of palu'imide, **50**. The valine residue in the structure was identified by the nitrogen resonating at 115.5 ppm in an HSQC spectrum. The imide nitrogen, resonating at 165.1 ppm, was established from a 4 Hz optimized HMBC experiment.

50
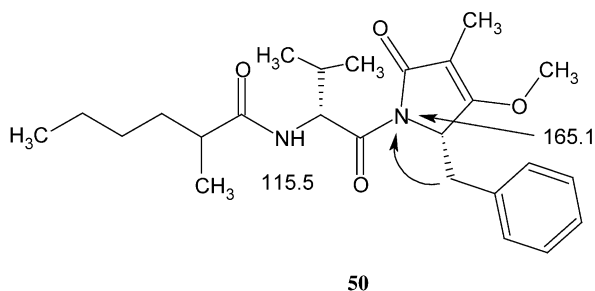
Gluconeogenesis inhibitors FR225659 and FR225656. Yoshimura and co-workers[101] reported the elucidation of the structure of two new gluconeogenesis inhibitors from a *Helicomyces* sp. and used long-range ^{1}H–^{15}N data in the confirmation of the structure. The two structures are analogues and differed from one another only in the nature of a side-chain R group, which was either a methyl or ethyl group. The authors comment that the HMBC data acquired in the study were optimized for 8 Hz but do not clearly specify that the same optimization was used for both proton–carbon and proton–nitrogen long-range experiments. Nevertheless, long-range ^{1}H–^{15}N HMBC data were successfully used to locate the nitrogen atoms in the skeletal framework of the methyl analogue, **51**, R=–CH$_3$. Once the first structure was established, long-range ^{1}H–^{15}N data were not necessary to establish the structure of the ethyl analogue.

51
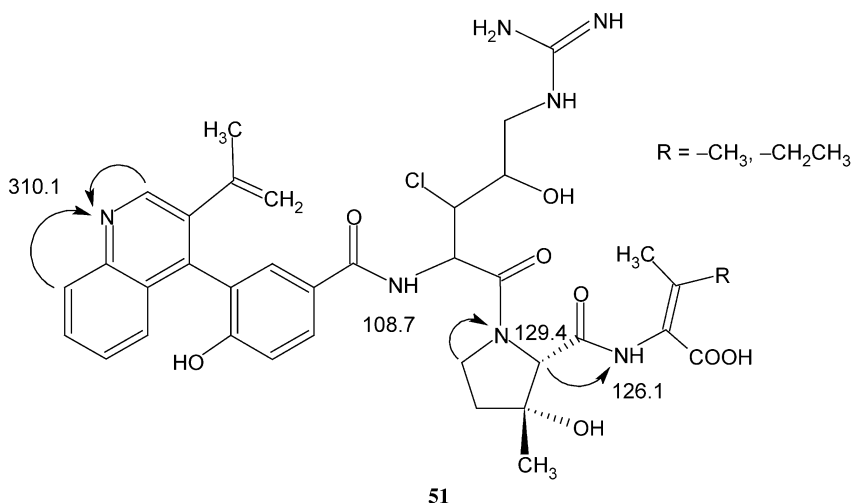
Revision of the structure of tetrapetalone-A. In late 2003, Hirota and co-workers[102] reported the results of a study employing long-range ^{1}H–^{15}N data that resulted in the revision of the structure of the lipoxygenase inhibitor tetrapetalone-A. The structure of tetrapetalone-A was originally assigned as **52** in an earlier communication using a suite of 2D NMR experiments consisting of COSY, HMQC, ^{1}H–^{13}C HMBC, and ^{13}C–^{13}C 2D INADEQUATE experiments.[103] Long-range ^{1}H–^{15}N heteronuclear shift correlation data, however, were not used in the initial structure characterization study.
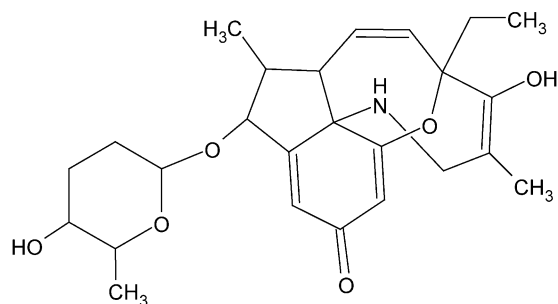
52

When the molecule was investigated using long-range ^{1}H–^{15}N 2D NMR methods, it was possible to revise the structure as shown by **53** on the basis of the observed long-range correlations to the single nitrogen resonating at 123.0 ppm. In the process of revising the structure, the complete stereochemistry of the molecule was also assigned.
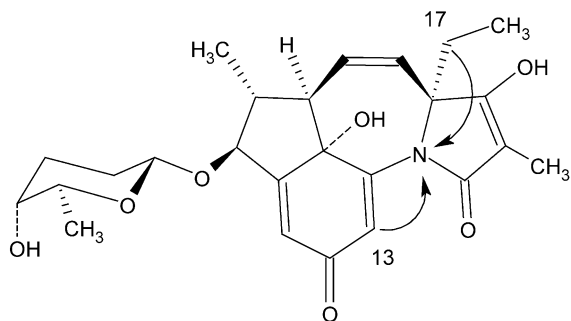
53

Pyrrolizidine alkaloids from Onosma leptantha. Chinou and co-workers[104] utilized long-range ^{1}H–^{15}N data in the characterization of several new pyrrolizidine alkaloids from *Onosma leptantha*. The authors in particular used the ^{15}N chemical shift to confirm the presence of the N-oxide of **54** and the tertiary amine, **55**. The chemical shift difference of 80.5 ppm between **54** and **55** is consistent with differences observed for other N-oxides.[9,22]
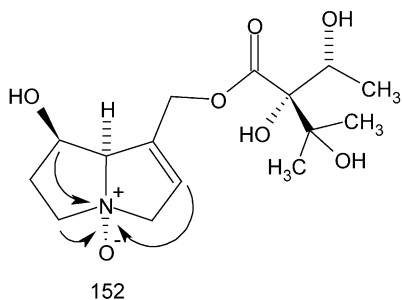
54
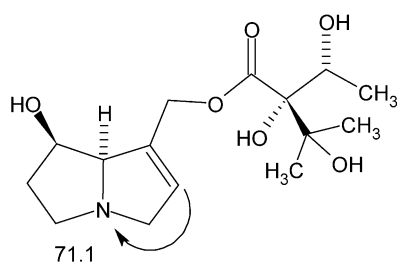
55

5.1.2.2. Imidazoles and related systems

Bacteriochlorophyll/imidazole and chlorophyll/imidazole complexes. In a late 2000 report, de Groot and co-workers reported the results of a study of bacteriochlorophyll and chlorophyll complexes with imidazole that relied on long-range ^{1}H–^{15}N correlation data.[105] The authors were able to make unambiguous assignments of the two imidazole nitrogens of imidazole ligated to the magnesium of bacteriochlorophyll *a* or chlorophyll *a*. The imidazole in each case was deprotonated when complexed, implying that the chlorophyll/imidazole carries a full negative charge despite the apolar solvent environment. The authors inferred that their data may have potential utility in the characterization of the nature of magnesium–histidine interaction and the charge state of chlorophylls coordinated by histidine in photosynthetic pigment protein complexes.

Naamidines – anticryptococcal and nitric oxide synthetase inhibitory imidazole alkaloids. Hamann and co-workers[106] isolated and characterized a series of imidazole-derived alkaloids with anticryptococcal and nitric oxide synthetase inhibitory activity from the calcareous sponge *Leucetta chagosensis*. The authors used long-range ^{1}H–^{15}N to locate the protonated imidazole nitrogen of naamidine D (**56**), resonating at 135.2 ppm, in the molecular skeleton. In addition to a correlation from the directly attached proton resonating at 11.35 ppm, a long-range correlation was also observed from the benzylic methylene protons resonating at 3.80 ppm.
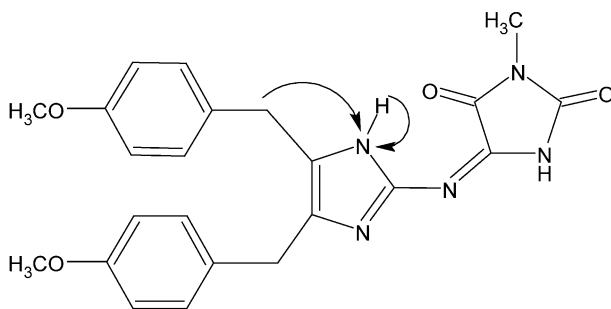
56

Cholera toxin induced PGE$_2$ activity. In an interesting study of mediators of cholera toxin induced fluid secretion, it was found that the administration of histidine significantly reduced the net secretory response into the small intestine of mice challenged with cholera toxin.[107] The authors were able to demonstrate using a 90 ms
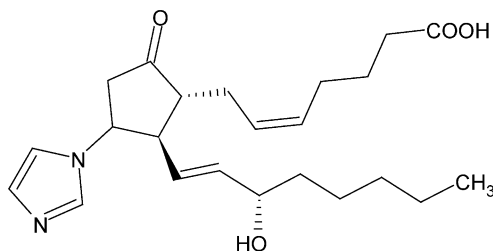
57

long-range ^{1}H–^{15}N 2D NMR data that a complex is formed between PGE$_2$ at the 11-position and imidazole as shown by **57**.

Archerine. Cimninello and co-workers[108] reported the isolation and structural characterization of the complex bromotyrosine-derived imidazole alkaloid archerine (**62**) that was isolated from the Caribbean marine sponge *Aplysina archeri*. The authors used long-range ^{1}H–^{15}N correlation data to assemble four substructural fragments, **58**–**61**. ^{15}N chemical shift data reported in conjunction with these fragments are shown with the individual fragments. The final structure was assembled from the substructural components through the use of long-range ^{1}H–^{13}C correlation data.

58

59

60

142.5, 178.7

61

62
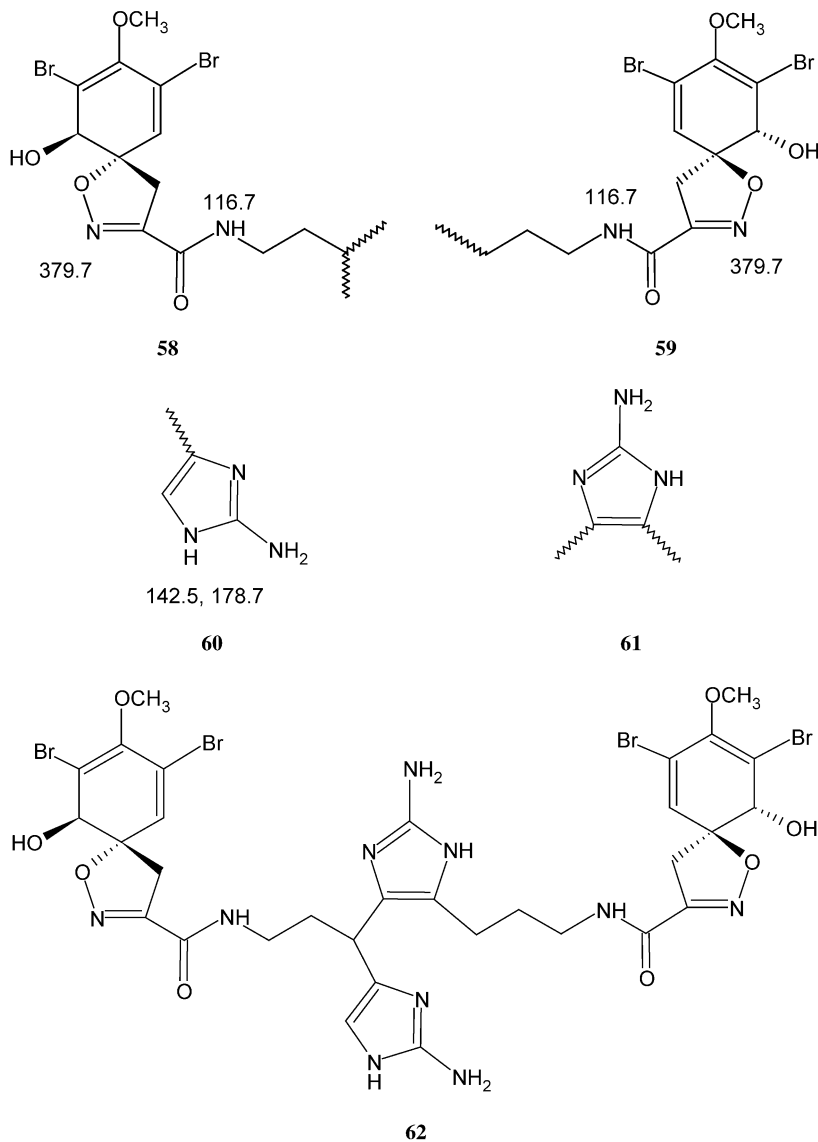
Visoltricin. Rieder and Lepschy[109] reported a revision of the structure of visoltricin (**63**) made on the basis of a long-range ^{1}H–^{15}N HMBC study. Visoltricin had been reported to be an active metabolite of *Fusarium tricinctum*, with toxicity to human tumor cell lines. The structure of visoltricin was elucidated spectroscopically, the data interpreted to be consistent with the structure as shown by **63**. Independently, fungerin (**64**) was isolated from a strain of *Fusarium* sp. and shown to have activity against a number of species, including *Penicillium chrysogenum*, *Colletotrichu langenarium*, *Alternaria mali*, and *Pyricularia oryzae*. When visoltricin and fungerin were both synthesized, the preliminary spectral data were inconsistent with the proposed structure of visoltricin.

63   **64**
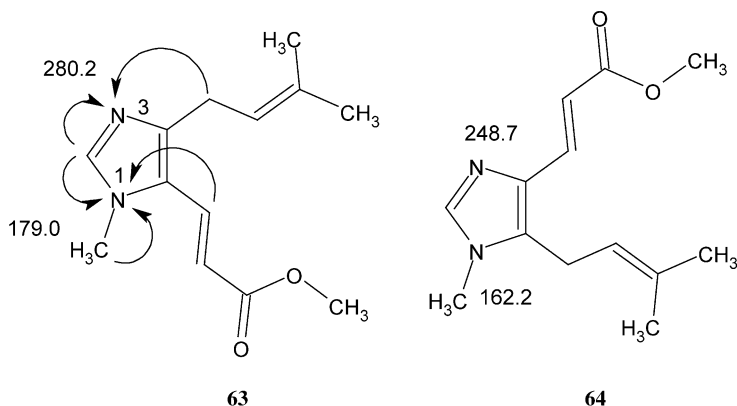
The structure of visoltricin was revised on the basis of long-range ^{1}H–^{15}N HMBC data. The H2 resonance of the imidazole ring of the synthesized sample, **63**, gave correlations to both the imidazole nitrogens. The N1 methyl-bearing nitrogen resonates as 179.0 ppm; the assignment was confirmed by a correlation from the N-methyl group and the side chain vinyl proton. N3, in contrast, resonates at 280.2 ppm, that assignment confirmed by a correlation from one of the side-chain methylene protons. In contrast, the reported ^{15}N chemical shift assignments for fungerin, **64**, are 162.2 for the methyl-bearing N1 resonance, and 248.7 for the N3 resonance.[110] When the long-range ^{1}H–^{15}N data for an 'authentic' sample of visoltricin were acquired, they were identical to those for isolated fungerin, **64**. GC retention time comparison and mass spectral fragmentation pathways and fragment ion intensities were also identical for 'authentic' visoltricin and fungerin. On the basis of these data, the structure of visoltricin was revised and shown to be identical to fungerin, **64**.

Cribostatin 6. Pettit and co-workers[111] in an investigation of the antineoplastic agents elaborated by the marine sponge *Cribrochalina* sp. reported the isolation and elucidation of the structure of cribrostatin 6. When the suite of routine 2D NMR experiments, including long-range ^{1}H–^{13}C HMBC were acquired for the compound, it was not possible to distinguish between structures **65** and **66**.

65   **66**
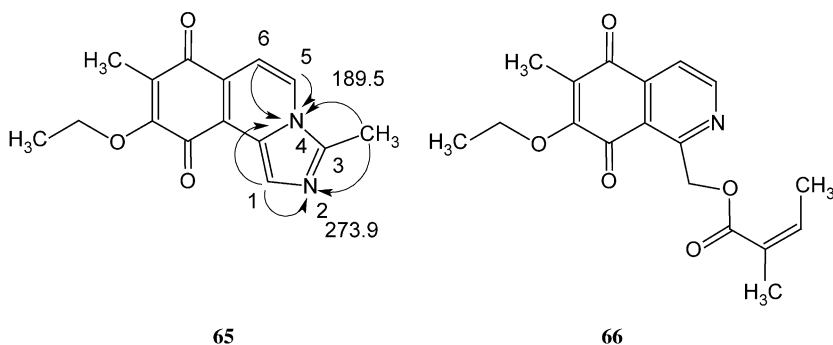
Acquisition of 5 Hz optimized ^{1}H–^{15}N HMBC spectrum resolved the ambiguity. Long-range correlations were observed to two nitrogen atoms, eliminating **66** from consideration as a possible structure. Correlations were observed from both H1 and the 3-methyl group to both nitrogens which resonated at 189.5 and 273.9 ppm. The former was assigned as N2, and the latter as N4, which also showed two- and three-bond correlations to H5 and H6, respectively, confirming the structure of cribostatin 6 as **65**.

5.1.2.3. Oxazole, isoxazole and related systems

Isomeric siderophores from the freshwater cyanobacterium Anabaena cylindrica. Itou et al.[112] reported the structural characterization of a pair of iron chelating siderophores isolated from the freshwater cyanobacterium *Anabaena cylindrica*. Both direct and long-range ^{1}H–^{15}N HSQC and HMBC data were used in the characterization of the structures. The amide nitrogen resonances along the backbone of the molecule were assigned from HSQC data. Long-range data were used in the assembly of the tetrahydroquinoline portion of the structure via the correlations shown. Unfortunately, no long-range correlations were observed to the oxazoline nitrogen resonance.

67
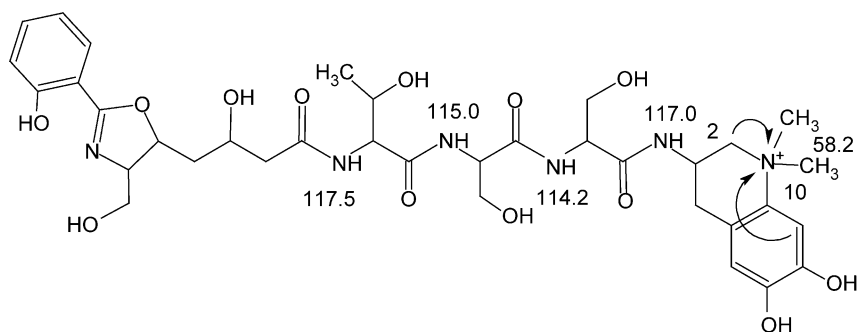
Desymmetrization of C$_2$-symmetric diazidobutane-1,4-diol with benzaldehyde. Scheurer and co-workers[113] reported an interesting study of the reaction of C$_2$-symmetric diazidobutane-1,4-diol with benzaldehyde. Although quantum mechanical studies favored the reaction of the substrate with two equivalents of benzaldehyde to produce
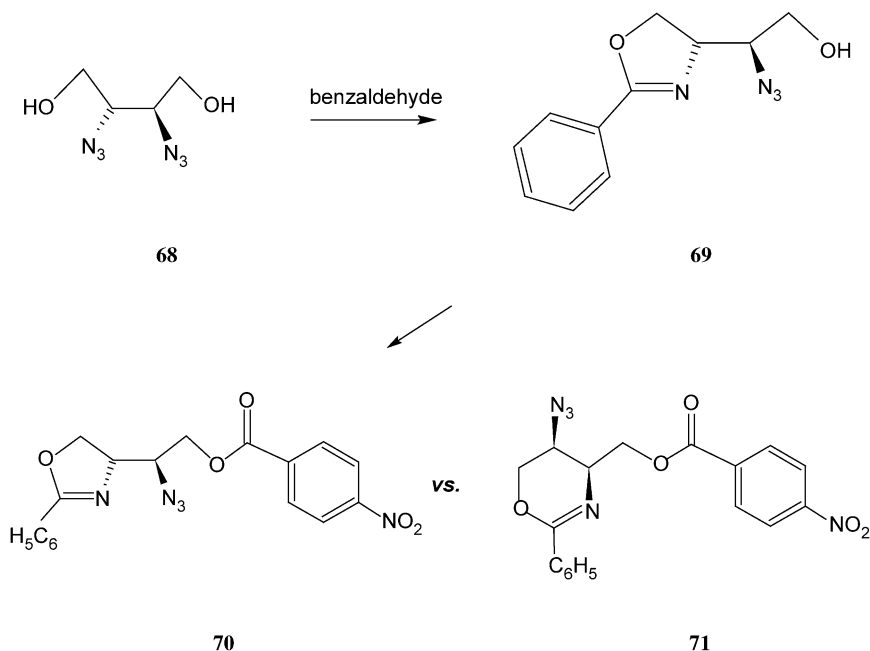
Scheme 3.

a bioxazoline system, only a single equivalent of benzaldehyde was consumed to afford **69** as shown in Scheme 3. To confirm the structure of the product, the authors further reacted **69** with *p*-nitrobenzaldehyde, which could afford either **70** or **71** as products. The authors used long-range ^{1}H–^{15}N HMBC data to confirm the structure as **70**.

5.1.3. Alicyclic and aromatic six-membered ring containing natural products

5.1.3.1. Pyridine, quinoline, isoquinoline and related systems

Sarcomejine. Skaltsounis and co-workers[114] employed long-range ^{1}H–^{15}N data to differentiate between possible alternative structures during the elucidation of the structure of sarcomejine. The two structures differed in the attachments of the side chains and are shown by **72** and **73**. Correlations from the side-chain methine proton to the quinolyl nitrogen resonating at 118.3 ppm were used to assign the structure of sarcomejine as **72**, based on the reasoning that these correlations would not be readily observable if structure **73** were the correct structure. Given the optimization of the delays of their long-range ^{1}H–^{15}N HMBC experiment for 5 Hz, this is a valid assumption since a smaller optimization would likely be necessary to observe the corresponding $^{4}J_{NH}$ correlation to the quinolyl nitrogen if **73** were the correct structure.

Araguspongines K and L. Orabi and co-workers[115] reported the elucidation of the structures of several bis-1-oxaquinolizidine *N*-oxide alkaloids from Red Sea specimens of *Xestospongia exigua*, employing long-range ^{1}H–^{15}N HMBC data in the process. Two of the compounds were known, araguspongine A and araguspongine-C, however, their corresponding *N*-oxide, araguspongine-K (**74**) and araguspongine-L (**75**) were new
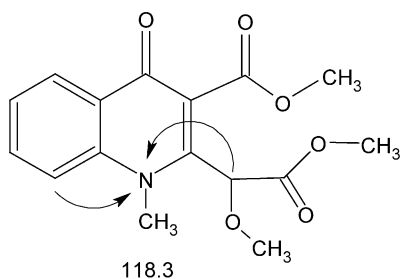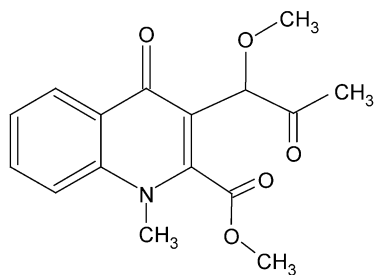
72   **73**

compounds. Only partial ^{15}N data were reported for **74**, specifically the shift of the N5-oxide nitrogen, which resonated at 117.1 ppm. Both shifts were reported for the symmetric **75**. In the case of the latter, N5 resonated at 43.1 ppm, while the N5′-oxide nitrogen resonated at 117.0 ppm, which represents a downfield shift of +73.4 ppm due to the *N*-oxidation. The downfield shift observed following *N*-oxidation is consistent with the downfield ^{15}N shifts following *N*-oxidation reported from these laboratories.[116–118]

Total synthesis of the fumiquinazoline alkaloids. Wang and Ganesan,[119] in the process of synthesizing a series of fumiquinazoline alkaloids, reported the extensive use of long-range ^{1}H–^{15}N correlation data. The authors reported chemical shift and long-range correlations observed for fiscalin-B (**76**) as well as for several of the substituted analogs
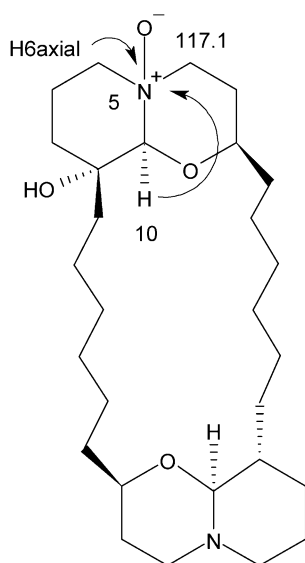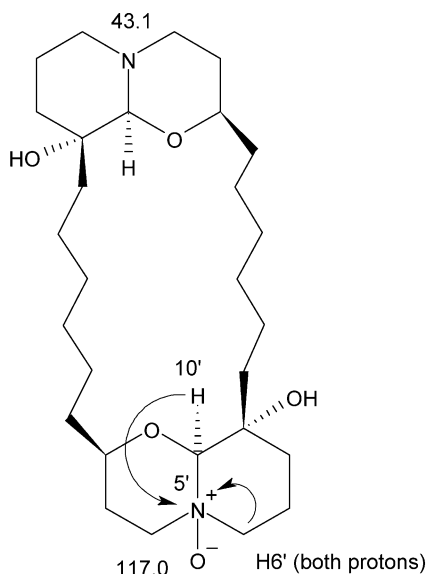
74   **75**

shown in Scheme 4. ^{15}N chemical shift data for analogues of **77** are collected in Table 4, while the ^{15}N chemical shifts for the one product, **78**, for which they were reported are shown on the structure. The original report also contains ^{15}N chemical shift data for a number of synthetic intermediates to which the interested reader is referred.

76
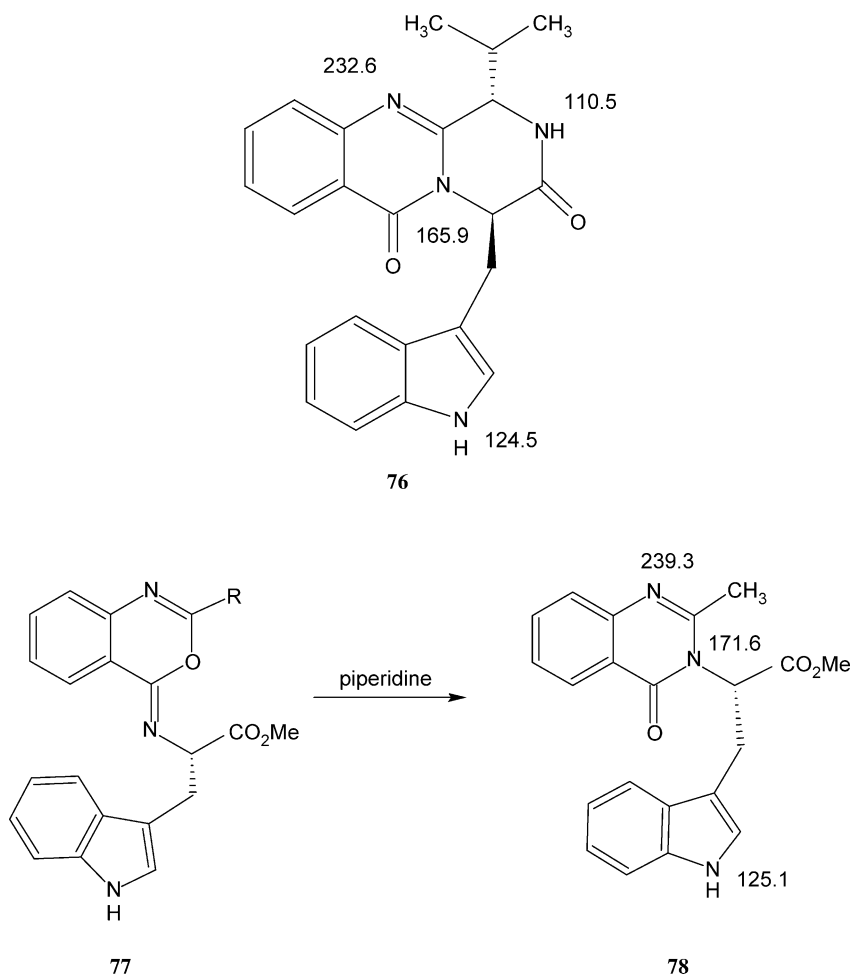
Scheme 4.

Table 4. ^{15}N chemical shift assignments for several analogues of **77**[119]

Substituent (R)	Indole NH	Exo C=N	Benzoxazine C=N
–CH$_3$	122.2	224.2	223.0
–C$_6$H$_5$	121.7	222.6	223.4
–CH$_2$CH(CH$_3$)$_2$	123.4	221.9	225.0

The authors also reported ^{15}N chemical shift assignments for one additional compound. Refluxing the *t*-butyl substituted precursor of **77** in methylene chloride with triphenylphosphine, iodine and triethylamine led to the formation of the substituted β-carboline, **79**.
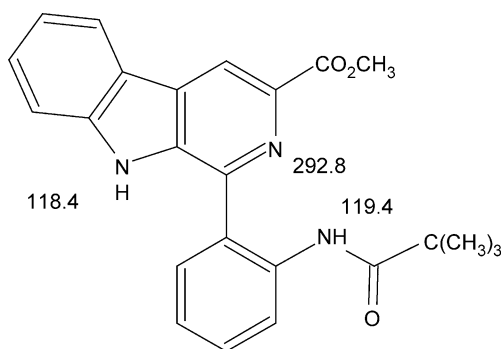
79

Spectral characterization of bisbenzylisoquinolines from Isolona ghesquiereina. The investigation of bisbenzylisoquinolines has been an active area of natural products research that has been relatively recently reviewed.[120] Frappier and co-workers[121] have studied and characterized some antiplasmodial bisbenzylisoquinoline alkaloids from *Isolona ghesquiereina* using long-range ^{1}H–^{15}N HMBC data in their study. The authors characterized (−)curine (**80**) and chondrofoline (**81**), for which ^{15}N chemical shift data were reported. Unfortunately, the observed long-range ^{1}H–^{15}N correlations were not reported. The N2 and N2′ resonances of **80** were assigned as 22.5 and 34.7 ppm, respectively. The corresponding resonance assignments for N2 and N2′ of **81** were quite comparable at 23.2 and 35.4 ppm.

Antifungal alkaloids from Duguetia hadrantha. Muhammad and co-workers[122] reported the isolation and structural characterization of two alkaloids from *Duguetia hadrantha*, hadranthine-A and -B (**82**) that were related to the known alkaloid imbiline-1. To confirm the placement of the annular nitrogen atoms in the skeletal framework, the authors utilized long-range ^{1}H–^{15}N HMBC data. Thus, correlations from protons resonating at 9.11 and 8.22 ppm to a nitrogen resonating at 321.0 were used to position N1 of hadranthine-A (**82**, R$_1$=–CH$_3$; R$_2$=–OCH$_3$). A correlation from the amide methyl group to a nitrogen resonating at 135.6 ppm located N6. To provide confirmation of the structural assignment, imbiline-1 (**82**, R$_1$=–CH$_3$, R$_2$=–H) was also examined by long-range ^{1}H–^{15}N methods. Identical long-range correlations were observed to nitrogens resonating at 321.9 and 135.4 ppm, confirming the structural assignment. Only partial ^{15}N data were reported by the authors for hadranthine-B (**82**, R$_1$=–CH$_3$; R$_2$=–H); the N1 resonance was observed at 321.5 ppm. The ^{15}N chemical shift of the N6 resonance was not reported.
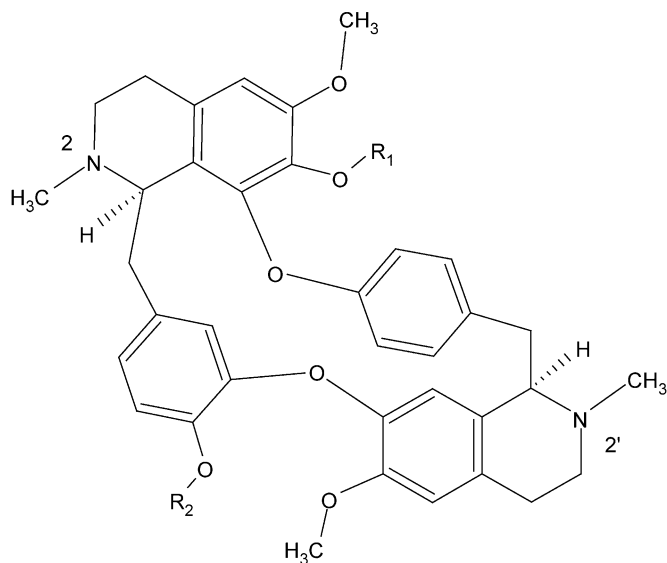
80 $R_1 = R_2 = -H$

81 $R_1 = -CH_3, R_2 = -H$
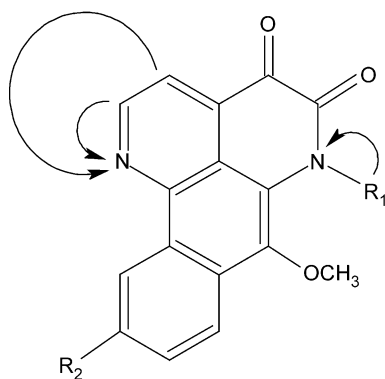
82

Assignment of the ^{15}N *spectrum of streptonigrin.* Anderberg *et al.*[123] reported the assignment of the ^{13}C and ^{15}N spectra of the antitumor antibiotic streptonigrin (**83**). The aromatic nitrogens, N1 and N1′, were assigned via long-range correlations from the proton at the 3-position and the methyl group, of the respective rings. Initial ^1H–^{15}N HMBC spectra recorded at 300 K gave a correlation that allowed the assignment of the N10 amino group at 65.0 ppm. But, no signal was observed for the N7′ resonance.

However, by lowering the temperature to 240 K, the authors were able to assign both the N10 resonance at 65.0 ppm and the N7′ resonance at 75.0 ppm. The authors note that these assignments were similar to those previously reported for analogous systems.[203]
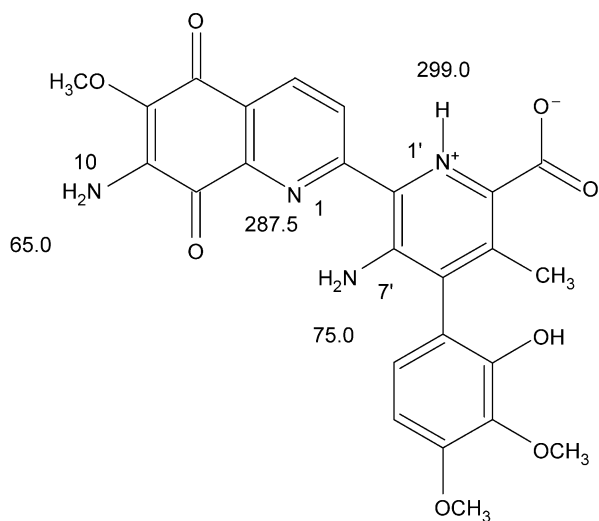
83

¹⁵N *chemical shift assignments of isoquinoline alkaloids.* Marek and co-workers[124] in a continuation of their prior work in the area of ¹⁵N NMR of isoquinoline alkaloids[125] reported the ¹⁵N chemical shift assignment and long-range coupling pathways for numerous tertiary and quaternary isoquinoline alkaloids of a number of different classes. The included stylopine (**84**), corydaline and thalictricavine (**85a, 85b**), mecambridine (**86**), cyclanolie iodide (**87**), 8-hydroxy-7,8-dihydroberberine (**88**), palmatine chloride and jatrorrhizine chloride (**89a** and **89b**), norchelerythine (**90**), isothebaine (**91**), mecambrine (**92**), argemonine (**93**), rhoeadine (**94**), and bicuculine (**95**). The authors employed both conventional ¹H–¹⁵N HMBC and ¹H–¹⁵N GSQMBC[126] experiments for this work but did not report the optimization of the long-range delays used.
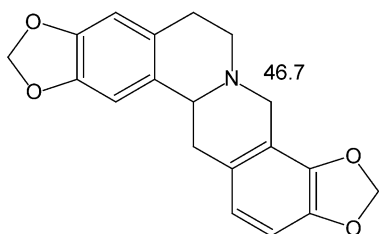
84
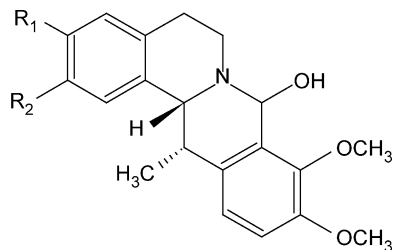
85a   R₁ = R₂ = -OCH₃ -- 40.1ppm

85b   R₁ + R₂ = -OCH₂O- -- 40.2 ppm
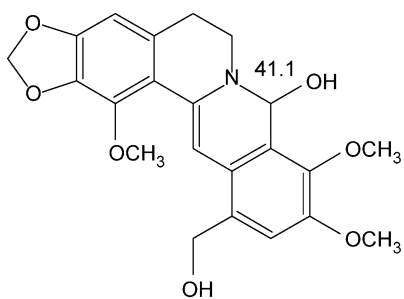
86
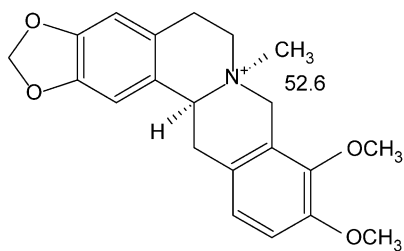
87
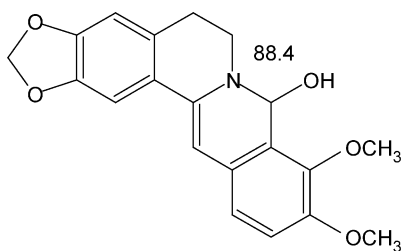
88
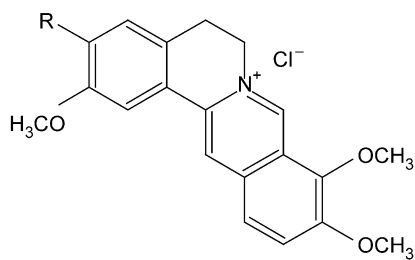
89a   R = -CH₃– 194.5 ppm

89b   R = -H – 194.4 ppm

90

91

92

93

94

95
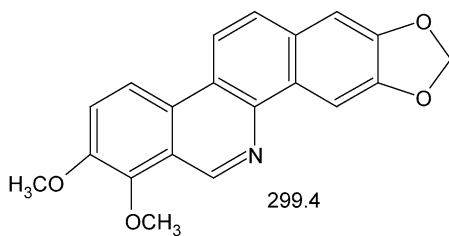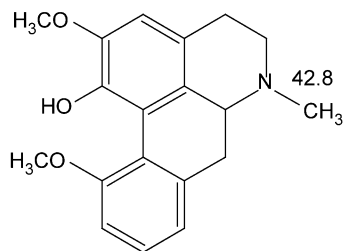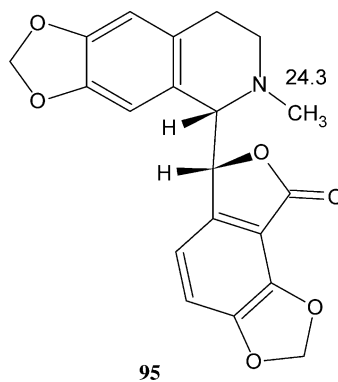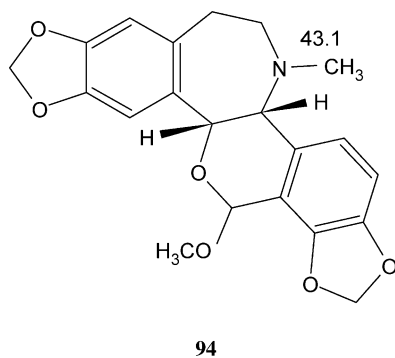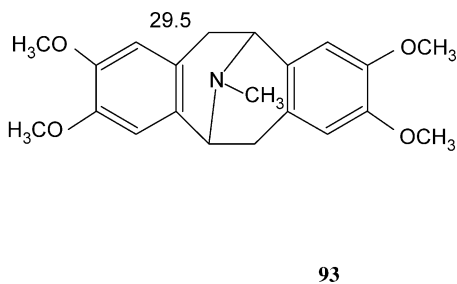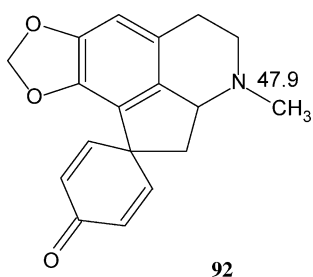
Macaridine – a constituent of Lepidium meyenii 'maca'. Muhammad and co-workers,[127] in an investigation of *Lepidium meyenii* 'maca' isolated and characterized maciridine (**96**) in part through the use of long-range ^{1}H–^{15}N data. The lack of an NH moiety in the structure was ruled out by the lack of an ∼90 Hz doublet that would have been observed if the structure contained an NH. The shift of the single ^{15}N in the structure was observed at 159.7 ppm, far upfield of a pyridine and considerably downfield of what would be expected for a piperidine-like NH even with the double bonds in the ring. The ^{15}N chemical shift is, however, consistent with the presence of an *N*–OH substituent even though no correlation was observed from the hydroxylamine proton to the nitrogen.

96
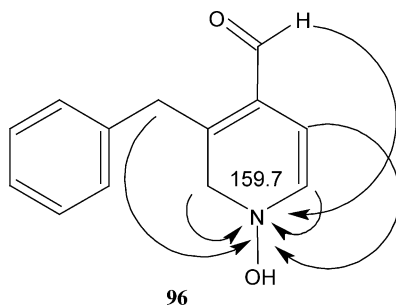
Pyridoacridine alkaloids isodiplamine and lissoclinidine. Copp and co-workers[128] reported the isolation of two new pyridoacridine analogues, isodiplamine (**97**) and lissoclinidine (**98**) from the New Zealand ascidian *Lissoclinum notti*. The authors utilized 6 Hz optimized ^{1}H–^{15}N HMBC data in the process of characterizing these novel compounds. The ^{15}N chemical shifts and observed long-range couplings are shown on the structures.

97   **98**
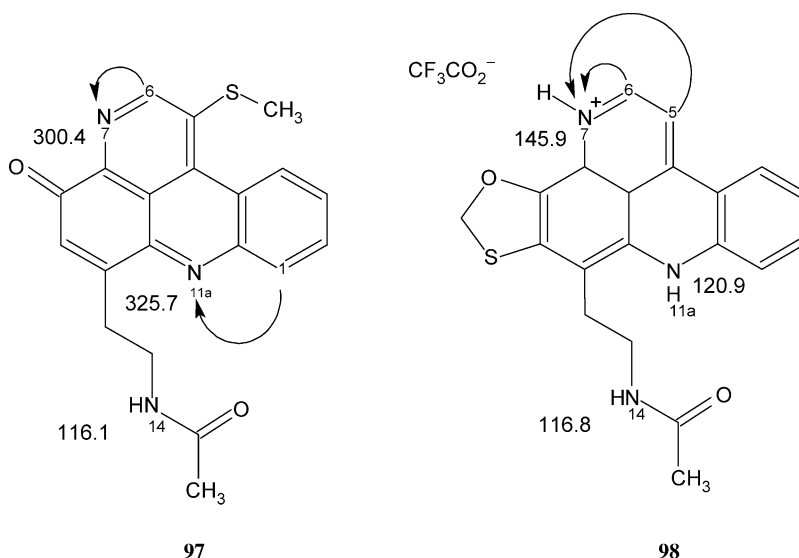
Palmitine and berberine isolation artifacts. Marek and co-workers[129] have reported a study of the structures of common isolation artifacts of the widely distributed alkaloids palmitine and berberine (**99**) that are frequently formed from adduction of simple solvent molecules during isolation. The authors reported ^{15}N chemical shift assignments for the reported molecules that were established from ^{1}H–^{15}N HMBC data (Table 5).

99
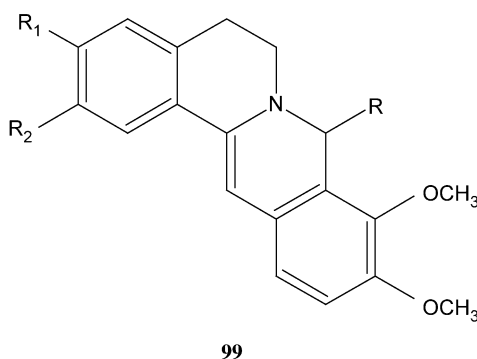
Table 5. ^{15}N chemical shift assignments for isolation artifacts of palmitine and berberine (**99**)[129]

Substituents			^{15}N shift	Solvent
R	R$_1$	R$_2$		
–OH	–OCH$_3$	–OCH$_3$	88.5	CD$_2$Cl$_2$
–OCH$_3$	–O–CH$_2$–O–		83.6	CD$_2$Cl$_2$
–CCl$_3$	–O–CH$_2$–O–		64.9	CD$_2$Cl$_2$
–CCl$_3$	–O–CH$_2$–O–		65.0	CDCl$_3$
–CCl$_3$	–O–CH$_2$–O–		64.6	DMSO-d_6

Tetrahydroisoquinoline alkaloids and 2-deoxyribonolactones from Aristolochia arcuata. Lopes and co-workers[130] made use of long-range ^{1}H–^{15}N HMBC data in differentiating between the previously assigned structure of 6,7-dihydroxy-1,1-dimethyl-isochromane (**100**)[131] and the revised structure, 6,7-dihydroxy-1,1-dimethyl-1,2,3,4-tetrahydroisoquinoline (**101**). The observation that the ^{13}C chemical shifts of C1 and C3 in the structure of the isolate were lower than expected for carbinolic carbons prompted the authors to investigate more rigorously. Conventional ^{1}H–^{13}C HMQC and HMBC data provided the means of assembling the carbon skeleton of the molecule while ^{1}H–^{15}N HMBC data confirmed that the molecule was a 1,2,3,4-tetrahydroisoquinoline as shown by **101**.

100   **101**
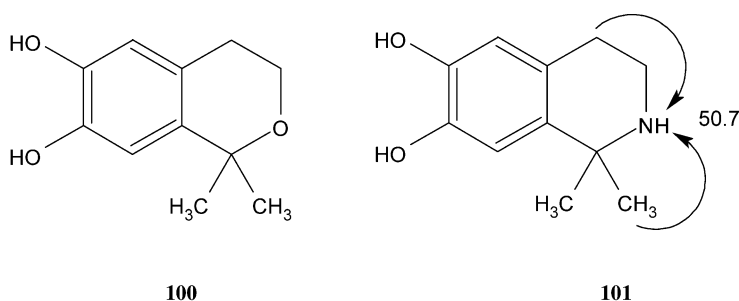
Ancisheynin, a novel naphthylisoquinolinium alkaloid from Ancistrocladus heyneanus. Plants of the genera *Ancistrocladaceae* and *Dinocophyllaceae* are rich sources of naphthylisoquinoline alkaloids that vary in the degree of hydroxylation and O-methylation. Butler and co-workers[132] reported the isolation and structural characterization of a novel naphthylisoquinolinium alkaloid, ancisheynine (**102**) from *Ancistrocladus heyneanus*. The authors used long-range ^{1}H–^{15}N HMBC data to confirm the linkage between the naphthyl and isoquinoline subunits as C8′–N2 based on long-range correlations from H7′, and the 1- and 3-methyl groups and H4 resonance to the isoquinolinium nitrogen resonating at 197.0 ppm.

102
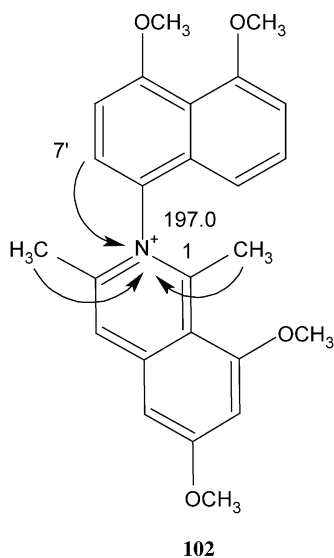
5.1.3.2. Diazoles, triazoles, diazines, triazines and related systems

Barrenazine A and B. Chill *et al.*[133] reported the utilization of long-range ^{1}H–^{15}N HMBC data in the characterization of the structures of barrenazine-A and -B, **103**, two new cytotoxic alkaloids from an unidentified tunicate collected off the Barren Islands, Madagascar. The authors varied much more widely the optimization of the ^{1}H–^{15}N HMBC experiment than is typical of natural product structure elucidation efforts. The authors report acquiring data with optimizations of 60, 90, 120, and 150 ms and that further, the best results were obtained with the pair of compounds characterized with a 120 ms optimization was employed. Barrenazine-A, R=–CH$_2$–CH$_3$, gave the long-range correlations and chemical shift assignments shown with the structure. The long-range ^{1}H–^{15}N HMBC data also allowed the authors to differentiate between the assigned structure, **103**, and the alternative isomeric structure, **104**. Long-range ^{1}H–^{15}N HMBC data were neither recorded or necessary for the characterization of the isomeric alkaloid barrenazine-B (R=–CH=CH$_2$).

103
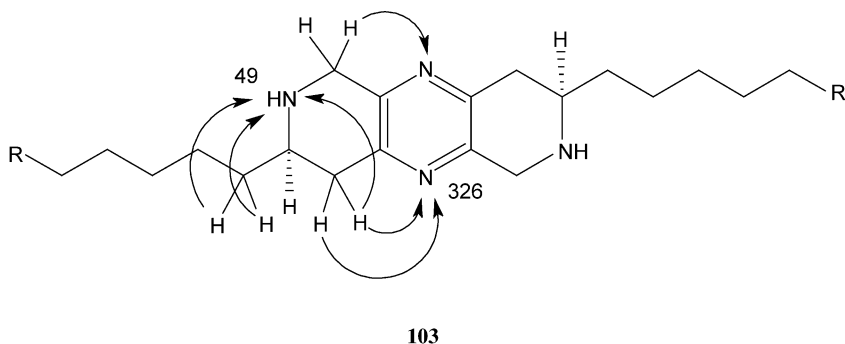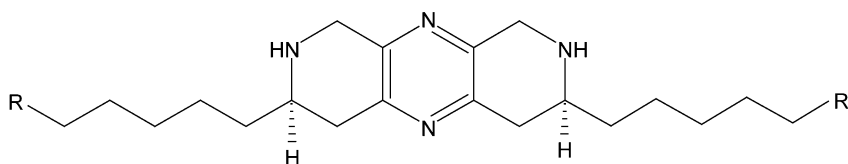
104

5.1.4. *Cyclic peptide natural products*

Argifin. Ōmura and co-workers[134] reported the application of long-range ^{1}H–^{15}N correlation data in the determination of the structure of the cyclic peptide argifin (**105**) isolated from a culture broth of the fungal strain *Gliocladium* sp. FTD-0668. The authors unfortunately did not report any details of the optimization of the proton–nitrogen experiments performed.
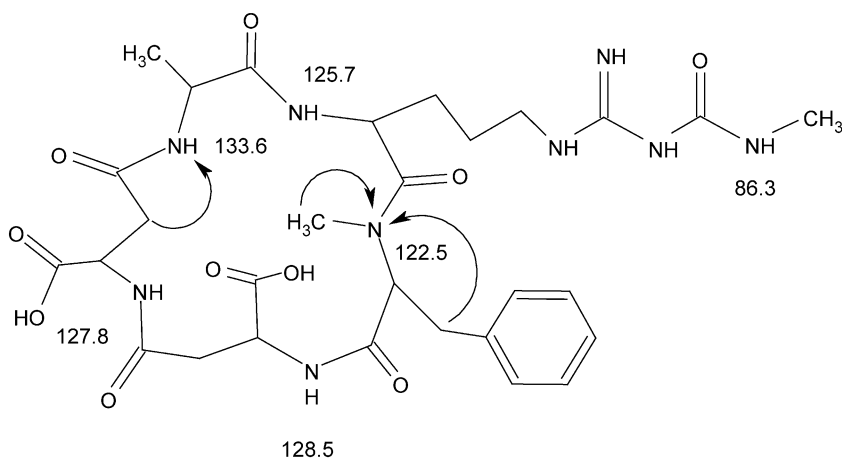
105

Microcyclamide. Ishida *et al.*[135] reported the utilization of long-range ^{1}H–^{15}N HMBC data in the characterization of the cytotoxic cyclic hexapeptide microcycla-mide (**106**), from the cyanobacterium *Microcystis aeruginosa*. The authors also noted that the availability of these data were crucial to successfully linking the thiazole–isoleucinyl subunit of the structure to the methyloxazole–alanyl subunit during the elucidation of the structure. The authors also noted that the HMBC data provided confirmation of the eight nitrogen atoms in the empirical formula of the molecule. ^{15}N chemical shifts in their original report were referenced to formamide.

106
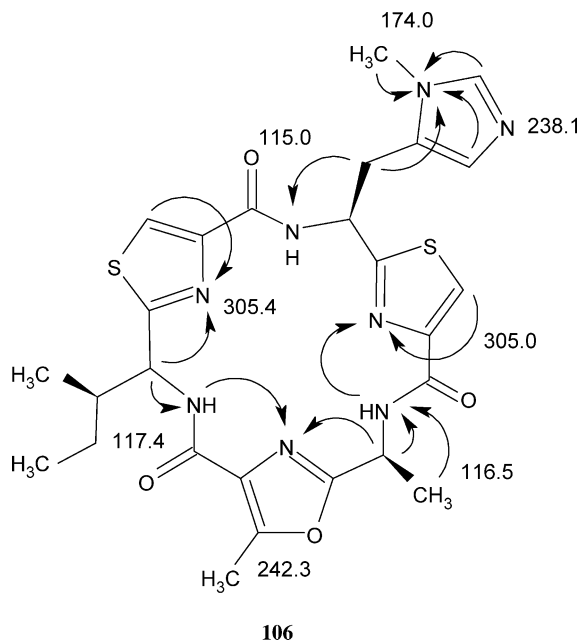
Lyngbyabellin B. Gerwick and co-workers[136] also employed ^{1}H–^{15}N heteronculear correlation data in assembling the structure of the cyclic peptide lyngbyabellin B (**107**). ^{1}H–^{15}N PEP-HSQC-TOCSY data, which are not commonly employed in natural product structure elucidation studies, were utilized to assemble the individual amino acid subunits of the structure. Unfortunately, neither the ^{15}N chemical shifts nor the observed long-range

107
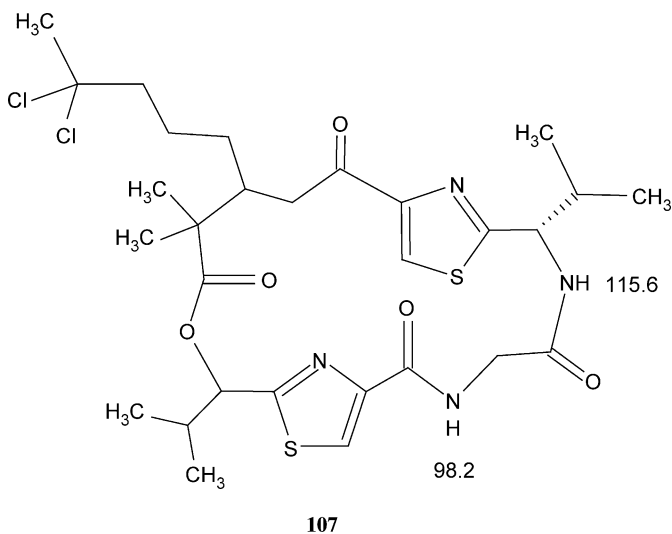
couplings were reported in the article itself. Amide ^{15}N chemical shifts shown were extracted visually from the ^{1}H–^{15}N HMBC spectrum published as supplemental information to the report. The ^{1}H–^{15}N HMBC spectrum in the supplemental information did not show a region where responses for the thiazole and thiazoline nitrogen resonances would be observed.

Cis, cis- and *trans, trans-ceratospongamide*. Gerwick and co-workers[137] reported the isolation of additional cyclic peptides in 2000. *Cis*, *cis-* and *trans*, *trans-*ceratospongamides (**108**), which are bioactive cyclic heptapeptides, were isolated from the Indonesian red algae *Ceratodictyon spongium* and the symbiotic sponge *Sigmadocia symbiotica*. The authors used HMQC-TOCSY data to establish the individual spin systems present in the molecule in conjunction with long-range ^{1}H–^{15}N HMBC data to link the individual spin systems together as shown on the structure. It should be noted that on a comparative basis, HSQC-TOCSY spectra offer much better resolution than the corresponding HMQC-TOCSY variant, and that the former should be the preferred choice for structure elucidation studies.[138] Although the authors did not report ^{15}N chemical shift data in their study, they did note that the ^{1}H–^{15}N HMBC correlation data were particularly useful in establishing the Pro-thiazole-Phe sequence in the molecular structure.
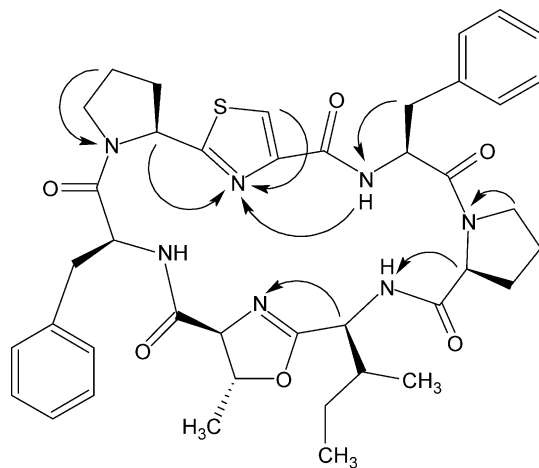
108

In the original report of the structure,[137] the authors stated that heating *cis, cis-*ceratospongamide in DMSO converted it to the *trans, trans* isomer. A subsequent total synthesis by Yokokawa and co-workers[139] showed that heating *cis, cis-*ceratospongamide in DMSO, rather than converting it to the *trans, trans-*isomer instead converted it to *trans, trans-*[D-allo-Ile]-ceratospongamide on the basis of total synthesis.

Nostocyclopeptides A1 and A2. Moore and co-workers[140] employed long-range ^{1}H–^{15}N data in the characterization of the first member of the nostocyclopeptide series. The determination of the structure of nostocyclopeptide A1 (**109**) relied on the use of long-range correlation data. From an 8 Hz optimized ^{1}H–^{15}N HMBC spectrum, the presence of an imine moiety in the structure was established and positioned within the skeletal framework. The acquisition of a 4 Hz optimized spectrum gave additional

long-range correlations, the most noteworthy of which were from the H3′ methylene proton to the tyrosine amide nitrogen and from the H2 resonance of the 2-methylproline to the 2-methylproline nitrogen resonance. Following the determination of the structure of nostocyclopeptide A1, it was possible to assemble the structure of the related cyclic peptide, A2, without resorting to long-range ^{1}H–^{15}N data.

109
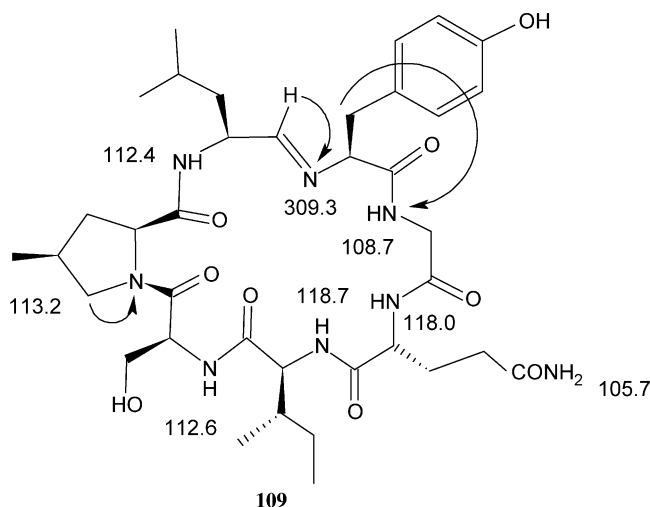
Application of CROPSY to gramicidin-A. Farès *et al.*[141] reported a study of the cyclic peptide antibiotic gramicidin-A that employed cross polarization heteronuclear shift correlation (CROPSY) as a means of exploring the dispersion and resolution of amide signals of membrane polypeptides. The spectrum was recorded in dimyristoyl-phosphati-dylcholine (DMPC-d_{67}). While this is not specifically an application of long-range ^{1}H–^{15}N spectroscopy, the paper is interesting nevertheless in that it does illustrate another possible direction in which proton–nitrogen correlation spectroscopy may diverge.

Characterization of JM47, a cyclic tetrapeptide HC-toxin analogue. Burgess and co-workers[142] extracted a known metabolite, enniatin B and a new cyclic tetrapeptide,

110
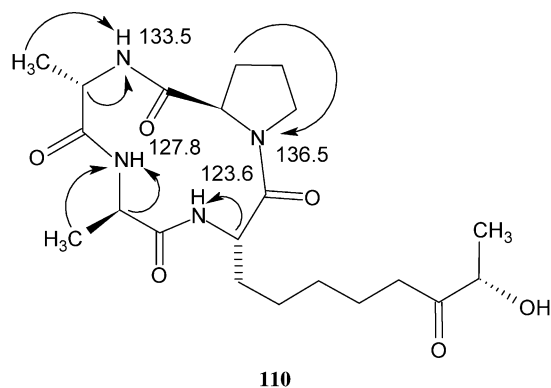
JM47 (**110**), from brown rice cultures of a marine fungus identified as a *Fusarium* species isolated from the marine algae *Codium fragile*. The structure of the cyclic tetrapeptide was characterized using both ^{1}H–^{15}N HSQC and HMBC data. The molecule contains one unnatural amino acid, (*2S,9S*)-2-amino-8-oxo-9-hydroxydecanoic acid in its structure.

Nocathiacins. Leet and co-workers[143] reported the isolation and characterization of several new thiazolyl peptide antibiotics from *Nocardia* sp. The authors utilized long-range ^{1}H–^{15}N HMBC data in the determination of the structure of nocathiacin-I (**111**) but were able to establish the structures of II and III without resorting to long-range ^{1}H–^{15}N data once the structure of the first member of the series was determined. Key long-range

111
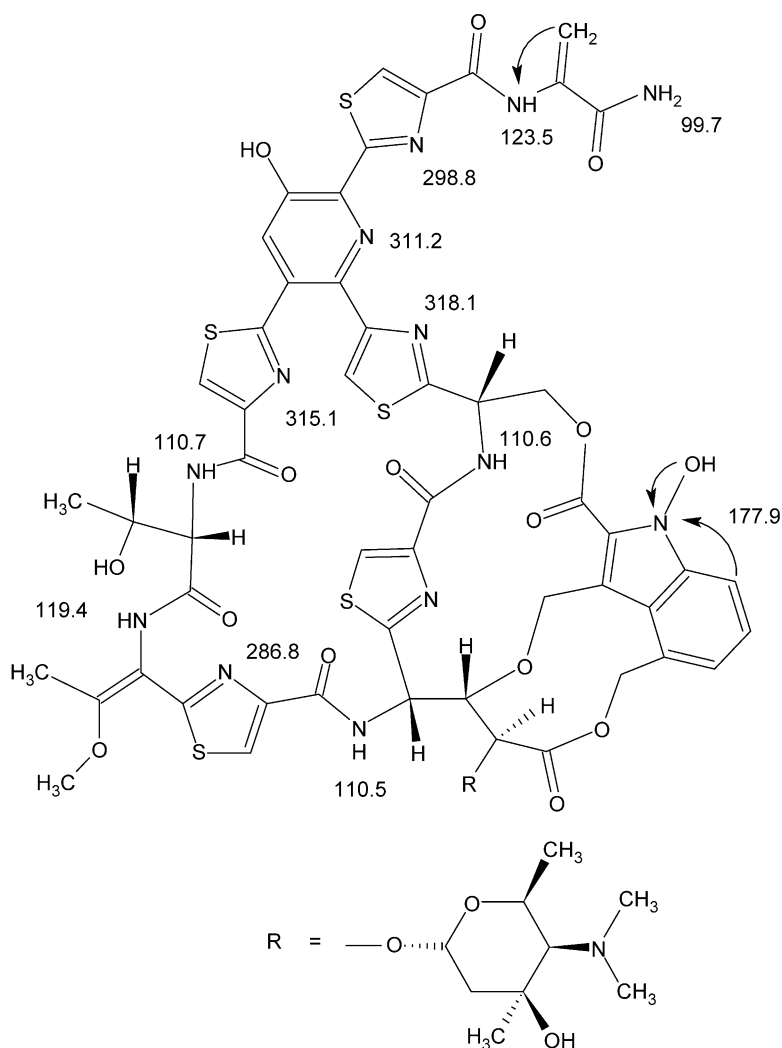
correlations to ^{15}N are shown on the structure. The interested reader is referred to the original reference, where further long-range correlation information is presented.

In a corollary report also published in 2003, Constantine, *et al.*,[144] were able to establish the conformation and absolute configuration of this complex molecule by a combination of NMR spectroscopic and chiral capillary electrophoresis methods, the former utilizing ^{1}H–^{15}N HSQC data.

Protease inhibitors from a toxic waterbloom of the cyanobacterium Aplanktothrix rubescens. Grach-Pogrebinsky *et al.*[145] in late 2003 reported the isolation and structural characterization of several novel protease inhibitory cyclic peptides and several known compounds isolated from a toxic waterbloom in Slovenian Lake Bled of the cyanobacterium *Aplanktothrix rubescens*. Long-range ^{1}H–^{15}N HMBC data were utilized in the determination of two of the new planktopeptin structures reported by the authors. The structure of planktopeptin BL1125 is shown by **112** and that of planktopeptin BL1061 is shown by **113**.

112

113
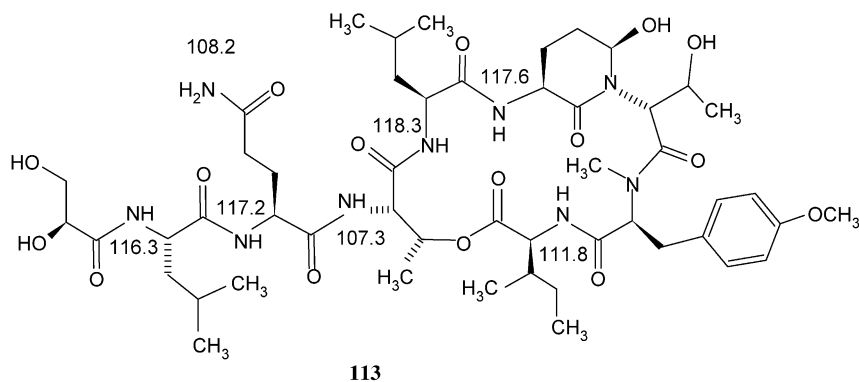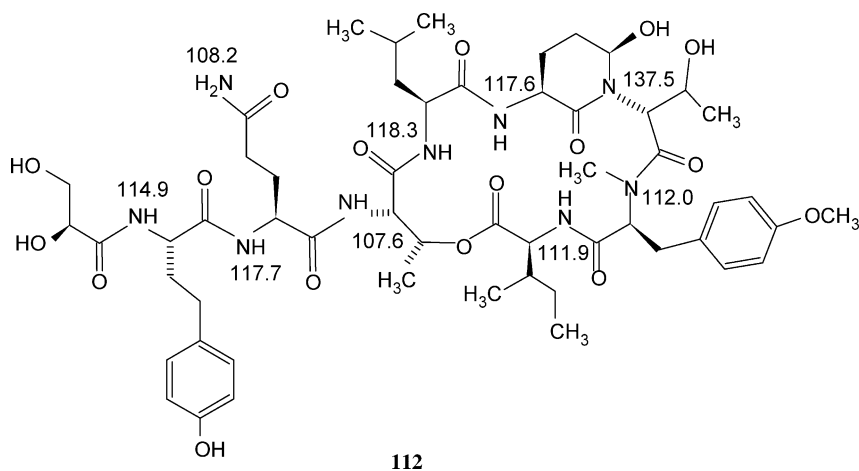
5.1.5. *Purines, pterins and related natural products*

Toxoflavin and fervenulin. Koshino and co-workers[146] explored the utility of long-range ^{1}H–^{15}N 2D NMR methods in the structural characterization of toxoflavin and fervenulin. Prior to their study, antibiotics in the pyrimidotriazine class of molecules had typically been characterized by single crystal X-ray methods or synthesis since the high nitrogen content of these molecules made the assembly of the substructural components very difficult. Observing long-range ^{1}H–^{15}N correlations necessary to verify these structures required Koshino and co-workers to resort to very long delay optimization for the long-range magnetization transfers. Delays of 150, 225 and 300 ms were used in this study to observe the various long-range correlations shown on the structures of toxoflavin (**114**) and fervenulin (**115**). In the specific case of the assignment of the N8 resonance of **114** at 172.8 ppm, the 300 ms data were necessary to observe the $^4J_{NH}$ correlations from the N1-methyl and N6-methyl groups since there are no $^2J_{NH}$ or $^3J_{NH}$ correlations possible to the N8 resonance.

114   **115**
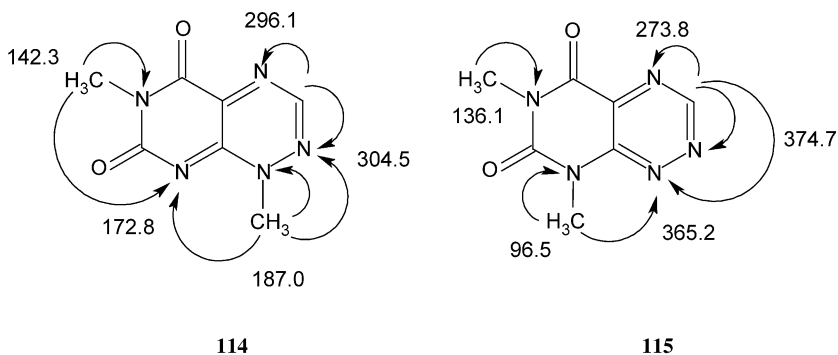
2-Methylfervenulon. Pallen and co-workers[147] utilized long-range ^{1}H–^{15}N HMBC data optimized for 8 and 2 Hz to characterize three novel compounds from *Streptomyces* sp. IM 2096. The first of these, **116**, was a novel glycocyamidine. As would be expected

116
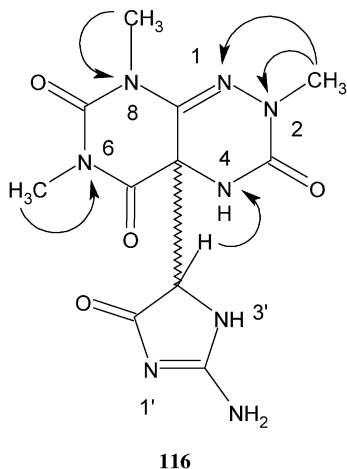
Table 6.   [15]N chemical shifts of 2-methylfervenulon (**117**) and related compounds as the free base and salt[147]

Position	116		117		118	
	Free base	TFA salt	Free base	TFA salt	Free base	TFA salt
N1	285.3	286.0	323.2	314.6	293.3	288.1
	(279.8)[a]	(283.1)[a]				
N2–Me	130.9	130.8	187.3	181.9	166.7	163.8
	(132.1)	(130.8)				
N4–H	81.3	77.4	Not obs.	Not obs.	–	231.9
	(81.3)	(78.6)				
N5–Me	–	–	–	–	121.8	122.8
N6–Me	143.9 (142.0)	142.7	155.3	153.6	–	–
		(142.0)				
N7–Me	–	–	–	–	105.2	106.5
N8–Me	108.7	107.4	109.8	110.5	–	–
	(111.0)	(109.1)				
N2′–NH$_2$	–	87.2	–	–	–	–
		(87.0)				
N3′	84.7	86.9	–	–	–	–
	(85.7)					

[a]Possible diastereomer.

given the structure, the use of the small 2 Hz optimization was necessary to observe some of the long-range correlations possible to assign the ^{15}N shifts reported in Table 6. 2-Methylfervenulon (**117**) and the biologically inactive imidazo[4,5-*e*]-1,2,4-triazine (**118**) were also isolated and the authors speculated that **118** may have been a degradation product of 2-methylfervenulon (**117**).

117   **118**
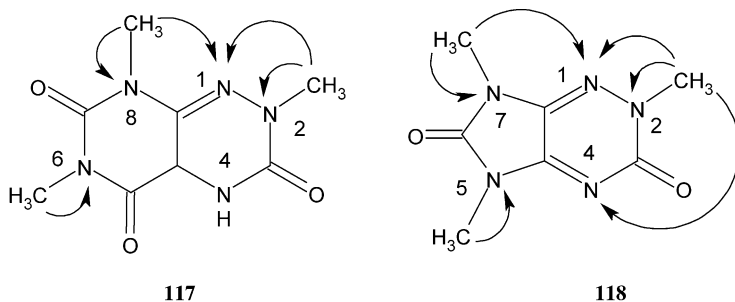
Characterization of 3,7-dimethylguanine. Ireland and co-workers[148] utilized long-range ^{1}H–^{15}N HMBC data in the elucidation of the structure of 3,7-dimethylguanine (**119**) from the Phillipine sponge *Zyzzya fuliginosa*. The authors utilized a combination of long-range [1]H–[13]C and [1]H–[15]N experiments, both optimized for 8 Hz, to establish the methyl substitution.
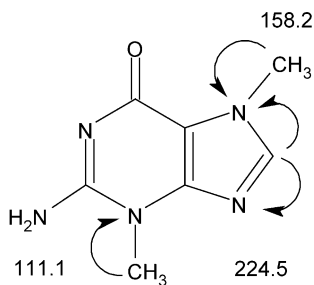
119

Novel pterins from a Eudistoma species Ascidian. In another report, Ireland and co-workers[149] reported the isolation and structural characterization of several novel pterins from a methanol extract of an Indonesian *Eudistoma* sp. ascidian. In characterizing the 1,3,O^7-trimethylisoxanthopterin skeleton, **120**, the authors acquired both 10 and 4 Hz optimized ^{1}H–^{15}H HMBC data. From these experiments, the authors were able to assign three of the four nitrogens as shown on the structure. The chemical shift of the N5 resonance at 338 ppm was noteworthy in that it is shifted considerably downfield of the corresponding N9 resonance at 230 ppm of the known compound, **121**. The downfield shift observed for N5 of **120** vs. the N9 resonance of **121** is fully consistent with the pyrazine moiety incorporated into the structure of **120** (see Section 5.1.3.2).
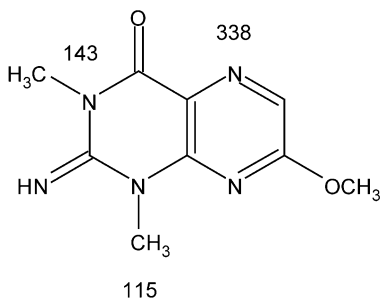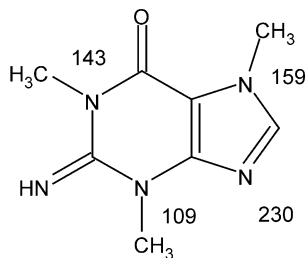
120   **121**

5.1.6. *Miscellaneous natural product studies*

N-Acetylpalytoxin. Iwashita and co-workers[150] in reporting the complete ^{1}H, ^{13}C and ^{15}N spectral assignment of *N*-acetylpalytoxin (**122**) have succeeded in what is undoubtedly the most monumental natural product spectral assignment exercise of all time. Palytoxin is a huge molecule with an empirical formula of $C_{129}H_{223}N_3O_{54}$. The assignment of the ^{15}N resonances is a trivial undertaking relative to the ^{1}H and ^{13}C assignment challenges, which required the authors to resort to 3D heteronuclear NMR experiments, which is almost never done for natural products because of the inherent insensitivity of these experiments that were developed for use with labeled proteins.

Nevertheless, the authors did complete the total assignment, including the three nitrogen resonances as shown.
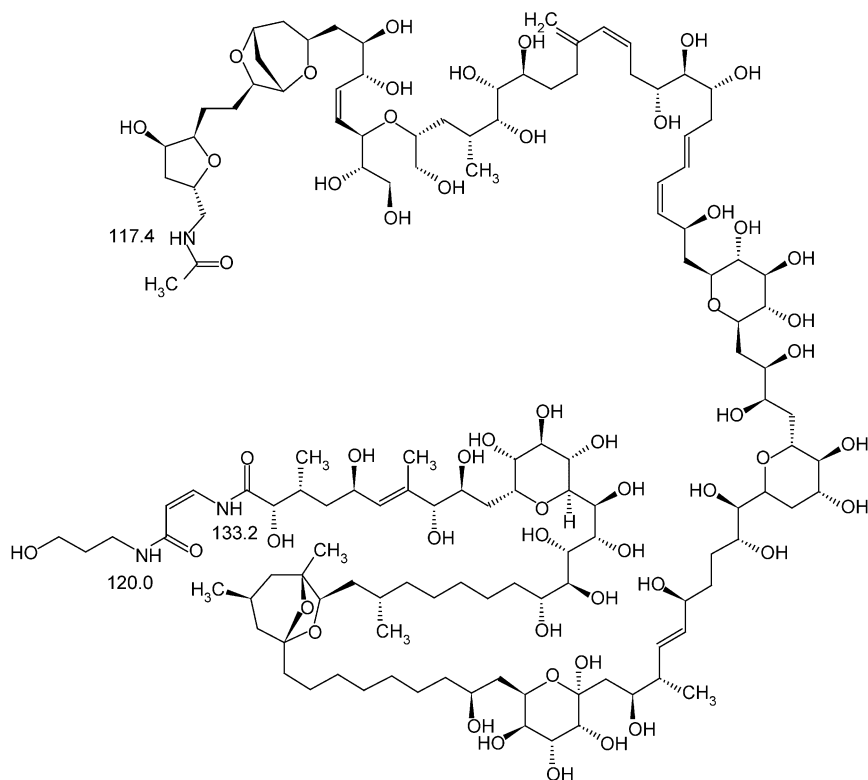
122

Exiguamide. Uy and co-workers[151] reported a new spirocyclic sesquiterpene, exiguamide (**123**) from the marine sponge *Geodia exigua* that required the use of ^{1}H–^{15}N HMBC data to confirm the structure. The presence of the formylamino group was
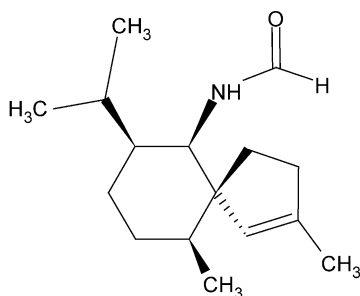
123

confirmed by a correlation from the formyl proton to the amino nitrogen. Unfortunately, the authors did not report the ^{15}N shift of the formylamino group.

Identification of the axial ligand of Cobalt(III)bleomycin. Xia et al.[152] reported a study directed at the identification of the internal axial ligand of hydroperoxy–cobalt(III)–bleomycin using a combination of ^{1}H–^{15}N HSQC and HMBC data. Using this approach, the authors were able to assign all the non-aromatic ^{15}N resonances of bleomycin, **124**, as well as deglycobleomycin and the hydroperoxide–cobalt(III) complexes. Readers interested in the ^{15}N chemical shift data for the aromatic nitrogen resonances of bleomycin are referred to the much earlier work of Naganawa and co-workers.[153] Assigned ^{15}N chemical shifts for bleomycin-A$_2$, deglycobleomycin-A$_2$ and the hydroproxy-Co(III) complexes of both are presented in Table 7.

124
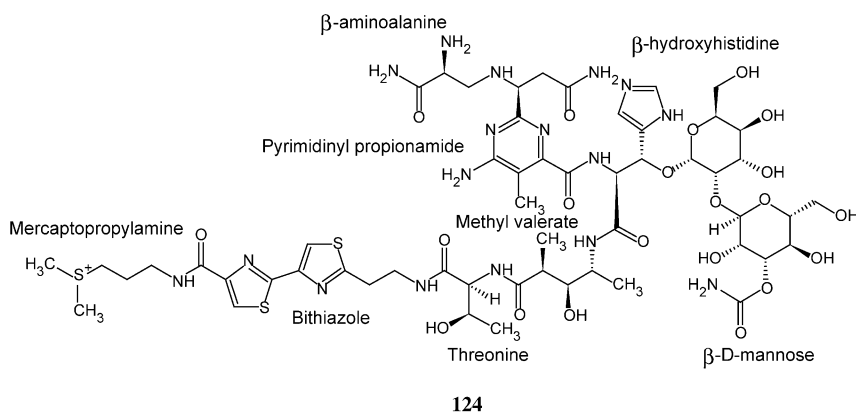
Table 7. Protonated ^{15}N chemical shift assignments for bleomycin-A$_2$ (**124**), deglycobleomycin-A$_2$ and the hydroperoxy–Co(III) complexes of both[152]

Position	Protonated ^{15}N chemical shift assignments			
	Bleomycin-A$_2$	Deglycobleomycin-A$_2$	HO$_2$–CO(III)–bleomycin-A$_2$	HO$_2$–CO(III)–deglycobleomycin-A$_2$
Mercaptopropyl-amine	116.8	116.6	115.9	116.3
Bithiazole amide	119.4	119.4	117.6	117.9
Threonine	118.4	119.2	114.4	115.4
Methyl valerate	133.9	136.0	133.6	133.7
β-Hydroxyhistidine	118.8	120.3	94.8	–
β-Aminoalanine amide	108.9	108.7	108.5	110.2
Pyrimidinyl propionamide amide	113.6	113.1	112.5	111.6
Mannose amide	75.9	–	76.1	–
Pyrimidinyl propionamide amino	84.1	–	96.2	94.4
β-Aminoalanine–NH	35.1 or 36.5	–	11.2	12.9
β-Aminoalanine–NH$_2$	36.5 or 35.1	–	−9.7	−7.8

5.2. Long-range ^{1}H–^{15}N heteronuclear shift correlation studies involving synthetic compounds

5.2.1. *Studies of non-ring nitrogen containing compounds*

Structural characterization of α-phenylsulfonyl-N-arylacetamides. Kolehmainen and co-workers[164] reported the structural characterization of a series of α-phenylsulfonyl-*N*-arylacetamides of the type shown by **125** using multinuclear NMR methods. Among the NMR data employed by the authors were long-range ^{1}H–^{15}N HMBC spectral data. The ^{15}N chemical shift assignments are collected in Table 8.
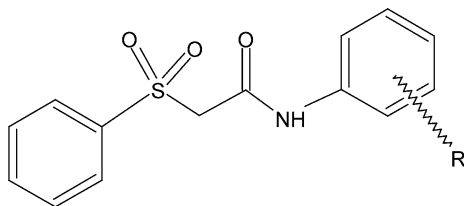
125

Structure assignment of aminoconduritols. Hudlicky and co-workers[155] reported the utilization of ^{1}H–^{15}N HMBC data in the synthesis of aminoconduritol analogues. One of the intermediates, **126**, was characterized using long-range ^{1}H–^{15}N. Curiously,
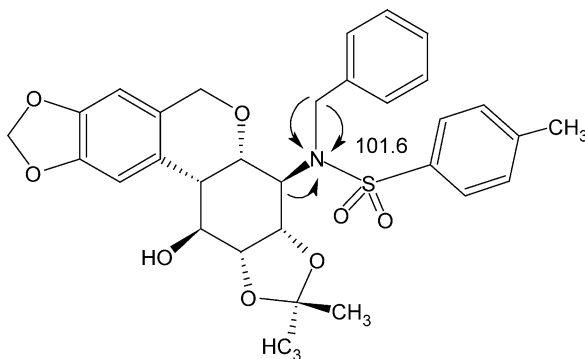
126

Table 8. ^{15}N chemical shift assignments of a series of α-phenylsulfonyl-*N*-arylacetamides, **125**[154]

Substituent	Acetamide ^{15}N	Other ^{15}N
–H	132.2	–
3-OCH$_3$	132.7	–
4-NO$_2$	132.4	356.4
4-N(CH$_3$)$_2$	131.0	43.0

despite our experience which has shown that long-range ^{1}H–^{15}N HMBC experiments can be performed on very small samples, the authors report synthesizing 100 mg of **126** to obtain 'enough sample' to perform the ^{1}H–^{15}N HMBC experiment. Clearly a sample of only a couple of mg of material with even a conventional 5 mm inverse detection probe with a 400 or 500 MHz spectrometer would have been more than adequate to allow the data to be acquired overnight.

4-Fluoroanilines: *synthesis and decomposition*. Gawinecki and co-workers[156] reported the synthesis of a series of 4-fluoroanilines as well as the results of a study of their decomposition. The authors used long-range ^{1}H–^{15}N HMBC data in the characterization and study of the decomposition of these molecules. ^{15}N chemical shifts are collected in Table 9 for the 4-fluorinated anilines synthesized in the study. The reader interested in the applications of long-range ^{1}H–^{15}N HMBC data in the decomposition study is referred back to the original report for further details.

127
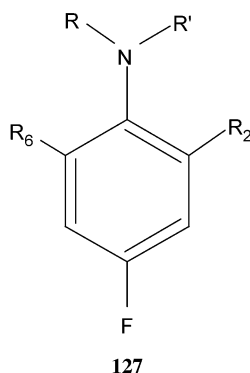
Table 9. ^{15}N chemical shifts of a series of 4-fluoroanilines (**127**)[156]

Substituents				^{15}N shift
R	R$'$	R$_2$	R$_6$	
–H	–H	–H	–H	50.0
–CH$_3$	–H	–H	–H	48.3
–H	–CH$_3$	–H	–H	47.3
–H	–C$_2$H$_5$	–H	–H	66.3
–H	–CH$_3$	–CH$_3$	–H	40.1
–H	–C$_2$H$_5$	–CH$_3$	–H	52.3
–H	–C$_2$H$_5$	–C$_2$H$_5$	–H	66.3
–CH$_3$	–CH$_3$	–CH$_3$	–H	66.7
–H	–(CH$_2$)$_4$–		–H	68.4
–H	–(CH$_2$)$_5$–		–H	63.9
–(CH$_2$)$_2$–		–CH$_3$	–H	61.3
–(CH$_2$)$_3$–		–H	–H	58.3
–(CH$_2$)$_3$–		–CH$_3$	–H	51.8
–(CH$_2$)$_3$–		–(CH$_2$)$_3$–		60.9
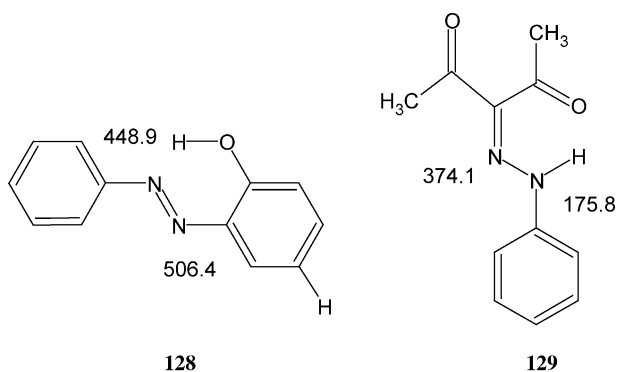
Scheme 5.
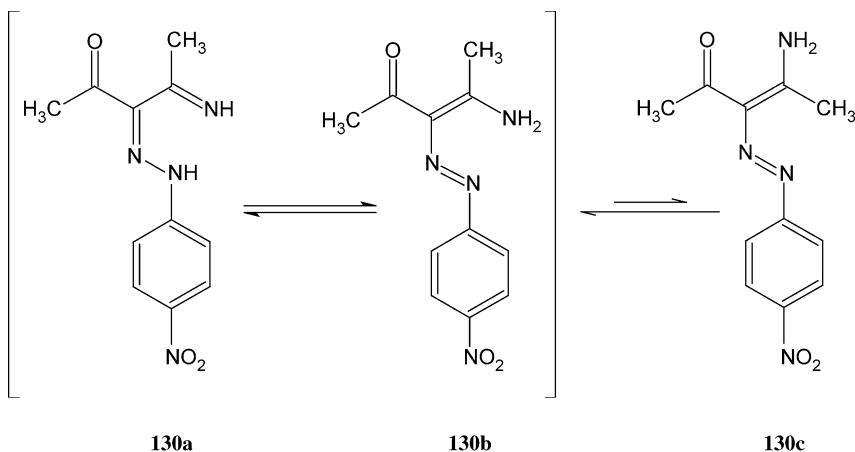
Tautomerism and hydrogen bonding in reaction products from 4-aminopent-3-en-2-one. Šimůnek and co-workers[157] utilized long-range ^1H–^{15}N correlation to establish the major and minor tautomeric forms of 4-aminopent-3-en-2-one in solution. As model compounds, the authors employed the diazo and hydrazone compounds, **128** and **129** whose ^{15}N chemical shifts are shown on the structures. Compound **130** was found to be only sparingly soluble in deuterochloroform and despite ^{15}N labeling, the authors were only able to collect ^1H–^{15}N HMBC data for the major form in solution. The ^{15}N chemical shifts observed were 315.3 and 447.1 ppm and on this basis, the authors conclude that **130** exists in solution as an equilibrium mixture of the azo and hydrazone forms, as shown in Scheme 5. Using the ^{15}N data for **128** and **129**, the authors were able to calculate that **130** was 45% in the hydrazone form and 55% in the azo form.

Selective conversion of O-succinimidyl carbamates to N-(O-carbamoyl)-succinmono-amides and ureas. Vasilevich and co-workers[158] utilized long-range ^1H–^{15}N

heteronuclear shift correlation data to characterize reaction products in the conversion of *O*-succinimidyl carbamates to the corresponding *N*-(*O*-carbamoyl)-succinmonoamides and ureas. ^{15}N chemical shift assignments for the various compounds elaborated in this study are shown on the structures.
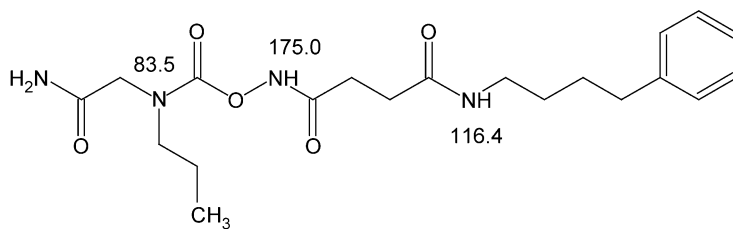
131
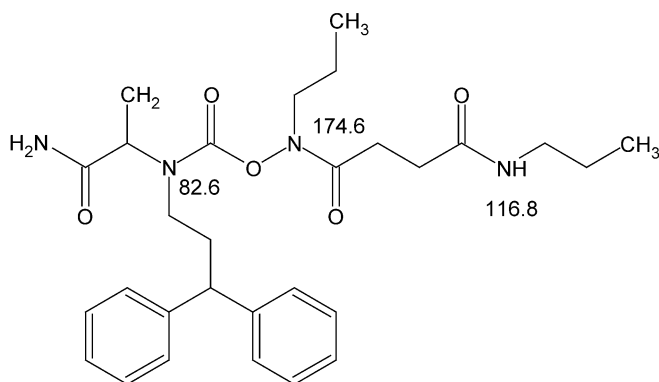
132
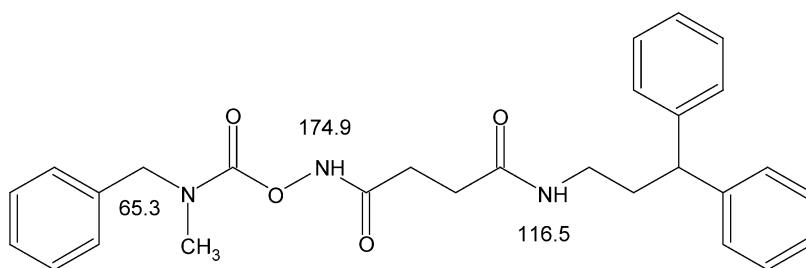
133
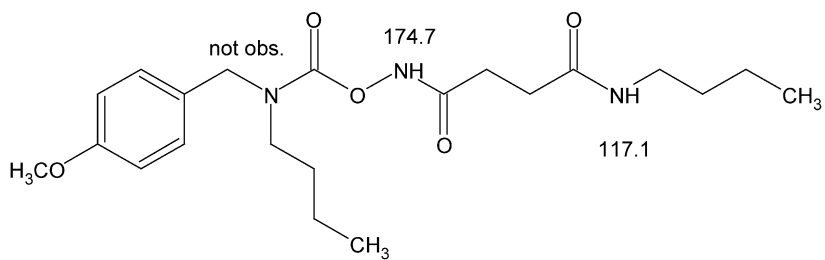
134
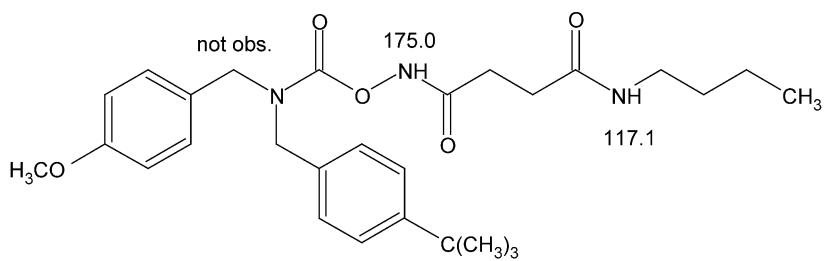
135
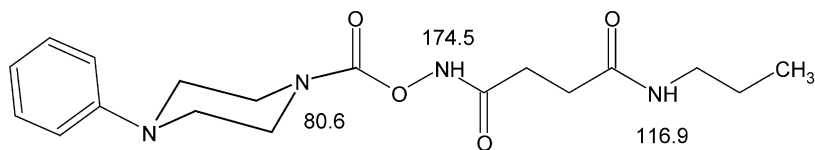
136
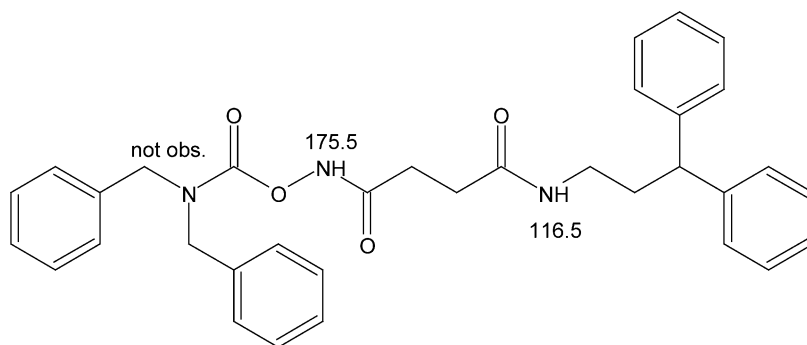
137
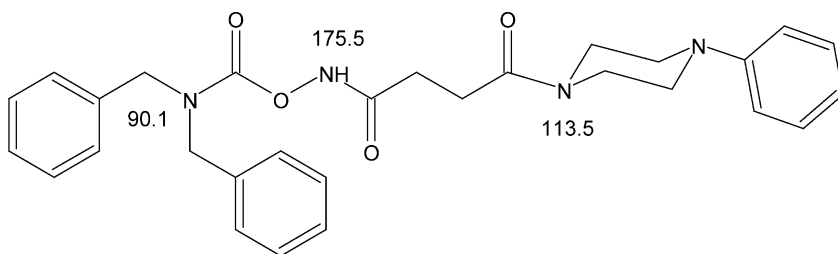
138
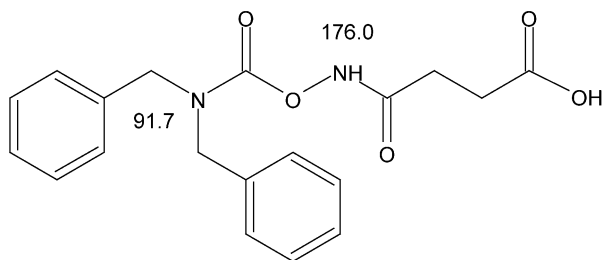
139
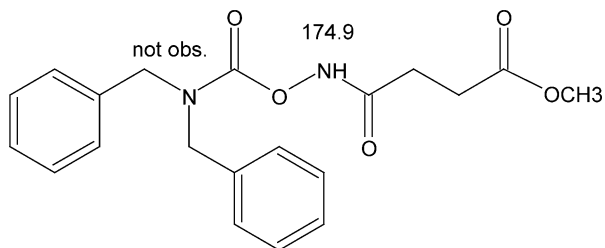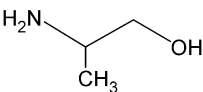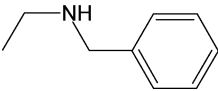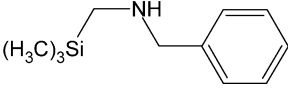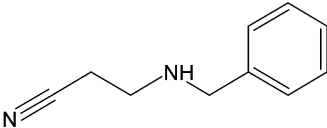
140

Investigation of the robustness of ^{15}*N-optimized CIGAR-HMBC*. Kline and Cheatham[21] in developing a ^{15}N-optimized variant of CIGAR-HMBC (see Section 2.2) extensively applied the experiment in an effort to determine its robustness relative to conventional ^{1}H–^{15}N HMBC for structural characterization. ^{15}N assignments reported by the authors for a series of anilines are reported in Table 10. ^{15}N chemical shifts for a series of primary and secondary amines are collected in Table 11; shift data for a series of pyridines are collected in Table 12; and finally, data for a series of pyrazoles and imidazoles are gathered in Table 13.

Table 10.   [15]N chemical shifts for a series of anilines measured using ^{15}N-optimized CIGAR-HMBC[21]
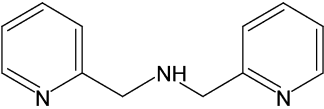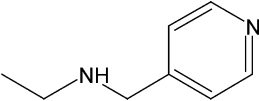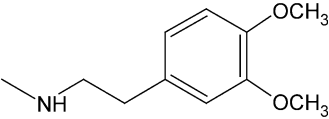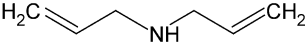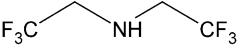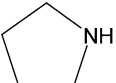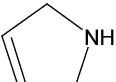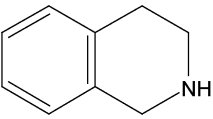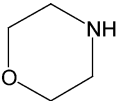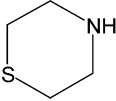
Compound	[15]N chemical shift
3,5-Dichloroaniline	67.6
3-Chloro-4-methoxyaniline	57.8
3,4-Difluoroaniline	61.9
3-Trifloromethoxyaniline	60.4
3-Nitroaniline	61.4
4-Methylaniline	59.4
3-Methoxyaniline	63.1
4-Methoxyaniline	56.4
2-Fluoroaniline	51.5
2-Chloroaniline	62.6
2-Iodoaniline	73.9
3-Chloroaniline	64.7
3-Bromoaniline	64.5
4-Chloroaniline	63.1
4-Bromoaniline	62.6

Table 11.   [15]N chemical shifts for a series of primary and secondary amines measured using ^{15}N-optimized CIGAR-HMBC [21]

Ethyl amine	30.1
n-Propyl amine	25.1
Isopropyl amine	47.9
Sec-butylamine	43.2

36.2

44.9

28.6

39.2
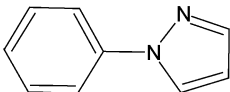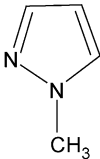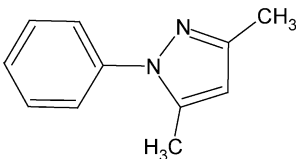
Table 11.   Continued.

	33.3
	40.6
	25.9
N,N-bis-*n*-propylamine	40.1
	40.3
	8.2
	40.3
	25.9
	30.2
	33.1
	36.7

Table 12.   [15]N chemical shifts for a series of pyridines measured using ^{15}N-optimized CIGAR-HMBC[21]
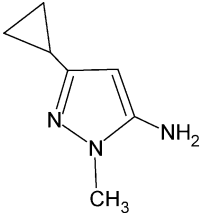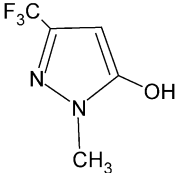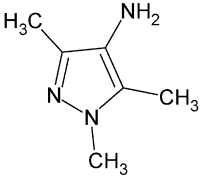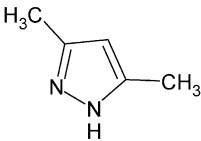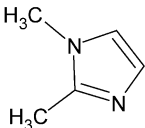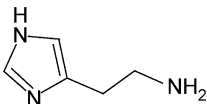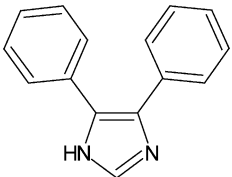
Compound	[15]N chemical shift
4-Methoxypyridine	296.9
4-*t*-Butylpyridine	311.7
2,4-Dimethylpyridine	310.4
2,5-Dimethylpyridine	318.4
2,3-Dimethylpyridine	318.2
3,5-Dimethylpyridine	319.0
2-methyl-5-*n*-Butylpyridine	318.4
3,5-Dinitropyridine	319.5
2-methyl-5-Hydroxypyridine	321.5
2-Fluoropyridine	276.6
2-Chloropyridine	310.0
2-Bromopyridine	318.3
4-Methylpyridine	311.0
3-Methylpyridine	319.2
2-Methylpyridine	318.4
4-Bromopyridine	322.1

Table 13.   [15]N chemical shifts for a series of pyrazoles and imidazoles measured using ^{15}N-optimized CIGAR-HMBC[21]

Pyrazole derivatives	N1	N2
	221.7	–
	205.0	311.5
	215.0	305.7
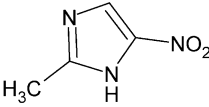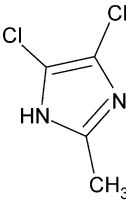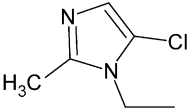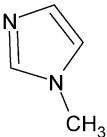
(*continued*)

Table 13.   Continued.

Pyrazole derivatives	N1	N2
	174.5	279.9
	187.1	238.6
	185.7	297.0
	205.5	295.7

Imidazoles	N1	N3
	160.1	261.4
	183.5	288.6
	173.7	266.1

Table 13.   Continued.

Pyrazole derivatives	N1	N2
	177.1	250.9
	174.3	260.9
	175.7	259.9
	164.1	–

17β-Estradiol nitration. d'Ischia and co-workers[159] in early 2004 reported the use of long-range ^{1}H–^{15}N HMBC data in a study of the nitration of 17β-estradiol using ^{15}N labeled nitrate in the presence of various peroxidases. The long-range data were used to differentiate and assign the 2- and 4-nitrogroups.

141
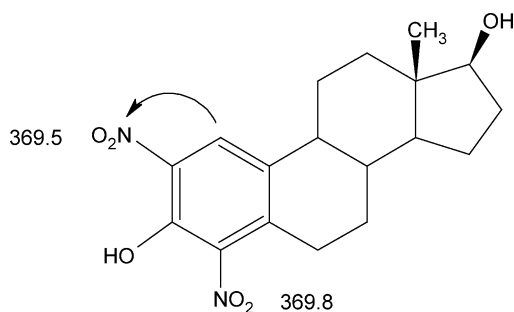
5.2.2. Studies involving five-membered nitrogen containing rings

Determination of the protecting group locations of N^m protected histidines. Heinonen and co-workers[160] reported a practical application of long-range ^{1}H–^{15}N HMBC data for the location of protecting groups of N^m protected histidines. As would be expected for imidazoles in general, the 'pyridine'-like nitrogen resonates considerably downfield of the N-alkylated 'pyrrole'-like nitrogen (Table 14).

142   **143**
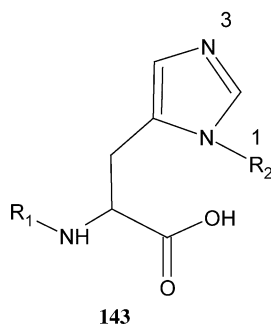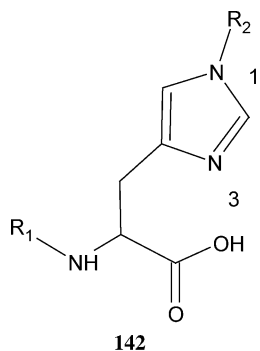
Pyrazolo[1,5-a]pyrimidine. In a study of a series of pyrazolo[1,5-*a*]pyrimidines, Kolehmainen and co-workers[161] reported ^{15}N shift assignments for all but one nitrogen resonance in the series of 10 molecules studied providing a useful compilation of chemical shift data for this series of molecules (Table 15).

144
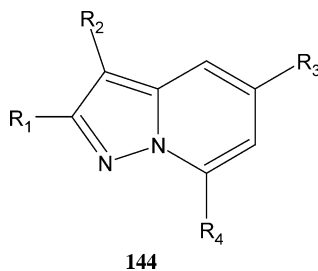
Table 14. ^{15}N chemical shifts of some variously N^m protected histidine analogues[160]

Compound	Protecting groups		^{15}N chemical shifts	
	R$_1$	R$_2$	N1	N3
142	Boc	Boc	188.6	272.2
142	Boc	Tos	207.3	273.8
142	Boc	Dnp	170.1	267.6
142	Fmoc	Trt	188.1	261.5
142	Fmoc	2,6-Dmbz	210.8	274.2
143	Boc	Bom	256.5	179.0
143	Fmoc	2,6-Dmbz	267.0	207.8

Boc, *tert*-butoxycarbonyl; Tos, tosyl; Dnp, 2,4-dinitrophenyl; Fmoc, 9-fluorenylmethoxycarbonyl; Trt, trityl; 2,6-Dmbz, 2,6-dimethoxybenzoyl; Bom, benzyloxymethyl.

Table 15. ^{15}N chemical shifts for a series of pyrazolo[1,5-a]pyrimidines[161]

Substituents				^{15}N chemical shifts		
R1	R2	R3	R4	N1	N4	N7a
$-C_6H_5$	$-H$	$-CF_3$	$-CF_3$	275.1	286.6	213.1
$-H$	$-C_6H_5$	$-CF_3$	$-CF_3$	281.0	287.5	213.8
$-CH_3$	$-C_6H_5$	$-CF_3$	$-CF_3$	278.3	285.7	209.3
$-C_6H_5$	$-H$	$-C(CH_3)_3$	$-CF_3$	269.0	284.5	208.1
$-H$	$-C_6H_5$	$-C_6H_5$	$-CH_3$	271.7	263.6	224.7
$-C_6H_5$	$-H$	$-CH_3$	$-C_6H_5$	266.3	274.1	216.5
$-C_6H_5$	$-H$	$-C_6H_5$	$-CH_3$	266.2	264.1	222.9
$-H$	$-C_6H_5$	$-C_6H_5$	$4-Br-C_6H_4$	273.0	Not obs.	218.8
$-C_6H_5$	$-H$	$-C(CH_3)_3$	$-CF_2CH_2CF_3$	270.6	283.7	209.1
$-CH_3$	$-C_6H_5$	$-CH_3$	$-CF_3$	271.6	286.3	204.7

2,6-Dihydroimidazo[1,5-c]quinazoline-3,5-diones. Klásek and co-workers[162] observed an interesting rearrangement and cyclization during the reaction of a series of quinoline-2,4-diones (**145**) to afford a series of 2,6-dihydroimidazo[1,5-c]quinazoline-3,5-diones (**146**). Because of the rearrangement, coupled with the fact that the imidazo[1,5-c] quinazoline system formed is not common in the literature, the structure was confirmed through the acquisition of long-range ^{1}H–^{15}N HMBC data.

145   **146**
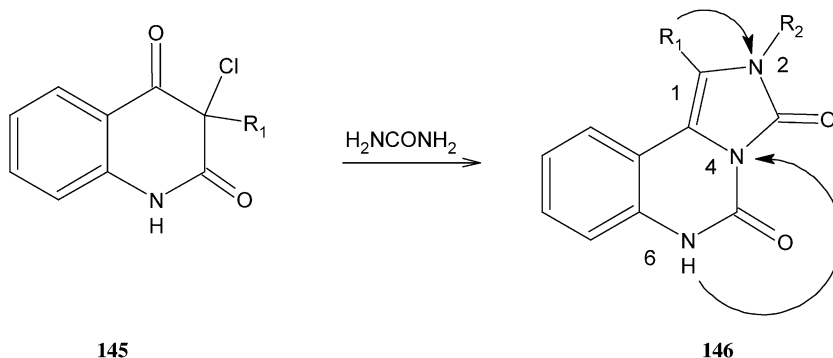
The N6 proton established the ^{15}N shift of the N6 resonance and was also long-range coupled to the N4 resonance. Side chain methylene protons of the R$_1$ substituent facilitated the assignment of the N2 resonance. These data, in conjunction with conventional 2D NMR homo- and heteronuclear shift correlation data, confirmed the structures (Table 16).

Imidazo[4,5-c]quinolin-2-ones. In a continuation of the work that led to the isolation and characterization of the series of 2,6-dihydroimidazo[1,5-c]quinazoline-3,5-diones described in this section, Klásek and co-workers[163] investigated the reaction of analogues of **145** bearing 3-amino substituents as shown in Scheme 6. To characterize these products, the authors again resorted to long-range ^{1}H–^{15}N correlation data. For **148**,

Table 16. ^{15}N chemical shift assignments for selected 2,6-dihydroimidazo[1,5-c] quinazoline-3,5-diones (**146**)[162]

Substituents		^{15}N chemical shift assignments		
		N2	N4	N6
–C$_4$H$_9$	–CH$_2$C$_6$H$_5$	137.7	147.5	114.9
–C$_6$H$_5$	–C$_4$H$_9$	138.5	148.1	115.0

the N1 resonated downfield, as would be expected for this nitrogen environment, at 306.8 ppm. The N3 and N5 resonances were assigned at 125.8 and 120.0 ppm, respectively. Following the reduction of **148** to afford **149**, the N1 resonance shifted upfield to 88.8 ppm and was observed with an 88.3 Hz $^1J_{NH}$ coupling. The N3 and N5 chemical shifts were less perturbed and were assigned at 104.5 and 128.4 ppm, respectively.
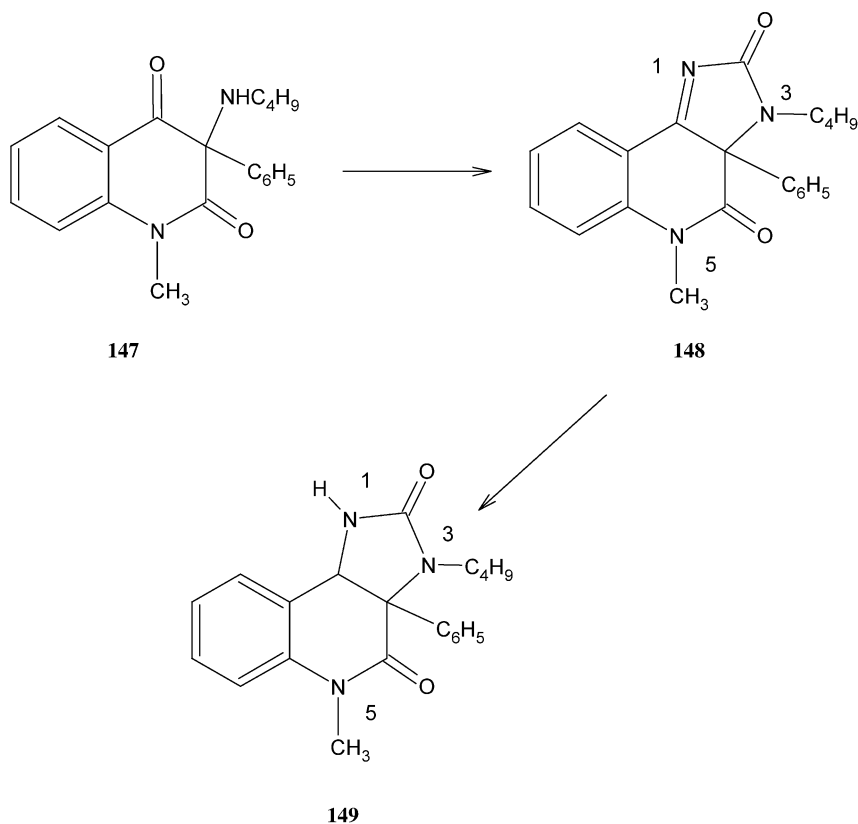
Scheme 6.

2-Aryl-1,3,4-oxadiazoles. Nowak-Wydra *et al.*[165] reported the results of the study of a series of 2-arylsubstituted 1,3,4-oxadiazole analogs in which long-range ^1H–^{15}N HMBC data were used to unequivocally differentiate the two nitrogen resonances. Examining the data contained in Table 17 for the series of 2-aryl-1,3,4-oxadiazoles studied, there was relatively little effect on the ^{15}N shift of either of the oxadiazole nitrogens as the nature of the substituent at the 4-position of the aryl group was varied.

150
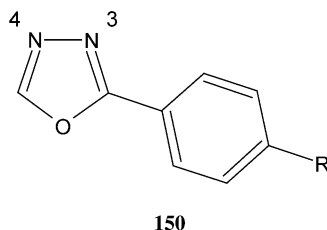
Isomeric N-methyltriazolopyridazines. During the synthesis of a pair of isomeric *N*-methyl-[1,2,3]triazolo[4,5*d*]-pyridazines, Csámpai and co-workers[166] utilized long-range ^1H–^{15}N correlation data to determine the position of the N-methyl group on the 1,2,3-triazole ring. In the case of the N1 methyl analogue, **151**, correlations were observed from the methyl group to only two of the three nitrogen resonances, N1, resonating upfield at 231.0 ppm and N2 resonating downfield at 383.8 ppm. In contrast, for the isomer assigned as the N2 methyl analogue, **152**, correlations were observed for all three nitrogens. N2 resonated furthest upfield at 264.5 ppm. N1 flanking the carbonyl was assigned at 325.3 ppm, while the N3 resonance was assigned downfield at 329.2 ppm, although the authors note that the N1 and N3 assignments may be interchangeable.

Table 17. ^{15}N chemical shifts of a series of 2-aryl substituted 1,3,4-oxadiazoles[165]

Substituent	^{15}N chemical shift		
	N3	N4	Other N
–NMe$_2$	283.2	304.4	51.2
–NH$_2$	284.8	304.3	58.1
–OMe	287.7	304.6	–
–Me	290.9	305.8	–
–H	292.7	306.1	–
–C$_6$H$_5$	293.3	306.8	–
–F	292.6	306.6	–
–Br	294.9	307.1	–
–CN	300.5	308.6	257.2
–NO$_2$	301.3	309.3	364.8
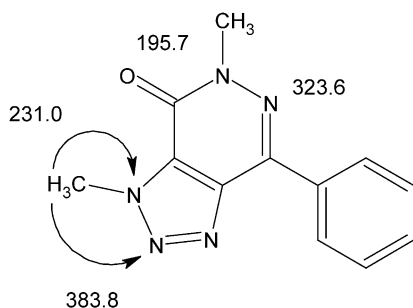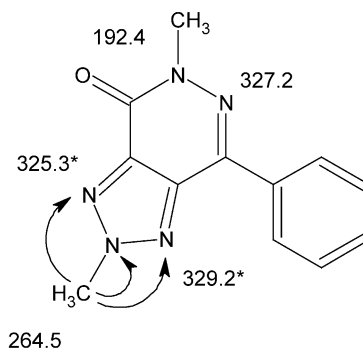
151   **152**

5-Carboxymethyl-1,2,4-triazole and 5-oxo-1,2,4-triazine derivatives. Bednarek and co-workers[167] as a part of a synthetic effort to develop novel compounds with fungicidal or bacteriostatic activity, prepared a number of 5-carboxymethyl-1,2,4-triazole (**153**) and 5-oxo-1,2,4-triazine (**154**) derivatives. During the synthesis employed, dimethyl 2-[(1-arylamino-1-arylmethylidene)hydrazono]succinate cyclizes, based on mass spectrometric and preliminary ^{1}H-NMR data, to the corresponding 5-oxo-1,2,4-triazines (**154**). The reaction could, however, lead to the alternative formation of the 5-carboxymethyl-1,2,4-triazoles (**153**), which prompted the authors to do a more rigorous structural characterization that involved the acquisition of long-range ^{1}H–^{15}N HMBC data.
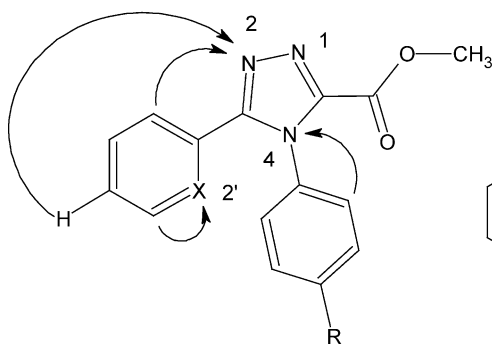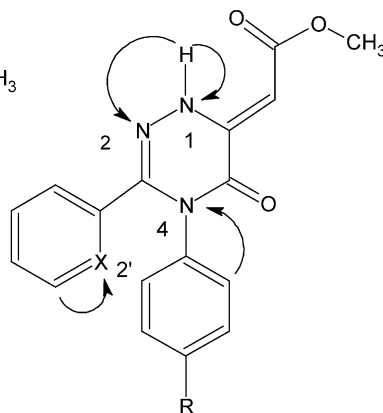
153   **154**

From the synthesis, both series of compounds were formed. The structures were confirmed by a combination of 2D NMR methods and X-ray single crystal studies. The authors note that the assignment of the three or four nitrogen resonances of each of the molecules was a non-trivial challenge, requiring the acquisition of both 8 and 1 Hz optimized ^{1}H–^{15}N long-range data. The 8 Hz optimized data allowed the assignment of the N4 resonance, and in those analogues with a 2-pyridyl substituent, the pyridine nitrogen. In the 1 Hz optimized data, there were two correlations observed from protons

Table 18. ^{15}N chemical shift assignments for a series of 5-carboxymethyl-1,2,4-triazole (**153**) and 5-oxo-1,2,4-triazine (**154**) analogues[167]

Compound	Substituent		^{15}N chemical shift			
	R'	R''	N1	N2	N4	Pyridyl
153	$-C_6H_5$	$-C_6H_5$	329.4	318.7	178.2	–
153	2-C_5H_4N	$-C_6H_5$	329.5	318.6	179.0	311.7
153	2-C_5H_4N	$-C_6H_4-CH_3$	329.3	318.6	178.9	311.8
154	$-C_6H_5$	$-C_6H_5$	271.4	254.6	160.6	–
154	2-C_5H_4N	$-C_6H_5$	271.4	256.8	159.0	312.1
154	2-C_5H_4N	$-C_6H_4-CH_3$	271.4	256.6	158.5	311.8

on the 3-aryl substituent to the N2 resonance via $^4J_{NH}$ and $^6J_{NH}$ couplings as shown for **153**. The assignment of the N1 resonance was subsequently made from the 1D ^{15}N NMR data. The ^{15}N assignments for the series of analogues studied are collected in Table 18.

Molecular structures of 4-tert-butylpyrazoles. Trofimenko and co-workers[168] reported an interesting study of the buttressing effects observed for three *tert*-butyl substituted pyrazoles in both the solution and solid state that employed X-ray crystallography and ^{15}N measurements. The authors found that the major tautomers in solution were consistent with the X-ray single crystal tautomeric preferences for the three analogues. The ^{15}N shifts shown for the structures are solid-state data. The pairs of ^{15}N resonances for N2 are explained as a result of *tert*-butyl groups existing in different conformations in the solid state.

155   156   157
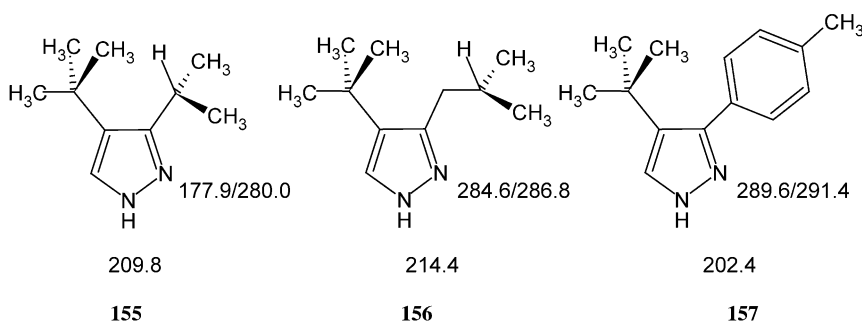
Halogeno-1,2,4-triazoles. Claramunt and co-workers[169] reported a study of a series of 1,2,4-triazole analogues in both the solution and solid states. ^{15}N chemical shift data were reported in both the solution state (DMSO, methanol) and in the solid state for three analogues, the 3-bromo-, 3-chloro- and parent 1,2,4-triazole. As would be expected for the 1,2,4-triazole system, there are various forms in tautomeric equilibrium, as shown by **158a–c**. The authors present a discussion of the estimation of chemical shifts for the various tautomers; the interested reader is referred back to the original reference for more details as that discussion is beyond the scope of this work. ^{15}N chemical shift assignments for the bromo-substituted analogue, **158**, the chloro analogue, **159**, and the parent 1,2,4-triazole, **160**, are collected in Table 19.

Table 19. ^{15}N chemical shifts for selected 1,2,4-triazoles, **158–160**[169]

Compound	Solvent	^{15}N chemical shift		
		N1	N2	N4
158	CPMAS	222.8	289.7	249.1
	DMSO-d_6	224.8	281.9	253.7
	CD$_3$OD	214.9	Not obs.	243.0
159	CPMAS	219.6	280.6	241.9
	DMSO-d_6	218.3	278.7	248.7
	CD$_3$OD	211.9	Not obs.	236.5
160	CPMAS	219.6	284.9	237.9
	DMSO-d_6	252.9	252.9	243.8
	CD$_3$OD	209.9	279.3	234.2

158a   **158b**   **158c**

159   **160**
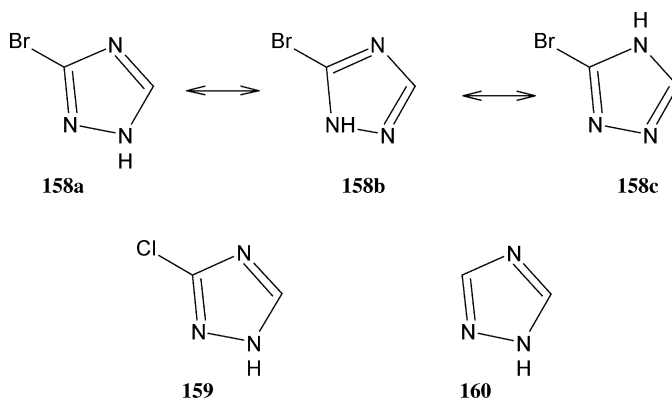
Porphyrin inner proton exchange. Ribó and co-workers[170] reported a study of the effect of steric factors due to bridge substitution on the modulation of proton exchange rates in a water soluble porphyrin, **161**. The authors utilized both ^{1}H–^{15}N HSQC and HMBC data and were able to assign the N21, N22, N23 and N24 resonances. The N22

161
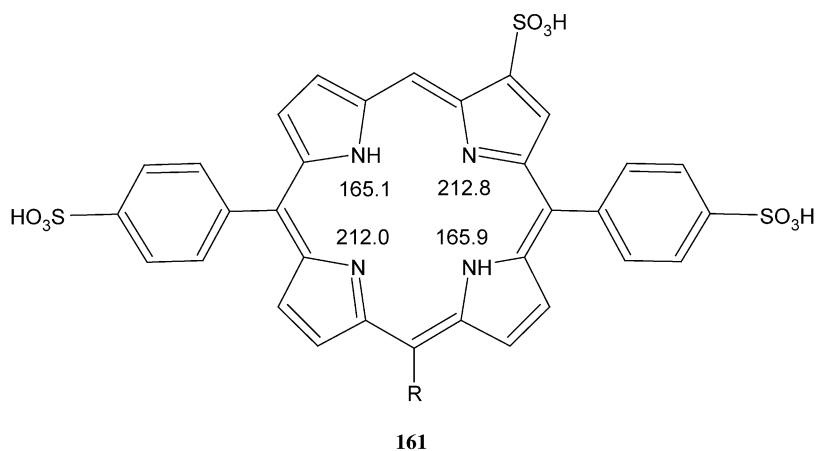
and N24 resonances of **161** resonated upfield of N21 and N23 but the differences between the resonance chemical shifts pairwise were small.

Synthesis and characterization of lithocholic acid derived dipyrromethanes. Koivukorpi *et al.*[171] in early 2004 reported the synthesis of a series of steroidal dipyrromethane analogues that can be exploited for the synthesis of pyrrole–steroidal macrocycles. The authors used long-range ¹H–¹⁵N HMBC data to confirm the structure.

162
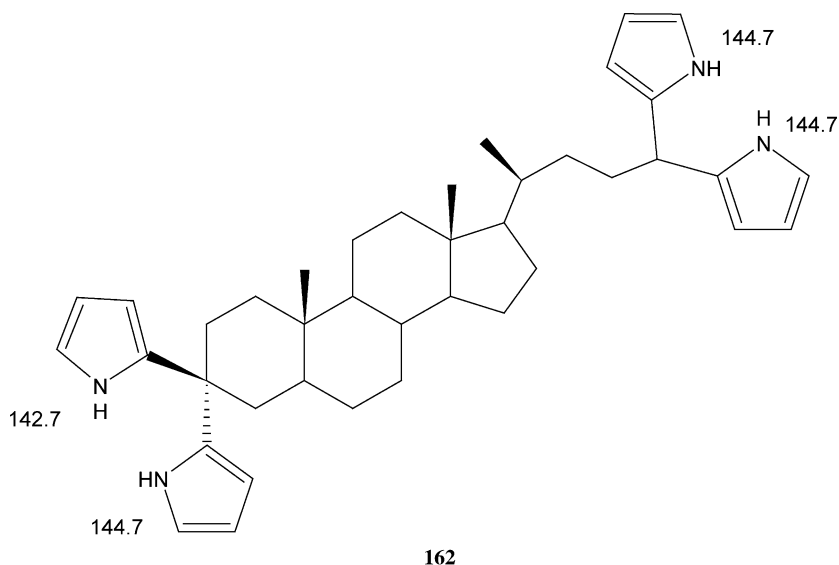
5.2.3. *Studies involving six-membered nitrogen containing rings*

Quinoacridinium salts. There has been considerable interest in pyridoacridines and related compounds due to their biological activity (cytotoxicity, mutagenicity or antibacterial activity). Wawer and co-workers[172] reported the study of a pair of quino-acridinium salts from this broad family of compounds utilizing long-range ¹⁵N hetero-nuclear shift correlation data in their study. There are numerous resonance structures, two of the 18 that the authors report as possible are shown, **163** and **164**. The authors were able to differentiate the chemical shifts of the two N-ethyl groups at N8 and N13 on the basis of calculated nitrogen shielding constants and by heteronuclear shift correlation spectra. Based on their work, the authors conclude that N8 is significantly more shielded than N13, giving rise to the chemical shift assignments contained in Table 20.

Table 20. ¹⁵N chemical shift assignments for two quinoacridinium salts[172]

Substituent (R)	N8	N13
–H	135.6	143.7
–CH₃	134.9	142.7

163   **164**
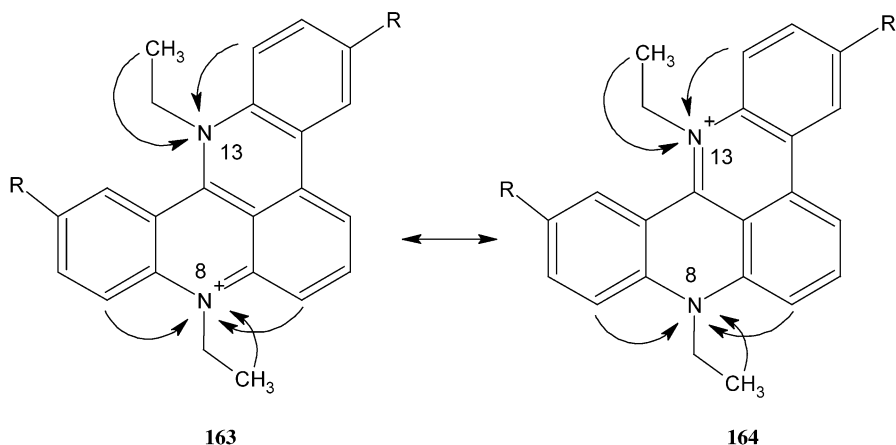
Configurational dissimilarity of N-methyl-1,2-dihydro-2-benzoylmethylenequinolines and their desmethyl congeners. Gawinecki and co-workers[173] reported a study of 1-methyl-1,2-dihydro- and 1,2-dihydro-2-benzoylmethylenequinolines which demonstrated that the molecules in both the solution and crystalline state are in the Z- and E-form, respectively. Long-range ^{1}H–^{15}N spectra were used to measure the ^{15}N chemical shifts reported for analogues of **165** in Table 21. In the case of the 1,2-dihydro- form, the nitrogen resonated ∼30 ppm downfield of the nitrogen shift of the corresponding 1-methyl-1,2-dihydro- form. The observed downfield shift was attributed to hydrogen bonding as shown by **166**.[215]

165

166
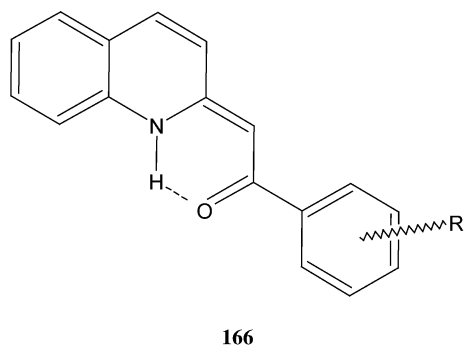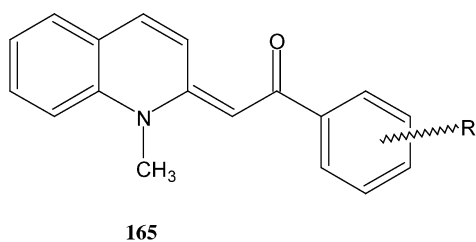
Table 21. ^{15}N chemical shifts of a series of *N*-methyl-1,2-dihydro-2-benzoylmethylene-quinolines, **165**[173]

Substituent (–R)	N1	Other nitrogen
p-OCH$_3$	118.1	–
p-CH$_3$	119.3	–
m-CH$_3$	119.0	–
–H	119.3	–
p-F	119.7	–
p-Cl	120.7	–
p-Br	120.5	–
m-F	120.8	–
m-Br	121.3	–
m-CF$_3$	121.7	–
p-CF$_3$	121.7	–
p-NO$_2$	123.9	267.3
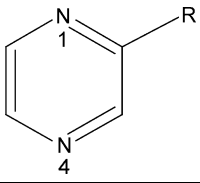
1,3-Bis(2-quinolyl)-2-(p-chlorophenyl)-2-propanol. Later in 2000, Gawinecki and co-workers[174] reported the results of a multinuclear NMR and X-ray study of 1,3-bis(2-quinolyl)-2-(*p*-chlorophenyl)-2-propanol (**167**) in which they found that the methylene protons of the molecule were non-equivalent. Long-range ^{1}H–^{15}N HMBC data showed the two 2-quinolyl species to be equivalent in solution despite the inequivalence of the methylene protons.

167
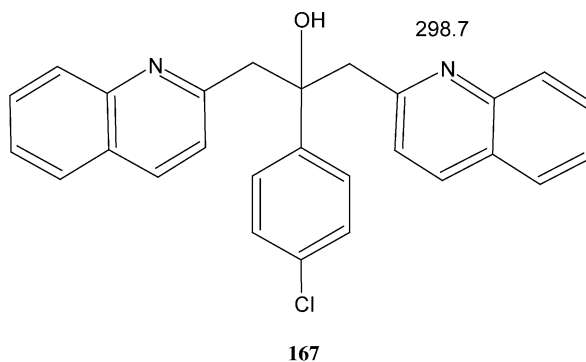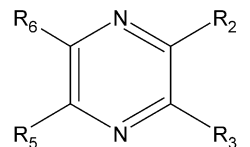
Determination of the substitution pattern of di- and tri-substituted pyrazines. Disubstituted pyrazines, as a chemical class, are important in the flavor industry. The ability to differentiate between 2,3-, 2,5- and 2,6-di-substituted isomers is provided, in part, through the use of long-range ^{1}H–^{15}N GHMBC data. Sommer and co-workers[175] reported a study a large series of di- and tri-substituted pyrazines. The possible two- and three-bond long-range ^{1}H–^{15}N correlations of di- and tri-substituted pyrazines are shown by **168–170**. ^{15}N chemical shift assignments for a selected group of mono-substituted pyrazines are collected in Table 22. ^{15}N chemical shift assignments for a much more extensive series of di-substituted pyrazines are contained in Table 23.

168   **169**   **170**
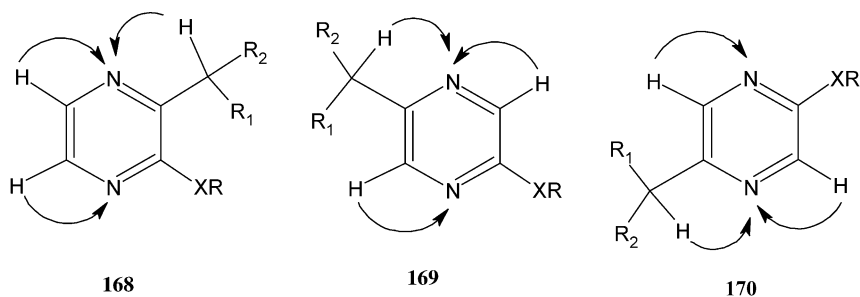
Table 22. ^{15}N chemical shift assignments of a group of mono-substituted pyrazines[175]
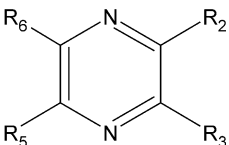
Substituent (R)	N1	N4
–H	335.6	335.6
–CH$_3$	334.3	335.4
–OCH$_3$	281.9	342.2
–SCH$_3$	320.1	332.1
–C(=O)CH$_3$	333.9	338.5

Table 23. ^{15}N chemical shift assignments of a series of di- and tri-substituted pyrazines[175]

Substituents				^{15}N chemical shifts	
R$_2$	R$_3$	R$_5$	R$_6$	N1	N4
–CH$_3$	–CH$_3$	–H	–H	332.9	332.9
–CH$_3$	–H	–CH$_3$	–H	333.9	333.9
–CH$_3$	–H	–H	–CH$_3$	335.0	332.3
–C$_2$H$_5$	–CH$_3$	–CH$_3$	–H	331.4	333.1
–C$_2$H$_5$	–CH$_3$	=H	–CH$_3$	331.4	333.9
2-Methyl-propyl	–CH$_3$	–CH$_3$	–H	334.7	332.7
2-Methyl-propyl	–CH$_3$	–H	–CH$_3$	334.4	333.5

(*continued*)

Table 23.   Continued.

Substituents				^{15}N chemical shifts	
R$_2$	R$_3$	R$_5$	R$_6$	N1	N4
2-Methyl-propyl	–CH$_3$	–H	–H	334.4	333.6
–OCH$_3$	–CH$_3$	–H	–H	278.6	337.8
–OCH$_3$	–H	–H	–CH$_3$	285.1	341.6
–OCH$_3$	–C$_2$H$_5$	–H	–H	278.6	335.9
–OCH$_3$	–Pr	–H	–H	279.4	336.7
–OCH$_3$	1-Methyl-ethyl	–H	–H	279.7	333.8
–OCH$_3$	2-Methyl-propyl	–H	–H	278.7	339.2
–OCH$_3$	–H	–H	2-Methyl-propyl	284.9	340.9
–OCH$_3$	1-Methyl-propyl	–H	–H	279.2	335.0
–OCH$_3$	3-Methyl-butyl	–H	–H	278.7	336.9
-Propoxy	–CH$_3$	–H	–H	278.8	337.4
-Propoxy	–H	–H	–CH$_3$	285.9	341.3
1-Methyl-ethoxy	–CH$_3$	–H	–H	279.7	337.1
1-Methyl-ethoxy	–H	–H	–CH$_3$	286.5	337.8
–SCH$_3$	–CH$_3$	–H	–H	318.1	329.5
–SCH$_3$	–H	–H	–CH$_3$	321.1	332.9
–SCH$_3$	1-Methyl-ethyl	–H	–H	320.5	325.5
–Cl	–CH$_3$	–H	–H	327.5	342.5
–Cl	–H	–H	–CH$_3$	326.6	344.4
-Acetyl	–CH$_3$	–CH$_3$	–H	337.2	338.9
-Acetyl	–CH$_3$	–H	–CH$_3$	335.4	340.9
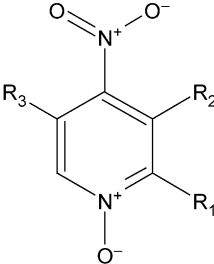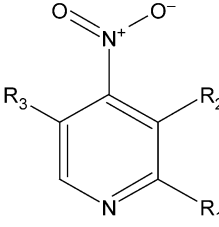
Controlled metalations of pyrazines. Quéguiner and co-workers[176] in a study directed at developing a new route for the synthesis of septorin (**171**) employed the controlled metalation of substituted pyrazines. To differentiate possible metalation sites in these analogues, which present the same problem as determining substitution patterns of pyrazines discussed above, it was necessary to utilize long-range ^{1}H–^{15}N HMBC data to establish the structures. To differentiate between structures **172** and **173**, the authors relied on long-range coupling pathways to the N4 resonance. As shown, for **172**, there are two long-range couplings observed, allowing the unequivocal assignment of both nitrogens. In contrast, for **173**, a single correlation to N4 is observed consistent with the structure shown.
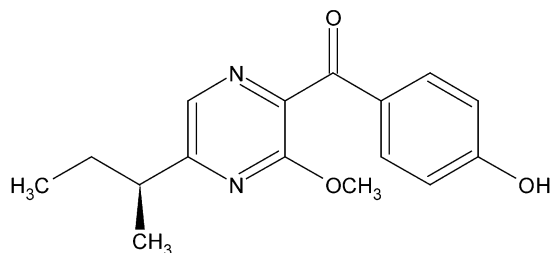
171
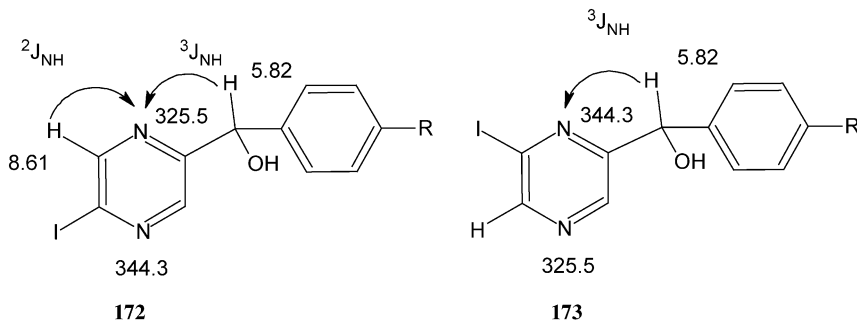
172   **173**

Multinuclear NMR study of substituted 2-amino-4-nitropyridines and their N-oxides. Laihia and co-workers[177] reported the results of a study of three 4-nitropyridine *N*-oxides and four nitropyridines. ^{15}N chemical shift assignments were made using long-range ^{1}H–^{15}N methods; the assignments are contained in Table 24. The first study of a limited number of pyridine and pyridine-*N*-oxides was followed in 2003 by the same basic group of authors[178] with a more comprehensive study of a broader group of pyridine and pyridine-*N*-oxides (Table 25).

Androsteno [17,16-d]pyrimidine derivatives. Forgo and Vincze[179] in a study of the reactions of 16-hydroxymethylene- and 16-aminomethylene androstenone analogues with formamide and guanidine reported the isolation and characterization of androsteno[17,16-*d*]pyrimidine analogues, which were characterized, in part, using
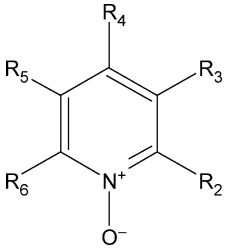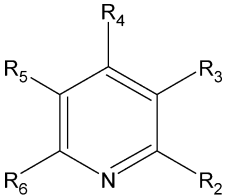
Table 24. ^{15}N chemical shift assignments of a series of nitropyridines and nitropyridine-N-oxides[177]

	174				175		

N-oxide	Substituents			^{15}N chemical shifts			
	R$_1$	R$_2$	R$_3$	$-NO_2$	N$-NO_2$	Pyridine	NHCH$_3$ or NCH$_3$NO$_2$
	Pyridine-N-oxide			–	–	258.9	–
	Pyridine			–	–	321.9	–
N–O	–NHCH$_3$	–H	–CH$_3$	368.3	–	265.9	61.9
N–O	–NHCH$_3$	–CH$_3$	–H	370.6	–	266.7	60.5
N–O	–NHCH$_3$NO$_2$	–CH$_3$	–H	365.7	348.2	296.6	–
–	–NHCH$_3$	–H	–CH$_3$	373.7	–	273.3	69.8
–	–NHCH$_3$	–CH$_3$	–H	376.3	–	265.0	73.8
–	–NHCH$_3$NO$_2$	–CH$_3$	–H	369.5	350.6	313.2	–
–	–NHCH$_3$NO$_2$	–H	–CH$_3$	369.0	347.6	310.1	81.9
N–O	–H	–H	–H	352.4	–	306.1	–
N–O	–H	–CH$_3$	–H	366.6	–	304.0	–
–	–H	–H	–H	367.2	–	333.5	–
–	–H	–CH$_3$	–H	371.4	–	330.2	–

long-range ^{1}H–^{15}N HMBC data. The ^{15}N chemical shift assignments for the analogues described in this report are contained in Table 26.
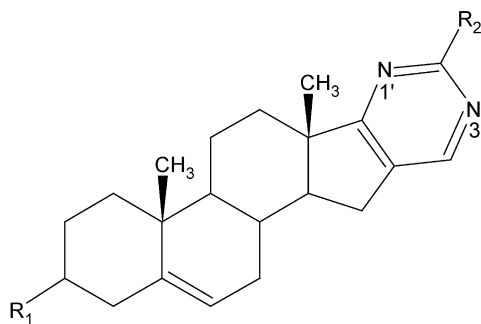
178

Table 25. ^{15}N chemical shifts of a series of pyridine-N-oxides (**176**) and pyridines (**177**)[178]

176

177

Substituents					^{15}N chemical shifts			
R_2	R_3	R_4	R_5	R_6	N_{ring}	N_{amino}	N_{nitro}	Ar_{nitro}
Pyridine-N-oxides								
–NHNO$_2$	–H	–H	–H	–H	236.4	224.0	359.2	–
–H	–NHNO$_2$	–H	–H	–H	292.6	183.0	346.1	–
–H	–H	–NHNO$_2$	–H	–H	240.9	230.1	358.3	–
–NHNO$_2$	–CH$_3$	–H	–H	–H	285.1	180.0	350.5	–
–NHNO$_2$	–H	–CH$_3$	–H	–H	217.7	237.8	–	–
–NHNO$_2$	–H	–H	–CH$_3$	–H	239.6	213.4	–	–
–NHNO$_2$	–H	–H	–H	–CH$_3$	255.4	208.4	–	–
–NHNO$_2$	–H	–H	–NO$_2$	–H	210.8	258.5	–	360.5
–NHCH$_3$	–H	–NO$_2$	–H	–H	266.7	65.8	–	365.0
–NHC$_2$H$_5$	–H	–NO$_2$	–H	–H	266.5	81.3	–	364.9
–N(C$_2$H$_5$)$_2$	–H	–NO$_2$	–H	–H	286.8	74.5	–	364.2
–NHC$_4$H$_9$	–H	–NO$_2$	–H	–H	266.2	57.6	–	365.1
–N(CH$_2$)$_5$	–H	–NO$_2$	–H	–H	286.9	70.8	–	364.3
–N(CH$_2$)$_4$O	–H	–NO$_2$	–H	–H	286.5	66.5	–	364.3
–NHCH$_3$	–H	–NO$_2$	–H	–CH$_3$	266.0	65.7	–	364.2
–NHC$_2$H$_5$	–H	–NO$_2$	–H	–CH$_3$	265.6	81.2	–	364.3
–NHCH$_3$	–H	–NO$_2$	–NO$_2$	–CH$_3$	259.2	78.9	–	361.4
–NHC$_2$H$_5$	–H	–NO$_2$	–NO$_2$	–CH$_3$	258.6	84.3	–	361.5
Pyridine compounds								
–NHNO$_2$	–CH$_3$	–H	–H	–H	186.6	241.7	–	–
–NHNO$_2$	–H	–CH$_3$	–H	–H	182.5	242.2	–	–
–NHNO$_2$	–H	–H	–CH$_3$	–H	208.6	232.7	–	–
–NHNO$_2$	–H	–H	–H	–CH$_3$	204.0	–	–	–
–NCH$_3$NO$_2$	–H	–NO$_2$	–H	–H	311.9	188.2	346.8	364.2
–NHCH$_3$	–H	–NO$_2$	–H	–CH$_3$	274.3	73.7	–	369.9
–NHC$_2$H$_5$	–H	–NO$_2$	–H	–CH$_3$	273.8	91.1	–	369.6
–NCH$_3$NO$_2$	–H	–NO$_2$	–H	–CH$_3$	311.7	187.8	347.8	364.8
–NC$_2$H$_5$NO$_2$	–H	–NO$_2$	–H	–CH$_3$	312.4	198.6	345.8	364.6

Table 26. ^{15}N chemical shifts of several androsteno[17,16-*d*]pyrimidine (**178**) derivatives[179]

Substituents		^{15}N chemical Shifts		
R$_1$	R$_2$	Other ^{15}N	N1$'$	N3$'$
–H	–NH$_2$	82.0	241.9	241.9
–H	–H	–	283.0	283.0
–C(=O)NHC$_2$H$_5$	–H	88.9	283.0	283.0

^{15}N chemical shift assignments and substituent effects on a series of N-phenoxy-ethylanilines. Jios and co-workers[180] reported the results of a comprehensive study of substituent effects in a series of *N*-phenyoxyethylanilines of the type shown by **179** (Table 27).

179
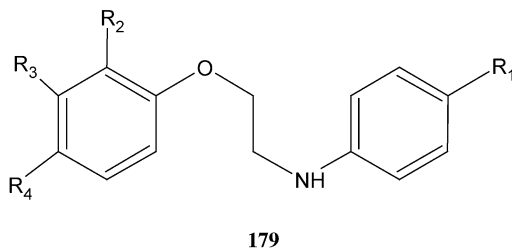
Structural characterization of β-2$'$-pyridylaminocrotonoyl-2-pyridylamide. Gawi-necki and co-workers [181] reported the results of a solution and X-ray crystal study of β-2$'$-pyridylaminocrotonoyl-2-pyridylamide (**180**) that have yielded interesting insights into the solution behavior of the molecule. The amide studied has a dimeric form whereas the monomer molecules are held together by two intermolecular hydrogen bonds. The NMR data also show that there is an intramolecular hydrogen bond in each monomer subunit.

180
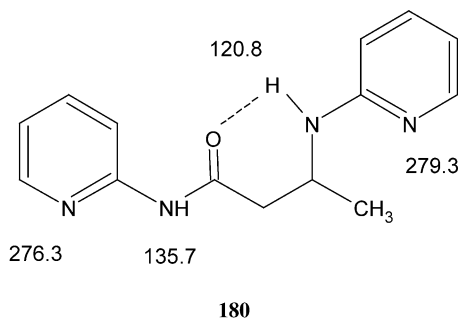
Table 27. ^{15}N chemical shift assignments for a series of substituted *N*-phenoxyethyl-anilines (**179**)[180]

Substituents				^{15}N shift
R$_1$	R$_2$	R$_3$	R$_4$	
–H	–H	–H	–H	60.5
–H	–H–	–H	–OCH$_3$	60.0
–H	–H	–H	–CH$_3$	60.1
–H	–H	–H	–Cl	59.7
–H	–H	–H	–Br	59.6
–H	–H	–H	–NO$_2$	59.7
–H	–Br	–H	–Cl	59.4
–H	–OCH$_3$	–H	–H	60.5
–H	–Br	–H	–H	59.7
–H	–NO$_2$	–H	–H	59.2
–H	–H	–NO$_2$	–H	59.1
–OCH$_3$	–H	–H	–H	55.9
–CH$_3$	–H	–H	–H	57.4
–Cl	–H	–H	–H	59.8
–NO$_2$	–H	–H	–H	73.7
–OCH$_3$	–H	–H	–Cl	55.3
–OCH$_3$	–NO$_2$	–H	–H	54.4
–Cl	–OCH$_3$	–H	–H	59.9
–Cl	–Br	–H	–H	59.5
–Br	–OCH$_3$	–H	–H	60.4

Synthesis of carba-analogues of myoseverin. Hocek *et al.*[182] reported a study dealing with the synthesis of carba-analogues of the cytostatic myoseverin via the reactions of 2,6-dichloro-9-isopropylpurine. Three families of compounds, **181–183**, were prepared by varying the substituents on the 9-isopropyl purine substrate used in the reactions. Long-range ^{1}H–^{15}N HMBC spectra were recorded with the long-range delay optimized in the range of 50–60 ms. ^{15}N chemical shift assignments are collected in Table 28.

Table 28. ^{15}N chemical shift assignments for carba-analogues, **181–183**, of myoseverin[182]

Compound	^{15}N chemical shift assignments			
	N1	N3	N7	N9
181	267.3	242.9	238.7	172.7
182	270.6	Not obs.	236.8	174.7
183	277.4	245.6	237.7	174.6

181   **182**

183
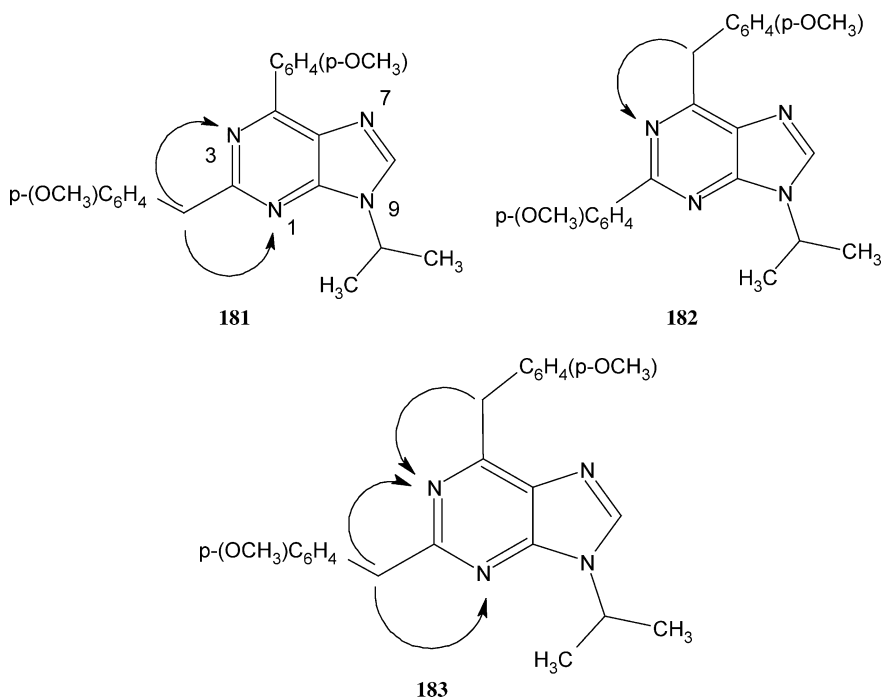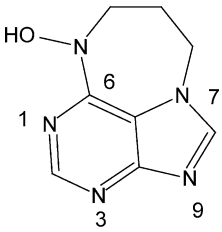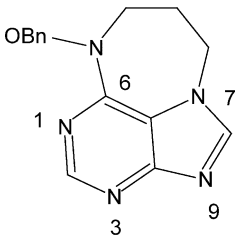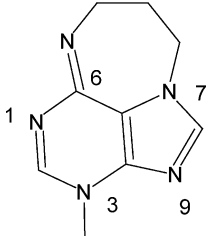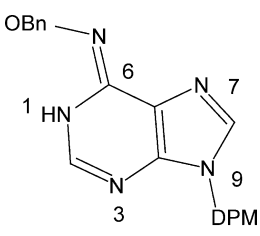
Synthesis of 9-substituted tetrahydrodiazepinopurine asmarine A analogues. Pappo and Kashman[183] made extensive use of long-range ^1H–^{15}N HMBC data during the course of efforts to synthesize 9-substituted tetrahydrodiazepinopurine analogues of the marine sponge metabolite asmarine-A (**184**) (Table 29).

184   **185**   **186**
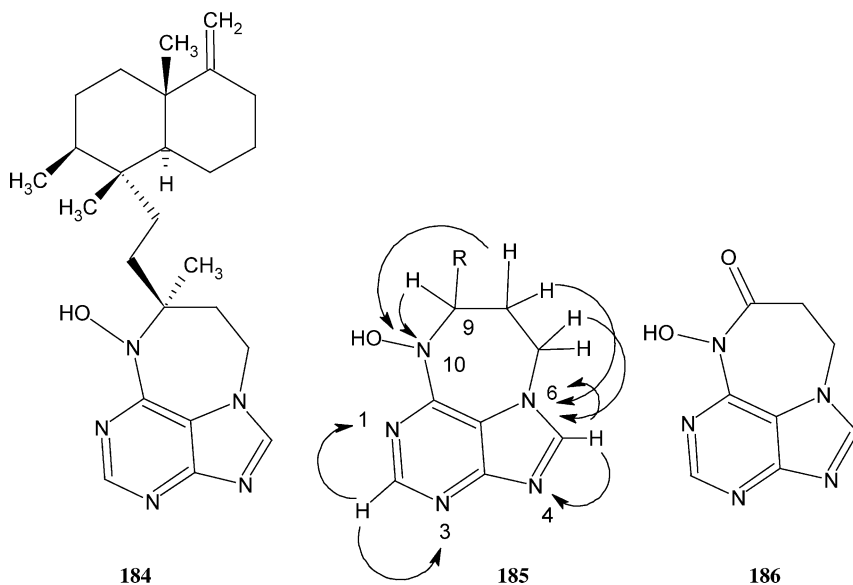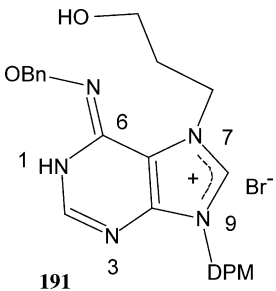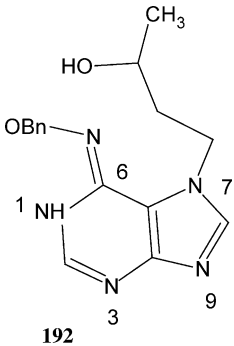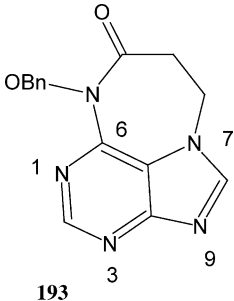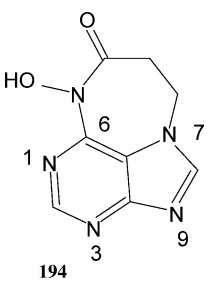
Table 29. ^{15}N chemical shifts of tetrahydrodiazepinopurine analogues of asmarine-A[183]

Compound	^{15}N Chemical shifts				
	N1	N3	N7	N9	N6
187	245.0	235.3	156.0	245.5	149.3
188	250.8	237.9	155.6	245.0	92.6
189	234.0	161.3	167.3	231.9	119.2
190	136.9	207.9	247.4	173.9	285.3
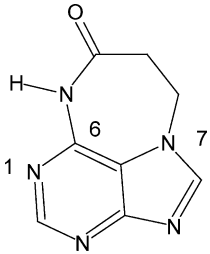
(*continued*)

Table 29.   Continued.

Compound	¹⁵N Chemical shifts				
	N1	N3	N7	N9	N6
191	141.8	204.0	172.2	180.0	288.2
192	134.4	226.7	164.5	250.0	280.0
193	Not obs.	263.5	155.9	244.5	203.9
194	Not obs.	262.6	155.7	244.2	188.3

(*continued*)

Table 29.   Continued.

Compound	^{15}N Chemical shifts				
	N1	N3	N7	N9	N6
195	248.0	260.5	154.7	245.4	150.7 (HSQC)

TMPM, (3,4,5-timethoxyphenyl)methyl; DPM, diphenylmethyl.

Asmarines G and H. Kashman and co-workers[184] in a continuation of the preceeding study above, reported the isolation of two known and two novel asmarines from the Indian Ocean sponge *Raspailia* sp. ^{15}N chemical shift assignments for the compounds reported were derived from long-range ^{1}H–^{15}N HMBC data. The authors note in this communication that their previously reported ^{15}N chemical shift assignments for asmarine-A (**184**)[183] were incorrect due to a referencing problem. The revised assignments are presented in Table 30.

Table 30. ^{15}N chemical shifts for asmarine-A (**184**), -F (**196**), -G (**197**) and -H (**198**)[184]

Compound	–R	^{15}N chemical shift				
		N1$'$	N3$'$	N7$'$	N9$'$	N10$'$
184	–OH	233.3	147.0	245.8	153.9	166.5
196	–OCH$_3$ 5-epi, 8-oxo	224.0	239.2	120.0	113.5	186.9
197	–OCH$_3$	236.7	231.2	243.8	152.9	189.9
198	–H	243.0	231.2	243.8	155.9	116.6

Complete structure analysis of OR-1746. Pollesello and Nore[185] reported the elucidation of the complex structure formed by the condensation of two molecules of levosimendan in the presence of ethanol. The condensation product, which contains a number of clusters of protonated and unprotonated nitrogens could not be confirmed on the basis of conventional 2D NMR data; long-range ^{1}H–^{15}N HMBC data were necessary to assemble the final structure of the molecule. Protonated nitrogens in the structure were assigned on the basis of the direct correlation doublets observed in the spectrum.

199
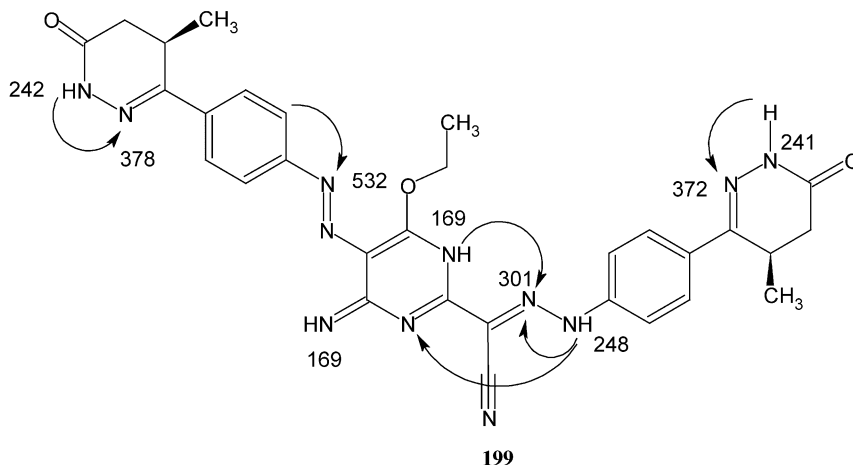
1-Oxo-2-hydroxy-1,2-dihydroacronycine. The pyranolacridone alkaloid acronycine has been shown to be a potent anticancer agent. During a campaign to synthesize analogues of this naturally occurring alkaloid as potential new anticancer agents, Skaltsounis and co-workers [186] utilized long-range ^{1}H–^{15}N HMBC data to establish the position of nitrogen substituents at the 6-position. Long-range ^{1}H–^{15}N correlation and chemical shift data were only reported for a single compound of the series, **200**.

200
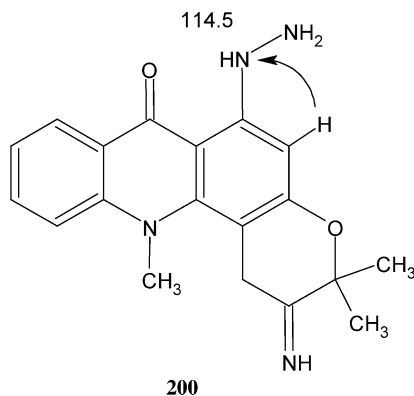
5.3. Biosynthesis, degradation, metabolic and toxicologic studies involving long-range ^{1}H–^{15}N data

5.3.1. Biosynthesis studies

Barbamide and dechlorobarbamide. Gerwick and co-workers, in a study of the halogenated marine natural products barbamide (**201**, R = –CCl$_3$) and dechlorobarbamide (**202**, R = –CHCl$_2$) have also employed long-range ^{1}H–^{15}N data in the elucidation of the biosynthetic pathway leading to these interesting marine natural products.[187] The authors were able to demonstrate that the nitrogen of the thiazole ring is derived biosynthetically from glycine by feeding the organism, *Lyngbya majuscula* doubly labeled ^{13}C,^{15}N glycine. Unfortunately, ^{15}N chemical shift data were not reported.
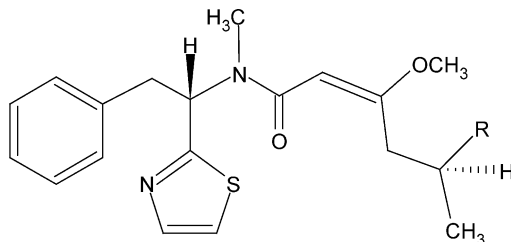
201   R = –CCl$_3$

202   R = –CHCl$_2$

5.3.2. Degradation chemistry studies

Thermal degradation pathway products of the oxazolidinone antibiotic Zyvox™. In a study of the degradation chemistry of the drug Zyvox, the first member of a new class of oxazolidinone antibiotics, Hadden *et al.* utilized long-range ^{1}H–^{15}N GHMBC data to characterize the state of the oxazolidinone ring nitrogen and side chain amide nitrogen in the series of degradants formed.[188] Typical long-range ^{1}H–^{15}N couplings to the parent molecule are shown by **203**.

203
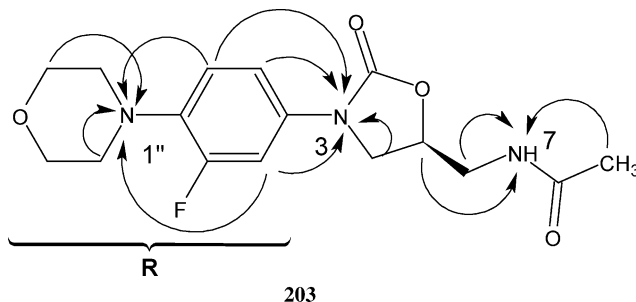
The structures of the degradants of the thermal degradation cascade are shown by **204–207**, and assignments for all of the nitrogens of each of the degradants are summarized in Table 31. While not a high sensitivity means of identifying degradant structures, the approach, which utilized 8 Hz optimized ^{1}H–^{15}N GHMBC data, is useful when

the chemical state of nitrogen is varied between structures in the series of degradants. It is also quite likely that the greatly enhanced sensitivity of cryogenic NMR probes (see Section 3.2) will make this approach to degradant characterization more viable in the future.

204   **205**

206   **207**
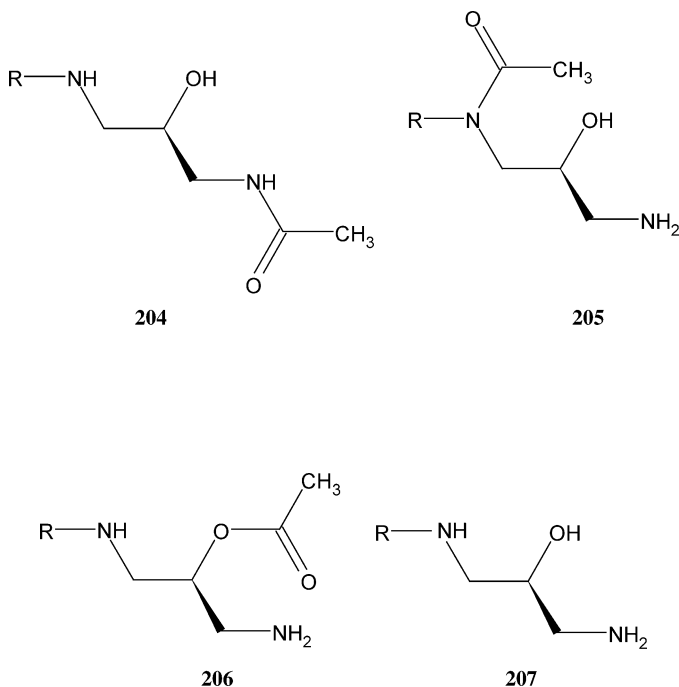
Oxidative degradation of ^{15}N *labeled paracetamol.* d'Ichia and colleagues[189] reported a novel application of the ^1H–^{15}N HMBC experiment in a study of the oxidative decomposition of ^{15}N labeled paracetamol (**208**). Among the compounds they were successfully able to identify in the study were acetamide (**209**), oxalamide, 4-acetylaminocatechol (**210**), 3-(acetylamino-2,4-dihydroxy-2-penedioic acid (**211**), 2-(acetylamino)-3-dihydroxybutyric acid (**212**), and acetylaminoglyoxylic acid (**213**).

Table 31. ^{15}N chemical shifts of the oxazolidinone antibotic Zyvox™ (**203**) and a series of thermal degradants, **204–207**[188]

Position	203	204	205	206	207
N3	93.8	56.7	109.1	53.8	54.9
N7	105.3	105.9	23.9	23.7	22.0
N1″	47.9	43.1	50.3	43.5	43.0

208   **209**   **210**

211   **212**   **213**
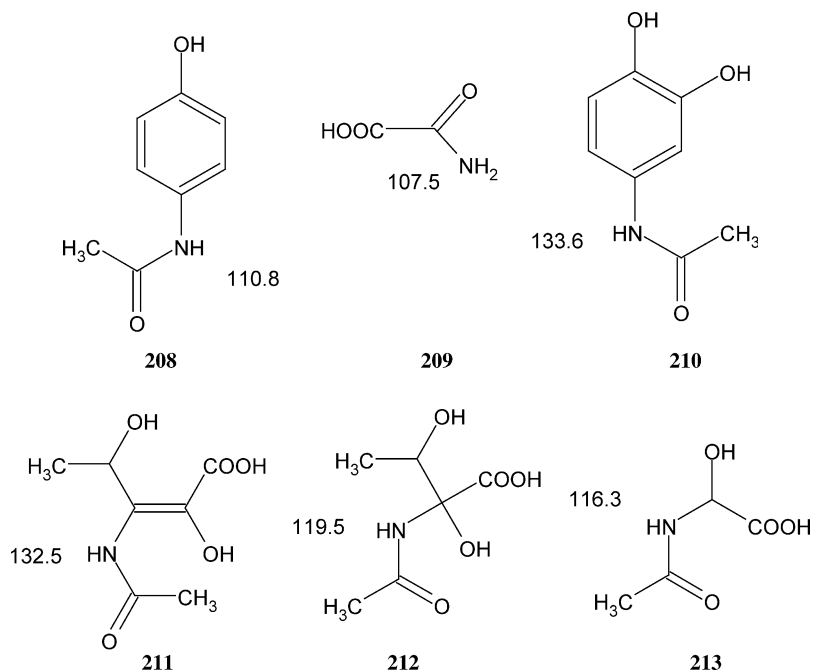
Characterization of unexpected degradation products of an analogue of Nifedipine. Gössnitzer and co-workers[190] during the course of saponification experiments with an analogue of nifedipine, **214a**, observed the formation of three unexpected degradation products. The characterization of these degradants relied, in part, on 10 Hz optimized long-range ¹H–¹⁵N HMBC data. The degradants formed were an *N*-hydroxylindole carboxylic acid, **215**, a β-carbolin-9-ol, **216**, and a [2,7]naphthyridine analogue, **217**. Since there were no examples in the literature to provide ¹⁵N chemical shift verification for **215** and **216**, the authors made extensive comparisons to a number of model compounds. The reader interested in the compounds used for comparison and their ¹⁵N chemical shifts is referred back to the original report for further details.
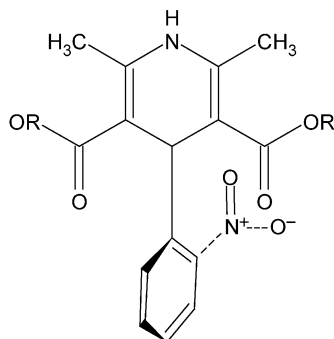
214a – R = –H, NH = 124.7 ppm; –NO$_2$ = 369.4 ppm

214b – nifedipine – R = -CH$_3$, NH = 135.4 ppm, –NO$_2$ = 371.2 ppm

215   **216**   **217**
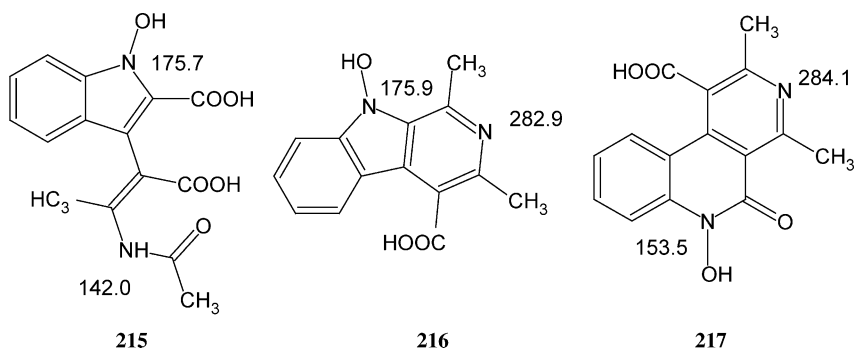
5.3.3. Metabolic studies

Degradation of benzothiazoles by Rhodococcus strains. In an interesting environmental application of long-range ^{1}H–^{15}N 2D results at natural abundance, Delort and co-workers[191] reported the results of a study of the degradation of benzothiazoles by two *Rhodococcus* strains as shown in Scheme 7. The authors acquired long-range ^{1}H–^{15}N data with optimization of the long-range delays for 80 or 140 ms for the characterization of 2,6-dihydroxybenzothiazole. In the former experiment, only the $^3J_{NH}$ correlation from the H4 resonance to N1 was observed in the experiment while in the latter experiment, $^4J_{NH}$ correlations were observed from both H5 and H7 to the N1 nitrogen resonance at 135.5 ppm.

218   **219**

220
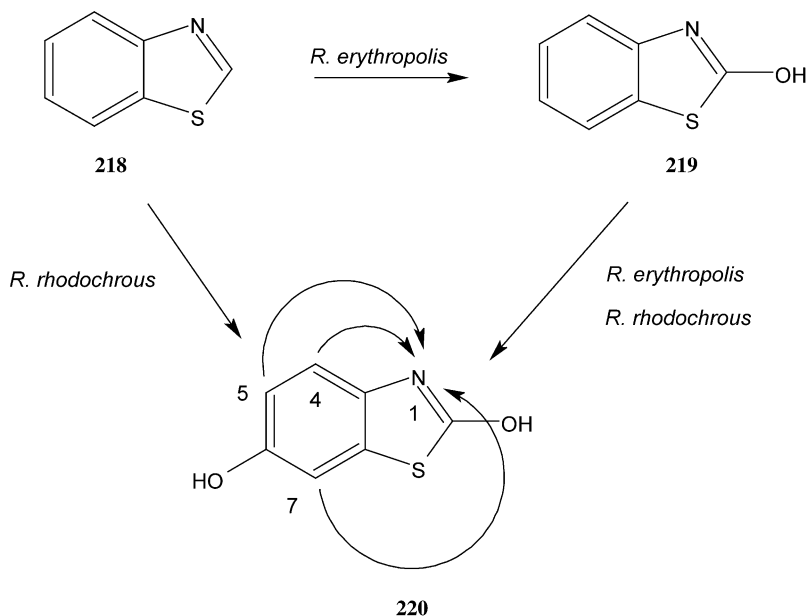
Scheme 7.

2-Aminobenzothiazole. In a later study of the metabolic fate of 2-amino-benzothiazole, Delort and co-workers[192] were again able to establish the site of ring hydroxylation at the 6-position on the basis of long-range ^{1}H–^{15}N HMBC data optimized for 80 and 140 ms. The N3 resonance was observed at 226.4 ppm and was long-range coupled to the H4 and H5 resonances via ^3J–$_{NH}$ and ^4J–$_{NH}$ correlations. Again, only the ^3J–$_{NH}$ correlation was observed in the 80 ms experiment while both long-range correlations were observed in the 140 ms data. No correlation was observed to the H7 proton in the 140 ms optimized long-range experiment. It is also interesting to note that there was only a very small shift in the resonant position of N3 following 6-hydroxylation, the N3 resonance was observed at 226.0 ppm for the parent molecule.

221
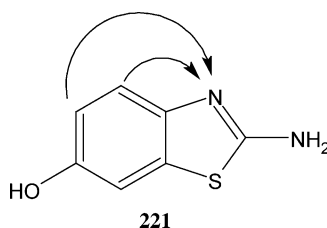
Metabolic activity in Nicotiana plumbaginifola cell-suspension cultures. Mesnard and co-workers[193] reported an interesting study of the nitrogen metabolism in suspension cultured cells of *Nicotiniana plumbaginifola*. Using a combination of ^{1}H–^{15}N HSQC and HMBC, the authors were able to monitor the formation of a number of amino acids by feeding ^{15}N labeled ammonium sulfate and potassium nitrate to the cell culture. In addition to the amino acids normally detected by 1D ^{15}N NMR spectra (glutamine, aspartate and alanine), several other amino acids could be resolved. The newly resolved amino acids included serine, glycine and proline. The authors also found that the peak normally assigned to the non-protein amino acid γ-aminobutyric acid in 1D ^{15}N NMR spectra was resolved into several components in the 2D spectra recorded. Further, a number of *N*-acetylated compounds were resolved, possibly composed of the intermediates of arginine biosynthesis. An intermediate of putrescine degradation was also observed. The occurrence of ^{15}N labeled agmatine and the detection of labeled putrescine suggested that crucial intermediates of the pathway from glutamate to polyamines and/or the formation of tobacco alkaloids could be monitored by this method.

Monitoring nitrogen metabolism in a transformed root culture of Datura stramonium. Fliniaux and colleagues[194] reported the application of long-range ^{1}H–^{15}N data in their efforts to monitor nitrogen metabolism in a transformed root culture of *Datura stramonium*. The culture was fed ^{15}N labeled potassium nitrate and ammonium sulfate for two days. The authors were able to determine the presence of alanine, asparagines, glutamine, glutamate, glycine, an *N*-acetyl compound, and serine. Perhaps more

interestingly, the authors were also able to correlate the biosynthetic relationships between compounds with the HMBC data acquired.

5.4.   Long-range ^{1}H–^{15}N studies of organometallic compounds

Novel bile acids N-(2-aminoethyl)amides and their Cd^{2+} complexes. One of the wide variety of studies utilizing long-range ^{1}H–^{15}N shift correlation data reported by Kohlemainen and co-workers[195] dealt with a multinuclear NMR study of novel bile acids and their Cd^{2+} complexes that were part of an effort to design bile acid conjugates suitable for specific recognition of cations. Since Cd^{2+} can replace Zn^{2+} and Ca^{2+} in many biologically important molecules and can further be detected by NMR, Cd^{2+} was selected for the study. ^{15}N chemical shift data for several analogues and their respective Cd^{2+} complexes are reported in Table 32. The HMBC data used in this study were acquired with a long-range delay optimization of 50 ms (10 Hz).

222
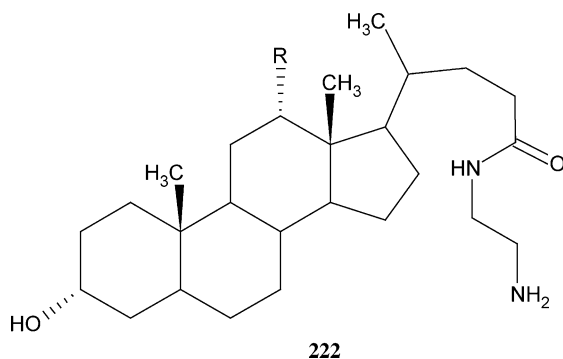
1,2,4-triazolo[1,5-a]pyrimidines and the ^{15}N shifts of the Au(III) complexes. Szlyk and co-workers[196] reported the ^{15}N chemical shifts of a series of 1,2,4-triazolo[1,5-a] pyrimidines. Chemical shifts were determined using GHMQC data, the delays optimized

Table 32. ^{15}N and ^{113}Cd chemical shifts of novel bile acids, **222**, and their Cd^{+2} conjugates[195]

Substituent (R)	^{15}N –NH$_2$	^{15}N –NHCO	^{113}Cd
–H (CDCl$_3$)	17.5	111.5	–
–H (CD$_3$OD)	15.5	115.8	–
–H+Cd^a (CD$_3$OD)	9.2	116.5	92
–OH (CD$_3$OD)	15.3	115.7	–
–OH+Cd^a (CD$_3$OD)	19.5	115.9	84

^{a}Solution saturated with Cd(NO$_3$)$_2$·4H$_2$O.

223
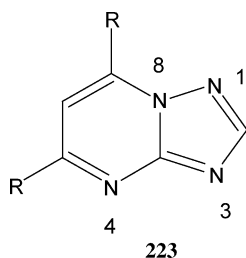
Table 33. ^{15}N chemical shifts of a series of 1,2,4-triazolo[1,5-*a*]pyrimidines and their corresponding Au(III) complexes measured using ^{1}H–^{15}N GHMQC[196]

Substituent	N1	N3	N4	N8
–H	273.5	228.2	276.3	225.2
–H	276.0	156.1	266.8	217.3
Au(III)	(+2.5)	(−72.1)	(−9.5)	(−7.9)
–CH$_3$	267.7	225.6	263.7	224.2
–CH$_3$	270.8	153.7	255.1	221.6
Au(III)	(+3.1)	(−71.9)	(−8.6)	(−2.6)
–C$_6$H$_5$	269.0	228.8	259.1	220.2
–C$_6$H$_5$	271.0	155.1	246.6	223.0
Au(III)	(+2.0)	(−73.7)	(−12.5)	(+2.8)

Chemical shift changes following Au(III) complexation are given parenthetically.

for long-range couplings. Chemical shift data for the three compounds used in the study and their Au(III) complexes are collected in Table 33.

   Analysis of palladium(II) pyridinylpyrazole complexes. Satake *et al.*[197] have reported the results of a study of the complexation of palladium(II) chloride with several pyridinylpyrazole analogues and their characterization in part through the use of long-range ^{1}H–^{15}N HMBC data. ^{15}N chemical shift data were reported for a number of complexes and are collected in Table 34. Long-range ^{1}H–^{15}N correlation responses observed for one of these compounds, **224**, are shown below.

224

225

226

227

228
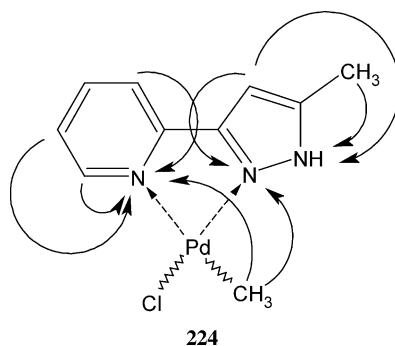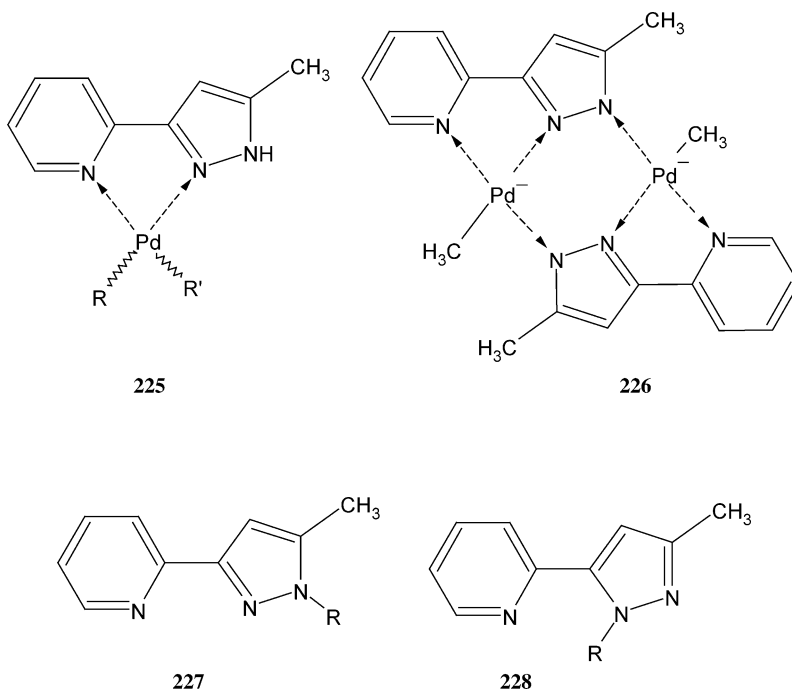
1,2,4-Triazolo[1,5-a]pyrimidine and the Zn(II) halide and thiocyanate complexes.
Szłyk and co-workers[198] reported a study of the complexation of 1,2,4-Triazolo[1,5-*a*]
pyrimidine (**229**) with Zn(II) halides and thiocyanate. The authors studied these
complexes both in solution, using long-range ^{1}H–^{15}N HMBC data and also in the solid
state via magic angle spinning studies. Usefully, the authors also report the measured
long-range ^{1}H–^{15}N coupling constants for **229** from a 1D direct observe ^{15}N experiment.
The authors also compare the results from the 1D and 2D spectra of **229**, which showed
the results to be within about ±0.5 ppm. Following complexation with various Zn(II)
halides and Zn(II) thiocyanate, only minor changes in the assigned ^{15}N shifts are
observed, as shown in Table 35.

Table 34. ^{15}N chemical shift assignments for a series of pyridinylpyrazole complexes with
palladium(II)chloride[197]

Compound or substituents	Pyridine N	Pyrazole C=N	Pyrazole NH
225 (R=–Cl, R′=–CH$_3$)	238.2	200.0	177.0
225 (R=–CH$_3$, R′=–Cl)	201.8	235.8	178.3
225 (R, R′=–Cl)	193.8	187.1	184.6
226	202.7	260.7	212.8
227/228 (R=–H)	273.2	Not detected	Not detected
227 (R=–CH$_3$)	284.4	281.4	179.6
228 (R=–CH$_3$)	286.1	172.7	291.5
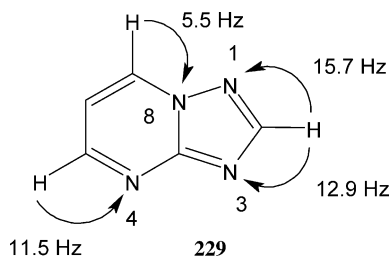
Table 35. ^{15}N shifts of 1,2,4-triazolo[1,5-α]pyrimidine (**229**) and a series of Zn(II) complexes[198]

Compound	N1	N3	N4	N8
229 1D ^{15}N	274.3	229.9	277.2	225.9
229 2D ^{15}N	273.9	229.4	276.9	226.3
229 + ZnCl$_2$	273.9	228.4	276.8	226.2
229 + ZnBr$_2$	273.9	228.4	276.7	226.3
229 + ZnI$_2$	273.8	228.4	276.8	226.2
229 + Zn(NCS)$_2$	273.9	229.0	276.8	226.4

Binding site of Zn^{2+} in ATP. Du and Mao[199] reported the results of an interesting investigation of the binding of Zn^{2+} with ATP (**230**) using long-range ^{1}H–^{15}N HMBC data as a function of pH. ^{15}N shifts for the four ring nitrogen resonances of the adenosine were measured for both free ATP and an equimolar solution of ATP and ZnCl$_2$, the data collected in Table 36.
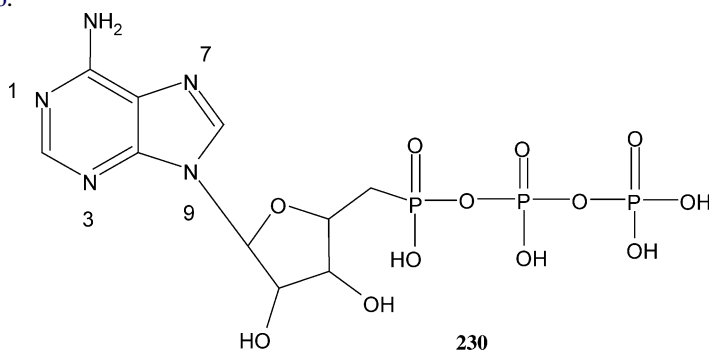
Table 36. ^{15}N chemical shift assignments for free ATP and a 1:1 equimolar solution of ATP and ZnCl$_2$ at a range of pH values[199]

pH	N1		N3		N7		N9	
	ATP	ATP + Zn	ATP	ATP + Zn	ATP	ATP + Zn	ATP	ATP + Zn
2.86	165.9	181.6	229.6	228.7	245.1	237.8	183.9	182.8
3.73	178.9	203.1	228.6	226.5	245.1	237.8	183.9	181.5
5.00	219.1	224.3	225.7	224.3	241.2	228.0	179.5	179.8
7.10	234.2	230.8	224.8	224.2	240.4	226.3	177.5	178.9

Evidence for Mg(II) binding to N1 of ATP. In a later study reported by Jiang and Mao[200] the authors present evidence for the binding of Mg^{2+} to N1 of ATP. When a solution of magnesium chloride at an equimolar concentration to a solution of ATP at pH 3.7 was added to the ATP solution, the authors observed a 10 ppm downfield shift of the N1 resonance in a ^{1}H–^{15}N HMBC experiment relative to the chemical shift of N1 in an HMBC spectrum acquired just prior to the addition of the magnesium chloride solution. None of the other nitrogen chemical shifts of the ATP were shifted upfield or downfield.

Cisplatin complexes with ATP. In a continuation of previous studies, Jiang and Mao[201] reported the results of a study of the complexation of the anticancer drug cisplatin with ATP. The authors made use of long-range ^{1}H–^{15}N HMBC data in the study, and although they did not report ^{15}N chemical shift data in the paper, they did show representative contour plots of their data. The authors concluded that a 2:1 complex is formed between ATP and cisplatin at the N7 position of ATP. At pH 2.1, a more complicated spectrum is observed. The authors interpreted the low pH data to represent the formation of an additional 1:1 complex between the N1 of ATP and cisplatin.

Polyaza[n]paracyclophanes. Albelda *et al.*[202] described the results of an ^{15}N study of several aliphatic amines, **231–233** as well as two polyaza[n]paracyclophanes by **234** and **235**. ^{15}N chemical shifts are shown, the downfield shift of the ^{15}N resonance on protonation shown parenthetically. The authors also reported some data observed for several of the polyaza[n]paracyclophanes on binding with Zn^{2+}. ^{15}N chemical shifts of **235** after binding with Zn^{2+} are presented in square braces with the structure. The reader interested in these phenomena is referred back to the cited reference for further details.
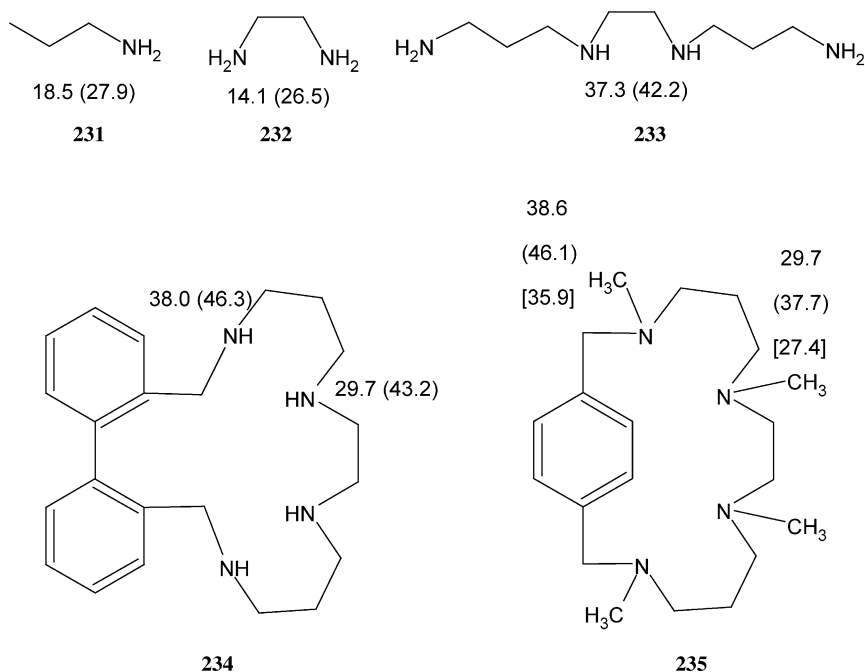
Ruthenium complexes of analogues of the antitumor antibiotic Streptonigrin. Harding and co-workers[203] in a follow-up to their work dealing with the assignment of the ^{15}N spectrum of streptonigrin (**83**) also reported a study of ruthenium complexes of several model ligands that have implications for the metal binding of streptonigrin that cleaves DNA in the presence of metal ions. In the presence of metal ions, streptonigrin is presumed to form a complex involving binding of the metal ion by the quinone carbonyl, the carboxylate group, and the quinoline and pyridine nitrogens as shown by **236**. To model metal binding by streptonigrin (**83**) several model ligands were prepared, **237** (R=–H, or –NH$_2$) and **238** (R=–CH$_3$, or –C(=O)CH$_3$).

236

237   **238**
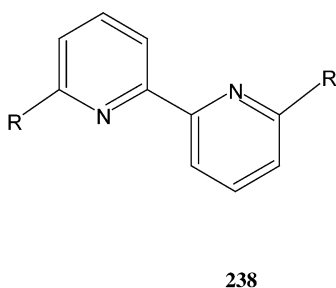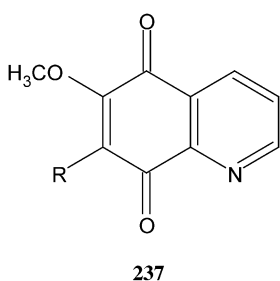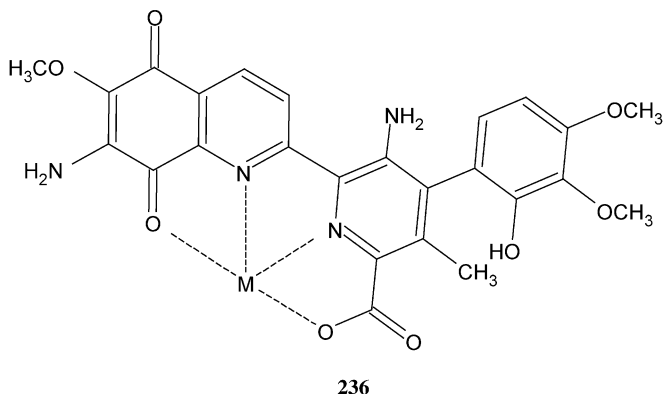
When ruthenium complexes were formed with the two **237** analogues, two different ruthenium complexes were formed as shown by **240** and **241** depending on the substituent on the quinone ring. ^{15}N chemical shifts for the free ligands and ruthenium complexes are collected in Table 37. When ligand **238**, which contains the key metal binding site of streptonigrin (**83**), was employed, both ^{1}H–^{15}N HMBC and X-ray single crystal data were obtained. The X-ray showed that despite the steric hinderance of the 6,6′-diacetyl-2,2-bipyridine (**238**, R=–C(=O)CH$_3$), the ligand was still able to form an octahedral complex with the ruthenium atom.

Table 37. ^{15}N chemical shifts for model streptonigrin ligands, **237** and **238**, and ruthenium complexes[203]

Compound	Substituent (R)	Pyridine ^{15}N	Amino ^{15}N
237	–H	315	–
237 + Ru	–H	330	–
237	–NH$_2$	314	62
237 + Ru	–NH$_2$	258	60
238	– CH$_3$	307	–
238 + Ru	– CH$_3$	231, 247	–
238	–C(=O)CH$_3$	307	–
238 + Ru	–C(=O)CH$_3$	255	–
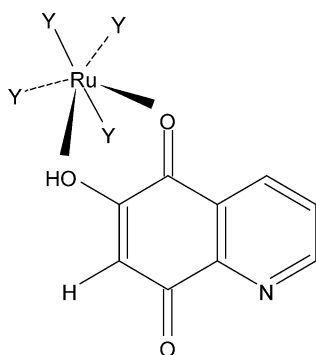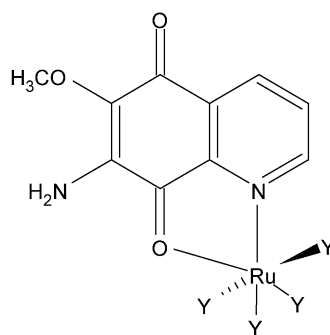
239   Y = 2Cl and 2C = O   **240**

Chelation vs. cyclometalation in a cationic dipyridylpyridazine–Rh(I) complex. Milstein and co-workers[204] reported the results of a study of the interaction of rhodium norbornadiene tetrafluoroborate (Rh(NBD)$_2$) with the tetradentate ligand 3,6-bis-(2-pyridyl)pyridazine (DPPN) (**241**). Mononuclear complexes, **242**, were obtained quantitatively. Treatment of the complex of DPPN:Rh(NBD)$_2$BF$_4$ with a second equivalent of the metal precursor (Rh(NBD)(CH$_3$CN)$_2$)BF$_4$ led to a dinuclear complex, **243**, that involves a unique rearrangement of the norbornadienyl moiety.

241

242   243
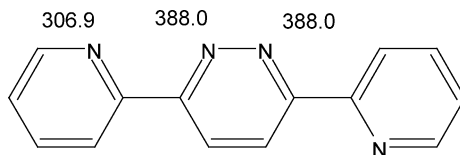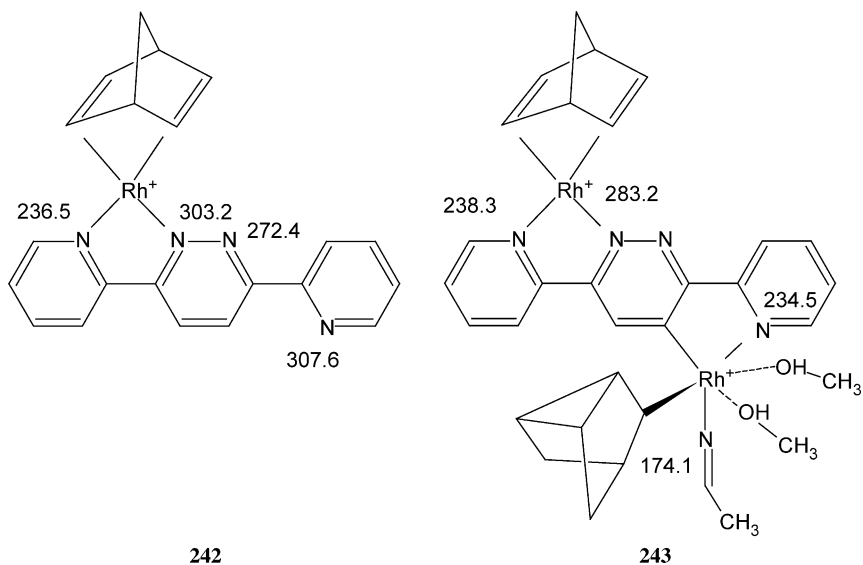
Studies of a supramolecular complex of silver(I) and a cholaphane. Virtanen and co-workers reported the results of a study involving a supramolecular complex of a cholaphane analogue (**244**) with Ag(I).[205] The authors used a 50 ms optimized ^{1}H–^{15}N HMBC spectrum to assign the piperazine nitrogen shifts with and without Ag(I).

244
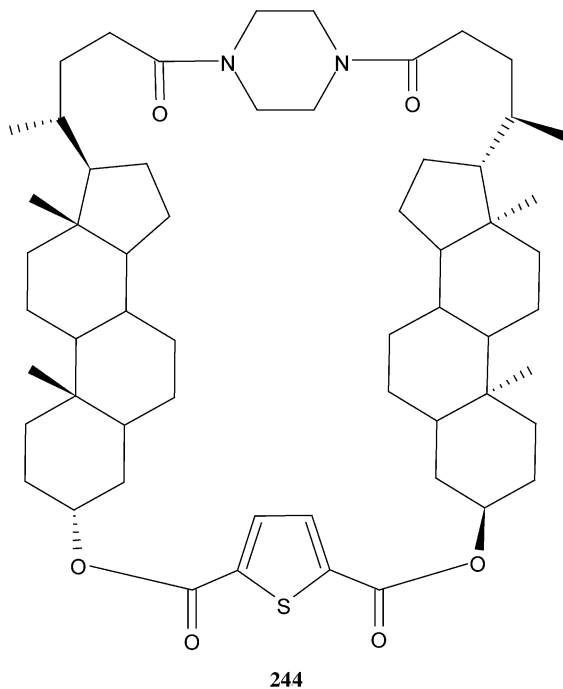
The piperazine nitrogens resonated at 111.9 ppm in the starting cholaphane and shifted downfield to 115.1 ppm on complexation with Ag(I).

Structure of a novel spirotin compound. Wrackmeyer and co-workers[206] reported an interesting multinuclear NMR study in which they demonstrated that 2,3-dichloro-1,3-bis-(trimethylsilyl)-1,3,2-diazastanna-[3]ferrocenophane reacts with lithium alkynides to give the corresponding di(alkyn-1-yl)tin derivatives, **246**, that on subsequent organo-boration with triethylborane affords a novel spirotin compound that contains both ferrocenophane and a stannacyclopentadiene ring.

245   **246**
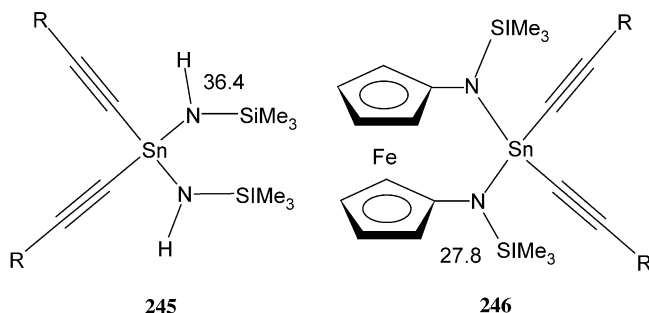
New catalysts for asymmetric hydrosilylation of ketones. Finn and co-workers[207] in another organometallic application reported the use of long-range ^{1}H–^{15}N HMBC data in characterizing a new catalyst for asymmetric hydrosilylation of ketones. In the case of one of the catalysts, that bears an *N,N*-dimethylamino group, the authors reported ^{15}N chemical shift data for the free catalyst, **247**, and the rhodium complex **248**.

247   **248**
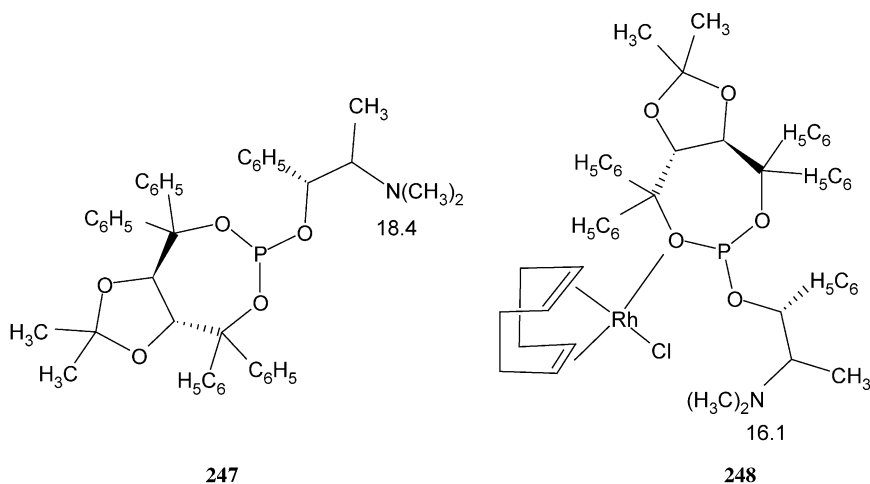
Organotin(IV) complexes containing the 4-phenyl-2,4-butanedionebenzoylhydrazone ligand. Another application of long-range ^{1}H–^{15}N HMBC in the characterization of an organotin(IV) complex was reported by Rosair and co-workers.[208] Two complexes were

prepared but only **249** had sufficient solubility for multinuclear NMR measurements; the reported ^{15}N chemical shifts are shown with the structure.

249
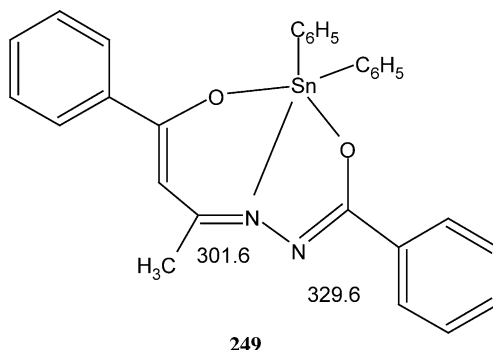
5.5. Long-range ^{15}N studies involving correlation or interaction with other nuclides or atoms – ^{19}F, ^{31}P, Sb

Characterization of hypervalent Sb···^{15}N bonding in triarylstibanes. Yamaguchi and co-workers, first in a communication[209] followed later in 2000 by a comprehensive study,[210] reported the use of long-range ^{1}H–^{15}N data to probe interactions between hypervalent antimony and ^{15}N. The authors observed a downfield shift with each of the three dimethylamino substrates studied. Hence, beginning with *N,N*-dimethylbenzyl amine, **250**, the ^{15}N resonance shifts from 25.9 to 28.8 ppm on formation of the bis-*p*-tolylstibane, **251**, and shifts still further downfield to 36.6 ppm when the antimony has two chlorine atoms attached in **252**. The authors surmise that the downfield shift may be caused by electron deficiency around the nitrogen atom due to the delocalization of a pair of electrons that would be consistent with an Sb···^{15}N bond. A similar trend is generally observed for the other two series of compounds studied in this report. The exception was an upfield shift in going from **253** to **254**. From an X-ray study of these compounds that was also a part of this comprehensive study, the authors note that the Sb···N bonding distances in **252**, **255**, and **258** are shorter than the corresponding Sb···N bonding distances in **251**, **254** and **257**. Finally, the authors also note a correlation between the Sb···N distances and ^{15}N chemical shifts.

250   **251**   **252**

253   **254**   **255**

256   **257**   **258**
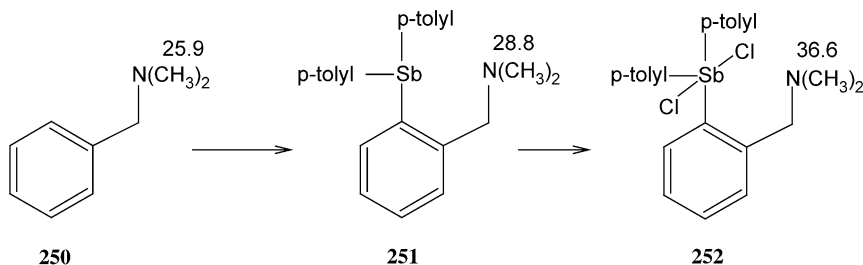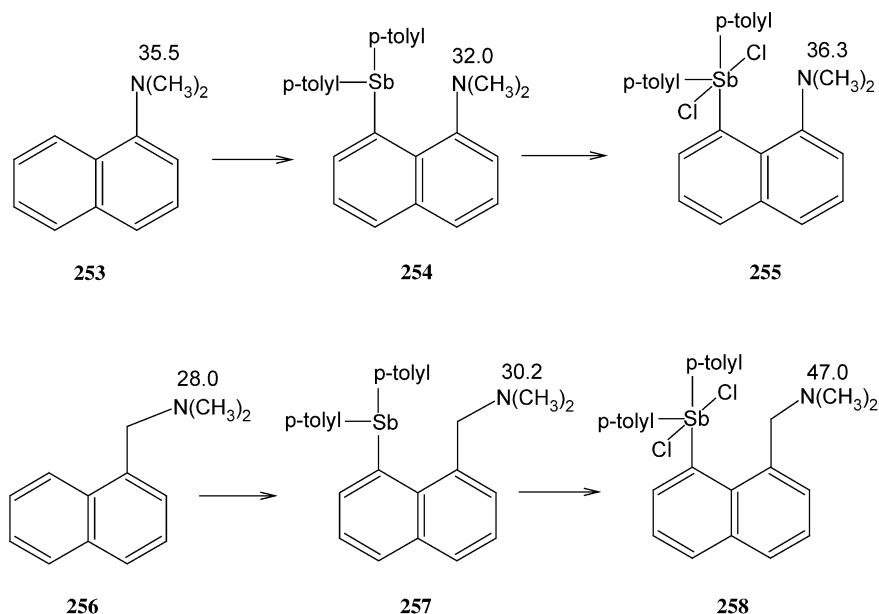
Bis(diphenylphorpanyl)amine – application of the INEPT-HEED pulse sequence. Wrackmeyer and co-workers communicated the results of a study of $^{31}P–^{15}N$ measurements for bis(diphenylphosphanyl)amine, as well as the disulfide and diselenide using the INEPT-HEED (Hahn-Echo ExtendeD) pulse sequence.[211] The authors used the experiment to measure $^{31}P–^{15}N$ heteronuclear coupling constants at natural abundance, detecting the ^{15}N via the much more sensitive ^{31}P.

Detection of ^{15}N at natural abundance via ^{31}P. Another report that dealt with the observation of ^{15}N at natural abundance via ^{31}P inverse-detection methods was that of Carbajo and López-Ortiz.[212] The authors report that enhanced sensitivity $^{15}N–^{31}P$ HSQC experiments could be recorded artifact free with good signal-to-noise, allowing accurate measurement of ^{15}N parameters including coupling constants.

Long-range $^{19}F–^{15}N$ heteronuclear shift correlation. Russell et al.[213] have demonstrated the viability of ^{19}F-detected long-range $^{19}F–^{15}N$ IMPEACH-MBC experiments which may be of use for the characterization of some nitrogen-containing heterocycles that also bear trifluoromethyl groups, for example, 2-acyl derivatives of 5-trifluoromethyl-1,3,4-thiadizole. The large difference between the $^2J_{NF}$ and $^3J_{NF}$ couplings, -52 and -3.6 Hz, for 2- and 3-fluoropyridine, respectively, almost mandates the use of an accordion-optimized pulse sequence if performing multiple experiments is to be avoided.

Two-bond $^{19}F–^{15}N$ spin–spin coupling constants ($^2J_{F–N}$) across F–H$\cdots$N hydrogen bonds. Del Bene and co-workers[214] reported the results of a study of two-bond $^{19}F–^{15}N$ spin–spin coupling constants across ^{19}F–H$\cdots^{15}N$ hydrogen bonds. Coupling constants were measured for 13 neutral compounds stabilized by F–H$\cdots$N hydrogen bonds. The proton acceptors included nitrogens that are sp (HCN and derivatives), sp^2 (aromatic azines) and sp^3 (NH$_3$ and derivatives).

Reactivity and spectroscopic properties of N-substituted secondary thioamiodes. Spychala[215] reported the results of an interesting study in 2003 involving proton complexes based on thiamide ligation. The author utilized both ^{1}H–^{15}N HSQC and HMBC data in the study although no ^{15}N chemical shifts were reported in the paper. The interested reader is referred back to the original reference for more details.

6. CONCLUSIONS

Long-range ^{1}H–^{15}N 2D NMR spectroscopy at natural abundance has become a very active area of investigation for many researchers studying a diverse assortment of structural problems and chemical phenomena. The area has been reviewed twice previously.[9,10] The most active area of investigation continues to be natural product structure elucidation. Applications have begun to appear in natural product synthesis and other synthetic studies and there are also numerous applications being reported in the organometallic area. Several new experiments have been developed since 2000 that are applicable to long-range ^{1}H–^{15}N investigations. Accordion-optimized experiments provide the means of circumventing the variability of long-range ^{1}H–^{15}N coupling constants[12] that can be problematic with statically optimized HMBC experiments that have required some investigators to run multiple experiments with different optimization to ensure that all possible correlations to the nitrogens in a given molecule are observed.[133,146] The work of Kline and Cheatham[21] in modifying the CIGAR-HMBC[19] experiment for ^{15}N has shown it to be robust for long-range ^{1}H–^{15}N measurements. If use of the IMPEACH-MBC[12] or ^{15}N-optimized CIGAR-HMBC[21] experiments becomes more widespread, we may witness continued growth in this already very active area of investigation. Finally, expanding access to cryogenic NMR probe technology can also be expected to promote further growth in the area of long-range ^{1}H–^{15}N spectroscopy.[43] The tremendous increase in sensitivity and the corresponding reduction in sample requirements as a result of cryogenic probes will make it possible for more investigators to exploit long-range ^{1}H–^{15}N measurements in their structural chemistry investigations. Some investigations utilizing cryogenic NMR probe technology have already been reported from the author's laboratory – more will undoubtedly follow.[25,26]

REFERENCES

1. J. Uzawa, H. Utumi, H. Koshino, T. Hinomoto and K. Anzai, 32nd NMR Conference, Tokyo, Japan, November 4–6, 1993, pp. 147–150.
2. G. E. Martin, R. C. Crouch, M. H. M. Sharaf and P. L. Schiff, Jr., 34th Annual Meeting of the American Society of Pharmacognosy, San Diego, CA, July 18–22, 1993, Abstract P101.
3. S. Carmeli, R. E. Moore, G. M. L. Patterson, T. H. Corbett and F. A. Valeriote, *J. Am. Chem. Soc.*, 1990, **112**, 8195.
4. R. E. Hurd and B. K. John, *J. Magn. Reson.*, 1991, **91**, 648.
5. J. Ruiz-Cabello, G. W. Vuister, C. T. W. Moonen, P. van Geldern, J. S. Cohen and P. C. M. van Zilj, *J. Magn. Reson.*, 1992, **100**, 282.
6. R. C. Crouch and G. E. Martin, *J. Heterocyclic Chem.*, 1995, **32**, 1665.

7. G. E. Martin, R. C. Crouch and C. W. Andrews, *J. Heterocyclic Chem.*, 1995, **32**, 1759.

8. G. E. Martin and R. C. Crouch, *J. Heterocyclic Chem.*, 1995, **32**, 1839.

9. G. E. Martin and C. E. Hadden, *J. Nat. Prod.*, 2000, **65**, 543.

10. R. Marek and A. Lycka, *Curr. Org. Chem.*, 2002, **6**, 35.

11. G. E. Martin, Qualitative and quantitative exploitation of heteronuclear coupling constants, in *Annual Reports on NMR Spectroscopy*, G. A. Webb, ed., Vol. 46, Academic Press, London, 2002, 37–100.

12. C. E. Hadden, G. E. Martin and V. V. Krishnamurthy, *J. Magn. Reson.*, 1999, **140**, 274.

13. G. E. Martin and C. E. Hadden, *Magn. Reson. Chem.*, 2000, **38**, 251.

14. A. Meissner and O. W. Sørensen, *Magn. Reson. Chem.*, 2000, **38**, 981.

15. D. A. Craig and G. E. Martin, *J. Nat. Prod.*, 1986, **49**, 456.

16. A. M. Torres, W. A. Bubb and P. W. Kuchel, *J. Magn. Reson.*, 2002, **156**, 249.

17. T. Sprang and P. Bigler, *Magn. Reson. Chem.*, 2003, **41**, 177.

18. T. Sprang and P. Bigler, *Magn. Reson. Chem.*, 2004, **42**, 55.

19. V. V. Krishnamurthy, D. J. Russell, C. E. Hadden and G. E. Martin, *J. Magn. Reson.*, 2000, **146**, 232.

20. R. Berger, C. Schorn and P. Bigler, *J. Magn. Reson.*, 2001, **148**, 88.

21. M. Kline and S. Cheatham, *Magn. Reson. Chem.*, 2003, **41**, 307.

22. K. A. Farley, G. S. Walker and G. E. Martin, *Magn. Reson. Chem.*, 1997, **35**, 671.

23. J.-M. Nuzillard, J. D. Connolly, C. Delaude, B. Richard, M. Zèches-Hanrot and L. Le Men-Olivier, *Tetrahedron*, 1999, **55**, 11511.

24. M. Köck, J. Junker and T. Lindel, *Org. Lett.*, 1999, **1**, 2041.

25. G. E. Martin, C. E. Hadden, D. J. Russell, B. D. Kaluzny, J. E. Guido, W. K. Duholke, B. A. Stiemsma, T. J. Thamann, R. C. Crouch, K. Blinov, M. Elyashberg, E. R. Martirosian, S. G. Molodtsov, A. J. Williams and P. L. Schiff Jr., *J. Heterocyclic Chem.*, 2002, **39**, 1241.

26. K. Blinov, M. Elyashberg, E. R. Martirosian, S. G. Molodtsov, A. J. Williams, A. N. Tackie, M. H. M. Sharaf, P. L. Schiff Jr., R. C. Crouch, G. E. Martin, C. E. Hadden, J. E. Guido and K. A. Mills, *Magn. Reson. Chem.*, 2003, **41**, 577.

27. M. E. Elyashberg, K. A. Blinov, E. R. Martirosian, S. G. Molodtsov, A. J. Williams and G. E. Martin, *J. Heterocyclic Chem.*, 2003, **40**, 1017.

28. M. E. Elyashberg, K. A. Blinov, A. J. Williams, S. G. Molodtsov, G. E. Martin and E. R. Martirosian, *J. Chem. Inf. Comput. Sci.*, 2004, **44**, 771.

29. G. E. Martin, C. E. Hadden and D. J. Russell, unpublished data.

30. T. Parella and J. Bellow, *Magn. Reson. Chem.*, 2002, **40**, 133.

31. R. C. Crouch and G. E. Martin, *J. Nat. Prod.*, 1992, **55**, 1343.

32. R. C. Crouch and G. E. Martin, *Magn. Reson. Chem.*, 1992, **30**, S66.

33. G. E. Martin, R. C. Crouch and A. P. Zens, *Magn. Reson. Chem.*, 1998, **36**, 551.

34. G. E. Martin, J. E. Guido, R. H. Robins, M. H. M. Sharaf, A. N. Tackie and P. L. Schiff Jr., *J. Nat. Prod.*, 1998, **61**, 555.

35. G. Schlotterbeck, A. Ross, H. Senn, R. Hochstrasser, H. Tschirky, R. Seydoux, D. Marek, T. Kühn, O. Schett and M. Warden, *42nd Experimental NMR Conference*, Orlando, FL, March 11–16, 2001, Abst. W&Th, p. 202.

36. G. Schlotterbeck, A. Ross, R. Hochstrasser, H. Senn, T. Kühn, D. Marek and O. Schett, *Anal. Chem.*, 2002, **74**, 4464.

37. G. E. Martin, Microprobes and methodologies for spectral assignments: applications, in *Encyclopedia of Nuclear Magnetic Resonance*, D. M. Grant and R. K. Harris, eds., *Advances in NMR,* Vol. 9, Wiley, Chichester, 2002, 98–112.

38. P. Styles, N. F. Soffe, C. A. Scott, D. A. Cragg, F. Row, D. White and P. C. J. White, *J. Magn. Reson.*, 1983, **60**, 397.

39. P. Styles, N. F. Soffe and C. A. Scott, *J. Magn. Reson.*, 1989, **84**, 376.

40. W. A. Anderson, W. W. Brey, A. I. Brooke, B. Cole, K. A. Delin, L. H. Fuks, H. D. W. Hill, M. E. Johanson, V. Y. Kotsubo, R. Nast, R. S. Withers and W. H. Wong, *Bull. Magn. Reson.*, 1995, **17**, 98.

41. H. D. W. Hill, *IEEE Trans. Appl. Superconduct.*, 1997, **7**, 3750.

42. G. E. Martin, Cryogenic NMR Probes: Applications, in *Encyclopedia of Nuclear Magnetic Resonance*, D. M. Grant and R. K. Harris, eds., *Advances in NMR,* Vol. 9, Wiley, Chichester, 2002, 33–35.

43. R. C. Crouch, W. Llanos, K. G. Mehr, C. E. Hadden, D. J. Russell and G. E. Martin, *Magn. Reson. Chem.*, 2001, **39**, 555.

44. M. E. Elyashberg, K. A. Blinov and E. R. Martirosian, *Lab. Automat. Inf. Manage.*, 1999, **34**, 15; K. A. Blinov, M. E. Elyashberg, S. G. Molodtsov, A. J. Williams and E. R. Martirosian, *Fresenius J. Anal. Chem.*, 2001, **369**, 709.

45. M. E. Elyashberg, K. A. Blinov, A. J. Williams, E. R. Martirosian and S. G. Molodtsov, *J. Nat. Prod.*, 2002, **65**, 693.

46. K. A. Blinov, D. A. Carlson, M. E. Elyashberg, G. E. Martin, E. R. Martirosian, S. Molodtsov and A. J. Williams, *Magn. Reson. Chem.*, 2003, **41**, 359.

47. S. G. Molodtsov, M. E. Elyashberg, K. A. Blinov, A. J. Williams, E. R. Martirosian, G. E. Martin and B. Lefebvre, *J. Chem. Inf. Comp. Sci.*, 2004, **44**, 1737.

48. B. D. Christie and M. E. Munk, *J. Am. Chem. Soc.*, 1991, **113**, 3750.

49. M. E. Munk, *J. Chem. Inf. Comput. Sci.*, 1998, **38**, 997.

50. K. Funatsu and S. Sasaki, *J. Chem. Inf. Comput. Sci.*, 1996, **36**, 190.

51. C. Peng, S. Yuan, C. Zheng and Y. Hui, *J. Chem. Inf. Comput. Sci.*, 1994, **34**, 805.

52. C. Peng, S. Yuan, C. Zheng, Y. Hui, H. We, K. Ma and X. Han, *J. Chem. Inf. Comput. Sci.*, 1994, **34**, 814.

53. C. Peng, S. Yuan, C. Zheng, Z. Shi and H. Wu, *J. Chem. Inf. Comput. Sci.*, 1995, **35**, 539.

54. C. Peng, G. Bodenhausen, S. Qiu, H. H. S. Fong, N. R. Farnsworth, S. Yuan and C. Zheng, *Magn. Reson. Chem.*, 1998, **36**, 267.

55. J.-M. Nuzzillard and G. Massiot, *Tetrahedron*, 1991, **47**, 3655.

56. J.-M. Nuzillard, J. D. Connolly, C. Delaude, B. Richard, M. Zeches-Hanrot and L. Le Men-Livier, *Tetrahedron*, 1999, **55**, 11511.

57. C. Steinbeck, *Angew. Chem. Int. Ed. Engl.*, 1996, **35**, 1984.

58. T. Lindel, J. Junker and M. Köck, *Eur. J. Org. Chem.*, 1999, **3**, 573.

59. M. Köck, J. Junker and T. Lindel, *Org. Lett.*, 1999, **1**, 2041.

60. M. Jaspers, *Nat. Prod. Rep.*, 1999, **16**, 241.

61. G. E. Martin and A. J. Williams, Probes, Pulse Sequences, and CASE Programs: Advances in the Characterization of Novel Structures Using NMR-Based Methods, ACD/Labs North American User's Meeting, Princeton, NJ, March 7–8, 2002.

62. Advanced Chemistry Development, Inc., 90 Adelaide St. West, Suite 600, Toronto, Ont., Canada MH5 3V9.

63. W. Bremser, *Anal. Chim. Acta*, 1978, **103**, 355.

64. G. E. Martin and A. J. Williams, Validation of NNMR predictor, ACD/Labs user meeting, ENC 2004, Monterey, April 18, 2004.

65. I. Wiedermannová, J. Slouka, O. Humpa and K. Lemr, *J. Heterocyclic Chem.*, 2003, **40**, 357.

66. G. E. Martin, D. J. Russell, K. A. Blinov, M. E. Elyashberg and A. J. Williams, *Ann. Magn. Reson.*, 2003, **2**, 1.

67. K. Blinov, M. Elyashberg, E. R. Martirosian, S. G. Molodtsov, A. J. Williams, A. N. Tackie, M. H. M. Sharf, P. L. Schiff Jr., R. C. Crouch, G. E. Martin, C. E. Hadden, J. E. Guido and K. A. Mills, *Magn. Reson. Chem.*, 2003, **41**, 577.

68. R. C. Crouch, A. O. Davis, T. D. Spitzer, G. E. Martin, M. H. M. Sharaf, P. L. Schiff Jr., C. H. Phoebe Jr. and A. N. Tackie, *J. Heterocyclic Chem.*, 1995, **32**, 1077.

69. M. H. M. Sharaf, P. L. Schiff Jr., A. N. Tackie, C. H. Phoebe Jr., R. L. Johnson, D. Minick, C. W. Andrews, R. C. Crouch and G. E. Martin, *J. Heterocyclic Chem.*, 1996, **33**, 789.

70. A. N. Tackie, G. N. Boye, M. H. M. Sharaf, P. L. Schiff Jr., R. C. Crouch, T. D. Spitzer, R. L. Johnson, J. Dunn, D. Minick and G. E. Martin, *J. Nat. Prod.*, 1993, **56**, 653.

71. C. E. Hadden, G. E. Martin, A. N. Tackie and P. L. Schiff Jr., *J. Heterocyclic Chem.*, 1999, **36**, 1115.

72. G. E. Martin, C. E. Hadden, A. N. Tackie, M. H. M. Sharaf and P. L. Schiff Jr., *Magn. Reson. Chem.*, 1999, **37**, 529.

73. A. Bax and M. F. Summers, *J. Am. Chem. Soc.*, 1986, **108**, 2093.

74. D. Gudat, Applications of heteronuclear X/Y-correlation spectroscopy in organometallic and organoelement chemistry: recent developments, in *Annual Reports on NMR Spectroscopy*, G. A. Webb, ed., Vol. 51, Academic Press, London, 2002, 60–103.

75. K. Shin-Ya, J.-S. Kim, K. Furihata, Y. Hayakawa and H. Seto, *J. Asian Nat. Prod. Rep.*, 2000, **2**, 121.

76. H. Seki, T. Tokunaga, H. Utsumi and K. Yamaguchi, *Tetrahedron*, 2000, **56**, 2935.
77. X.-C. Li, D. C. Dunbar, H. N. El Sohly, L. A. Walker and A. M. Clark, *Phytochemistry*, 2001, **58**, 627.
78. Z. Zhang, H. N. El Sohly, M. R. Jacob, D. S. Pasco, L. A. Walker and A. M. Clark, *J. Nat. Prod.*, 2001, **64**, 1001.
79. I. Muhammad, D. C. Dunbar, R. A. Khan, M. Ganzera and I. A. Kahn, *Phytochemistry*, 2001, **57**, 781.
80. M. Horiuchi, T. Maoka, N. Iwase and K. Ohnishi, *J. Nat. Prod.*, 2002, **65**, 1204.
81. R. Suemitsu, K. Ohnishi, M. Horiuchi, A. Kitagichi and Odamura, *Phytochemistry*, 1992, **31**, 2325.
82. D. R. Appleton, M. J. Page, G. Lambert, M. V. Berridge and B. R. Copp, *J. Org. Chem.*, 2002, **67**, 5402.
83. D. R. Appleton and B. R. Copp, *Tetrahedron*, 2003, **44**, 8963.
84. C. E. Hadden, D. J. Richard, M. M. Joullié and G. E. Martin, *J. Heterocyclic Chem.*, 2003, **40**, 359.
85. Y. Liu, W. W. McWhorter Jr. and C. E. Hadden, *Org. Lett.*, 2003, **5**, 333.
86. M. Tsuda, T. Mugishima, K. Komatsu, T. Sone, M. Tanaka, Y. Mikami, M. Shiro, M. Hirai, Y. Ohizumi and J. Kobayashi, *Tetrahedron*, 2003, **59**, 3227.
87. S.-Y. Jeong, K. Ishida, Y. Ito, S. Okada and M. Murakami, *Tetrahedron Lett.*, 2003, **44**, 8005.
88. R. M. Claramunt, C. Lopze, D. Sanz, I. Alkorta and J. Elguero, *Heterocycles*, 2001, **55**, 2109.
89. M. Moreno-Mañas, R. M. Sebastián, A. Vallribera, J. F. Piniella, A. Álvarez-Larena, M. L. Jimeno and J. Elguero, *New J. Chem.*, 2001, **25**, 329.
90. S. Trofimenko, A. L. Rheingold, L. M. Liable-Sands, R. M. Claramunt, C. López, M. D. Santa Maria and J. Elguero, *New J. Chem.*, 2001, **25**, 819.
91. R. M. Claramunt, C. López, M. A. García, M. D. Otero, M. R. Torres, E. Pinilla, S. H. Alarcón, I. Alkorta and J. Elguero, *New J. Chem.*, 2001, **25**, 1061.
92. M. A. P. Martins, C. M. P. Pereira, A. P. Sinhorin, A. Rosa, N. E. K. Zimmermann, H. G. Bonacorso and N. Zanatta, *Magn. Reson. Chem.*, 2002, **40**, 182.
93. J. R. Malpass, D. Belkacemi and D. R. Russell, *Tetrahedron*, 2002, **58**, 197.
94. J. A. Guerrero-Alvarez, A. Moncayo-Bautista and A. Ariza-Castolo, *Magn. Reson. Chem.*, 2004, **42**, 524.
95. J. Ford and R. J. Capon, *J. Nat. Prod.*, 2000, **63**, 1527.
96. Y. Kan, B. Sakamoto, T. Fujita and H. Nagai, *J. Nat. Prod.*, 2000, **63**, 1599.
97. K. A. El Sayed, A. M. S. Mayer, M. Kelly and M. T. Hamann, *J. Org. Chem.*, 1999, **64**, 9258.
98. T.-P. Loh, Y.-K. Chok and Z. Yin, *Tetrahedron Lett.*, 2001, **42**, 7893.
99. K. Shin-ya, J.-S. Kim, K. Furihata, Y. Hayakawa and H. Seto, *Tetrahedron Lett.*, 1997, **38**, 7079.
100. H. Luesh, W. Y. Yoshida, R. E. Moore and V. J. Paul, *Tetrahedron*, 2002, **58**, 7959.
101. T. Zenkoh, Y. Ohtsu, S. Yoshimura, N. Shigematsu, S. Takase and M. Hino, *J. Antibiotics*, 2003, **56**, 694.
102. T. Komoda, Y. Sugiyama, N. Abe, M. Imachi, H. Hirota, H. Koshino and A. Hirota, *Tetrahedron Lett.*, 2003, **44**, 7417.
103. T. Komoda, Y. Sugiyama, N. Abe, M. Imachi, H. Hirota and A. Hirota, *Tetrahedron Lett.*, 2003, **44**, 1659.
104. O. Kretsi, N. Aligiannis, A.-L. Skaltsounis and I. B. Chinou, *Helv. Chim. Acta*, 2003, **86**, 3136.
105. Alia, J. Matysik, C. Erkelens, F. B. Hulsbergen, P. Gast, J. Lugtenberg and H. J. M. de Groot, *Chem. Phys. Lett.*, 2000, **330**, 325.
106. D. C. Dunbar, J. M. Rimoldi, A. M. Clark, M. Kelly and M. T. Hamann, *Tetrahedron*, 2000, **56**, 8795.
107. J. W. Peterson, D. King, E. L. Ezell, M. Rogers, D. Gelssell, J. Hoffpauer, L. Reuss, A. Chopra and D. Gorenstein, *Biochem. Biophys. Acta*, 2001, **1537**, 27.
108. P. Ciminello, C. Dall'Aversano, E. Gattoruso and S. Magno, *Eur. J. Org. Chem.*, 2001, 55.
109. J. M. Rieder and J. Lepschy, *Tetrahedron Lett.*, 2002, **42**, 2375.
110. Y. Kato, H. Koshino, J. Uzawa and K. Anzai, *Biosci. Biotech. Biochem.*, 1996, **60**, 2081.
111. G. R. Pettit, J. C. Collins, J. C. Knight, D. L. Herald, R. A. Nieman, M. D. Williams and R. K. Pettit, *J. Nat. Prod.*, 2003, **66**, 544.
112. Y. Itou, S. Okada and M. Murakami, *Tetrahedron*, 2001, **57**, 9093.
113. A. Scheurer, W. Bauer, F. Hampel, C. Schidt, R. W. Saalfrank, P. Mosset, R. Puchta and N. J. R. van Eikema Hommes, *Tetrahedron Assym.*, 2004, **15**, 867.
114. N. Fokialakis, P. Magiatis, A.-L. Skaltsounis, F. Tillequin and T. Sévenet, *J. Nat. Prod.*, 2000, **63**, 1004.
115. K. Y. Orabi, K. A. El Sayed, M. T. Harmann, C. D. Dunbar, M. S. Al-Said, T. Higa and M. Kelly, *J. Nat. Prod.*, 2000, **65**, 1782.

116. K. A. Farley, P. B. Bowman, J. C. Brumfield, F. W. Crow, W. K. Duholke, J. E. Guido, R. H. Robins, S. M. Sims, R. F. Smith, T. J. Thamann, B. S. Vonderwell and G. E. Martin, *Magn. Reson. Chem.*, 1998, **36**, S11.

117. G. E. Martin, C. E. Hadden, J. R. Blinn, M. H. M. Sharaf, A. N. Tackie and P. L. Schiff Jr., *Magn. Reson. Chem.*, 1999, **37**, 1.

118. C. E. Hadden, B. D. Kaluzny, R. H. Robins and G. E. Martin, *Magn. Reson. Chem.*, 1999, **37**, 325.

119. H. Wang and A. Ganesan, *J. Org. Chem.*, 2000, **65**, 1022.

120. P. L. Schiff Jr., *Alkaloids: Chem. Biol. Perspect.*, 1999, **14**, 1.

121. L. Mambu, M.-T. Martin, D. Razafimahefa, D. Ramanitrahasimbola, P. Rasoanaivo and F. Frappier, *Planta Med.*, 2000, **66**, 537.

122. I. Muhammad, D. C. Dunbar, S. Takamatsu, L. A. Walker and A. M. Clark, *J. Nat. Prod.*, 2001, **64**, 559.

123. P. I. Anderberg, I. J. Luck and M. M. Harding, *Magn. Reson. Chem.*, 2002, **40**, 313.

124. R. Marek, J. Marek, J. Dostál, E. Táborská, J. Slavík and R. Dommisse, *Magn. Reson. Chem.*, 2002, **40**, 687.

125. R. Marek, O. Humpa, J. Dostál, J. Slavík and V. Sklenář, *Magn. Reson. Chem.*, 1999, **37**, 195.

126. R. Marek, L. Kárlik and V. Slkenář, *Tetrahedron Lett.*, 1997, **38**, 665.

127. I. Muhammad, J. Zhao, D. C. Dunbar and I. A. Khan, *Phytochemistry*, 2002, **59**, 105.

128. D. R. Appleton, A. N. Pearce, G. Lambert, R. C. Babcock and B. R. Copp, *Tetrahedron*, 2002, **58**, 9779.

129. R. Marek, P. Sečkářová, D. Hulová, J. Marek, J. Dostál and V. Sklenař, *J. Nat. Prod.*, 2003, **66**, 481.

130. M. C. Francisco, A. L. M. Nasser and L. M. X. Lopes, *Phytochemistry*, 2003, **62**, 1265.

131. F.-L. Hsu and J.-Y. Chen, *Phytochemistry*, 1993, **34**, 1625.

132. L.-K. Yang, R. P. Glover, K. Yoganathan, J. P. Sarnaik, A. J. Godbole, D. D. Soejarto, A. D. Buss and M. S. Butler, *Tetrahedron Lett.*, 2003, **44**, 5827.

133. L. Chill, M. Aknin and Y. Kashman, *Org. Lett.*, 2003, **5**, 2433.

134. N. Arai, K. Shiomi, Y. Iwai and S. Ōmura, *J. Antibiotics*, 2000, **53**, 609.

135. K. Ishida, H. Nakagawa and M. Murakami, *J. Nat. Prod.*, 2000, **63**, 1315.

136. K. E. Milligan, B. L. Marquez, R. T. Williamson and W. H. Gerwick, *J. Nat. Prod.*, 2000, **63**, 1440.

137. L. T. Tan, R. T. Williamson, W. H. Gerwick, K. S. Watts, K. McGouch and R. Jacobs, *J. Org. Chem.*, 2000, **65**, 419.

138. C. E. Hadden, G. E. Martin, J.-K. Luo and R. N. Castle, *J. Heterocylic Chem.*, 1999, **36**, 533.

139. F. Yokokawa, H. Sameshima, Y. In, K. Minoura, T. Ishida and T. Shioiri, *Tetrahedron*, 2002, **58**, 8127.

140. T. Golakoti, W. Y. Yoshida, S. Chaganty and R. E. Moore, *J. Nat. Prod.*, 2001, **64**, 54.

141. C. Farès, F. J. Sharom and J. H. Davis, *J. Am. Chem. Soc.*, 2002, **124**, 11232.

142. Z. Jiang, M.-O. Barret, K. G. Boyd, D. R. Adams, A. S. F. Boyd and J. G. Burgess, *Phytochemistry*, 2002, **60**, 33.

143. J. E. Leet, W. Li, H. A. Ax, J. A. Matson, S. Huang, R. Huang, J. L. Cantone, D. Drexler, R. A. Dalterio and K. S. Lam, *J. Antibiotics*, 2003, **56**, 232.

144. K. L. Constantine, L. Mueller, S. Huang, S. Abid, K. S. Lam, W. Li and J. E. Leet, *J. Am. Chem. Soc.*, 2003, **124**, 7284.

145. O. Grach-Pogrebinsky, B. Sedmak and S. Carmeli, *Tetrahedron*, 2003, **59**, 8329.

146. H. Koshino, Y. Kono, K. Yoneyama and J. Uzawa, *Heterocycles*, 2000, **52**, 811.

147. H. Wang, K. L. Lim, S. L. Yeo, X. Xu, M. M. Sim, A. E. Ting, Y. Wang, S. Yee, Y. H. Tan and C. J. Pallen, *J. Nat. Prod.*, 2000, **63**, 1641.

148. D. Tasdemir, G. C. Mangalindan, G. P. Concepción, M. K. Harper and C. M. Ireland, *Chem. Pharm. Bull.*, 2001, **49**, 1628.

149. R. M. Van Wagoner, J. Jompa, A. Tahir and C. M. Ireland, *J. Nat. Prod.*, 2001, **64**, 1100.

150. Y. Kan, D. Uemura, Y. Hirata, M. Ishiguro and T. Iwashita, *Tetrahedron Lett.*, 2001, **42**, 3197.

151. M. M. Uy, S. Ohta, M. Yanai, E. Ohta, T. Hirata and S. Ikegami, *Bioorg. Med. Chem. Lett.*, 2002, **12**, 3037.

152. C. Xia, H. Fösterling and D. H. Petering, *Biochemistry*, 2003, **42**, 6559.

153. H. Naanawa, T. Takita, H. Umezawa and W. E. Hull, *J. Antibiotics*, 1979, **32**, 539.

154. E. Kolehmainen, H. Janota, R. Gawinecki, K. Laihia and R. Kauppinen, *Magn. Reson. Chem.*, 2000, **38**, 384.

155. S. Schilling, U. Rinner, C. Chan, I. Tghiviriga and T. Hudlicky, *Can. J. Chem.*, 2001, **79**, 1659.

156. A. Zakrzewska, E. Kolehmainen, B. Osmialowski and R. Gawinecki, *J. Fluor. Chem.*, 2001, **111**, 1.

157. P. Šimůnek, V. Bertolasi and V. Macháček, *J. Mol. Struct.*, 2002, **642**, 41.

158. N. I. Vasilevich, N. D. Sachinvala, K. Maskoks and D. H. Coy, *Tetrahedron Lett.*, 2002, **43**, 3443.

159. A. Pezzella, P. Manini, P. Di Donato, R. Boni, A. Napolitano, A. Palumbo and M. d'Ischia, *Bioorg. Med. Chem.*, 2004, **12**, 2927.

160. S. Zaramella, P. Heinonen, E. Yeheskielyh and R. Strömberg, *J. Org. Chem.*, 2003, **68**, 7521.

161. E. Kolehmainen, K. Laihia, A. V. Firsov, V. I. Zayzev, E. E. Emelina and A. A. Petrov, *Magn. Reson. Chem.*, 2002, **40**, 480.

162. A. Klásek, K. Kořistek, A. Lyčka and M. Holčapek, *Tetrahedron*, 2003, **59**, 1283.

163. A. Klásek, K. Kořistek, A. Lyčka and M. Holčapek, *Tetrahedron*, 2003, **59**, 5279.

164. E. Kolehmainen, B. Ośmiałowski, T. M. Krygowski, R. Kauppinen, M. Nissinen and R. Gawinecki, Originally reported as manuscript in preparation although to the best of the author's knowledge, this manuscript was never published.

165. B. Nowak-Wydra, B. Gierczyk and G. Schroeder, *Magn. Reson. Chem.*, 2003, **41**, 689.

166. A. Csámpai, P. Kövér, G. Hajós and Z. Riedl, *J. Mol. Struct.*, 2002, **616**, 73.

167. E. Bednarek, B. Modzelewska-Banachiewicz, M. K. Cyrański, J. Sitkowski and I. Wawer, *J. Mol. Struct.*, 2001, **562**, 167.

168. S. Trofimenko, A. L. Theingold, L. M. Liable-Sands, R. M. Claramunt, C. López, M. D. Santa Maria and J. Elguero, *New J. Chem.*, 2001, **25**, 819.

169. R. M. Claramunt, C. López, M. A. Garcia, M. D. Otero, M. R. Torres, E. Pinilla, S. H. Alarcón, I. Alkorta and J. Elguero, *New J. Chem.*, 2001, **25**, 1061.

170. H. García-Ortega, J. Crusats, M. Feliz and J. M. Ribó, *J. Org. Chem.*, 2002, **67**, 4170.

171. J. Koivukorpi, A. Valkonen and E. Kolehmainen, *J. Mol. Struct.*, 2004, **693**, 81.

172. J. Joroszewska-Manaj, D. Maciejewska and I. Wawer, *Magn. Reson. Chem.*, 2000, **38**, 482.

173. R. Gawinecki, B. Ośmiałowski, E. Kolehmainnen and M. Nissinen, *J. Mol. Struct.*, 2000, **525**, 233.

174. B. Ośmiałowski, M. Nissinen, E. Kolehmainen and R. Gawinecki, *J. Mol. Struct.*, 2000, **525**, 241.

175. H. Sommer, H.-J. Bertram, G. E. Krammer, C. O. Schmidt, W. Stumpe, P. Werkhoff and M. Zviley, *Magn. Reson. Chem.*, 2000, **38**, 907.

176. C. Fruit, A. Turck, N. Plé, L. Mojovic and G. Quéguiner, *Tetrahedron*, 2001, **57**, 9429.

177. K. Laihia, E. Kolehmainen, R. Kauppinen, J. Lorenc and A. Puszko, *Spectrochim. Acta A*, 2002, **58**, 1425.

178. K. Laihia, E. Kolehmainen, E. Virtanen, M. Nissinen, A. Puszko and Z. Talik, *Magn. Reson. Chem.*, 2003, **41**, 721.

179. P. Forgo and I. Vincze, *Steroids*, 2002, **67**, 749.

180. J. L. Jios, G. P. Romanelli, J. C. Autino, D. Magiera and H. Duddeck, *Z. Naturforsh.*, 2002, **57b**, 226.

181. B. Ośmiałowski, K. Laihia, E. Virtanen, M. Nissinen, E. Kolehmainen and R. Gawinecki, *J. Mol. Struct.*, 2003, **654**, 61.

182. M. Hocek, I. Votruba and H. Dvořáková, *Tetrahedron*, 2003, **59**, 607.

183. D. Pappo and Y. Kashman, *Tetrahedron*, 2003, **59**, 6493.

184. A. Rudi, H. Shalom, M. Schleyer, Y. Benayahu and Y. Kashman, *J. Nat. Prod.*, 2004, **67**, 106.

185. P. Pollesello and P. Nore, *J. Pharm. Biomed. Anal.*, 2003, **31**, 125.

186. P. Magiatis, S. Mitaku, A.-L. Skaltsounis and F. Tillequin, *Chem. Pharm. Bull.*, 2003, **49**, 1304.

187. N. Sitachitta, B. L. Márquez, R. T. Williamson, J. Rossi, M. A. Roberts, W. H. Gerwick, V.-A. Nguyen and C. L. Willis, *Tetrahedron*, 2000, **56**, 9103.

188. C. E. Hadden, P. B. Bowman, W. H. Duholke, J. E. Guido, B. D. Kaluzny, R. H. Robins, D. J. Russell, S. M. Sims, T. J. Thamann and G. E. Martin, *J. Heterocyclic Chem.*, 2000, **37**, 1623.

189. D. Vogna, R. Marotta, A. Napolitano and M. d'Ischia, *J. Org. Chem.*, 2002, **67**, 6143.

190. E. Gössnitzer, K. Görlitzer and H. J. Baltrusch, *Magn. Reson. Chem.*, 2002, **40**, 467.

191. P. Besse, B. Combourieu, G. Boyse, M. Sancelme, H. de Wever and A.-M. Delort, *Appl. Environ. Microbiol.*, 2001, **67**, 1412.

192. N. Haroune, B. Combourieu, B. Besse, M. Sanmcelme and A.-M. Delort, *Compt. Rend. Acad. Sci., Paris*, 2001, **4**, 759.

193. F. Mesnard, N. Azaroual, D. Marty, M.-A. Fliniax, R. J. Robins, G. Vermeersch and J.-P. Monti, *Planta*, 2000, **210**, 446.

194. O. Fliniaux, F. Mesnard, S. Raynaud, S. Baltora, R. J. Robins and M.-A. Fliniaux, *Compt. Rend. Acad. Sci., Paris, Chim.*, 2001, **4**, 775.

195. J. Tamminen, E. Kolehmainen, J. Linnanto, P. Vainiotalo, S. Vuorikoski and R. Kauppinen, *J. Incl. Phenom. Macrocyclic Chem.*, 2000, **37**, 121.

196. E. Szlyk, L. Pazderski, I. Łakomska, L. Kozerski and J. Sitkowski, *Magn. Reson. Chem.*, 2002, **40**, 529.

197. A. Satake, H. Koshino and T. Nakata, *J. Organomet. Chem.*, 2000, **595**, 208.

198. E. Szłyk, A. Grodzicki, L. Pazderski, E. Bednarek and B. Kamieński, *Polyhedron*, 2000, **19**, 965.

199. F. Du and X.-A. Mao, *Spectrochim. Acta A*, 2000, **56**, 2391.

200. L. Jiang and X.-A. Mao, *Spectrochim. Acta A*, 2001, **57**, 1711.

201. L. Jiang and X.-A. Mao, *Polyhedron*, 2003, **22**, 611.

202. M. T. Albelda, M. I. Burguete, J. C. Frías, E. García-España, S. V. Luis, J. F. Miravet and M. Querol, *J. Org. Chem.*, 2001, **66**, 7505.

203. P. I. Anderberg, M. M. Harding, I. J. Luck and P. Turner, *Inorg. Chem.*, 2002, **41**, 1365.

204. R. Dorata, L. Konstantinovski, L. J. W. Simon, Y. Ben-David and D. Milstein, *Eur. J. Inorg. Chem.*, 2003, 70.

205. E. Virtanen, J. Koviukorpi, J. Tamminen, P. Mänttäri and E. Kolehmainen, *J. Organomet. Chem.*, 2003, **668**, 43.

206. B. Wrackmeyer, H. E. Maisel, W. Milius and M. Herbrhold, *J. Organomet. Chem.*, 2003, **680**, 271.

207. S. Yao, J.-C. Meng, S. Siuzdak and M. G. Finn, *J. Org. Chem.*, 2003, **68**, 2540.

208. D. K. Dey, A. Lycka, S. Mitra and G. M. Rosair, *J. Organomet. Chem.*, 2004, **689**, 88.

209. T. Tokunaga, H. Seki, S. Yasuike, M. Ikoma, J. Kurita and K. Yamaguchi, *Tetrahedron Lett.*, 2000, **41**, 1031.

210. T. Tokunaga, H. Seki, S. Yasuike, M. Ikoma, J. Kurita and K. Yamaguchi, *Tetrahedron*, 2000, **56**, 8833.

211. B. Wrackmeyer, E. Garcia-Baez, F. J. Zuno-Cruz, G. Sanchez-Cabrera and M. R. Rosales, *Z. Naturforsch.*, 2000, **55b**, 186.

212. R. J. Carbajo and F. López-Ortiz, *J. Magn. Reson.*, 2001, **148**, 165.

213. D. J. Russell, C. E. Hadden, G. E. Martin and K. Krishnamurthy, *Magn. Reson. Chem.*, 2002, **40**, 207.

214. J. E. Del Bene, S. A. Perera, R. J. Bartlett, M. Yáñez, O. Mó, J. Elguero and I. Alkkorta, *J. Phys. Chem. A*, 2003, **107**, 3121.

215. J. Spychala, *Magn. Reson. Chem.*, 2003, **41**, 169.

Magic-Angle-Spinning Solid-State NMR Applied to Polypeptides and Proteins

COLAN E. HUGHES AND MARC BALDUS

Department for NMR-Based Structural Biology, Max-Planck-Institute for Biophysical Chemistry, Am Fassberg 11, 37077 Göttingen, Germany

This chapter deals with the topic of polypeptide structure elucidation using the technique of magic-angle-spinning (MAS) solid-state NMR. We discuss various aspects of sample preparation and recent progress in establishing high-resolution conditions for MAS-based structural studies. Approaches for obtaining structural parameters in multiply or uniformly labelled polypeptides are reviewed. Recent applications to globular and membrane-associated proteins are summarized.

1. INTRODUCTION

For a long time, magic-angle spinning (MAS[1]) has helped biomolecular NMR applications in cases where slow molecular tumbling or susceptibility effects prohibit high-resolution spectroscopy under static conditions. For example, the beneficial effect of MAS has been observed for structural studies on biopolymers,[2] model membranes,[3–5]

membrane proteins[6] and DNA complexes.[7] Moreover, MAS has long been applied to probe protein dynamics[8,9] and has become a standard technique in modern combinatorial chemistry.[10,11]

With the advent of efficient isotope-labelling schemes and solid-state NMR instruments operating at 500 MHz and above, significant progress is currently being made in studying multiply or uniformly labelled proteins by solid-state NMR methods. In particular, experimental approaches have appeared that enable the study of the three-dimensional structure of an immobilized molecule at atomic resolution. As recently reviewed by Opella and Marassi,[12] the majority of these three-dimensional structures based on solid-state NMR have, thus far, been obtained using macroscopically aligned (membrane-embedded) peptides. For such studies, a variety of sample preparation methods, NMR pulse schemes and data analysis approaches have been suggested and the interested reader is referred to a series of reviews.[12–16] The purpose of the current manuscript is to discuss progress in the design and use of MAS-based solid-state NMR spectroscopy to study structure and dynamics in peptides and proteins. As we will show in the following sections, such methods can be used on samples consisting of microcrystalline proteins or protein aggregates and those involving proteoliposomes. MAS has also been applied to study (membrane) proteins mechanically oriented on glass plates,[17] films[18] or polymer surfaces.[19,20]

Ideally, a maximal number of parameters defining molecular structure or dynamics should be obtained from a single sample. Because of the limited use of ^{1}H NMR spectroscopy, such information has, thus far, been acquired predominantly from spectral analysis of a multiply or uniformly [^{13}C,^{15}N]-labelled polypeptide variant. As in the solution state, protein synthesis and the preparation of NMR samples amendable to MAS-based studies have increased in importance. Consequently, this chapter begins with a discussion of sample preparation methods. A subsequent structural analysis usually requires, in the first stage, resonance assignments of the isotope-labelled biomolecule of interest. Such information is intimately related to the use of radio-frequency (r.f.) based pulse schemes that drive polarization across the polypeptide spin network. In Section 2.2 we briefly review the theoretical basics that permit an understanding of the details of such through-space and through-bond polarization transfer methods. To observe correlations at high resolution, multi-dimensional correlation spectroscopy is applied. In Section 2.3, we discuss recent progress in optimizing spectral resolution in evolution and detection periods using state-of-the-art decoupling schemes and we consider three-dimensional correlation methods. In Sections 2.4 and 2.5 we show how polarization transfer can be established and how multiple-quantum coherences (MQCs) can be excited, whilst Section 2.6 describes how these techniques may be used to arrive at *de novo* resonance assignments in a polypeptide. Finally, in Section 2.7, we conclude our methodological part by discussing routes currently pursued to infer three-dimensional protein structures under MAS conditions.

Many of the experimental approaches to study protein structure by solid-state MAS NMR have been devised relatively recently. Not surprisingly, the number of biophysical applications using such methods is still limited. Nevertheless, we will present in Chapter 3 different areas of research where MAS-based solid-state NMR has already been applied and which may pave the way for future applications. We also refer the interested reader to

other review articles dealing with the methodological improvements of MAS-based solid-state NMR[21–23] and its application to structural biology.[24–33]

2. METHODS

2.1. Sample preparation

There are two key aspects to the preparation of protein samples for measurement by solid-state NMR. The first is the chemical or biochemical process by which the protein molecules are produced, with particular emphasis on the inclusion or exclusion of particular nuclear isotopes. The second is the means by which the protein molecules are prepared for the actual measurement, with possibilities including lyophilization, crystallization and insertion into lipid bilayers or liposomes.

At the present time, most protein samples used in structural determination studies are produced by micro-organism expression (usually in *Escherichia coli*) or chemical synthesis. Although significant progress has been achieved in enhancing the spectral resolution of ^{1}H protein resonances by ultra-fast MAS approaches[34,35] or the use of chemical deuteration,[36–38] structural analysis thus far usually involves the use of carbon (^{13}C) and nitrogen (^{15}N) spectroscopy. Hence, isotope labelling (see, for example, Ref. 39) is, in general, necessary and is often most easily achieved using bacterial cell lines. For expression in *E. coli*, isotope labelling may be achieved by controlling the source of nutrition to the bacteria, whilst the use of pre-prepared, isotopically labelled amino acids allows labelling during chemical synthesis. Broadly, labelling methods can be divided into three classes, referred to here as uniform, specific and selective, illustrated in Fig. 1.

Uniform labelling (Fig. 1a) involves the complete replacement of the naturally occurring isotope distribution for a particular element with a single isotope. In the context of polypeptides, this is most commonly carried out with ^{2}H, ^{13}C or ^{15}N. In the context of bacterial expression systems, uniform isotope labelling is often easily achieved by supplying U-[^{13}C]-labelled glucose and ^{15}N-labelled NH$_4$Cl. A similar degree of isotope labelling can be achieved for specific residues by supplying U-[^{13}C,^{15}N]-labelled amino acids. In principle, uniform labelling offers the possibility of extracting a maximum amount of structural information from a single sample. However, as discussed in further detail below, the spin system dynamics are, in this case, often dominated by nearest-neighbour interactions and medium to long-range internuclear interactions, which are most informative about the 3D structure of the protein, are difficult to detect.

A variant of uniform labelling, where molecules of the same protein are prepared with different elements uniformly labelled and then mixed at the molecular level into a single sample, has recently been investigated in our group. This sample preparation method, which allows the investigation of dimerization and other intermolecular contacts, will be more fully discussed in Section 3.3.

Specific labelling (Fig. 1b) refers to the placement of certain isotopes at particular positions in a molecule whilst ensuring that, at all other positions of that element in the molecule, the natural isotope distribution is present. NMR of specifically labelled samples is an extremely powerful method for delivering information about the
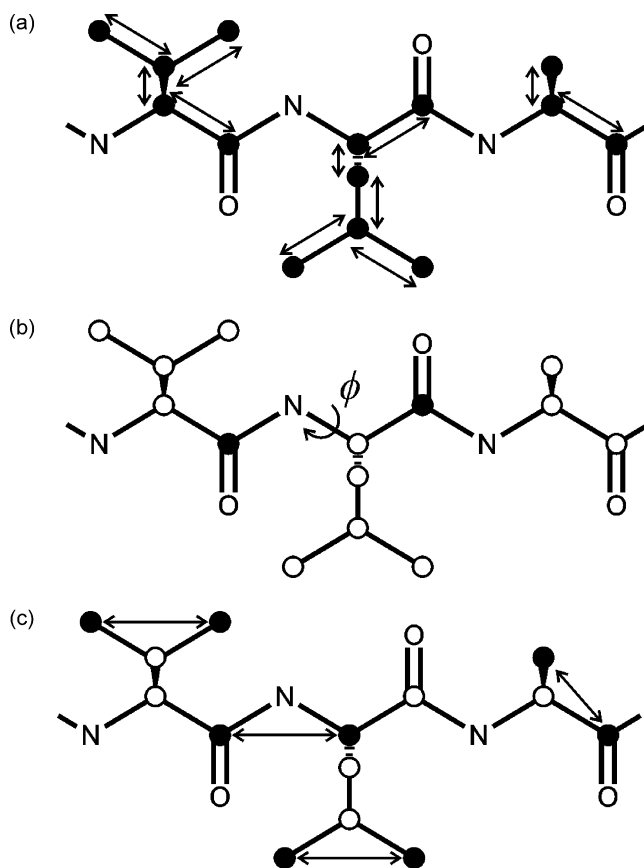
Fig. 1.   Different ^{13}C labelling schemes, illustrated for the three-residue stretch VLA. (a) Uniform, (b) specific, (c) selective, block labelling using [1,3-^{13}C]-glycerol.[40] Also shown are which pieces of structural information can be obtained from such samples. Distances are indicated by straight arrows, torsional angles by curved arrows.

labelled sites. Because NMR spectra of specifically labelled molecules can be assigned using one-dimensional spectroscopy, structural information, for example, resulting from the measurement of a single internuclear distance, can be readily obtained. However, specific labelling suffers from a significant weakness in the context of complete protein structure determination, namely that many different samples are required in order to acquire a set of structural constraints sufficient to construct a three-dimensional molecular structure. Specific labelling can be achieved in chemical synthesis by using appropriately labelled amino acids at specific point(s) during the synthesis.

A compromise between specific and uniform labelling of proteins is selective labelling, where certain amino acids or parts of amino acids are labelled. Bacteria fed with isotope-labelled versions of the amino acids Arg, Cys, His, Ile, Leu, Lys, Met, Phe, Pro, Trp, Tyr and Val will produce proteins with these amino acids labelled due to

the direct incorporation of the fed molecules into the proteins. Selective labelling of the amino acids Ala, Asn, Asp, Glu, Gln, Gly, Ser and Thr is, however, difficult, due to their additional roles in the metabolic pathways (see, for example, Ref. 39).

One other particularly useful method of selective labelling is block labelling (Fig. 1c),[40] where consistent labelling patterns are achieved in some amino acids types. Block labelling is carried out by feeding the bacteria on a diet containing a single source for a particular element which is only labelled at certain positions, such as [1,3-^{13}C]- or [2-^{13}C]-glycerol. Through the mechanism of synthesis of the amino acids, this ensures that amino acids are labelled only at certain positions and unlabelled at others, thus diluting the labels to a significant extent. Using [1,3-^{13}C] or [2-^{13}C]-glycerol, six amino acids (Ala, Cys, Gly, Leu, Ser and Val) can be prepared with all carbon sites either fully labelled ($>90\%$ ^{13}C) or unlabelled (1% ^{13}C) (see Fig. 1 in Ref. 40). Of the remaining residue types, all except Arg, Gln, Glu and Pro have the CO, Cα and Cβ sites either fully labelled or unlabelled. In most cases, nearest neighbour ^{13}C pairs are avoided. However, one-bond (^{13}C,^{13}C) interactions must be taken into account for several residue types, in particular Ile, Leu and Val.

Scattering methods for structure determination rely upon the availability of crystalline samples. On the other hand, NMR can make use of samples which have an isotropic orientation distribution and/or amorphous structures. This greater range of sample possibilities not only makes NMR applicable to studies of biomolecular structure with different macroscopic properties but also raises opportunities for different experimental procedures leading to increased amounts of structural information. However, attention must always be paid to the effect sample preparation may have on the conformation of the protein molecules relative to the naturally occurring structure.

After expression and purification, protein samples are often initially available as lyophilized solids, in which the proteins are correctly folded but in an amorphous arrangement with an isotropic distribution of orientations. This form of the protein may be used for NMR studies but the lack of water can significantly affect the structures of the individual protein molecules. One simple way to overcome this is to rehydrate the sample with small amounts of water.[41–43] The effect can be quite significant, as illustrated in Fig. 2 for a sample of the 76-residue protein ubiquitin. Flash freezing offers the opportunity of preparing solid samples of proteins in which the solution-state structure is largely preserved.[44,45]

If a protein can be obtained in large enough crystals, techniques such as X-ray crystallography may be used for structure determination. However, it is sometimes the case that only small crystals can be prepared. Samples composed of many isotopically oriented micro- or nanocrystalline samples are amenable to solid-state NMR. In order to produce microcrystals, precipitants, such as 2-methyl-2,4-pentanediol (MPD[9]) and polyethylene glycol (PEG[45–48]), may be added to solutions of the protein. The use of micro- and nanocrystalline samples in NMR has one significant advantage over the use of amorphous samples in that the greater regularity of the molecular structure minimizes inhomogeneous broadening effects and hence often gives rise to sharper lines in the NMR spectra.

For membrane proteins, an alternative sample preparation method is available which seeks to provide a more natural environment for the molecules by using lipid molecules

(a)

(b)
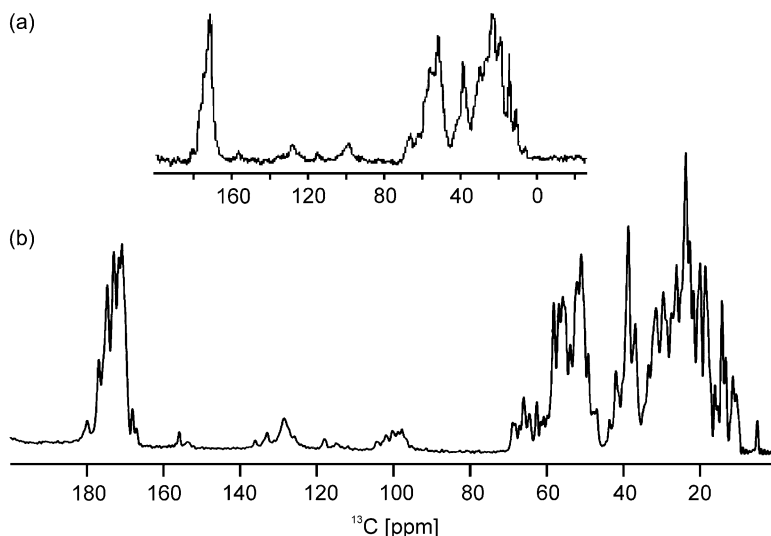
Fig. 2. ^{13}C NMR spectra of uniformly (^{13}C,^{15}N) labelled ubiquitin. (a) Lyophilized and (b) hydrated after lyophilization.

to create artificial membranes in which the proteins insert themselves. The artificial membranes are composed of lipid bilayers, either macroscopically oriented on a surface (glass or plastic) or creating randomly oriented liposomes.[49] Macroscopic sample alignment offers the possibility to readily determine the protein orientation relative to the membrane frame under static[16] or MAS[17] conditions. Using polymer films,[19] MAS rates of up to 10 kHz have been achieved, a regime where radio-frequency-based modulation schemes can be employed to infer structural parameters with high spectral resolution.[20] Liposomal samples, which create an isotropic distribution of protein orientations, may be used at relatively high MAS frequencies but controlling temperature and hydration level are of crucial importance.

A key difference between crystalline samples and hydrated or lipid-embedded proteins can be the different degrees of molecular mobility. This aspect will impact on the utility of those solid-state NMR experiments that exploit anisotropic interactions in the magnetic field. Such aspects can, for example, play an important role if proteins reconstituted into lipid bilayers are studied at high temperatures (i.e., in the liquid crystalline phase). Here, the degree of molecular mobility may depend on the polypeptide topology in the membrane and a theoretical understanding how solid-state NMR parameters are affected by molecular motion is crucial. The basic interactions, present in a solid-state NMR experiment on spin-½ nuclei, are introduced in the next section.

2.2. Theoretical background

The information which may be obtained from proteins by solid-state NMR is contained in the effect the immediate electronic environment has on the magnetic field experienced by

the nuclei (Fig. 3a), the interactions between the nuclear spins (Fig. 3b) and the effect of molecular motion on the nuclear spins.[50] Unfortunately, the spin–spin and spin–field interactions cause very broad spectral lines in solid samples. This is in contrast to solution-state samples where, except for very large molecules, the tumbling motion of the molecules averages out the anisotropic parts of these interactions, giving narrow spectral lines. In the solid state, this tumbling may be mimicked by MAS,[1] that is, sample rotation around an axis which is tilted at $54.7°$ from the static applied magnetic field. MAS is effective because of the dependence of the spin-spin and spin-field interactions upon the orientations of vectors fixed within the molecule.

The effect of the magnetic field experienced by the nuclei is seen in the chemical shielding of the nuclear resonance. It is often convenient to distinguish an isotropic part, independent of the molecular orientation, and an anisotropic part, known as the CSA. Under MAS, the anisotropic part becomes time dependent, unless the spinning frequency is sufficiently high, in which case it vanishes. The chemical shift Hamiltonian under MAS may be expressed as

$$\hat{H}^{CS} = \left(C_{0,0}^{CS} + \sum_{n=-2}^{+2} C_{2,n}^{CS} D_{n,0}^2(\Omega_{PL}^{CS}(t)) \right) \hat{I}_z,$$

$$C_{0,0}^{CS} = \omega_{CS}^{iso}, \quad C_{2,0}^{CS} = \omega_{CS}^{aniso}, \quad C_{2,\pm1}^{CS} = 0, \quad C_{2,\pm2}^{CS} = -\frac{1}{\sqrt{6}}\eta\omega_{CS}^{aniso}, \tag{1}$$

$$\omega_{CS}^{iso} = -\gamma B_0 \delta^{iso}, \quad \omega_{CS}^{aniso} = -\gamma B_0 \delta^{aniso}.$$

The factor $-\gamma B_0$ is the Larmor frequency of the nucleus, ω_0. The terms δ^{iso}, δ^{aniso} and η are the isotropic chemical shift (in parts per million, ppm), the anisotropy (also in ppm)
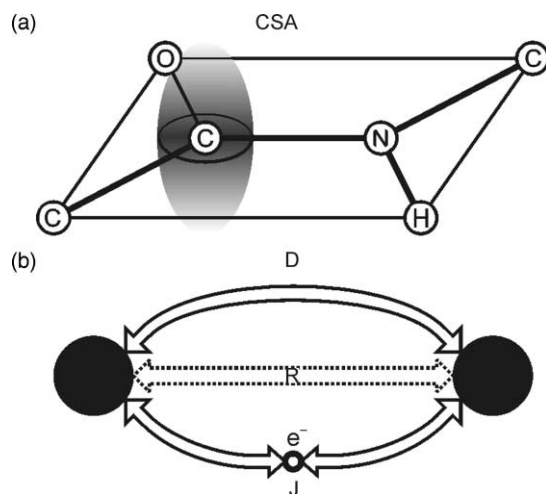
Fig. 3. (a) A representation of the chemical shift, showing the orientation adopted at carbonyl sites relative to the peptide plane. (b) The two-spin interactions utilized in solid-state NMR: dipolar (D), *J*-coupling and relaxation (R).

and the asymmetry parameter. These are all given in terms of the components of the second-rank tensor which describes the chemical shift interaction:

$$\delta^{iso} = \frac{1}{3}(\delta_{xx}^{P} + \delta_{yy}^{P} + \delta_{zz}^{P}), \quad \delta^{aniso} = \delta^{iso} - \delta_{zz}^{P}, \quad \eta = \frac{\delta_{yy}^{P} - \delta_{xx}^{P}}{\delta_{zz}^{P} - \delta^{iso}}. \tag{2}$$

P indicates that the components are those for the principal axis system (PAS) of the tensor. The terms $D_{n,0}^2(\Omega_{PL}^{CS}(t))$ are Wigner rotation matrix elements. They are functions of the set of Euler angles, $\Omega_{PL}^{CS}(t)$, which relates the PAS of the chemical shift to the laboratory frame. Due to MAS, these angles are time dependent. A full treatment of the orientation dependence of the chemical shift requires the transformation between several different reference frames.

If the MAS frequency is significantly greater than ω_{CS}^{aniso}, the anisotropic part of the chemical shift Hamiltonian is averaged out. If the MAS frequency is not sufficiently high, the effect of the time-dependent terms is to generate spinning side bands in the spectrum. These are additional lines in the spectrum, positioned at frequencies separated from δ^{iso} by integer multiples of the MAS frequency. For carbonyl (CO) ^{13}C nuclei in single amino acids, values of δ^{aniso} are typically in the range 60–90 ppm whilst values are on the order of 10–25 ppm for Cα nuclei.[51] Few values of δ^{aniso} have been measured for polypeptides but those available fall into the same ranges. Because ω_{CS}^{aniso} depends upon the value of B_0, the magnitude of the static field has an effect on the size of the CSA. At a field of 14.1 T, ω_{CS}^{aniso} for carbonyls is approximately 12 kHz, within the available range of many MAS units.

The range of chemical shifts observed in proteins are highly significant as, together with the line widths, they determine the spectral resolution (*vide infra*). With increasing static magnetic field, the size and orientation of the chemical shielding anisotropy become important. For the CO nuclei, one CSA orientation relative to the surrounding C, O and N atoms (illustrated in Fig. 3a) is generally observed. Empirical studies in model systems also have greatly refined the orientation of the ^{15}N backbone CSA tensor in the molecular frame but such information is still limited for other important resonances such as Cα or Cβ. Nevertheless, significant progress has been made in establishing a correlation between the isotropic chemical shifts of the Cα and Cβ nuclei and the peptide backbone torsional angles ϕ and ψ.

There are two kinds of spin–spin interaction, direct (through space) and indirect (through bond). The direct couplings, known as dipolar interactions, are anisotropic. A similar formalism may be used to describe the dipolar coupling under MAS as was used to describe the chemical shift (Eqs. (1) and (2))

$$\hat{H}^D = \left(\sum_{n=-2}^{+2} C_{2,n}^D D_{n,0}^2(\Omega_{PL}^D(t))\right)\hat{F}^D, \tag{3}$$

noting that there is no isotropic (0,0) term. The values of $C_{2,n}^D$ and $\hat{F}^D$ depend upon whether the two nuclei are of the same type or different. For the homonuclear case (denoted jk)

$$\hat{F}^{D_{jk}} = \frac{1}{\sqrt{6}}(3\hat{I}_{jz}\hat{I}_{kz} - \hat{\vec{I}}_j \cdot \hat{\vec{I}}_k),$$

$$C_{2,0}^{D_{jk}} = \sqrt{6}b_{jk}, \quad C_{2,\pm1}^{D_{jk}} = C_{2,\pm2}^{D_{jk}} = 0, \tag{4}$$

$$b_{jk} = -\frac{\mu_0 \gamma_I^2 \hbar}{4\pi|\vec{r}|^3}.$$

The term b_{jk} is the dipolar coupling constant. It depends upon the gyromagnetic ratio, γ_I, and is inversely proportional to the internuclear distance cubed. There is only a single non-zero term in the Hamiltonian and there is no asymmetry parameter. As with the chemical shift, the terms $D_{n,0}^2(\Omega_{PL}^D(t))$ are Wigner rotation matrix elements which are functions of the time-dependent set of Euler angles $\Omega_{PL}^{CS}(t)$ relating the PAS of the dipolar coupling (aligned along the internuclear vector) to the laboratory frame.

For heteronuclear dipolar couplings (denoted *IS*), the elements for Eq. (3) are given by

$$\hat{F}^{D_{IS}} = \sqrt{\frac{2}{3}}\hat{I}_z\hat{S}_z,$$

$$C_{2,0}^{D_{IS}} = \sqrt{6}b_{IS}, \quad C_{2,\pm1}^{D_{IS}} = C_{2,\pm2}^{D_{IS}} = 0, \tag{5}$$

$$b_{IS} = -\frac{\mu_0 \gamma_I \gamma_S \hbar}{4\pi|\vec{r}|^3}.$$

The key difference is in the form of the part which describes the spin dependence of the Hamiltonian, $\hat{F}^{D_{IS}}$. For both homo- and heteronuclear couplings, if the MAS frequency significantly exceeds the magnitude of the dipolar coupling, the entire Hamiltonian is averaged out. Because of the dependence upon the gyromagnetic ratios, dipolar couplings to or between ^{1}H nuclei are considerably greater than others commonly found in proteins. Typical single bond ^{13}C–^{13}C dipole–dipole coupling constants are around 2 kHz, well within the range of available MAS frequencies, whilst ^{1}H–^{13}C coupling constants are on the order of 20 kHz, which lies towards the upper end of MAS frequencies available to most spectroscopists. Thus, MAS is usually applied at frequencies sufficient to ensure that

$$\hat{H}_{CC}^D = 0, \tag{6}$$

but often not sufficient to eliminate $\hat{H}_{HC}^D$ and $\hat{H}_{HH}^D$. These remain as significant, time-dependent terms.

The through-bond or indirect couplings are also known as scalar or *J*-couplings. They are mediated by bonding electrons and are therefore indicative of bonding between nuclei, with *J*-couplings measurable over more than one covalent bond and across hydrogen bonds. Using the same formalism as above for the *J*-coupling Hamiltonian gives

$$\hat{H}^J = C_{0,0}^J\hat{F}^J, \tag{7}$$

This Hamiltonian only contains an isotropic (0,0) term, i.e., it is independent of molecular orientation. As with the dipolar coupling, the precise form of the *J*-coupling Hamiltonian

depends upon whether the spins are of the same species or different:

$$\hat{F}^{J_{jk}} = \hat{\vec{I}}_j \cdot \hat{\vec{I}}_k, \quad C_{0,0}^{J_{jk}} = 2\pi J_{jk},$$

$$\hat{F}^{J_{IS}} = \hat{I}_z \hat{S}_z, \quad C_{0,0}^{J_{IS}} = 2\pi J_{IS}. \tag{8}$$

J_{jk} and J_{IS} are the J-coupling coefficients. J-couplings are much smaller in magnitude than one-bond dipolar couplings, with ^{13}C–^{13}C couplings on the order of 50 Hz and ^{1}H–^{13}C couplings around 170 Hz. In spite of their relatively small magnitude, J-couplings carry important information regarding molecular connectivity and have been successfully exploited in a variety of applications.

In solid-state NMR of proteins there are three main contributions to the molecular motion: MAS, motion of the whole protein molecule and motion of parts of the protein relative to the rest of the molecule. As discussed above, MAS is always present as it is necessary for reasons of spectral resolution. The remaining two motional types will depend upon the details of the sample preparation. Highly hydrated samples will often exhibit a certain degree of motion of the whole protein molecule, whilst membrane proteins inserted into lipid bilayers may show significant motion only for lipophobic protein sections. If sufficiently rapid, molecular motion can average anisotropic interactions such as the dipolar interaction or CSA. A limited degree of motion causes a partial averaging of anisotropic interactions. As a consequence, in relatively rigid molecules, experiments which exploit the dipolar couplings are generally used in order to transfer magnetization between spins. However, in more mobile systems, techniques exploiting the isotropic J-couplings are to be favoured.

2.3. Spectral resolution

Spectral assignment critically depends upon the spectral resolution, which may be estimated from the ratio of the empirically observed chemical shift range and the NMR resonance line width. For ^{13}C, the spectral dispersion in the side-chain region spans up to 70 ppm between Thr Cβ and the methyl carbons. For ^{1}H side-chain resonances and ^{15}NH backbone shifts, typical values are 5 and 30 ppm, respectively. In well-ordered proteins, ^{13}C and ^{15}N resonance line widths are often found in the range of 0.5–1 ppm. Hence, obtaining spectral separation of the NMR resonances comparable to (^{13}C,^{13}C) or (^{13}C,^{15}N) correlation spectroscopy for ^{1}H spectra would require ^{1}H line widths between 0.04 and 0.17 ppm. While the combination of ultra-high magnetic fields, proton dilution, fast MAS and r.f. decoupling schemes has been shown to significantly improve the spectral resolution of ^{1}H spectroscopy, all protein resonance assignments reported to date are based on (^{13}C,^{15}N) correlation spectroscopy.

In addition to MAS, ^{1}H r.f. decoupling schemes are usually employed to enhance the resolution of (^{13}C,^{15}N) evolution and detection periods. Decoupling seeks to eliminate the effect of ^{1}H–^{13}C and ^{1}H–^{15}N dipole–dipole couplings, which are generally too large to be removed by MAS. Moreover, modulation of the spatial components of the system Hamiltonian (such as in the case of MAS) is unable to suppress isotropic through-bond interactions such as (^{1}H,^{13}C) one-bond J-couplings. The simplest ^{1}H decoupling

scheme involves application of r.f. irradiation at a fixed amplitude and phase, known as continuous wave (CW) decoupling.[2] More sophisticated schemes have been developed, where the phase of the irradiation is varied over time. These include TPPM,[52] XiX[53] and the various SPINAL sequences.[54] Furthermore, r.f. schemes that suppress broadening effects due to scalar (^{13}C,^{13}C) couplings have also been shown to improve spectral resolution in uniformly labelled proteins.[55] As in the case of macroscopically oriented systems,[56] extending the MAS NMR experiment to three spectral dimensions enhances the possibilities for resonance assignments in larger proteins.[57]

2.4. Magnetization transfer

In solid-state NMR, assignment of resonances to specific nuclei relies upon correlation spectroscopy.[23,58] This involves the acquisition of spectra in which the transfer of magnetization between nearby nuclei can be traced. The patterns of transfer may then be used to assign the individual resonances to the correct positions in the protein. Three mechanisms for magnetization transfer are available: through-space, through-bond or relaxation mediated.

Through-space methods utilize the direct dipolar interaction. For ^{13}C and ^{15}N, these interactions are removed by MAS. Hence, some form of recoupling is required. Recoupling does not simply restore the static Hamiltonian. Although the Hamiltonian may be of the same form, it will be smaller in scale and can have different angle dependencies or spin terms. For magnetization transfer, the choice of which recoupling scheme to use may depend upon all these factors.

Nuclei of the same species may have the through-space coupling between them restored by various r.f.-driven schemes or by utilizing the rotational resonance effect (*vide infra*). Many r.f.-driven homonuclear dipolar-recoupling schemes have been devised. In some, discrete r.f. pulses are applied at certain points in each period of sample rotation with patterns of pulse phases chosen to achieve the desired average Hamiltonian over the complete sequence. Examples include RFDR[59] and DRAMA.[60] Others methods involve the continuous application of r.f. irradiation and are often referred to as rotating-frame methods. The nutation frequency generated by the irradiation is set to a fixed relationship with the MAS frequency and, for some methods, changes in the phase are applied in a manner synchronous with the sample rotation. Examples include HORROR,[61] MELODRAMA,[62] and DRAWS,[63] together with various symmetry-based sequences,[22] such as C7[64] and SPC5.[65] Some r.f.-driven recoupling methods are largely unaffected by the magnitude of the chemical shifts (isotropic and anisotropic) of the nuclei involved. These sequences, including C7 and SPC5, may be described as broadband. Other sequences, including HORROR, are more seriously affected by large chemical shift differences or anisotropies and therefore recouple in a selective manner. Finally, the combination of laboratory and rotating-frame dipolar recoupling, possibly in conjunction with offset compensation by phase switching (RIL[66]), is possible.

Variations in MAS rate or r.f. field may enhance the efficiency of the polarization transfer. For rotating-frame polarization transfer, higher spinning rates (and, hence, stronger r.f. recoupling fields) improve the offset compensation. Unfortunately, a second

consideration may limit the extent to which this path may be taken. As with detection periods, it is often necessary to apply an r.f. field to the proton resonances during a polarization transfer period in order to remove the effects of ^{1}H–^{13}C and/or ^{1}H–^{15}N dipolar couplings not completely suppressed by MAS. This r.f. field must avoid any resonance conditions with the r.f. field being used to recouple the rare spins and, consequently, it is often applied with a nutation frequency in excess of 2.5 times the recoupling nutation frequency.[67] Thus, higher spinning rates mean higher recoupling powers and even higher decoupling powers, all of which significantly increases the risk of sample damage due to heating or may simply be limited by the r.f. circuitry.

The effect of the decoupling power on the efficiency of recoupling can be seen in Fig. 4. As the nutation frequency increases, the efficiency of the rotating-frame
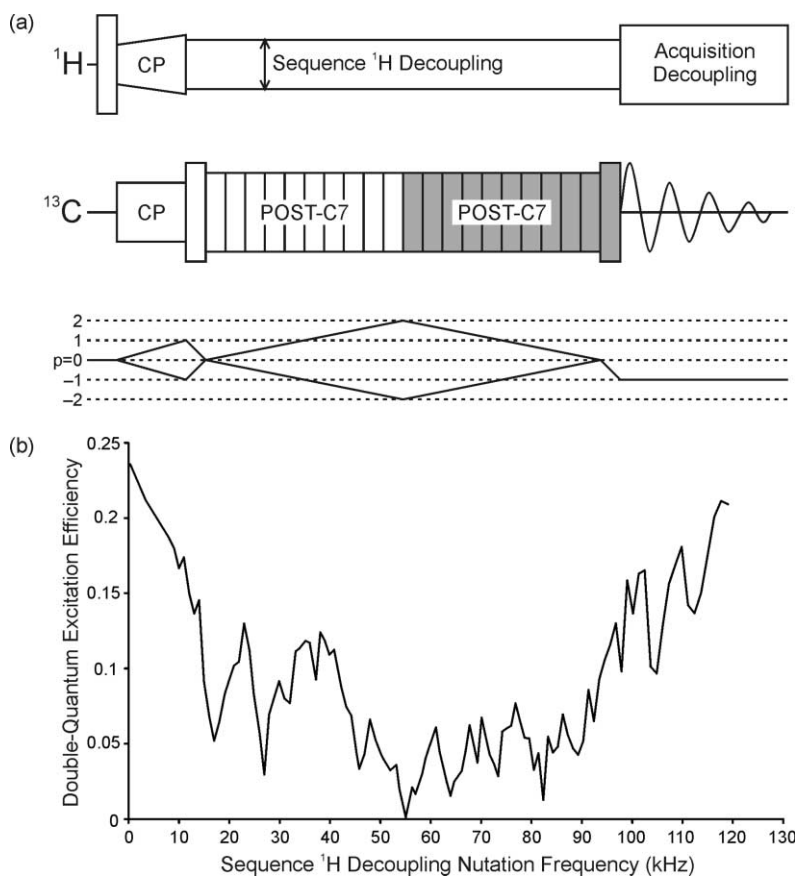
Fig. 4.   (a) A (^{13}C–^{13}C) double-quantum filtration pulse sequence using the POST-C7 sequence for excitation and reconversion (shaded). (b) The dependence of double-quantum filtering efficiency in U-^{13}C-Gly upon the decoupling field strength applied during the excitation and reconversion sequences.

polarization transfer scheme, POST-C7 improves. However, the increase in efficiency is oscillatory. To avoid using too high a decoupling power, the decoupling field strength can be carefully calibrated to achieve a compromise between decoupling effectiveness and irradiation level. Applying a field corresponding to the top of one oscillation provides one solution to the problem. However, as may also be seen in Fig. 4, the recoupling sequences in question, POST-C7, also operate effectively when no decoupling is applied.[68] This is due to the fact that, in the absence of r.f. irradiation on the ^{1}H resonances, this sequence also performs heteronuclear decoupling at the same time as homonuclear recoupling. Consequently, by choosing the correct recoupling scheme, decoupling may be eliminated during periods of magnetization transfer, significantly cutting the risk of sample or instrumental damage.

Rotational resonance[69,70] is an effect whereby the dipolar coupling between two nuclei is restored under MAS by matching the isotropic chemical shift difference between the two spins (expressed in Hz) to an integer multiple of the MAS frequency (ν_r), i.e.,

$$|(\delta_j^{iso} - \delta_k^{iso})\omega_0/2\pi| = n\nu_r, \quad n = 1, 2, \ldots \tag{9}$$

Because of its dependence on the isotropic chemical shifts, rotational resonance methods are selective, i.e., they will only cause transfer of magnetization between some of the pairs of nuclei in close spatial proximity and with isotropic chemical shift values that fulfil Eq. (9). The efficiency of magnetization transfer may be enhanced by varying the MAS rate[71] or by applying r.f. fields,[72] thus allowing dipolar interactions to be measured.[73,74]

Heteronuclear dipolar interactions may also be utilized for magnetization transfer. This is most commonly performed using REDOR-type[75] pulse schemes or cross polarization (CP).[76] Cross polarization ideally involves the application of r.f. fields to both nuclear species at nutation frequencies which differ by either one or two times the MAS frequency (known as the Hartmann–Hahn condition). This creates a resonance between the two nuclear species, allowing the dipolar coupling to effect magnetization transfer. Consequently, the large polarization on ^{1}H nuclei (due to their high gyromagnetic ratio) may be transferred to spins such as ^{13}C and ^{15}N (which have much lower gyromagnetic ratios), thus significantly increasing sensitivity. In addition, CP can also be used to transfer magnetization between nuclei at various points in an experiment. By varying the position of irradiation and the r.f. fields used, CP can be made to be specific to resonances in certain regions of the spectrum.[77]

Through-bond methods for magnetization transfer utilize the indirect J-coupling between nuclei. These couplings are not affected by MAS but, due to their small magnitude, can only be used if they are isolated from the other remaining interactions. For homonuclear spins, the TOBSY sequence[78,79] achieves this isolation by applying a continuous r.f. irradiation which removes those interactions not removed by the MAS (principally the isotropic chemical shift) whilst not reintroducing any other interactions. Heteronuclear J-couplings may be exploited using the INEPT experiment[80] to transfer magnetization between nuclear species. Since INEPT involves the creation of transversal antiphase magnetization that evolves under the heteronuclear scalar coupling, controlling T_2 relaxation is of crucial importance. In solids, proton–proton dipolar interactions are often the prominent source of ^{1}H T_2 relaxation such that homonuclear decoupling

schemes (as demonstrated by Emsley and co-workers[81]) must be employed. Alternatively, molecular motion may lead to a strong reduction of dipolar interactions and hence favourable T_2 relaxation rates. INEPT spectroscopy is also applicable to systems that exhibit a high degree of molecular mobility. As is well known from solution-state NMR,[82] one-bond scalar couplings show little variation with the respect to amino acid type. Through-bond correlation spectroscopy can hence be easily applied for the characterization of polypeptides and proteins.

Relaxation-mediated magnetization transfer is often dominated by the effects of a strongly coupled proton bath. The influence of the corresponding homonuclear and heteronuclear dipolar interactions may indirectly enhance the rate of polarization exchange between rare spins such as ^{13}C by a process called proton-driven spin diffusion (PDSD[83]). In this case, longitudinal ($^{13}C,^{13}C$) mixing schemes are used in the absence of proton decoupling and lead to the occurrence of cross peaks in a time frame given by the product of the ^{13}C zero-quantum relaxation rate and the internuclear ($^{13}C,^{13}C$) distance.[84–86] This effect can be further enhanced by the use of rotational resonance in conjunction with ^1H irradiation in a scheme known as dipolar-assisted rotational resonance (DARR[87]). The exploitation of spin diffusion is also possible in ($^1H,^1H$) correlation spectroscopy under MAS conditions. Because of the larger gyromagnetic ratio, proton–proton mixing is two orders of magnitudes faster than ($^{13}C,^{13}C$) polarization exchange and less sensitive to resonance offsets.[88]

2.5. Multiple-quantum spectroscopy

In addition to experimental procedures which correlate transverse magnetization of nuclei to one another, a second form of multi-dimensional experiment is available which makes use of magnetization states in which more than one nucleus is involved. Such states are known as MQCs, with transverse magnetization being considered a single-quantum coherence (1QC). As with magnetization transfer techniques, the excitation of multiple-quantum states and their reconversion to single-quantum for observation (MQCs cannot be directly observed) requires the presence of some form of interaction between the nuclei. The various dipolar-recoupling schemes discussed above for magnetization transfer can also be used to create MQCs, predominantly, in the context of the works described here, double-quantum coherences (2QC). Such excitation and reconversion can be carried out directly (using, for example, C7[64] or SPC5[65]) or by combining the recoupling sequence with 90° pulses (e.g., RFDR[59] or HORROR[61]). As is the case for magnetization transfer, J-couplings can be exploited to excite MQCs. This may be achieved using the INADEQUATE experiment.[89]

During a period of evolution in which multiple-quantum states are present, the magnetization acquires a modulation due to the nutation frequency of the MQCs. Thus, signals which are due to single sites during other evolution periods will have the same spectral frequency in a multiple-quantum domain as those signals which had passed through the same MQC. This can therefore easily be read in a multi-dimensional spectrum as a correlation between these nuclear sites. In addition, a multiple-quantum domain as part of a multi-dimensional spectrum removes the auto-correlation peaks on

the principle diagonal. As these peaks are often strong and can dominate the spectrum, their removal can provide significant advantages in terms of spectral clarity.

These aspects can be of particular relevance in three-dimensional homonuclear correlation experiments, where a cubic diagonal may prohibit a detailed structural analysis. As visible from Fig. 5, these effects can be minimized by conducting a 3D 2QC–1QC–1QC experiment. The general transfer pathway carried out by the pulse sequence shown in Fig. 5a is as follows:

$$2QC \xrightarrow{t_1} 1QC \xrightarrow{t_2} CCmix \xrightarrow{t_3} \tag{10}$$
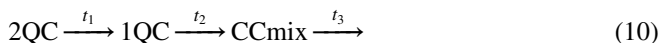
where 2QC excitation and reconversion was established using the $R18_{10}^5$ scheme[90] and ($^{13}C,^{13}C$) mixing after t_2 is conventional ^1H-driven spin diffusion. Figure 5b shows a spectrum acquired using this pulse scheme on ubiquitin. Signals appear symmetrically
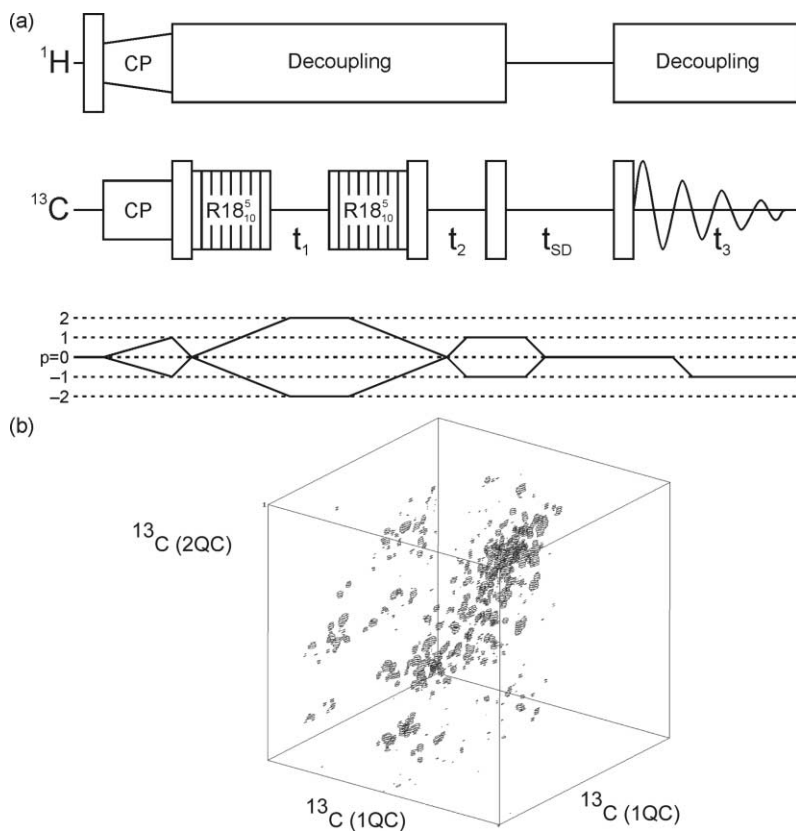
Fig. 5. (a) A pulse sequence for acquiring a three-dimensional spectrum with ($^{13}C-^{13}C$) double-quantum coherence in t_1 and ^{13}C single-quantum coherence in t_2 and t_3. Proton-driven spin diffusion is employed between t_2 and t_3, for a time t_{SD}. (b) A three-dimensional spectrum of ubiquitin, acquired using the pulse sequence in (a).

either side of the (F1,F2) diagonal, eliminating the cubic diagonal. This spectrum will be further discussed in Section 3.1.

As with magnetization transfer, the build-up of MQCs as a function of the recoupling time is indicative of the strength of the coupling between the nuclei involved. Of particular importance is the excitation of 2QC by dipolar recoupling, whose dynamics can be related, through comparison with simulations, to the internuclear distances.

2.6. Protein spectral assignment

For soluble molecules, resonance assignment methods for $[^{13}C,^{15}N]$-labelled proteins were pioneered by Bax and co-workers[91,92] and today represent an integral part of the tool box of modern solution-state NMR.[82,93] While these methods make extensive use of the *J*-coupling to direct polarization along the polypeptide chain, solid-state NMR mixing schemes can, as detailed below, employ through-bond or through-space transfer mechanisms to achieve sequential resonance assignments under MAS conditions.

With optimized spectral resolution, ^{13}C and ^{15}N evolution and detection dimensions can be connected by through-space, through-bond or relaxation-mediated transfer pathways along the polypeptide chain (Fig. 6). Amino acid types and intraresidue interactions are, perhaps, most easily obtained from $(^{13}C,^{13}C)$ broadband correlation spectra. Such experiments can involve through-bond or through-space interactions. For the latter, $(^{13}C,^{13}C)$ interactions may be actively recoupled (see Refs. 23,25,94 for recent reviews) or they may rely upon $(^{13}C,^{13}C)$ transfer facilitated by multiple-(^{1}H)-spin effects. Intraresidue correlations are also often easily identified by the inspection of double-quantum single-quantum (2Q,1Q) spectra.

Discrimination of intra- and interresidue transfer can be easily established by rendering the dipolar $(^{15}N,^{13}C)$ transfer chemical-shift selective, for N_i (in the *i*th residue) to either $C\alpha_i$ or CO_{i-1}. For this purpose, the conventional Hartmann–Hahn cross polarization condition can be modified by adjusting the r.f. field strength and carrier offset frequency. Because spectral resolution among CO resonances is usually limited, an additional homonuclear transfer step (i.e., $CO_{i-1} \rightarrow C\alpha_{i-1}$) is often mandatory. This second transfer step is also often implemented following transfer to $C\alpha_i$ in order to transfer magnetization along the amino acid side chain. The combination of N–$C\alpha_i$–$C\beta_i$ (known as NCACB, Fig. 6a) and N–CO_{i-1}–$C\alpha_{i-1}$ (NCOCA, Fig. 6b) transfer schemes provides the basis for sequential assignments. Figure 7a shows the general pulse scheme employed for both these types of experiments. The only difference is the choice of irradiation point on the ^{13}C channel during the second CP. For NCOCA this is on the CO resonances and for NCACB this is on the $C\alpha$ resonances. In Fig. 7a $(^{13}C,^{13}C)$ mixing is established using a longitudinal mixing block without proton decoupling. Other polarization transfer schemes (discussed in Section 2.4) are also possible.

At ultra-high magnetic fields, the final mixing step in these sequences is required over a chemical shift difference $\delta^{iso}(CO_{i-1}) - \delta^{iso}(C\alpha_{i-1})$ of 120 ppm, corresponding to a frequency difference ranging from 18 kHz (600 MHz ^{1}H frequency) to
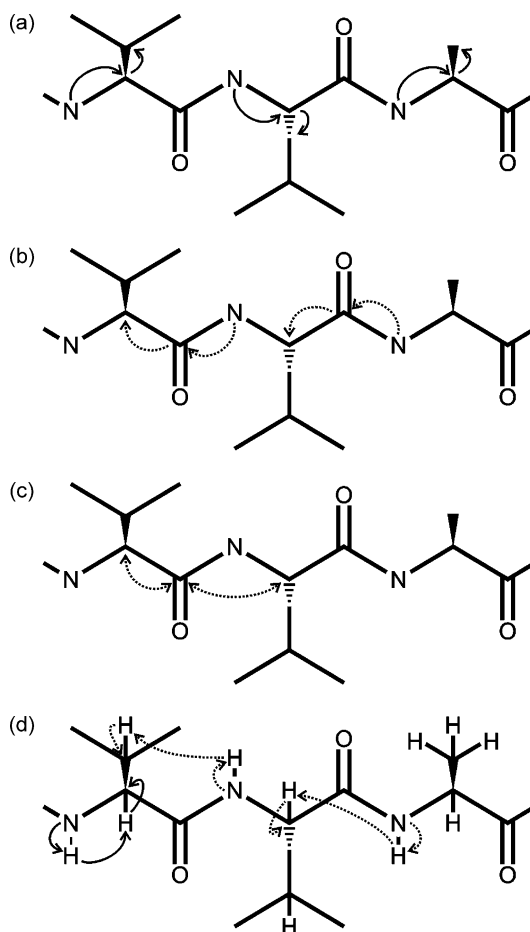
Fig. 6.   Examples of magnetization transfer pathways used for spectral assignment, illustrated for the three-residue stretch VLA. Solid arrows denote intraresidue transfer, dotted arrows denote interresidue transfer. (a) NCACB generates intraresidue magnetization transfer. (b) NCOCA generates interresidue magnetization transfer. (c) CACA generates interresidue transfer via weakly coupled (CO,Cα) spin pairs.[97] (d) NHHC generates both intra- and interresidue magnetization transfer.

27 kHz (900 MHz). This transfer step hence necessitates a very efficient suppression of chemical shift terms during a broadband polarization transfer or can rely on polarization transfer schemes such as RR,[69] RRTR[95] or RFDR[59] that operate most efficiently[96] at a rotational resonance condition, i.e.,

$$|(\delta^{\mathrm{iso}}(\mathrm{CO}_{i-1}) - \delta^{\mathrm{iso}}(\mathrm{C}\alpha_{i-1}))\omega_0/2\pi| = n\nu_{\mathrm{r}}, \quad n = 1, 2, \ldots, \tag{11}$$

described earlier.

A very recent development in spectral assignment methodology allows the correlation of Cα resonances (and additional side-chain resonances) in consecutive residues by
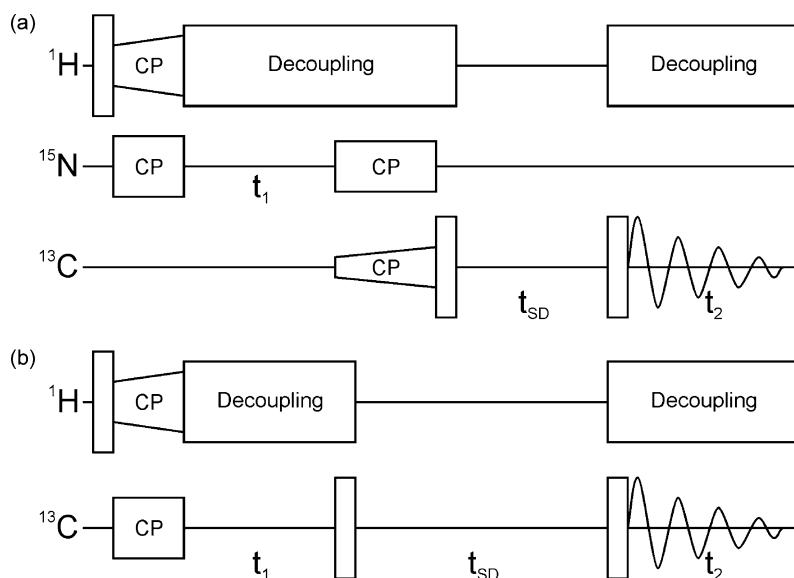
Fig. 7. (a) Pulse sequence for NCACB- or NCOCA-type experiment. To implement NCACB selectivity, the ^{13}C CP pulse has a weak r.f. field and is on resonance with the Cα spectral region. To implement NCOCA selectivity, the ^{13}C CP pulse again has a weak r.f. field but is on resonance with the CO spectral region. (b) Pulse sequence for CACA correlation spectroscopy.[97] All ^{13}C pulses have strong r.f. fields since no selectivity is required. The MAS frequency is set to the Hz equivalent of 62.5 ppm at the ^{13}C Larmor frequency.

exploiting a near rotational resonance effect.[97] The protein sample is spun at an MAS frequency near to, but not exactly at, half the isotropic chemical shift difference between the CO and Cα resonances. This spinning frequency does not give rise to highly undesirable rotational resonance line broadening but does cause magnetization transfer between both intra- and interresidue CO–Cα pairs (Fig. 6c). Consequently, in a (^{13}C,^{13}C) correlation spectrum with a long (>100 ms) mixing time, cross peaks are seen not only due to PDSD but also between consecutive side-chain residues. Such spectra recorded under 'weak coupling' conditions can lead to (^{13}C,^{13}C) spectra that assist NC-type resonance assignment experiments. The general scheme for these experiments is shown in Fig. 7b.

As illustrated in Fig. 6d, sequential resonance assignments can also be obtained from proton–proton[98] or ^{1}H–^{13}C-mediated[99] correlation spectroscopy. Such experiments also give information regarding the proximities of different secondary structure elements of the protein, since the outer surface of the polypeptide chain is largely made up of hydrogen atoms. In Fig. 8, we graphically summarize structural parameters that can be determined in the context of a multiply or uniformly labelled polypeptide sample under MAS conditions and allow for the determination of local structural motifs ($\Delta\delta$) and overall 3D structure (d_{CC}, d_{NC}, d_{HH}). In the latter case, distance measurements require the analysis of medium- or long-range interactions.
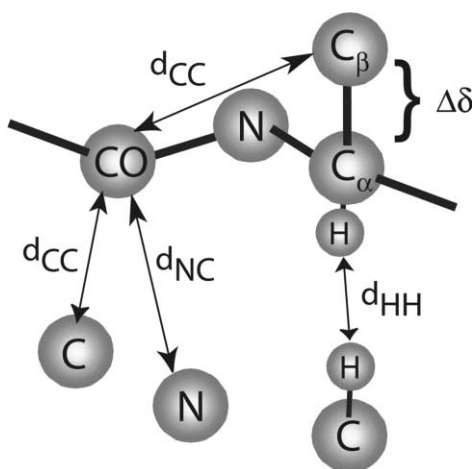
Fig. 8. A representation of the roles played by the different parameters measured by solid-state NMR in the structure determination of proteins.

2.7. Structure determination

Concepts with which to construct three-dimensional structure from solid-state NMR data are currently being developed in many laboratories. All of these approaches aim at determining both the secondary structure (the backbone conformation) and tertiary structure (the overall fold) of proteins in an efficient manner. As in the solution state, solid-state NMR structure determination involves the calculation of families of molecular conformations that are consistent with the experimentally derived distance and/or angle constraints. The number and precision of these parameters determine the accuracy of the resulting three-dimensional structure.

The isotropic chemical shift, such as those of the Cα and Cβ sites, can be a strong indicator of local molecular conformation. Empirical[100,101] and theoretical[102] results can be used to define an average ('random coil') chemical shift for each amino acid residue type. It has been found[100,103,104] that deviations from these reference values can be interpreted in terms of the local backbone conformation. In particular, the quantity $\Delta\delta$, defined as

$$\Delta\delta = \{\delta^{iso}(C\alpha)_{obs} - \delta^{iso}(C\alpha)_{rc}\} - \{\delta^{iso}(C\beta)_{obs} - \delta^{iso}(C\beta)_{rc}\}, \qquad (12)$$

is found to be positive for residues in α-helical conformations and negative for β-sheet conformations.[104] In Fig. 9, this aspect is demonstrated for sequential resonance assignments obtained for the α-spectrin SH3 domain.[105] Because of a rapidly increasing database of protein resonance assignments using solution-state NMR methods, several approaches have been published to establish a functional relationship between protein structure and measured chemical shift. As in the case of TALOS[106] such a concept may invoke primary sequence homology as an additional criterion to predict polypeptide backbone structure from a given set of NMR resonance assignments or they may combine
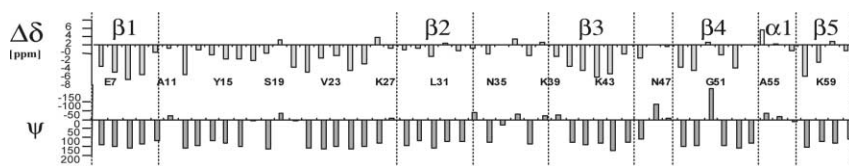
Fig. 9. Example of secondary chemical shift correlating to secondary structure, illustrated for the case of the α-spectrin SH3 domain.

empirical NMR data with DFT calculations to predict NMR resonance assignments from 3D structure.[107]

Complementary to the analysis of conformation-dependent chemical shifts, two-dimensional experiments that correlate anisotropic interactions may be used to study backbone conformation by MAS NMR. This is possible in particular for dipolar interactions, whose orientations are along the internuclear vector, and for the carbonyl CSAs, which generally adopt a particular orientation with respect to the peptide plane (Fig. 3a). Under MAS, these interactions may be recoupled during the evolution and/or detection period of a two-dimensional correlation experiment, as discussed earlier. The resulting spectrum will contain cross peaks whose pattern is characteristic of the relative orientation of the two interactions being correlated. An alternative approach is to excite a state of 2QC between two neighbouring nuclei, which then evolves under the influence of two anisotropic interactions.

The correlation of two bonds separated by a third results directly in a measurement of the torsional angle around the middle bond. For proteins, the backbone torsional angles ϕ and ψ (see Fig. 10) can be measured using such techniques. The ϕ angle may be measured using an HN/CH[108,109] correlation experiment whilst the ψ angle may be measured with an NC/CN experiment.[110,111] HC/CH experiments can be used to measure some of the torsional angles χ_i in the amino acid side chain. Experiments correlating NH/NH dipolar tensors[112] can also be used to acquire backbone structure information, as can experiments measuring the relative orientation of sequential carbonyl CSAs.[113] In a double-quantum correlation experiment with evolution due to the CN dipole–dipole coupling, the decay in signal amplitude is directly related to the backbone torsional angle. This experiment may be conveniently applied to multiply labelled polypeptides.[23]

In addition, the measurement of a dipolar coupling constant (and hence of internuclear distance) provides a rich source of structural information in MAS solid-state NMR.
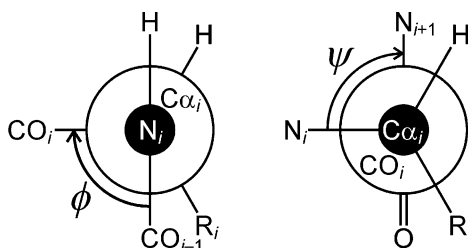
Fig. 10. Representations of the ϕ and ψ torsional angles in protein backbones.

Such measurements can be made by comparing the build-up of a state of 2QC between the two nuclei in question to simulations for the spin system (see Section 2.5). Uniform labelling of ^{13}C and ^{15}N produces samples in which many strong (^{13}C–^{13}C) and (^{15}N–^{13}C) couplings are present. The measurement of weaker, longer distance couplings can be achieved using specific or selective labelling,[114,115] or by using chemical-shift-selective r.f. pulse sequences to recouple the interaction of interest.[116] In particular, because the carbonyl ^{13}C resonances are well separated from the other resonances in the spectrum, couplings to these nuclei may be recoupled selectively. The use of samples prepared with proton dilution by deuterons has also been demonstrated to allow the measurement of longer range distances, in particular between NH moieties.[37]

As is visible from Fig. 11, proton spins are not only more abundant than ^{13}C or ^{15}N nuclei in proteins but (^{1}H–^{1}H) contacts provide key constraints defining secondary and tertiary protein structure. Because of the limited spectral resolution of ^{1}H MAS NMR spectroscopy, indirect detection schemes have been employed for a long time
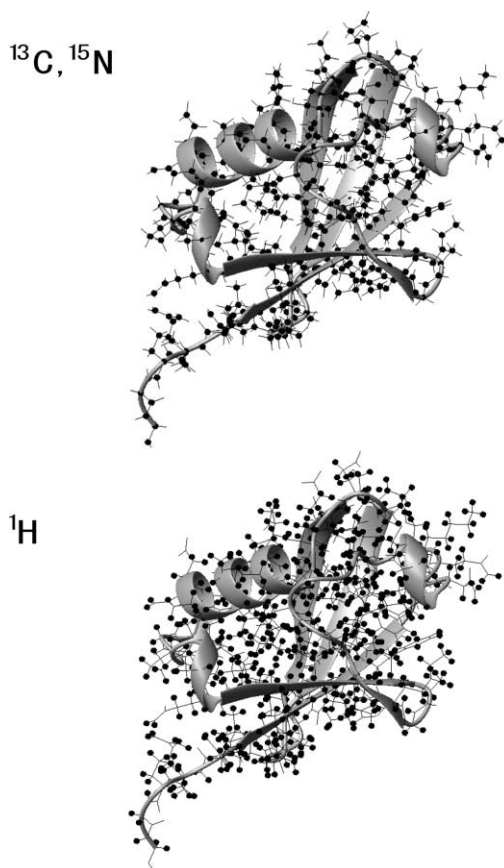
Fig. 11. Comparison of the density of ^{1}H nuclei (below) and ^{13}C and ^{15}N nuclei (above) in the same protein, ubiquitin.

(see, for example, Refs. 88,98,117–122). For a reliable structural interpretation of proton–proton interactions in the solid state, a detailed understanding of the underlying polarization transfer dynamics and their dependence on experimental parameters such as MAS rate or r.f. mixing scheme is imperative. As detailed in Ref. 88, such an analysis can be performed using test compounds of known 3D structure and permits the construction of calibration curves that establish a functional relationship between proton–proton distance and mixing time for a variety of experimental settings. Such information is useful for the spectroscopic study of protein–protein interfaces,[99] molecular dynamics[123] and, as detailed below, for the determination of the three-dimensional structure of uniformly [^{13}C,^{15}N]-labelled (poly)peptides under MAS conditions.[88,124] We note that similar information may help to study macromolecular assemblies[125,126] by 2D solid-state MAS NMR.

3. APPLICATIONS

3.1. Spectral assignments in globular proteins

For reasons of sensitivity and spectral resolution, an initial analysis of multiply labelled biomolecules under MAS conditions often calls for the application of homonuclear (^{13}C,^{13}C) correlation experiments. Such studies have been reported on proteins such as ubiquitin,[98,127,128] BPTI[129] and the α-spectrin SH3 domain.[105,130] Other fully labelled biomolecules include chlorophyll-a water aggregates,[131] erythromycin A,[132] TEE,[123,133] antamanide,[134,135] kaliotoxin[124,136] and a variety of tripeptides.[104,137,138]

NCOCA- and NCACB-type experiments, such as those discussed in Section 2.6, were used to obtain an almost complete set of *de novo* resonance assignments for the SH3 domain of α-spectrin (62 residues, 7.2 kDa) under MAS conditions.[105] As discussed above, correlation of these (^{15}N,^{13}C) chemical shift assignments with random coil values subsequently showed[104] that secondary chemical shifts provide a straightforward and powerful instrument with which to monitor secondary structure in solid-phase proteins under MAS conditions. Moreover, these resonance assignments represented the starting point for an investigation of the proton resonance frequencies[139] and for the structural analysis of the three-dimensional structure of a set of [^{13}C]-block-labelled[40,114] protein variants.[115]

As in methodological studies using solution-state NMR, ubiquitin (76 residues, 8.6 kDa) is becoming an attractive model protein for high-resolution solid-state NMR investigations. The three-dimensional structure of ubiquitin has been determined using X-ray crystallography[140] and solution-state NMR[141] and exhibits a rich variation in secondary structure (one α-helix, three ½ turns and a twisted, anti-parallel β-sheet). The first solid-state NMR studies were reported by Ernst and co-workers[127] using two-dimensional (^{13}C,^{15}N) chemical shift correlation spectroscopy. Subsequently, lyophilized ubiquitin was investigated by Hong *et al.*[114,128] Both studies yielded partial (∼25%), site-specific assignments of ubiquitin at moderate applied magnetic field strengths. Recently, McDermott and co-workers reported backbone[142] and side-chain[143]

[13]C assignments obtained at 800 MHz. The uniformly [^{13}C,^{15}N]-labelled sample was crystallized by batch methods in 60% MPD and 20 mM citrate buffer at pH 4.0–4.2.

High-resolution spectra of ubiquitin can also be obtained after rehydration[43,144] or after precipitation from PEG.[48] Using the latter method, a three-dimensional 2QC–1QC–1QC (^{13}C,[13]C,[13]C) correlation experiment was recorded under sensitivity-optimized conditions[145] in the manner described in Section 2.5 and depicted in Fig. 5. Notably, this spectrum was recorded on a narrow-bore 800 MHz instrument using a triple-resonance (^{1}H,[13]C,[15]N) 4 mm probe (Bruker Biospin, Germany) and SPINAL64[146] decoupling in evolution and detection periods. Combined with a set of two- and three-dimensional (^{15}N,[13]C) correlation experiments, resonance assignments for ubiquitin precipitated from PEG can be derived (K. Seidel *et al.*, submitted). These spectral assignments differ from results reported for the MPD-derived form and may help to further investigate the influence of sample preparation upon protein structure. Structural insight may also come from proteins such as the immunoglobin-binding domain B1 of streptococcal protein G[147] and thioredoxin[148] for which sequential (^{13}C,[15]N) assignments have been reported very recently.

Finally, we have obtained (^{13}C,[15]N) resonance assignments for the 38-amino acid polypeptide kaliotoxin (KTX),[124,136] a 38-residue peptide found in the venom of the scorpion *Androctonus mauretanicus mauretanicus*.[149] KTX has been shown to block voltage-dependent eukaryotic potassium (Kv) channels (e.g., Shaker and Kv1.3) in high affinity and with a 1:1 stoichiometry.[150] Uniformly [^{13}C,^{15}N]-labelled KTX was expressed recombinantly as an intein fusion protein[151] in *E. coli*. Electrophysiological experiments measuring the blockage of KcsA-Kv1.3 potassium channels[152] show that the purified KTX is fully functional. For our structural analysis, a lyophilized sample of uniformly [^{13}C,^{15}N]-labelled KTX was rehydrated and investigated under MAS conditions. No additional attempts were made to improve the structural homogeneity of the sample. Two-dimensional (^{15}N,[13]C) and weakly coupled (^{13}C,[13]C) correlation experiments (see Section 2.6) resulted in sequential assignment of 87% of all protein residues. This value may be further increased by the application of three-dimensional correlation spectroscopy. To conclude this section, Table 1 summarizes information about globular proteins thus far studied by MAS-based correlation methods. In addition to sequence and molecular mass, we have also included an overview of spectroscopic methods applied for each system.

3.2. 3D structure determination of polypeptides

Determining the three-dimensional (3D) structures of proteins at atomic resolution is fundamental to the understanding of many biological processes such as signal transduction in membrane proteins or protein aggregation and fibril formation. In these cases, application of the two principal experimental methods for 3D structure determination, X-ray crystallography and solution-state NMR, can be challenging. 3D molecular structures have previously been obtained from a spectral analysis of several polypeptide variants containing isotope labels at well-defined atomic positions or residue types.[12,115,153–156] Such approaches were successful in the context of

Table 1.   A summary of globular proteins studied by solid-state MAS NMR

Protein	Sequence	Mass	PDB	Method	Ref.
Ubiquitin	MQIFVKTLTGKTITL EVEPSDTIENVKAKI QDKEGIPPDQQRLIF AGKQLEDGRTLSDY NIQKESTLHLVLRLR GG	8.5 kDa	1UBQ 1D3Z	X-ray Solution-state NMR Solid-state NMR	140 141 98,127,128
BPTI	RPDFCLEPPYTGPCK ARIIRYFYNAKAGLC QTFVYGGCRAKRNN FKSAEDCMRTCGGA	6.5 kDa	6PTI	X-ray Solid-state NMR	198 129
α-Spectrin SH3 domain	MDETGKELVLALYDY QEKSPREVTMKKGDI LTLLNSTNKDWWKVE VNDRQGFVPAAYVKK LD	7.2 kDa	1SHG 1AEY 1M8M	X-ray Solution-state NMR Solid-state NMR	199 200 115
Crh	MVQQKVEVRLKTGLQ ARPAALFVQEANRFT SDVFLEKDGKKVNAK SIMGLMSLAVSTGTE VTLIAQGEDEQEALE KLAAYVQEEV	2×10.4 kDa	1K1C 1MU4	Solution-state NMR X-ray Solid-state NMR	201 202 47
Kaliotoxin	GVEINVKCSGSPQCL KPCKDAGMRFGKCM NRKCHCTPK	4.1 kDa	2KTX	Solution-state NMR Solid-state NMR	203 124
B1 domain streptococcal protein G	MTYKLILNGKTLKGE TTTEAVDAATAEKVF KQYANDNGVDGEWT YDDATKTFTVTE	6.2 kDa	1PGA 1PGB	X-ray X-ray Solid-state NMR	204 147
Thioredoxin	MVKQIESKTAFQEAL DAAGDKLVVVDFSA TWCGPCKMIKPFFHS LSEKYSNVIFLEVDVD DCQDVASECEVKCMP TFQFFKKGQKVGEFS GANKEKLEATINELV	11.7 kDa	1AUC	X-ray Solid-state NMR	205 148

membrane-embedded proteins oriented on glass plates[12,13] or involved peptides,[155] amyloid fibrils[153,154,156] or a solid-phase protein[115] under MAS conditions. Up to date, 10 three-dimensional structures of polypeptides derived with the help of solid-state NMR methods have been deposited in the Protein Data Bank (PDB[157]).

In Figs. 12 and 13, structures determined in oriented bilayer samples and under MAS conditions are shown, respectively. If available, PDB codes are given. The first structure
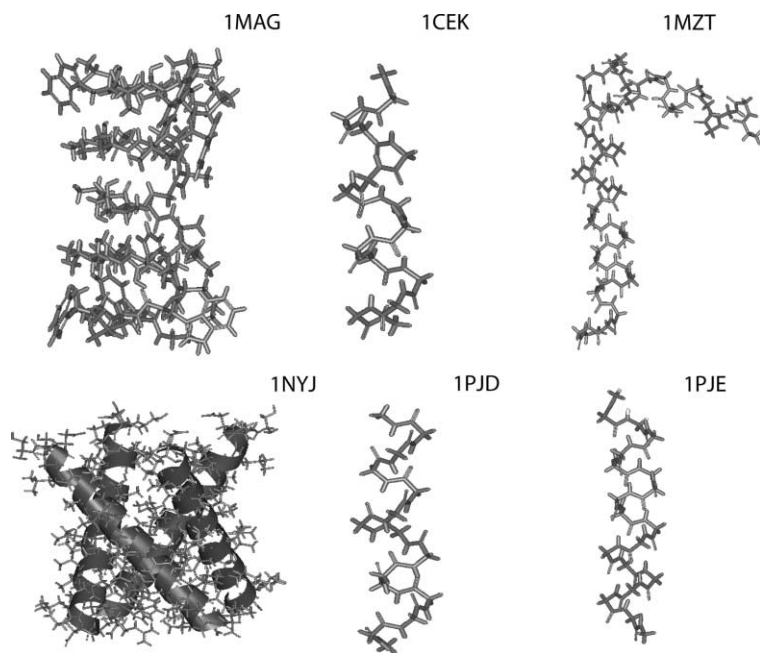
Fig. 12. Structures determined by solid-state NMR in oriented bilayers. The PDB file numbers are shown, see text for details. (Adapted from Ref. 12.)

reported using solid-state NMR methods relates to gramicidin A (1MAG[158]). Additional studies of membrane-embedded peptides relate to the M2 channel-lining segment from the nicotinic acetylcholine receptor (1CEK[159]), the Fd bacteriophage coat protein in lipid bilayer membranes (1MZT[160]), the closed state structure of M2 protein H^+ channel (1NYJ[161]), a peptide segment of the sixth transmembrane domain of the *Saccharomyces cerevisiae* α-factor receptor (1PJD[162]) and the structure of the channel-forming transmembrane domain of virus protein 'U' (Vpu) from HIV-1 (1PJE[163]). MAS-based 3D structures (Fig. 13) were reported for the dipeptide glycyl isoleucine,[138] the tripeptide *N*-formyl-L-Met-L-Leu-L-Phe-OH,[155] the α-spectrin SH3 domain (1M8M[115]) and an 11-amino acid stretch of transthyretin (TTR[105–115,156]).

In Fig. 14, we present recent applications to solid-phase molecules of small molecular weight. In both cases, the three-dimensional molecular structure was obtained from a single, uniformly labelled sample. For example, in Fig. 14a results of an NHHC[98] experiment were used to rapidly construct the 3D structure of the tripeptide Ala-Gly-Gly.[88] In Fig. 14b, the 3D structure of L-tyrosine ethylester determined from a single uniformly labelled sample[123] is shown. The corresponding CHHC data set shows a ($^{13}C,^{13}C$) correlation spectrum containing nearest neighbour ($^1H,^1H$) interactions that can be used to construct the 3D structure of the molecule in the polycrystalline state. Additional successful applications by our group relate to the anticancer agent epothilone B, the 38-amino acid polypeptide kaliotoxin[124] and ubiquitin (K. Seidel *et al.*, submitted).
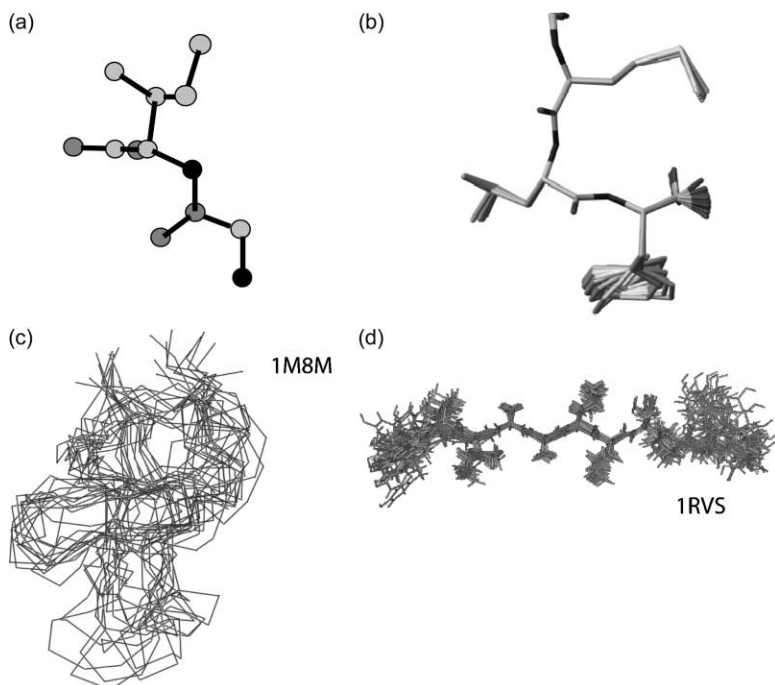
Fig. 13. Structures of polypeptides determined by MAS solid-state NMR. The PDB file numbers are shown where available. (a) The dipeptide glycyl isoleucine. (b) The tripeptide *N*-formyl-L-Met-L-Leu-L-Phe-OH. (c) The α-spectrin SH3 domain. (d) An 11-amino acid stretch of transthyretin (TTR[105–115]).
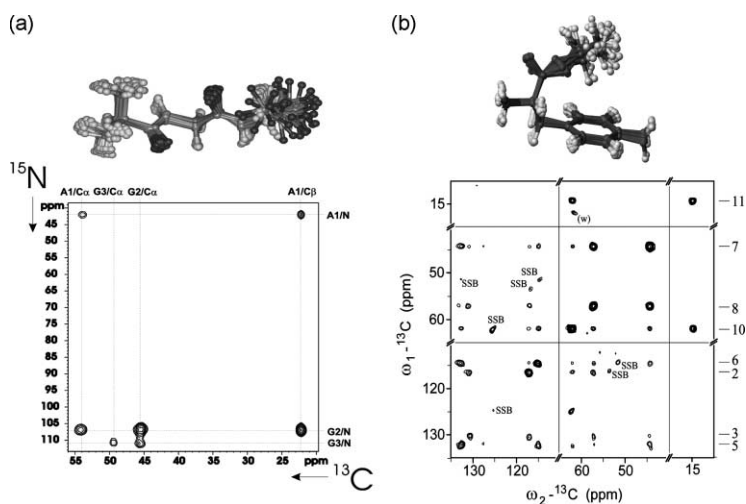
Fig. 14. Examples of 3D structures of U-[^{13}C,^{15}N]-labelled molecules obtained using proton–proton distance restraints. (a) The tripeptide Ala-Gly-Gly. (b) A CNS-based structure calculation for L-tyrosine ethylester.

3.3. Protein folding and dynamics

For a long time, solid-state methods have been successfully used to study molecular dynamics in material science applications, ranging from the investigation of chain order in elastomers (see, for example, Ref. [164] for a recent application) to the investigation of the mechanism of proton conduction in fuel cell polymer electrolyte membranes.[165] While solution-state NMR techniques have provided unprecedented insight into the structural details of unfolded or partially structured proteins,[166,167] recent progress in solid-state NMR spectroscopy offers new means to investigate protein folding and, in particular, aggregation and fibril formation. For example, a nearly complete assignment of ^{13}C NMR signals was obtained for amyloid fibrils formed from a uniformly labelled seven-residue fragment of the 40-residue Alzheimer Aβ peptide.[103] Recently, a structural model for the full-length Aβ amyloid fibrils could be proposed based on solid-state NMR studies on samples containing 5–7 selected, uniformly labelled amino acids.[154] Full sequential assignment of ^{13}C and ^{15}N resonances was also reported for a 11-residue peptide fragment of transthyretin (TTR) in an amyloid fibril based on a spectral analysis of samples containing different stretches of four consecutive uniformly labelled amino acids.[153,156] Using these three samples, a total, of 76 structural constraints, including 41 dihedral angle constraints and 35 [13]C–[15]N distances were measured and reveal an extended β-strand conformation for TTR.[105–115,156]

Together with A. Böckmann *et al.*, we have begun investigating the structure and folding of the 85-residue catabolite repression histidine containing protein (Crh) that regulates gene expression and can exist in a monomeric and a domain-swapped dimeric form. Domain swapping is defined as a process by which two or more protein molecules exchange parts of their structure to form intertwined oligomers. Similar folding events have been observed for amyloid-forming proteins, suggesting that domain swapping and amyloid formation may share similar folding intermediates. In a first step, we have reported[47] solid-state NMR resonance assignments for the microcrystalline form of Crh in the solid state. In Fig. 15, deviations between the solid-state NMR-based backbone structure of the microcrystalline state of Crh and (a) the solution-state monomer and (b) the single-crystal dimer are indicated in black. These results suggest that Crh also forms a domain-swapped dimer in the microcrystalline form.

To directly probe intermolecular monomer–monomer contacts, we have recently[99] suggested an approach that is based on the spectroscopic analysis of mixtures composed of different molecules, uniformly labelled with spin species X or Y (denoted X:Y). For example, to reliably detect intermolecular contacts in a [[13]C:^{15}N]-labelled sample, ^{15}N and ^{13}C evolution and detection periods must be combined with a polarization transfer technique sensitive to the interface region only. Such mechanisms could involve (a) a direct N→C dipolar (cross polarization) transfer[168] or adiabatic versions thereof,[169] (b) an NH→C cross (NHC) polarization transfer[123,170] or (c) (^{1}H,[1]H) transfer encoding NH–HC spin pairs (NHHC[88,98]). As shown in Ref. 99, all the NMR schemes considered are capable of probing intermolecular interactions with high spectral resolution. Application of the NHHC concept maximizes spectral resolution and the detectability of the distance between the two proteins of interest. Unlike the NC approach, the NHHC scheme does not necessitate careful optimization of CP transfer steps involving weak (intermolecular)
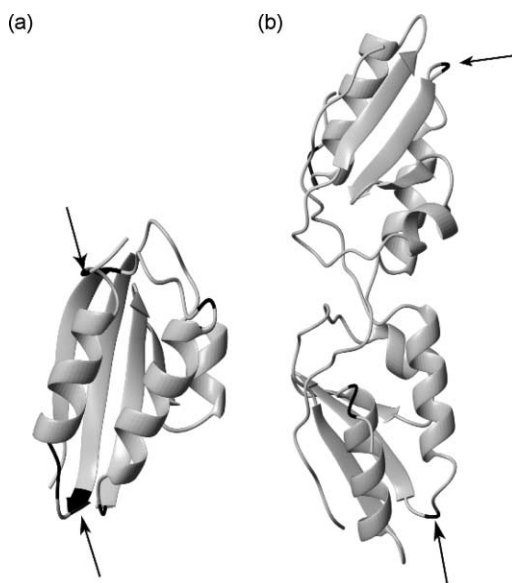
Fig. 15.   Comparison of backbone dihedral angles obtained for a microcrystalline sample of Crh[47] in comparison to (a) the monomer structure obtained in the solution state (PDB: 1K1C) and the (b) the single crystal structure (PDB: 1MU4). Largest deviations are indicated in black along the polypeptide backbone chain and by additional arrows.

dipolar interactions. Since NC and NHC transfers are based on a non-vanishing dipolar coupling element, they may be favourable in the case of applications under ultra-fast MAS, where relaxation-mediated transfer is attenuated,[88] or for the investigation of non-protonated target spins.

A [^{13}C:^{15}N]-labelled sample of Crh was prepared by mixing equal amounts of [^{15}N]- and [^{13}C]-labelled protein under denaturing conditions, followed by renaturation and microcrystallization. Application of the NHHC technique reveals a variety of intermolecular contacts (shown in Fig. 16) that, apart from differences in terms of local protein dynamics, suggest that domain swapping also occurs in the microcrystalline state of Crh.

We have also begun to structurally characterize fibrillar states of α-synuclein (140 residues) and of the K19 domain of protein tau. Both systems are involved in possibly related neuro-degenerative diseases.[171] Preliminary results of two- and three-dimensional correlation spectroscopy, as outlined above, reveal that many of the NMR detectable resonances exhibit narrow ^{13}C or ^{15}N line widths, consistent with the occurrence of well-ordered domains in both proteins. On the other hand, other segments of the considered proteins cannot readily be detected suggesting that they may display static or dynamic disorder under the experimental conditions considered. While the effect of molecular dynamics of NMR relaxation parameters has been studied in the context of solution- or solid-state NMR for a long time, recent progress in the study of uniformly labelled proteins by MAS NMR has created novel means by which to study dynamics of entire polypeptide sequences using 2D methods. For example, Böckmann and Emsley have
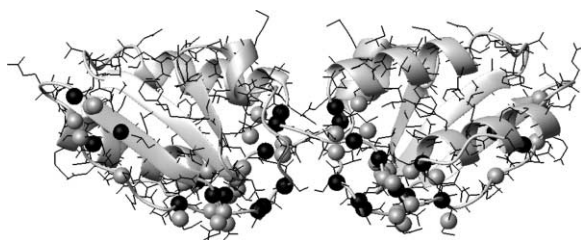
Fig. 16. Summary of monomer–monomer contacts observed in a microcrystalline sample of Crh. NH–HC correlations observed in an NHHC experiment conducted on a [^{13}C:^{15}N]-labelled sample are indicated by grey and black spheres, respectively.[99]

shown that ^{15}N T_1 relaxation rates can be conveniently recorded in a 2D NCC correlation experiment[172] and may provide a powerful instrument to monitor backbone dynamics in a single 2D experiment.

Solid-state NMR can not only report on 3D structure and the motional rates[123] of solid-phase molecules but it also, in principle, allows the inference of motional amplitudes in disordered systems. We have recently investigated this aspect on neurotensin, a neurotransmitter known to be unstructured in the absence of its membrane receptor (see the following section). For this purpose, we have developed a general strategy[173] to relate conformational heterogeneity to two-dimensional cross-peak patterns that provide a spectroscopic snapshot of all backbone conformations present in the polypeptide of interest. These dependencies reveal that the degree of backbone disorder detected for individual residues of neurotensin is in qualitative agreement with the residue-specific free energies, ΔG, calculated for a transfer from an aqueous to a lipid environment.

3.4. Membrane peptides and proteins

MAS has long been employed to obtain site-specific structural information in membrane proteins such as bacteriorhodopsin or rhodopsin (for recent reviews see, for example, Refs. 27,174). In addition, MAS-based solid-state NMR studies were also conducted using selectively labelled membrane peptides[175,176] or peptides reconstituted into deuterated model lipids.[177–179] Such experimental conditions can also easily be modified for the case of macroscopically oriented systems.[19,180] Uniformly [^{13}C,^{15}N]-labelled peptides studied recently by high-resolution correlation techniques include neurotensin,[181] mastoparan-X[182] and a variety of fusion peptides.[183] Irrespective of whether measured in the gel or liquid-crystalline phase, secondary chemical shifts can report on local backbone conformation.[20,183,184]

Membrane protein (i.e., receptor) function often involves interactions with ligand molecules and represents an area of great pharmacological relevance. Until recently, no structural information of a high-affinity ligand bound to a G-protein-coupled receptor (GPCR) was available. Unlike rhodopsin, the recombinant expression of GPCR in large

quantities is usually difficult and must involve carefully optimized biochemical procedures. Restrictions regarding the availability of functional receptors also affect ligand quantities that can be studied. Moreover, the chemical environment including lipids and receptor protein can hamper the unambiguous spectral identification of a bound ligand in a solid-state NMR experiment.[185]

We have shown how 2D (double-quantum) solid-state NMR correlation experiments can be utilized to detect microgram quantities of bound neurotensin, a 13-residue neuropeptide that interacts in high affinity with its NTS-1 (101 kDa) receptor.[181] To elucidate the backbone conformation of neurotensin in complex with its receptor, we conducted a series of double-quantum filter (2QF) 2D correlation experiments to identify the peptide bound signal, assign the side-chain resonances and, finally, to derive the backbone structure using TALOS.[106] In Fig. 17a, the general approach to identify intraresidue correlations in the considered peptide fragment is outlined: Knowledge of amino acid-specific chemical shift ranges is used to establish a spectral grid that serves to identify the different residue types. As detailed in Ref. 181, this analysis does not allow for discrimination of Arg8 and Arg9 in neurotensin, but suffices to identify backbone and side-chain resonances of
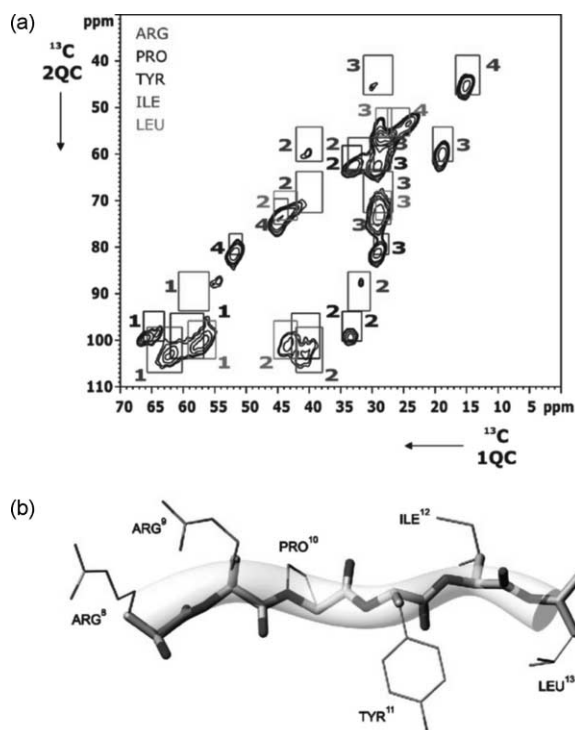
Fig. 17. (a) A 2Q–1Q spectrum of neurotensin (NT$^{9-13}$). (b) The backbone conformation of neurotensin in complex with its GPCR, as determined by solid-state NMR.[181]

NT[9–13] (Fig. 17a). A subsequent analysis of the resonance assignments obtained on receptor-bound NT[8–13] suggests that neurotensin adopts a β-strand conformation when bound to NTS-1 (Fig. 17b). Further evidence that the structure consistent with the solid-state NMR data represents the bioactive conformation of neurotensin comes from a recent report by Gmeiner and co-workers[186] who rigidized NT by chemical synthesis (using 4,4-spirolactam) around the Pro10 backbone angle to (A) $\psi = 120°$ and (B) $\psi = -120°$. While compound A exhibits a dihedral angle close to the value predicted from the 2D solid-state NMR data and has a nM binding affinity to the NT-receptor, compound B is characterized by a binding affinity that is three orders of magnitude lower.

Two-dimensional (^{13}C,^{15}N) correlation spectroscopy was also applied to a uniformly [^{13}C,^{15}N]-labelled version of the LH2 light-harvesting complex[187] from the purple non-sulphur photosynthetic bacterium *Rhodopseudomonas acidophila* 10050 strain,[188] one of the largest systems (approx. 150 kDa) studied by solid-state NMR to date. Here, the application of ultra-high magnetic fields (up to 750 MHz) was crucial to establish high-resolution conditions in the solid state. Two-dimensional (^{15}N,^{13}C) correlation experiments were conducted to assign the backbone and side-chain resonances at different temperatures. From two-dimensional correlation spectra shown in Ref. 187, a significant number of individual (^{15}N,^{13}C) correlations can be identified that are characterized by line widths below 1 ppm in both spectral dimensions. Combined with an NCOCA experiment, a variety of spectral assignments within the transmembrane sections of the protein were possible and are indicated in black in Fig. 18. Additional correlations occur at temperatures below $-10°C$, consistent with the immobilization of flexible loop regions of the protein. A more detailed structural study of membrane proteins could include (^{13}C,^{13}C) or indirect (^{1}H,^{1}H) correlation experiments, possibly in conjunction with advanced isotope labelling approaches, to determine the complete 3D structure of a membrane protein in the solid state.
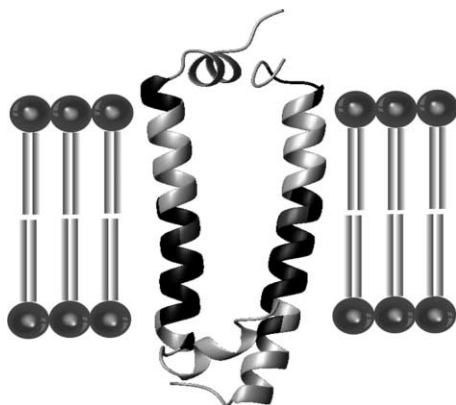
Fig. 18. Schematic view of the backbone structure of the LH2 protomer complex embedded in a model membrane. Assigned residues[187] are given in black.

4. CONCLUSIONS

MAS-based solid-state NMR has recently made considerable progress in the structural study of polypeptides and proteins. In many of these investigations, spectral assignments provide the basis for further investigations of 3D structure or dynamics. Recent applications include a variety of protein aggregates and fibrils, membrane-interacting peptides and proteins and the analysis of protein–protein interactions. Advances regarding sample preparation (for example, including modular labelling, *in vitro* expression and intein technology[189]) and improvements in NMR hardware instrumentation could open up new areas of solid-state NMR research such as the investigation of large protein–protein complexes or the complete 3D characterization of larger membrane proteins.

For such applications, further improvements of the applied spectral assignment methods will be beneficial and may result from numerically optimized decoupling and polarization transfer schemes. While in the earlier stages, the theoretical details of polarization and the development of general principles in designing mixing schemes were the focus of many research groups, sensitivity-optimized concepts, for example, in the context of three- or higher-dimensional correlation spectroscopy,[57] will likely play an increasing role in MAS solid-state NMR applications. Likewise, conducting solid-state NMR experiments at higher magnetic fields and a further optimization of the macroscopic sample conditions will likely expand the utility of biological solid-state NMR. Similar to other spectroscopic methods, the applicability of solid-state NMR to investigate structural problems is often determined by the spectral resolution and the signal-to-noise ratio. Recent studies have shown that both parameters can be significantly improved by increasing the strength of the static magnetic field in which the sample of interest is placed and by employing state-of-the-art NMR instrumentation. Pioneered by Griffin and co-workers,[190] a further dramatic increase in sensitivity may result from the widespread application of dynamic nuclear polarization (DNP) methods in MAS solid-state NMR. In addition, techniques that aim at enhancing spectral resolution by the application of state-of-the-art MAS hardware or r.f.-based selection schemes may further improve spectral resolution.

With the existing approaches at hand, the solid-state NMR spectroscopist already can address structural problems in chemistry and biophysics with greater flexibility. As shown for the neurotensin case, solid-state NMR can play a key role in investigating high-affinity ligand binding in membrane proteins, an area of great pharmacological relevance.[191–193] In parallel, novel routes to study protein dynamics and folding are emerging.

Clearly, additional efforts to streamline 3D protein structure determination by MAS NMR are necessary. Novel concepts may make extensive use of the rapidly increasing power of bioinformatics and computational chemistry. Already, general approaches have appeared to predict 3D structure from a limited set of solution-state NMR data.[194] In parallel, the ability to relate molecular structure to NMR detectable parameters by *ab initio* quantum chemistry calculations and DFT approaches is dramatically improving.[195,196] These techniques already have empowered novel material science applications of solid-state NMR[197] and will greatly expand the use of MAS solid-state NMR for the study of polypeptides and proteins. Complementary to crystallographic

methods and solution-state NMR techniques, MAS solid-state NMR methods may hence provide a very efficient means to study protein structure, folding and function under biologically relevant conditions.

ACKNOWLEDGEMENTS

REFERENCES

1. E. R. Andrew, A. Bradbury and R. G. Eades, *Nature*, 1958, **182**, 1659.
2. J. Schaefer and E. O. Stejskal, *J. Am. Chem. Soc.*, 1976, **98**, 1031–1032.
3. J. Herzfeld, A. Roufosse, R. A. Haberkorn, R. G. Griffin and M. J. Glimcher, *Philos. Trans. R. Soc. Lond. Ser. B – Biol. Sci.*, 1980, **289**, 459–469.
4. E. Oldfield, J. L. Bowers and J. Forbes, *Biochemistry*, 1987, **26**, 6919–6923.
5. P. L. Yeagle and J. Frye, *Biochim. Biophys. Acta*, 1987, **899**, 137–142.
6. F. Creuzet, A. McDermott, R. Gebhard, K. Vanderhoef, M. B. Spijkerassink, J. Herzfeld, J. Lugtenburg, M. H. Levitt and R. G. Griffin, *Science*, 1991, **251**, 783–786.
7. P. Tang, C. L. Juang and G. S. Harbison, *Science*, 1990, **249**, 70–72.
8. D. A. Torchia, *Annu. Rev. Biophys. Bioeng.*, 1984, **13**, 125–144.
9. H. B. R. Cole and D. A. Torchia, *Chem. Phys.*, 1991, **158**, 271–281.
10. P. A. Keifer, *Drug Discov. Today*, 1997, **2**, 468–478.
11. M. J. Shapiro and J. R. Wareing, *Curr. Opin. Chem. Biol.*, 1998, **2**, 372–375.
12. S. J. Opella and F. M. Marassi, *Chem. Rev.*, 2004, **104**, 3587–3606.
13. T. A. Cross and S. J. Opella, *Curr. Opin. Struct. Biol.*, 1994, **4**, 574–581.
14. F. M. Marassi and S. J. Opella, *Curr. Opin. Struct. Biol.*, 1998, **8**, 640–648.
15. B. Bechinger, R. Kinder, M. Helmle, T. C. B. Vogt, U. Harzer and S. Schinzel, *Biopolymers*, 1999, **51**, 174–190.
16. T. A. Cross and J. R. Quine, *Concepts Magn. Reson.*, 2000, **12**, 55–70.
17. C. Glaubitz and A. Watts, *J. Magn. Reson.*, 1998, **130**, 305–316.
18. N. A. Oyler and R. Tycko, *J. Am. Chem. Soc.*, 2004, **126**, 4478–4479.
19. C. Sizun and B. Bechinger, *J. Am. Chem. Soc.*, 2002, **124**, 1146–1147.
20. O. C. Andronesi, J. R. Pfeifer, L. Al-Momani, S. Özdirekcan, D. T. S. Rijkers, B. Angerstein, S. Luca, U. Koert, J. A. Killian and M. Baldus, *J. Biomol. NMR*, 2004, **30**, 253–265.
21. S. P. Brown and H. W. Spiess, *Chem. Rev.*, 2001, **101**, 4125–4155.
22. M. H. Levitt, Symmetry-based pulse sequences in magic-angle spinning solid-state NMR, in Encyclopedia of Nuclear Magnetic Resonance: Supplementary Volume, R. K. Harris, ed., Wiley, Chichester, 2002, 165–196.
23. M. Baldus, *Prog. NMR Spectrosc.*, 2002, **41**, 1–47.
24. L. M. McDowell and J. Schaefer, *Curr. Opin. Struct. Biol.*, 1996, **6**, 624–629.
25. R. G. Griffin, *Nat. Struct. Biol.*, 1998, **5**, 508–512.
26. A. Watts, *Curr. Opin. Biotechnol.*, 1999, **10**, 48–53.
27. J. H. Davis and M. Auger, *Prog. NMR Spectrosc.*, 1999, **35**, 1–84.
28. L. K. Thompson, *Curr. Opin. Struct. Biol.*, 2002, **12**, 661–669.
29. R. Tycko, *Biochemistry*, 2003, **42**, 3151–3159.
30. R. Tycko, *Prog. NMR Spectrosc.*, 2003, **42**, 53–68.
31. S. Luca, H. Heise and M. Baldus, *Acc. Chem. Res.*, 2003, **36**, 858–865.

32. N. C. Nielsen, A. Malmendal and T. Vosegaard, *Mol. Membr. Biol.*, 2004, **21**, 129–141.

33. S. K. Straus, *Philos. Trans. R. Soc. Lond. Ser. B – Biol. Sci.*, 2004, **359**, 997–1008.

34. M. Ernst, A. Detken, A. Bockmann and B. H. Meier, *J. Am. Chem. Soc.*, 2003, **125**, 15807–15810.

35. E. H. Hardy, A. Detken and B. H. Meier, *J. Magn. Reson.*, 2003, **165**, 208–218.

36. A. E. McDermott, F. J. Creuzet, A. C. Kolbert and R. G. Griffin, *J. Magn. Reson.*, 1992, **98**, 408–413.

37. B. Reif, B. J. van Rossum, F. Castellani, K. Rehbein, A. Diehl and H. Oschkinat, *J. Am. Chem. Soc.*, 2003, **125**, 1488–1489.

38. E. K. Paulson, C. R. Morcombe, V. Gaponenko, B. Dancheck, R. A. Byrd and K. W. Zilm, *J. Am. Chem. Soc.*, 2003, **125**, 15831–15836.

39. L.-Y. Lian and D. A. Middleton, *Prog. NMR Spectrosc.*, 2001, **39**, 171–190.

40. D. M. LeMaster and D. M. Kushlan, *J. Am. Chem. Soc.*, 1996, **118**, 9255–9264.

41. R. B. Gregory, M. Gangoda, R. K. Gilpin and W. Su, *Biopolymers*, 1993, **33**, 513–519.

42. R. B. Gregory, M. Gangoda, R. K. Gilpin and W. Su, *Biopolymers*, 1993, **33**, 1871–1876.

43. S. Luca and M. Baldus, *J. Magn. Reson.*, 2002, **159**, 243–249.

44. J. N. S. Evans, R. J. Appleyard and W. A. Shuttleworth, *J. Am. Chem. Soc.*, 1993, **115**, 1588–1590.

45. D. L. Jakeman, D. J. Mitchell, W. A. Shuttleworth and J. N. S. Evans, *J. Biomol. NMR*, 1998, **12**, 417–421.

46. Y. Tomita, E. J. Oconnor and A. McDermott, *J. Am. Chem. Soc.*, 1994, **116**, 8766–8771.

47. A. Böckmann, A. Lange, A. Galinier, S. Luca, N. Giraud, H. Heise, M. Juy, R. Montserret, F. Penin and M. Baldus, *J. Biomol. NMR*, 2003, **27**, 323–339.

48. R. W. Martin and K. W. Zilm, *J. Magn. Reson.*, 2003, **165**, 162–174.

49. R. B. Gennis, *Biomembranes. Molecular Structure and Function*, Springer, New York, 1989.

50. M. Mehring, Internal spin interactions & rotations in solids, in Encyclopedia of Nuclear Magnetic Resonance, D.M. Grant and R.K. Harris, eds., Wiley, Chichester, 1996, 2585–2603.

51. C. H. Ye, R. Q. Fu, J. Z. Hu, L. Hou and S. W. Ding, *Magn. Reson. Chem.*, 1993, **31**, 699–704.

52. A. E. Bennett, C. M. Rienstra, M. Auger, K. V. Lakshmi and R. G. Griffin, *J. Chem. Phys.*, 1995, **103**, 6951–6958.

53. A. Detken, E. H. Hardy, M. Ernst and B. H. Meier, *Chem. Phys. Lett.*, 2002, **356**, 298–304.

54. A. Khitrin and B. M. Fung, *J. Chem. Phys.*, 2000, **112**, 2392–2398.

55. L. Duma, S. Hediger, B. Brutscher, A. Bockmann and L. Emsley, *J. Am. Chem. Soc.*, 2003, **125**, 11816–11817.

56. A. Ramamoorthy, F. M. Marassi, M. Zasloff and S. J. Opella, *J. Biomol. NMR*, 1995, **6**, 329–334.

57. H. Heise, K. Seidel, M. Etzkorn, S. Becker and M. Baldus, *J. Magn. Reson.*, 2005, **173**, 64–74.

58. R. R. Ernst, G. Bodenhausen and A. Wokaun, *Principles of Nuclear Magnetic Resonance in One and Two Dimensions*, Clarendon Press, Oxford, 1987.

59. A. E. Bennett, J. H. Ok, R. G. Griffin and S. Vega, *J. Chem. Phys.*, 1992, **96**, 8624–8627.

60. R. Tycko and G. Dabbagh, *Chem. Phys. Lett.*, 1990, **173**, 461–465.

61. N. C. Nielsen, H. Bildsøe, H. J. Jakobsen and M. H. Levitt, *J. Chem. Phys.*, 1994, **101**, 1805–1812.

62. B. Q. Sun, P. R. Costa, D. Kocisko, P. T. Lansbury and R. G. Griffin, *J. Chem. Phys.*, 1995, **102**, 702–707.

63. D. M. Gregory, D. J. Mitchell, J. A. Stringer, S. Kiihne, J. C. Shiels, J. Callahan, M. A. Mehta and G. P. Drobny, *Chem. Phys. Lett.*, 1995, **246**, 654–663.

64. Y. K. Lee, N. D. Kurur, M. Helmle, O. G. Johannessen, N. C. Nielsen and M. H. Levitt, *Chem. Phys. Lett.*, 1995, **242**, 304–309.

65. M. Hohwy, C. M. Rienstra, C. P. Jaroniec and R. G. Griffin, *J. Chem. Phys.*, 1999, **110**, 7983–7992.

66. M. Baldus, M. Tomaselli, B. H. Meier and R. R. Ernst, *Chem. Phys. Lett.*, 1994, **230**, 329–336.

67. Y. Ishii, J. Ashida and T. Terao, *Chem. Phys. Lett.*, 1995, **246**, 439–445.

68. C. E. Hughes, S. Luca and M. Baldus, *Chem. Phys. Lett.*, 2004, **385**, 435–440.

69. D. P. Raleigh, M. H. Levitt and R. G. Griffin, *Chem. Phys. Lett.*, 1988, **146**, 71–76.

70. E. R. Andrew, A. Bradbury, R. G. Eades and V. T. Wynn, *Phys. Lett.*, 1963, **4**, 99–100.

71. R. Verel, M. Baldus, M. Nijman, J. W. M. van Os and B. H. Meier, *Chem. Phys. Lett.*, 1997, **280**, 31–39.

72. R. Verel, M. Baldus, M. Ernst and B. H. Meier, *Chem. Phys. Lett.*, 1998, **287**, 421–428.

73. R. Ramachandran, V. Ladizhansky, V. S. Bajaj and R. G. Griffin, *J. Am. Chem. Soc.*, 2003, **125**, 15623–15629.

74. V. Ladizhansky and R. G. Griffin, *J. Am. Chem. Soc.*, 2004, **126**, 948–958.

75. T. Gullion and J. Schaefer, *J. Magn. Reson.*, 1989, **81**, 196–200.
76. S. R. Hartmann and E. L. Hahn, *Phys. Rev.*, 1962, **128**, 2042–2053.
77. M. Baldus, A. T. Petkova, J. Herzfeld and R. G. Griffin, *Mol. Phys.*, 1998, **95**, 1197–1207.
78. M. Baldus and B. H. Meier, *J. Magn. Reson. Ser. A*, 1996, **121**, 65–69.
79. M. Baldus, R. J. Iuliucci and B. H. Meier, *J. Am. Chem. Soc.*, 1997, **119**, 1121–1124.
80. G. A. Morris and R. Freeman, *J. Am. Chem. Soc.*, 1979, **101**, 760–762.
81. A. Lesage, P. Charmont, S. Steuernagel and L. Emsley, *J. Am. Chem. Soc.*, 2000, **122**, 9739–9744.
82. J. Cavanagh, W. J. Fairbrother, A. G. Palmer and N. J. Skelton, *Protein NMR Spectroscopy, Principles and Practice*, Academic Press, San Diego, CA, 1996.
83. N. Bloembergen, *Physica*, 1949, **15**, 386–426.
84. A. Kubo and C. A. McDowell, *J. Chem. Soc., Faraday Trans. I*, 1988, **84**, 3713–3730.
85. D. Suter and R. R. Ernst, *Phys. Rev. B*, 1982, **25**, 6038–6041.
86. D. Suter and R. R. Ernst, *Phys. Rev. B*, 1985, **32**, 5608–5627.
87. K. Takegoshi, S. Nakamura and T. Terao, *Chem. Phys. Lett.*, 2001, **344**, 631–637.
88. A. Lange, K. Seidel, L. Verdier, S. Luca and M. Baldus, *J. Am. Chem. Soc.*, 2003, **125**, 12640–12648.
89. A. Bax, R. Freeman and S. P. Kempsell, *J. Am. Chem. Soc.*, 1980, **102**, 4849–4851.
90. P. E. Kristiansen, D. J. Mitchell and J. N. S. Evans, *J. Magn. Reson.*, 2002, **157**, 253–266.
91. M. Ikura, L. E. Kay and A. Bax, *Biochemistry*, 1990, **29**, 4659–4667.
92. M. Ikura, L. E. Kay, R. Tschudin and A. Bax, *J. Magn. Reson.*, 1990, **86**, 204–209.
93. F. J. M. van de Ven, *Multidimensional NMR in Liquids: Basic Principles and Experimental Methods*, VCH Publishers, New York, 1995.
94. S. Dusold and A. Sebald, *Annu. Rep. NMR Spectrosc.*, 2000, **41**, 185–264.
95. K. Takegoshi, K. Nomura and T. Terao, *Chem. Phys. Lett.*, 1995, **232**, 424–428.
96. M. Baldus, D. G. Geurts and B. H. Meier, *Solid State Nucl. Magn. Reson.*, 1998, **11**, 157–168.
97. K. Seidel, A. Lange, S. Becker, C. E. Hughes, H. Heise and M. Baldus, *Phys. Chem. Chem. Phys.*, 2004, **6**, 5090–5093.
98. A. Lange, S. Luca and M. Baldus, *J. Am. Chem. Soc.*, 2002, **124**, 9704–9705.
99. M. Etzkorn, A. Böckmann, A. Lange and M. Baldus, *J. Am. Chem. Soc.*, 2004, **126**, 14746–14751.
100. H. Saito, *Magn. Reson. Chem.*, 1986, **24**, 835–852.
101. S. Spera and A. Bax, *J. Am. Chem. Soc.*, 1991, **113**, 5490–5492.
102. A. C. Dedios, J. G. Pearson and E. Oldfield, *Science*, 1993, **260**, 1491–1496.
103. J. J. Balbach, Y. Ishii, O. N. Antzutkin, R. D. Leapman, N. W. Rizzo, F. Dyda, J. Reed and R. Tycko, *Biochemistry*, 2000, **39**, 13748–13759.
104. S. Luca, D. V. Filippov, J. H. van Boom, H. Oschkinat, H. J. M. de Groot and M. Baldus, *J. Biomol. NMR*, 2001, **20**, 325–331.
105. J. Pauli, M. Baldus, B. van Rossum, H. de Groot and H. Oschkinat, *ChemBioChem*, 2001, **2**, 272–281.
106. G. Cornilescu, F. Delaglio and A. Bax, *J. Biomol. NMR*, 1999, **13**, 289–302.
107. S. Neal, A. M. Nip, H. Y. Zhang and D. S. Wishart, *J. Biomol. NMR*, 2003, **26**, 215–240.
108. C. M. Rienstra, M. Hohwy, M. Mueller, C. P. Jaroniec, B. Reif and R. G. Griffin, *J. Am. Chem. Soc.*, 2002, **124**, 11908–11922.
109. M. Hong, J. D. Gross and R. G. Griffin, *J. Phys. Chem. B*, 1997, **101**, 5869–5874.
110. P. R. Costa, J. D. Gross, M. Hong and R. G. Griffin, *Chem. Phys. Lett.*, 1997, **280**, 95–103.
111. X. Feng, M. Edén, A. Brinkmann, H. Luthman, L. Eriksson, A. Gräslund, O. N. Antzutkin and M. H. Levitt, *J. Am. Chem. Soc.*, 1997, **119**, 12006–12007.
112. B. Reif, M. Hohwy, C. P. Jaroniec, C. M. Rienstra and R. G. Griffin, *J. Magn. Reson.*, 2000, **145**, 132–141.
113. F. J. Blanco and R. Tycko, *J. Magn. Reson.*, 2001, **149**, 131–138.
114. M. Hong and K. Jakes, *J. Biomol. NMR*, 1999, **14**, 71–74.
115. F. Castellani, B. van Rossum, A. Diehl, M. Schubert, K. Rehbein and H. Oschkinat, *Nature*, 2002, **420**, 98–102.
116. L. Sonnenberg, S. Luca and M. Baldus, *J. Magn. Reson.*, 2004, **166**, 100–110.
117. X. L. Wu, S. M. Zhang and X. W. Wu, *Phys. Rev. B*, 1988, **37**, 9827–9829.
118. S. Zhang, B. H. Meier and R. R. Ernst, *Phys. Rev. Lett.*, 1992, **69**, 2149–2151.
119. M. Tomaselli, S. Hediger, D. Suter and R. R. Ernst, *J. Chem. Phys.*, 1996, **105**, 10672–10681.

120. M. Wilhelm, H. Feng, U. Tracht and H. W. Spiess, *J. Magn. Reson.*, 1998, **134**, 255–260.
121. F. M. Mulder, W. Heinen, M. van Duin, J. Lugtenburg and H. J. M. de Groot, *J. Am. Chem. Soc.*, 1998, **120**, 12891–12894.
122. Y. Matsuki, H. Akutsu and T. Fujiwara, *Magn. Reson. Chem.*, 2004, **42**, 291–300.
123. K. Seidel, M. Etzkorn, L. Sonnenberg, A. Sebald and M. Baldus, *J. Phys. Chem. A*, 2005, in press.
124. A. Lange, S. Becker, K. Seidel, O. Pongs and M. Baldus, *Angew. Chem.-Int. Edit.*, 2005, in press
125. R. Tycko and Y. Ishii, *J. Am. Chem. Soc.*, 2003, **125**, 6606–6607.
126. I. de Boer, J. Matysik, M. Amakawa, S. Yagai, H. Tamiaki, A. R. Holzwarth and H. J. M. de Groot, *J. Am. Chem. Soc.*, 2003, **125**, 13374–13375.
127. S. K. Straus, T. Bremi and R. R. Ernst, *J. Biomol. NMR*, 1998, **12**, 39–50.
128. M. Hong, *J. Biomol. NMR*, 1999, **15**, 1–14.
129. A. McDermott, T. Polenova, A. Bockmann, K. W. Zilm, E. K. Paulsen, R. W. Martin and G. T. Montelione, *J. Biomol. NMR*, 2000, **16**, 209–219.
130. J. Pauli, B. van Rossum, H. Forster, H. J. M. de Groot and H. Oschkinat, *J. Magn. Reson.*, 2000, **143**, 411–416.
131. G. J. Boender, J. Raap, S. Prytulla, H. Oschkinat and H. J. M. de Groot, *Chem. Phys. Lett.*, 1995, **237**, 502–508.
132. C. M. Rienstra, M. E. Hatcher, L. J. Mueller, B. Q. Sun, S. W. Fesik and R. G. Griffin, *J. Am. Chem. Soc.*, 1998, **120**, 10602–10612.
133. X. Helluy and A. Sebald, *J. Phys. Chem. B*, 2003, **107**, 3290–3296.
134. S. K. Straus, T. Bremi and R. R. Ernst, *J. Biomol. NMR*, 1997, **10**, 119–128.
135. A. Detken, E. H. Hardy, M. Ernst, M. Kainosho, T. Kawakami, S. Aimoto and B. H. Meier, *J. Biomol. NMR*, 2001, **20**, 203–221.
136. S. Becker, A. Lange, K. Giller, K. Morick, H. Kratzin, C. Legros, O. Pongs and M. Baldus, XXth ICMRBS, Toronto, 2002.
137. M. Hong and R. G. Griffin, *J. Am. Chem. Soc.*, 1998, **120**, 7113–7114.
138. K. Nomura, K. Takegoshi, T. Terao, K. Uchida and M. Kainosho, *J. Am. Chem. Soc.*, 1999, **121**, 4064–4065.
139. B. J. van Rossum, F. Castellani, K. Rehbein, J. Pauli and H. Oschkinat, *ChemBioChem*, 2001, **2**, 906–914.
140. S. Vijay-Kumar, C. E. Bugg and W. J. Cook, *J. Mol. Biol.*, 1987, **194**, 531–544.
141. G. Cornilescu, J. L. Marquardt, M. Ottiger and A. Bax, *J. Am. Chem. Soc.*, 1998, **120**, 6836–6837.
142. T. I. Igumenova, A. J. Wand and A. E. McDermott, *J. Am. Chem. Soc.*, 2004, **126**, 5323–5331.
143. T. I. Igumenova, A. E. McDermott, K. W. Zilm, R. W. Martin, E. K. Paulson and A. J. Wand, *J. Am. Chem. Soc.*, 2004, **126**, 6720–6727.
144. S. Luca, Ph.D. Thesis, MPI for Biophysical Chemistry, 2003.
145. H. Heise, K. Seidel, M. Etzkorn, S. Becker and M. Baldus, 2004, submitted for publication.
146. B. M. Fung, A. K. Khitrin and K. Ermolaev, *J. Magn. Reson.*, 2000, **142**, 97–101.
147. C. M. Rienstra, T. Franks, D. Donghua Zhou, B. Wylie, B. Money, D. Graesser and G. Sahota, The 45th ENC Conference, Asilomar, CA, 2004.
148. T. Polenova, M. L. Tasayco, A. E. McDermott, D. Marulanda, M. Cataldi, V. Arriaran and S. Bai, The 45th ENC Conference, Asilomar, CA, 2004.
149. M. Crest, G. Jacquet, M. Gola, H. Zerrouk, A. Benslimane, H. Rochat, P. Mansuelle and M. F. Martineauclaire, *J. Biol. Chem.*, 1992, **267**, 1640–1647.
150. S. Grissmer, A. N. Nguyen, J. Aiyar, D. C. Hanson, R. J. Mather, G. A. Gutman, M. J. Karmilowicz, D. D. Auperin and K. G. Chandy, *Mol. Pharmacol.*, 1994, **45**, 1227–1234.
151. S. R. Chong, F. B. Mersha, D. G. Comb, M. E. Scott, D. Landry, L. M. Vence, F. B. Perler, J. Benner, R. B. Kucera, C. A. Hirvonen, J. J. Pelletier, H. Paulus and M. Q. Xu, *Gene*, 1997, **192**, 271–281.
152. C. Legros, V. Pollmann, H. G. Knaus, A. M. Farrell, H. Darbon, P. E. Bougis, M. F. Martin-Eauclaire and O. Pongs, *J. Biol. Chem.*, 2000, **275**, 16918–16924.
153. C. P. Jaroniec, C. E. MacPhee, N. S. Astrof, C. M. Dobson and R. G. Griffin, *Proc. Natl Acad. Sci.*, 2002, **99**, 16748–16753.
154. A. T. Petkova, Y. Ishii, J. J. Balbach, O. N. Antzutkin, R. D. Leapman, F. Delaglio and R. Tycko, *Proc. Natl Acad. Sci.*, 2002, **99**, 16742–16747.

155. C. M. Rienstra, L. Tucker-Kellogg, C. P. Jaroniec, M. Hohwy, B. Reif, M. T. McMahon, B. Tidor, T. Lozano-Perez and R. G. Griffin, *Proc. Natl Acad. Sci.*, 2002, **99**, 10260–10265.

156. C. P. Jaroniec, C. E. MacPhee, V. S. Bajaj, M. T. McMahon, C. M. Dobson and R. G. Griffin, *Proc. Natl Acad. Sci.*, 2004, **101**, 711–716.

157. H. M. Berman, J. Westbrook, Z. Feng, G. Gilliland, T. N. Bhat, H. Weissig, I. N. Shindyalov and P. E. Bourne, *Nucleic Acids Res.*, 2000, **28**, 235–242.

158. R. R. Ketchem, W. Hu and T. A. Cross, *Science*, 1993, **261**, 1457–1460.

159. S. J. Opella, F. M. Marassi, J. J. Gesell, A. P. Valente, Y. Kim, M. Oblatt-Montal and M. Montal, *Nat. Struct. Biol.*, 1999, **6**, 374–379.

160. F. M. Marassi and S. J. Opella, *Protein Sci.*, 2003, **12**, 403–411.

161. J. F. Wang, S. Kim, F. Kovacs and T. A. Cross, *Protein Sci.*, 2001, **10**, 2241–2250.

162. K. G. Valentine, S. F. Liu, F. M. Marassi, G. Veglia, S. J. Opella, F. X. Ding, S. H. Wang, B. Arshava, J. M. Becker and F. Naider, *Biopolymers*, 2001, **59**, 243–256.

163. S. H. Park, A. A. Mrse, A. A. Nevzorov, M. F. Mesleh, M. Oblatt-Montal, M. Montal and S. J. Opella, *J. Mol. Biol.*, 2003, **333**, 409–424.

164. M. F. Wang, M. Bertmer, D. E. Demco and B. Blumich, *J. Phys. Chem. B*, 2004, **108**, 10911–10918.

165. C. E. Hughes, S. Haufe, B. Angerstein, R. Kalim, U. Maehr, A. Reiche and M. Baldus, *J. Phys. Chem. B*, 2004, **108**, 13626–13631.

166. H. J. Dyson and P. E. Wright, *Nat. Struct. Biol.*, 1998, **5**, 499–503.

167. C. M. Dobson, *Philos. Trans. R. Soc. Lond. Ser. B – Biol. Sci.*, 2001, **356**, 133–145.

168. J. Schaefer, R. A. McKay and E. O. Stejskal, *J. Magn. Reson.*, 1979, **34**, 443–447.

169. M. Baldus, D. G. Geurts, S. Hediger and B. H. Meier, *J. Magn. Reson. Ser. A*, 1996, **118**, 140–144.

170. A. Lange, Diploma Thesis, University of Göttingen, 2002.

171. B. I. Giasson, M. S. Forman, M. Higuchi, L. I. Golbe, C. L. Graves, P. T. Kotzbauer, J. Q. Trojanowski and V. M. Y. Lee, *Science*, 2003, **300**, 636–640.

172. N. Giraud, A. Böckmann, A. Lesage, F. Penin, M. Blackledge and L. Emsley, *J. Am. Chem. Soc.*, 2004, **126**, 11422–11423.

173. H. Heise, S. Luca, B. de Groot, H. Grubmüller and M. Baldus, 2004, submitted for publication.

174. S. O. Smith, K. Aschheim and M. Groesbeek, *Q. Rev. Biophys.*, 1996, **29**, 395–449.

175. O. B. Peersen, S. Yoshimura, H. Hojo, S. Aimoto and S. O. Smith, *J. Am. Chem. Soc.*, 1992, **114**, 4332–4335.

176. D. J. Hirsh, J. Hammer, W. L. Maloy, J. Blazyk and J. Schaefer, *Biochemistry*, 1996, **35**, 12733–12741.

177. M. Bouchard, J. H. Davis and M. Auger, *Biophys. J.*, 1995, **69**, 1933–1938.

178. J. H. Davis, M. Auger and R. S. Hodges, *Biophys. J.*, 1995, **69**, 1917–1932.

179. W. Y. Zhang, E. Crocker, S. McLaughlin and S. O. Smith, *J. Biol. Chem.*, 2003, **278**, 21459–21466.

180. C. Glaubitz, *Concepts Magn. Reson.*, 2000, **12**, 137–151.

181. S. Luca, J. F. White, A. K. Sohal, D. V. Filippov, J. H. van Boom, R. Grisshammer and M. Baldus, *Proc. Natl Acad. Sci.*, 2003, **100**, 10706–10711.

182. T. Fujiwara, Y. Todokoro, H. Yanagishita, M. Tawarayama, T. Kohno, K. Wakamatsu and H. Akutsu, *J. Biomol. NMR*, 2004, **28**, 311–325.

183. M. L. Bodner, C. M. Gabrys, P. D. Parkanzky, J. Yang, C. A. Duskin and D. P. Weliky, *Magn. Reson. Chem.*, 2004, **42**, 187–194.

184. P. Barre, O. Zschornig, K. Arnold and D. Huster, *Biochemistry*, 2003, **42**, 8377–8386.

185. A. Lange and M. Baldus, *Novel Solid-state NMR methods for structural studies on GPCRs*. Marcel Dekker Inc., New York, 2005, in press

186. H. Bittermann, J. Einsiedel, J. Hubner and P. Gmeiner, *J. Med. Chem.*, 2004, **47**, 5587–5590.

187. T. A. Egorova-Zachernyuk, J. Hollander, N. Fraser, P. Gast, A. J. Hoff, R. Cogdell, H. J. M. de Groot and M. Baldus, *J. Biomol. NMR*, 2001, **19**, 243–253.

188. G. McDermott, S. M. Prince, A. A. Freer, A. M. Hawthornthwaitelawless, M. Z. Papiz, R. J. Cogdell and N. W. Isaacs, *Nature*, 1995, **374**, 517–521.

189. D. Staunton, J. Owen and I. D. Campbell, *Acc. Chem. Res.*, 2003, **36**, 207–214.

190. M. Rosay, A. C. Zeri, N. S. Astrof, S. J. Opella, J. Herzfeld and R. G. Griffin, *J. Am. Chem. Soc.*, 2001, **123**, 1010–1011.

191. S. Farley, *Nat. Rev. Drug Discov.*, 2003, **2**, 862–862.
192. T. Bartfai, J. L. Benovic, J. Bockaert, R. A. Bond, M. Bouvier, A. Christopoulos, O. Civelli, L. A. Devi, S. R. George, A. Inui, B. Kobilka, R. Leurs, R. Neubig, J. P. Pin, R. Quirion, B. P. Roques, T. P. Sakmar, R. Seifert, R. E. Stenkamp and P. G. Strange, *Nat. Rev. Drug Discov.*, 2004, **3**, 574–626.
193. S. Luca, A. Lange, H. Heise and M. Baldus, 2004, submitted for publication.
194. J. Meiler and D. Baker, *Proc. Natl Acad. Sci.*, 2003, **100**, 15404–15409.
195. C. Ochsenfeld, *Phys. Chem. Chem. Phys.*, 2000, **2**, 2153–2159.
196. C. Ochsenfeld, J. Kussmann and F. Koziol, *Angew. Chem. Int. Ed.*, 2004, **43**, 4485–4489.
197. T. M. Clark and P. J. Grandinetti, *J. Phys. Condens. Matter*, 2003, **15**, S2387–S2395.
198. A. Wlodawer, J. Nachman, G. L. Gilliland, W. Gallagher and C. Woodward, *J. Mol. Biol.*, 1987, **198**, 469.
199. A. Musacchio, M. Noble, R. Pauptit, R. Wierenga and M. Saraste, *Nature*, 1992, **359**, 851–855.
200. F. J. Blanco, A. R. Ortiz and L. Serrano, *J. Biomol. NMR*, 1997, **9**, 347–357.
201. A. Favier, B. Brutscher, M. Blackledge, A. Galinier, J. Deutscher, F. Penin and D. Marion, *J. Mol. Biol.*, 2002, **317**, 131–144.
202. M. R. Juy, F. Penin, A. Favier, A. Galinier, R. Montserret, R. Haser, J. Deutscher and A. Böckmann, *J. Mol. Biol.*, 2003, **332**, 767–776.
203. M. Gairi, R. Romi, I. Fernandez, H. Rochat, M.-F. Martin-Eauclaire, J. Van Rietschtoten, M. Pons and E. Giralt, *J. Pept. Sci.*, 1997, **3**, 314–319.
204. T. Gallagher, P. Alexander, P. Bryan and G. L. Gilliland, *Biochemistry*, 1994, **33**, 4721–4729.
205. J. F. Andersen, D. A. Sanders, J. R. Gasdaska, A. Weichsel, G. Powis and W. R. Montfort, *Biochemistry*, 1997, **36**, 13979–13988.

NMR Studies of Dynamic Processes in Organic Solids

D. REICHERT

Univ. Halle, FB Physik, Friedemann-Bach-Platz 6, 06108 Halle, Germany
E-mail: reichert@physik.uni-halle.de

Similar to molecular structure, molecular dynamics is crucial for understanding the macroscopic properties of the material, such as the biological activity in proteins, application properties in construction polymers, electrical properties in conducting material and transport phenomena in nanoporous solids. The molecular dynamics covers a wide range of motional frequencies and involves dynamic modes that might have different effects on the properties of the material. It is therefore desirable to determine both the characteristic time (correlation time of motion, τ_c) and the topology (like jump angles and population of sites) of the processes with a reasonable spectral and thus molecular resolution. This chapter describes the principles and applications of dynamic solid-state NMR spectroscopy for the investigation of molecular dynamic processes in organic materials. It covers the major experimental methods and briefly comments on their application in a variety of materials up to the year 2003.

1. INTRODUCTION

Since the relevant NMR interactions like chemical shift and dipolar coupling provide primarily information about the chemical and spatial structure of the sample material, the majority of reported NMR studies naturally aim to obtain structural data: the search

term 'NMR and structure' obtains about 85,000 hits in the Web-of-Science database (http://isiknowledge.com/, August 2004) while 'NMR and dynamic' delivers just about 19,500 hits. The relation is similar for solid state (about 12,500 vs. 3500) which in addition might be owed to the common opinion that molecules in solid-state materials are rigid and do not have any appreciable internal mobility. However, on the contrary, these materials exhibit a sometimes astonishing variety of segmental motions as well as molecular reorientations. Many of these motions were previously found to take place in solution, usually but not necessarily at higher rates. NMR spectroscopy is a particular convenient and versatile tool to search, investigate and characterize dynamic processes in the solid state. Soon after NMR was discovered and long before the discovery of the chemical shift and the J-coupling (which provide the basis of chemical applications), the relation of molecular dynamics and NMR relaxation parameters was elucidated. Likewise, the broadening of the NMR lines due to dipole–dipole coupling and the influence of molecular dynamic processes on this broadening were discovered early on. Nowadays available solid-state NMR methods span a dynamic range of more than 10 orders of magnitude, from shorter than nanoseconds in NMR relaxation up to tens of seconds in exchange experiments. Dynamic NMR also provides information about the topology of the dynamic processes, i.e., about the amplitude of reorientations, detailed information of jump angles, the number of interchanging sites or even the details of the correlation function of motion. The extraction of this information from the experimental NMR data often requires a simplified assumption of the correlation function of motion or a motional model for which the relation between relaxation time and correlation function has to be calculated or relies on the simulation of spectra or other NMR data and comparison with the experimental data. In a few cases of exchange NMR experiments, the dynamic information can be extracted completely model free. While the early experiments were mostly 'low-resolution' experiments on abundant nuclei like ^{1}H, the possibility of isotopic labeling as well as advances in line narrowing approaches and multi-dimensional NMR provide an increased molecular resolution and sensitivity, making dynamic NMR a unique tool for the detailed investigation of dynamic processes in organic solids.

In the framework of this chapter, the term 'organic solids' covers molecular crystals, organic glasses, synthetic and biopolymers, liquid crystals in certain phases as well as organic–inorganic hybrid compounds. The latter include substances like organically modified inorganic materials, organic matrices doped with inorganic substances and nano- and mesoporous inorganic materials filled with organic molecules. All these 'organic solids' have in common is that the macroscopic properties depend crucially on the molecular dynamics of the organic material, for example, the application properties of polymers, the biological functionality of biopolymers, transport properties of adsorbed molecules in zeolites, stability of food-related materials, electrical conductivity of organic charge carriers and the behavior of amorphous glasses and polymers. The understanding and improvement of these properties require knowledge about the time scale, amplitude and molecular origin of the dynamic processes. This in turn requires the development of experimental methods for their reliable and accurate detection. The aim of the present paper is a compilation of the major experimental methods in dynamic solid-state NMR, put into historical

perspective, as well as its applications. The chapter does not cover the detection of translational motions which are accessible by PFG-NMR experiments, or methods beyond the T_1-limit. Also, for the publications included in this review, full details and results are not being discussed.

2. EXPERIMENTAL METHODS

To describe molecular dynamics, the investigator would like to quantify the time scale as well as the geometry of the molecular process. The time dependence of the correlation function of motion contains the potentially available dynamic information. The shape of the correlation function can be as simple as a single exponential for an isotropic reorientation or as complicated as a multi-component and non-exponential function for more complicated motions in larger and structured molecules. In most of the cases, this information is not completely accessible and approximations have to be made. The most common approach is to apply a general model (see model-free approach below) and determine at least the correlation time and some information about the amplitude of motion, either in terms of an order parameter or more detailed as jump angles, number and population of sites involved in the process, etc. In most cases, jump motions can be distinguished from rotational diffusions. Dynamic solid-state NMR spans a dynamic window from very fast processes with correlation times of nanoseconds down to very slow motions that occur on the time scale of seconds. For that, different experimental approaches have been developed: fast processes in the range of the inverse Larmor frequency efficiently stimulate transitions of spins between the Zeeman levels and drive NMR relaxation. Thus, these experiments provide accurate information about fast motions while in their absence, spin-dynamic processes that do not contain information about the molecular dynamic contribute substantially to the relaxation data and make a faithful determination of dynamic parameters difficult. Slower motion, however, can either be investigated by relaxation experiments in lower effective fields or one can make use of the fact that processes with correlation time on the order of the lifetime of the solid-state NMR signal, i.e., microseconds, have an effect on the appearance of the NMR spectrum due to a modulation of the resonance frequencies or interference with external perturbations. Even slower processes are the domain of exchange experiments that basically are capable to investigate processes with correlation times as long as the relaxation time T_1. In the framework of this chapter, we will distinguish these different dynamic regimes according to their relation to the lifetime of the NMR signal (relaxation time T_2): we will call the dynamic processes fast, intermediate or slow if their characteristic time is short, comparable or long compared to T_2. Roughly, these three regimes match the three sections of the abscissa in Fig. 1. In the following sections, we will briefly introduce these methods and outline their main features which are of importance for dynamic NMR experiments on organic solids.
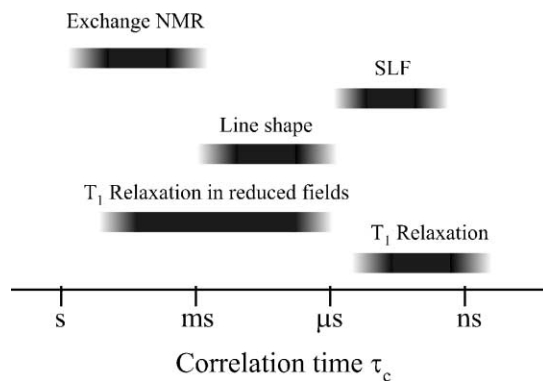
Fig. 1.   Dynamic range of the different NMR methods.

2.1. NMR relaxation

The NMR relaxation time T_1 was introduced in the Bloch equations to describe the return of a magnetization to thermal equilibrium after a perturbation of the spin system. It was soon realized that T_1 depends on the molecular mobility of the 'lattice' in which the spin system is embedded: the T_1 relaxation is most efficient when the lattice provides dynamic degrees of freedom in a frequency range close to the Larmor frequency and thus enables transition between the Zeeman levels. A quantitative understanding was developed in 1948[1] and further advanced.[2] Many more elaborate theories have been developed, relating the relaxation times T_1 and T_2 to molecular dynamic parameters by various approaches, e.g., with the aid of the density matrix formalism,[3–6] Kubo's method[7–10] or the Fokker–Planck equation.[11] The first relaxation experiments in solids were performed on the abundant and easily detectable nuclei ^1H and ^{19}F.[12] Soon after it was suspected as a result of dielectric and mechanical relaxation experiments that organic solids which are believed to be rigid exhibit a considerable amount of motion a degree of freedom that in turn permits rotational motions which should be detectable by NMR.[13] The method was quickly applied to more complex systems like synthetic polymers,[14,15] amino acids and biomolecular components.[16–18] It soon became clear that the dynamic behavior of more complicated materials like polymers cannot be described by a single correlation time but might require a distribution (Fig. 2)[19–23] (for which one has to distinguish between homogeneous and heterogeneous distributions that can be discriminated in NMR experiments[24]). A particularly useful tool in NMR relaxation is the ^2H-T_1 in organic solids since it reveals two important features:[25] (i) the inherent anisotropy of the relaxation time can be easily detected and (ii) this anisotropy depends on the correlation time τ_c (Fig. 3). Thus, partially relaxed spectra make it possible to determine τ_c from a single set of relaxation data and provide a tool for the discrimination between different models. Theoretical expressions can be derived for detailed models and provide unique dynamic information.[26,27]

While the most common approach to sample relaxation data is to record the NMR relaxation time as a function of temperature and make use of the temperature–frequency
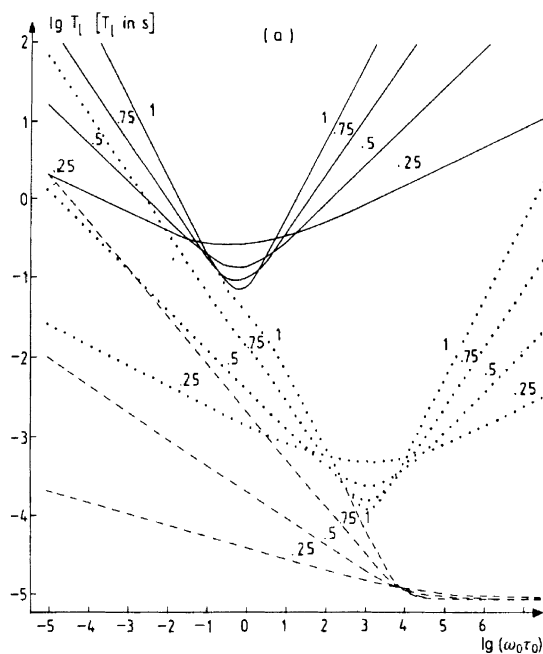
Fig. 2. Relaxation times vs. correlation times for T_1 (full lines), $T_{1\rho}$ (dotted lines) and T_2 (dashed lines). The numbers at the curves are the width parameters of a Fouss–Kirkwood distribution.[660] (Adapted with permission from Ref. 24.)
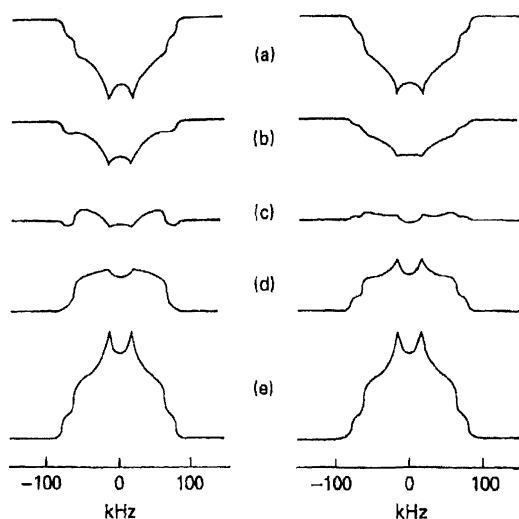
Fig. 3. Simulated partially relaxed ^{2}H powder spectra, calculated assuming a two-site jump and for an inversion recovery sequence with a solid echo for detection and recovery times of (a) 1.5 ms, (b) 5 ms, (c) 10 ms, (d) 20 ms and (e) 500 ms. Correlation times are 0.35 and 20 ns for the left and right columns, demonstrating the different T_1 anisotropy for short and long correlation times. (Adapted with permission from Ref. 456.)

relationship of thermally activated dynamic processes, a detailed treatment of relaxation data for more complicated motional processes requires the sampling of the frequency dependence of the NMR relaxation time. However, the commonly available ranges of Larmor frequencies provide less than one order of magnitude variation only. Since the sensitivity of the NMR signal decreases with decreasing Larmor frequency, the construction of very low-field spectrometers is not a feasible option. An intriguing approach to solve this problem is to polarize the samples and detect the signal at high field but mechanically switch them to a defined lower field for relaxation. This technique is termed field cycling and was first realized in the early days of NMR,[28] developed later on[29–31] and applied to rigid solids.[32] However, since it requires very special NMR hardware,[33–36] its application is limited to a few labs around the world.

T_1 relaxation probes dynamic processes in the MHz range. To tackle slower motions that are more closely related to the properties of the materials, it is desirable to extend the dynamic window to lower frequencies. The most important step towards this goal is the development of relaxation experiments in a spin lock field which is of the order of some tens of kHz. The NMR relaxation is governed by the relaxation time in the rotating frame, $T_{1\rho}$.[37,38] When double-resonance experiments on rare heteronuclei became routine by means of cross-polarization (CP), X-nuclei $T_{1\rho}$ became a very popular dynamic parameter in dynamic experiments.[39,40] The interpretation of these relaxation data is, however, not straightforward since both molecular and spin processes can contribute to the relaxation. If the spin–spin processes become dominant, the value of $T_{1\rho}$ cannot be considered as a measure of the molecular dynamics. To obtain reliable information, it is therefore very important to evaluate the share of these two contributions. It was shown that this can be estimated by comparison of the values of $T_{1\rho}$ to T_{CH}^{ADRF},[41] where the latter is the characteristic CP time using adiabatic demagnetization in the rotating frame.[39,42–45] It became clear that the value of $T_{1\rho}$ is dominated by molecular dynamics only if the strength of the ^1H field is larger than the local dipolar field while in rigid materials where there is no molecular motion, $T_{1\rho}$ becomes equal to T_{CH}^{ADRF}. Special r.f. schemes have been suggested to accomplish this condition.[46,47] An alternative option to decrease the effective relaxation field is the application of pulse trains. In such experiments, the magnetization decays with a relaxation time T_{2e} which asymptotically merges with $T_{1\rho}$ and permits one to sample the relaxation over a wider range of effective fields.[48–51] Even slower effective fields of the order of Hz can be archived by double-rotating frame experiments[52–55] or in the triple-rotating frame.[56] To obtain consistent results over a wide frequency range, simultaneous processing of the different relaxation data, which are sensitive to different parts of the dynamic spectrum, is desirable.[57]

To obtain qualitative dynamic information, the usual approach involves the use of dynamic models that are based on physical intuition and/or the ease of the formulation. In this procedure, there is always the problem of overinterpretation of a limited data set and/or the possibility that the resulting physical picture is not unambiguous: models can never be proven, just be eliminated. The so-called 'model-free approach'[58–65] completely describes the information on fast dynamic processes by just two parameters with model-independent significance, namely a generalized order parameter which is a measure of the spatial restriction of motion and an effective correlation time which is a measure of the rate of the motion. This model is reasonably well suited for the description of internal

motion in globular proteins in the liquid state; however, it does not hold for most of the dynamic investigations in organic solids. Thus, the ambition to obtain quantitative information about the correlation function of motion is dropped sometimes and relaxation experiments are used to compare between different samples, conditions, etc., without exploring the full potential of the method. Unlike NMR relaxation experiments, some of the tools described in the next section provide real model-free dynamic information, either on the correlation time, the geometry of motion or on both.

2.2. Dynamic line shape

The earliest NMR experiments in solids revealed broad lines and it was realized that this was due to static dipolar interaction. In isotropic liquids, however, much narrower lines were detected and it was understood that is due to the averaging of static interactions that scaled with the factor $(3 \cos^2\theta - 1)$, the time average of which is zero. It is therefore straightforward to apply the simple measurements of line widths depending on temperature to the study of dynamic processes: the temperature dependence of the second moment of the dipolar interaction, which is proportional to the dipolar line width, allows the identification of different motional modes that move through the dynamic window of the method on increasing temperature.[66] It is interesting to note that the introduction of magic-angle spinning (MAS), certainly the most influential innovation in solid-state NMR, was initiated by the idea to check the effect of motion on the second moment. According to theory, the second moment must remain constant even under motion and thus the spectral narrowing must be accompanied by the formation of spinning sidebands (SSBs) appearing at *random* frequency positions, determined by the stochastic nature of the molecular process and being invisible due to their vanishing spectral intensity. In contrast, a coherent motion like sample spinning should produce the SSBs at fixed frequency positions and thus should become observable in the NMR spectrum. This experiment was performed at an angle of 90° (rather than at the magic angle)[67] and the idea was later developed to what became MAS.[68,69]

The application of temperature-dependent line shapes and the measurements of second moments in more complex organic solids like polymers followed soon after.[70–74] Even nowadays, this simple method still has its place in the characterization of materials like solid polymer electrolytes where the line widths and T_1 relaxation of the charge carriers provide information about their mobility that can be correlated with the electrical conductivity of the material.[75,76] More detailed information can be obtained from cases in which the interaction is well defined, i.e., when an anisotropic single-spin interaction dominates the spectrum. Typical cases are the chemical shielding anisotropy (CSA) and quadrupolar interaction for which the theory is well developed.[77–79]

Almost any textbook on NMR describes the classical phenomenon of 'chemical exchange': a spin system can exist in two or more different states with different resonance frequencies, giving rise to different lines in a liquid-like spectrum. A dynamic process that interconverts the two states affects the NMR spectrum: if the rate of the process is of the order of the difference of the resonance frequencies, the spectrum broadens due to a loss of phase coherences of the two frequencies. Eventually, a single broad line forms

and re-narrows upon increasing the rate of the process into a single line, representing the weighted average of the original resonance frequencies (Fig. 4). Under favorable conditions, this *chemical* process can be observed in solid-state experiments in either single crystals or under MAS conditions.[80,81] However, since it relies on the *isotropic* chemical shift, no information about the topology of the process can be extracted. It should be mentioned that chemical-exchange effects can show up in relaxation experiments (although applications in solid-state NMR are still missing but might be reported soon). In Carr–Purcell–Meiboom–Gill (CPMG) experiments,[82,83] the effective relaxation time depends on the repetition rate of the π-pulses (CPMG dispersion[84–90]). This can be understood from the fact that the exchange contribution of the signal decay is not refocused by the pulses and the longer the pulse spacing, the faster is the apparent relaxation for a given exchange rate. Similarly, the dispersion of the relaxation time $T_{1\rho}$ provides analogous information.[91]

In spectra dominated by anisotropic interactions like quadrupolar interactions and chemical shifts, the concept of dynamic broadening due to *chemical* exchange can be applied to the detection of *molecular* processes: the resonance frequency of a nucleus depends not only on its chemical identity (isotropic chemical shift) but also on its
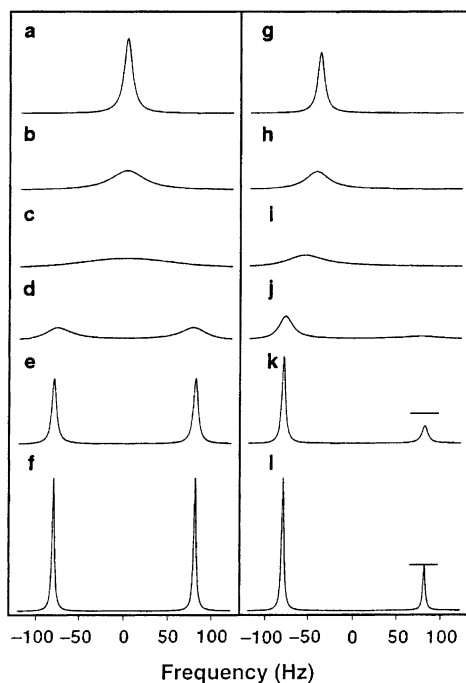
Fig. 4. Calculated chemical-exchange line shapes for two exchanging sites. (a–f) Symmetric exchange with equal populations $p_a = p_b = 0.5$ and (g–l) unequal population $p_a = 0.75$, $p_b = 0.25$. Exchange rates $k = (2\tau_c)^{-1}$ are (a,g) 10,000 s^{-1}, (b,h) 2000 s^{-1}, (c,i) 900 s^{-1}, (d,j) 200 s^{-1}, (e,k) 20 s^{-1} and (f,l) 0 s^{-1}. (Adapted with permission from Ref. 661.)

orientation relative to the external magnetic field. A molecular reorientation alters the resonance frequency, thus permitting the detection of reorientations simply by monitoring exchange broadening in anisotropic spectra[92,93] (Fig. 5). In contrast to exchange experiments by means of the *isotropic* chemical shift as mentioned above, the utilization of *anisotropic* interactions permits the extraction of both the time scale and topology of the dynamic processes.

In a typical organic solid, experiments on abundant nuclei like ^{1}H are far too unselective: one of the powers of NMR, the chemical selectivity or molecular resolution, is lost due to the strong dipolar interaction between the spins that broadens the spectra and prevents the extraction of the desired detailed information. This drawback was overcome by the introduction of specifically isotopically labeled samples where the ^{2}H nucleus[94,95]
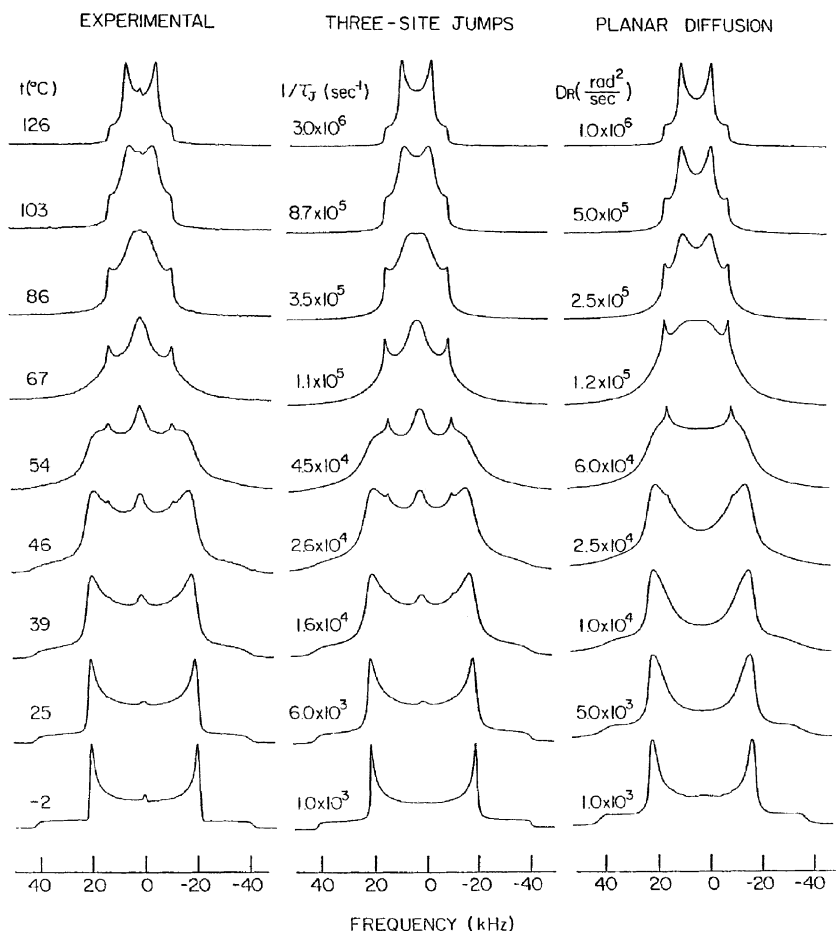
Fig. 5. ^{2}H-NMR line shapes for trimethylsulfonium iodide. Experimental quadrupole-echo spectra (left) and simulations for three-site jumps (middle) and planar diffusion (right). Courtesy of R. Poupko and Z. Luz, Weizmann Institute of Science, Israel.

has particularly favorable properties: (i) it is a non-disturbing spin label since its molecular properties are almost identical to those of the ^{1}H, (ii) its dominant quadrupolar interaction is large compared to homonuclear dipolar interactions, resulting in well-structured NMR spectra and (iii) the orientation of the quadrupolar tensor is to a good approximation parallel to the C–D bond, making the simulation of NMR experiments and the data processing straightforward. Nowadays available desktop computer performance allows a fast fitting of the line shape and extraction of dynamic parameters.[96] However, the ^{2}H quadrupolar interaction of the order of about 100 kHz and the resulting fast decay of the free induction decay make it difficult to record undistorted spectra. It was first shown for a dipolar-coupled spin pair that it is possible to excite the so-called dipolar order by a pair of pulses resulting in a 'solid echo'.[97] Likewise, quadrupolar order can be created in a ^{2}H-solid echo (^{2}H-SE) or quadrupolar echo experiment to overcome the dead-time problem.[98] It appeared that the delay between the two pulses can be used as another experimental parameter to distinguish between motional models.[99] First applications of the ^{2}H-SE technique were found in polymer science.[100,101] Numerical procedures to simulate spectra for discrete jumps[102] as well as diffusive motions are available.[103] In addition to the shape of the spectra, the integrated spectral intensity provides another valuable experimental parameter to distinguish between different dynamic parameters (Fig. 6). The signal intensity in ^{2}H-CPMG experiments decays with
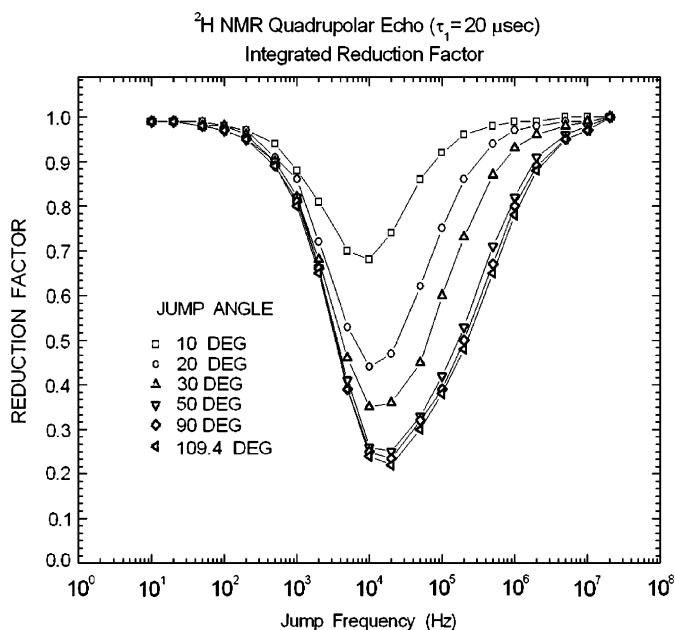
Fig. 6. Theoretical integrated reduction factor of the powder spectrum (amplitude at the top of solid echo) for a two-site jump motion ($p_a = p_b$) as the function of jump frequency l/τ_c and for different jump angles 2β. (Reprinted with permission from Ref. 112. Copyright 1990 American Chemical Society.)

a relaxation time T_2^{SE} (Fig. 7).[104–110] Its dispersion can be indicative for different motional models, the origin of which is similar to the CPMG dispersion in cases of chemical exchange as discussed above.

Dynamic line shape combined with selective isotopic labeling has found numerous applications, in particular, in polymer science (mainly ^{2}H),[111,112] for biopolymers (both ^{2}H and ^{15}N)[113–115] and for the investigation of host–guest systems like inclusion compounds.[116] However, in natural abundance, the overlap of the broad anisotropic lines belonging to different chemically inequivalent nuclei prohibits the application of this powerful method. A partial solution has been found in 2D experiments correlating the isotropic with the anisotropic chemical shift[117–119] or correlating ^{13}C isotropic chemical shifts with ^{2}H line shapes of directly bonded deuterons[120] and thus achieving the necessary spectral resolution. A particularly interesting approach is dynamic off-MAS spinning in which the widths of the anisotropic line is scaled according to the angle deviation from the magic angle and, thus, different dynamic regimes can be realized at a single temperature[121]: they are realized by different ratios between anisotropic line width and MAS rate, i.e., a fast-limit line shape is
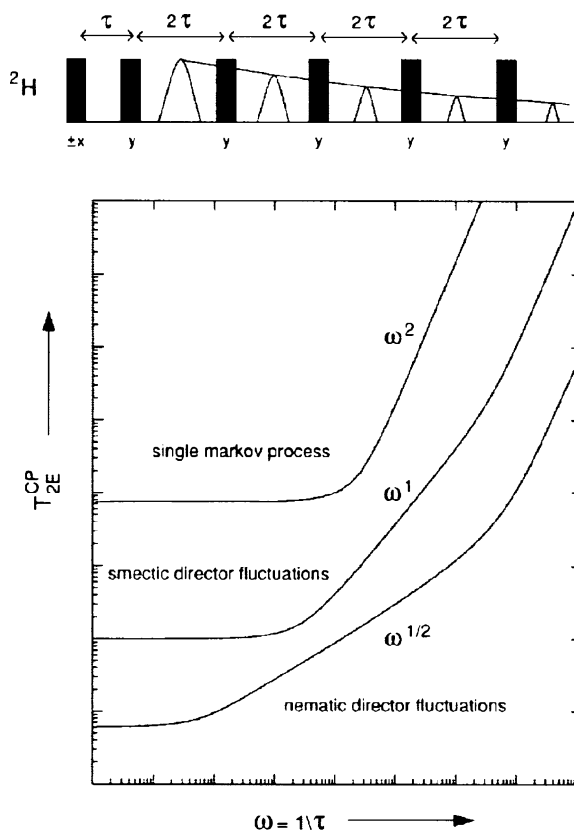
Fig. 7. ^{2}H version of the CPMG experiment for measuring T_{2E}^{CP} (top) and the dispersion profiles (bottom) of T_{2E}^{CP} calculated for different processes. (Adapted with permission from Ref. 107.)

acquired by setting the angle between the sample spinning axis and the external field close to the magic angle while the most sensitive case of dynamic broadening is achieved by setting the angle such that the resulting widths of the spectrum are approximately equal to the rate of the dynamic process.

In the MAS experiments of rare nuclei like ^{13}C, both heteronuclear ^{1}H decoupling and MAS are applied to achieve reasonably narrow lines by coherent averaging of the heteronuclear dipolar interaction and CSA, respectively. However, any stochastic molecular motion with a frequency close to the characteristic frequencies of these experimental measures (some tens of kHz for ^{1}H decoupling[122] and some kHz for MAS[123]) interferes with the line narrowing approaches, resulting in its decreased performance. This undesired effect can be turned into an advantage since it allows the easy detection of such dynamic processes, just by recording the spectra and monitoring line broadening. In particular, the effect of MAS ('dynamic MAS') is theoretically well understood either in the framework of the Floquet theory[124,125] or extended exchange theory,[126,127] permitting the efficient calculation of spectra that can be used for comparison with experimental data. Alternatively, numerical integration of the density matrix provides calculated spectra in comparable CPU times.[128–131] The broadening effect depends on the relation between molecular exchange rate and MAS frequency and permits quantitative results on both the time scale and the geometry of the dynamic process[132] (Fig. 8). We like to note that in contrast to relaxation experiments, at
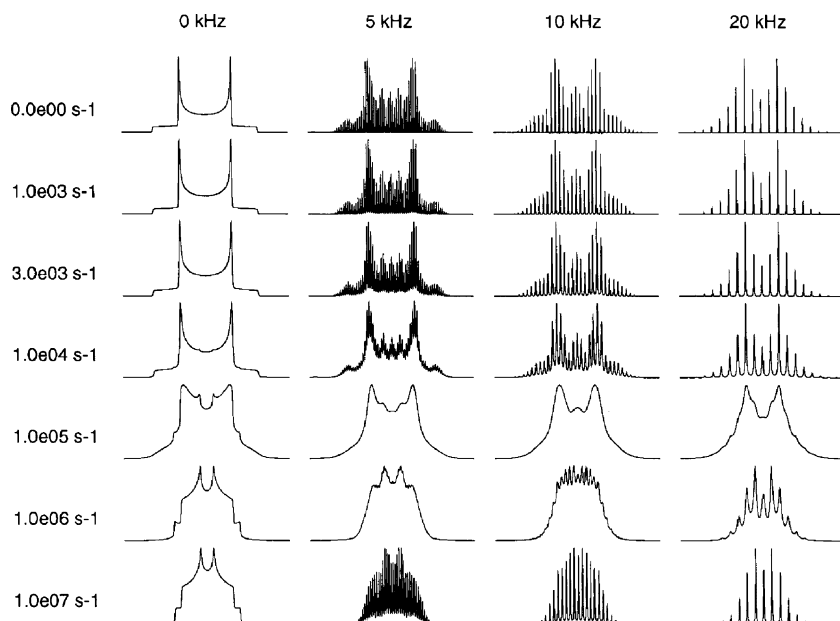
Fig. 8. ^{2}H-MAS NMR line shapes with different MAS rates for deuterons undergoing 180° flips at rates indicated. The deuteron quadrupole interaction tensors are taken to be axially symmetric, oriented at 60° to the jump axis with a quadrupole coupling constant of 170 kHz. (Adapted with permission from Ref. 132; http://www.tandf.co.uk/journals/.)

least the approximate value of the correlation time can be estimated from the r.f. power of the decoupling field (in frequency units) or the MAS frequency, i.e., completely model free. A special yet simple experimental approach allows one to separate the homogeneous line widths which are associated in part with motion from the inhomogeneous line widths which have causes such as a distribution of local packing environments.[133]

2.3. Exchange NMR

Molecular dynamics with correlation times slower than the lifetime of the NMR signals (approx. T_2) does not affect the NMR spectrum. In this case, 2D-exchange NMR[134] is a powerful tool to extract both the correlation time and the geometry of the dynamic process. In these experiments, the NMR frequencies are sampled before and after an adjustable mixing period τ_m during which the dynamic process that may change the resonance frequency happens on a time scale longer than T_2 and shorter than or comparable to T_1. In solids, molecular reorientations cause exchange of the orientation-dependent resonance frequencies of the probe nucleus which in turn leads to characteristic off-diagonal features in the 2D-exchange spectra[135] (although the process detected in this original paper was spin exchange which, however, is generally difficult to separate from molecular dynamic processes[136,137]). In favorable cases, the reorientation angle can be read off from the spectra in a real model-free fashion (Fig. 9).[138–140] τ_m-dependent exchange experiments provide information about the correlation time. In particular, ^2H experiments that achieve molecular selectivity by isotopic labeling have found numerous applications in polymer science.[141] As in dynamic NMR experiments, natural abundance samples with more than a single isotropic NMR signal require combination with correlation techniques.[142] Further methodical developments include the acquisition of spectra containing only the mobile components[143] and the application of this method to the reorientation of a dipolar vector connecting two nuclei.[144]

The general drawback of the static 2D-exchange method in natural abundance samples is the lack of chemical selectivity due to the overlap of the broad anisotropic resonances. This can be overcome by switching to rotor-synchronized 2D-MAS exchange experiments in which the exchange process shows up in cross-peaks linking the MAS SSBs under slow-MAS conditions (Fig. 10). The experiment was first performed for ^{13}C and CSA,[145,146] received continuous further development[147–151] and extension to $I = 1$ nuclei[152] (Fig. 11). The 2D-MAS exchange experiment permits, in particular, to distinguish easily between chemical processes (more precise: processes that change the *isotropic* chemical shift; this could very well be molecular processes like chain diffusion between crystalline and amorphous regions[153] or conformational exchange[154]) and reorientations (processes that affect the *anisotropic* chemical shift only)[155] (Fig. 12) and permits the correlation of molecular dynamics and orientation in anisotropic materials[156,157] in higher dimensional experiments.

The 2D experiments are time consuming due to the necessity of acquiring many t_1 increments in the indirect time dimension. It was realized that 'time-domain experiments', in which only a limited number of t_1 increments (or even a single delay
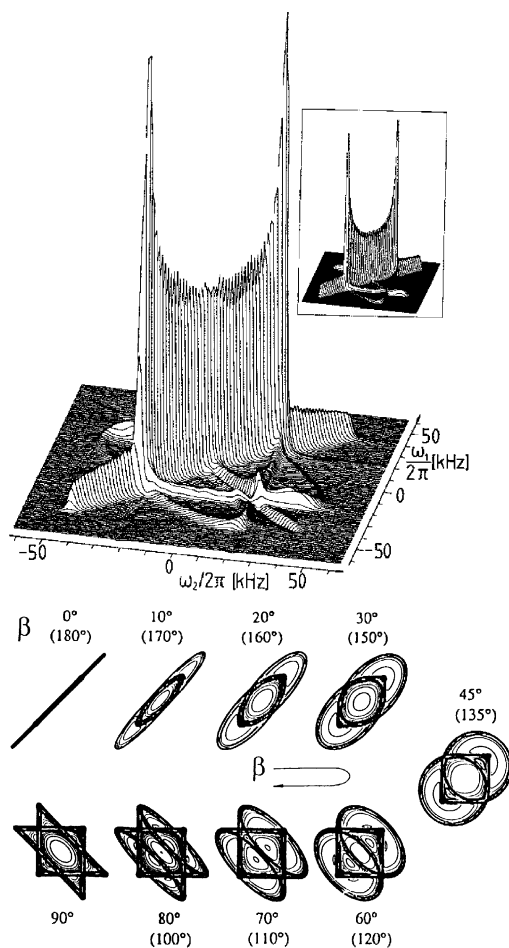
Fig. 9. Top: ^{2}H-2D exchange spectrum of dimethylsulfone. The inset shows the corresponding theoretical spectrum for a two-site jump with a jump angle of 106°. The angular information is encoded in the shape of the elliptical ridges perpendicular to the main-diagonal spectrum. Bottom: Theoretical ridge pattern (contour plots) for different jump angles. (Adapted with permission from Refs. 138,140.)

time) are sampled and the second FT over t_1 is omitted, contain equivalent information as do the 2D spectra. First pulse sequences for this purpose utilize the creation of dipolar[158] or quadrupolar order.[159–161] For the latter, analogies to quasi-elastic neutron scattering were found.[162] Higher dimensional experiments were developed to extract more detailed dynamic information in complex systems like synthetic polymers at the glass transition temperature.[163,164] As for static 2D experiments, MAS versions are desirable to increase the spectral resolution and overall sensitivity of the experiment. Again, one has to distinguish between *chemical* processes (like H exchange) and *molecular* reorientations.[155] For the former, magnetization-transfer experiments are used that create a
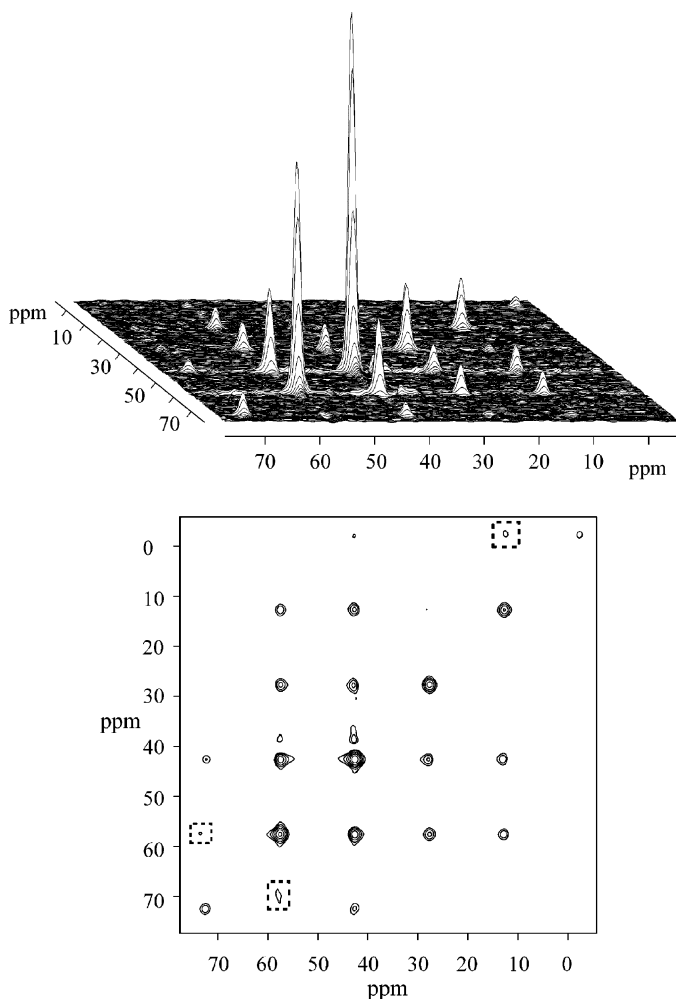
Fig. 10.   Rotor-synchronized ^{13}C-2D MAS exchange spectrum of dimethylsulfone at a MAS rate $\nu_R = 1.5$ kHz and a mixing time $\tau_m = 20$ ms. Top: stack plot. Bottom: contour plot. The marked cross-peaks denote negative intensity. (Adapted with permission from Ref. 155.)

non-equilibrium between the magnetizations of the interchanging spins and the return to equilibrium is observed.[165] In the absence of couplings, these experiments can well be described in the well-known simple 'magnetization-vector picture' for an isolated spin $I = 1/2$. It is tempting to apply the same concept to molecular reorientations: under slow-MAS conditions, spectra exhibit a series of SSBs resembling a 'liquid-like' spectrum. However, these must not be considered as 'real-NMR lines' but are the spectral representation of the periodicity of the MAS signal and cannot be described in the simple magnetization-vector picture. Thus, a more elaborate theory must be applied to design these experiments properly.[155,166] In particular, a non-equilibrium between
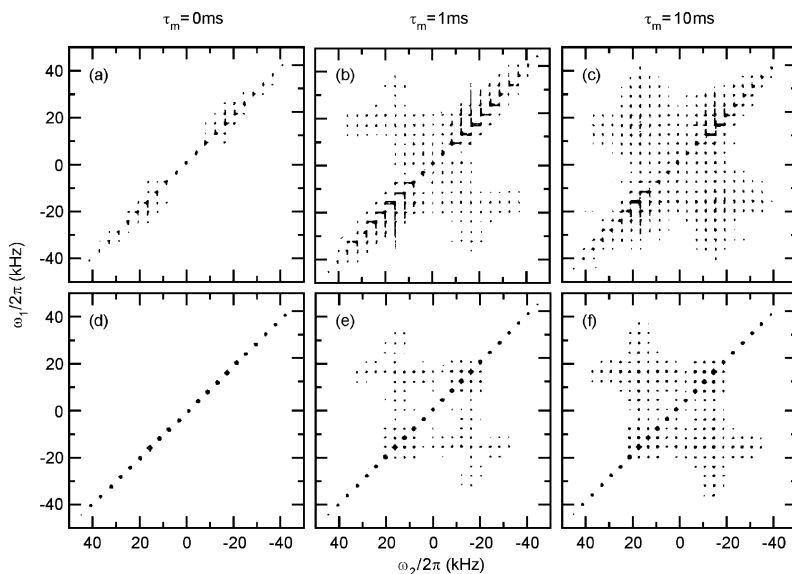
Fig. 11. Rotor-synchronized ^{2}H-2D MAS exchange spectra of dimethylsulfone. (a), (b) and (c) are experimental and were recorded with $\nu_R = 4.06$ kHz at 30°C and nominal mixing times as indicated. (d), (e) and (f) are calculated using an axially symmetric quadrupole tensor with a jump angle of 108°. (Adapted with permission from Ref. 152.)
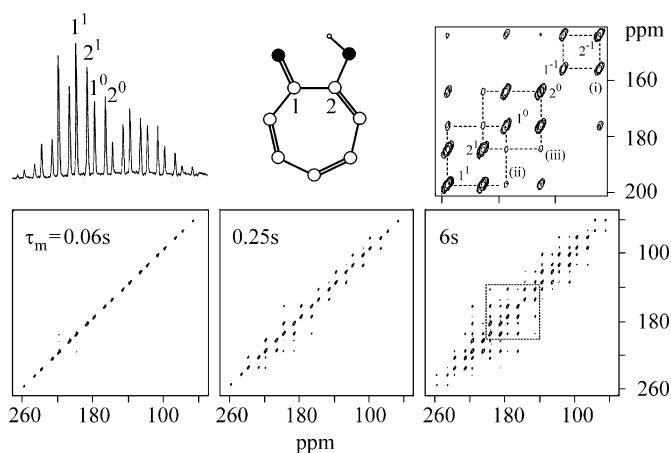
Fig. 12. ^{13}C rotor-synchronized 2D-MAS exchange spectra of a tropolone sample enriched to 25% in carbons 1 and 2 (in different molecules) for the indicated mixing times at room temperature, $\nu_R = 1.5$ kHz. Also shown are the structural formula of tropolone (top middle), the 1D-MAS spectrum of the enriched sample (top left) and an expanded part of the right-most 2D-MAS spectrum. In the latter, the peaks along the main diagonal are labeled as j^N where j labels the carbon and N the order of the SSB. The cross-peak (i) is a hetero cross-peak between the SSB 1^{-1} and 2^{-1}, while (ii) and (iii) are auto cross-peaks linking 1^1 with 1^0 and 2^1 with 2^0, respectively. (Adapted with permission from Ref. 155.)
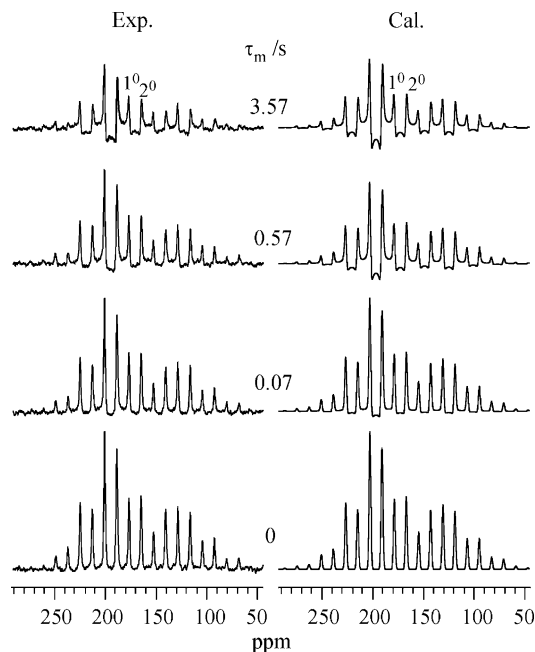
Fig. 13. Experimental (left) and simulated (right) tr-ODESSA[169] spectra of the tropolone sample (Fig. 10), taken at a MAS rate of $\nu_R = 1.40$ kHz for different mixing times. The decrease in spectral intensity and increase of dephasing with increasing length of the mixing period indicated exchange between chemically equivalent as well as inequivalent carbons. (Adapted with permission from Ref. 170.)

the SSBs belonging to the same resonance must be created. This was first achieved in the so-called EIS method using a TOSS-building block under slow MAS.[167] Later, more efficient methods (ODESSA, tr-ODESSA, Fig. 13) were developed[168,169] and further improved.[170,171] All these methods rely on the evolution of the CSA under MAS that is reasonably efficient only under slow-MAS conditions. In some cases, this might result in a crowded spectrum and spoil the spectral resolution. A similar 1D-MAS exchange method (CODEX) that recouples the CSA evolution and thus works in principle at any MAS rate was introduced soon after[172,173] and received further development.[174,175] In this method, another improvement introduced a reference experiment to eliminate the effect of T_1 relaxation and to obtain data at normalized intensity (Fig. 14). Higher dimensional versions are also available.[173,176]

A yet exotic experimental approach in exchange experiments are the so-called 'hole-burning experiments' in which a part of the anisotropic line shape (i.e., a certain orientation of molecules) is selected by either selective excitation or saturation and the redistribution of spins into this orientation is observed during a mixing period that may exceed T_2 (see Chapter 7.2 of Ref. 140). This idea has found a few applications in systems with reasonably broad spectra like ^{14}N[177] and ^2H[178] (Fig. 15).[179]
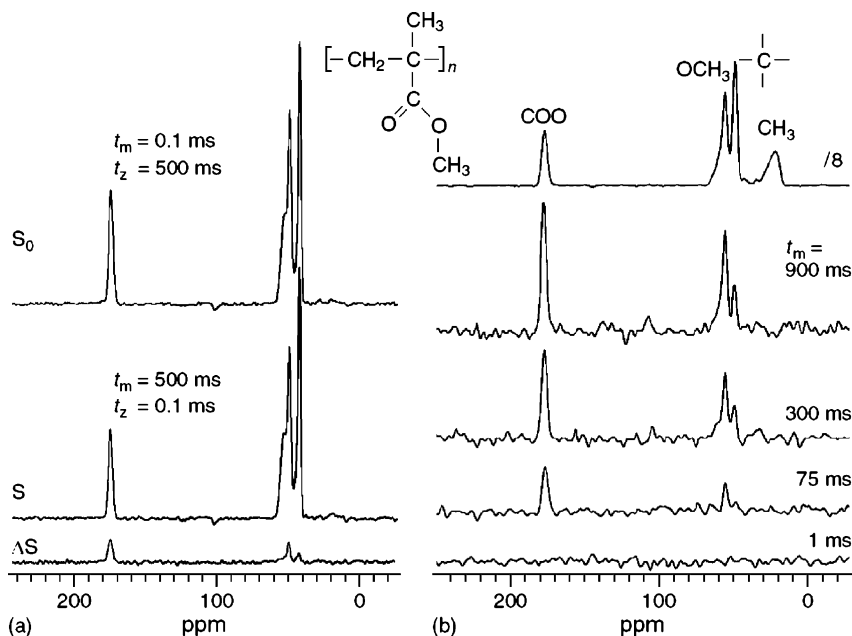
Fig. 14. (a) Full reference spectrum S_0, spectrum S after CODEX dephasing and pure-exchange CODEX spectrum $\Delta S = S_0 - S$ of natural abundance PMMA at 300 K, for $\tau_m = 500$ ms. The intensity of ΔS is low since only a minority of the side groups (35%) are undergoing flips. (b) Series of pure-exchange CODEX spectra of PMMA at 300 K, $\nu_R = 6.5$ kHz, as a function of τ_m as indicated. Large-amplitude side group and smaller-amplitude backbone motions are observed. (Adapted with permission from Ref. 662.)

2.4. Effective dipolar coupling

As stated above, the magnitude of the dipolar coupling is a valuable source not only to gain structural information but also for extracting dynamic parameters: the ratio between the theoretical 'rigid-lattice value' and the experimentally determined reduced dipolar coupling indicates fast molecular processes that average, i.e., reduce the dipolar interaction. Besides simple dipolar line shape and relaxation experiments as discussed above, some more elaborate approaches deserve special attention: CP dynamics, separated-local field (SLF) and double-quantum (DQ) experiments. The first relies on the heteronuclear dipolar coupling between abundant (like ^{1}H) and rare spins (like ^{13}C) in CP experiments. The increase of rare-spin magnetization happens with the relaxation time T_{CH} that is – similar to the relaxation time $T_{1\rho}$ – sensitive to dynamic processes in the kHz range[180] and correlates with important mechanical parameters like dynamic moduli.[181–183] The measurement of T_{CH} has become rather popular in dynamic investigations of organic solids, however, care must be taken in the interpretation of the data.[184] SLF experiments measure chemical shifts and dipolar couplings separately but in a way that they can be correlated.[185–188] Popular versions of SLF experiments are
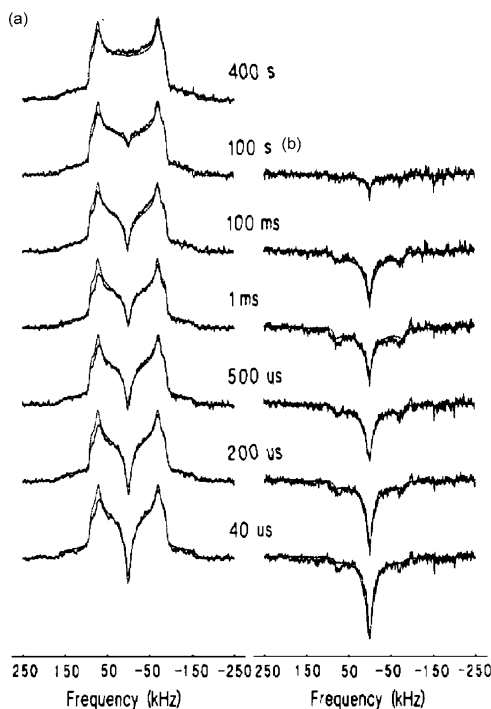
Fig. 15. ^{2}H quadrupole echo spectra of *p*-nitroaniline-*N,N-d$_2$* recorded using a hole-burning pulse sequence. The selective excitation was achieved by a selective low-power soft pulse. In the left-hand column are shown (a) seven out of 12 spectra obtained in the experiment and in the right-hand column (b) the result of subtracting the spectrum obtained at $\tau = 400$ s from spectra obtained at shorter τ values. The dashed spectra in A and B are the result of calculations using a 180° flip rate, $k = 2.0 \times 10^3$ s^{-1}. (Reprinted with permission from Ref. 178. Copyright 1991 American Chemical Society.)

dipolar-rotational spin echoes (DRSEs)[188–191] (Fig. 16) and wide-line separation (WISE) experiments. The latter approach was first suggested as a dynamic filter[192] to separate mobile and rigid components in ^{13}C spectra and was later turned into an easy-to-implement 2D method[193] (Fig. 17). Further developments of WISE include the suppression of ^{1}H-spin diffusion during the CP step[194,195] and the use of *through-bond* *J*-coupling, rather the much stronger direct *through-space* dipolar coupling.[196] Further SLF variants that deserve attention are the efficient DIPSHIFT experiment[197,198] and the Lee–Goldberg CP experiment.[199] All these experiments determine the dipolar coupling strength that is reduced by fast molecular dynamics (τ_c of the order of 10^{-6}–10^{-4} s). Information about the amplitude of the molecular process can be extracted from the reduction ratio with respect to the static value of the dipolar coupling.

DQ experiments on abundant spins were first performed on ^{19}F.[200] Advances in NMR hardware recently paved the way for ultra-fast MAS experiments with commercially available MAS rates of about 35 kHz.[201] These spinning speeds enable solid-state ^{1}H experiments with an improved (as compared to wide-line experiments) but still limited
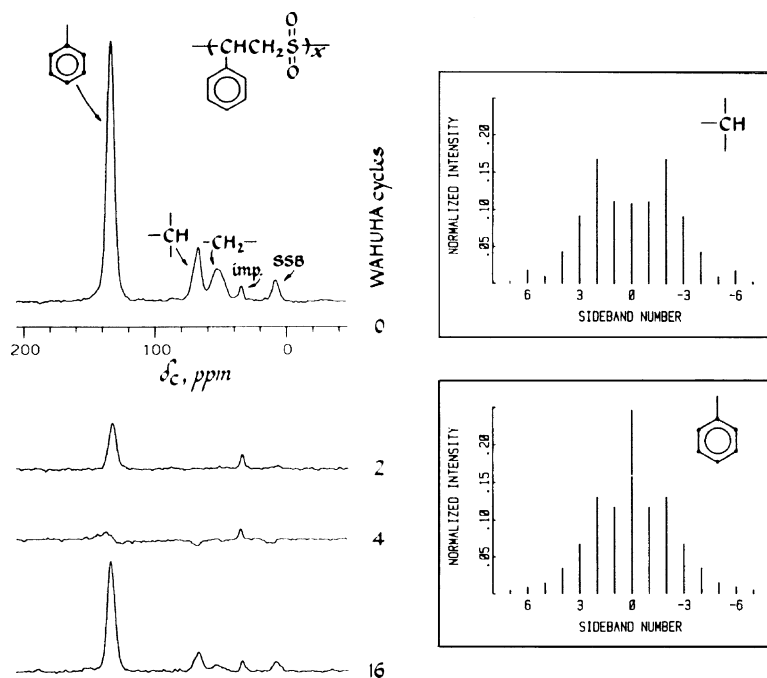
Fig. 16. Dipolar rotational spin-echo ^{13}C-NMR spectra of poly(styrene-*co*-sulfone) as a function of the number of evolution cycles used during ^{1}H–^{13}C dipolar evolution (left). Experimental dipolar sideband patterns for the two CH pairs of the polymer under magic-angle spinning at $\nu_R = 1.894$ kHz are shown at the right of the figure. (Reprinted with permission from Ref. 190. Copyright 1984 American Chemical Society.)
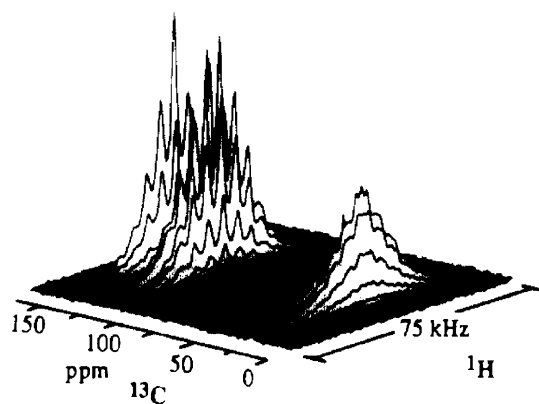
Fig. 17. WISE-NMR spectrum of polycarbonate. The phenyl signals exhibit pronounced ^{1}H spinning sidebands, due to the phenyl flip motion, while the methyl protons show a simple ^{1}H line, with a width of 20 kHz. (Reprinted with permission from Ref. 193. Copyright 1992 American Chemical Society.)

spectral resolution. These MAS rates efficiently suppress the homonuclear dipolar interaction between more remote nuclei but do not much affect those between directly neighbored nuclei.[202,203] DQ experiments select only the coupled nuclei and exhibit connectivities. The precise value of the dipolar coupling that carries the information about molecular distances and/or fast molecular dynamics can be extracted from the DQ-sideband intensities.[204,205] These experiments have found some application in organic solids,[206–209] however, the limited resolution still leaves it far from being a routine method. The extension to DQ–DQ exchange experiments permits the investigation of slow processes.[210]

3. APPLICATIONS OF DYNAMIC SOLID-STATE NMR IN ORGANIC SOLIDS

In this section, applications of the methods reviewed in Section 2 are reported without the claim of completeness. They are presented in order of increasing molecular complexity from small molecules in molecular crystals to macromolecular and composite materials.

3.1. Molecular crystals and organic glass formers

We consider here small molecules forming crystalline structures with long-range order at the molecular level over the entire sample (single crystals) or over smaller parts, forming a macroscopically disordered sample (polycrystalline material). Such a molecule was one of the first objects of dynamic solid-state NMR.[13] Most experiments have been reported for polycrystalline materials; a prominent example is dimethylsulfone (DMS) which is sometimes considered being the 'rosetta stone of solid-state NMR'. It is a handy substance that exhibits a two-site molecular jump that can be monitored by dynamic line shape and exchange experiments at ambient temperatures. It is thus a convenient test substance for the development of dynamic NMR methods that are aimed at the determination of both the time scale and topology of motion. Correlation times obtained by a variety of NMR methods have been compiled.[211] A few other examples of dynamic NMR investigations of small molecules are the application of ^{2}H-SE experiments to trioxane,[212] dimethylmalonic acid[213] and the application of dynamic MAS and ^{2}H-2D- and 1D-MAS exchange NMR to phenyl flips in polyaryl ethers.[127,214] Tropolone is a molecule which in the solid performs both pseudo-reorientations by jumps between lattice sites at which the molecule is differently oriented and chemical exchange due to a intramolecular proton shift. The latter was studied by 1D-MAS magnetization transfer[165] while all processes can be studied by 2D-MAS exchange.[215] Another molecule exhibiting a similar interesting internal dynamic is bullvalene which – together with its derivatives – was extensively studied by 2D-MAS exchange,[216–219] dynamic MAS[217–219] and dynamic line shape in a single crystal.[220] The electron conductor imidazol in which the electric properties are related to the molecular dynamics was investigated by ^{15}N-2D exchange[221,222] and ^{1}H-DQ NMR.[223] Chemical-exchange line shapes were used to monitor ^{1}H transfers, flip motions and configurational motions in cyclohexane,[224] penicillin derivates,[225] pyrazoles[226] and 'triple-rotor' molecules.[227] ^{2}H-T_1 experiments provided detailed dynamic information about baskatene,[228]

acenaphthylene[229] and plastic crystals.[230] Dynamic MAS was applied to sulfanilamide[231] and 2D-MAS and static exchange to organosilicon compounds.[232] [13]C and ^{1}H relaxation experiments were conducted to probe the dynamic of *tert*-butyl groups,[233] naphthalene derivates,[234] vitamin A,[235] hormones,[236,237] adrenaline[238] and the dynamics of molecular disorder[239] while the interference of molecular dynamics with ^{1}H decoupling (dynamic decoupling) provided dynamic data for aspirin,[240] the methyl group dynamics in methyl *p*-nitrobenzenesulfonate[241] and the plastic-crystal phase of cyclohexane.[242]

Only a few experiments (both 1D and 2D) have been reported for single crystals, since they rely on the preparation of a suitable sample.[243–251] A particularly nice application is the separation of chemical exchange from the competing spin exchange effect.[252] Some experiments investigate the tunneling regime of rotating methyl groups.[253–258]

In contrast to polycrystalline solids discussed above, organic glasses lack from translational order even on the molecular level. However, their molecular dynamics, in particular, in relation to the glass transition and the detection of dynamic heterogeneities, is of considerable interest. Here, the ^{2}H experiments (in particular, 1D[259–263] (Fig. 18) and *n*D[264,265]) offer their full potential for the investigation of details of the molecular dynamics. More applications to amorphous matter, namely amorphous synthetic polymers, with special emphasis on the glass transition are reported in the next section.

3.2. Synthetic and natural polymers

Synthetic polymers were among the first solid samples to be investigated by dynamic NMR[14,15] and they still form the major share of dynamic NMR applications. There are numerous studies by [1]H-spectra[266] and [1]H-relaxation studies of polymers,[267–279] [13]C relaxation[280–285] (including the effect of hydration[286]), field-cycling relaxometry,[287–289] investigations using the dynamic-decoupling effect[290,291] (Fig. 19)[292–297] and dynamic line shapes both for static samples[298–301] and under MAS conditions.[302–306] Differences in *isotropic* chemical shift due to different local conformations permit the application of the 'chemical-exchange scenario' to the study of conformational transitions, both for 1D[307–310] and 2D experiments (Fig. 20).[154,274,306,311–317] Exchange experiments aimed at molecular reorientations, i.e., the detection of changes of the *anisotropic* chemical shift, both static[306] and under MAS conditions[318,319] and 1D variants[136,319–322] aimed at slow dynamic processes with correlation times in the millisecond range. Experiments based on the CP dynamics[314,323–327] detected processes with rates in the kHz range while DRSE[328–334] and WISE experiments[335–338] focus on faster processes. Information about the amplitude of fast motions can be extracted from the determination of averaged CAS tensor elements, for example, for phenyl flips.[339,340]

^{2}H-NMR became particularly popular in polymer science, both in [2]H-relaxation and quadrupolar echo experiments[112,297,341–364] and in [2]H-2D exchange experiments.[359,365] The dynamics of molten polymer chains confined between air and a solid[366] and low-molecular probes dissolve in stretched polymers[367] was also studied by ^{2}H-NMR.

Polymer complexes like blends and copolymers have been investigated by [1]H-,[368–370] [13]C-[371–376] and [2]H-relaxation,[377,378] dynamic line shape,[379] dynamic MAS[380] and
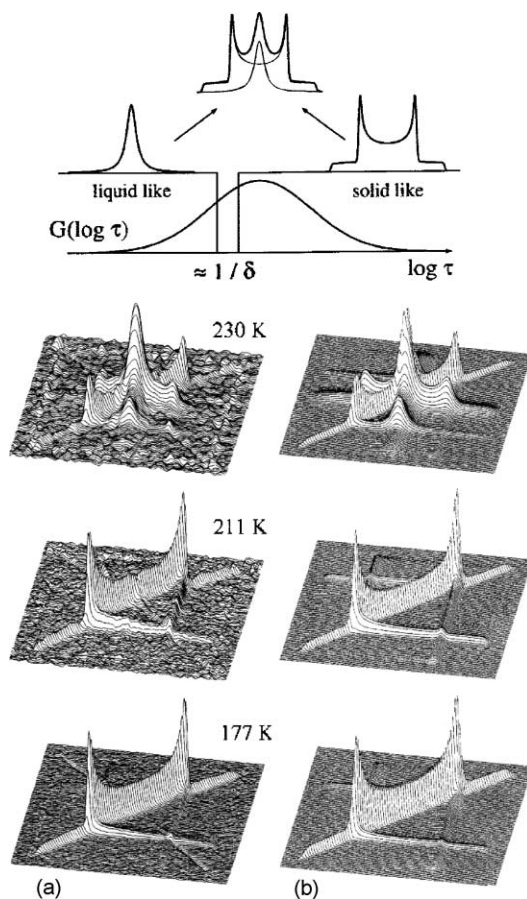
Fig. 18. Top: Sketch of a broad distribution of correlation times (logarithmic scaling of the *x*-axis), illustrating the origin of the 'two-phase' ^{2}H-spectra. Bottom: Measured (left) and calculated (right) ^{2}H-2D exchange spectra of 26 wt% benzene-d_6 in oligo-styrene ($M_w = 1020$ g/mol) at $T < T_g$ ($\tau_m = 100$ ms). (Adapted with permission from Ref. 263.)

dynamic decoupling,[375] ^{2}H-quadrupolar echo experiments,[381,382] ^{2}H-2D exchange,[383–385] ^{13}C-2D exchange,[383,386] CP dynamics,[372] ^{1}H-2D exchange[387] and SLF (both DRSE[388,389] and WISE[387,390,391]). Of particular importance are dynamic studies under a mechanical load like pressure or deformation, since they directly connect molecular structure and dynamics with the macroscopic properties of the material and are thus particularly interesting for materials science. Such experiments have been conducted by ^{13}C relaxation,[392] ^{2}H-quadrupolar echo[393–396] and ^{2}H-2D exchange.[393,396,397] The dynamic behavior of elastomers and gels – often in its relation to structural properties – has been investigated by CP dynamics and under deformation,[398] ^{13}C relaxation,[399,400] ^{2}H-T_1,[401] ^{1}H- and ^{2}H-T_2,[402–405] ^{31}P-2D exchange[406] and DQ NMR[407,408] (Fig. 21).

The success of the Mainz group certainly deserves an extra paragraph. The consequent application of ^{2}H-1D experiments and the development of *n*D methods represent
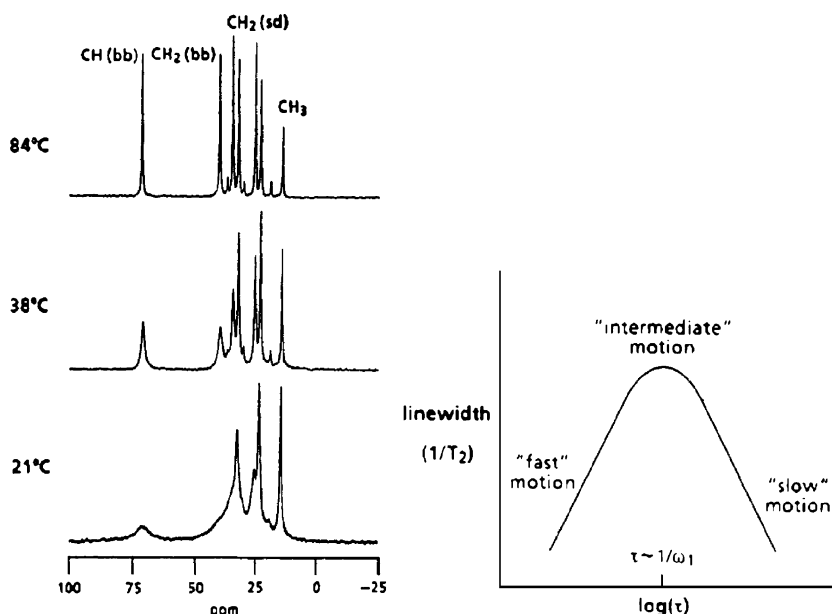
Fig. 19. Top: ^{13}C-NMR spectra of the amorphous component of solid poly(β-hydroxyalkanoates) as a function of temperature. Spectra were obtained without MAS. Only the aliphatic region is shown, and the backbone and side-chain carbons are labeled bb and sd, respectively. The differential dynamics of the backbone and side chains is evident in the differential line widths. Bottom: Schematic behavior of the ^{13}C line width, under conditions of ^{1}H decoupling, when the frequency of the motion of the ^{13}C–^{1}H internuclear vectors is on the order of the strength of the decoupling field (expressed in frequency units) which is about 50–100 kHz in most solid-state NMR experiments. (Reprinted with permission from Ref. 291. Copyright 1992 American Chemical Society.)

a qualitative progress in polymer science. The main tools for the detailed investigations of the polymer dynamics are ^{2}H-quadrupolar echo experiments,[101,409–414] ^{2}H-2D exchange methods[303,304,414–419] and higher dimensional versions.[303,304,420–423] Alternative methods like ^{13}C-2D exchange,[416,424,425] 2D-echo[426] and WISE experiments[427] have been applied as well. Most of the NMR methods developed before 1994 have been presented in detail.[140] Recently, methodical developments have concentrated on DQ experiments[208,428,429] and new classes of supermolecular systems such as 'dendri-dendrimers',[430] 'molecular tweezers'[431] and 'hairy rods'[432] have attracted considerable interest. These molecules are constructed from stiff units that start growing from a central spot and develop branches such that the molecular density increases on increasing distance from the starting point, eventually forming molecular caves. The molecular dynamics of which was investigated by ^{1}H-DQ and ^{13}C-CODEX experiments.[430,433,434]

Polymers in natural organic materials are more challenging as compared to synthetic materials, since the possibility of isotopic labeling and thus the application of the powerful ^{2}H methods are limited and often impossible. Thus, methods that work in natural abundance become more important in this field. The option to run solid-state ^{2}H
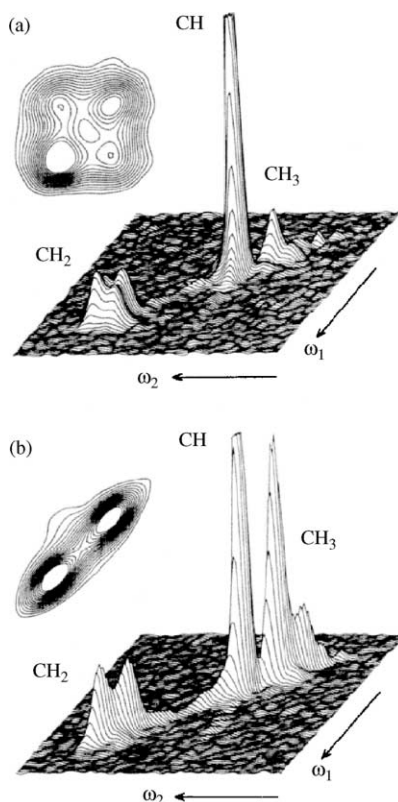
Fig. 20. ^{13}C-2D CPMAS NMR spectra of atactic polypropylene at 250 K acquired with mixing times of (a) 500 ms and (b) 5 ms. The CH signals have been truncated to display the methylene (CH$_2$) peaks more clearly. A contour plot of the CH$_2$ chemical shift region is shown as an inset for each spectrum. The cross-peaks indicate conformational transitions. (Reprinted with permission from Ref. 154. Copyright 1991 American Chemical Society.)

experiments in natural abundance has been demonstrated[435] and even low-resolution ^{1}H experiments found ample applications. Food-related samples like saccharides and starch[436–441] were investigated by ^{1}H relaxation with ^{13}C detection, ^{2}H relaxation[442] and ^{2}H line shape,[442,443] static ^{2}H exchange,[444] 2D-echo experiments,[445] CP dynamics and WISE experiments.[446] Cell walls of potatoes, onions and cork have been investigated by ^{1}H-[447] and ^{13}C-relaxation[448,449] and WISE experiments,[448,450] as well as cutin and suberin in plants.[451]

3.3. Biomolecules

This section covers the investigation of simple amino acids, proteins, lipids and nucleic acids. In particular, in proteins, molecular dynamics is an important link between molecular structure and function.[452–454] Among the first experimental approaches of
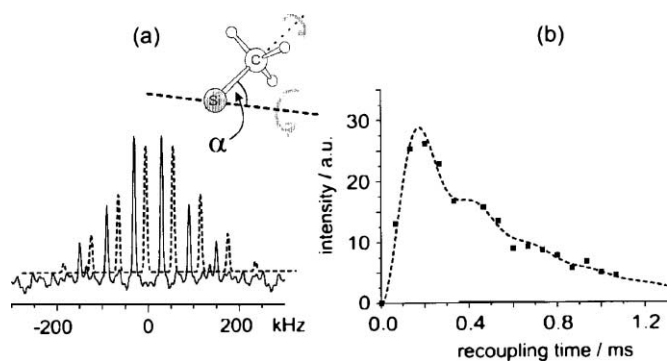
Fig. 21. Quantitative determination of the ^{1}H–^{13}C dipolar coupling constant for the methyl groups of the PDMS chain at 30 kHz MAS. (a) Spinning sideband pattern. (b) 1D intensity build-up as a function of the recoupling time. The dashed lines represent fits to the experimental data. (Adapted with permission from Ref. 408.)

dynamic solid-state NMR in biological samples were ^{2}H experiments[455,456] and ^{1}H relaxation measurements.[457]

The complex structure of biomolecules is the main reason for their elaborate molecular dynamics that is very likely inhomogeneous across the molecule in both time scale and amplitude. The different relaxation processes contributing to ^{1}H relaxation in solid proteins were identified[458,459] and ^{1}H relaxation became a popular tool for amino acids,[460] solid proteins,[461,462] biological complexes,[463] model membranes[464] and wheat proteins.[465] Owing to the lack of proper models, in some cases, information about the *relative* dynamic state of different subunits according to Fig. 22 can only be made. Remarkable is the investigation of
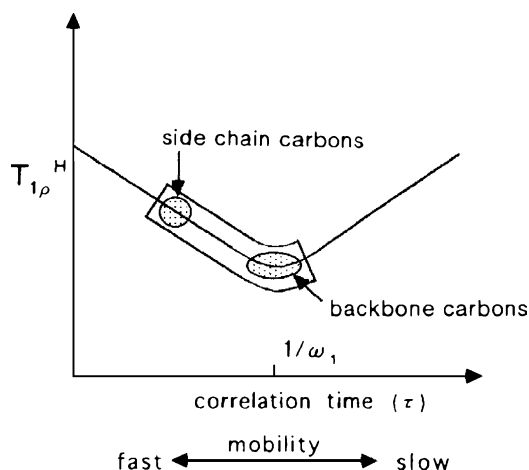
Fig. 22. General relationship between $T_{1\rho}$ value and correlation time τ_c. ω_1 is the Larmor precession frequency of ^{1}H in a rotating frame. The shaded areas indicate hypothetical fragments with different molecular mobility. (Adapted with permission from Ref. 463.)
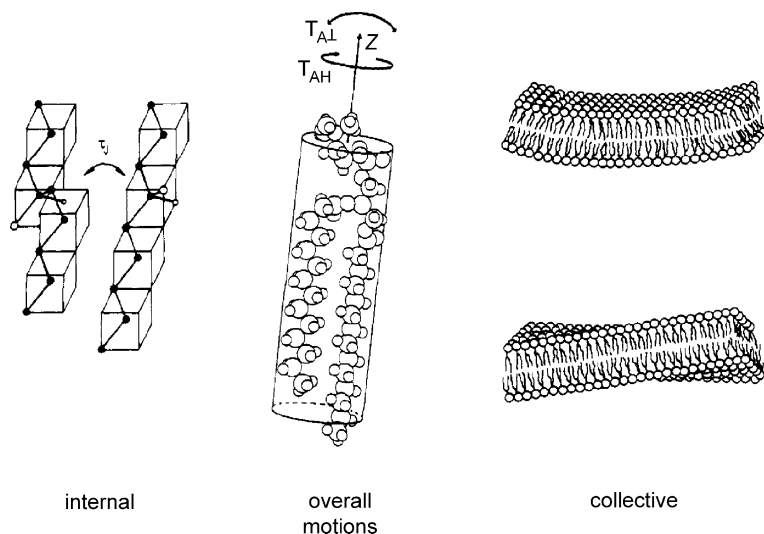
Fig. 23. Schematic representation of the various motional modes in bilayer membranes that can be studied by ^{2}H line shape and relaxation experiments: internal τ_J, overall τ_R and collective lipid motions. (Reprinted with permission from Ref. 501. Copyright 1992 American Chemical Society.)

real biological material like lenses[466] and cartilage.[467–469] Field cycling found its applications, too.[470,471] Other relaxation techniques include CP dynamics,[472] ^{13}C relaxation for the study of lipids[473] and peptides[474] as well as ^{31}P[475] and ^{2}H relaxation.[476,477] Conformational motions have been studied.[478–480] Other line shape experiments include ^{13}C,[481,482] ^{31}P in freeze-dried liposomes,[483] DNA,[484] cytochrome[485] and ^{15}N spectra of lipids.[486] The complex dynamics in lipid bilayers was studied by ^{2}H-2D exchange.[487] Dynamic decoupling found its application[488] as well as ^{1}H multipulse experiments.[489] SLF experiments like LG-CP,[490] DIPSHIFT[491,492] and DRSE[493] determine the amplitudes of fast motions. The effect of hydration was investigated by ^{1}H relaxation,[494] MAS line shape studies,[495,496] ^{13}C relaxation,[497] WISE[498] and CP dynamics.[499,500] ^{2}H-solid echo experiments were applied to the application of membranes in which different motional modes exist[501] (Fig. 23),[502,503] amino acids,[504,505] peptides,[506] proteins.[456,472,507–514] The dynamic properties of the perhaps most abundant protein on earth, collagen, attracted considerable attention[515–519] as well as spider's silk.[520–522] Last but not least are DNA and RNA studied by ^{2}H-quadrupolar echo experiments.[476,523,524] Recently, the 1D-MAS exchange method tr-ODESSA[525] as well as CODEX[174,490,526,527] were employed to biological solids, however, the influence of competing spin dynamics like proton-driven spin diffusion[135,528–535] and the so-called RIDER[536–538] limits their application so far.

3.4. Liquid crystals

The majority of dynamic NMR investigations of liquid crystals (LCs) and LC polymers aims at the properties of the mesophases, i.e., to a very mobile state. These studies will

thus not be considered in this report. However, a few experiments were performed in the solid phases, for example, by line shape experiments,[539–542] [13]C[543–545] and ^{2}H relaxation,[546] field-cycling relaxometry,[547–549] [2]H-line shape,[550–558] WISE,[545] dynamic line shape,[559] dynamic MAS,[558,560,561] [2]H-static exchange,[550–552,556] [13]C 2D-MAS[558] and 1D-MAS exchange.[176] Of particular importance are studies under the influence of external fields.[562]

3.5. Host–guest systems and organic–inorganic hybrid materials

Dynamic studies in host–guest systems like inclusion compounds[116] are commonly aimed at the study of dynamic details of the mobile guest molecules that are included in the more rigid hosts. A few studies by ^{13}C relaxation[563,564] and [2]H-quadrupolar echo[565] are aimed at polymeric guests while small molecules form the mobile part in the majority of the investigated materials. Experimental techniques include [1]H-,[566]
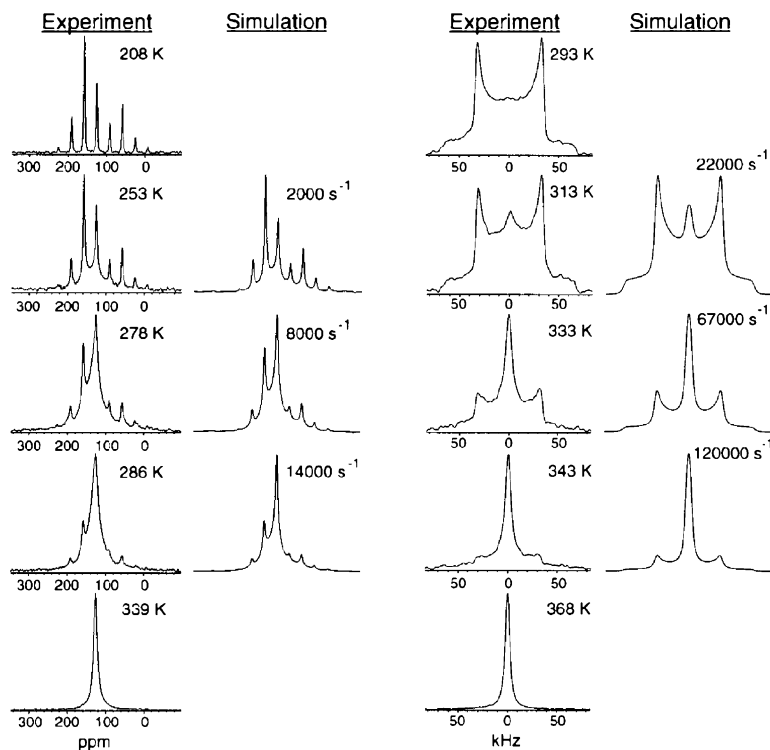
Fig. 24.   Variable-temperature experimental and simulated ^{13}C dynamic MAS NMR (left) and [2]H-solid echo spectra (right) for a bulk loading of two adsorbed benzene molecules per Ag–Y zeolite supercage. The numerical values accompanying the simulated MAS ^{13}C-NMR spectra are the centers of a 1.9 decade FWHM log-normal rate distribution, which was varied to obtain the simulations. (Reprinted with permission from Ref. 626. Copyright 1999 American Chemical Society.)

[2]H-[567–570] and ^{13}C-relaxation,[571,572] 2D-MAS exchange[573] and [2]H-quadrupolar echo experiments.[570,574–588] While there are no covalent chemical bonds between guest and host molecules in inclusion compounds, there are materials in which the organic phase is chemically bonded to the inorganic template. Examples are organic molecules or polymers attached to silica or alumina that have been investigated by [2]H-quadrupolar echo,[589–594] CP dynamics,[595,596] dynamic line shape[597] and WISE.[598,599] Polymer–metal complexes have been investigated by line shape[600] and relaxation studies,[601] [2]H-quadrupolar echo[602,603] and dynamic decoupling.[604] Other hybrid materials have been investigated by ^{1}H relaxation,[605] field-cycling relaxometry,[606,607] CP dynamics,[608–610]
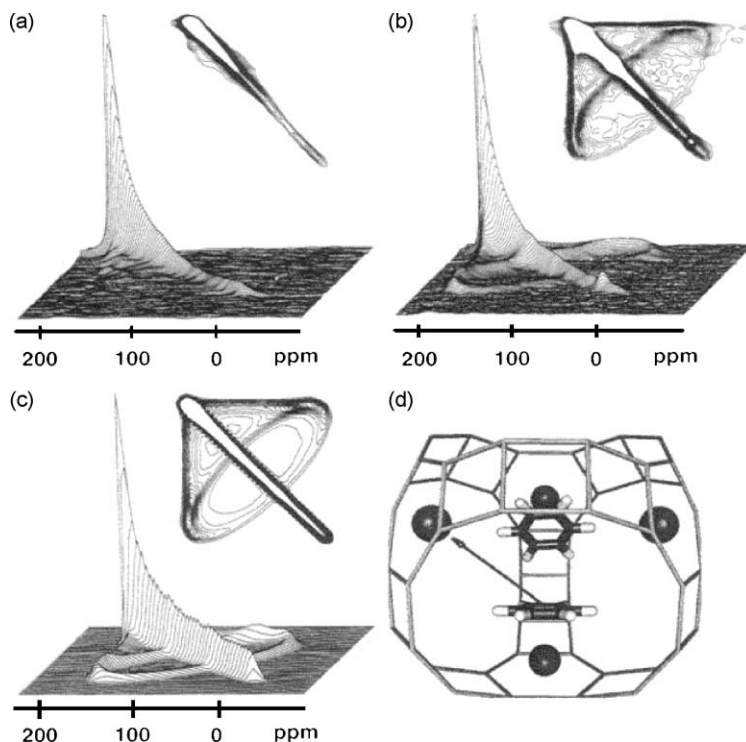
Fig. 25. (a–c) Experimental and simulated 2D-exchange ^{13}C-NMR spectra of benzene adsorbed in the supercages of Ca-LSX zeolite: (a) $T = 298$ K, $\tau_m = 1$ ms: little or no exchange of benzene molecules occurs among adsorption sites with different orientations on this time scale; (b) $T = 298$ K, $\tau_m = 300$ ms: the off-diagonal exchange features are consistent with a sizable fraction of benzene molecules reorienting among different well-defined environments $\beta = 109° \pm 3°$ with respect to one another; (c) simulated exchange NMR spectrum for an isotropic distribution of axially symmetric chemical shift tensors that exchange with a correlation time on the order of the mixing time among discrete tetrahedrally arranged sites $\beta = 109.5°$. (d) Schematic diagram of benzene molecules adsorbed at Ca^{2+} cation sites in a Ca–LSX zeolite supercage. Up to four such cation sites may exist which are arranged tetrahedrally in each LSX supercage. (Reprinted with permission from Ref. 631. Copyright 1995 American Chemical Society.)

WISE,[609,611–613] [1]H DQ[431] and [2]H-quadrupolar echo.[614–617] The interaction between proteins and biomineral surfaces was studied by ^{13}C MAS NMR.[618]

Although inorganic nano- and mesoporous materials like zeolites can hardly be considered as 'organic solids', the dynamic behavior of guest molecules in these materials is of particular importance for the properties of the material and is accessible by the NMR methods described above. These include [1]H-[619–621] and [2]H-relaxation,[110] [2]H-quadrupolar echo,[622–629] [13]C dynamic MAS[626] (Fig. 24) [2]H-2D exchange[624,630,631] (Fig. 25),[626,632,633] [13]C reduced 3D-exchange experiments,[626] as well as 1D-static[625,633] and MAS-exchange experiments.[632,634,635] A kind of inverse material (as compared to zeolites) is solid-polymer electrolytes in which salts are dissolved in an organic matrix which provides both a mechanical stability for the hybrid material and a sufficiently low viscosity to enable efficient ion mobility. Relaxation experiments aimed at both the ions (with lithium being a prominent example)[636–645] and the polymer (often PEO)[639,646,647] are common. Since the mobility of the organic matrix is directly related to that of the charge carriers, the investigation of its dynamic details attracted attention by [2]H-quadrupolar echo,[648] CP dynamics,[649] WISE[650] and advanced 2D- and 1D-exchange techniques.[651–653] It is also desirable to do line shape and relaxation experiments on both the ions and the matrix simultaneously.[654,655] A class of materials that has recently attracted the attention of dynamic NMR are self-assembled monolayers (SAMs) on substrates which has been investigated by ^{13}C relaxation,[656] [2]H-quadrupolar echo[657] and SLF.[658,659]

4. CONCLUSIONS

A variety of conformational and reorientational motions have been found in organic solids. Such processes are not an exception; the solid state is not entirely rigid. In most cases, the dynamic phenomena are strongly correlated with macroscopic properties of the material and, thus, their investigation is of particular interest for materials science. NMR is a versatile tool for the extraction of detailed information about both the time scale and the amplitude/geometry, as it does not require labeling other than isotopic exchange (as compared to spin-marker molecules in electron-spin resonance, ESR) and provides molecular resolution, i.e., the identification of dynamic units at the level of the molecule or even the identification of smaller heterogeneous dynamic units within the molecule.

REFERENCES

1. N. Bloembergen, E. M. Purcell and R. V. Pound, *Phys. Rev.*, 1948, **73**, 679.
2. H. S. Gutowsky and G. E. Pake, *J. Chem. Phys.*, 1950, **18**, 162.
3. P. S. Hubbard, *Rev. Mod. Phys.*, 1961, **33**, 249.
4. A. Abragam, *The Principles of Nuclear Magnetism*, Claredon Press, Oxford, 1962.
5. H. Pfeifer, *Ann. Physik*, 1964, **13**, 174.
6. U. Haeberlen and J. S. Waugh, *Phys. Rev.*, 1969, **185**, 420.
7. R. Kubo and K. Tomita, *J. Phys. Soc. Jpn.*, 1954, **9**, 888.

8. J. M. Deutch and J. S. Waugh, *J. Chem. Phys.*, 1965, **43**, 1914.

9. D. Sames, *Ann. Physik*, 1965, **15**, 363.

10. A. A. Samokhin, *Physica*, 1966, **32**, 823.

11. H. Nakano and A. Yoshimori, *Prog. Theor. Phys.*, 1964, **32**, 685.

12. J. F. Darby and B. V. Rollin, *Nature*, 1949, **164**, 66.

13. E. R. Andrew, *J. Chem. Phys.*, 1950, **18**, 607.

14. C. W. Wilson and G. E. Pake, *J. Polym. Sci.*, 1953, **10**, 503.

15. J. G. Powles, J. H. Strange and D. J. H. Sandiford, *Polymer*, 1963, **4**, 401.

16. E. R. Andrew, W. S. Hinshaw, M. G. Hutchins, R. O. I. Sjoblom and P. C. Canepa, *Mol. Phys.*, 1976, **32**, 795.

17. E. R. Andrew, W. S. Hinshaw, M. G. Hutchins and R. O. I. Sjoblom, *Mol. Phys.*, 1976, **31**, 1479.

18. E. R. Andrew, R. Gaspar and W. Vennart, *Biopolymers*, 1978, **17**, 1913.

19. A. Miyake, *J. Polym. Sci.*, 1958, **28**, 476.

20. V. P. Grigorev and A. I. Maklakov, *Vysokomol. Soedin. Ser. A*, 1973, **15**, 2576.

21. V. P. Grigorev, A. I. Maklakov and V. S. Derinovs, *Vysokomol. Soedin. Ser. B*, 1974, **16**, 737.

22. V. J. McBrierty and D. C. Douglass, *Phys. Rep. – Rev. Sect. Phys. Lett.*, 1980, **63**, 63.

23. V. J. McBrierty and D. C. Douglass, *Macromol. Rev. Part D – J. Polym. Sci.*, 1981, **16**, 295.

24. V. Fedotov and H. Schneider, *NMR Basic Principles and Progress*, Vol. 21, Springer, Berlin, 1989, 1.

25. D. A. Torchia and A. Szabo, *J. Magn. Reson.*, 1982, **49**, 107.

26. S. Benz, U. Haeberlen and J. Tegenfeldt, *J. Magn. Reson.*, 1986, **66**, 125.

27. A. Heuer and U. Haeberlen, *J. Chem. Phys.*, 1991, **95**, 4201.

28. N. F. Ramsey and R. V. Pound, *Phys. Rev.*, 1951, **81**, 278.

29. F. Noack, *Prog. NMR Spectrosc.*, 1986, **18**, 171.

30. E. Anoardo, G. Galli and G. Ferrante, *Appl. Magn. Reson.*, 2001, **20**, 365.

31. R. Kimmich and E. Anoardo, *Prog. NMR Spectrosc.*, 2004, **44**, 257.

32. Y. L. Wang and P. S. Belton, *Chem. Phys. Lett.*, 2000, **325**, 33.

33. G. Schauer, W. Nusser, M. Blanz and R. Kimmich, *J. Phys. E – Sci. Instrum.*, 1987, **20**, 43.

34. K. H. Schweikert, R. Krieg and F. Noack, *J. Magn. Reson.*, 1988, **78**, 77.

35. M. Blanz, T. J. Rayner and J. A. S. Smith, *Meas. Sci. Technol.*, 1993, **4**, 48.

36. C. Job, J. Zajicek and M. F. Brown, *Rev. Sci. Instrum.*, 1996, **67**, 2113.

37. D. Ailion and C. P. Slichter, *Phys. Rev. Lett.*, 1964, **12**, 168.

38. C. P. Slichter and D. Ailion, *Phys. Rev. A – Gen. Phys.*, 1964, **135**, 1099.

39. J. Schaefer, E. O. Stejskal and R. Buchdahl, *Macromolecules*, 1977, **10**, 384.

40. D. L. Vanderhart and A. N. Garroway, *Bull. Am. Phys. Soc.*, 1978, **23**, 271.

41. A. N. Garroway, D. L. Vanderhart and W. L. Earl, *Philos. Trans. R. Soc. Lond. Ser. A – Math. Phys. Eng. Sci.*, 1981, **299**, 609.

42. D. L. Vanderhart and A. N. Garroway, *J. Chem. Phys.*, 1979, **71**, 2773.

43. J. Schaefer, E. O. Stejskal, T. R. Steger, M. D. Sefcik and R. A. McKay, *Macromolecules*, 1980, **13**, 1121.

44. C. S. Yannoni, *Acc. Chem. Res.*, 1982, **15**, 201.

45. K. Akasaka, S. Ganapathy, C. A. McDowell and A. Naito, *J. Chem. Phys.*, 1983, **78**, 3567.

46. P. Tekely, D. Canet, J. J. Delpuech and J. Virlet, *Magn. Reson. Chem.*, 1990, **28**, S10.

47. A. Krushelnitsky, R. Kurbanov, D. Reichert, G. Hempel, H. Schneider and V. Fedotov, *Solid State Nucl. Magn. Reson.*, 2002, **22**, 423.

48. W. Grunder, *Wiss. Z., Karl-Marx-Univ. Leipzig, Math.-Naturwiss. Reihe*, 1974, **23**, 506.

49. A. J. Vega and R. W. Vaughan, *J. Chem. Phys.*, 1978, **68**, 1958.

50. W. Hiller and H. Schneider, *Acta Polym.*, 1988, **39**, 276.

51. H. Schneider and W. Hiller, *J. Polym. Sci. Part B – Polym. Phys.*, 1990, **28**, 1001.

52. A. E. Mefed and V. A. Atsarkin, *JETP Lett.*, 1977, **25**, 215.

53. A. E. Mefed, V. A. Atsarkin and M. E. Zhabotinsky, *Zh. Eksp. Teor. Fiz.*, 1986, **91**, 671.

54. A. E. Mefed and V. A. Atsarkin, *Phys. Status Solidi A – Appl. Res.*, 1986, **93**, K21.

55. A. G. Krushelnitsky, A. E. Mefed, A. A. Kharitonov and V. D. Fedotov, *Appl. Magn. Reson.*, 2001, **20**, 207.

56. A. E. Mefed, *Appl. Magn. Reson.*, 2001, **21**, 127.

57. A. G. Krushelnitsky, G. Hempel and D. Reichert, *Biochim. Biophys. Acta – Proteins Proteomics*, 2003, **1650**, 117.

58. R. King and O. Jardetzky, *Chem. Phys. Lett.*, 1978, **55**, 15.
59. G. Lipari and A. Szabo, *Biophys. J.*, 1981, **33**, A307.
60. G. Lipari, A. Szabo and R. M. Levy, *Nature*, 1982, **300**, 197.
61. G. Lipari and A. Szabo, *J. Am. Chem. Soc.*, 1982, **104**, 4546.
62. G. Lipari and A. Szabo, *J. Am. Chem. Soc.*, 1982, **104**, 4559.
63. G. Lipari and A. Szabo, *Biophys. J.*, 1982, **37**, A380.
64. V. D. Fedotov and L. S. Kivayeva, *J. Biomol. Struct. Dyn.*, 1987, **4**, 599.
65. G. M. Clore, A. Szabo, A. Bax, L. E. Kay, P. C. Driscoll and A. M. Gronenborn, *J. Am. Chem. Soc.*, 1990, **112**, 4989.
66. E. R. Andrew and R. G. Eades, *Proc. R. Soc. Lond. Ser. A – Math. Phys. Sci.*, 1953, **218**, 537.
67. E. R. Andrew, A. Bradbury and R. G. Eades, *Nature*, 1958, **182**, 1659.
68. E. R. Andrew, A. Bradbury and R. G. Eades, *Nature*, 1959, **183**, 1802.
69. I. J. Lowe, *Phys. Rev. Lett.*, 1959, **2**, 285.
70. W. P. Slichter, *Makromol. Chem.*, 1959, **34**, 67.
71. W. P. Slichter, *Ann. NY Acad. Sci.*, 1959, **83**, 60.
72. W. P. Slichter and E. R. Mandell, *J. Appl. Phys.*, 1959, **30**, 1473.
73. W. P. Slichter, *J. Polym. Sci.*, 1959, **35**, 77.
74. K. H. Illers and R. Kosfeld, *Makromol. Chem.*, 1960, **42**, 44.
75. Z. Gadjourova, Y. G. Andreev, D. P. Tunstall and P. G. Bruce, *Nature*, 2001, **412**, 520.
76. W. H. Hou, C. Y. Chen and C. C. Wang, *Polymer*, 2003, **44**, 2983.
77. S. Alexander, A. Baram and Z. Luz, *J. Chem. Phys.*, 1974, **61**, 992.
78. A. Baram, Z. Luz and S. Alexander, *J. Chem. Phys.*, 1976, **64**, 4321.
79. S. Zamir, R. Poupko, Z. Luz and S. Alexander, *J. Chem. Phys.*, 1991, **94**, 5939.
80. W. Domalewski, F. G. Riddell and L. Stefaniak, *Bull. Pol. Acad. Sci. – Chem.*, 1998, **46**, 35.
81. O. Klein, M. M. Bonvehi, F. Aguilar-Parrilla, N. Jagerovic, J. Elguero and H. H. Limbach, *Isr. J. Chem.*, 1999, **39**, 291.
82. H. Y. Carr and E. M. Purcell, *Phys. Rev.*, 1954, **94**, 630.
83. S. Meiboom and D. Gill, *Rev. Sci. Instrum.*, 1958, **29**, 688.
84. Z. Luz and S. Meiboom, *J. Chem. Phys.*, 1963, **39**, 366.
85. J. P. Carver and R. E. Richards, *J. Magn. Reson.*, 1972, **6**, 89.
86. R. Ishima, J. M. Louis and D. A. Torchia, *J. Am. Chem. Soc.*, 1999, **121**, 11589.
87. R. Ishima and D. A. Torchia, *J. Biomol. NMR*, 1999, **14**, 369.
88. R. Ishima and D. A. Torchia, *Nat. Struct. Biol.*, 2000, **7**, 740.
89. F. A. A. Mulder, N. R. Skrynnikov, B. Hon, F. W. Dahlquist and L. E. Kay, *J. Am. Chem. Soc.*, 2001, **123**, 967.
90. N. R. Skrynnikov, F. A. A. Mulder, B. Hon, F. W. Dahlquist and L. E. Kay, *J. Am. Chem. Soc.*, 2001, **123**, 4556.
91. S. Meiboom, *J. Chem. Phys.*, 1961, **34**, 375.
92. H. W. Spiess, *Chem. Phys.*, 1974, **6**, 217.
93. H. W. Spiess, R. Grosescu and U. Haeberlen, *Chem. Phys.*, 1974, **6**, 226.
94. D. Hentschel, H. Sillescu and H. W. Spiess, *Makromol. Chem. – Macromol. Chem. Phys.*, 1979, **180**, 241.
95. R. Hentschel and H. W. Spiess, *J. Magn. Reson.*, 1979, **35**, 157.
96. A. E. Aliev and K. D. M. Harris, *Magn. Reson. Chem.*, 1998, **36**, 855.
97. J. G. Powles and J. H. Strange, *Proc. Phys. Soc. Lond.*, 1963, **82**, 6.
98. J. H. Davis, K. R. Jeffrey, M. Bloom, M. I. Valic and T. P. Higgs, *Chem. Phys. Lett.*, 1976, **42**, 390.
99. H. W. Spiess and H. Sillescu, *J. Magn. Reson.*, 1981, **42**, 381.
100. D. Hentschel, H. Sillescu and H. W. Spiess, *Macromolecules*, 1981, **14**, 1605.
101. E. Rossler, H. Sillescu and H. W. Spiess, *Polymer*, 1985, **26**, 203.
102. A. J. Vega and Z. Luz, *J. Chem. Phys.*, 1987, **86**, 1803.
103. D. E. Woessner, B. S. Snowden and G. H. Meyer, *J. Chem. Phys.*, 1969, **51**, 2968.
104. A. J. Vega, R. Poupko and Z. Luz, *J. Magn. Reson.*, 1989, **83**, 111.
105. K. Muller, R. Poupko and Z. Luz, *J. Magn. Reson.*, 1990, **90**, 19.
106. K. Muller, R. Poupko and Z. Luz, *J. Magn. Reson.*, 1991, **93**, 291.
107. N. Heaton, D. Reimer and G. Kothe, *Ber. Bunsen-Gesellschaft – Phys. Chem. Chem. Phys.*, 1993, **97**, 1320.
108. N. Heaton, D. Reimer and G. Kothe, *J. Non-Cryst. Solids*, 1994, **172**, 917.

109. D. Reimer, N. Heaton, A. Schleicher, K. Muller, G. Kothe and M. Vilfan, *J. Chem. Phys.*, 1994, **100**, 1693.
110. A. G. Stepanov, T. O. Shegai, M. V. Luzgin and H. Jobic, *Eur. Phys. J. E*, 2003, **12**, 57.
111. H. W. Spiess, *Colloid Polym. Sci.*, 1983, **261**, 193.
112. J. Hirschinger, H. Miura, K. H. Gardner and A. D. English, *Macromolecules*, 1990, **23**, 2153.
113. S. J. Opella, *Methods Enzymol.*, 1986, **131**, 327.
114. A. G. Palmer, J. Williams and A. McDermott, *J. Phys. Chem.*, 1996, **100**, 13293.
115. D. J. Siminovitch, *Biochem. Cell Biol. – Biochim. Biol. Cell.*, 1998, **76**, 411.
116. K. D. M. Harris, *J. Mol. Struct.*, 1996, **374**, 241.
117. L. Frydman, S. Vallabhaneni, Y. K. Lee and L. Emsley, *J. Chem. Phys.*, 1994, **101**, 111.
118. H. Ishida and F. Horii, *Macromolecules*, 2002, **35**, 5550.
119. M. Murakami, H. Ishida, M. Miyazaki, H. Kaji and F. Horii, *Macromolecules*, 2003, **36**, 4160.
120. D. Sandstrom, M. Hong and K. Schmidt-Rohr, *Chem. Phys. Lett.*, 1999, **300**, 213.
121. A. Schmidt and S. Vega, *Chem. Phys. Lett.*, 1989, **157**, 539.
122. W. P. Rothwell and J. S. Waugh, *J. Chem. Phys.*, 1981, **74**, 2721.
123. D. Suwelack, W. P. Rothwell and J. S. Waugh, *J. Chem. Phys.*, 1980, **73**, 2559.
124. A. Schmidt, S. O. Smith, D. P. Raleigh, J. E. Roberts, R. G. Griffin and S. Vega, *J. Chem. Phys.*, 1986, **85**, 4248.
125. A. Schmidt and S. Vega, *J. Chem. Phys.*, 1987, **87**, 6895.
126. Z. Luz, R. Poupko and S. Alexander, *J. Chem. Phys.*, 1993, **99**, 7544.
127. D. Reichert, G. Hempel, H. Zimmermann, H. Schneider and Z. Luz, *Solid State Nucl. Magn. Reson.*, 2000, **18**, 17.
128. J. H. Kristensen, H. Bildsoe, H. J. Jakobsen and N. C. Nielsen, *J. Magn. Reson.*, 1991, **92**, 443.
129. J. H. Kristensen, H. Bildsoe, H. J. Jakobsen and N. C. Nielsen, *J. Magn. Reson.*, 1992, **100**, 437.
130. J. H. Kristensen, G. L. Hoatson and R. L. Vold, *Solid State Nucl. Magn. Reson.*, 1998, **13**, 1.
131. J. H. Kristensen, G. L. Hoatson and R. L. Vold, *J. Chem. Phys.*, 1999, **110**, 4533.
132. N. J. Heaton, *Mol. Phys.*, 1997, **92**, 251.
133. P. M. Henrichs and V. A. Nicely, *Macromolecules*, 1991, **24**, 2506.
134. J. Jeener, B. H. Meier, P. Bachmann and R. R. Ernst, *J. Chem. Phys.*, 1979, **71**, 4546.
135. H. T. Edzes and J. P. C. Bernards, *J. Am. Chem. Soc.*, 1984, **106**, 1515.
136. O. Pascui, M. Beiner and D. Reichert, *Macromolecules*, 2003, **36**, 3992.
137. D. Reichert, T. J. Bonagamba and K. Schmidt-Rohr, *J. Magn. Reson.*, 2001, **151**, 129.
138. C. Schmidt, S. Wefing, B. Blumich and H. W. Spiess, *Chem. Phys. Lett.*, 1986, **130**, 84.
139. C. Schmidt, B. Blumich and H. W. Spiess, *J. Magn. Reson.*, 1988, **79**, 269.
140. K. Schmidt-Rohr and H. W. Spiess, *Multidimensional Solid-State NMR and Polymers*, Academic Press, London, 1994.
141. H. W. Spiess, *Chem. Rev.*, 1991, **91**, 1321.
142. L. Frydman, Y. K. Lee, L. Emsley, G. C. Chingas and A. Pines, *J. Am. Chem. Soc.*, 1993, **115**, 4825.
143. E. R. deAzevedo, T. J. Bonagamba and K. Schmidt-Rohr, *J. Magn. Reson.*, 2000, **142**, 86.
144. W. G. Hu, C. Boeffel and K. Schmidt-Rohr, *Macromolecules*, 1999, **32**, 1611.
145. A. F. Dejong, A. P. M. Kentgens and W. S. Veeman, *Chem. Phys. Lett.*, 1984, **109**, 337.
146. A. P. M. Kentgens, A. F. DeJong, E. Deboer and W. S. Veeman, *Macromolecules*, 1985, **18**, 1045.
147. A. Hagemeyer, K. Schmidt-Rohr and H. W. Spiess, *Adv. Magn. Reson.*, 1989, **13**, 85.
148. G. J. Boender and S. Vega, *J. Magn. Reson.*, 1998, **133**, 281.
149. D. Reichert, G. Hempel and H. Schneider, *Solid State Nucl. Magn. Reson.*, 1998, **11**, 259.
150. M. Ernst, A. P. M. Kentgens and B. H. Meier, *J. Magn. Reson.*, 1999, **138**, 66.
151. R. Tycko and A. E. Berger, *J. Magn. Reson.*, 1999, **141**, 141.
152. D. Reichert, Z. Olender, R. Poupko, H. Zimmermann and Z. Luz, *J. Chem. Phys.*, 1993, **98**, 7699.
153. K. Schmidtrohr and H. W. Spiess, *Macromolecules*, 1991, **24**, 5288.
154. K. Zemke, B. F. Chmelka, K. Schmidtrohr and H. W. Spiess, *Macromolecules*, 1991, **24**, 6874.
155. Z. Luz, P. Tekely and D. Reichert, *Prog. NMR Spectrosc.*, 2002, **41**, 83.
156. Y. Yang, A. Hagemeyer and H. W. Spiess, *Macromolecules*, 1989, **22**, 1004.
157. Y. Yang, A. Hagemeyer, K. Zemke and H. W. Spiess, *J. Chem. Phys.*, 1990, **93**, 7740.
158. J. Jeener and P. Broekaert, *Phys. Rev.*, 1967, **157**, 232.
159. M. Lausch and H. W. Spiess, *Chem. Phys. Lett.*, 1980, **71**, 182.
160. H. W. Spiess, *J. Chem. Phys.*, 1980, **72**, 6755.

161. M. Lausch and H. W. Spiess, *J. Magn. Reson.*, 1983, **54**, 466.

162. F. Fujara, S. Wefing and H. W. Spiess, *J. Chem. Phys.*, 1986, **84**, 4579.

163. S. C. Kuebler, A. Heuer and H. W. Spiess, *Macromolecules*, 1996, **29**, 7089.

164. A. Heuer, M. Wilhelm, H. Zimmermann and H. W. Spiess, *Phys. Rev. Lett.*, 1995, **75**, 2851.

165. N. M. Szeverenyi, A. Bax and G. E. Maciel, *J. Am. Chem. Soc.*, 1983, **105**, 2579.

166. M. Mehring, *NMR – Basic Principles and Progress*, Springer, Berlin, 1976, 40.

167. Y. Yang, M. Schuster, B. Blumich and H. W. Spiess, *Chem. Phys. Lett.*, 1987, **139**, 239.

168. V. Gerardy-Montouillout, C. Malveau, P. Tekely, Z. Olender and Z. Luz, *J. Magn. Reson. Ser. A*, 1996, **123**, 7.

169. D. Reichert, H. Zimmermann, P. Tekely, R. Poupko and Z. Luz, *J. Magn. Reson.*, 1997, **125**, 245.

170. P. Tekely, D. Reichert, H. Zimmermann and Z. Luz, *J. Magn. Reson.*, 2000, **145**, 173.

171. D. Reichert, G. Hempel, Z. Luz, P. Tekely and H. Schneider, *J. Magn. Reson.*, 2000, **146**, 311.

172. E. R. deAzevedo, W. G. Hu, T. J. Bonagamba and K. Schmidt-Rohr, *J. Am. Chem. Soc.*, 1999, **121**, 8411.

173. E. R. deAzevedo, W. G. Hu, T. J. Bonagamba and K. Schmidt-Rohr, *J. Chem. Phys.*, 2000, **112**, 8988.

174. E. R. deAzevedo, S. B. Kennedy and M. Hong, *Chem. Phys. Lett.*, 2000, **321**, 43.

175. D. Reichert, O. Pascui, T. J. Bonagamba, E. R. deAzevedo and A. Schmidt, *Chem. Phys. Lett.*, 2003, **380**, 583.

176. I. Fischbach, T. Pakula, P. Minkin, A. Fechtenkotter, K. Mullen, H. W. Spiess and K. Saalwachter, *J. Phys. Chem. B*, 2002, **106**, 6408.

177. E. A. Hill and J. P. Yesinowski, *J. Chem. Phys.*, 1997, **107**, 346.

178. T. H. Lin and R. R. Vold, *J. Phys. Chem.*, 1991, **95**, 9032.

179. J. C. Williams and A. E. McDermott, *J. Phys. Chem.*, 1993, **97**, 12393.

180. D. G. Cory and W. M. Ritchey, *Macromolecules*, 1989, **22**, 1611.

181. A. A. Parker, J. J. Marcinko, P. Rinaldi, D. P. Hedrick and W. M. Ritchey, *J. Appl. Polym. Sci.*, 1993, **48**, 677.

182. J. J. Marcinko, A. A. Parker, P. L. Rinaldi and W. M. Ritchey, *J. Appl. Polym. Sci.*, 1994, **51**, 1777.

183. J. J. Marcinko, A. A. Parker, Y. T. Shieh and W. M. Ritchey, *J. Appl. Polym. Sci.*, 1992, **45**, 391.

184. I. Klur, J. F. Jacquinot, F. Brunet, T. Charpentier, J. Virlet, C. Schneider and P. Tekely, *J. Phys. Chem. B*, 2000, **104**, 10162.

185. R. K. Hester, J. L. Ackerman, B. L. Neff and J. S. Waugh, *Phys. Rev. Lett.*, 1976, **36**, 1081.

186. E. F. Rybaczewski, B. L. Neff, J. S. Waugh and J. S. Sherfinski, *J. Chem. Phys.*, 1977, **67**, 1231.

187. M. Linder, A. Hohener and R. R. Ernst, *J. Chem. Phys.*, 1980, **73**, 4959.

188. M. G. Munowitz, R. G. Griffin, G. Bodenhausen and T. H. Huang, *J. Am. Chem. Soc.*, 1981, **103**, 2529.

189. J. Schaefer, R. A. McKay and E. O. Stejskal, *J. Magn. Reson.*, 1983, **52**, 123.

190. J. Schaefer, M. D. Sefcik, E. O. Stejskal, R. A. McKay, W. T. Dixon and R. E. Cais, *Macromolecules*, 1984, **17**, 1107.

191. S. Swanson, S. Ganapathy, S. Kennedy, P. M. Henrichs and R. G. Bryant, *J. Magn. Reson.*, 1986, **69**, 531.

192. P. Tekely, D. Nicole, J. Brondeau and J. J. Delpuech, *J. Phys. Chem.*, 1986, **90**, 5608.

193. K. Schmidtrohr, J. Clauss and H. W. Spiess, *Macromolecules*, 1992, **25**, 3273.

194. X. H. Qiu and P. A. Mirau, *J. Magn. Reson.*, 2000, **142**, 183.

195. J. Lu, P. A. Mirau and A. E. Tonelli, *Macromolecules*, 2001, **34**, 3276.

196. S. Hediger, A. Lesage and L. Emsley, *Macromolecules*, 2002, **35**, 5078.

197. A. C. Kolbert, H. J. M. de Groot, M. H. Levitt, M. G. Munowitz, J. E. Roberts, G. S. Harbison, J. Herzfeld and R. G. Griffin, *Multinuclear Magnetic Resonance in Liquids and Solids – Chemical Applications*, Kluwer, Dordrecht, 1990., 339.

198. M. Hong, J. D. Gross and R. G. Griffin, *J. Phys. Chem. B*, 1997, **101**, 5869.

199. B. J. van Rossum, C. P. de Groot, V. Ladizhansky, S. Vega and H. J. M. de Groot, *J. Am. Chem. Soc.*, 2000, **122**, 3465.

200. D. A. Lathrop and K. K. Gleason, *Macromolecules*, 1993, **26**, 4652.

201. H. J. Jacobson, *Encyclopedia of Nuclear Magnetic Resonance*, Wiley, Chichester, 1996, 398.

202. H. Geen, J. J. Titman, J. Gottwald and H. W. Spiess, *Chem. Phys. Lett.*, 1994, **227**, 79.

203. S. Hafner and H. W. Spiess, *Concepts Magn. Reson.*, 1998, **10**, 99.

204. J. Gottwald, D. E. Demco, R. Graf and H. W. Spiess, *Chem. Phys. Lett.*, 1995, **243**, 314.

205. U. Friedrich, I. Schnell, S. P. Brown, A. Lupulescu, D. E. Demco and H. W. Spiess, *Mol. Phys.*, 1998, **95**, 1209.

206. R. Graf, D. E. Demco, S. Hafner and H. W. Spiess, *Solid State Nucl. Magn. Reson.*, 1998, **12**, 139.

207. R. Graf, A. Heuer and H. W. Spiess, *Phys. Rev. Lett.*, 1998, **80**, 5738.

208. T. Dollase, R. Graf, A. Heuer and H. W. Spiess, *Macromolecules*, 2001, **34**, 298.

209. S. P. Brown and H. W. Spiess, *Chem. Rev.*, 2001, **101**, 4125.

210. I. Schnell, A. Watts and H. W. Spiess, *J. Magn. Reson.*, 2001, **149**, 90.

211. D. E. Favre, D. J. Schaefer and B. F. Chmelka, *J. Magn. Reson.*, 1998, **134**, 261.

212. E. Gelerinter, Z. Luz, R. Poupko and H. Zimmermann, *J. Phys. Chem.*, 1990, **94**, 8845.

213. W. Scheubel, H. Zimmermann and U. Haeberlen, *J. Magn. Reson.*, 1988, **80**, 401.

214. D. Reichert, G. Hempel, H. Zimmermann, P. Tekely, R. Poupko, Z. Luz, D. E. Favre and B. F. Chmelka, *Appl. Magn. Reson.*, 1999, **17**, 315.

215. J. J. Titman, Z. Luz and H. W. Spiess, *J. Am. Chem. Soc.*, 1992, **114**, 3756.

216. J. J. Titman, Z. Luz and H. W. Spiess, *J. Am. Chem. Soc.*, 1992, **114**, 3765.

217. Z. Luz, L. Olivier, R. Poupko, K. Muller, C. Krieger and H. Zimmermann, *J. Am. Chem. Soc.*, 1998, **120**, 5526.

218. K. Muller, H. Zimmermann, C. Krieger, R. Poupko and Z. Luz, *J. Am. Chem. Soc.*, 1996, **118**, 8006.

219. R. Poupko, K. Muller, C. Krieger, H. Zimmermann and Z. Luz, *J. Am. Chem. Soc.*, 1996, **118**, 8015.

220. S. Schlick, Z. Luz, R. Poupko and H. Zimmermann, *J. Am. Chem. Soc.*, 1992, **114**, 4315.

221. B. S. Hickman, M. Mascal, J. J. Titman and I. G. Wood, *J. Am. Chem. Soc.*, 1999, **121**, 11486.

222. T. Ueda, H. Masui and N. Nakamura, *Solid State Nucl. Magn. Reson.*, 2001, **20**, 145.

223. G. R. Goward, K. Saalwachter, I. Fischbach and H. W. Spiess, *Solid State Nucl. Magn. Reson.*, 2003, **24**, 150.

224. D. Casarini, L. Lunazzi, A. Mazzanti and G. Simon, *J. Org. Chem.*, 2000, **65**, 3207.

225. J. Fattah, J. M. Twyman, S. J. Heyes, D. J. Watkin, A. J. Edwards, K. Prout and C. M. Dobson, *J. Am. Chem. Soc.*, 1993, **115**, 5636.

226. F. Aguilar-Parrilla, O. Klein, J. Elguero and H. H. Limbach, *Ber. Bunsen-Gesellschaft – Phys. Chem. Chem. Phys.*, 1997, **101**, 889.

227. J. E. Anderson, D. Casarini and L. Lunazzi, *J. Org. Chem.*, 1996, **61**, 1290.

228. A. Muller, H. Zimmermann, U. Haeberlen, J. J. Wolff, R. Poupko and Z. Luz, *J. Phys. Chem.*, 1996, **100**, 13911.

229. T. Brauniger, R. Poupko, H. Zimmermann and Z. Luz, *J. Chem. Soc., Perkin Trans. 2*, 1997, 1255.

230. M. Winterlich, H. Zimmermann and R. Bohmer, *J. Non-Cryst. Solids*, 2002, **307**, 442.

231. L. Frydman, A. C. Olivieri, L. E. Diaz, B. Frydman, A. Schmidt and S. Vega, *Mol. Phys.*, 1990, **70**, 563.

232. X. Helluy, J. Kummerlen and A. Sebald, *Organometallics*, 1997, **16**, 5218.

233. F. G. Riddell, S. Arumugam, K. D. M. Harris, M. Rogerson and J. H. Strange, *J. Am. Chem. Soc.*, 1993, **115**, 1881.

234. P. A. Beckmann, K. S. Burbank, K. M. Clemo, E. N. Slonaker, K. Averill, C. Dybowski, J. S. Figueroa, A. Glatfelter, S. Koch, L. M. Liable-Sands and A. L. Rheingold, *J. Chem. Phys.*, 2000, **113**, 1958.

235. E. R. Andrew and B. Peplinska, *Solid State Nucl. Magn. Reson.*, 1998, **13**, 39.

236. E. R. Andrew and M. Kempka, *Solid State Nucl. Magn. Reson.*, 1995, **4**, 249.

237. E. R. Andrew, M. Kempka, J. M. Radomski and E. Szczesniak, *Solid State Nucl. Magn. Reson.*, 1999, **14**, 91.

238. E. R. Andrew, B. Peplinska and M. Kempka, *Solid State Nucl. Magn. Reson.*, 1998, **10**, 117.

239. J. Tegenfeldt, L. Ojamae and C. Svensson, *J. Chem. Phys.*, 1991, **95**, 2696.

240. S. J. Kitchin and T. K. Halstead, *Appl. Magn. Reson.*, 1999, **17**, 283.

241. T. Hiraoki, T. Hamada and A. Tsutsumi, *J. Mol. Struct.*, 1995, **355**, 143.

242. K. J. McGrath and R. G. Weiss, *Langmuir*, 1997, **13**, 4474.

243. T. Brauniger, R. Poupko, Z. Luz, P. Gutsche, C. Meinel, H. Zimmermann and U. Haeberlen, *J. Chem. Phys.*, 2000, **112**, 10858.

244. P. Speier, H. Zimmermann, U. Haeberlen and Z. Luz, *Mol. Phys.*, 1998, **95**, 1153.

245. A. Detken, H. Zimmermann, U. Haeberlen and Z. Luz, *J. Magn. Reson.*, 1997, **126**, 95.

246. P. Speier, G. Prigl, H. Zimmermann, U. Haeberlen, E. Zaborowski and S. Vega, *Appl. Magn. Reson.*, 1995, **9**, 81.

247. A. Muller, U. Haeberlen, H. Zimmermann, R. Poupko and Z. Luz, *Mol. Phys.*, 1994, **81**, 1239.

248. A. Birczynski, Z. Sulek, A. Muller and U. Haeberlen, *Z. Phys. Chem. – Int. J. Res. Phys. Chem. Chem. Phys.*, 1992, **178**, 133.

249. T. Bernhard, H. Zimmermann and U. Haeberlen, *Mol. Phys.*, 1992, **77**, 1123.

250. S. Idziak, U. Haeberlen and H. Zimmermann, *Mol. Phys.*, 1991, **73**, 571.

251. T. Brauniger, R. Poupko, Z. Luz, D. Reichert, H. Zimmermann, H. Schmitt and U. Haeberlen, *Phys. Chem. Chem. Phys.*, 2001, **3**, 1891.

252. P. Speier, A. Muller, C. Meinel and U. Haeberlen, *Mol. Phys.*, 1998, **95**, 859.

253. Z. Olejniczak, Z. T. Lalowicz, T. Schmidt, H. Zimmermann, U. Haeberlen and H. Schmitt, *J. Chem. Phys.*, 2002, **116**, 10343.

254. A. Detken, H. Zimmermann and U. Haeberlen, *Mol. Phys.*, 1999, **96**, 927.

255. A. Detken, P. Schiebel, M. R. Johnson, H. Zimmermann and U. Haeberlen, *Chem. Phys.*, 1998, **238**, 301.

256. A. Detken, P. Focke, H. Zimmermann, U. Haeberlen, Z. Olejniczak and Z. T. Lalowicz, *Z. Naturforsch. Sect. A – J. Phys. Sci.*, 1995, **50**, 95.

257. A. Detken and H. Zimmermann, *J. Chem. Phys.*, 1998, **109**, 6791.

258. A. Detken and H. Zimmermann, *J. Chem. Phys.*, 1998, **108**, 5845.

259. T. Dries, F. Fujara, M. Kiebel, E. Rossler and H. Sillescu, *J. Chem. Phys.*, 1988, **88**, 2139.

260. M. Vogel and E. Rossler, *J. Phys. Chem. B*, 2000, **104**, 4285.

261. M. Vogel and E. Rossler, *J. Chem. Phys.*, 2001, **115**, 10883.

262. M. Vogel, C. Tschirwitz, G. Schneider, C. Koplin, P. Medick and E. Rossler, *J. Non-Cryst. Solids*, 2002, **307**, 326.

263. P. Medick, T. Blochowicz, M. Vogel and E. Rossler, *J. Non-Cryst. Solids*, 2002, **307**, 565.

264. S. C. Kuebler, A. Heuer and H. W. Spiess, *Phys. Rev. E*, 1997, **56**, 741.

265. S. A. Reinsberg, X. H. Qiu, M. Wilhelm, H. W. Spiess and M. D. Ediger, *J. Chem. Phys.*, 2001, **114**, 7299.

266. R. Soltani, F. Laupretre, L. Monnerie and S. Krause, *Polymer*, 1995, **36**, 275.

267. T. R. Steger, J. Schaefer, E. O. Stejskal and R. A. McKay, *Macromolecules*, 1980, **13**, 1127.

268. M. Wobst, *J. Polym. Sci. Part B – Polym. Phys.*, 1988, **26**, 527.

269. A. C. Kolbert, N. S. Sariciftci, K. U. Gaudl, P. Bauerle and M. Mehring, *J. Am. Chem. Soc.*, 1991, **113**, 8243.

270. M. I. B. Tavares and E. E. C. Monteiro, *Polym. Test.*, 1995, **14**, 273.

271. M. Forsyth, P. Meakin and D. R. MacFarlane, *J. Mater. Chem.*, 1997, **7**, 193.

272. A. R. Lim, J. R. Stewart and B. M. Novak, *Solid State Commun.*, 1999, **110**, 23.

273. M. I. B. Tavares, *Polym. Test.*, 2000, **19**, 899.

274. K. Kuwabara, H. Kaji and F. Horii, *Macromolecules*, 2000, **33**, 4453.

275. O. Dupont, A. M. Jonas, B. Nysten, R. Legras, P. Adriaensens and J. Gelan, *Macromolecules*, 2000, **33**, 562.

276. H. Y. Lee and S. Y. Kwak, *Polymer*, 2001, **42**, 1375.

277. A. Mercier, S. Kuroki, I. Ando, H. Deleuze and O. Mondain-Monval, *J. Polym. Sci. Part B – Polym. Phys.*, 2001, **39**, 956.

278. M. I. B. Tavares, *J. Appl. Polym. Sci.*, 2003, **87**, 473.

279. P. Adriaensens, R. Rego, R. Carleer, B. Ottenbourgs and J. Gelan, *Polym. Int.*, 2003, **52**, 1647.

280. M. Wobst, *Acta Polym.*, 1985, **36**, 492.

281. H. Kikuchi, H. Tokumitsu and K. Seki, *Macromolecules*, 1993, **26**, 7326.

282. J. Spevacek and J. Straka, *Makromol. Chem. – Macromol. Symp.*, 1993, **72**, 201.

283. S. Z. D. Cheng, T. M. Chalmers, Y. Gu, Y. Yoon, F. W. Harris, J. L. Cheng, M. Fone and J. L. Koenig, *Macromol. Chem. Phys.*, 1995, **196**, 1439.

284. P. G. Klein, B. W. Evans and I. M. Ward, *Polymer*, 1998, **39**, 3349.

285. M. D. Shelby, A. J. Hill, M. I. Burgar and G. L. Wilkes, *J. Polym. Sci. Part B – Polym. Phys.*, 2001, **39**, 32.

286. P. X. Wang and I. Ando, *J. Mol. Struct.*, 1998, **447**, 81.

287. R. Kimmich and R. Bachus, *Colloid Polym. Sci.*, 1982, **260**, 911.

288. R. Kimmich, S. Stapf, M. Moller, R. Out and R. O. Seitter, *Macromolecules*, 1994, **27**, 1505.

289. N. Fatkullin and R. Kimmich, *J. Chem. Phys.*, 1994, **101**, 822.

290. K. Takegoshi and K. Hikichi, *J. Chem. Phys.*, 1991, **94**, 3200.

291. F. G. Morin and R. H. Marchessault, *Macromolecules*, 1992, **25**, 576.

292. K. J. McGrath, K. L. Ngai and C. M. Roland, *Macromolecules*, 1992, **25**, 4911.

293. C. Lemenestrel, A. M. Kenwright, P. Sergot, F. Laupretre and L. Monnerie, *Macromolecules*, 1992, **25**, 3020.

294. X. Q. Zhang, K. Takegoshi and K. Hikichi, *Macromolecules*, 1993, **26**, 2198.

295. E. Katoh, H. Kurosu and I. Ando, *J. Mol. Struct.*, 1994, **318**, 123.

296. K. J. McGrath, K. L. Ngai and C. M. Roland, *Macromolecules*, 1995, **28**, 2825.

297. J. L. White, A. J. Dias and J. R. Ashbaugh, *Macromolecules*, 1998, **31**, 1880.

298. L. A. Belfiore, P. M. Henrichs, D. J. Massa, N. Zumbulyadis, W. P. Rothwell and S. L. Cooper, *Macromolecules*, 1983, **16**, 1744.
299. B. J. Cauley, C. Cipriani, K. Ellis, A. K. Roy, A. A. Jones, P. T. Inglefield, B. J. McKinley and R. P. Kambour, *Macromolecules*, 1991, **24**, 403.
300. Y. Liu, M. M. Turnbull, A. A. Jones, P. T. Inglefield and R. P. Kambour, *Solid State Nucl. Magn. Reson.*, 1993, **2**, 289.
301. A. S. Kulik, D. Radloff and H. W. Spiess, *Macromolecules*, 1994, **27**, 3111.
302. K. J. McGrath and C. M. Roland, *J. Non-Cryst. Solids*, 1994, **172**, 891.
303. K. Schmidtrohr, A. S. Kulik, H. W. Beckham, A. Ohlemacher, U. Pawelzik, C. Boeffel and H. W. Spiess, *Macromolecules*, 1994, **27**, 4733.
304. A. S. Kulik, H. W. Beckham, K. Schmidtrohr, D. Radloff, U. Pawelzik, C. Boeffel and H. W. Spiess, *Macromolecules*, 1994, **27**, 4746.
305. K. Kuwabara, H. Kaji, M. Tsuji and F. Horii, *Macromolecules*, 2000, **33**, 7093.
306. H. Kaji, N. Miura and K. Schmidt-Rohr, *Macromolecules*, 2003, **36**, 6100.
307. A. N. Garroway, W. M. Ritchey and W. B. Moniz, *Macromolecules*, 1982, **15**, 1051.
308. J. R. Lyerla, C. S. Yannoni and C. A. Fyfe, *Acc. Chem. Res.*, 1982, **15**, 208.
309. H. Kaji, T. Tai and F. Horii, *Macromolecules*, 2001, **34**, 6318.
310. T. Miyoshi, S. Hayashi, F. Imashiro and A. Kaito, *Macromolecules*, 2002, **35**, 6060.
311. K. Schmidtrohr and H. W. Spiess, *Macromolecules*, 1991, **24**, 5288.
312. A. E. Tonelli, *J. Mol. Struct.*, 1995, **355**, 105.
313. J. Zhao, A. A. Jones, P. T. Inglefield and J. T. Bendler, *Polymer*, 1998, **39**, 1339.
314. P. Wang and I. Ando, *J. Mol. Struct.*, 1999, **508**, 103.
315. T. Miyoshi, K. Takegoshi and T. Terao, *Macromolecules*, 1999, **32**, 8914.
316. T. Miyoshi, S. Hayashi, F. Imashiro and A. Kaito, *Macromolecules*, 2002, **35**, 2624.
317. J. E. Wolak, J. Knutson, J. D. Martin, P. Boyle, A. L. Sargent and J. L. White, *J. Phys. Chem. B*, 2003, **107**, 13293.
318. W. Domberger, D. Reichert, F. Garwe, H. Schneider and E. Donth, *J. Phys. – Condens. Matter*, 1995, **7**, 7419.
319. E. R. deAzevedo, R. W. A. Franco, A. Marletta, R. M. Faria and T. J. Bonagamba, *J. Chem. Phys.*, 2003, **119**, 2923.
320. T. J. Bonagamba, F. Becker-Guedes, E. R. deAzevedo and K. Schmidt-Rohr, *J. Polym. Sci. Part B – Polym. Phys.*, 2001, **39**, 2444.
321. D. Reichert, O. Pascui and M. Beiner, *Macromol. Symp.*, 2002, **184**, 175.
322. T. Miyoshi, O. Pascui and D. Reichert, *Macromolecules*, 2002, **35**, 7178.
323. F. Laupretre, R. P. Eustache and L. Monnerie, *Polymer*, 1995, **36**, 267.
324. L. Heux, J. L. Halary, F. Laupretre and L. Monnerie, *Polymer*, 1997, **38**, 1767.
325. L. Heux, F. Laupretre, J. L. Halary and L. Monnerie, *Polymer*, 1998, **39**, 1269.
326. R. F. Nogueira and M. I. B. Tavares, *Polym. Test.*, 2001, **20**, 379.
327. M. K. Cheung, P. Gao and S. W. Li, *Polymer*, 2003, **44**, 3299.
328. J. Schaefer, E. O. Stejskal, R. A. McKay and W. T. Dixon, *Macromolecules*, 1984, **17**, 1479.
329. J. R. Garbow and J. Schaefer, *Macromolecules*, 1987, **20**, 819.
330. M. D. Poliks and J. Schaefer, *Macromolecules*, 1990, **23**, 3426.
331. M. D. Poliks and J. Schaefer, *Macromolecules*, 1990, **23**, 2682.
332. M. D. Poliks, T. Gullion and J. Schaefer, *Macromolecules*, 1990, **23**, 2678.
333. J. R. Garbow, J. Goetz and J. Asrar, *Macromolecules*, 1998, **31**, 3925.
334. J. H. Wu, C. D. Xiao, A. F. Yee, J. M. Goetz and J. Schaefer, *Macromolecules*, 2000, **33**, 6849.
335. Y. H. Chin and S. Kaplan, *Magn. Reson. Chem.*, 1994, **32**, S53.
336. S. Reddy, P. Desai, A. S. Abhiraman, H. W. Beckham, A. S. Kulik and H. W. Spiess, *Macromolecules*, 1997, **30**, 3293.
337. K. Nagapudi, J. Hunt, C. Shepherd, J. Baker and H. W. Beckham, *Macromol. Chem. Phys.*, 1999, **200**, 2541.
338. K. Nagapudi, J. Leisen, H. W. Beckham and H. W. Gibson, *Macromolecules*, 1999, **32**, 3025.
339. F. Laupretre, A. Gerard, U. Wiesner and L. Monnerie, *Mol. Cryst. Liq. Cryst. Sci. Technol. Sect. A – Mol. Cryst. Liq. Cryst.*, 1994, **254**, 61.
340. U. Wiesner, F. Laupretre and L. Monnerie, *Macromolecules*, 1994, **27**, 3632.
341. L. W. Jelinski, J. J. Dumais and A. K. Engel, *Macromolecules*, 1983, **16**, 492.

342. L. W. Jelinski, J. J. Dumais and A. K. Engel, *ACS Symp. Ser.*, 1984, **247**, 55.
343. A. L. Cholli, J. J. Dumais, A. K. Engel and L. W. Jelinski, *Macromolecules*, 1984, **17**, 2399.
344. F. A. Bovey and L. W. Jelinski, *J. Phys. Chem.*, 1985, **89**, 571.
345. J. J. Dumais, L. W. Jelinski, L. M. Leung, I. Gancarz, A. Galambos and J. T. Koberstein, *Macromolecules*, 1985, **18**, 116.
346. L. W. Jelinski, *Annu. Rev. Mater. Sci.*, 1985, **15**, 359.
347. C. Schmidt, K. J. Kuhn and H. W. Spiess, *Prog. Colloid Polym. Sci.*, 1985, **71**, 71.
348. A. Kintanar, L. W. Jelinski, I. Gancarz and J. T. Koberstein, *Macromolecules*, 1986, **19**, 1876.
349. J. Hirschinger and A. D. English, *J. Magn. Reson.*, 1989, **85**, 542.
350. H. Miura, J. Hirschinger and A. D. English, *Macromolecules*, 1990, **23**, 2169.
351. P. M. Henrichs and T. E. Long, *Macromolecules*, 1991, **24**, 55.
352. L. J. Mathias and R. F. Colletti, *Macromolecules*, 1991, **24**, 5515.
353. S. Kitazawa, T. Hiraoki and A. Tsutsumi, *J. Mol. Struct.*, 1995, **355**, 87.
354. J. Zhao, Y. H. Chin, Y. Liu, A. A. Jones, P. T. Inglefield, R. P. Kambour and D. M. White, *Macromolecules*, 1995, **28**, 3881.
355. J. F. Shi, P. T. Inglefield, A. A. Jones and M. D. Meadows, *Macromolecules*, 1996, **29**, 605.
356. A. D. English, *Korea Polym. J.*, 1996, **4**, 100.
357. F. Horii, H. Kaji, H. Ishida, K. Kuwabara, K. Masuda and T. Tai, *J. Mol. Struct.*, 1998, **441**, 303.
358. T. Kawaguchi, A. Mamada, Y. Hosokawa and F. Horii, *Polymer*, 1998, **39**, 2725.
359. R. D. O'Connor, F. D. Blum, E. Ginsburg and R. D. Miller, *Macromolecules*, 1998, **31**, 4852.
360. C. Hellermark, U. W. Gedde, A. Hult, C. Boeffel, R. H. Boyd and F. Liu, *Macromolecules*, 1998, **31**, 4531.
361. K. Kulbaba, P. M. Macdonald and I. Manners, *Macromolecules*, 1999, **32**, 1321.
362. J. P. Kujanpaa and F. G. Riddell, *J. Chem. Soc., Perkin Trans. 2*, 2000, 2225.
363. R. D. O'Connor, E. J. Ginsburg and F. D. Blum, *J. Chem. Phys.*, 2000, **112**, 7247.
364. S. V. Primak, T. Jin, A. C. Dagger, D. Finotello and E. K. Mann, *Phys. Rev. E*, 2002, **65**.
365. D. J. Schaefer and A. D. English, *Polymer*, 1995, **36**, 2517.
366. S. Rivillon, P. Auroy and B. Deloche, *Phys. Rev. Lett.*, 2000, **84**, 499.
367. H. E. Gottlieb and Z. Luz, *Macromolecules*, 1984, **17**, 1959.
368. T. Miyoshi, K. Takegoshi and K. Hikichi, *Polymer*, 1996, **37**, 11.
369. S. Y. Kwak, S. Y. Kim and N. Nakajima, *J. Polym. Sci. Part B – Polym. Phys.*, 1997, **35**, 709.
370. M. Kanekiyo, M. Kobayashi, I. Ando, H. Kurosu and S. Amiya, *Macromolecules*, 2000, **33**, 7971.
371. S. Schantz and N. Ljungqvist, *Macromolecules*, 1993, **26**, 6517.
372. F. O. Garces, K. Sivadasan, P. Somasundaran and N. J. Turro, *Macromolecules*, 1994, **27**, 272.
373. H. Y. Chien, D. McIntyre, J. L. Cheng and M. Fone, *Polymer*, 1995, **36**, 2559.
374. S. Schantz, *Macromolecules*, 1997, **30**, 1419.
375. T. Miyoshi, K. Takegoshi and K. Hikichi, *Polymer*, 1997, **38**, 2315.
376. C. Wastlund, M. Schmidt, S. Schantz and F. H. J. Maurer, *Polym. Eng. Sci.*, 1998, **38**, 1286.
377. T. R. Lutz, Y. Y. He, M. D. Ediger, H. H. Cao, G. X. Lin and A. A. Jones, *Macromolecules*, 2003, **36**, 1724.
378. Y. Y. He, T. R. Lutz and M. D. Ediger, *Macromolecules*, 2003, **36**, 8040.
379. P. Bergquist, J. F. Shi, J. Zhao, A. A. Jones, P. T. Inglefield and R. P. Kambour, *Macromolecules*, 1998, **31**, 3632.
380. J. B. Miller, K. J. McGrath, C. M. Roland, C. A. Trask and A. N. Garroway, *Macromolecules*, 1990, **23**, 4543.
381. S. Saxena, D. Cizmeciyan and J. A. Kornfield, *Solid State Nucl. Magn. Reson.*, 1998, **12**, 165.
382. A. Tezuka, K. Takegoshi and K. Hikichi, *J. Mol. Struct.*, 1995, **355**, 1.
383. Y. H. Chin, P. T. Inglefield and A. A. Jones, *Macromolecules*, 1993, **26**, 5372.
384. G. C. Chung, J. A. Kornfield and S. D. Smith, *Macromolecules*, 1994, **27**, 964.
385. U. Mukai, K. K. Gleason, A. S. Argon and R. E. Cohen, *Macromolecules*, 1995, **28**, 4899.
386. Y. H. Chin, C. Zhang, P. Wang, P. T. Inglefield, A. A. Jones, R. P. Kambour, J. T. Bendler and D. M. White, *Macromolecules*, 1992, **25**, 3031.
387. J. Brus, J. Dybal, P. Schmidt, J. Kratochvil and J. Baldrian, *Macromolecules*, 2000, **33**, 6448.
388. M. Afeworki and J. Schaefer, *Macromolecules*, 1992, **25**, 4097.
389. J. M. Goetz, J. H. Wu, A. F. Yee and J. Schaefer, *Macromolecules*, 1998, **31**, 3016.
390. E. Lindner, M. Kemmler, T. Schneller and H. A. Mayer, *Inorg. Chem.*, 1995, **34**, 5489.

391. I. Quijada-Garrido, M. Wilhelm, H. W. Spiess and J. M. Barrales-Rienda, *Macromol. Chem. Phys.*, 1998, **199**, 985.
392. T. Miyoshi, K. Takegoshi and T. Terao, *Macromolecules*, 1997, **30**, 6582.
393. D. J. Schaefer, R. J. Schadt, K. H. Gardner, V. Gabara, S. R. Allen and A. D. English, *Macromolecules*, 1995, **28**, 1152.
394. L. S. Loo, R. E. Cohen and K. K. Gleason, *Science*, 2000, **288**, 116.
395. M. de Langen, H. Luigjes and K. O. Prins, *Polymer*, 2000, **41**, 1183.
396. A. G. S. Hollander and K. O. Prins, *Int. J. Thermophys.*, 2001, **22**, 357.
397. M. T. Hansen, B. Blumich, C. Boeffel, H. W. Spiess, L. Morbitzer and A. Zembrod, *Macromolecules*, 1992, **25**, 5542.
398. T. Kameda and T. Asakura, *Polymer*, 2003, **44**, 7539.
399. M. Geppi, F. Ciardelli, C. A. Veracini, C. Forte, G. Cecchin and P. Ferrari, *Polymer*, 1997, **38**, 5713.
400. G. Xue, G. D. Ji, H. Yan and M. M. Guo, *Macromolecules*, 1998, **31**, 7706.
401. P. Sotta and B. Deloche, *J. Chem. Phys.*, 1994, **100**, 4591.
402. U. Heuert, M. Knorgen, H. Menge, G. Scheler and H. Schneider, *Polym. Bull.*, 1996, **37**, 489.
403. H. Menge, S. Hotopf and H. Schneider, *Kautsch. Gummi Kunstst.*, 1997, **50**, 268.
404. P. Ekanayake, H. Menge and H. Schneider, *Polym. Bull.*, 2000, **44**, 173.
405. P. Ekanayake, H. Menge, H. Schneider, M. E. Ries, M. G. Brereton and P. G. Klein, *Macromolecules*, 2000, **33**, 1807.
406. J. F. Shi, L. C. Dickinson, W. J. MacKnight, J. C. W. Chien, C. G. Zhang, Y. Liu, Y. H. Chin, A. A. Jones and P. T. Inglefield, *Macromolecules*, 1993, **26**, 1008.
407. K. Saalwachter, *Chem. Phys. Lett.*, 2002, **362**, 331.
408. K. Saalwachter, *Macromol. Rapid Commun.*, 2002, **23**, 286.
409. H. W. Spiess, *Adv. Polym. Sci.*, 1985, **66**, 23.
410. H. W. Spiess, *Pure Appl. Chem.*, 1985, **57**, 1617.
411. H. W. Spiess, *Makromol. Chem. – Macromol. Symp.*, 1986, **4**, 227.
412. J. A. Kornfield, H. W. Spiess, H. Nefzger, H. Hayen and C. D. Eisenbach, *Macromolecules*, 1991, **24**, 4787.
413. H. W. Spiess, *Annu. Rev. Mater. Sci.*, 1991, **21**, 131.
414. S. C. Kuebler, D. J. Schaefer, C. Boeffel, U. Pawelzik and H. W. Spiess, *Macromolecules*, 1997, **30**, 6597.
415. C. Schmidt, B. Blumich, S. Wefing, S. Kaufmann and H. W. Spiess, *Ber. Bunsen-Gesellschaft – Phys. Chem. Chem. Phys.*, 1987, **91**, 1141.
416. S. Wefing, S. Kaufmann and H. W. Spiess, *J. Chem. Phys.*, 1988, **89**, 1234.
417. U. Pschorn, E. Rossler, H. Sillescu, S. Kaufmann, D. Schaefer and H. W. Spiess, *Macromolecules*, 1991, **24**, 398.
418. J. Hirschinger, D. Schaefer, H. W. Spiess and A. J. Lovinger, *Macromolecules*, 1991, **24**, 2428.
419. D. Schaefer and H. W. Spiess, *J. Chem. Phys.*, 1992, **97**, 7944.
420. A. Heuer, J. Leisen, S. C. Kuebler and H. W. Spiess, *J. Chem. Phys.*, 1996, **105**, 7088.
421. U. Wiesner, H. W. Spiess, M. Muller, F. Kremer, F. Laupretre, J. L. Halary and L. Monnerie, *Acta Polym.*, 1996, **47**, 429.
422. U. Tracht, M. Wilhelm, A. Heuer, H. Feng, K. Schmidt-Rohr and H. W. Spiess, *Phys. Rev. Lett.*, 1998, **81**, 2727.
423. U. Tracht, H. Wilhelm, A. Heuer and H. W. Spiess, *J. Magn. Reson.*, 1999, **140**, 460.
424. M. Wilhelm and H. W. Spiess, *Macromolecules*, 1996, **29**, 1088.
425. M. Wind, R. Graf, A. Heuer and H. W. Spiess, *Phys. Rev. Lett.*, 2003, **91**.
426. U. Tracht, A. Heuer and H. W. Spiess, *J. Chem. Phys.*, 1999, **111**, 3720.
427. J. Clauss, K. Schmidtrohr, A. Adam, C. Boeffel and H. W. Spiess, *Macromolecules*, 1992, **25**, 5208.
428. S. P. Brown, I. Schnell, J. D. Brand, K. Mullen and H. W. Spiess, *J. Mol. Struct.*, 2000, **521**, 179.
429. H. W. Spiess, *Macromol. Symp.*, 2001, **174**, 111.
430. M. Wind, U. M. Wiesler, K. Saalwachter, K. Mullen and H. W. Spiess, *Adv. Mater.*, 2001, **13**, 752.
431. S. P. Brown, T. Schaller, U. P. Seelbach, F. Koziol, C. Ochsenfeld, F. G. Klarner and H. W. Spiess, *Angew. Chem., Int. Ed.*, 2001, **40**, 717.
432. A. Schmidt, S. Lehmann, M. Georgelin, G. Katana, K. Mathauer, F. Kremer, K. Schmidtrohr, C. Boeffel, G. Wegner and W. Knoll, *Macromolecules*, 1995, **28**, 5487.
433. M. Wind, K. Saalwachter, U. M. Wiesler, K. Mullen and H. W. Spiess, *Macromolecules*, 2002, **35**, 10071.

434. M. Mierzwa, G. Floudas, M. Neidhofer, R. Graf, H. W. Spiess, W. H. Meyer and G. Wegner, *J. Chem. Phys.*, 2002, **117**, 6289.

435. R. Poupko, Z. Olender, D. Reichert and Z. Luz, *J. Magn. Reson. Ser. A*, 1994, **106**, 113.

436. E. C. Reynhardt and L. Latanowicz, *Chem. Phys. Lett.*, 1996, **251**, 235.

437. H. R. Tang and P. S. Belton, *Solid State Nucl. Magn. Reson.*, 1998, **12**, 21.

438. Y. L. Wang, H. R. Tang and P. S. Belton, *J. Phys. Chem. B*, 2002, **106**, 12834.

439. H. R. Tang and P. S. Belton, *Solid State Nucl. Magn. Reson.*, 2002, **21**, 117.

440. M. I. B. Tavares, A. L. B. S. Bathista, E. O. Silva, N. P. Filho and J. S. Nogueira, *Carbohydr. Polym.*, 2003, **53**, 213.

441. H. R. Tang and B. P. Hills, *Biomacromolecules*, 2003, **4**, 1269.

442. B. Stevensson, C. Hoog, K. Ulfstedt-Jakel, Z. Huang, G. Widmalm and A. Maliniak, *J. Phys. Chem. B*, 2000, **104**, 6065.

443. S. J. Kitchin and T. K. Halstead, *Solid State Nucl. Magn. Reson.*, 1996, **7**, 27.

444. A. S. Kulik and J. Haverkamp, *Carbohydr. Polym.*, 1997, **34**, 49.

445. D. van Dusschoten, U. Tracht, A. Heuer and H. W. Spiess, *J. Phys. Chem. A*, 1999, **103**, 8359.

446. M. Paris, H. Bizot, J. Emery, J. Y. Buzare and A. Buleon, *Int. J. Biol. Macromol.*, 2001, **29**, 137.

447. H. R. Tang, P. S. Belton, A. Ng, K. W. Waldron and P. Ryden, *Spectrochim. Acta Part A – Mol. Biomol. Spectrosc.*, 1999, **55**, 883.

448. S. Hediger, L. Emsley and M. Fischer, *Carbohydr. Res.*, 1999, **322**, 102.

449. A. M. Gil, M. Lopes, J. Rocha and C. P. Neto, *Int. J. Biol. Macromol.*, 1997, **20**, 293.

450. B. Yan and R. E. Stark, *Macromolecules*, 1998, **31**, 2600.

451. R. E. Stark, B. Yan, A. K. Ray, Z. Chen, X. Fang and J. R. Garbow, *Solid State Nucl. Magn. Reson.*, 2000, **16**, 37.

452. A. J. Wand, *Nat. Struct. Biol.*, 2001, **8**, 926.

453. N. Sinha and S. J. Smith-Gill, *Protein Pept. Lett.*, 2002, **9**, 367.

454. F. Parak, *Rep. Prog. Phys.*, 2004, **66**, 103.

455. E. Oldfield, D. Chapman and W. Derbyshi, *Chem. Phys. Lipids*, 1972, **9**, 69.

456. D. A. Torchia, *Annu. Rev. Biophys. Bioeng.*, 1984, **13**, 125.

457. E. R. Andrew, D. N. Bone, D. J. Bryant, E. M. Cashell, R. Gaspar and Q. A. Meng, *Pure Appl. Chem.*, 1982, **54**, 585.

458. E. R. Andrew, *Polymer*, 1985, **26**, 190.

459. J. P. Korb and R. G. Bryant, *J. Chem. Phys.*, 2001, **115**, 10964.

460. Y. L. Wang, P. S. Belton and H. R. Tang, *Chem. Phys. Lett.*, 1997, **268**, 387.

461. V. D. Fedotov, N. P. Obuchov, R. A. Zadikhanov, J. Spevacek and J. Straka, *Appl. Magn. Reson.*, 1993, **4**, 491.

462. A. G. Krushelnitsky, V. D. Fedotov, J. Spevacek and J. Straka, *J. Biomol. Struct. Dyn.*, 1996, **14**, 211.

463. K. Yoza, Z. Y. Wang, M. Kobayashi and T. Nozawa, *Photosynth. Res.*, 1997, **52**, 167.

464. M. Bouchard, C. Le Guerneve and M. Auger, *Biochim. Biophys. Acta – Biomembr.*, 1998, **1415**, 181.

465. L. Calucci, C. Forte, L. Galleschi, M. Geppi and S. Ghiringhelli, *Int. J. Biol. Macromol.*, 2003, **32**, 179.

466. J. M. Rydzewski, S. X. Wang, A. Stevens, C. Serdahl and T. Schleich, *Exp. Eye Res.*, 1993, **56**, 305.

467. K. Arnold, J. Kaufmann, L. Naji, J. Schiller and D. Huster, *Biophys. J.*, 2000, **78**, 2844Pos.

468. D. Huster, J. Schiller and K. Arnold, *Magn. Reson. Med.*, 2002, **48**, 624.

469. L. Naji, J. Kaufmann, D. Huster, J. Schiller and K. Arnold, *Carbohydr. Res.*, 2000, **327**, 439.

470. W. Nusser and R. Kimmich, *J. Phys. Chem.*, 1990, **94**, 5637.

471. P. Belton and Y. L. Wang, *J. Mol. Struct.*, 2002, **602**, 71.

472. J. Kikuchi, M. P. Williamson, K. Shimada and T. Asakura, *Photosynth. Res.*, 2000, **63**, 259.

473. M. D. Sefcik, J. Schaefer, E. O. Stejskal, R. A. McKay, J. F. Ellena, S. W. Dodd and M. F. Brown, *Biochem. Biophys. Res. Commun.*, 1983, **114**, 1048.

474. S. K. Straus, T. Bremi and R. R. Ernst, *J. Biomol. NMR*, 1997, **10**, 119.

475. P. J. R. Spooner and A. Watts, *Biochemistry*, 1991, **30**, 3880.

476. T. M. Alam and G. P. Drobny, *Chem. Rev.*, 1991, **91**, 1545.

477. P. Tsang, D. R. Kearns and R. R. Vold, *J. Am. Chem. Soc.*, 1992, **114**, 6585.

478. M. Stumber, M. Geyer, R. Graf, H. R. Kalbitzer, K. Scheffzek and U. Haeberlen, *J. Mol. Biol.*, 2002, **323**, 899.

479. H. Saito, K. Yamamoto, S. Tuzi and S. Yamaguchi, *Biochim. Biophys. Acta – Biomembr.*, 2003, **1616**, 127.

480. M. A. Danielson and J. J. Falke, *Annu. Rev. Biophys. Biomol. Struct.*, 1996, **25**, 163.

481. S. K. Sarkar, C. E. Sullivan and D. A. Torchia, *J. Biol. Chem.*, 1983, **258**, 9762.

482. A. Perry, M. P. Stypa, B. K. Tenn and K. K. Kumashiro, *Biophys. J.*, 2002, **82**, 1086.

483. N. M. Tsvetkova, B. L. Phillips, L. M. Crowe, J. H. Crowe and S. H. Risbud, *Biophys. J.*, 1998, **75**, 2947.

484. T. Odahara, S. Nishimoto, N. Katsutani, Y. Kyogoku, Y. Morimoto, A. Matsushiro and H. Akutsu, *J. Biochem.*, 1994, **115**, 270.

485. A. Kim, I. C. Jeong, Y. B. Shim, S. W. Kang and J. S. Park, *J. Biochem. Mol. Biol.*, 2001, **34**, 446.

486. B. Bechinger, M. Zasloff and S. J. Opella, *Biophys. J.*, 1998, **74**, 981.

487. M. Auger, I. C. P. Smith and H. C. Jarrell, *Biophys. J.*, 1991, **59**, 31.

488. T. Arakawa, K. Shimono, S. Yamaguchi, S. Tuzi, Y. Sudo, N. Kamo and H. Saito, *FEBS Lett.*, 2003, **536**, 237.

489. J. R. Long, B. Q. Sun, A. Bowen and R. G. Griffin, *J. Am. Chem. Soc.*, 1994, **116**, 11950.

490. J. J. Buffy, A. J. Waring, R. I. Lehrer and M. Hong, *Biochemistry*, 2003, **42**, 13725.

491. P. Barre, O. Zschornig, K. Arnold and D. Huster, *Biochemistry*, 2003, **42**, 8377.

492. P. Barre, S. Yamaguchi, H. Saito and D. Huster, *Eur. Biophys. J. Biophys. Lett.*, 2003, **32**, 578.

493. J. R. Garbow, G. S. Jacob, E. O. Stejskal and J. Schaefer, *Biochemistry*, 1989, **28**, 1362.

494. P. S. Belton, *Prog. Biophys. Mol. Biol.*, 1994, **61**, 61.

495. J. M. Zanotti, M. C. Bellissent-Funel and J. Parello, *Physica B*, 1997, **234**, 228.

496. J. M. Zanotti, M. C. Bellissent-Funel and J. Parello, *Biophys. J.*, 1999, **76**, 2390.

497. E. Alberti, S. M. Gilbert, A. S. Tatham, P. R. Shewry, A. Naito, K. Okuda, H. Saito and A. M. Gil, *Biopolymers*, 2002, **65**, 158.

498. M. J. Duer, N. McDougal and R. C. Murray, *Phys. Chem. Chem. Phys.*, 2003, **5**, 2894.

499. S. D. Swanson and R. G. Bryant, *Biopolymers*, 1991, **31**, 967.

500. A. M. Gil, K. Masui, A. Naito, A. S. Tatham, P. S. Belton and H. Saito, *Biopolymers*, 1997, **41**, 289.

501. K. Weisz, G. Grobner, C. Mayer, J. Stohrer and G. Kothe, *Biochemistry*, 1992, **31**, 1100.

502. M. H. P. vanGenderen, M. Pfaadt, C. Moller, S. Valiyaveettil and H. W. Spiess, *J. Am. Chem. Soc.*, 1996, **118**, 3661.

503. P. T. F. Williamson, J. A. Watts, G. H. Addona, K. W. Miller and A. Watts, *Proc. Natl Acad. Sci. USA*, 2001, **98**, 2346.

504. C. M. Gall, J. A. Diverdi and S. J. Opella, *J. Am. Chem. Soc.*, 1981, **103**, 5039.

505. T. Hiraoki, A. Kogame, N. Nishi and A. Tsutsumi, *J. Mol. Struct.*, 1998, **441**, 243.

506. M. G. Usha, W. L. Peticolas and R. J. Wittebort, *Biochemistry*, 1991, **30**, 3955.

507. C. M. Gall, T. A. Cross, J. A. Diverdi and S. J. Opella, *Proc. Natl Acad. Sci. USA – Biol. Sci.*, 1982, **79**, 101.

508. P. J. R. Spooner and A. Watts, *Biochemistry*, 1991, **30**, 3871.

509. K. J. Shon, Y. G. Kim, L. A. Colnago and S. J. Opella, *Science*, 1991, **252**, 1303.

510. V. Copie, A. E. McDermott, K. Beshah, J. C. Williams, M. Spijkerassink, R. Gebhard, J. Lugtenburg, J. Herzfeld and R. G. Griffin, *Biochemistry*, 1994, **33**, 3280.

511. A. Naito, T. Iizuka, S. Tuzi, W. S. Price, K. Hayamizu and H. Saito, *J. Mol. Struct.*, 1995, **355**, 55.

512. A. Tamura, M. Matsushita, A. Naito, S. Kojima, K. I. Miura and K. Akasaka, *Protein Sci.*, 1996, **5**, 127.

513. M. Kamihira, A. Naito, S. Tuzi and H. Saito, *J. Phys. Chem. A*, 1999, **103**, 3356.

514. J. W. Mack, M. G. Usha, J. Long, R. G. Griffin and R. J. Wittebort, *Biopolymers*, 2000, **53**, 9.

515. L. W. Jelinski, C. E. Sullivan, L. S. Batchelder and D. A. Torchia, *Biophys. J.*, 1980, **32**, 515.

516. L. W. Jelinski, C. E. Sullivan and D. A. Torchia, *Nature*, 1980, **284**, 531.

517. L. S. Batchelder, C. E. Sullivan, L. W. Jelinski and D. A. Torchia, *Proc. Natl Acad. Sci. USA – Biol. Sci.*, 1982, **79**, 386.

518. D. A. Torchia, L. S. Batchelder, W. W. Fleming, L. W. Jelinski, S. K. Sarkar and C. E. Sullivan, *Ciba Found. Symp.*, 1983, **93**, 98.

519. D. Reichert, O. Pascui, E. R. deAzevedo, T. J. Bonagamba, K. Arnold and D. Huster, *Magn. Reson. Chem.*, 2004, **42**, 276.

520. A. H. Simmons, C. A. Michal and L. W. Jelinski, *Science*, 1996, **271**, 84.

521. Z. T. Yang, O. Liivak, A. Seidel, G. LaVerde, D. B. Zax and L. W. Jelinski, *J. Am. Chem. Soc.*, 2000, **122**, 9019.

522. A. I. Kishore, M. E. Herberstein, C. L. Craig and F. Separovic, *Biopolymers*, 2001, **61**, 287.

523. A. C. Wang, M. A. Kennedy, B. R. Reid and G. P. Drobny, *J. Magn. Reson. Ser. B*, 1994, **105**, 1.

524. G. A. Meints and G. P. Drobny, *Biochemistry*, 2001, **40**, 12436.

525. A. Krushelnitsky, D. Reichert, G. Hempel, V. Fedotov, H. Schneider, L. Yagodina and A. Schulga, *J. Magn. Reson.*, 1999, **138**, 244.

526. D. Huster, L. S. Xiao and M. Hong, *Biochemistry*, 2001, **40**, 7662.

527. S. B. Kennedy, E. R. deAzevedo, W. A. Petka, T. P. Russell, D. A. Tirrell and M. Hong, *Macromolecules*, 2001, **34**, 8675.

528. C. E. Bronniman, N. M. Szeverenyi and G. E. Maciel, *J. Chem. Phys.*, 1983, **79**, 3694.

529. D. L. Vanderhart, *J. Magn. Reson.*, 1987, **72**, 13.

530. H. H. Limbach, B. Wehrle, M. Schlabach, R. Kendrick and C. S. Yannoni, *J. Magn. Reson.*, 1988, **77**, 84.

531. R. Tycko and G. Dabbagh, *Isr. J. Chem.*, 1992, **32**, 179.

532. B. H. Meier, *Adv. Magn. Opt. Reson.*, 1994, **18**, 1.

533. Z. Olender, D. Reichert, A. Muller, H. Zimmermann, R. Poupko and Z. Luz, *J. Magn. Reson. Ser. A*, 1996, **120**, 31.

534. D. Reichert, G. Hempel, R. Poupko, Z. Luz, Z. Olejniczak and P. Tekely, *Solid State Nucl. Magn. Reson.*, 1998, **13**, 137.

535. P. Tekely, M. J. Potrzebowski, Y. Dusausoy and Z. Luz, *Chem. Phys. Lett.*, 1998, **291**, 471.

536. J. R. Sachleben, V. Frydman and L. Frydman, *J. Am. Chem. Soc.*, 1996, **118**, 9786.

537. D. P. Weliky and R. Tycko, *J. Am. Chem. Soc.*, 1996, **118**, 8487.

538. K. Saalwachter and K. Schmidt-Rohr, *J. Magn. Reson.*, 2000, **145**, 161.

539. P. Tekely, *Mol. Phys.*, 1992, **75**, 747.

540. M. Bender, P. Holstein and D. Geschke, *Mol. Cryst. Liq. Cryst.*, 2001, **363**, 85.

541. M. Gentzler, S. Patil, J. A. Reimer and M. M. Denn, *Solid State Nucl. Magn. Reson.*, 1998, **12**, 97.

542. M. Matsui, Y. Yamane, H. Kimura, S. Kuroki, I. Ando, K. Fu and J. Watanabe, *J. Mol. Struct.*, 2003, **650**, 175.

543. R. L. Silvestri, J. L. Koenig, W. R. Likavec and W. M. Ritchey, *Polymer*, 1995, **36**, 2347.

544. M. Giotto, D. Azar, J. Gosselin, P. T. Inglefield and A. A. Jones, *J. Polym. Sci. Part B – Polym. Phys.*, 2001, **39**, 1548.

545. M. Mizuno, A. Hirai, H. Matsuzawa, K. Endo, M. Suhara, M. Kenmotsu and C. D. Han, *Macromolecules*, 2002, **35**, 2595.

546. M. Geppi, S. Pizzanelli and C. A. Veracini, *Chem. Phys. Lett.*, 2001, **343**, 513.

547. P. J. Sebastiao, A. C. Ribeiro, H. T. Nguyen and F. Noack, *J. Physique II*, 1995, **5**, 1707.

548. F. Noack, M. Notter and W. Weiss, *Liq. Cryst.*, 1988, **3**, 907.

549. U. Zeuner, T. Dippel, F. Noack, K. Muller, C. Mayer, N. Heaton and G. Kothe, *J. Chem. Phys.*, 1992, **97**, 3794.

550. J. Leisen, A. Ohlemacher, C. Boeffel and H. W. Spiess, *Ber. Bunsen-Gesellschaft – Phys. Chem. Chem. Phys.*, 1993, **97**, 1306.

551. J. Leisen, M. Werth, C. Boeffel and H. W. Spiess, *J. Chem. Phys.*, 1992, **97**, 3749.

552. M. Werth, J. Leisen, C. Boeffel, R. Y. Dong and H. W. Spiess, *J. Physique II*, 1993, **3**, 53.

553. A. Maliniak, S. Greenbaum, R. Poupko, H. Zimmermann and Z. Luz, *J. Phys. Chem.*, 1993, **97**, 4832.

554. S. Zamir, R. Poupko, Z. Luz, B. Huser, C. Boeffel and H. Zimmermann, *J. Am. Chem. Soc.*, 1994, **116**, 1973.

555. D. Pressner, C. Goltner, H. W. Spiess and K. Mullen, *Acta Polym.*, 1994, **45**, 188.

556. J. Leisen, C. Boeffel, H. W. Spiess, D. Y. Yoon, M. H. Sherwood, M. Kawasumi and V. Percec, *Macromolecules*, 1995, **28**, 6937.

557. L. Calucci, H. Zimmermann, R. Poupko and Z. Luz, *J. Phys. Chem.*, 1995, **99**, 14942.

558. R. Kannan, T. Sen, R. Poupko, Z. Luz and H. Zimmermann, *J. Phys. Chem. B*, 2003, **107**, 13033.

559. T. Yamanobe, M. Tsukahara, T. Komoto, J. Watanabe, I. Ando, I. Uematsu, K. Deguchi, T. Fujito and M. Imanari, *Macromolecules*, 1988, **21**, 48.

560. H. Zimmermann, V. Bader, R. Poupko, E. J. Wachtel and Z. Luz, *J. Am. Chem. Soc.*, 2002, **124**, 15286.

561. Z. Luz, R. Poupko, E. J. Wachtel, H. Zimmermann and V. Bader, *Mol. Cryst. Liq. Cryst.*, 2003, **397**, 367.

562. P. Holstein, M. Bender, M. Winkler and D. Geschke, *Polym. Adv. Technol.*, 1998, **9**, 659.

563. J. Lu, P. A. Mirau, I. D. Shin, S. Nojima and A. E. Tonelli, *Macromol. Chem. Phys.*, 2002, **203**, 71.

564. F. C. Schilling, P. Sozzani and F. A. Bovey, *Macromolecules*, 1991, **24**, 4369.

565. F. C. Schilling, K. R. Amundson and P. Sozzani, *Macromolecules*, 1994, **27**, 6498.

566. S. Matsui, T. Terao and A. Saika, *J. Chem. Phys.*, 1982, **77**, 1788.

567. R. L. Vold, R. R. Vold and N. J. Heaton, *Adv. Magn. Reson.*, 1989, **131**, 17.

568. D. W. Aksnes, L. Gjerdaker and L. Kimtys, *J. Mol. Struct.*, 1999, **509**, 297.

569. R. Decressain, E. Cochin and L. Carpentier, *J. Physique IV*, 2000, **10**, 299.
570. J. Schmider and K. Muller, *J. Phys. Chem. A*, 1998, **102**, 1181.
571. A. Comotti, M. C. Gallazzi, R. Simonutti and P. Sozzani, *Chem. Mater.*, 1998, **10**, 3589.
572. A. Comotti, R. Simonutti, S. Stramare and P. Sozzani, *Nanotechnology*, 1999, **10**, 70.
573. C. A. Fyfe and A. C. Diaz, *J. Phys. Chem. B*, 2002, **106**, 2261.
574. E. Meirovitch, S. B. Rananavare and J. H. Freed, *J. Phys. Chem.*, 1987, **91**, 5014.
575. E. Gelerinter, Z. Luz, R. Poupko and H. Zimmermann, *J. Phys. Chem.*, 1990, **94**, 5391.
576. R. Poupko, E. Furman, K. Muller and Z. Luz, *J. Phys. Chem.*, 1991, **95**, 407.
577. G. H. Penner, J. M. Polson, C. Stuart, G. Ferguson and B. Kaitner, *J. Phys. Chem.*, 1992, **96**, 5121.
578. P. Girard, A. E. Aliev, F. Guillaume, K. D. M. Harris, M. D. Hollingsworth, A. J. Dianoux and P. Jonsen, *Physica B*, 1997, **234**, 112.
579. P. S. Sidhu, G. H. Penner, K. R. Jeffrey, B. Y. Zhao, Z. L. Wang and I. Goh, *J. Phys. Chem. B*, 1997, **101**, 9087.
580. A. E. Aliev and K. D. M. Harris, *J. Phys. Chem. A*, 1997, **101**, 4541.
581. E. Zaborowski, H. Zimmermann and S. Vega, *J. Am. Chem. Soc.*, 1998, **120**, 8113.
582. P. Girard, A. E. Aliev, F. Guillaume, K. D. M. Harris, M. D. Hollingsworth, A. J. Dianoux and P. Jonsen, *J. Chem. Phys.*, 1998, **109**, 4078.
583. A. Desmedt, S. J. Kitchin, F. Guillaume, M. Couzi, K. D. M. Harris and E. H. Bocanegra, *Phys. Rev. B*, 2001, **6405**.
584. K. Nagashima and F. D. Blum, *Colloids Surf. A – Physicochem. Eng. Aspects*, 2001, **176**, 17.
585. M. Bach-Verges, S. J. Kitchin, K. D. M. Harris, M. Zugic and C. A. Koh, *J. Phys. Chem. B*, 2001, **105**, 2699.
586. Z. Tosner, J. Lang, D. Sandstrom, O. Petrov and J. Kowalewski, *J. Phys. Chem. A*, 2002, **106**, 8870.
587. P. S. Sidhu, G. A. Enright, J. A. Ripmeester and G. H. Penner, *J. Phys. Chem. B*, 2002, **106**, 8569.
588. M. Bach-Verges, S. J. Kitchin, G. B. Hix, K. D. M. Harris and A. E. Aliev, *Chem. Mater.*, 2002, **14**, 2656.
589. R. C. Zeigler and G. E. Maciel, *J. Am. Chem. Soc.*, 1991, **113**, 6349.
590. F. D. Blum, G. Xu, M. H. Liang and C. G. Wade, *Macromolecules*, 1996, **29**, 8740.
591. W. Y. Lin and F. D. Blum, *Macromolecules*, 1997, **30**, 5331.
592. W. Y. Lin and F. D. Blum, *Macromolecules*, 1998, **31**, 4135.
593. W. Y. Lin and F. D. Blum, *J. Am. Chem. Soc.*, 2001, **123**, 2032.
594. F. D. Blum, W. Y. Lin and C. E. Porter, *Colloid Polym. Sci.*, 2003, **281**, 197.
595. G. P. Wang, T. C. Chang, Y. S. Hong and Y. S. Chiu, *Polymer*, 2002, **43**, 2191.
596. Y. S. Chiu, K. H. Wu and T. C. Chang, *Eur. Polym. J.*, 2003, **39**, 2253.
597. F. Aguilar-Parrilla, R. M. Claramunt, C. Lopez, D. Sanz, H. H. Limbach and J. Elguero, *J. Phys. Chem.*, 1994, **98**, 8752.
598. N. A. Melosh, P. Lipic, F. S. Bates, F. Wudl, G. D. Stucky, G. H. Fredrickson and B. F. Chmelka, *Macromolecules*, 1999, **32**, 4332.
599. M. Pursch, L. C. Sander, H. J. Egelhaaf, M. Raitza, S. A. Wise, D. Oelkrug and K. Albert, *J. Am. Chem. Soc.*, 1999, **121**, 3201.
600. A. Badia, W. Gao, S. Singh, L. Demers, L. Cuccia and L. Reven, *Langmuir*, 1996, **12**, 1262.
601. S. Aime, D. Braga, R. Gobetto, F. Grepioni and A. Orlandi, *Inorg. Chem.*, 1991, **30**, 951.
602. M. I. Altbach, Y. Hiyama, R. J. Wittebort and L. G. Butler, *Inorg. Chem.*, 1990, **29**, 741.
603. K. Kulbaba, I. Manners and P. M. Macdonald, *Macromolecules*, 2002, **35**, 10014.
604. G. W. Wagner and B. E. Hanson, *Inorg. Chem.*, 1987, **26**, 2019.
605. S. Bachmann, C. Hellriegel, J. Wegmann, H. Handel and K. Albert, *Solid State Nucl. Magn. Reson.*, 2000, **17**, 39.
606. S. Stapf and R. Kimmich, *Macromolecules*, 1996, **29**, 1638.
607. T. Zavada and R. Kimmich, *Phys. Rev. E*, 1999, **59**, 5848.
608. Y. Z. Khimyak and J. Klinowski, *Phys. Chem. Chem. Phys.*, 2001, **3**, 616.
609. L. Q. Wang and G. J. Exarhos, *J. Phys. Chem. B*, 2003, **107**, 443.
610. R. Suresh, S. Vasudevan and K. V. Ramanathan, *Chem. Phys. Lett.*, 2003, **371**, 118.
611. S. M. De Paul, J. W. Zwanziger, R. Ulrich, U. Wiesner and H. W. Spiess, *J. Am. Chem. Soc.*, 1999, **121**, 5727.
612. L. Q. Wang, J. Liu, G. J. Exarhos, K. Y. Flanigan and R. Bordia, *J. Phys. Chem. B*, 2000, **104**, 2810.
613. V. Nasreddine, J. Halla and L. Reven, *Macromolecules*, 2001, **34**, 7403.
614. H. E. Gottlieb and Z. Luz, *J. Magn. Reson.*, 1983, **54**, 257.

615. E. Lifshitz, A. H. Francis, S. Vega and Z. Luz, *Abstr. Pap. Am. Chem. Soc.*, 1987, **194**, 100.

616. J. E. Gambogi and F. D. Blum, *Macromolecules*, 1992, **25**, 4526.

617. E. Lindner, F. Hoehn, T. Salesch, H. A. Mayer, S. Singh and K. Muller, *Z. Anorg. Allg. Chem.*, 2002, **628**, 1124.

618. W. J. Shaw, J. R. Long, A. A. Campbell, P. S. Stayton and G. P. Drobny, *J. Am. Chem. Soc.*, 2000, **122**, 7118.

619. D. W. Aksnes and L. Kimty, *Magn. Reson. Chem.*, 1998, **36**, 747.

620. W. Bohlmann, D. Michel and J. Roland, *Magn. Reson. Chem.*, 1999, **37**, S126.

621. D. W. Aksnes, L. Gjerdaker, L. Kimtys and K. Forland, *Phys. Chem. Chem. Phys.*, 2003, **5**, 2680.

622. Z. Luz and A. J. Vega, *J. Phys. Chem.*, 1986, **90**, 4903.

623. A. J. Vega and Z. Luz, *Zeolites*, 1988, **8**, 19.

624. I. Kustanovich, Z. Luz, S. Vega and A. J. Vega, *J. Phys. Chem.*, 1990, **94**, 3138.

625. O. Isfort, B. Boddenberg, F. Fujara and R. Grosse, *Chem. Phys. Lett.*, 1998, **288**, 71.

626. A. Gedeon, D. E. Favre, D. Reichert, J. MacNeil and B. F. Chmelka, *J. Phys. Chem. A*, 1999, **103**, 6691.

627. T. Sato, K. Kunimori and S. Hayashi, *Phys. Chem. Chem. Phys.*, 1999, **1**, 3839.

628. E. Gedat, A. Schreiber, J. Albrecht, T. Emmler, I. Shenderovich, G. H. Findenegg, H. H. Limbach and G. Buntkowsky, *J. Phys. Chem. B*, 2002, **106**, 1977.

629. S. Hayashi, *Microporous Mesoporous Mater.*, 2003, **66**, 253.

630. I. Kustanovich, D. Fraenkel, Z. Luz, S. Vega and H. Zimmermann, *J. Phys. Chem.*, 1988, **92**, 4134.

631. M. Wilhelm, A. Firouzi, D. E. Favre, L. M. Bull, D. J. Schaefer and B. F. Chmelka, *J. Am. Chem. Soc.*, 1995, **117**, 2923.

632. D. J. Schaefer, D. E. Favre, M. Wilhelm, S. J. Weigel and B. F. Chmelka, *J. Am. Chem. Soc.*, 1997, **119**, 9252.

633. B. Geil, O. Isfort, B. Boddenberg, D. E. Favre, B. F. Chmelka and F. Fujara, *J. Chem. Phys.*, 2002, **116**, 2184.

634. D. E. Favre, D. J. Schaefer, S. M. Auerbach and B. F. Chmelka, *Phys. Rev. Lett.*, 1998, **81**, 5852.

635. P. C. M. M. Magusin, D. Schuring, E. M. van Oers, J. W. de Haan and R. A. van Santen, *Magn. Reson. Chem.*, 1999, **37**, S108.

636. P. Judeinstein, J. Titman, M. Stamm and H. Schmidt, *Chem. Mater.*, 1994, **6**, 127.

637. M. Forsyth, M. Garcia, D. R. MacFarlane, S. Ng, M. E. Smith and J. H. Strange, *Solid State Ionics*, 1996, **86-8**, 1365.

638. S. Wong and D. B. Zax, *Electrochim. Acta*, 1997, **42**, 3513.

639. S. T. C. Ng, M. Forsyth, M. Garcia, D. R. MacFarlane and M. E. Smith, *Electrochim. Acta*, 1998, **43**, 1551.

640. D. K. Yang and D. B. Zax, *J. Chem. Phys.*, 1999, **110**, 5325.

641. P. Mustarelli, C. Capiglia, E. Quartarone, C. Tomasi, P. Ferloni and L. Linati, *Phys. Rev. B*, 1999, **60**, 7228.

642. C. E. Tambelli, J. P. Donoso, A. M. Regiani, A. Pawlicka, A. Gandini and J. F. LeNest, *Electrochim. Acta*, 2001, **46**, 1665.

643. K. Hayamizu, Y. Aihara and W. S. Price, *Electrochim. Acta*, 2001, **46**, 1475.

644. N. Arun, S. Vasudevan and K. V. Ramanathan, *J. Chem. Phys.*, 2003, **119**, 2849.

645. P. H. de Souza, R. F. Bianchi, K. Dahmouche, P. Judeinstein, R. M. Faria and T. J. Bonagamba, *Chem. Mater.*, 2001, **13**, 3685.

646. A. E. Wolfenson, R. M. Torresi, T. J. Bonagamba, M. A. DePaoli and H. Panepucci, *J. Phys. Chem. B*, 1997, **101**, 3469.

647. A. Lauenstein and J. Tegenfeldt, *J. Phys. Chem. B*, 1998, **102**, 6702.

648. S. Wong, R. A. Vaia, E. P. Giannelis and D. B. Zax, *Solid State Ionics*, 1996, **86-8**, 547.

649. M. E. Brik, J. J. Titman, J. P. Bayle and P. Judeinstein, *J. Polym. Sci. Part B – Polym. Phys.*, 1996, **34**, 2533.

650. D. J. Harris, T. J. Bonagamba, K. Schmidt-Rohr, P. P. Soo, D. R. Sadoway and A. M. Mayes, *Macromolecules*, 2002, **35**, 3772.

651. R. Bohmer, T. Jorg, F. Qi and A. Titze, *Chem. Phys. Lett.*, 2000, **316**, 419.

652. F. Qi, T. Jorg and R. Bohmer, *Solid State Nucl. Magn. Reson.*, 2002, **22**, 484.

653. E. R. deAzevedo, D. Reichert, E. L. G. Vidoto, K. Dahmouche, P. Judeinstein and T. J. Bonagamba, *Chem. Mater.*, 2003, **15**, 2070.

654. N. C. Mello, T. J. Bonagamba, H. Panepucci, K. Dahmouche, P. Judeinstein and M. A. Aegerter, *Macromolecules*, 2000, **33**, 1280.

655. M. V. Giotto, C. L. Sangiorge, D. J. Harris, A. L. deOliveira, K. Schmidt-Rohr and T. J. Bonagamba, *Macromolecules*, 2002, **35**, 3576.

656. M. Pursch, D. L. Vanderhart, L. C. Sander, X. H. Gu, T. Nguyen, S. A. Wise and D. A. Gajewski, *J. Am. Chem. Soc.*, 2000, **122**, 6997.
657. A. Badia, L. Cuccia, L. Demers, F. Morin and R. B. Lennox, *J. Am. Chem. Soc.*, 1997, **119**, 2682.
658. A. Badia, R. B. Lennox and L. Reven, *Acc. Chem. Res.*, 2000, **33**, 475.
659. H. Schmitt, A. Badia, L. Dickinson, L. Reven and R. B. Lennox, *Adv. Mater.*, 1998, **10**, 475.
660. R. M. Fouss and J. G. Kirkwood, *J. Am. Chem. Soc.*, 1941, **63**, 385.
661. A. G. Palmer, C. D. Kroenke and J. P. Loria, *Methods Enzymol.*, 2001, **339**, 204.
662. K. Schmidtrohr, E. deAzevedo and T. J. Bonagamba, *Encyclopedia of Nuclear Magnetic Resonance*, Wiley, Chichester, 2002, 633.

NMR Studies of Nanoparticles

CHRISTIAN MAYER

Institut für Chemie, Universität Duisburg-Essen, 47048 Duisburg, Germany
E-mail: hi408ma@uni-duisburg.de

Different experimental approaches for the application of NMR spectroscopy to dispersed nanoparticles are summarized and briefly discussed regarding their specific advantages and disadvantages. A general numeric approach for the analysis of the obtained data is introduced which accounts for rotational and lateral diffusion of the particles in a fluid medium. The applicability of the NMR experiments together with the numerical analysis of the resulting spectra is demonstrated on various examples which cover the particle structure, phase transitions, decomposition pathways, molecular exchange at phase boundaries, and release processes.

1. INTRODUCTION

The analysis of nanoparticles still represents a considerable challenge for common methods of NMR spectroscopy. Most problems are connected to the fact that the samples

of interest are necessarily inhomogeneous, with a corresponding spatial variation of the magnetic susceptibility along the phase boundaries.[1] In addition, motional inhomogeneity complicates the spectral analysis: while the fluid constituents exhibit rapid rotational diffusion, the solid contributions mostly lack the rapid isotropic tumbling which could lead to a desired motional averaging of the chemical shift tensors. Finally, spectroscopists who deal with dispersed nanoparticles have to be concerned about the long-term stability of their samples, as agglomeration and precipitation may occur especially under experimental conditions such as magic angle spinning (MAS).

On the other hand, the approaches of NMR offer various advantages compared to other analytical techniques[2]: except for sample spinning, the methods in general are completely non-destructive and allow for long-term studies on sensitive particle systems. At the same time, NMR spectroscopy offers the unique benefit of rendering simultaneous information on the chemical identity as well as the molecular mobility of individual components in a complex inhomogeneous mixture. Further, it yields data which give access to domain sizes, chemical exchange, proximity to paramagnetic centres, or reaction kinetics. Unlike common techniques for nanoparticle characterization such as electron and scanning probe microscopy, it does not require any sample preparation procedures which always include the risk of causing artefacts or structural deterioration. All these advantages given, NMR may prove to be a valuable asset in the analysis of dispersed nanoparticles.

The definition of the term 'nanoparticles' varies significantly depending on the scientific community where it is used. While in material sciences, the prefix 'nano' is generally restricted to structures smaller than 10 nm[3] or, at the most, 100 nm,[4,5] the same term in pharmaceutical sciences may refer to particles with up to 1000 nm in diameter.[6,7] However, when dealing with nanoparticles, there is general agreement on the phase state of the particles themselves which are supposed to be solid and dispersed in a continuous solid or fluid medium. In the following, we stick to a nomenclature that is common in pharmaceutical applications and has been proposed by Kreuter[6]: spherical nanoparticles with a compact solid structure are referred to as nanospheres, while hollow nanoparticles with a fluid content are named nanocapsules.

The following article deals with the application of NMR to dispersed nanoparticles. It will put an emphasis on organic nanoparticles of up to 1000 nm in size which serve as carrier systems for pharmaceutical applications, because the NMR approach seems to be especially promising in this field. However, most techniques can be generalized to other organic systems and to inorganic particles as well. In Section 1, a choice of suitable NMR experiments will be introduced. Section 2 deals with a numeric simulation procedure, which is capable of reproducing the regarded NMR experiments on the time scale under the influence of slow lateral and rotational diffusion. The final sections show examples which demonstrate the applicability of NMR experiments together with the numerical simulation for the analysis of various nanoparticle characteristics.

2. NUCLEAR MAGNETIC RESONANCE TECHNIQUES

Due to the general problems of diluted and inhomogeneous systems, the choice of NMR experiments suitable for the analysis of nanoparticles is somewhat restricted. With low

concentrations of the observed constituents, insensitive nuclei such as ^{13}C and significant line broadening due to hindered rotational diffusion, the use of sophisticated multidimensional NMR becomes tedious if not impossible. Therefore, the following examples are restricted to simple and straightforward experimental conditions which are among the classical representatives of solid state and high resolution NMR spectroscopy[2]:

(a) Direct excitation (de) of isolated $I=1/2$-nuclei (e.g., ^{13}C) under high power heteronuclear decoupling on static samples.

(b) Cross-polarization (cp) between an abundant nucleus I with nuclear spin $I_N=1/2$ (e.g., ^{1}H) and a rare nucleus S, also with spin 1/2 (e.g., ^{13}C) on static samples.

(c) Direct excitation or cross-polarization on spinning samples (e.g., sample spinning under MAS conditions).

(d) Echo experiments such as Hahn or stimulated echo sequences under application of pulsed field gradients (PFG).

Rotational diffusion of individual molecules in the fluid phase and particle tumbling of the solid particle matrix lead to more or less efficient motional averaging and directly affect NMR data in the time and frequency domain (Fig. 1). Each of the experiments mentioned above has its individual preference for a certain fraction of system components depending on their molecular dynamics.

In case of spectra taken under simple direct excitation conditions on static samples (case a), the integral of the spectral lines are directly proportional to the number of spins. Therefore, strong signal amplitudes are observed for rapid tumbling (Fig. 1c), while signals for components undergoing slower rotational diffusion are hardly detectable (Fig. 1a,b). This way, the direct excitation experiment (de) can be regarded as a filter for the components in the fluid phase. This approach has been used extensively on dispersed nanoparticles.[1,2,8–18]

The opposite rule holds for NMR experiments taken by cross-polarization between abundant and rare nuclei, such as (^{1}H)-^{13}C measurements (case b). The efficiency of the cp process is especially high in absence of motional averaging, therefore rigid components (Fig. 1a) give rise to the highest signal amplitudes, while mobile fractions tend to be undetectable. Therefore, the cross-polarization (cp) experiment generally acts as a filter for those components which make up the solid matrix of the particles. This approach has been used to put focus on the solid constituents and to study mobile components adsorbing on the particle surface.[2,19–21] A general disadvantage of the cp experiment under the given circumstances is the loss of the proportionality between the number of observed spins and the signal integrals, a fact which severely complicates the quantitative analysis of cp spectra.[22]

In order to improve the spectral resolution for the solid-state contributions, both methods (a) and (b) can be combined with sample spinning (case c). It leads to a significantly improved spectral resolution and increased signal-to-noise ratio for all components of the solid particle matrix, as long as the particle tumbling is slow compared to the spinning rate.[23] On the other hand, sample spinning gives rise to the generation of spinning sidebands which complicate the spectrum and may overlap with other signals. In addition, sample spinning is accompanied by gravitational fields of up to $10^6 g$, conditions
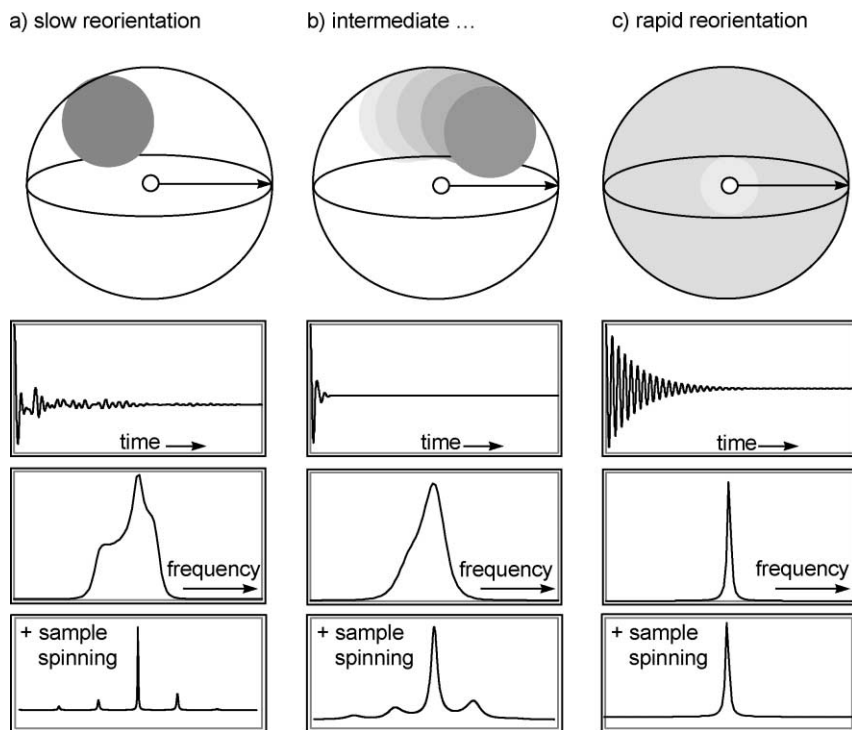
Fig. 1. Dependence of an NMR time signal and the corresponding frequency spectrum on the dynamics of rotational diffusion. The grey circle is meant to symbolize a general local interaction centre (e.g., causing an anisotropic chemical shift) next to the observed spin system. (a) Extremely slow reorientation in an isotropic sample leads to a superposition of angular dependent lineshapes coming close to the ideal powder pattern. Corresponding high resolution spectra are accessible by sample spinning at the magic angle (bottom line). (b) Reorientation in the most sensitive time scale (e.g., in the ms range for ^{13}C chemical shift anisotropy in common hydrocarbons) leads to short free induction decays and characteristic frequency line shapes strongly depending on motional correlation times. Spectra with improved resolution are accessible by sample spinning (bottom line). (c) Rapid reorientation leads to almost complete averaging of all angular dependent contributions, represented by a narrow line in the spectrum. Magic angle spinning has no significant effect (bottom line).

which are comparable to an ultracentrifugation experiment.[2] Therefore, this type of experiment on particle dispersions may easily lead to macroscopic phase separation, either by radial sedimentation or flotation of the particles during the observation period. However, as long as the dispersion is either well stabilized against sedimentation or as long as the density of the particles is well adjusted to the density of the solvent, sample spinning represents a perfect experimental approach to study the solid particle matrix.

The use of PFGs in combination with echo sequences (case d) allows for the observation of the lateral mobility of any observed component. Experimentally, the echo intensity of any observable resonance in a given echo experiment (most commonly, Hahn echoes or stimulated echoes are used) is studied as a function of the gradient strength and the diffusion

time. This approach is especially suitable for the differentiation between the liquid contents and the liquid continuous phase in a nanocapsule system, which otherwise cannot be achieved. Applied to nanocapsule dispersions, the obtained data set yields information on the nature of liquid capsule contents, the capsule size, and the capsule wall permeability.[2,24]

This set of experiments can be regarded as a basic toolbox for systematic studies on dispersed nanoparticles. It simultaneously yields data on the chemical identity and on rotational as well as lateral mobility. Hence, it allows for a clear assignment of all chemical constituents to the various system components such as particle matrix, capsule contents, or the continuous phase. Further, it gives access to data on the size and shape of the particles and the chemical exchange on the particle surface.

Of course, under favourable circumstances, the full variety of high resolution and solid-state NMR experiments may be applied to elucidate further details. Recent examples include REDOR studies on core-shell nanoparticles containing fluorinated polymers[25,26] or spin-diffusion measurements on isolated nanoparticles to elucidate matrix inhomo-geneities.[27] However, the simpler set of standard experiments mentioned above offers the advantage of being well understood regarding their effect on dispersed systems with nanoparticles undergoing slow isotropic tumbling. In the following section, a general approach is described which simulates the response of a spin system on the given experimental conditions under the influence of slow rotational and lateral self-diffusion. The numerical procedure can be implemented as a computer program and is suitable for the systematic analysis of line spectra or relaxation patterns corresponding to the NMR methods outlined above. It yields data on the nanoparticle size, its structure and different kinds of dynamic processes related to chemical exchange, release and particle degradation.

3. NUMERICAL SIMULATION PROCEDURE

3.1. Introduction of finite elements

For the simulation of the described NMR experiments on dispersed nanoparticles, one needs to account for a number of key variables: the time, the orientation of a given particle in space and its location with respect to a local reference system. In addition, in case of sample spinning experiments, the time-dependent orientation of the rotor has to be considered. For numerical calculation, all these parameters are approximated in a finite element scheme[2,22,23,28]:

(a) The time axis, starting at a point $t = 0$, is segmented into a total number of n_t time intervals of equal duration Δt.

(b) The orientation of each particle in space is determined by a set of three Euler angles Φ, Θ, and Ψ which is segmented according to the following rules[2,29]:

$$n_\Phi \text{ sites between } \Phi_{min} = 0 \text{ and } \Phi_{max} = 2\pi \quad \text{with } \Delta_\Phi = 2\pi/n_\Phi$$
$$n_\Theta \text{ sites between } \Theta_{min} = 0 \text{ and } \Theta_{max} = \pi \quad \text{with } \Delta_\Theta = \pi/n_\Theta$$
$$n_\Psi \text{ sites between } \Psi_{min} = 0 \text{ and } \Psi_{max} = 2\pi \quad \text{with } \Delta_\Psi = 2\pi/n_\Psi$$

Consequently, the full continuum of all possible orientations in space is approximated by a total number of $n_\Phi n_\Theta n_\Psi$ discrete sites.

(c) The location of a particle in three-dimensional space is determined by coordinates x, y, and z, which in turn are segmented into a total number of $n_x n_y n_z$ sites of equal size $\Delta x = \Delta y = \Delta z$. In many cases (as, e.g., for common PFG experiments), one may restrict to a single coordinate z which points along the direction of the magnetic field gradient.[2]

(d) The time-dependent position of a rotor in case of sample spinning experiments is determined by two angles $\alpha(t)$ and β, where $\alpha(t) = \omega_r t$ describes the rotation with an angular velocity of ω_r while β stands for the (static) orientation of the rotor axis with respect to the magnetic field.[23] The segmentation of $\alpha(t)$ is defined by the duration of the time interval Δt according to $\alpha(0) = 0$, $\alpha(\Delta t) = \omega_r \Delta t$, $\alpha(2\Delta t) = \omega_r 2\Delta t$, $\alpha(3\Delta t) = \omega_r 3\Delta t$, etc.

During the simulation process, all sites which refer to orientation $\Phi/\Theta/\Psi$ and location $x/y/z$ have time independent equilibrium populations which correspond to the degree of anisotropy and to the shape of the sample container. Rotational diffusion is simulated by introducing exchange between adjacent sites in the $\Phi/\Theta/\Psi$-domain, while lateral self-diffusion is connected to a corresponding exchange in the $x/y/z$-domain. This process is strictly limited to the exchange of physical properties such as lateral magnetization, while the equilibrium populations remain unchanged. The population of all sites is assumed to be large enough for this physical property to be treated classically.

3.2. Equilibrium state and the effect of an initial $\pi/2$-pulse

In the state of thermal equilibrium, the magnetization vector of each site is considered to point along the axis of the external magnetic field. Consequently, the complex lateral magnetization $M(\Phi_k \Theta_l \Psi_m x_i y_j z_k t)$ of each site $klmijk$ with the given orientation $\Phi_k/\Theta_l/\Psi_m$ and the lateral location $x_i/y_j/z_k$ is zero, as well as its corresponding value in the rotating x'–y'-frame $M'(\Phi_k \Theta_l \Psi_m x_i y_j z_k t)$. A $\pi/2$-pulse at a time t transfers the equilibrium longitudinal magnetization into the transversal direction, hence leading to a total complex lateral magnetization M' in the rotating frame according to[2,28]

$$\mathrm{Re}\, M' = \sum_{k,l,m,i,j,k} \mathrm{Re}\, M'(\Phi_k \Theta_l \Psi_m x_i y_j z_k t) = \sum_{k,l,m,i,j,k} c P_{eq}(\Phi_k \Theta_l \Psi_m x_i y_j z_k) \tag{1}$$

$$\mathrm{Im}\, M' = \sum_{k,l,m,i,j,k} \mathrm{Im}\, M'(\Phi_k \Theta_l \Psi_m x_i y_j z_k t) = 0 \tag{2}$$

where the proportionality constant c is of an arbitrary value. $P_{eq}(\Phi_k \Theta_l \Psi_m x_i y_j z_k)$ denotes the equilibrium population of the site $klmijk$ given by

$$P_{eq}(\Phi_k \Theta_l \Psi_m x_i y_j z_k) = P'_{eq}(\Phi_k \Theta_l \Psi_m) P''_{eq}(x_i y_j z_k) = \frac{\sin \Theta_l}{n_\Phi n_\Psi \sum_{l'} \sin \Theta_{l'}} P''_{eq}(x_i y_j z_k) \tag{3}$$

The population of spatial positions $P_{eq}''(x_i y_j z_k)$ depends on the shape of the sample container[2] or other diffusion barriers[2,24] and has to be adapted to reflect the given circumstances. The starting values of the site dependent lateral magnetizations $M'(\Phi_k \Theta_l \Psi_m x_i y_j z_k t)$ as given by Eqs. (1)–(3) mark the beginning of an NMR experiment starting with an initial $\pi/2$-pulse. Subsequently, the complex value of $M'(\Phi_k \Theta_l \Psi_m x_i y_j z_k t)$ develops in time according to the local Larmor frequency and the diffusion-related exchange of magnetization elements with adjacent sites which will be treated in the following sections.

3.3. Time development caused by local variations of the Larmor frequency

As mentioned in Section 2, we basically focus on experiments with nuclei with $I = 1/2$ (as, e.g., ^{13}C or ^{31}P) under high power decoupling. In this case, the dominating interaction of the nucleus with its molecular surroundings consists of the anisotropic chemical shift. It is fully determined by three principal values σ_{11}, σ_{22}, and σ_{33} which correspond to the diagonal values σ_{XX}^M, σ_{YY}^M, and σ_{ZZ}^M of the chemical shift tensor in a magnetic tensor system M (Fig. 2):

$$\boldsymbol{\sigma}^M = \begin{pmatrix} \sigma_{XX}^M & 0 & 0 \\ 0 & \sigma_{YY}^M & 0 \\ 0 & 0 & \sigma_{ZZ}^M \end{pmatrix} \tag{4}$$
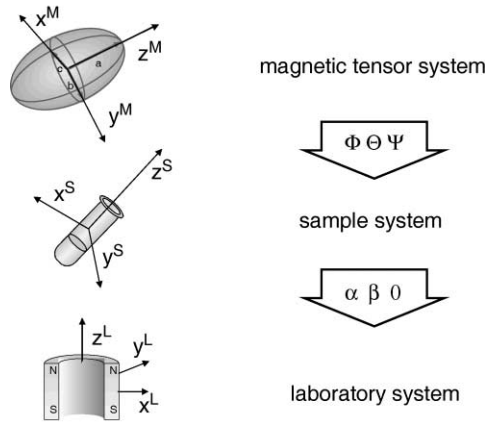
Fig. 2. Reference frames and sets of Euler angles required for the description of rotational diffusion and sample spinning in a general NMR experiment.[29] The magnetic tensor system (top, left) is characterized by a diagonal chemical shift tensor $\boldsymbol{\sigma}^M$. The sample system (centre, left) is defined by the axis z^S of sample spinning while the laboratory system is determined by the direction z^L of the external magnetic field. For a transformation from the magnetic tensor system into the sample system, a full set of three Euler angles Φ, Θ, and Ψ is needed. For the transformation from the sample system into the laboratory system, only two Euler angles α and β are required as the external magnetic field is assumed to be of rotational symmetry.

The Larmor frequency of spins in an orientation $\Phi_k/\Theta_l/\Psi_m$ depends on the element σ^L_{ZZ} of the chemical shift tensor in the laboratory system L which is defined by the direction of the external magnetic field.[30] In general, two coordinate transformations are needed to derive σ^L_{ZZ} from the elements of $\boldsymbol{\sigma}^M$ (Fig. 2).

The first one leads from the magnetic tensor system to the sample system, while the second one finally transforms into the laboratory system[2]:

$$\boldsymbol{\sigma}^S = \mathbf{T}^{DS}(\Phi_k\Theta_l\Psi_m)\boldsymbol{\sigma}^M\mathbf{T}^{DS-1}(\Phi_k\Theta_l\Psi_m) \tag{5}$$

$$\boldsymbol{\sigma}^L = \mathbf{T}^{SL}(\alpha\beta 0)\boldsymbol{\sigma}^S\mathbf{T}^{SL-1}(\alpha\beta 0) \tag{6}$$

where the transformation matrices $\mathbf{T}$ and $\mathbf{T}^{-1}$ are derived according to the following general definition:

$$\mathbf{T}(\Phi\Theta\Psi) =$$
$$\begin{pmatrix} \cos\Phi\cos\Psi - \cos\Theta\sin\Phi\sin\Psi & -\cos\Psi\sin\Phi - \cos\Theta\sin\Psi\cos\Phi & \sin\Theta\sin\Psi \\ \sin\Psi\cos\Phi + \cos\Theta\cos\Psi\sin\Phi & -\sin\Psi\sin\Phi + \cos\Phi\cos\Theta\cos\Psi & -\sin\Theta\cos\Psi \\ \sin\Theta\sin\Phi & \sin\Theta\cos\Phi & \cos\Theta \end{pmatrix} \tag{7}$$

$$\mathbf{T}^{-1}(\Phi\Theta\Psi) =$$
$$\begin{pmatrix} \cos\Phi\cos\Psi - \cos\Theta\sin\Phi\sin\Psi & \sin\Psi\cos\Phi + \cos\Theta\cos\Psi\sin\Phi & \sin\Theta\sin\Phi \\ -\cos\Psi\sin\Phi - \cos\Theta\sin\Psi\cos\Phi & -\sin\Psi\sin\Phi + \cos\Phi\cos\Theta\cos\Psi & \sin\Theta\cos\Phi \\ \sin\Theta\sin\Psi & -\sin\Theta\cos\Psi & \cos\Theta \end{pmatrix} \tag{8}$$

If we assume sample spinning at a tilt angle β with a time-dependent angle $\alpha = \omega_r t$, the crucial element σ^L_{ZZ} for a given angular orientation $\Phi_k/\Theta_l/\Psi_m$ is derived by[23]:

$$\begin{aligned} \sigma^L_{ZZ}(\Phi_k\Theta_l\Psi_m t) = {} & [\cos^2\beta\sigma^S_{ZZ}(\Phi_k\Theta_l\Psi_m)] + \sin^2(\omega_r t)[\sin^2\beta\sigma^S_{YY}(\Phi_k\Theta_l\Psi_m)] \\ & + \cos^2(\omega_r t)[\sin^2\beta\sigma^S_{XX}(\Phi_k\Theta_l\Psi_m)] \\ & + \sin(\omega_r t)\cos(\omega_r t)[\sin^2\beta(\sigma^S_{XY}(\Phi_k\Theta_l\Psi_m) + \sigma^S_{YX}(\Phi_k\Theta_l\Psi_m))] \\ & + \sin(\omega_r t)[\sin\beta\cos\beta(\sigma^S_{YZ}(\Phi_k\Theta_l\Psi_m) + \sigma^S_{ZY}(\Phi_k\Theta_l\Psi_m))] \\ & + \cos(\omega_r t)[\sin\beta\cos\beta(\sigma^S_{XZ}(\Phi_k\Theta_l\Psi_m) + \sigma^S_{ZX}(\Phi_k\Theta_l\Psi_m))] \end{aligned} \tag{9}$$

In case of static samples, the angle β and the angular velocity ω_r can be set to zero and Eq. (9) simplifies accordingly, leading to $\sigma^L_{ZZ}(\Phi_k\Theta_l\Psi_m t) = \sigma^S_{ZZ}(\Phi_k\Theta_l\Psi_m t)$.

In absence of field gradients or other local variations of the external magnetic field, the time-dependent Larmor frequency ω of spins in a given orientation $\Phi_k/\Theta_l/\Psi_m$ at any location $x_i/y_j/z_k$ is given by

$$\omega(\Phi_k\Theta_l\Psi_m x_i y_j z_k t) = \omega_0 \sigma^L_{ZZ}(\Phi_k\Theta_l\Psi_m t) \tag{10}$$

In general, however, one has to account for spatial field inhomogeneities which may be induced by local variations of the magnetic susceptibility.[31] Another very important cause for spatial dependence of the magnetic field is the presence of external field gradients which may be applied temporarily during the experiment in order to observe lateral diffusion processes. With a field gradient of time-dependent strength $G(t)$ along the z-axis of the laboratory system, the Larmor frequency of spins in a given orientation $\Phi_k/\Theta_l/\Psi_m$ at a given location $x_i/y_j/z_k$ becomes[2]:

$$\omega(\Phi_k\Theta_l\Psi_m x_i y_j z_k t) = \omega_0 \sigma^L_{ZZ}(\Phi_k\Theta_l\Psi_m t) - \gamma G(t) z_k [1 - \sigma^L_{ZZ}(\Phi_k\Theta_l\Psi_m t)] \tag{11}$$

In any case, all contributions $M'(\Omega_n t) = M'(\Phi_k\Theta_l\Psi_m x_i y_j z_k t)$ to the complex lateral magnetization M' are subject to a time development according to the corresponding Larmor frequency:

$$M'(\Omega_n t + \Delta t) = M'(\Omega_n t)\exp[i\omega(\Omega_n t)\Delta t] \tag{12}$$

where Ω_n stands for the relevant combination of the values Φ_k, Θ_l, Ψ_m, x_i, y_j and z_k.

3.4. The effect of lateral self-diffusion

As mentioned in Section 3.1, a self-diffusion process is accounted for by introducing a corresponding exchange of magnetization between adjacent sites. If this is introduced in the time evolution according to Eq. (12), one has to simultaneously account for the evolution of the lateral magnetization and the diffusion-related exchange, a problem which is difficult to solve numerically. In good approximation, one may assume that the lateral magnetization only develops according to the Larmor frequency during the time interval Δt, while the exchange of site-specific magnetization occurs discontinuously at the end of the interval. This given, the effect of diffusion is introduced into Eq. (12)[28]:

$$M'(\Omega_n t + \Delta t) = M'(\Omega_n t)\exp[i\omega(\Omega_n t)\Delta t] + \sum_{n'} \left\{ -k_{nn'}\Delta t M'(\Omega_n t)\exp[i\omega(\Omega_n t)\Delta t] \right.$$
$$\left. + k_{n'n}\Delta t M'(\Omega_{n'} t)\exp[i\omega(\Omega_{n'} t)\Delta t] \right\} \tag{13}$$

where again Ω_n and $\Omega_{n'}$ stand for two given combinations of the values Φ_k, Θ_l, Ψ_m, x_i, y_j and z_k. While this may be a rough approximation for long periods Δt, it rapidly converges into the ideal simulation of the diffusive exchange for $\Delta t \to 0$. The rate constants $k_{nn'}$ denote the efficiency of the exchange between different sites Ω_n and $\Omega_{n'}$ and relate to the lateral diffusion constant D and to the equilibrium populations P''_{eq}

(see Eq. (3)) according to[2,24]

$$k_{i(i\pm1)} = D\sqrt{\frac{P''_{eq}(x_{i\pm1}y_jz_k)}{P''_{eq}(x_iy_jz_k)}}\left(\frac{1}{(\Delta x^2)}\right) \qquad (14)$$

$$k_{j(j\pm1)} = D\sqrt{\frac{P''_{eq}(x_iy_{j\pm1}z_k)}{P''_{eq}(x_iy_jz_k)}}\left(\frac{1}{(\Delta y^2)}\right) \qquad (15)$$

$$k_{k(k\pm1)} = D\sqrt{\frac{P''_{eq}(x_iy_jz_{k\pm1})}{P''_{eq}(x_iy_jz_k)}}\left(\frac{1}{(\Delta z^2)}\right) \qquad (16)$$

where $k_{i(i\pm1)}$ ($k_{j(j\pm1)}$, $k_{k(k\pm1)}$) stand for the rate constants connecting those locations Ω_n and $\Omega_{n'}$ which differ only in the position x_i (y_j, z_k) by one positive or negative step Δx (Δy, Δz). All other rate constants $k_{nn'}$ in Eq. (13) are assumed to be zero. The sample geometry is defined by the equilibrium populations P''_{eq} and by the definition of 'internal' and 'external' sites.[2,31] The rate constants k connecting internal with external sites as well as all populations of external sites are set to zero. Hereby, almost any sample geometry with or without internal barriers can be described numerically.[31]

In case of one-dimensional PFG experiments, one can take advantage of the fact that the gradient-induced phase shift is a periodical function of the gradient axis z. In this case, one may neglect the x and y axes and restrict to the simulation of a small unit cell along the z axis which fulfils the condition that the outer limits z_{min} and z_{max} have identical phase shifts with $z_{max}+\Delta z$ and $z_{min}-\Delta z$, respectively. In this case, additional rate constants connecting z_{min} with z_{max} are introduced which account for the exchange between adjacent unit cells.[24]

Within the unit cell, subspaces may be defined which represent nanocapsules with liquid content. The equilibrium population $P'''_{eq}(z_i)$ of a given subspace at the position z_i reflects the individual shape of the capsule. Generally spherical geometries are assumed which leads to[2,24]:

$$P'''_{eq}(z_i) = c\cdot[R^2 - (z_i - z_0)^2] \quad \text{with } (z_0 - R) \le z_i \le (z_0 + R) \qquad (17)$$

where R is the capsule radius, z_0 the location of the capsule centre and c a normalization constant which has to be adjusted to yield the correct encapsulated fraction of the observed molecules. The self-diffusion of chemical components inside the nanocapsules is then defined by a diffusion constant D_{in} which, in the general case, may differ from the corresponding value of the continuous medium D_{out}. Otherwise, the internal self-diffusion along the z axis is treated as given by Eq. (16). In general, the capsule walls may allow a certain degree of molecular exchange between the encapsulated and the continuous phase of the system. This exchange process is accounted for by rate constants $k_i(\text{in}\rightarrow\text{out})$ and $k_i(\text{out}\rightarrow\text{in})$ which describe the flow through the capsule walls in both

directions at a location z_i and relate to an average exchange rate $\bar{k}_{ex}$ by[24]

$$k_i(\text{in} \rightarrow \text{out}) = \bar{k}_{ex} \left(\frac{A_i}{V_i} \right) \sqrt{\frac{P''_{eq}(z_i)}{P'''_{eq}(z_i)}} \tag{18}$$

$$k_i(\text{out} \rightarrow \text{in}) = \bar{k}_{ex} \left(\frac{A_i}{V_i} \right) \sqrt{\frac{P'''_{eq}(z_i)}{P''_{eq}(z_i)}} \tag{19}$$

where $P''_{eq}(z_i)$ refers to the local equilibrium population in the continuous phase, A_i to the relative surface area and V_i to the relative volume fraction of the capsule in the location z_i. The factor (A_i/V_i) in Eqs. (18) and (19) derives from the fact that the exchange rate for a given slice i of the capsule is proportional to its relative surface A_i as well as to its reciprocal volume contribution V_i^{-1}.[24]

In all cases mentioned above, the system is assumed to be free of net flow processes. In consequence, the exchange between two adjacent sites Ω_n and $\Omega_{n'}$ is always balanced according to

$$k_{nn'} P_{eq}(\Omega_n) = k_{n'n} P_{eq}(\Omega_{n'}) \tag{20}$$

This condition is fulfilled by all rate constants k and equilibrium populations P_{eq} in Eqs. (14)–(16), (18) and (19).

3.5. The effect of rotational diffusion

Rotational diffusion, which in fact is a self-diffusion process in the angular domain, leads to an exchange of magnetization contributions between different angular orientations $\Phi_k/\Theta_l/\Psi_m$. The general operator which describes rotational diffusion for an ellipsoidal particle of rotational symmetry can be adapted to the finite element scheme which leads to five different sets of rate constants[23]:

$$k_{k(k+1)} = k_{k(k-1)} \left(\frac{1}{6\tau_\parallel} + \frac{1}{6\tau_\perp} \cot^2\Theta_l \right) \frac{1}{(\Delta\Phi)^2} \tag{21}$$

$$k_{l(l\pm1)} = \frac{1}{6\tau_\perp} \frac{\sqrt{\sin\Theta_{l\pm1}}}{\sqrt{\sin\Theta_l}} \frac{1}{(\Delta\Theta)^2} \tag{22}$$

$$k_{m(m+1)} = k_{m(m-1)} = \frac{1}{6\tau_\perp} \frac{1}{\sin^2\Theta_l} \frac{1}{(\Delta\Psi)^2} \tag{23}$$

$$k_{m(m+1)}^{k(k+1)} = k_{m(m-1)}^{k(k-1)} = -\frac{1}{6\tau_\perp} 2\frac{\cot\Theta_l}{\sin\Theta_l} \frac{1}{4(\Delta\Phi)(\Delta\Psi)} \tag{24}$$

$$k_{m(m-1)}^{k(k+1)} = k_{m(m+1)}^{k(k-1)} = \frac{1}{6\tau_\perp} 2\frac{\cot\Theta_l}{\sin\Theta_l} \frac{1}{4(\Delta\Phi)(\Delta\Psi)} \tag{25}$$

Here, the rate constant $k_{k(k\pm1)}$ ($k_{l(l\pm1)}$, $k_{m(m\pm1)}$) in Eqs. (21)–(23) refers to the independent exchange between adjacent sites in the angular domain Φ (Θ, Ψ), while the rate constants $k_{m(m\pm1)}^{k(k\pm1)}$ and $k_{m(m\mp1)}^{k(k\pm1)}$ in Eqs. (24) and (25) describe exchange processes with

simultaneous single steps in the Φ- and the Ψ-domain.[23] The velocity of the diffusive reorientation process of the ellipsoid is now defined by a correlation time $\tau_\parallel$ which denotes the rotational diffusion around the long axis, and a correlation time $\tau_\perp$ which refers to the rotational diffusion around the two short axes.[23] For spherical particles, both correlation times $\tau_\parallel$ and $\tau_\perp$ are equal and may be represented by a single correlation time for rotational diffusion τ. In any case, all rate constants together with the equilibrium populations given by Eq. (3) fulfil the balanced flow condition of Eq. (20).

3.6. The effect of π-pulses

So far, the simulation procedure for the observable NMR time signal is completely restricted to the magnetization in the (rotating) x'–y'-plane. Its value is determined by a set of site- and time-dependent complex numbers $M'(\Omega_n t)$. Within this description, it is easy to introduce the effect of π-pulses of any given phase angle φ. If an infinitesimally short π-pulse of a given phase φ acts on the system just between the time intervals t and $t + \Delta t$, one obtains[2]:

$$M'(\Omega_n t + \Delta t) = [e^{-i\varphi} M'(\Omega_n t)]^* e^{i\varphi} \tag{26}$$

where $[\ldots]^*$ denotes the complex conjugate of $[\ldots]$. In case of a π_x-pulse ($\varphi = 0$) or a π_y-pulse ($\varphi = \pi/2$), the result of this procedure is merely a reversal of the sign of the imaginary part or the real part of M', respectively. In both cases, the π-pulse will induce the formation of an echo signal corresponding to the Hahn echo under experimental conditions.

3.7. The effect of a cross-polarization sequence

Due to the complexity of the general cross-polarization (cp) process, the numerical simulation is restricted to the straightforward case of an I–S-system under the influence of additional I–I-coupling. In practice, such a system is most often represented by a CH-group, where the following procedure may be applied directly. However, with some restrictions, the results may also be generalized to other common organic residues like CH_2- and CH_3-groups.

The algorithm for the cross-polarization step can be introduced at any time period within the general simulation procedure which has been outlined in the Sections 3.1–3.6. At the beginning of the cp interval, the magnetization vector of the S-system, which so far has been described as a complex number referring to the rotating x'–y'-plane, is combined with the magnetization vector of the I-system. Together, their development is now regarded in a space which is spanned by four orthogonal single-transition operators[30]:

$$I_Z^{(1,4)} = \frac{1}{2}(I_Z + S_Z) \tag{27}$$

$$I_Z^{(2,3)} = \frac{1}{2}(I_Z - S_Z) \tag{28}$$

$$I_X^{(2,3)} = \frac{1}{2}(I^+S^- + I^-S^+) \tag{29}$$

$$I_Y^{(2,3)} = -\frac{i}{2}(I^+S^- - I^-S^+) \tag{30}$$

Within this basis, the evolution of the I–S-spin system is represented by a rotation of the weighted difference magnetization vector **d** in the three-dimensional subspace of the (2,3) transition while the component $I_Z^{(1,4)}$ remains constant.[22,30] Just like the real and the imaginary part of $M'(\Omega_n t)$ describes the development of the lateral magnetization vector for a given site Ω_n in absence of the cp-conditions, now the development of the I–S-system of each site is given by the three time- and site-dependent Cartesian components $d_X(\Omega_n t)$, $d_Y(\Omega_n t)$ and $d_Z(\Omega_n t)$ of the difference vector **d**. The non-exchange related part of this development is determined by two influences which cause the difference vector to undergo two simultaneous rotations[22]:

(a) The effect of dipolar coupling with a coupling constant D_{IS} leads to a rotation around the $I_X^{(2,3)}$ axis with an angular velocity ω_X of

$$\omega_X = \frac{1}{2} \frac{\omega_{1I}}{(\Delta_I^2 + \omega_{1I}^2)^{1/2}} \frac{\omega_{1S}}{(\Delta_S^2 + \omega_{1S}^2)^{1/2}} 2\pi D_{IS} \tag{31}$$

where Δ_I and Δ_S stand for the resonance offset frequencies, ω_{1I} and ω_{1S} for the precession frequencies in the RF field, respectively. The coupling constant D_{IS} is calculated according to

$$D_{IS} = \frac{1}{2\pi} \frac{\mu_0 \gamma_I \gamma_S \hbar}{4\pi r_{IS}^3} (1 - 3\cos^2\theta_{IS}) \tag{32}$$

with r_{IS} denoting the internuclear distance between I and S, and θ_{IS} representing the angle between the vector $\mathbf{r}_{IS}$ and the magnetic field.

(b) The effect of a deviation from the Hartmann–Hahn condition leads to a rotation around the $I_Z^{(2,3)}$ axis with an angular velocity ω_Z of

$$\omega_Z = (\Delta_I^2 + \omega_{1I}^2)^{1/2} - (\Delta_S^2 + \omega_{1S}^2)^{1/2} \tag{33}$$

These two superimposed rotations may be replaced by a single rotation with a precession frequency ω along an axis with a tilt angle φ with respect to the $I_Z^{(2,3)}$-direction, where

$$\omega = (\omega_X^2 + \omega_Z^2)^{1/2} \tag{34}$$

$$\sin\varphi = \frac{\omega_X}{\omega} \tag{35}$$

$$\cos\varphi = \frac{\omega_Z}{\omega} \tag{36}$$

$$\tan\varphi = \frac{\omega_X}{\omega_Z} \tag{37}$$

According to Eqs. (31)–(37), the values for ω and ϕ are calculated for the complete set of angular and spatial sites Ω_n to yield a set of parameters $\omega(\Omega_n t)$ and $\varphi(\Omega_n t)$. Then the non-exchange related time development of the three Cartesian components $d_X(\Omega_n t)$, $d_Y(\Omega_n t)$, and $d_Z(\Omega_n t)$ during the time interval Δt is given by[22]

$$d_{X'}(\Omega_n t) = \cos \varphi[(d_X(\Omega_n t)\cos \varphi - d_Z(\Omega_n t)\sin \varphi)\cos(\omega\Delta t)$$
$$+ d_Y(\Omega_n t)\sin(\omega\Delta t)] + \sin \varphi[d_X(\Omega_n t)\sin \varphi + d_Z(\Omega_n t)\cos \varphi] \quad (38)$$

$$d_{Y'}(\Omega_n t) = -(d_X(\Omega_n t)\cos \varphi - d_Z(\Omega_n t)\sin \varphi)\sin(\omega\Delta t) + d_Y(\Omega_n t)\cos(\omega\Delta t) \quad (39)$$

$$d_{Z'}(\Omega_n t) = -\sin \varphi[(d_X(\Omega_n t)\cos \varphi - d_Z(\Omega_n t)\sin \varphi)\cos(\omega\varDelta t)$$
$$+ d_Y(\Omega_n t)\sin(\omega\Delta t)] + \cos \varphi[d_X(\Omega_n t)\sin \varphi + d_Z(\Omega_n t)\cos \varphi] \quad (40)$$

with d_X, d_Y, and d_Z being the coefficients before the time period Δt and $d_{X'}$, $d_{Y'}$, and $d_{Z'}$ being the coefficients after the evolution period (the parameters $\omega(\Omega_n t)$ and $\varphi(\Omega_n t)$ are represented by ω and φ for reasons of readability). The influence of the dipolar interaction within the I-spin domain may be accounted for by an additional relaxation process with an empirical time constant T_d:

$$d_{X''} = d_{X'} \exp(-\Delta t/T_d) \quad (41)$$

$$d_{Y''} = d_{Y'} \exp(-\Delta t/T_d) \quad (42)$$

$$d_{Z''} = d_{Z'} \exp(-\Delta t/T_d) \quad (43)$$

Finally, the effect of diffusive motion is introduced by allowing for the partial exchange of vector components determined by the rate constants $k_{nn'}$ leading from any site n to an adjacent site n' (see Sections 3.4 and 3.5). With this, the 'new' Cartesian coefficients after a time interval Δt can be calculated according to

$$d_X(\Omega_n t + \Delta t) = d_{X''}(\Omega_n t) + \sum_{n'} \left[-k_{nn'}\Delta t d_{X''}(\Omega_n t) + k_{n'n}\Delta t d_{X''}(\Omega_{n'} t)\right] \quad (44)$$

$$d_Y(\Omega_n t + \Delta t) = d_{Y''}(\Omega_n t) + \sum_{n'} \left[-k_{nn'}\Delta t d_{Y''}(\Omega_n t) + k_{n'n}\Delta t d_{Y''}(\Omega_{n'} t)\right] \quad (45)$$

$$d_Z(\Omega_n t + \Delta t) = d_{Z''}(\Omega_n t) + \sum_{n'} \left[-k_{nn'}\Delta t d_{Z''}(\Omega_n t) + k_{n'n}\Delta t d_{Z''}(\Omega_{n'} t)\right] \quad (46)$$

Using Eqs. (38)–(46), the time development of the difference magnetization vector can be calculated during the complete mixing period. The most common starting condition for $t=0$ is a $\pi/2$-pulse on the I spins, which leads to the initial vector components:

$$d_X(\Omega_n 0) = 0 \quad (47)$$

$$d_Y(\Omega_n 0) = 0 \quad (48)$$

$$d_Z(\Omega_n 0) = P_{eq}(\Omega_n) \quad (49)$$

At the end of the mixing period at a given time t_{cp}, the magnetization vector in the single-transition operator system is transformed into the lateral magnetization vector of the S-system. The corresponding complex value for the rotating x'–y'-plane after the mixing period t_{cp} is given by[22]

$$\text{Re}[M'(\Omega_n t_{cp})] = \frac{\omega_{1S}}{(\Delta_S^2 + \omega_{1S}^2)^{1/2}} [P_{eq}(\Omega_n) - d_Z(\Omega_n t_{cp})] \tag{50}$$

$$\text{Im}[M'(\Omega_n t_{cp})] = 0 \tag{51}$$

which accounts for the fact that the cross-polarization is developing along the Z-axis of the tilted rotating frame which in general deviates from the x' axis of the classical rotating frame.[30] At the end of the mixing period, all contributions $M'(\Omega_n t_{cp})$ are real numbers as we assume that the signal is completely in phase after cross-polarization. This phase is determined by the phase of the spin-lock irradiation which is assumed to follow the x' axis of the rotating frame.

3.8. Calculation of the frequency spectrum

The simulation algorithm described in Sections 3.1–3.7 can be regarded as a general toolbox to deal with the various experimental conditions listed in Section 2. Principally, any combination of system parameters and experimental conditions is possible to be simulated. However, in most cases the numerical calculation is significantly simplified by certain restrictions, e.g.:

(a) Lateral diffusion of spins and particles only needs to be taken into account in case of experiments including PFGs or local field inhomogeneities, otherwise lateral motion is without any effect for the outcome of the experiment.

(b) In absence of sample spinning, the Larmor frequencies $\omega(\Phi_k \Theta_l \Psi_m x_i y_j z_k t)$ can be regarded as time independent.

(c) In case of very rapid intramolecular or intermolecular motion, one may restrict to a motionally averaged Hamiltonian with a corresponding set of Larmor frequencies.

After completion of the full experimental time scale, the analysis of the NMR time signal is restricted to the detection period, in general being referred to as the free induction decay. It is formed by addition over all complex magnetization contributions for all sites according to

$$M'(t) = \sum_n M'(\Omega_n t) \tag{52}$$

In some cases such as for relaxation or diffusion measurements, the focus is simply on the initial intensity of the time signal which can be directly determined at the initial data point of the detection period. Generally however, the overall time signal $M'(t)$ of the free

induction decay is Fourier transformed to give a corresponding frequency spectrum $S(\omega)$. In the simulation procedure, this is performed numerically following the standard equation:

$$S(\omega) = \int_{-\infty}^{\infty} M'(t)\exp(\mathrm{i}\omega t)\mathrm{d}t = 2\int_{0}^{\infty} M'(t)\exp(\mathrm{i}\omega t)\mathrm{d}t \tag{53}$$

The real part of the resulting frequency function $S(\omega)$ is identical to the common absorption spectrum.

4. GENERAL APPLICATIONS AND EXAMPLES

4.1. Rotational diffusion of particles

A very simple approach to study organic nanoparticles in a liquid dispersion is to apply a single $\pi/2$ pulse on the ^{13}C nuclei on a static sample and to observe the resulting free induction decay under proton decoupling. In this case, all dissolved and liquid components will show up as highly resolvable signals somewhat affected by local variations in the magnetic susceptibility. All solid constituents, on the other hand, will be represented by wide solid-state line shapes which strongly depend on the rotational diffusion of the particles. A typical simulated pattern for the dependence of a direct-excitation ^{13}C line shape on the correlation time for an isotropic rotational diffusion is shown in Fig. 3. A line shape analysis of the experimental spectrum would easily allow for the determination of the correlation time in the range between 1 and 200 μs. In practice however, the direct excitation (de) method on ^{13}C nuclei only yields unsatisfactory results due to its lack of sensitivity. In most cases, a dispersion of organic particles would either require extensive measuring times or yield spectra with bad s/n ratios.

A well-known tool for the enhancement of the spectral sensitivity for ^{13}C nuclei is cross-polarization (cp). However, it has to be taken into account that the cp approach necessarily leads to specific line shape distortions, especially under the influence of diffusive motion. In addition, the line shape will depend on the duration of the mixing period t_{cp}. Figure 4 shows a representative set of simulated (^{1}H)-^{13}C line shapes for various mixing periods and correlation times.[22] In general, the cp spectra show similar changes with the increase of rotational diffusion: wide, asymmetric line shapes (Fig. 4a) turn into narrow symmetric lines (Fig. 4e). Characteristic intensity oscillations are observed for longer correlation times (Fig. 4a–c). The oscillation frequency strongly depends on the angular orientation of the spectral contributions to the powder pattern and is determined by the orientation of the CH-vector with respect to the principal axis system of the chemical shift tensor.[22,32] Practically all cp line shapes differ significantly from those obtained by direct excitation.

The dependence of the cp line shape on the correlation time of isotropic rotational diffusion can be used to determine the rotational mobility of system components in
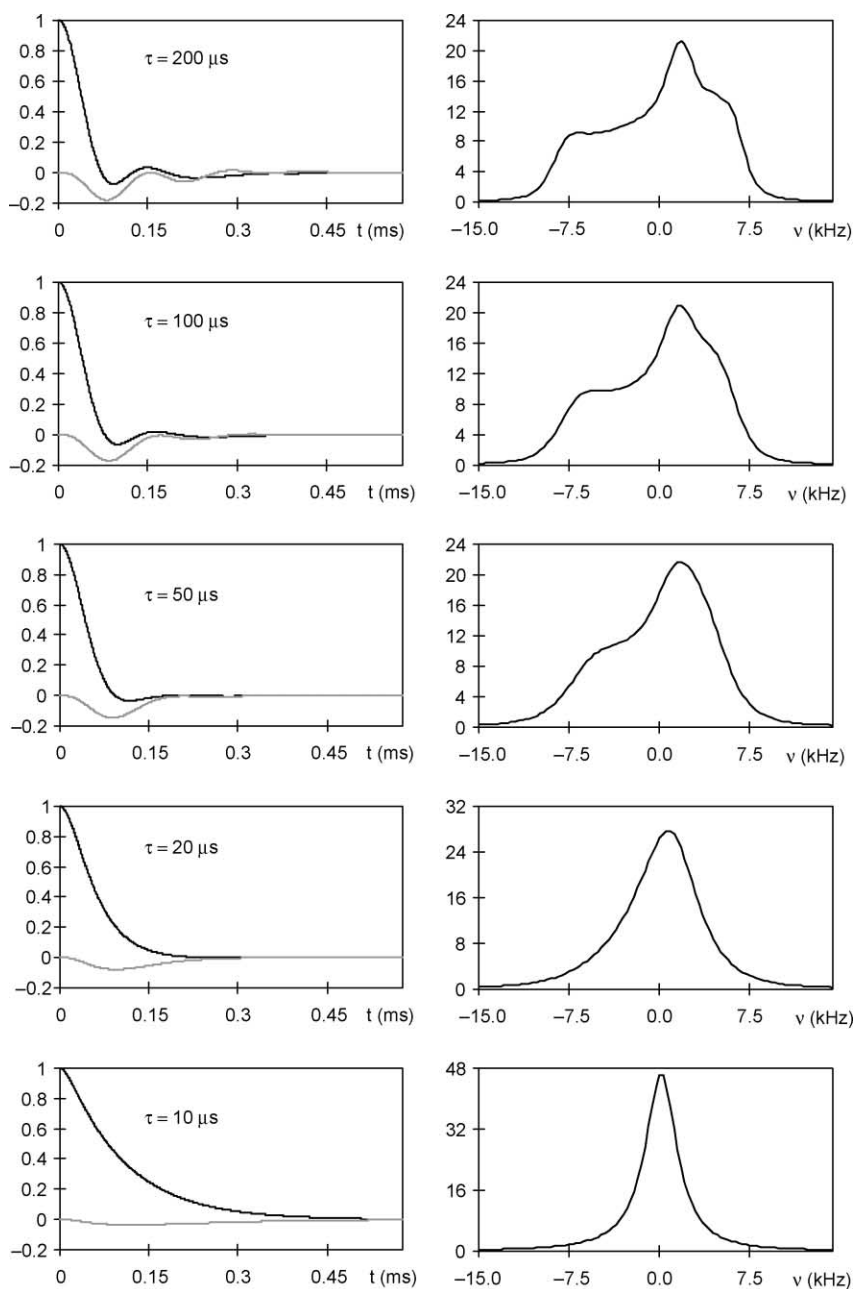
Fig. 3. Simulated time signals (left) and frequency spectra (right) of a ^{13}C nucleus with anisotropic chemical shielding ($\sigma_{11} = 8$ kHz, $\sigma_{22} = 2$ kHz, $\sigma_{33} = -10$ kHz) after direct excitation on a static sample. The correlation time of rotational diffusion $\tau = \tau_{\parallel} = \tau_{\perp}$ of the particles is varied between 200 (top) and 10 μs (bottom). The time signal consists of a real part Re M' (starting with 1.0) and an imaginary part Im M' (starting with 0.0) (reproduced from Ref. [28] with permission).
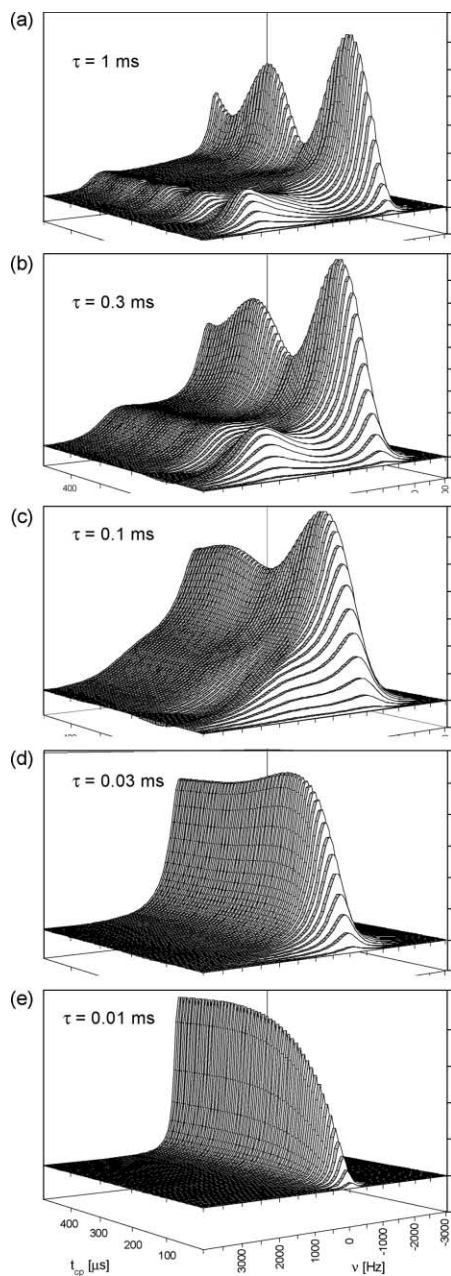
Fig. 4. Simulated (^{1}H)-^{13}C cross-polarization spectra of a with anisotropic chemical shielding ($\sigma_{11} = -1.5$ kHz, $\sigma_{22} = -1.5$ kHz, $\sigma_{33} = 3$ kHz). The correlation time of rotational diffusion $\tau = \tau_\parallel = \tau_\perp$ of the particles is varied between 300 (a) and 10 µs (e), while the mixing period is ranging from 10 to 500 µs in steps of 10 µs in each stacked plot (reproduced from Ref. [22] with permission).
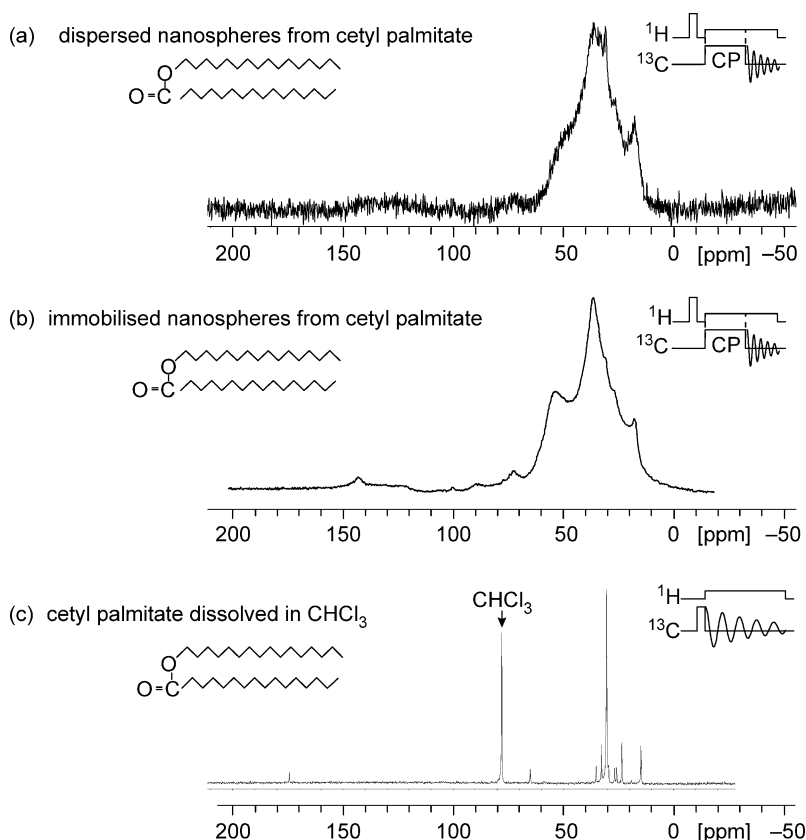
Fig. 5. (a) (^{1}H)-^{13}C cross-polarization spectrum of cetyl pamitate nanospheres dispersed in water at room temperature. (b) (^{1}H)-^{13}C cross-polarization spectrum of cetyl pamitate nanospheres after immobilization (removal of excess water). (c) High resolution ^{13}C spectrum (de) of cetyl palmitate dissolved in chloroform. The insets depict the molecular structure of cetyl palmitate and the relevant pulse programs, the resonance frequency for protons is 400 MHz in all cases.

dispersed nanoparticles. An example is given in Fig. 5, where the top spectrum (Fig. 5a) represents a cp (^{1}H)-^{13}C spectrum obtained on a dispersion of cetyl palmitate nanospheres, a representative of solid lipid nanoparticles (SLN).[11,33–35]

For comparison, the cp line shape of the same dispersion after immobilization of the particles by water removal is shown in Fig. 5b, and a corresponding high resolution spectrum of dissolved cetyl palmitate in Fig. 5c. Obviously, the solid-state spectra a and b represent a superposition of different frequency signals with averaged chemical shifts σ_{iso} ranging mainly between 13 and 80 ppm. These resonances may be approximated by using data of *n*-eicosane and polyethylene terephthalate, where the principal values of the chemical shift anisotropy are known (Table 1).[2,36–39] The resulting set of solid-state spectra for the spectral range between 0 and 80 ppm is shown in Fig. 6.

Based on the data in Table 1 (^{1}H)-^{13}C superposition spectra for a fixed contact time ($t_{cp} = 1$ ms) are calculated for a variety of rotational correlation times (Fig. 7).

Table 1. Tensor elements for the estimated anisotropy of the ^{13}C chemical shift interaction for characteristic CH$_n$-groups of cetyl palmitate. The values derive from n-eicosane[36] and polyethylene terephthalate (PET)[37–39] at room temperature and are given in ppm. All contributions with $\sigma_{iso} >$ 80 ppm are neglected

Carbon segment type	–CH$_2$–CH$_2$–CH$_2$–	–CH$_2$–CH$_3$	–CH$_2$–CH$_3$	–CH$_2$–OOCR
Number of represented carbons in cetyl palmitate	26	2	2	1
Model substance	n-Eicosane	n-Eicosane	n-Eicosane	PET
σ_{11} (ppm)	50	37	26	80
σ_{22} (ppm)	38	30	22	80
σ_{33} (ppm)	17	15	3	28
σ_{iso} (ppm)	35	27	17	63

The resulting set of line shapes allows for an easy estimation of rotational correlation times based on the solid-state spectrum of dispersed cetyl palmitate particles.

A rough comparison between Fig. 5a,b with Fig. 7 yields correlation times of $\tau \geq 2$ ms for the immobilized and $\tau = 0.5$ ms for the dispersed nanospheres (Fig. 8).[2]

The obvious deviations on the left side of the spectrum possibly reflect the differences between the actual chemical shift data and the ones listed in Table 1 which have been used for the calculations. On the other hand, all general features of the experimental line shapes are reproduced by the calculated spectra. Two significant conclusions can be drawn based on this finding:

(i) The absence of any narrow lines in the spectra of the particle systems indicate that the matrix material resides almost exclusively in the solid phase. Otherwise, any dissolved or liquid fraction would have led to the appearance of motionally narrowed signals, especially under direct excitation.
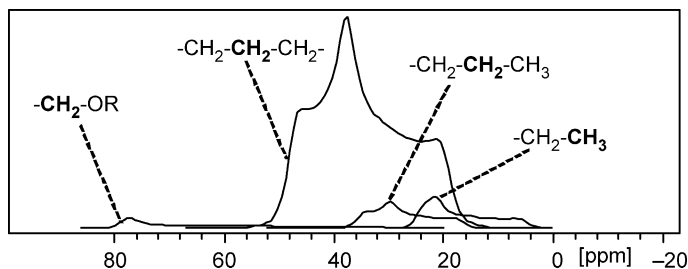
Fig. 6. Simulated spectral contributions of different methyl and methylene groups to the expected (^{1}H)-^{13}C cross-polarization spectrum of cetyl pamitate. The integral of each single spectrum corresponds to the number of carbon atoms being represented by the particular segment. All simulations are based on the data listed in Table 1.
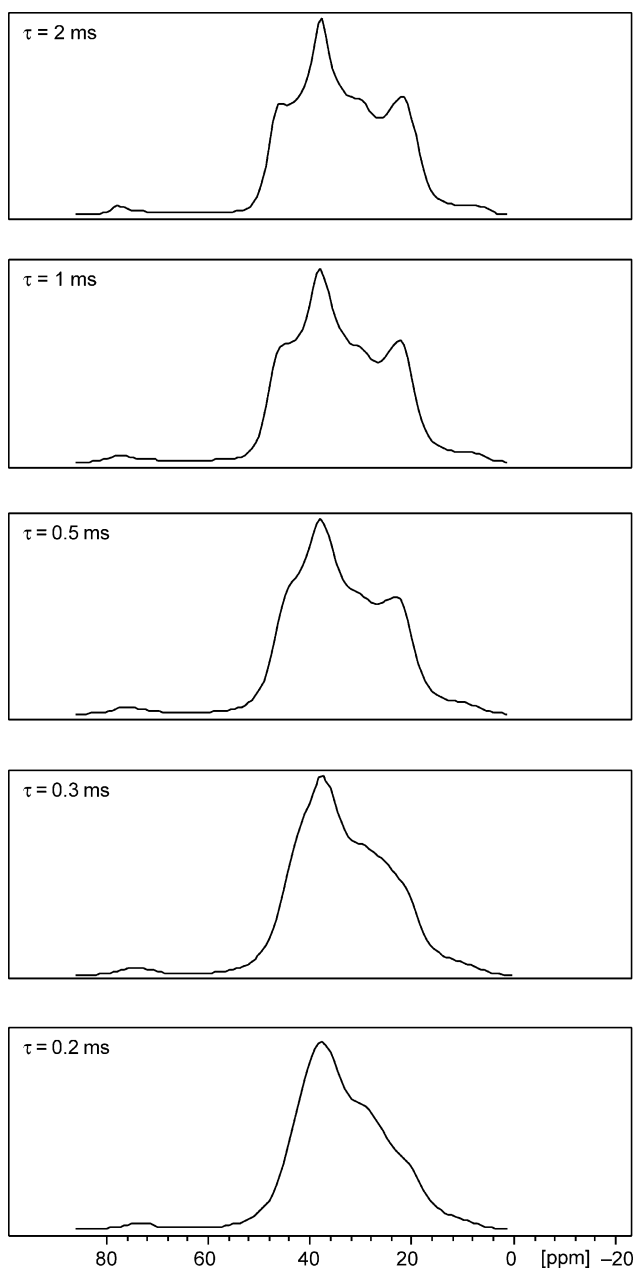
Fig. 7. Simulated (^{1}H)-^{13}C cross-polarization spectra of cetyl palmitate for various correlation times of rotational diffusion. The simulations are based on the data listed in Table 1 and a contact time of $t_{cp} = 1$ ms.
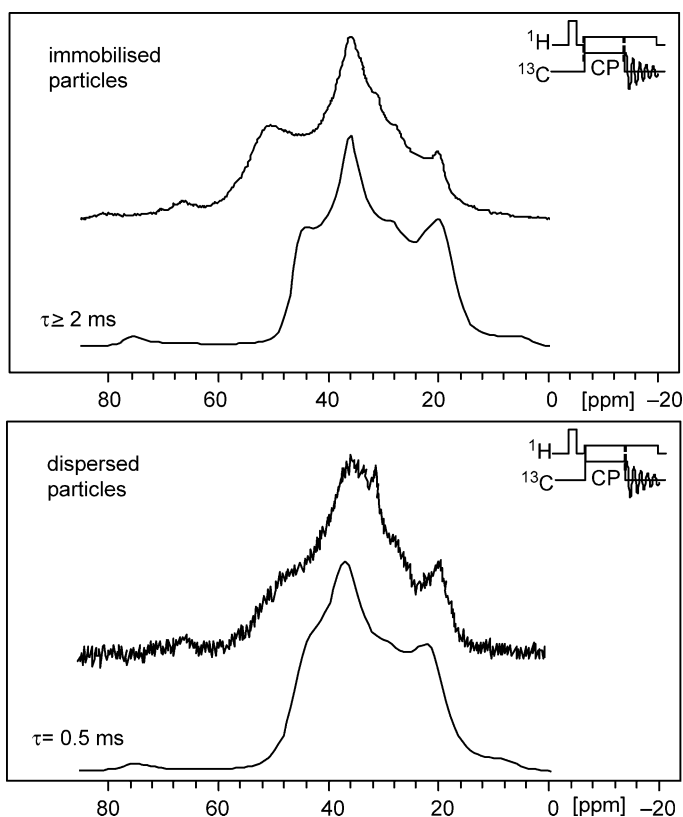
Fig. 8. Comparison between experimental and simulated (^{1}H)-^{13}C cross-polarization line shapes for immobilized (top) and dispersed cetyl palmitate nanospheres (bottom). The calculations are based on the chemical shift data for *n*-eicosane and polyethylene terephthalate which explains for the deviation of some resonance positions.

(ii) More important, the determination of the correlation time for isotropic rotational diffusion τ allows for a determination of the particle size. With the general dependence of τ on the particle radius a, the viscosity of the liquid phase η and the temperature T is given by[40]

$$\tau = \frac{4\pi\eta a^3}{3kT} \tag{54}$$

it is possible to estimate the radius of the dispersed cetyl palmitate nanospheres to approximately $a = 80$ nm under the given temperature conditions ($T = 298$ K in water).

Consequently, this approach may be used to differentiate between all solid constituents from those in the liquid phase. However, so far, one basic drawback of the method remains: the spectral resolution for solid components is very poor, not to

mention any option for their chemical identification. This deficiency asks for another element of the NMR toolbox: cross-polarization experiments under sample spinning. If sample rotation occurs around an axis tilted with an angle of $\beta = 54.74°$ with respect to the magnetic field, the technique is generally referred to as MAS. When applied to liquid particle dispersions, one has to take special care to avoid particle sedimentation or flotation, e.g., by adapting the density of the fluid medium. The outcome of a (^{1}H)-^{13}C MAS experiment on a liquid particle dispersion is similar to one on a solid sample: increasing resolution is accompanied by the formation of spinning sidebands at positions depending on the spinning velocity (Fig. 9).
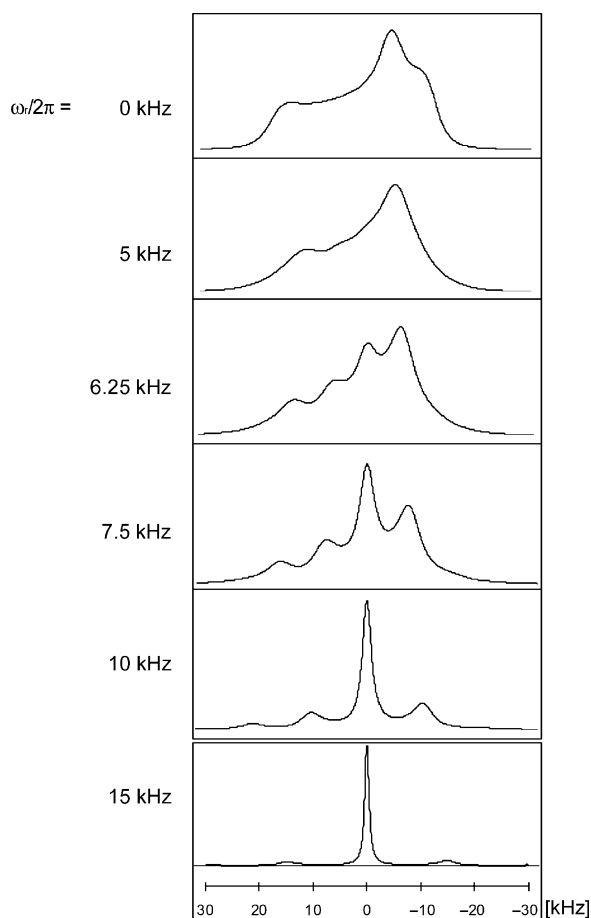
Fig. 9. Simulated ^{13}C MAS spectra under variation of the sample spinning rate ($\omega_r/2\pi =$ 0–15 kHz). The calculations are based on given anisotropic chemical shielding data ($\sigma_{11} = -15$ kHz, $\sigma_{22} = -5$ kHz, $\sigma_{33} = 20$ kHz) and isotropic rotational diffusion ($\tau = 0.1$ ms) (reproduced from Ref. [23] with permission).
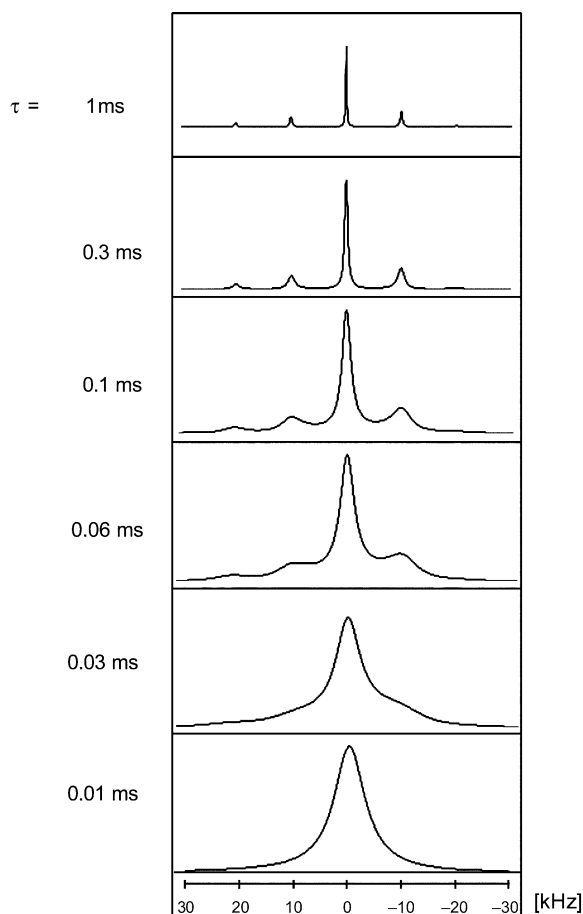
Fig. 10. Simulated ^{13}C MAS spectra under variation of the correlation time for rotational diffusion ($\tau=0.01$–1 ms). The calculations are based on given anisotropic chemical shielding data ($\sigma_{11}=-15$ kHz, $\sigma_{22}=-5$ kHz, $\sigma_{33}=20$ kHz) and a sample spinning rate of $\omega_r/2\pi=10$ kHz. In case of $\tau=0.01$ ms, the correlation time comes close to the reciprocal spinning frequency $1/\omega_r\approx0.016$ ms, leading to a near total loss of the MAS effect (reproduced from Ref. [23] with permission).

The slow rotational diffusion of the particles leads to a certain broadening of resonance lines and side bands (Fig. 10), finally resulting in a total loss of the MAS effect when the correlation time τ reaches the same order of magnitude as the reciprocal spinning velocity $1/\omega_r$ (Fig. 10, bottom).[23] The sideband integrals follow a pattern which is predicted by the method of Herzfeld and Berger.[41]

A typical experimental result (a) together with a simulated counterpart (b) is shown in Fig. 11. In the given case, the sample consists of an aqueous dispersion of polystyrene nanospheres with a particle radius of $a=285$ nm and is studied under a spinning frequency of $\omega_r/2\pi=2$ kHz at the magic angle.[42] Slow tumbling of the nanospheres leads
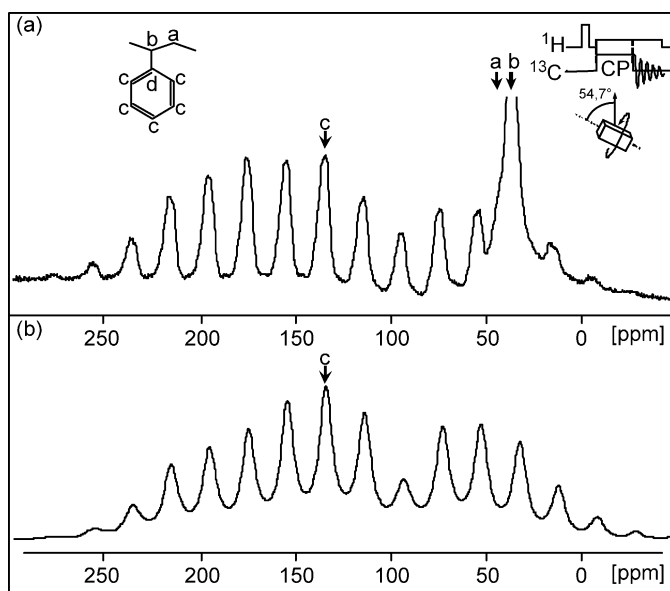
Fig. 11. (a) Experimental (^{1}H)-^{13}C cross-polarization spectrum ($\omega_H = 400$ MHz, full proton decoupling) of an aqueous dispersion of polystyrene nanospheres ($a = 285$ nm) under magic angle conditions at a spinning frequency of $\omega_r/2\pi = 2$ kHz. The overlapping signals a and b near 40 ppm derive from the aliphatic chain (see inset), while the centre band of the aromatic carbons appears at 135 ppm. The aromatic carbon of type d remains almost invisible due to the lack of adjacent hydrogen nuclei. (b) Corresponding simulated line shape for the aromatic carbons of type c assuming isotropic rotational diffusion with a correlation time of $\tau = 4$ ms.

to a significant broadening of the signals including the multiple side bands of the aromatic region, all of which is reproduced by the spectral simulation for a correlation time of 4 ms (for the signal of aromatic carbons c, see Fig. 11b).

Principally, the line broadening may be analysed to yield data on the rotational diffusion. However, the increase in line width by itself can be rather unspecific as multiple other sources of line broadening are possible. To avoid this uncertainty and to yield additional information on the particle dynamics, one may combine the advantages of the MAS approach with the ones of static NMR spectra by adjusting the spinning axis at an angle which slightly deviates from the magic one (off-MAS). In this case, the original powder pattern for long correlation times is scaled down to a narrow line shape which somewhat resembles the common solid-state spectrum, but shows better resolution and signal-to-noise ratio. A simulated example for a methyl group at $\beta = 52.5°$ is shown in Fig. 12.[43,44] With increasing tumbling rate, the scaled powder pattern turns into a broad line of Gaussian-like shape. A maximum of the line width is obtained for $\tau \approx 1/\omega_r$. For shorter correlation times, the line shape is subject to motional narrowing independent of the influence of sample spinning and finally turns into a sharp high resolution signal.
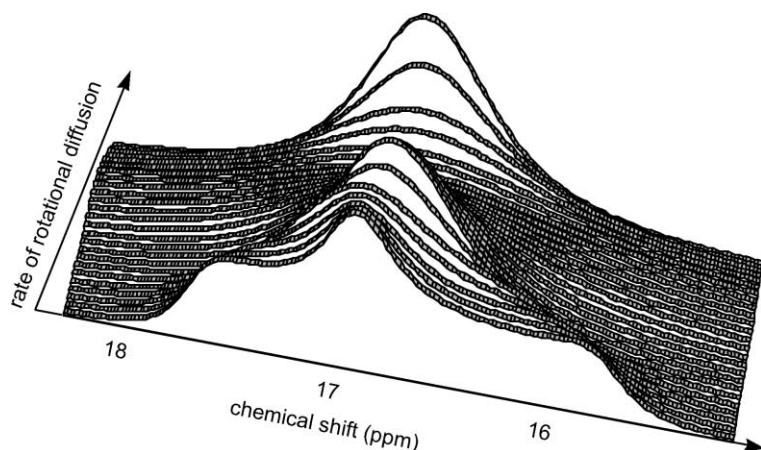
Fig. 12. Stacked plot of simulated ^{13}C off-MAS spectra ($\omega_C \approx 100$ MHz) for a typical methyl group at different rates of isotropic rotational diffusion.[42] Only the centre band is shown, all side bands are of very weak intensity. Within the stacked plot, the correlation time varies between 15 ms (front) and 15 µs (back). For all spectra, the spinning frequency is set to $\omega_r/2\pi = 1660$ Hz at an angle of $\beta = 52.5°$. Chemical shift data are as those given for the methyl group of *n*-eicosane in Table 1.

An example for the result of an off-MAS experiment is shown in Fig. 13. The spectrum (the display in Fig. 13 is restricted to the main signals of the aliphatic region) was obtained on an aqueous dispersion of cetyl palmitate nanospheres at $\omega_r/2\pi = 1660$ Hz and $\beta = 52.5°$. Under these conditions, the resolution is good enough to make a clear signal assignment to the three characteristic segments in the aliphatic chain[2,43]: the standard methylene groups (A), the terminal methylene group of each
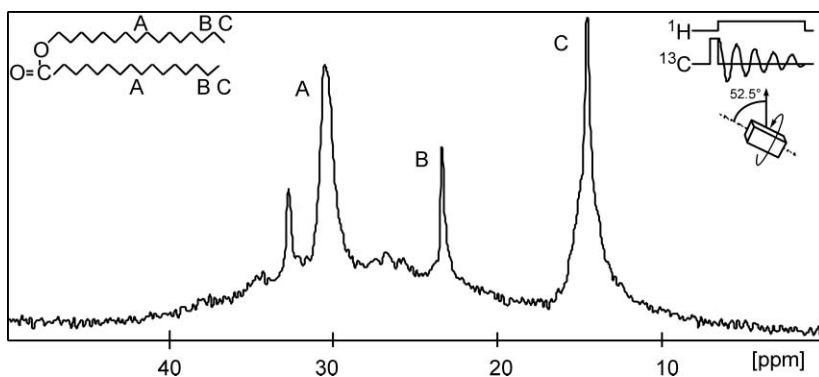
Fig. 13. Experimental ^{13}C off-MAS spectrum of an aqueous dispersion of cetyl palmitate nanospheres ($\omega_C \approx 100$ MHz, full proton decoupling). The spinning frequency has been adjusted to $\omega_r/2\pi = 1660$ Hz at an angle of $\beta = 52.5°$. The signals A, B, and C can be assigned to the standard methylene group, the terminal methylene group and the methyl end group, respectively.
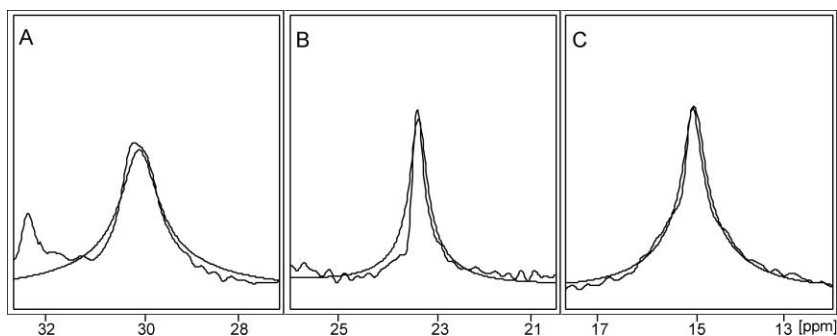
Fig. 14. Experimental ^{13}C off-MAS signals of cetyl palmitate carbons A, B, and C (see Fig. 13) together with their simulated counterparts (smooth lines). The calculations are based on the chemical shift parameters listed in Table 1 and an even distribution of correlation times between 0.1 and 1 ms. All other simulation parameters reflect the experimental conditions listed for Fig. 13.

chain (B) and the terminal methyl groups (C). Incomplete spin-lattice relaxation leads to the loss of proportionality between the signal integrals. All three signals show clearly different widths and line shapes which are supposed to reflect the isotropic tumbling of the nanospheres.

Figure 14 represents a corresponding best fit analysis of the three signals A, B and C. Except for the different chemical shift anisotropies (see Table 1, columns 1–3), a single data set has been used for the simulation of the three line shapes.[43] It combines the experimental parameters given above with the velocity of the isotropic tumbling. In order to obtain a simultaneous best fit for all three signals as shown in Fig. 14, one has to assume a continuous distribution of correlation times between 0.1 and 1 ms which corresponds to a particle radius ranging between 50 and 100 nm. This finding has been supported by independent measurements.[43]

The combination of direct excitation or cross-polarization NMR experiments with off-MAS sample spinning seems to be the most powerful approach for the study of rotational diffusion of all system constituents. It allows for a chemical identification of all organic system components and simultaneously yields data on their rotational diffusion. Hence, for detailed studies on particle tumbling in complex systems, it represents the preferred experimental condition for all particle dispersions which are stable enough to survive the inertial field during sample spinning for an adequate period of time.[2]

4.2. Assignment to structural elements of particle dispersions

The unique capability of NMR spectroscopy to differentiate by means of molecular mobility makes it a perfect tool to assign chemical constituents to structural elements of a particle dispersion. This is most straightforward in the case of dispersed nanospheres: every constituent which is part of the solid matrix will exhibit the slow particle tumbling, while all components of the liquid continuous phase undergo rapid rotational diffusion.
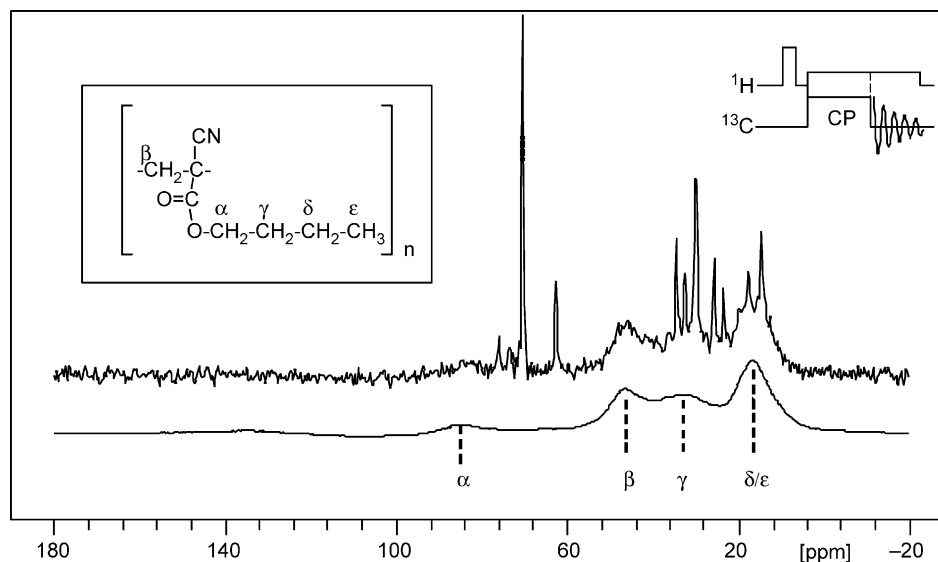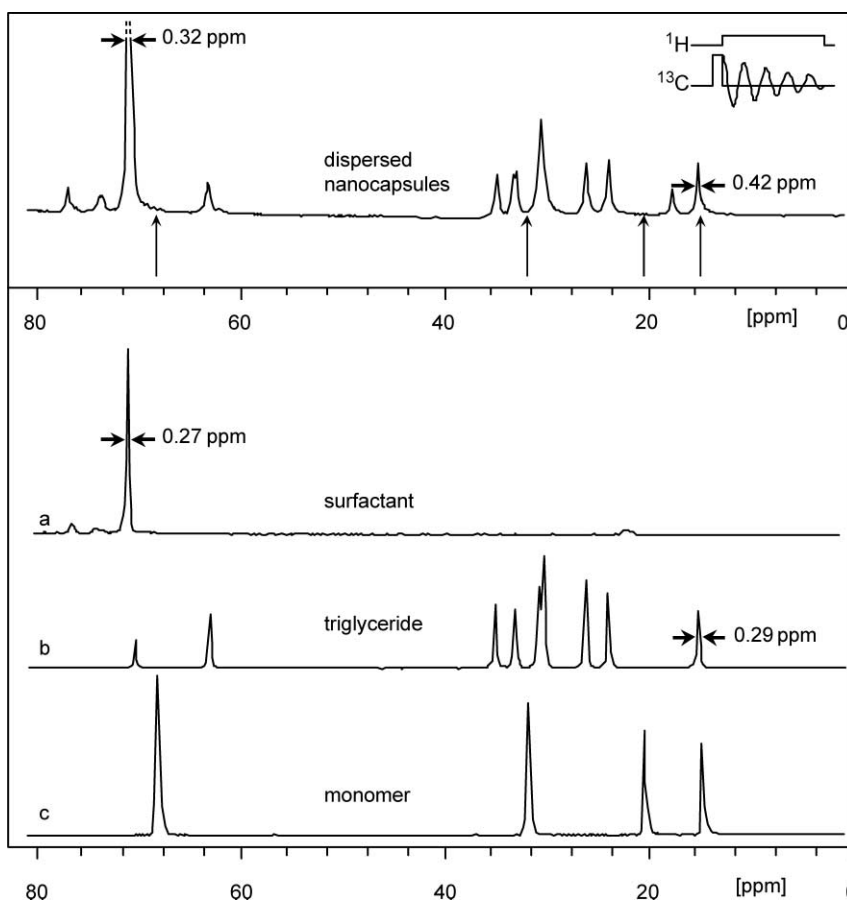
Fig. 15. Experimental (^{1}H)-^{13}C cross-polarization spectra of an aqueous dispersion of poly-*n*-butylcyanoacrylate nanocapsules (top) and of a solid reference sample of the same polymer (bottom). Both spectra are measured at a resonance frequency of $\omega_C \approx 100$ MHz after a contact time of $t_{cp} = 0.5$ ms under full proton decoupling. The assignment of the main solid-state resonances is indicated in the inset.[45]

The problem appears somewhat more complicated in the case of nanocapsules, where one deals with at least three different structural elements: a continuous liquid phase, the solid phase represented by the capsule walls and the encapsulated liquid domain. All techniques mentioned so far only allow for the differentiation of the solid phase from the two liquid phases. An example for poly-*n*-butylcyanoacrylate nanocapsules in aqueous dispersion[20] is shown in Figs. 15 and 16.

The system consists of hollow spheres made up from the polymer poly-*n*-butylcyanoacrylate which are filled with a triglyceride oil component and dispersed in an aqueous phase in presence of a surfactant. While the capsule walls are only a few nanometers thick, the capsule radius varies between 100 and 200 nm. A (^{1}H)-^{13}C cross-polarization spectrum which was obtained under static conditions after a contact period of $t_{cp} = 0.5$ ms (Fig. 15) shows a set of narrow lines superimposed on a broad solid-state line shape.[14,45] As the particle tumbling for the relatively large capsules is quite slow ($\tau \approx 10$ ms), the latter is almost identical to a reference spectrum of poly-*n*-butylcyanoacrylate (Fig. 15, bottom). Even without sample spinning, four contributions to the solid-state signal can be assigned to the aliphatic carbons of the polymer.[45] Clearly, all narrow lines can be attributed to liquid components. These can be selectively observed in a direct excitation spectrum (Fig. 16), where the solid contributions are not enhanced and therefore hardly detectable.

A comparison with reference spectra (Fig. 16a,b) allows one to identify all spectral contributions which belong to the liquid components: the surfactant dissolved in the

Fig. 16. Experimental ^{13}C direct excitation spectra of an aqueous dispersion of poly-*n*-butylcyanoacrylate nanocapsules (top) and of reference samples of liquid and dissolved constituents (a: aqueous solution of the block-copolymer surfactant Pluronic F68$^®$; b: the liquid oil component Miglyol 812$^®$ used as capsule content; c: the liquid monomer *n*-butylcyanoacry-late).[14] All spectra are measured at a resonance frequency of $\omega_C \approx 100$ MHz under full proton decoupling. In the spectrum of the dispersion, no narrow signals occur at the positions of the *n*-butylcyanoacrylate resonances (vertical arrows), indicating the complete absence of the monomer after the formation of the capsules. For the capsule dispersion, a slight increase in line width is observed for the characteristic resonances of the liquid components.

aqueous phase and the triglyceride which makes up the liquid core of the nanocapsules.[14] Further, a comparison with the spectrum of the liquid monomer (Fig. 16c) indicates that the polymerization reaction has been complete as no monomer residues are detectable. A certain increase of the signal line widths for the fluid components in the dispersion may be attributed to local variations of the magnetic susceptibility.

So far, the assignment to the structural elements is restricted to the separation of solid and fluid components. Neither direct excitation nor cross-polarization spectra give any indication whether the observed fluid components occur inside or outside of

the encapsulated spheres. The two liquid domains only differ in a single physical property: its lateral self-diffusion pattern. For very short diffusion times, the average lateral dislocation of individual molecules in the encapsulated and the continuous phase is practically identical. However, if self-diffusion is observed over longer time intervals, encapsulated molecules will experience the boundaries of their confinement, a condition which is known as restricted lateral diffusion.[46–49] Under these conditions, the propagator function deviates from a Gaussian profile and depends on the geometry of the capsules. In addition, it will begin to reflect the Brownian motion of the capsule as a whole, a phenomenon which generally can be neglected for short observation periods.

Consequently, the encapsulated fraction is easily identified by a PFG experiment. In case of free self-diffusion with a diffusion coefficient D, the decay of the relative signal intensity $I_{rel}(G_{max})$ follows the equation[49]

$$I_{rel}(G_{max}) = \frac{I(G_{max})}{I(0)} = \exp\left[-\gamma^2 G_{max}^2 \delta^2 D\left(\Delta - \frac{\delta}{3}\right)\right] \tag{55}$$

where $I(0)$ stands for the echo intensity in absence of the gradient, while Δ, G_{max}, and δ denote the separation, the strength and the individual duration of the two rectangular gradient pulses (see inset in Fig. 17). According to Eq. (55), a plot of the values $(-\ln I_{rel})$
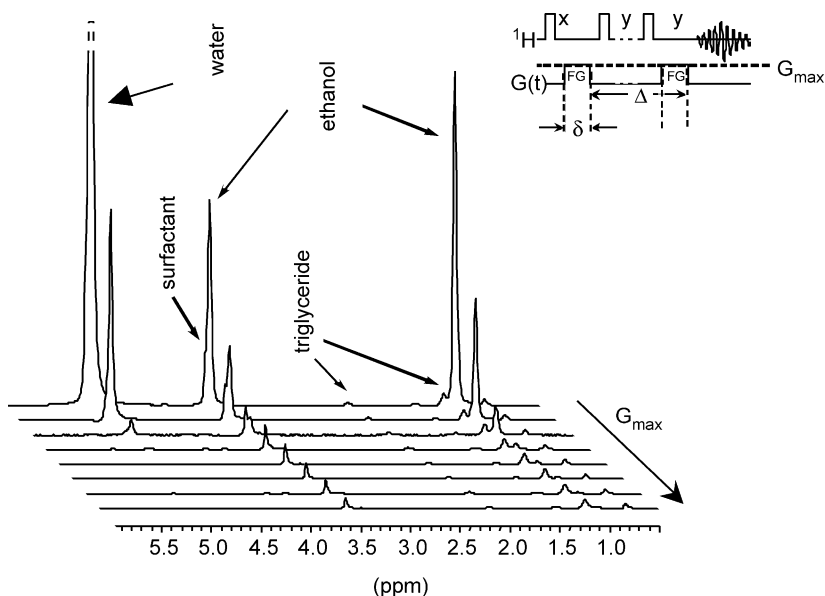

Fig. 17. Stacked plot of ^{1}H spectra resulting from a PFG experiment under variation of the maximum gradient strength G_{max} on a nanocapsule dispersion.[2,50] A stimulated echo sequence was used in combination with the pulsed field gradient (FG, see inset), the diffusion time was adjusted to $\Delta = 24$ ms. The echo decay with increasing gradient strength is related to the self-diffusion coefficient of the observed spin: rapidly diffusing water molecules lead to a steep loss of the corresponding ^{1}H signal (left), while the resonances of encapsulated components (e.g., of triglyceride at 2.1 and 1.3 ppm) exhibit much smaller dependencies.

against the expression $[\gamma^2 G_{max}^2 \delta^2(\Delta - \delta/3)]$ results in a straight line with a slope that is identical to the self-diffusion coefficient D. In case of restricted diffusion, Eq. (55) is not fully applicable and, instead of a true diffusion coefficient D, only yields an apparent diffusion coefficient D_{app} which strongly depends on the gradient pulse spacing Δ. Generally, the resulting parameter D_{app} comes close to D for the limit of small diffusion times Δ. The limiting value of D_{app} for long observation periods Δ reflects the motion of the individual capsules in the continuous medium.

A typical result for a poly-n-butylcyanoacrylate nanocapsule system using PFG combined with a stimulated echo experiment on protons[2,20,50] is shown in Fig. 17. The decay of the signal intensity with increasing pulsed gradient strength G_{max} directly depends on the average lateral displacement of the observed spins during the observation period Δ.[49] Rapid free diffusion of water and ethanol leads to a steep decay of the corresponding ^{1}H-signal. The surfactant, with its large molecular mass and its strong affinity to the particle surface, exhibits a much smaller dependence of its signal intensity on G_{max}. Finally, the resonance intensity of the encapsulated triglyceride oil component is only slightly affected by increasing gradient strength.

On detailed analysis, the signal decay of the encapsulated oil components reveals the characteristics of restricted diffusion (Fig. 18). For all diffusion times $\Delta \geq 10$ ms, the plots of the negative logarithmic relative intensities $(-\ln I_{rel})$ vs. the expression $[\gamma^2 G_{max}^2 \delta^2(\Delta - \delta/3)]$ show the expected linear dependency according to Eq. (55). However, their slopes strongly depend on the spacing of the gradient pulses, differing by more than a factor of 20 within the range of $\Delta = 9$–60 ms. Consequently, the apparent diffusion constants D_{app} vary distinctly with the duration of the diffusion time (Fig. 19).[50] For short observation periods, the experiment cannot distinguish between free and encapsulated triglyceride oil. The large majority of the oil molecules does not come into contact with the capsule walls during the relatively short PFG experiment, therefore the
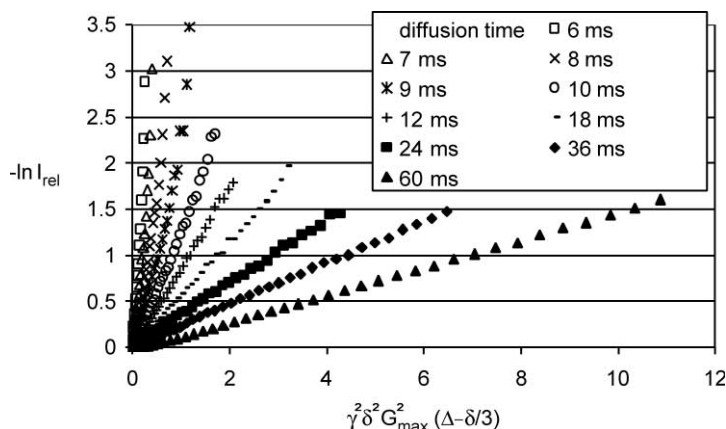
Fig. 18. Negative logarithmic echo intensities plotted vs. the parameter $[\gamma^2 G_{max}^2 \delta^2(\Delta - \delta/3)]$ as derived from the triglyceride ^{1}H signal at 2.1 ppm (see Fig. 17).[50] As typical for restricted diffusion, the observed slopes strongly depend on the diffusion time Δ. For $\Delta \geq 10$ ms, the plots are nearly linear and apparent diffusion constants D_{app} can be determined (see Fig. 19).
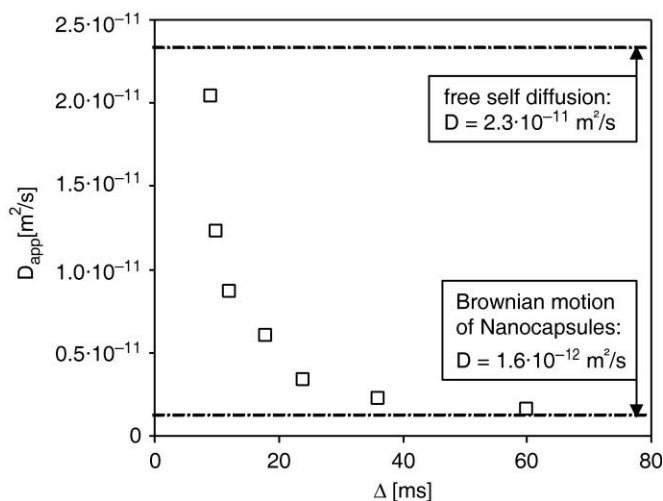
Fig. 19. Apparent self-diffusion constants D_{app} of the triglyceride oil component in a nanocapsule dispersion derived from the plots in Fig. 18. For short diffusion times Δ, the values for D_{app} come close to the self-diffusion coefficient of the bulk oil ($D = 2.3 \times 10^{-11}$ m²/s, top line). For long diffusion times, D_{app} approaches the diffusion constant which describes the Brownian motion of the capsules in the aqueous medium ($D = 1.6 \times 10^{-12}$ m²/s, bottom line).

apparent diffusion constant comes close to the self-diffusion constant of the free oil (top line in Fig. 19). With increasing duration of the observation period, the encapsulated oil will be restricted by the confinement limits, leading to a significant reduction of D_{app}. In the limit of extremely long diffusion times Δ, the position of each individual oil molecule is averaged out to the centre of the surrounding capsule. In this case, the apparent diffusion constant reflects the Brownian motion of the capsules, which for an average radius of $a = 120$ nm comes close to $D = 0.16 \times 10^{-11}$ m²/s (Fig. 19, bottom line).

In the given case, two conclusions can be drawn based on the observations[50]:

(i) The triglyceride oil represents the only strictly encapsulated liquid fraction, all other liquid components predominantly occur in the continuous phase.

(ii) The triglyceride oil fraction is absolutely limited to the encapsulated phase as, for long time intervals Δ, no contribution of some rapid signal decay with increasing gradient strength is observed.

(iii) The encapsulated domain can be regarded as a hollow sphere filled with liquid oil. The inside cavity of the capsules obviously lacks solid or dissolved fractions of the polymer; otherwise the short-time diffusion behaviour of the encapsulated oil molecules would differ from the one of the bulk oil.

This simple example shows the principle how PFG experiments can be used to discriminate the encapsulated liquid components against the ones occurring in the continuous phase. However, the real potential of the PFG experiment is established when studies are extended to time-resolved processes or to the observation of molecular exchange across the domain limits (see Section 4.5).

4.3. Phase transitions of the nanoparticle matrix

As in any other system, the phase state of the structural elements of nanoparticle dispersions may change induced by variation of physical parameters. This aspect becomes most interesting if the matrix material is affected, e.g., the bulk structure of a nanosphere or the wall material of a nanocapsule membrane. This case has very promising practical applications: a nanocapsule or a nanoparticle may be 'loaded' while being in one phase state and subsequently 'sealed' by a phase transition. This possibly allows one to produce prefabricated particle dispersions where the final encapsulation step is accomplished by addition of the active ingredient at any given point in time.

An example for a nanoparticle system undergoing a phase transition of the matrix is given by nanospheres and nanocapsules from poly-ε-caprolactone (PCL) formed by the emulsion-diffusion technique.[51,52] In this case, the mechanism of particle formation in an o/w emulsion is based on the diffusion of an organic solvent into the continuous phase followed by the deposition of the polymer around an oil droplet (Fig. 20).
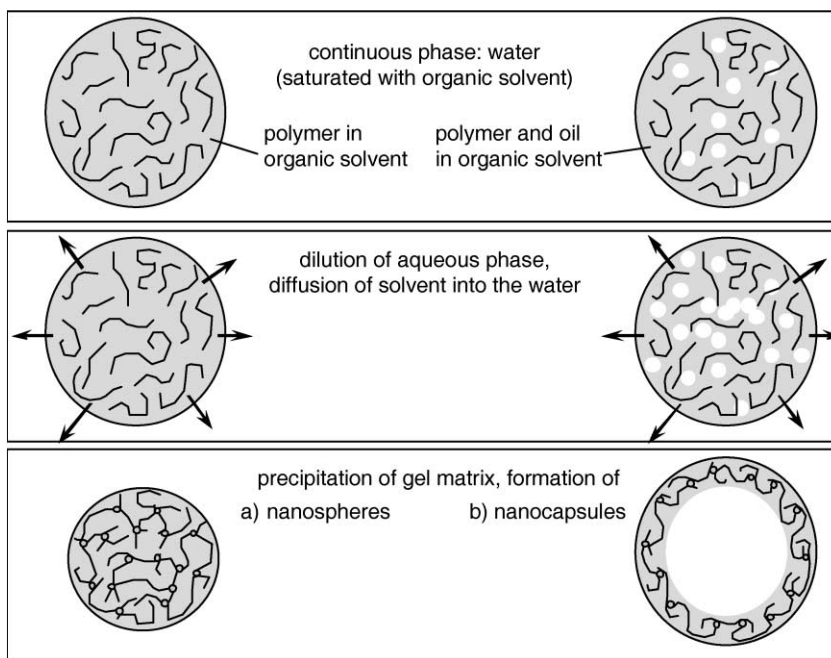
Fig. 20. Schematic representation of the emulsion-diffusion process leading to the formation of nanospheres (left) and nanocapsules (right).[52] Top row: an organic solvent containing a dissolved polymer (optionally together with an oil component, right) is dispersed in an aqueous phase and forms an o/w emulsion. Centre row: the aqueous phase is diluted with water, causing the organic solvent from the droplets to diffuse into the surrounding.[21] Bottom row: the polymer precipitates to form nanospheres (left) or nanocapsules (right).
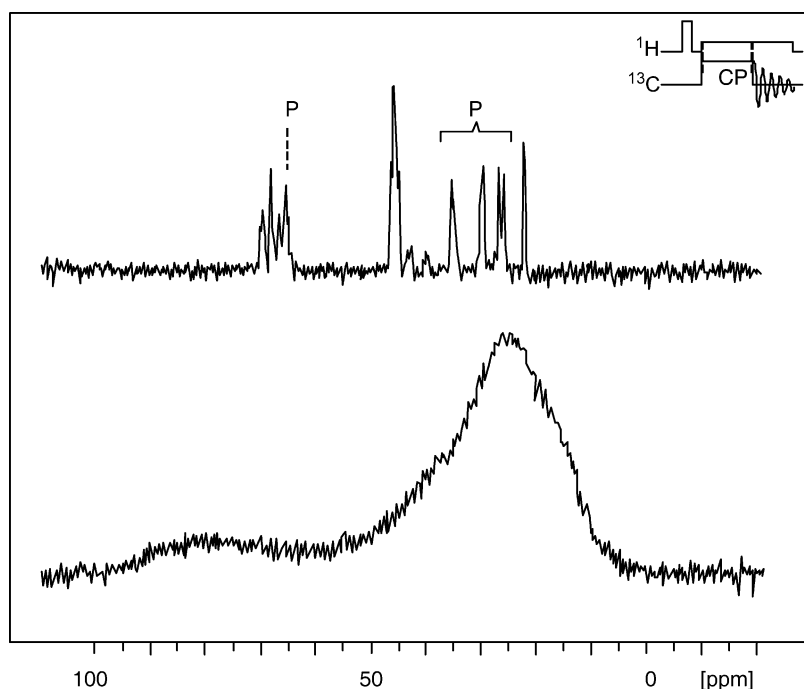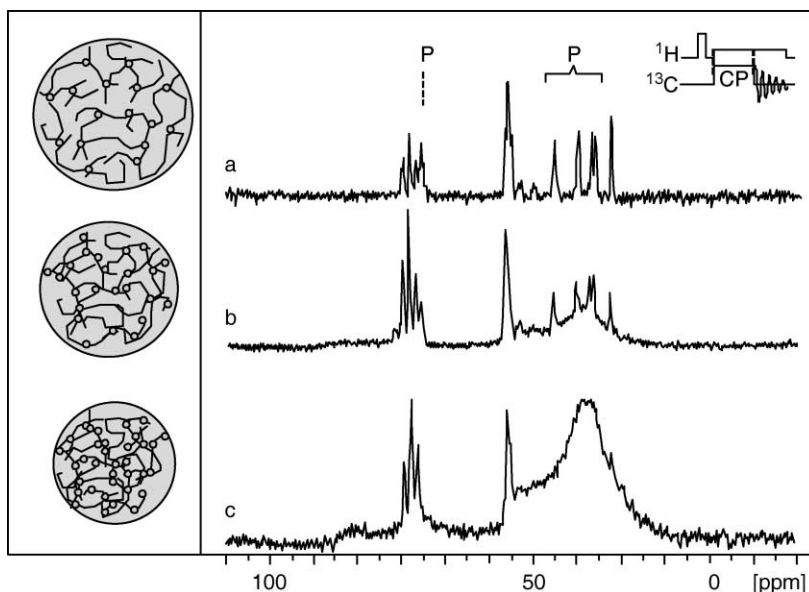
Fig. 21.   Top: Experimental (^{1}H)-^{13}C cross-polarization spectrum of freshly prepared poly-ε-caprolactone nanospheres in an aqueous dispersion ($\omega_C \approx 100$ MHz, full proton decoupling). Five polymer signals ('P') are detected within the given spectral range, other resonances can be assigned to the surfactant polyvinyl alcohol and small amounts of polyvinyl acetate.[21] Bottom: Corresponding (^{1}H)-^{13}C cross-polarization spectrum of a solid bulk sample of poly-ε-caprolactone under static conditions.

Figure 21 shows a cross-polarization (^{1}H)-^{13}C spectrum of the resulting particle dispersion in comparison with a corresponding spectrum of the solid polymer. Surprisingly, the expected wide lines for the solid polymer at slow particle tumbling cannot be detected. Instead, the polymer is represented by a set of relatively narrow ^{13}C resonances (indicated by 'P' in Fig. 21).[2,52] This indicates that the polymer chains, though being part of a solid structure, exhibit a considerable degree of molecular mobility, probably by incorporating a large amount of solvent molecules. In fact, the solid matrix of the freshly prepared nanoparticles can be considered as a swollen gel being formed by physical cross-linking of the polymer chains in presence of a large amount of solvent (Fig. 20, bottom row).

It is expected that the structure of the gel matrix will vary together with the concentration of the solvent. Figure 22 shows a series of (^{1}H)-^{13}C spectra obtained during a dehydration process. Being dried in a rotating flask under slightly reduced pressure, the particles lose approximately 50% of their water content and the original spectrum (Fig. 22a) gradually turns into the expected solid-state line shape (Fig. 22c). This process
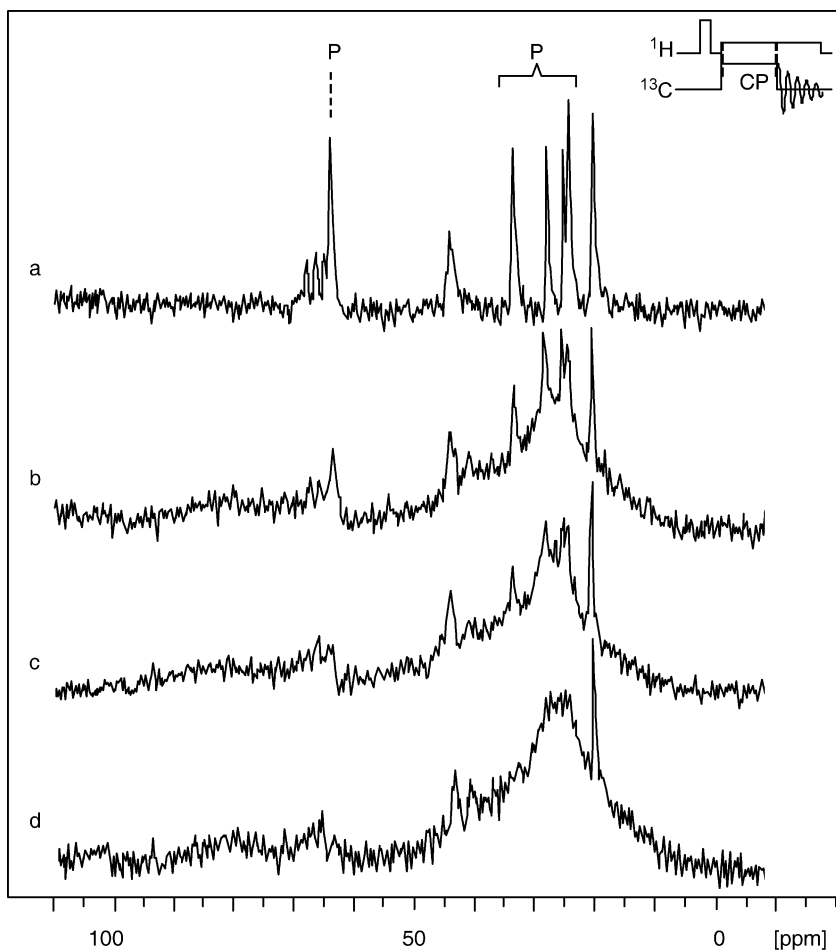
Fig. 22.   Experimental (^{1}H)-^{13}C cross-polarization spectra of poly-ε-caprolactone nanospheres in different states of dehydration ($\omega_C \approx 100$ MHz, full proton decoupling). With the original water content after the preparation, all polymer signals indicate a high degree of local chain mobility (a). After removal of approximately 50% of the matrix water, the complete polymer is irreversibly transformed into a rigid solid (c). Spectrum (b) represents an intermediate state.[21]

is irreversible, as the addition of water does not cause the system to return into the fully hydrated state.[2,52] In fact, the line shape represented in Fig. 22c is conserved even after the particles have been re-dispersed in water for an extended period of time. Obviously, the de-swelling of the gel has led to a dramatic increase of the number of cross-linking points in the polymer matrix accompanied by a corresponding loss in local chain mobility. At the same time, the particle size spectrum indicates a shift towards smaller particles.[52] In short, dehydration has reduced the particle size and turned the matrix into a classical polymer system with some residual solvent content.

Instead of removing water from the complete particle dispersion, one may induce the same process of matrix dehydration by simply freezing the aqueous phase and keeping it at $-10°$C for a limited duration.[52] During the freezing step, the concentration of liquid water in the continuous phase is virtually reduced to zero, causing a corresponding loss of water in the gel matrix of the particles while the swelling equilibrium is re-established. This process is most efficient if repeated by multiple freeze–thaw cycles (Fig. 23). After two freeze–thaw steps, the gel particles have irreversibly reached the de-swollen state while the original particle concentration of the dispersion is conserved throughout the process[52] (Fig. 23d).

Numerical simulation of the (^{1}H)-^{13}C spectra based on the given particle tumbling conditions allows for the quantitative analysis on a system which has undergone a partial phase transition.[2] An example for the poly-ε-caprolactone particles is shown in Fig. 24.

Fig. 23. Experimental (^{1}H)-^{13}C cross-polarization spectra of poly-ε-caprolactone nanospheres in aqueous dispersion after different freezing histories ($\omega_C \approx 100$ MHz, full proton decoupling): (a) dispersion after 4 weeks storage at room temperature, (b) after freezing for 1 h and thawing, (c) after freezing for 22 h and thawing, (d) after two freezing/thawing cycles. The signals at 23 and 45 ppm correspond to the surfactant polyvinyl alcohol and residual polyvinyl acetate, respectively.[21]

The experimental spectrum, which has been taken after a single 12 h freezing step, shows narrow lines superimposed on a solid-state spectrum for the polymer. The result was reproduced by a simulated spectrum based on data for an aliphatic chain (Table 1) assuming two fractions of different mobility. Fraction A represents the dehydrated solid and is merely subject to particle tumbling at a rate which is expected for particles of $a = 50$–70 nm in aqueous dispersion ($\tau = 0.1$ ms). Fraction B represents the particles with the gel matrix; in this case, the molecular reorientation is dominated by the internal mobility which is assumed to be equivalent to an isotropic tumbling of a short correlation time
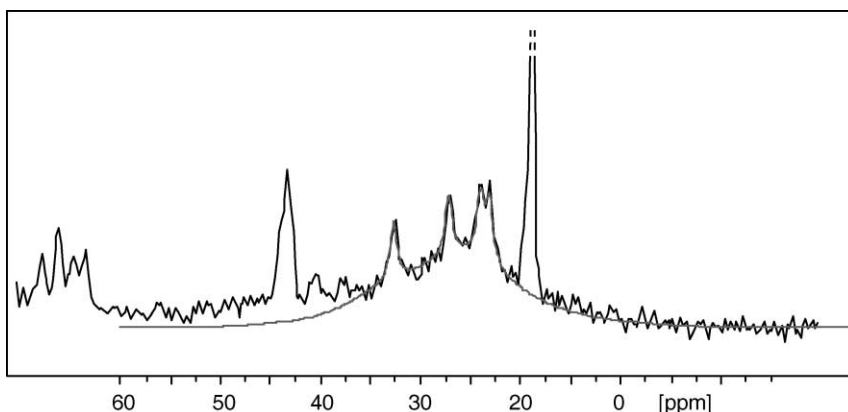
Fig. 24. Experimental and simulated (^{1}H)-^{13}C cross-polarization spectra of poly-ε-caprolactone nanospheres in aqueous suspension after 12 h freezing. The calculated spectrum reproduces the carbon spectrum of four different methylene groups based on the chemical shift anisotropy listed in Table 1. It represents a superposition of two fractions of different isotropic mobility (80%: $\tau = 0.1$ ms; 20%: $\tau = 0.007$ ms).

($\tau = 0.007$ ms). In case of the spectrum in Fig. 24, the best fit was found for a superposition of the contributions A and B in a 80%/20% relation.[2]

The practical applicability of such a system is quite clear: nanospheres or nanoparticles may be produced by the emulsion-diffusion method and stored in the gel state of the particle framework. At any later point of time, an active ingredient may be added to the dispersion which easily diffuses into or through the porous gel matrix. By a simple freezing step, the particles are sealed and the active ingredient is trapped inside the spheres or capsules. The whole process is easily monitored by solid-state NMR which, in this case, could hardly be replaced by any other analytical approach.

4.4. Molecular exchange on the nanoparticle surface

Usually, ^{13}C NMR techniques allow for a clear cut identification of the phase state of the observed component: while fluid components show narrow lines preferably observed by direct excitation, the solid constituents yield wide lines under static conditions and are most easily detectable by cross-polarization. However, several exceptions of this rule have to be taken into account:

(a) A polymer which forms a solid matrix may exhibit a high degree of internal mobility, hereby leading to motionally narrowed NMR signals which may be misinterpreted as being indicative for a liquid state. This situation is typical for the gel state (see, for example, the spectrum of poly-ε-caprolactone gel particles in Fig. 21).

(b) The inhomogeneity of the magnetic susceptibility, i.e., the local susceptibility drop at the particle surface, can possibly induce line width effects similar to those

due to restricted rotational molecular mobility. Hereby, liquid components may be falsely assigned to the solid phase.

(c) A component may take part in a rapid exchange between the liquid/dissolved and the solid state. In this case, its spectroscopic properties (line width, relaxation times, excitation behaviour) may reflect the typical features of both conditions.

An example for the latter phenomenon is illustrated in Fig. 25. For a given capsule system (the given example applies to a polyalkylcyanoacrylate nanocapsule), temporary adsorption processes are detected for the triglyceride oil component inside the capsules as well as for the dissolved surfactant molecules in the continuous phase.[14] A certain fraction P_{ads} of the triglyceride molecules as well as of surfactant molecules in aqueous solution is adsorbed by the inner and outer membrane surface. Both types of molecules undergo a continuous exchange process with another fraction P_{des} of the molecules in the bulk medium. This exchange is characterized by average residence times τ_{ads} and τ_{des} in the adsorbed and the desorbed state, respectively. A third fraction P_{free} of the bulk phase is excluded from this exchange process within a given observation period due to the limited lateral displacement.

The first experimental indication for the adsorption–desorption process is given by the development of the (^{1}H)-^{13}C cross-polarization spectrum of the nanocapsule dispersion
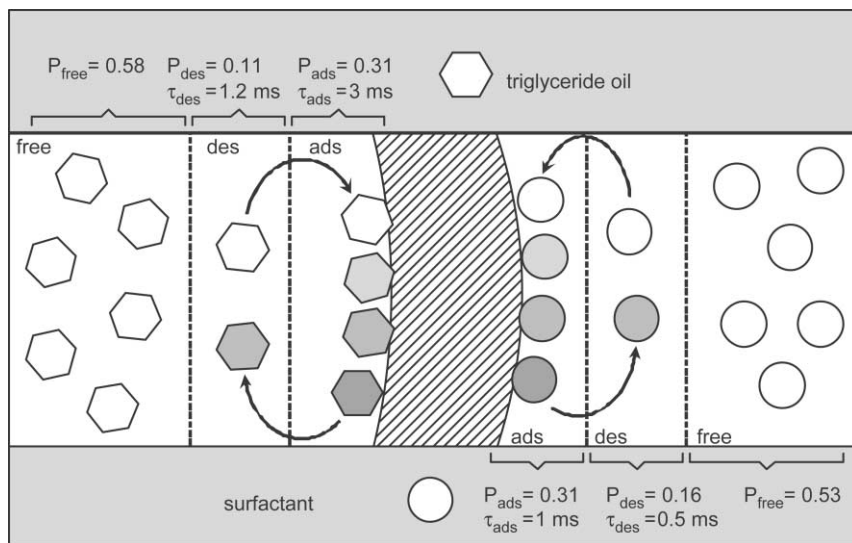
Fig. 25. Schematic representation of molecular adsorption processes at a nanocapsule membrane.[14] A certain fraction P_{ads} of the triglyceride molecules (hexagons) as well as of surfactant molecules in aqueous solution (circles) is adsorbed by the inner and outer membrane surface. They undergo a continuous exchange process with another fraction P_{des} of the molecules in the bulk medium. This exchange is characterized by average residence times in the adsorbed and the desorbed state τ_{ads} and τ_{des}. A third fraction P_{free} of the bulk phase is excluded from this exchange process within the experimental time frame by the limited self-diffusion. All numbers are discussed in Section 4.4.
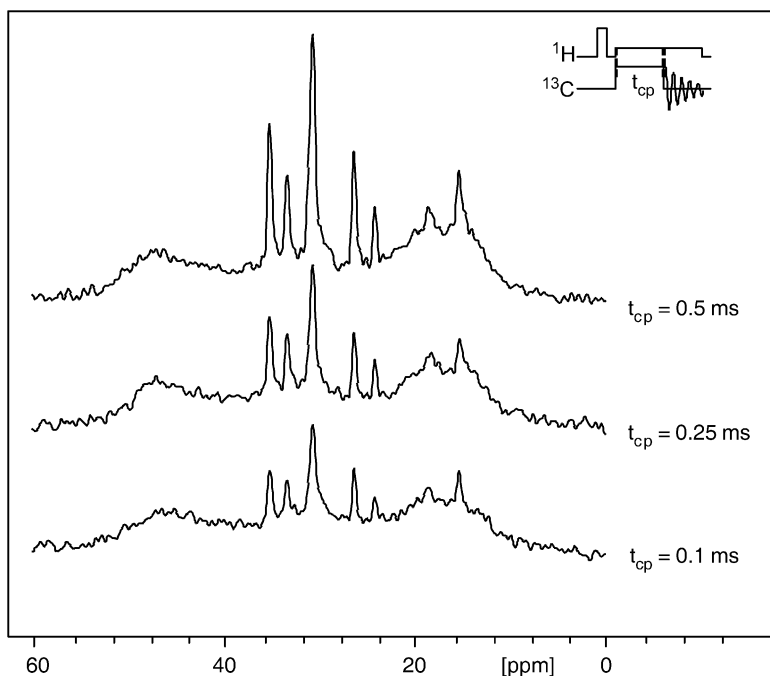
Fig. 26. Experimental (^{1}H)-^{13}C cross-polarization spectra of an aqueous dispersion of poly-*n*-butylcyanoacrylate nanocapsules at different mixing periods t_{cp}. The spectra are measured at a resonance frequency of $\omega_C \approx 100$ MHz after contact times of $t_{cp} = 0.1$, 0.25 and 0.5 ms under full proton decoupling. The wide lines derive from the polymer forming the capsule membrane while the narrow lines are assigned to the triglyceride oil. At $t_{cp} = 0.25$ ms, the broad signals of the polymer have almost developed to their full intensity, whereas the signals of the oil still gain amplitude.[2]

with an increasing mixing period t_{cp} (Fig. 26). At a mixing period as short as 0.25 ms, the wide lines of the solid matrix have already developed to their full intensity. In contrast, the signal amplitudes for the liquid components (only the resonances for the triglyceride are shown in Fig. 26) are still growing and only reach their maximum at $t_{cp} = 5$ ms. This observation is not really surprising as the mobile constituents in the liquid phase are expected to exhibit restricted growth of their cp amplitude (see Fig. 3). However, the further development of the cp amplitude is atypical and strongly deviates from the result obtained in absence of the particles: if the mixing time is extended up to 30 ms, the narrow signals do not exhibit the usual decay which is connected to the spin-lattice relaxation in the rotating frame. Instead, they remain at a constant level and, in some cases, even show some further growth.[2]

Given the process depicted in Fig. 25, this behaviour is quite easily understood: all molecules which are adsorbed onto the capsule surface become temporarily immobilized. In this state, they rapidly develop (^{1}H)-^{13}C cross-polarization signals which cannot be directly detected due to the overlap with the solid-state signal of the polymer. However, the polarization will still remain after the subsequent desorption step, leading to intensive

narrow lines in the spectrum. During the continuous exchange process, the polarized molecules are expected to accumulate in the vicinity of the particle surface. This is connected with a signal growth over time which partially or completely compensates for the signal relaxation.

Further details of the adsorption–desorption exchange process are accessible by measurements of $T_{1\rho}^{H}$, the spin-lattice relaxation time for the protons in the rotating frame.[2,14,19] The results of these measurements reveal a surprising difference depending on the experimental conditions of the $T_{1\rho}^{H}$ observation (Fig. 27). When determined under direct excitation, all plots of the signal intensities vs. the spin-lock duration t_{SL} can be fitted mono-exponentially, resulting in single relaxation times $T_{1\rho}^{H}$ (examples for two peaks of the oil component and the strongest peak of the surfactant are shown in Fig. 27, left column). However, if the same relaxation process is determined indirectly via the corresponding carbon nucleus in a cp experiment, all plots for oil and surfactant signals appear clearly biexponential (Fig. 27, right column). In all cases, an additional rapid decay is observed for $t_{SL} < 3$ ms which indicates rapid relaxation with time constants similar to those observed for the solid capsule wall.[2,14,19] During the relaxation process, the line shape is virtually unchanged, indicating that all detected molecules are in the liquid state while being observed in the NMR time signal.

Given the assumption of a rapid adsorption–desorption process, the fraction with the steep decay can be assigned to molecules which have undergone the adsorption and desorption step during the relaxation experiment and are in the liquid state during the observation of the FID. Their relative signal contribution is strongly enhanced by the cp condition, as the molecules are temporarily immobilized. At the same time, this immobilization is responsible for an accelerated spin-lattice relaxation with time constants close to those of the solid matrix. A quantitative analysis allows for the determination of the parameters of the molecular exchange on the capsule surface. Using a least square fit procedure (the best fit is represented by the solid lines in Fig. 27), the full set of parameters describing the adsorption–desorption cycle is obtained (see Fig. 25).[2,14,19]

4.5. Molecular exchange through nanocapsule walls

In general, nanocapsule walls are only a few molecular layers thin and often cannot be regarded as impermeable barriers. In most cases, especially if one deals with macromolecular capsule materials, they are more comparable to a sieve-like porous network than with a tight membrane. For most applications where active ingredients are encapsulated, it is essential to gather information on the capsule wall permeability. Nuclear magnetic resonance is the preferred and in some cases the only analytical approach to get access to permeability data. Two different approaches are possible and should be chosen depending on the time scale of the permeation process. Very slow leaking of the capsules may be studied under non-equilibrium conditions. In this case, a time-resolved NMR experiment (e.g., a series of consecutive ^{1}H spectra under the influence of a strong PFG) after a dilution of the sample easily reveals the decrease of the encapsulated fraction connected to the wall permeation. In many cases, however, the transfer through the capsule walls is too rapid to be followed in a time-resolved
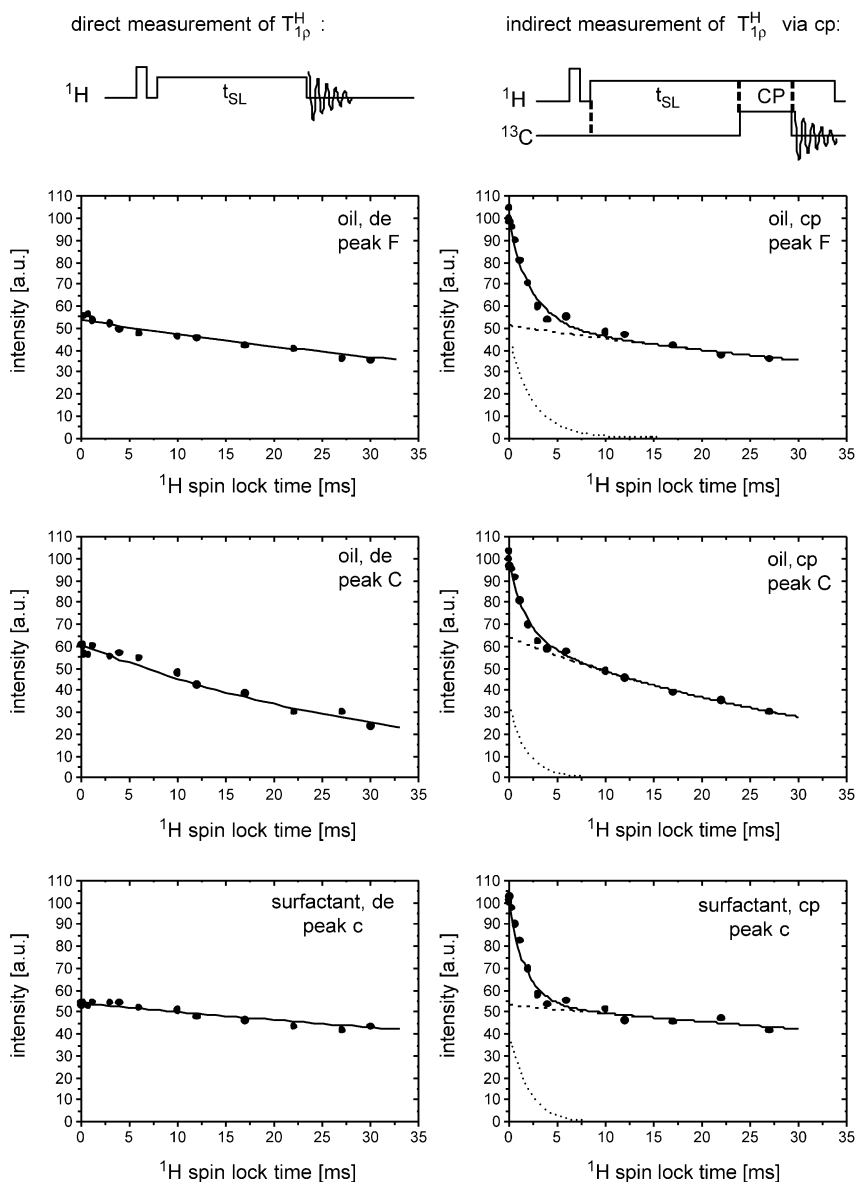
Fig. 27. Relaxation curves for an aqueous nanocapsule dispersion visualizing the spin-lattice relaxation of hydrogen nuclei in the rotating frame.[2,14] The curves refer to two different signals of the triglyceride oil (33 ppm, top row, and 35 ppm, centre row) and the most intensive signal of the surfactant (71 ppm, bottom row). The relaxation processes are obtained by variation of a spin-lock period t_{SL} either directly using a lone spin-lock signal on the protons (left column) or indirectly during a cross-polarization sequence (right column). Only in the first case could the relaxation curves be fitted by mono-exponential decays (solid lines) yielding the given relaxation times $T_{1\rho}^{H}$. The bi-exponential relaxation curves obtained in the cp mode (right column) have been fitted based on the parameters given in Fig. 25.

manner. Then the only alternative is the observation of the exchange process in the equilibrium state, which is possible using a PFG approach as well.[20,24,53]

An example for the latter case is given by polyethylene oxide molecules being partially encapsulated in block-copolymer vesicles.[54,55] Samples of polyethylene oxide (PEO) of different molecular masses are added to aqueous dispersions of vesicles from poly(2-vinylpyridine-*block*-ethyleneglycol).[24] As described in Section 4.2, the application of PFG methods allows for the assignment of the encapsulated and the non-encapsulated fraction of the active ingredient, even though both compartments are chemically identical. This approach has been successfully applied to micellar drug delivery systems in the past.[17,53] Figure 28a represents the result of such a PFG experiment for PEO 1500 with an average molecular mass of 1500 g/mol.[24] The plot of the logarithmic signal intensity vs. the gradient strength shows an initial steep decay which can be assigned to the non-encapsulated fraction of the PEO molecules. For gradients with $\gamma^2\delta^2 G^2(\Delta-\delta/3) > 3\times 10^9$ s/m^2, this contribution has virtually disappeared and the signal is dominated by the encapsulated fraction which exhibits a strongly reduced dependence on the gradient strength. The relative amount x_{in} of encapsulated PEO molecules can be estimated from an extrapolation of the shallow decay towards $G = 0$, yielding a value of $\ln(x_{in}) = -3.7$ or $x_{in} = 0.025$. With the pulse separation Δ increasing from 15 to 300 ms, this value shifts only marginally, indicating that the encapsulated fraction remains relatively constant on this time scale.

However, this situation already changes for PEO 600 with a molar mass of 600 g/mol (Fig. 28b).[24] More significant as in case of PEO 1500, the encapsulated fraction of PEO 600 seems to decrease with increasing pulse separation Δ because only those molecules which actually remain in the encapsulated state over the full duration of the PFG experiment are detected. Consequently, those molecules which have passed through the vesicle membrane into the continuous phase within the time period Δ lead to a corresponding drop in the plateau value of the PFG plot. Of course, this process is being part of a balanced equilibrium such that each molecule which is lost from the capsule content is simultaneously replaced by an originally non-encapsulated molecule entering the vesicle (which is not detected at higher gradient strengths). In case of even lower molecular masses, this phenomenon becomes more and more evident (Fig. 29a–c).[24] The signal decay plots for the various pulse spacings spread wider and wider with decreasing molecular mass of the PEO. In case of PEO 200 with a molecular mass of 200 g/mol and for a pulse spacing of $\Delta = 300$ ms, the signal of the encapsulated fraction is below the noise level and the system seems to consist exclusively of non-encapsulated PEO (Fig. 29c, filled circles).

All decay curves are analysed by numerical calculation as depicted in Section 3.4. A typical set of model calculations for different exchange rates is shown in Fig. 30.[24] The actual measurements for the individual PEO samples shown in Figs. 28 and 29 have been reproduced by fitting the exchange rate $\bar{k}_{ex}$ and the encapsulated fraction x_{in} as variable parameters.[24] The best fits are shown as solid lines in Figs. 28 and 29, the resulting exchange rates and fractions x_{in} are listed in Table 2.

Systematic studies of exchange rates under variation of the size of the tracer molecule are a potent tool for studies on the capsule membrane permeability. In the given case, the tracer molecules PEO 200 up to PEO 1500 are almost identical in
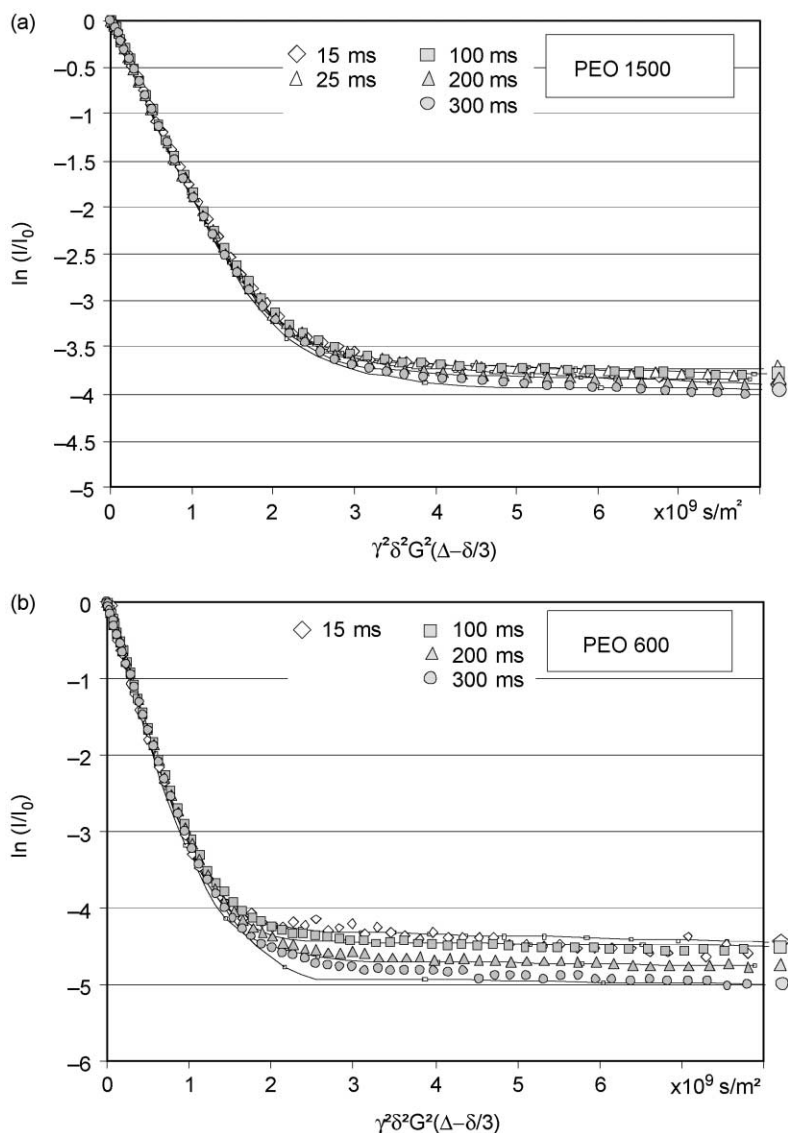
Fig. 28. Signal decay plots from stimulated echo PFG experiments on PEO 1500 (M_w = 1500 g/mol) (a) and PEO 600 (M_w = 600 g/mol) (b) in a dispersion of block-copolymer vesicles.[24] The solid lines represent the best fit calculations based on the parameters $\bar{k}_{ex}$ and x_{in} listed in Table 2, the assignments are given by symbols on the right margin.

their physical and chemical properties except for their size. Therefore, the set of exchange rates yields valuable information on pore sizes, permeation mechanisms and release properties. A plot of the exchange rates vs. the hydrodynamic radii of the tracer molecules is shown in Fig. 31. Interestingly, for PEO 200 up to PEO 600
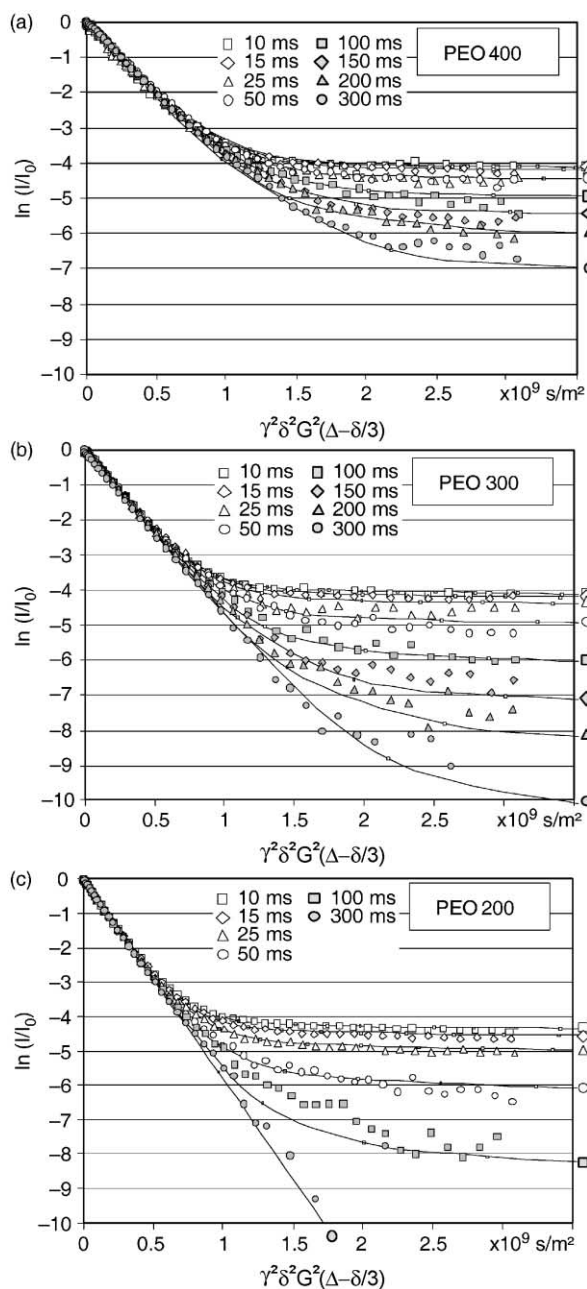
Fig. 29.   Signal decay plots from stimulated echo PFG experiments on PEO 400 ($M_w = 400$ g/mol) (a), PEO 300 ($M_w = 300$ g/mol) (b), and PEO 200 ($M_w = 200$ g/mol) (c) in a dispersion of block-copolymer vesicles.[24] The solid lines represent the best fit calculations based on the parameters $\bar{k}_{ex}$ and x_{in} listed in Table 2, the assignments are given by symbols on the right margin.
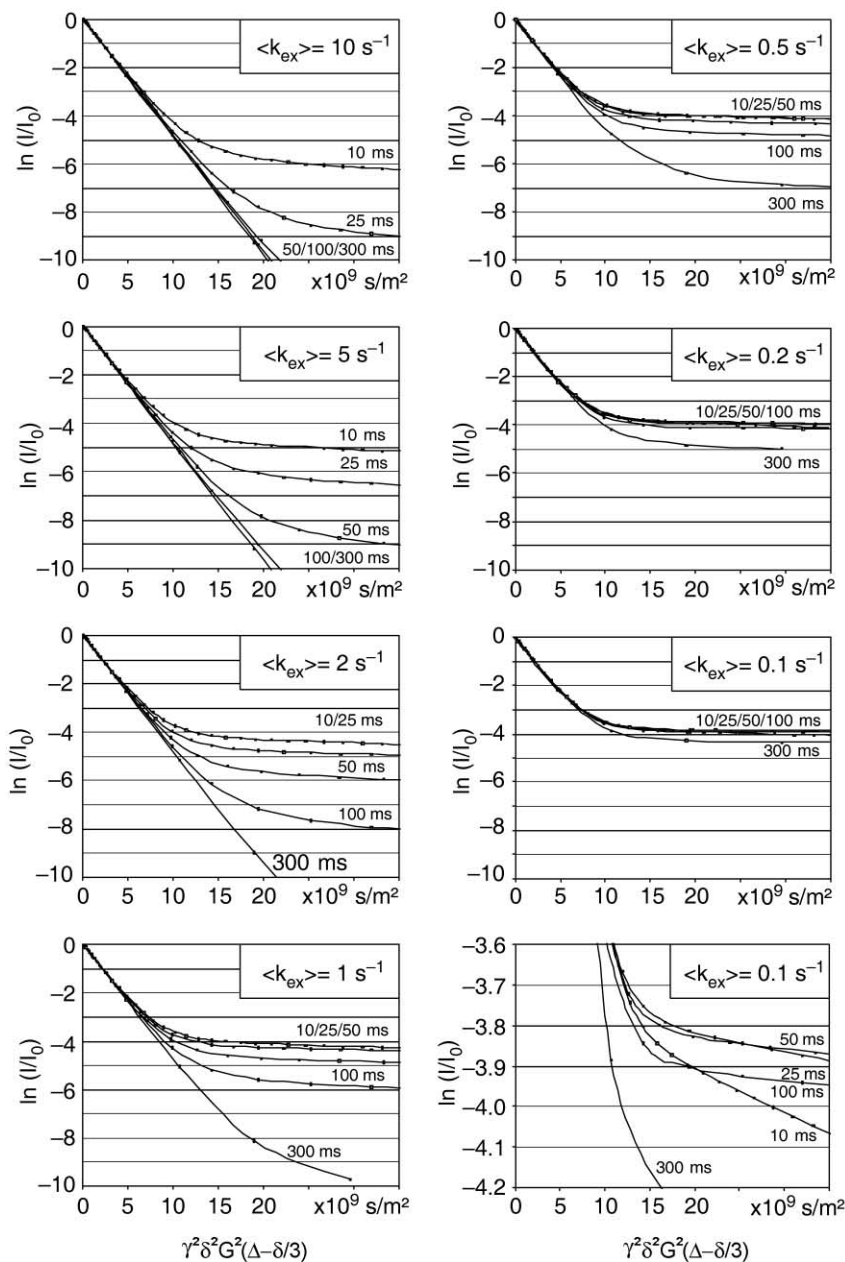
Fig. 30. Set of simulated PFG decay curves for different overall exchange rates $\langle k_{ex} \rangle$ and different pulse separations Δ (additional simulation parameters: pulse duration $\delta = 1.2$ ms, capsule radius $a = 1$ μm, $\gamma_H = 26.75 \times 10^7$ rad/s/T). For $\langle k_{ex} \rangle = 0.1$ s^{-1}, data are plotted separately in an expanded scale to show minor variations between the decay curves.[24]

Table 2. Simulation parameters used for the numerical reproduction of the echo decay curves for PEO samples in vesicle dispersions shown in Figs. 28 and 29

Model compound	Average molar mass (g/mol)	Encapsulated fraction x_{in}	Exchange rate $\bar{k}_{ex}$ [1/s]
PEO-200	~ 200	0.022 ± 0.001	1.6 ± 0.2
PEO-300	~ 300	0.023 ± 0.001	0.85 ± 0.05
PEO-400	~ 400	0.0205 ± 0.001	0.38 ± 0.02
PEO-600	~ 600	0.015 ± 0.001	0.075 ± 0.01
PEO-1500	~ 1500	0.028 ± 0.001	0.05 ± 0.01

the logarithmic exchange rate depends nearly linear on the hydrodynamic radius. If one assumes Arrhenius behaviour of the permeation process, this would mean that the activation energy for the transfer through the capsule membrane is proportional to the size of the tracer molecule. A strong deviation from this rule is detected for PEO 1500, which may be due to a different permeation mechanism.[24] Probably, this larger PEO molecule unfolds before the transfer through the membrane, leading to the reduced activation energy with respect to its size.

Similar to studies on the porosity of capsule membranes using series of tracer molecules of different size, one may use molecules of similar size which differ in a single other parameter like polarity, shape, flexibility, etc., to yield additional information about the membrane structure. As all these observations are performed in the state of equilibrium distribution, there are no restrictions in terms of the overall duration of the measurement. Overall, systematic studies on the membrane permeability could elucidate a variety of details on the capsule structure and the possible release properties.
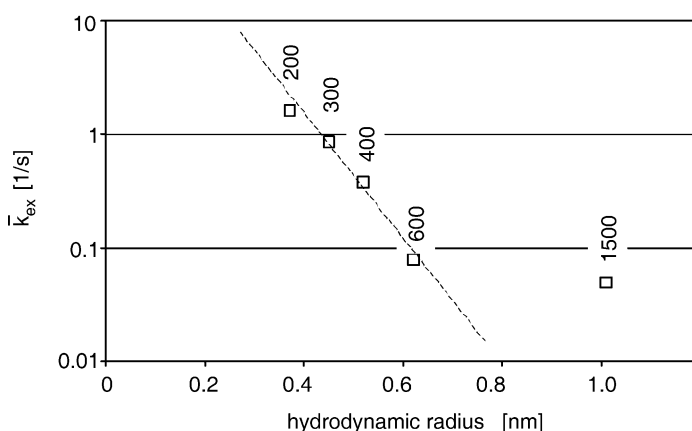
Fig. 31. Rate constants $\bar{k}_{ex}$ for the molecular exchange through the vesicle membranes as determined by the best fit simulations shown in Figs. 28 and 29. The values for $\bar{k}_{ex}$ are plotted in a logarithmic scale vs. the hydrodynamic radii of the tracer molecules PEO 200…1500 in water.

4.6. Local phase separations

When nanospheres are loaded with an active ingredient, it is often desired to obtain a homogeneous mixture of the particle matrix with the active component. However, in many cases, the system tends to undergo a local phase separation which may finally lead to inhomogeneous particles of various structures. These include core-shell type morphologies as well as particle matrices formed by solid-in-solid dispersions. NMR spectroscopy offers multiple approaches to elucidate the resulting structures. The location of active ingredients in core-shell nanoparticles, for example, has been successfully studied by REDOR NMR techniques.[25,56] In addition however, it is desirable to determine the dimensions of the homogeneous regions as these will influence their phase transition temperatures as well as the characteristics of solubility and uptake of the active ingredient.

An easy criterion for the observation of phase separation processes is offered by the spin-lattice relaxation time in the static as well as in the rotating frame, an idea which has been extensively used for the analysis of polymer blends.[57] Especially the spin-lattice relaxation time in the rotating frame of the protons $T_{1\rho}^{H}$, accessible by a single $\pi/2$-pulse followed by a spin-lock pulse of variable duration, allows for the discrimination between homogeneously mixed phases and heterogeneous systems with domain sizes exceeding 5 nm.[57] In case of a homogeneous mixture between two components A and B, both corresponding relaxation times $T_{1\rho}^{H}$ (A) and $T_{1\rho}^{H}$ (B) will be equal due to the rapid spin diffusion between the two proton reservoirs. In case of a heterogeneous system with the components A and B residing in two different phases, the spin diffusion will become less efficient leading to two generally different relaxation times $T_{1\rho}^{H}$ (A) and $T_{1\rho}^{H}$ (B).

An example for the application of this method on Q10-loaded SLN is shown in Figs. 32–34.[27]

A series of spectral line shapes obtained under MAS conditions and variation of the spin-lock duration t_{SL} (see representative examples in Fig. 32) is analysed for the variation of the relative contributions of the matrix component cetyl palmitate and the active ingredient Q10 (Fig. 33).[27]

A plot of the relative contributions against the spin-lock time t_{SL} (Fig. 34) shows a distinctly bi-exponential decay of the Q10-protons, while the protons of the matrix exhibits a largely mono-exponential decay down to values scattered by the background noise.[27] The initial slopes of both decays are identical within the given experimental error. However, for spin-lock durations of more than 2 ms, the Q10 contribution shows a much smaller relaxation rate, being detectable even after $t_{SL} = 10$ ms.

Identical relaxation times may occur accidentally; however, this is very unlikely under the given circumstances where two compounds (Q10 and cetyl palmitate) of significantly different chemical constitution and internal mobility are compared. Therefore, their common relaxation plot for $t_{SL} < 2$ ms can only mean that a homogeneous mixture of both components is observed in this range. After the decay of approximately 60% of the original Q10 signal, the residual 40% suddenly show a relaxation behaviour different from the one of the cetyl palmitate matrix. This must mean that a fraction of 40% of the Q10 form a separate domain which does not contain significant amounts of cetyl palmitate. In short, the Q10-loaded SLN clearly are
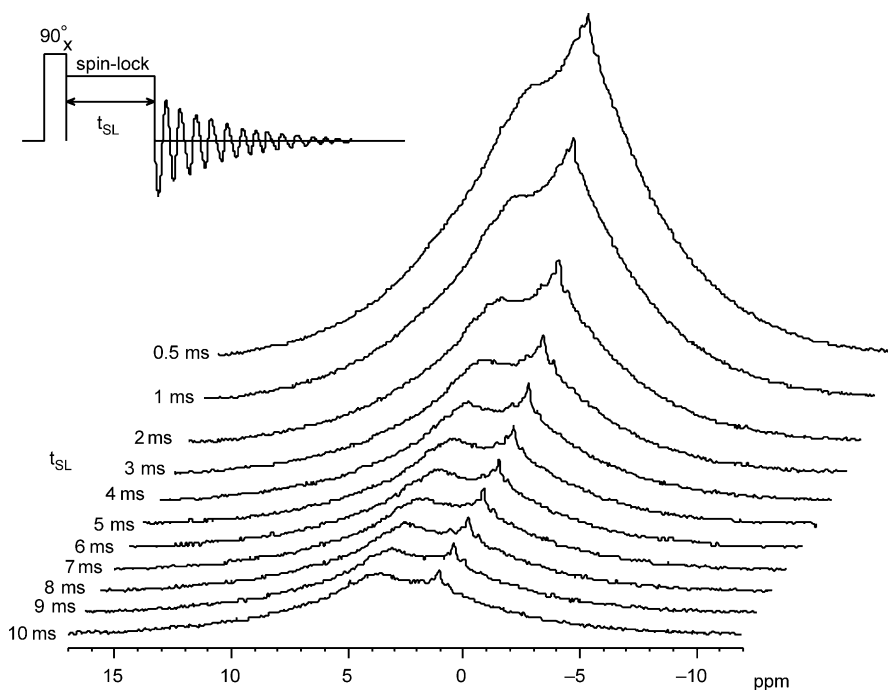
Fig. 32. Representative examples for proton spectra of Q10-loaded solid lipid particles obtained under MAS conditions and variation of the spin-lock duration t_{SL}. The pulse sequence used for the $T_{1\rho}^{H}$-measurements is depicted in the inset.[27]

inhomogeneous. A fraction of 60% of the active ingredient forms a mixture with the cetyl palmitate matrix, while 40% of the Q10 have separated into a second phase. The domain size must be larger than 5 nm, but also significantly smaller than 250 nm which is the average diameter of the SLN.[27]

4.7. Particle degradation

Under particle degradation, we understand any process that leads to an irreversible decomposition of the particle structure. The decomposition of the solid particle matrix may either lead to smaller solid fragments or to a complete disintegration into a fluid phase. In both cases, the decomposition process is reflected by the NMR spectrum of the matrix material. If the size of solid fragments decreases due to fractionation of the matrix, so does the correlation time for the isotropic tumbling according to Eq. (54). Consequently, one can expect the cross-polarization NMR signal to decrease in line width similar to the simulated pattern shown in Fig. 3. If the decomposition leads to a fluid phase via a phase transition or a solution, highly resolved signals are expected to appear in the direct excitation mode. In this respect, a time-resolved NMR observation during a decomposition process allows for the identification of a decomposition mechanism.
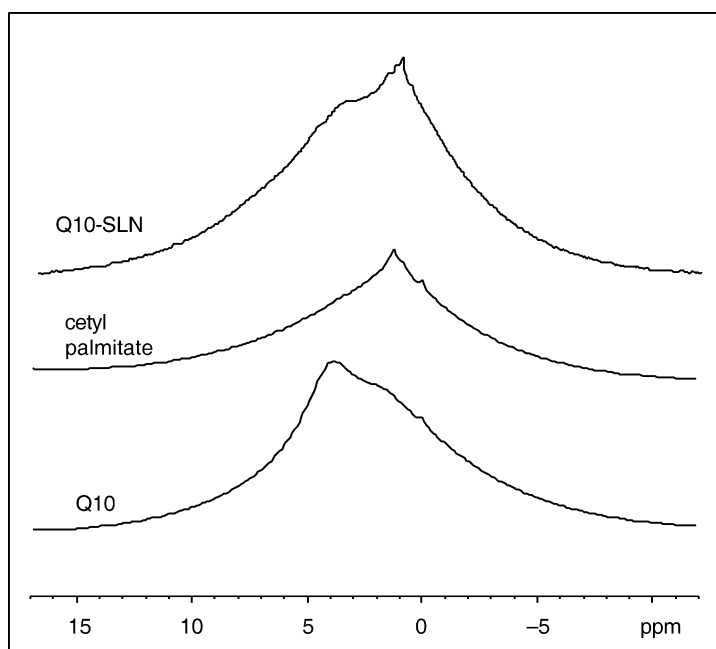
Fig. 33. Comparison of MAS proton spectra for Q10-loaded solid lipid particles (top) with corresponding spectra of the solid lipid cetyl palmitate (centre) and the active ingredient Q10 (bottom).[27]
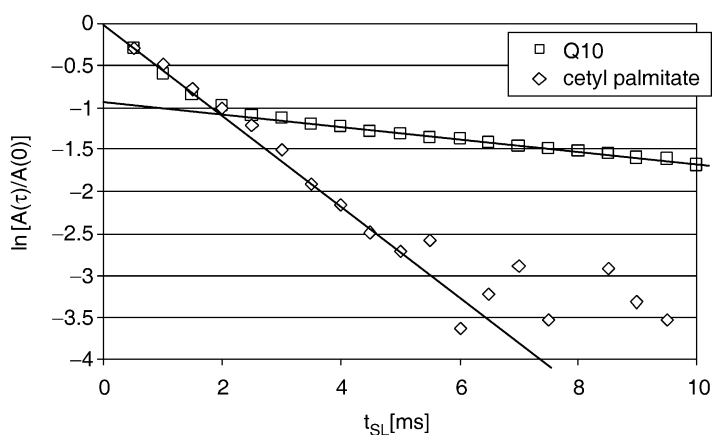
Fig. 34. Relative signal contributions for Q10 (squares) and for the lipid cetyl palmitate (diamonds) plotted logarithmically vs. the spin-lock duration t_{SL}. The grey lines indicate linear relaxation sections with relaxation times of 1.9 ms (lipid for the full duration as well as Q10 for $t_{SL} < 2$ ms) and 13 ms (Q10 for $t_{SL} > 2$ ms). The extrapolation of the latter curve toward $t_{SL} = 0$ yields the relative amount of the 'separate' fraction of Q10 which amounts to approximately 40%.
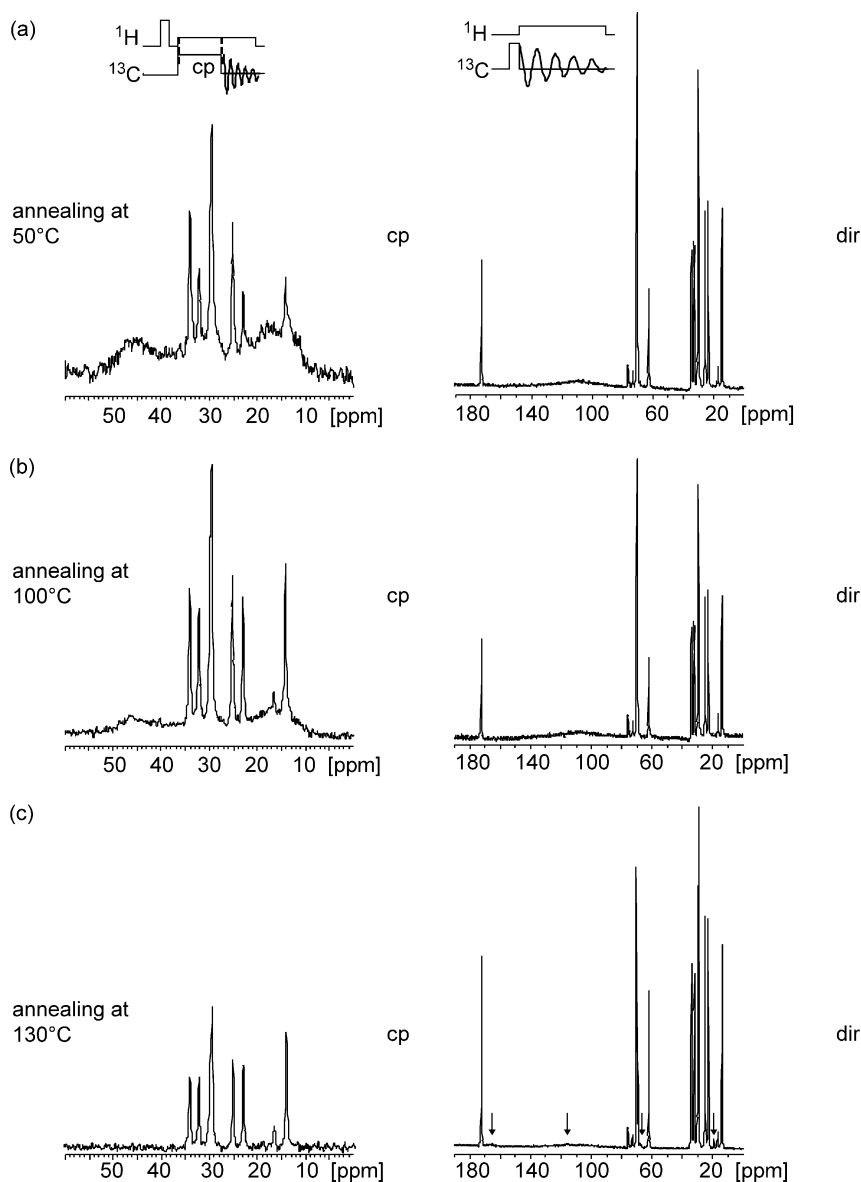
Fig. 35. ^{13}C-NMR-spectra of aqueous dispersions of poly-*n*-butylcyanoacrylate nanocapsules after 3 h of annealing at different temperatures: (a) 50°C, (b) 100°C, (c) 130°C. The (^{1}H)-^{13}C cross-polarization spectra ($t_{cp} = 1$ ms, left column) indicate the loss of the solid capsule wall at higher temperatures (see also Fig. 36). The narrow signals superimposed on the solid-state spectrum of the polymer derive partially from the adsorption of the triglyceride oil and the surfactant to the capsule surface (compare Section 4.4), partially from the residual cp in the liquid phase. The direct excitation ^{13}C spectra (right column) show the liquid and dissolved components with an increasing indication for traces of the *n*-butylcyanoacrylate monomer which results from depolymerization of the capsule wall material (arrows, see also Fig. 37).[19,58]

As an example, the NMR analysis of the thermal degradation of polybutylcyanoacrylate nanocapsules[19,58] is represented in Fig. 35. The decomposition is induced by a 3 h annealing step at different temperatures. After annealing at 50°C, the ^{13}C spectra (cp and direct excitation, line a in Fig. 35) remain virtually unchanged. Essentially, there is no detectable degradation under these circumstances. However, after annealing at 100°C, a significant loss of the solid-state signal in the cp spectrum is observed. With respect to the contributions of the triglyceride component, the contribution of the polymer signal is reduced to about 50% of its original intensity (Fig. 35b). Finally, after annealing at 130°C, the solid-state signal has completely disappeared (Fig. 35c). At the same time, small traces of new signals can be detected in the direct excitation spectrum.

A comparison between the cp polymer spectra a and b shows virtually no difference between the line shapes for samples being stored at 50 and 100°C, despite a significant decrease in intensity after the heat treatment at elevated temperature (Fig. 36). Obviously, the amount of the solid polymer in the capsule walls has been decreased by 50%, while at the same time the hydrodynamic size and the correlation time of isotropic tumbling has been conserved (the line shape indicates a rotational correlation time of $\tau = 10$ ms, see Section 4.2). This only allows for a single conclusion: The overall capsule structure stays largely intact, while the loss of polymer leads to a thinning and, possibly, increased porosity of the capsule wall. Only after 3 h annealing at 130°C, the polymer and with it the capsule wall has completely disappeared.[19,58] At the same time, the intensity of the cp triglyceride spectrum (narrow signals in the cp spectra in Fig. 35) suffers a significant loss as a large part of its original amplitude is owed to the temporary adsorption to the solid capsule walls (see Section 4.4).
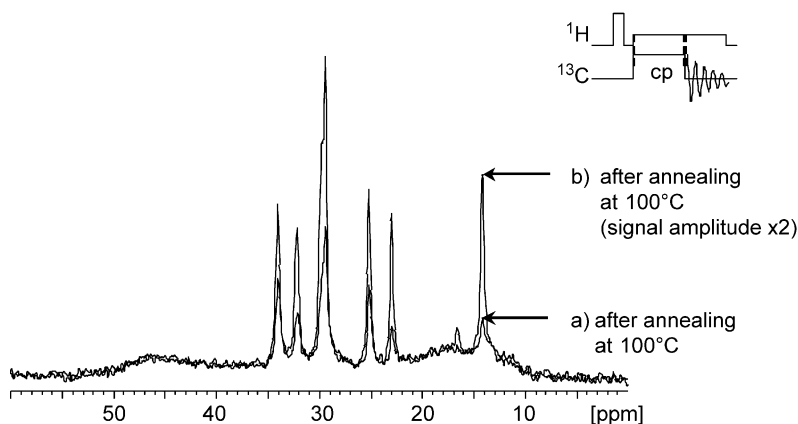
Fig. 36. Comparison between the (^{1}H)-^{13}C cross-polarization spectra of the dispersed nanocapsules after 3 h storage at (a) 50°C and (b) 100°C. For better comparability, the amplitude of the spectrum b has been multiplied by two. The underlying solid-state spectra show almost identical line shapes, indicating that the rotational diffusion and hence the size of the particle remains unchanged.[19,58] No additional narrow contributions corresponding to polymer particles of decreased size are observed in the cp spectrum.
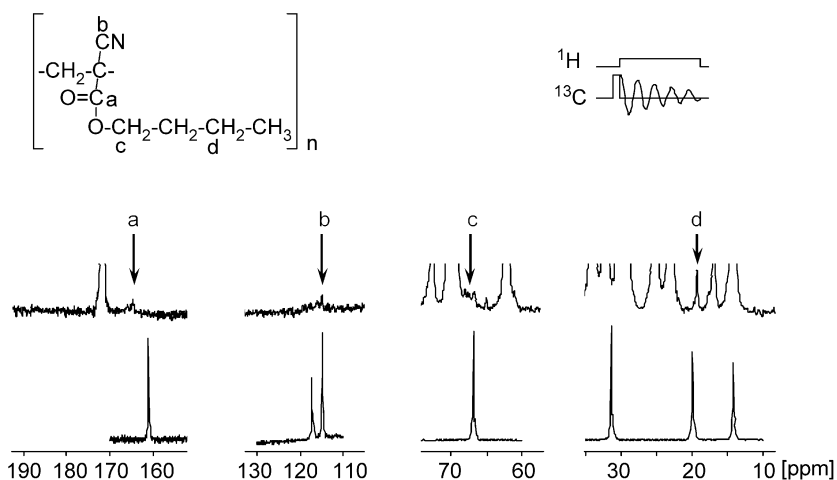
Fig. 37. Comparison between enlarged sections of direct excitation ^{13}C spectra of dispersed poly-*n*-butylcyanoacrylate nanocapsules after 3 h annealing at 130°C (top line) and a solution of *n*-butylcyanoacrylate in CHCl$_3$ (bottom line). The new signals appearing after the thermal treatment a, b, c, and d may be assigned to traces of the monomer resulting from the depolymerization of the capsule wall material. The shift variation observed for the carbonyl carbon signal (a) may result from an interaction with the solvent. The assignments to the monomer carbons are given in the insert.[19,58]

The question of the fate of the polymer material is answered by the direct excitation spectrum c. A comparison with a reference spectrum of the *n*-butylcyanoacrylate monomer (Fig. 37) shows that traces of the monomer spectrum appear after the last step of the degradation. Small changes in the chemical shift, especially observed for the carbonyl signal, can be assigned to the different solvent environment.

5. CONCLUSION

NMR spectroscopy represents a valuable and versatile tool for the characterization of dispersed nanoparticles. In contrast to alternative analytical techniques, it combines a distinctly non-invasive character with the ability to analyse for chemical composition as well as for local mobility of individual system components. Its main disadvantages – poor sensitivity and time consuming acquisition of experimental data – can be overcome by a suitable choice of the pulse sequence and the experimental conditions. The advantages of the NMR approach are especially promising for the study of nanoparticle dispersions used as drug carriers, where many important system characteristics such as release properties, surface exchange processes or decomposition pathways are readily available by relatively simple pulse experiments.

REFERENCES

1. T. Cosgrove and T. M. Obey, in *Encyclopedia of NMR*, D. M. Grant and R. K. Harris, eds., Wiley, Chichester, 1995, 1384.
2. C. Mayer, *Prog. NMR Spectrosc.*, 2002, **40**, 307.
3. H. Gleiter, *Encyclopedia of Materials Science and Engineering*. Suppl. Vol. 1, Pergamon Press, Oxford, 1988, 339.
4. K. E. Gonsalves and X. Chen, *Polymeric Materials Encyclopedia*, CRC Press, Boca Raton, 1996 electronic release.
5. B. H. Kear and G. Skandan, *Ullmann's Encyclopedia of Industrial Chemistry*, Wiley-VCH, New York, 2001 electronic release.
6. J. Kreuter, in *Colloidal Drug Delivery Systems*, J. Kreuter, ed., Marcel Dekker, New York, 1994.
7. W. Meier, *Chem. Soc. Rev.*, 2000, **29**, 295.
8. K. Westesen and T. Wehler, *J. Pharm. Sci.*, 1992, **81**, 777.
9. K. Westesen and T. Wehler, *J. Pharm. Sci.*, 1993, **82**, 1237.
10. K. Westesen, A. Gerke and M. H. J. Koch, *J. Pharm. Sci.*, 1995, **84**, 139.
11. K. Westesen, H. Bunjes and M. H. J. Koch, *J. Controlled Release*, 1997, **48**, 223.
12. E. Zimmermann, S. Liedtke, R. H. Müller and K. Mäder, *Proc. Int. Symp. Control. Rel. Bioact. Mater.*, 1999, **26**, 5407.
13. S. Liedtke, E. Zimmermann, R. H. Müller and K. Mäder, *Proc. Int. Symp. Control. Rel. Bioact. Mater.*, 1999, **26**, 5409.
14. D. Hoffmann and C. Mayer, *J. Chem. Phys.*, 2000, **112**, 4242.
15. V. Jenning, K. Mäder and S. H. Gohla, *Int. J. Pharm.*, 2000, **205**, 15.
16. K. Jores, W. Mehnert and K. Mäder, *Pharm. Res.*, 2003, **20**, 1274.
17. K. I. Momot, P. W. Kuchel, B. E. Chapman and D. Whittaker, *Langmuir*, 2003, **19**, 2088.
18. C. R. Heald, S. Stolnik, K. S. Kujawinski, C. De Matteis, M. C. Garnett, L. Illum, S. S. Davis, S. C. Purkiss, R. J. Barlow and P. R. Gellert, *Langmuir*, 2002, **18**, 3669.
19. D. Hoffmann, PhD thesis, University of Duisburg-Essen, 2000.
20. C. Mayer, D. Hoffmann and W. Wohlgemuth, *Int. J. Pharm.*, 2002, **242**, 37.
21. S. Guinebretière, S. Briancon, J. Lieto, C. Mayer and H. Fessi, *Drug Develop. Res.*, 2002, **57**, 18.
22. C. Mayer, *J. Magn. Reson.*, 2000, **145**, 216.
23. C. Mayer, *J. Magn. Reson.*, 1999, **139**, 132.
24. A. Rumplecker, S. Förster, M. Zähres and C. Mayer, *J. Chem. Phys.*, 2004, **120**, 8740.
25. H.-M. Kao, R. D. O'Connor, A. K. Mehta, H. Y. Huang, B. Poliks, K. L. Wooley and J. Schaefer, *Macromolecules*, 2000, **34**, 544.
26. H. Y. Huang, K. L. Wooley and J. Schaefer, *Macromolecules*, 2001, **34**, 547.
27. S. A. Wissing, R. H. Müller, L. Manthei and C. Mayer, *Pharm. Res.*, 2004, **21**, 400.
28. C. Mayer, *J. Magn. Reson.*, 1999, **138**, 1.
29. P. Meier, E. Ohmes and G. Kothe, *J. Chem. Phys.*, 1986, **85**, 3598.
30. R. R. Ernst, G. Bodenhausen and A. Wokaun, *Principles of Nuclear Magnetic Resonance in One and Two Dimensions*, Clarendon Press, Oxford, 1987.
31. C. Mayer and A. Terheiden, *J. Chem. Phys.*, 2003, **118**, 2775.
32. L. Müller, A. Kumar, T. Baumann and R. R. Ernst, *Phys. Rev. Lett.*, 1974, **32**, 1402.
33. C. Schwarz, W. Mehnert, J. S. Lucks and R. H. Müller, *J. Controlled Release*, 1994, **30**, 83.
34. R. H. Müller, D. Rühl, S. Runge, K. Schulze-Förster and W. Mehnert, *Pharm. Res.*, 1997, **14**, 458.
35. R. H. Müller, H. Weyhers, A. zur Mühlen, A. Dingler and W. Mehnert, *Pharm. Ind.*, 1997, **59**, 423.
36. D. L. VanderHart, *J. Chem. Phys.*, 1976, **64**, 830.
37. P. B. Murphy, T. Taki, B. C. Gerstein, P. M. Henrichs and D. J. Massa, *J. Magn. Reson.*, 1982, **49**, 99.
38. W. S. Veeman, *Prog. NMR Spectrosc.*, 1984, **16**, 193.
39. T. M. Duncan, *J. Phys. Chem. Ref. Data*, 1987, **16**, 125.
40. D. E. Woessner, *Brownian motion and correlation times. Encyclopedia of NMR*, Wiley, Chichester, 1995. 1068.
41. J. Herzfeld and A. E. Berger, *J. Chem. Phys.*, 1980, **73**, 6021.

42. F. Becker, Diploma Thesis, University of Duisburg, 1999.
43. C. Mayer and G. Lukowski, *Pharm. Res.*, 2000, **17**, 486.
44. G. Lukowski, D. Hoffmann, P. Pflegel and C. Mayer, *Proceedings of Third World Meeting APV/APGI*, Berlin, 2000.
45. D. Hoffmann, PhD Thesis, University of Duisburg, 2000.
46. B. Balinov, B. Jönsson, P. Linse and O. Södermann, *J. Magn. Reson. A*, 1993, **104**, 17.
47. P. T. Callaghan, *J. Magn. Reson. A*, 1995, **113**, 53.
48. S. L. Codd and P. T. Callaghan, *J. Magn. Reson.*, 1999, **137**, 358.
49. R. Kimmich, *NMR Tomography Diffusometry Relaxometry*, Springer, Berlin, 1997.
50. M. Wohlgemuth and C. Mayer, *J. Colloid Interface Sci.*, 2003, **260**, 324.
51. S. Guinebretière, S. Briançon, H. Fessi, V. S. Teodorescu and M. G. Blanchin, *Mater. Sci. Eng. C*, 2002, **21**, 137.
52. S. Guinebretière, S. Briançon, J. Lieto, C. Mayer and H. Fessi, *Drug Develop. Res.*, 2002, **57**, 18.
53. K. I. Momot and P. W. Kuchel, *Concepts Magn. Reson. Part A*, 2003, **19A**, 51.
54. D. E. Discher and A. Eisenberg, *Science*, 2002, **297**, 967.
55. E. Krämer, S. Förster, C. Göltner and M. Antonietti, *Langmuir*, 1998, **14**, 2027.
56. H. Y. Huang, K. L. Wooley and J. Schaefer, *Macromolecules*, 2001, **34**, 547.
57. W. S. Veeman and W. E. J. R. Maas, *NMR: Basic Principles and Progress*, Springer, Berlin, 1994, 131.
58. C. Mayer, *Kernmagnetische Resonanz an nanopartikulären Systemen*, Deutscher Wissenschafts-Verlag, Würzburg, 2001, 275.

Microscopy in Magnetic Resonance Imaging

P.T. NARASIMHAN AND RUSSELL E. JACOBS

Biological Imaging Center, 139-74 Beckman Institute, California Institute of Technology, Pasadena, CA 91125, USA

The notion of using magnetic resonance imaging (MRI) as a microscopic tool for obtaining three-dimensional images of living and nonliving material was envisioned early in the history of this technology. In this review we begin with a short discussion highlighting how imaging time is drastically lengthened as image resolution is increased. Obtaining sufficient signal and contrast is crucial in any imaging experiment and of particular importance in microscopic resolution MRI because of the intrinsically low sensitivity of the magnetic resonance phenomenon. In Section 2, we consider sources and ways to deal with signal and noise. In Sections 3 and 4, sample characteristics and how they can be taken advantage of with different MR imaging

methods to provide high information content images are discussed. q-Space (displacement) imaging discussed in Section 5 is somewhat peculiar to microscopic MRI, while the notion of multimodal imaging is gaining acceptance at all scales. Section 6 is devoted to recent applications across a broad spectrum, but emphasizing biological samples. We conclude with a brief discussion of prospects for achieving higher resolution images in reasonable time spans.

1. INTRODUCTION

Magnetic resonance imaging (MRI) is finding increasing application in areas that require microscopic resolution. While typical resolutions employed clinically are on the order of a millimeter, the notion of using MRI at microscopic resolutions arose early in the development of this technique.[1,2] The limitations to spatial resolution in MRI have been reviewed by several authors.[3–5] Theoretically, resolution is limited by molecular diffusion and is estimated to be of order 1–10 μm.[4] In practice, resolution is limited by the image signal-to-noise ratio (SNR). The achievable SNR is most often limited by the available time to acquire the image. For example, a clinical MR image with reasonable SNR can be obtained in about 5 min with a voxel (volume element) size of 1 mm^3. If one were to acquire the same image with a 100 μm^3 voxel size at the *same* SNR and all other experimental parameters constant (assuming this is possible), it would take approximately 10 years to complete the scan. The challenge in magnetic resonance microscopy (MRM) is to overcome the problem of excessive imaging time as the resolution is improved. This is achieved by optimizing the experimental setup, both hardware and software, to overcome the intrinsically poor SNR in order to obtain a respectable image in a reasonable amount of time. A number of laboratories now routinely obtain three-dimensional MR images of various samples with good SNR and contrast at spatial resolutions of 30–100 μm^3.[6–11] Applications range over a wide spectrum from the geological[12] to the biological.[13,14]

For the purposes of this review we define 'microscopic' MRI as studies with spatial resolution on the order of 100 μm or less and will concentrate on developments since 1999. We recommend texts by Callaghan,[5] Mansfield and Morris,[15] Morris,[16] Vlaardingerbroek and den Boer[17] and Haacke *et al.*[18] Two publications[12,19] contain papers presented at two conferences. Reviews by Balaban,[20] Bhakoo,[21] Blackband,[6] and Glover and Mansfield[22] cover earlier material. In the following sections we outline the basic challenge of improving signal to noise and the role of various factors that affect contrast and resolution in MRM images. Emphasis is laid on applications and illustrated with recent results. Our personal bias towards biological imaging is apparent and we refer the reader to texts by Blumich[23] and Blumler[12] for in-depth discussions of application in material sciences. We conclude with an evaluation of the prospects for routinely achieving higher resolution in MRM images.

2. SIGNAL AND NOISE IN MAGNETIC RESONANCE IMAGING

2.1. Signal and noise in MRM

MRM places heavy demands on the signal detection system on account of the small magnitude of the initially generated signal that then undergoes further processing as demanded by the experimental protocol. In order to generate the initial signal, one depends on the magnetization from a sample containing nuclear spins (usually protons) placed in a strong magnetic field. The magnitude of this magnetization at thermal equilibrium[24] is proportional to the number of spins in the sample as well as the strength of the magnetic field B_0 and the square of the magnetogyric ratio (γ) of the spins. Further, the magnetization is inversely proportional to the sample temperature.

For reasonable sizes of samples that can be accommodated in a magnet, this magnetization is small at room temperature and hence the voltage induced in the receiver coil of the magnetic resonance spectrometer is very low even for protons that have a large γ in comparison to most nuclei. The MR image can be viewed as the signal generated from individual volume elements (voxels). Hence, the image intensity is related to the number of spins in each voxel. In clinical MRI the voxel sizes are of the order of millimeters while the voxel sizes in MRM are in the range of microns. Considering a homogeneous sample, the reduction in the number of spins in going from a voxel size of 1 mm applicable to MRI to 10 μm for MRM could mean a reduction in the number of spins in the ratio $1:10^6$.

Apart from this problem of reduction in intensity, the signal is also corrupted with noise. The SNR can be improved by signal averaging. However, this process entails longer imaging times. By increasing the strength of the magnetic field, careful design of receiver coil and the gradient coils used for spatial encoding as well as design of pulse sequences, it has been possible in recent years to generate MR microscopy images of very high quality.

2.2. Signal-to-noise ratio and contrast-to-noise ratio

To glean useful information from data, especially imaging data, both high signal and good contrast versus noise are necessary. Thus, the SNR and contrast-to-noise ratio (CNR) are two important quantities that specify the quality of the MR image.[5,13,25] A good SNR value is necessary for the clear delineation of boundaries in an image. A low SNR leads to an image appearing noisy (although the visual system is quite adept at pulling features out of noise) and confounds quantitative analysis. The entire image is built up of discrete volume elements (called *pixels* in two dimensions and *voxels* in three dimensions) and a reduction in the size of the voxel reduces the number of spins contributing to the signal and thus lowers SNR. The basic challenge in micro-imaging as contrasted to macro-imaging comes from the size of the voxels.

At least two kinds of noise arise in MR imaging: random and systematic. Random noise (σ_r) arises from receiver electronics (e.g., Johnson noise), digitization, and from the sample. As the receiver bandwidth increases, noise also increases as the square root of

the bandwidth. Acquisition time (T_{acq}) and bandwidth are related as

$$T_{acq} = \frac{N}{\text{bandwidth}} \tag{1}$$

where N is the number of data points. Thus, for a given N, a longer acquisition time is favorable from an SNR point of view. Systematic noise (σ_s) arises from sample motion, blood flow, cerebrospinal fluid (CSF) motion, gradient coil movements, truncation effects in signal acquisition, etc. The total noise may be expressed as

$$\sigma = \sqrt{(\sigma_r^2 + \sigma_s^2)} \tag{2}$$

In the presence of random noise, signal averaging improves SNR by adding the signal repetitively and coherently in proportion to the number of scans, n. Due to its statistical nature, noise adds only in proportion to $\sqrt{n}$, thereby signal averaging leads to an overall increase in SNR. Noise contributions from periodic motion may be reduced by monitoring the motion and adopting gating techniques for signal acquisition. Thus, effects due to pulsatile motion on MR images may be reduced by monitoring the motion and gating the MR acquisition to it. The use of navigator echoes is also helpful in this context.

For two areas in an image to be distinguishable, a good CNR value is needed. If the signal from a region A is S_A and that of its neighbor B is S_B, then

$$CNR = \frac{(S_A - S_B)}{\sigma} \tag{3}$$

where σ is the noise which is generally taken as that of the background.

2.3. Hardware

2.3.1. *Main field magnets*

One of the most significant developments that has spurred activity in the area of MRM is the commercial availability of high field (e.g., 14.1 and 17.6 T) wide bore magnets. Assuming that the main source of noise is the receiver coil, SNR is proportional to the 7/4th power of the B_0 field. Therefore, imaging with high fields is preferable.

2.3.2. *RF receiver coils*

Sample sizes used in MRM are generally small and the filling factor and quality factor can be increased by the use of smaller RF receiver coils, usually of the solenoidal type. If the main source of noise is the thermal noise from the receiver coil, then cooling the receiver coil and preamplifier can result in significant improvement in SNR.[26–30] Several groups have investigated the use of high-temperature superconducting (HTS) receiver coils.[31–37] HTS coils have high Q and hence should be advantageous for SNR. However, the high Q value of the coil also implies a limited bandwidth that is problematic for imaging. At present it appears that imaging with HTS coils is technically more feasible at

lower fields. SNR in microscopy can be increased by the use of well-designed RF microcoils as demonstrated by many investigators.[38–42] Details of the design of solenoidal RF microcoils have been presented.[43–45] The use of microcoils seems to be preferred over the alternative of cryo-cooling the RF coil.[46]

With large-scale efforts in mouse mutagenics and transgenics underway, there is an increasing need for high throughput screening methods. In their present forms MRI and MRM are not high throughput imaging modalities. Matsuda *et al.*[47] and Henkelman and coworkers[48] have designed a parallel receiver coil system so that multiple mice can be imaged simultaneously, thus making MRM more amenable for use in phenotyping large numbers of animals.

2.3.3. *Gradient coils*

The design and development of gradient coils with good linearity over the sample volume and with capability to deliver large gradient strengths over the sample volume has received much attention in recent years. Along with this, efforts have been directed towards developing suitable power supplies. The main goal is to apply to the sample being imaged gradients of short duration and sufficient strength with extremely short rise/fall times so as to approach the diffusion limit for resolution.[5] Additionally, active screening of the gradient coils minimizes interaction with the environment. Due to the power dissipation, the gradient coil temperature may rise unduly and thus adversely affect the gradient coil as well as the receiver coil located in its proximity. Mechanical stability of the coils should also be ensured. From this point of view, an integrated approach to the design of the sample probe containing the receiver coil and the gradient coils can yield good results.[49,50] The advantage of using multilayer coils in gradient coil design for very large magnetic field gradients has been pointed out by Bowtell and coworkers.[51,52] Recently, Leggett *et al.*[53] have published designs for actively shielded multilayer gradient coil with improved cooling properties. Lee *et al.*[54] have given details of their probe that enabled them to obtain an image of their phantom at 1 μm in-plane resolution. The gradient coils could generate gradient strength > 1000 G/cm where cooling of the coil was essential. Seeber *et al.*[55,56] have described in detail their triaxial gradient system for use with a RF microcoil. Gradients strengths > 1500 G/cm could be produced in all three axes (x, y, and z) with ∼ 5000 G/cm in the x direction. The gradient switching time was ∼ 10 μs. The same group[42] was later able to employ gradient strength of 5800 G/cm in two directions and 4600 G/cm in the other direction in their imaging experiment.

3. CONTRAST

Perhaps the most basic sample characteristic contributing to contrast is the variation in proton density across the sample. Voxel intensity is directly proportional to proton concentration, all other factors being, thus proton concentration differences between voxels give rise to the well-known spin density contrast. Magnetization transfer (MT) contrast is finding increasing application in the clinical realm, but thus far is little used in MRM.[57]

3.1. T_1- and T_2-induced contrast

For data acquisition and signal averaging purposes, we need to repeat the pulse sequence many times in an imaging experiment. If we repeat the spin echo (SE) or gradient echo (GE) sequences at a repetition time, TR, which is long in comparison to the longitudinal relaxation time (T_1), we recover the full magnetization along the z-axis between excitations. From Eq. (4), it is clear that if we repeat the sequence at a faster pace, the longitudinal magnetization will not fully recover between excitations. In fact, for the SE sequences, it can be shown that the signal (S) depends on TR as well as on TE, T_1, the transverse relaxation time (T_2), the diffusion coefficient (D), the spin density (ρ), and the applied magnetic field gradient (G):

$$S(\text{SE}) \propto \rho\{1 - 2\, e^{-(\text{TR}-\text{TE}/2)/T_1} + e^{\text{TR}/T_1}\}e^{-\text{TE}/T_2^*}\, e^{-\gamma^2 D G^2 \text{TE}^3/12}$$

$$\propto \rho(\text{TR}, \text{TE}, T_1)e^{-\text{TE}/T_2^*}\, e^{-\gamma^2 D G^2 \text{TE}^3/12}, \qquad (4)$$

$$1/T_2^* = 1/T_2 + 1/T_{2\,\text{inhomogeniety}}$$

By manipulating the ratio TE/T_2, we can get T_2-weighted images. On the other hand, by adjusting the TR/T_1 ratio, we can get T_1-weighted images. In MR imaging, a careful choice of TR and TE can thus produce excellent contrast between different areas of the sample. In the brain, for example, the T_1 value of CSF is longer than most tissue T_1 values and, by choosing a shorter TR value, we can reduce the intensity from CSF in the SE image. To avoid T_2-weighting, we keep the value of TE short. T_1 values also depend on the main magnetic field strength (B_0). If the molecules bearing protons are mobile and rapidly moving in an isotropic fashion, T_1 equals T_2. If the motion is slow, as in the case of water bound to macromolecules, the T_2 value may be much lower than T_1. MR images can be produced with T_2-weighting to display variations in T_2 values in different areas of the sample. An analysis of FLASH versus SE imaging schemes with regard to SNR and CNR is available in the literature.[58] A number of groups have presented detailed considerations of the role of TR, TE, READ gradient strength, and sampling time on SNR and CNR in SE and GE imaging schemes.[5,59–63]

In the vicinity of paramagnetic ions, water molecules experience additional spin–lattice relaxation and thus exhibit shorter T_1 in comparison to those distant from the paramagnetic centers. This feature is exploited in imaging using 'contrast agents' typically composed of chelated paramagnetic ions. There is a rapidly growing body of literature demonstrating the clinical effectiveness of paramagnetic contrast agents. The capacity to differentiate regions/tissues that may be magnetically similar but histologically distinct is a major impetus for the preparation of these agents.[64] Local differences in relaxation times (T_1 and/or T_2) can be 'translated' into image contrast by the use of the appropriate MR imaging protocol. For example, regions associated with a gadolinium (Gd^{3+}) ion (near-by water molecules) appear bright in an MR image where the normal aqueous solution appears as dark background if T_1-weighted imaging schemes are used. Inversion recovery (IR) pulse sequence can be used in combination with an SE sequence for this purpose.

The lanthanide atom Gd^{3+} has generally been chosen as the metal atom for contrast agents because it has seven unpaired electrons, a high magnetic moment ($\mu^2 = 63BM^2$), and a symmetric electronic ground state (^8S). Transition metals such as high spin Mn(II) and Fe(III) are also candidates due to their relatively large number of unpaired electrons and high magnetic moments. Once the appropriate metal has been chosen, a suitable ligand or chelate must be found to render the complex nontoxic. Two examples of such chelators are: diethylenetriaminepentaacetic (DTPA) and the macrocyclic 1,4,7,10-tetraazacyclododecane-N,N',N'',N'''-tetracetic acid (DOTA).[65–68] Various features of the ligand can be manipulated to alter the physicochemical properties of the contrast agent – e.g., covalently bond a high molecular polymer to make the agent cell membrane impermeant or covalently bond a lipid to direct the agent to the cell membrane. Gd-DTPA–dextran (Mwt 20 kDa) and Gd-DTPA–lipid are two agents currently in use in our laboratory.

Fully oxygenated blood is diamagnetic in contrast to deoxygenated blood, which is paramagnetic.[69] Due to this, capillaries carrying deoxygenated blood show additional feature in brain images obtained with GE sequence. In the neighborhood of capillaries having deoxygenated blood, the induced magnetic field gives rise to magnetic field inhomogeneity. This inhomogeneity depends on oxygenation level, main magnetic field strength, capillary orientation with respect to the magnetic field, and the diameter of the capillary in comparison to the image voxel size. Water protons diffusing in and adjacent to capillaries carrying deoxygenated blood experience a shortening of T_2, and this gives rise to contrast in the GE image. This has been termed blood oxygenation level-dependent (BOLD) contrast.[70,71] The SE image is sensitive to T_2, while the GE image is sensitive to T_2^*, thus the BOLD effect is much more apparent in GE than SE images. Because blood flow is also a parameter that can contribute to MR signal intensity changes in functional MRI (fMRI) experiments, it is common to compare GE images with SE images to separate the BOLD effects from flow effects. The new field of fMRI of brain has been established on the basis of BOLD contrast changes in various regions of the brain following physiological stimulation. The BOLD approach to fMRI differs from the earlier dynamic fMRI, in which a bolus injection of a contrast agent is used.[72] Because fMR images must be obtained in very short periods of time, fast GE methods are employed. In this context, FLASH and GE versions of EPI have been used.[73,74] Excitation angles in FLASH are kept low, i.e., typically 10–50°. By combining the navigator echo approach with FLASH, it has been shown that ghosting artifacts in fMRI can be reduced.[75] The EPI technique is capable of producing images in the millisecond regime and is sensitive to T_2^* in its gradient echo version.

3.2. Diffusion-weighted imaging and the role of perfusion

Diffusion of nuclear spins in an inhomogeneous magnetic field can cause dephasing and contribute additionally to T_2, making it shorter.[76] Thus, the echo intensity observed in SE, as well as GE, methods is sensitive to T_1, T_2, and diffusion effects. MR images sensitive to diffusion effects, i.e., diffusion-weighted images, can be produced by

the use of additional gradients in the image pulse sequence. Diffusion in a constant gradient, G, contributes an additional term $e^{-\gamma^2 DG^2 (\text{TE})^3/12}$ in the description of signal intensity in the SE scheme, i.e.,

$$S(\text{SE}) = \rho(\text{TR}, \text{TE}, T_1) e^{-\text{TE}/T_2}\, e^{-\gamma^2 DG^2 (\text{TE})^3/12} \tag{5}$$

In the *pulsed* gradient spin echo (PGSE) MR imaging sequence, one introduces two pulsed gradients (one on either side of the 180° refocusing pulse) to obtain diffusion-weighted images.[77,78] The contribution to the loss of echo intensity from diffusion is now dependent on the term: $e^{-\gamma^2 G^2 \delta^2 (\Delta - \delta/3)D^*} = e^{-bD^*}$ instead of the last term in Eq. (5). G is the gradient pulse amplitude, δ its duration, and Δ the time between the leading edges of the two gradient pulses. By applying G in different directions, one can probe the anisotropy of D^*. These experiments refer to D^*, the apparent diffusion coefficient (ADC), rather than D, the true diffusion constant, because we are dealing in general with restricted diffusion. Restricted diffusion may also be usefully employed to highlight boundaries and interfaces.[79–81]

A number of recent studies have pointed out the importance of diffusion-weighted MR imaging of the brain. The anisotropy of D^* has been correlated with myelination. It has been pointed out that ~ 5700 capillary vessels traverse a cubic centimeter volume element in the brain cortex.[82] Diffusion-sensitized MR images of the working brain are likely to be affected by perfusion defined as the microcirculation of the blood at the capillary network level. A detailed analysis of such perfusion effects on MR brain images has been made and it is possible to separate diffusion and perfusion contributions by examining images obtained from specially designed imaging sequences.[83] This technique, which has been named the intravoxel incoherent motion (IVIM) method, has been applied to brain imaging. The EPI scheme has also been adopted for this purpose.[84] Reproducible D^* values can be obtained only if motional artifacts are suppressed. In this context, the use of navigator echo technique has considerably improved the quality of diffusion-weighted brain images and more progress in this direction is expected.[85]

3.3. i-MQCs

Intermolecular multiple quantum coherences (i-MQCs) created from the distant dipolar field have been employed for producing magnetic resonance images.[86–94] The creation of i-MQCs does not demand the presence of intramolecular spin couplings and can therefore be applied in a wide range of systems including biological specimens. Sequences for imaging with i-MQCs based on the CRAZED sequence of Warren and coworkers[86] have been used extensively. An RF pulse followed by a gradient pulse establishes a magnetization helix. The pitch length, p, of the helix is $2\pi/\gamma Gt$, where γ is the gyromagnetic ratio, G is the gradient strength, and t is the duration of the gradient. The signal is generated from spins within a correlation distance, $d = \pi/\gamma Gt$, that is half the repeat distance of the helix.[86] The ability to potentially manipulate image contrast by changing the helix pitch and thus altering the interaction distance between the spins makes this technique of interest for biological and clinical imaging as well as imaging of materials.

The intensity of the i-MQC signals involving higher order coherences is extremely low. For imaging purposes zero quantum (i-ZQC) and double quantum (i-DQC) are generally used and the signals from these are only 10–15% of the single quantum (SQC) signal that is acquired in MRI. The imaging time is therefore prolonged with i-MQC imaging. Higher field strengths provide increased polarization of the sample and are favored. Protons are the commonly employed nuclei for the same reason. We limit ourselves to i-DQC imaging for the present. The pulse sequence for i-DQC imaging starts with a 90° excitation pulse followed by a coherence gradient G_1 and a reconversion pulse with flip angle 120° to convert the DQC to SQC. A second gradient $G_2 = 2G_1$ acts as a gradient filter. The expression for i-DQC signal intensity is[92,95,96]

$$S(t_1, t_2) = iM_0\, e^{-i2\omega t_1}\, e^{i\omega t_2}\left(\frac{3\sqrt{3}}{4}\right)\left(\frac{2\tau_d}{t_2\Delta}\right) J_2\left(-\frac{t_2\Delta}{\tau_d}\right) e^{-t_1/T_{2,\text{i-DQC}}}\, e^{t_2/T_{2,\text{SQC}}} \qquad (6)$$

M_0 is the equilibrium magnetization per unit volume, 2ω is the frequency of i-DQC during the evolution period t_1, and ω is the frequency of the SQC converted from the i-DQC during the detection period t_2. τ_d is the dipolar demagnetization time: $\tau_d = 1/\gamma\mu_0 M_0$, where μ_0 is the magnetic permeability constant and J_2 is the second-order Bessel function. Δ is a factor that depends on the orientation of the coherence gradient (s) with respect to the main field z direction: $\Delta = (3(\vec{s}\cdot\vec{z})^2 - 1)/2$, where z is a unit vector lying along the coherence gradient direction. For the case of coherence gradient oriented along z, $\Delta = 1$; and for the gradient along x or y, $\Delta = -1/2$. If the gradient is oriented along the magic angle, then $\Delta = 0$. The i-DQC signal variation with gradient orientation therefore serves as a test for the integrity of the signal.

Equation (6) shows that the i-DQC signal scales as the square of M_0. The usual MRI signal is proportional to M_0. As a consequence, the regions where the normal image looks bright the i-DQC signal will appear to be brighter and in regions with less signal it will appear darker. Warren and coworkers[86,88,91,96] have emphasized that contrast in i-MQC images can be optimized by tuning the pitch length of the helix, thus varying the interaction distance between the spins that are correlated. The evolution period, t_1, of the i-MQCs can also be varied to produce $T_{2(\text{i-MQC})}^*$ contrast as opposed to $T_{2(\text{i-MQC})}$ contrast obtained by introducing a 180° pulse in the middle of the evolution period. This will refocus B_0 inhomogeneity and chemical shifts. By placing an additional pair of gradients symmetric to this 180° pulse, i-MQC diffusion contrast can be produced. The T_2 and diffusion coefficient D values for i-MQC are expected to increase proportionately with the coherence order. Although i-MQC signals are weaker than the SQCs employed in conventional imaging, the possibility of introducing a new kind of image contrast makes i-MQC imaging attractive.

Marques and Bowtell[97] have discussed the problem of optimization of sequence parameters in (DQ) CRAZED sequence for maximum sensitivity. i-MQC imaging has been employed to detect fMRI signals in the human brain.[90,98] 3D MRM images of the mouse brain with i-ZQCs and i-DQCs have been obtained by Narasimhan et al.[99] at 11.7 T. The usual procedure for i-DQC imaging is to phase encode the SQCs obtained from reconversion of the i-DQCs. Velan et al.[100] have shown that image resolution can be increased by a factor of 2 by phase encoding the i-DQCs during their evolution

period t_1. We note here that in the past the technique of phase encoding multiple quantum coherences has been carried out only in systems with intramolecular coupled spins.[101–103]

Phase cycling is essential for avoiding contamination of i-MQC signals by other order coherences. Using a phantom consisting of a closely packed array of parallel hollow cylinders and water filling all the space inside and outside, Bouchard et al.[104] were able to demonstrate signal intensity variation with the correlation distance, d. Capuani et al.[105] observed dips in the i-MQC signal from a phantom consisting of cylindrical glass capillary tubes filled with water that showed correlation between d and the structure of the sample. However, it is not often possible to demonstrate this dependence so nicely in highly heterogeneous samples presumably on account of diffusion and effect of local gradients on the integrity of the magnetization helix. Charles-Edwards et al.[106] have pointed out that misleading results can be obtained if residual SQCs are not eliminated from the i-DQC signal. After careful isolation of contaminating coherences, Chin et al.[94] were able to obtain i-DQC images of trabecular bone. These authors point out the feasibility of extracting structural parameters such as mean trabecular separation from such images. More applications of i-DQC imaging to porous and structured materials can be expected. By combining the RARE fast spin echo sequence with the i-MQC sequence, Narasimhan et al.[107] have been able to obtain i-DQC and i-ZQC images of good resolution of the mouse brain in a matter of minutes. The availability of fast i-DQC imaging schemes will make i-DQC imaging more attractive.

i-ZQC signals arise from the difference in frequencies of a correlated pair of spins whereas i-DQC signals are due to their sum. Thus, frequency differences arising from local field variations can contribute to i-ZQC. Local susceptibility differences at distance scales of the order of microns can therefore play an important factor in the contrast of i-ZQC images.[88] Examples of i-ZQC and i-DQC images of a fixed mouse brain recorded at 11.7 T are shown in Fig. 1.

3.4. Hyperpolarized nuclei

The proton equilibrium nuclear polarization in liquid samples at room temperature is only of the order of 10^{-5}. In gaseous samples it is even less due to the reduced number of spins in a unit volume. However, the nuclei of gases such as ^{3}He and ^{129}Xe can be prepared in a high state of nuclear polarization ($\sim 10^{-1}$) by the well-known technique of optical pumping.[108–110] Such a high degree of polarization is referred to as hyperpolarization (HP). Consequently, the SNR with these HP-gaseous samples can be quite large when utilized for MR imaging in comparison with normal samples. The two often-used gases for HP studies are ^{3}He and ^{129}Xe and both these have nuclear spin $I = 1/2$. ^{3}He can be directly polarized by using laser light of the appropriate frequency while ^{129}Xe HP is produced by optical pumping of rubidium vapor followed by spin exchange through collisions between rubidium and xenon.[111–113] The commercial availability of high power laser diode arrays has led to more efficient generation of these HP gases for MR imaging purposes.

The T_1 relaxation time of these HP gases is very long ($\sim$ hours, especially in containers with special coatings) in comparison to T_2^*. The diffusion coefficients are also much larger
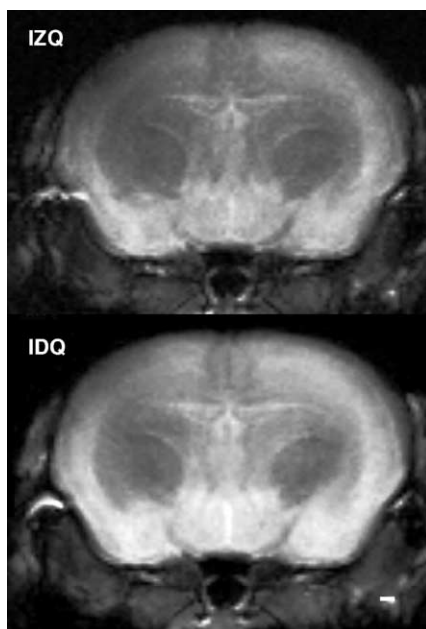
Fig. 1. MR images of a slice (thickness $= 2$ mm) through a fixed mouse brain acquired via intermolecular zero and double quantum coherences. A RARE imaging sequence was placed after the i-ZQC or i-DQC module in order to speed up data collection. Rare factor $= 8$; NA $= 64$; TR/TE$_{\text{effective}} = 3000$ ms/65 ms; FOV $= 12 \times 14$ mm^2 with a pixel resolution of 94×109 μm^2. Experiment time of 1 h. Scale bar $= 1$ mm (image courtesy: B. Boulat and P.T. Narasimhan).

than those of liquid water and this affects the resolution significantly. The FLASH method of imaging is generally chosen with very low ($\sim 10°$) tip angles so as to conserve as much of the longitudinal magnetization as possible. In order to improve the image SNR, centric phase encoding can be employed although this results in the loss of high frequency components. As the acquisition proceeds, the longitudinal magnetization necessarily gets depleted. This situation is quite unlike the usual imaging methods where the longitudinal magnetization recovers after on the order of a few seconds. A variable-flip-angle scheme can be used in order to maintain a constant transverse magnetization in the presence of a progressively decreasing longitudinal magnetization. In this connection non-Fourier encoding procedures, such as wavelet and direct encoding for imaging of HP gases, have been examined.[114] The image SNR using the radial projection encoding method has been evaluated for its performance in 3D microscopy of lungs with ^{3}H and ^{129}Xe[115] and good agreement with theory was obtained. Airways in the lung and void spaces in porous materials are accessible to HP gases and can yield images of high quality with contrast provided by the signal from the gas against the background of no signal from the porous material.[116] Johnson and coworkers[117] have shown that in images of lungs of small animals, resolution can be increased by acquiring 3D registered ^{1}H and ^{3}He images. An in-plane resolution of ~ 100 μm was demonstrated. These authors point out that restricted

diffusion in very narrow passages of the lung might limit the resolution but permit definition of anatomic structure. They conclude that in the case of lung imaging the resolution limit may be less than 200 μm. Xenon dissolves in blood and can reach the brain, thereby permitting images of the brain to be obtained with HP ^{129}Xe.[118–121]

When dissolved in a proton-bearing solvent HP ^{129}Xe has been shown to enhance the proton MR signal[122] by a process similar to the nuclear Overhauser effect and has been termed spin polarization-induced Overhauser effect (SPINOE). The original proposal for enhanced dynamic nuclear polarization (DNP) was based on the electron–nuclear interaction in metals and involved the irradiation of the electronic transition.[123] In proton-bearing liquids enhanced polarization has been obtained by irradiating the electron spin of dissolved free radicals. For observing the Overhauser signal from the protons at higher fields, one is forced to employ correspondingly high electron spin transition frequencies. The experimental arrangement that would permit MR imaging at the same time would be rather cumbersome. Wind and Ardenkjaer-Larsen[124] have pointed out that the equilibrium proton magnetization with a DNP set-up at 0.3 T would be enhanced to an equivalent field of 30 T. We also note that hyperpolarization of ^{13}C nuclei has been accomplished using DNP and used to assess cerebral perfusion in a rat model.[125] Although the depolarization rate is rapid in aqueous solution, the possibility of using HP ^{13}C in spectroscopic imaging applications *in vivo* is quite exciting.

4. IMAGING METHODS, PULSE SEQUENCES, AND THE POINT SPREAD FUNCTION

4.1. Imaging methods and pulse sequences

The MR characteristics of the sample to be imaged largely determine the suitability of an imaging procedure. The time required for imaging and the desired resolution need to be considered together. By reducing the demand on resolution, the number of points to be sampled in k-space can be reduced and hence the imaging time minimized. Our aim here is to highlight some of the points to be kept in mind in evaluating a method of imaging for a particular goal. Many of the pulse sequences chosen here are often used in imaging and the list of pulse sequences considered here is by no means exhaustive.

The two main imaging techniques that are to be considered are the projection reconstruction (PR) method and the Fourier imaging (FI) methods. PR is a frequency encoding-based method while FI in its usual form incorporates both frequency and phase encoding. The full phase encode version of 3D FI is a time-intensive procedure. However, signal loss due to diffusion is less than in the case of frequency encoding. With the PR method one can acquire the FID in the case of short T_2 samples or the echo using a short TE. The work of Toffanin *et al.*[126] serves as an illustration of the application of PR imaging method to a material with short T_2, namely, trabecular bone. These authors used a TE value of 3.0 ms and obtained a voxel resolution of 41 μm^3. Comparing the results with FI method Toffanin *et al.* conclude that PR yields better quantitative structural data.

For short T_2 materials the constant time imaging method (also called single point imaging method[127–129]), which is a phase-encode method, can be used to yield images

free of artifacts arising from B_0 inhomogeneity, susceptibility variations, and chemical shift. This is an FI-based technique. An extension of the constant time imaging method called SPRITE[130] cuts down imaging time and enables the introduction of T_1 contrast. By combining the RARE[131,132] and turboFLASH[133] imaging methods with the single point imaging method, Beyea *et al.*[134] have obtained good images of highly heterogeneous materials with long T_2 but short T_2^*.

The two main classes of pulse sequences that are used for imaging are the GE and SE sequences.[5,15,16,23] A large number of variants have been derived from these two classes. GE-based imaging is faster in general. However, it is prone to susceptibility artifacts. SE methods can provide immunity to artifacts arising from susceptibility, chemical shift, and B_0 inhomogeneity. It is well known that the image contrast can be varied by the choice of image parameters in SE and GE sequences. In general, high fields are used for MRM and the T_1 and T_2 values can be different from those at low fields. Echo time (TE) and repetition time (TR) have to be therefore re-evaluated. The choice of slice-selective pulses and slice-selection gradients can affect the image resolution and nature of artifacts. In recent years adiabatic pulses[135] have gained popularity. The amount of diffusion weighting in an SE image may be affected by the choice of placement of the read-gradient dephasing pulse in the pulse sequence and lead to errors in T_2 measurements.[136] In order to reduce signal loss due to T_2 relaxation, a short echo time is preferred. This may impact the duration of the phase encode and other gradients. With the choice of larger gradient values, diffusion attenuation will also come into play. If the rise/fall times of the phase encode gradients are not short, the phase encoding time cannot be unduly shortened. The line-narrowed 2DFT pulse sequence of Sharp *et al.*[137] can eliminate susceptibility distortions and reduce diffusion attenuation since it samples only the center of the echo. The echo planar method (EPI) is a fast imaging technique that enables an image to be obtained in one single excitation (shot). In its gradient echo version (MBEST) it is susceptible to artifacts. The spin-echo version (PEPI) using 180° refocusing pulses has yielded high-resolution images in a very short time at 11.7 T.[138]

With less demands on the hardware one can obtain good single shot images using pulse sequences such as FSE, RARE and its variants like UFLARE as well as FLASH and its variants. By proper choice of the magnetization preparation modules in the front end of an SE sequence, one can adapt it for a variety of tasks such as T_2-weighted, diffusion-weighted or flow-weighted imaging.[139] The FSE sequence, like the CPMG sequence on which it is based, can give rise to spin echoes provided the RF pulses are 90 and 180° pulses that obey the CPMG condition, namely, the initial transverse magnetization due to the 90° pulse lies on the axis of the refocusing 180° pulses. Any deviation in the phase relation between the 90 and 180° pulses or their flip angle results in echoes that are mixed with stimulated echoes (STEs) leading to artifacts. For T_2 and diffusion imaging this situation is undesirable. Further, the intensity of the CPMG echo train is attenuated. This problem is referred to as the non-CPMG problem. Several workers have addressed this problem.[140–142] A simple solution to this is to use crusher gradients flanking the 180° pulses and acquiring only a few echoes.[143] In this situation the full k-space data may not be available in one shot. Compensated π pulses like XY-4[144] have been incorporated in the FSE sequence with attendant increase in imaging time. The situation is more serious for the RARE imaging method where different echoes are phase encoded differently.

Hennig and Scheffler[145] have shown that for RARE sequences in which a low angle α pulse is used instead of the 90° pulse the signal can be significantly increased if the first refocusing pulse is $90° + \alpha/2$. Hennig and Scheffler[146] have proposed the use of hyperechoes in RARE imaging. In principle, imaging with the use of low RF power should be feasible. Samples with longer T_2 are well suited for RARE imaging. A sequence called fast large angle spin echo (FLASE) has also been proposed and demonstrated.[147] The sequence has yielded images of high resolution at 1.5 T. Two versions of the modified driven equilibrium FT (MDEFT) have been described.[148] The SE version is called MDEFT-SE and the GE version MDEFT-GRE. These sequences have been developed for 3D imaging and provide high T_1 contrast and have been used for human brain imaging at 4 T. DEFT-based methods have not yet found favor at higher fields. Pulse sequences based on steady-state precession have also proved efficient for MRM on account of their good SNR. Kohler et al.[149] have recently obtained good image resolution with TrueFISP with an imaging time on the order of a minute.

In phase-encoded imaging the choice of the order of phase encoding can affect the contrast and resolution in the images. Several ways of traversing the k-space to acquire data have been employed. The contributions from various signal-broadening mechanisms for a given pulse sequence can be evaluated by a point spread function (PSF) analysis (see Section 4.2). As stated earlier, the whole k-space data set may be acquired in a very short time with a single excitation or with the use of several excitations. In the latter case the time taken to acquire the data will be longer and the possibility of sample motion (e.g., live animals) exists. The incorporation of navigator echoes in the pulse sequence has to be considered in this situation.[85]

4.2. Spatial resolution and the point spread function

Resolution in MRM images of liquid-like samples depends upon the following important factors: SNR, diffusion, susceptibility, digitizer bandwidth, and T_2. A large value of T_1 might limit, in practical terms, the number of scans per unit time and thus affect the SNR per unit time, a quantity that is of importance in imaging studies. In solid-like samples the short T_2 calls for imaging strategies different from that for liquid-like samples. The pulse sequence chosen for imaging also affects resolution. We assume here that flow and sample motion are absent. A comprehensive analysis of the various factors affecting resolution in MRM in terms of their corresponding PSFs can offer better insight.[5,128,150,151] The full width at half height (FWHH) of the PSF in the spatial domain is considered as a useful measure of resolution. The total PSF is a convolution of all the individual PSFs. Thus,

$$PSF(total) = PSF(sampling) \otimes PSF(diffusion) \otimes PSF(relaxation) \otimes \cdots \qquad (7)$$

The symbol $\otimes$ denotes convolution. Thus, the effect of varying TE and TR in pulse sequences on resolution can be followed by a PSF analysis.[152,153] Robson et al.[154] have outlined an experimental method for measuring the PSF. Different schemes for the phase encoding employed in pulse sequences can lead to different k-space weighting functions and thus affect resolution. Zhou et al.[155] analyzed three different k-space sampling schemes and the corresponding PSFs for a fast spin echo sequence in order to

assess its suitability for MRM. Using numerical simulation procedure, Webb[156] was able to show that given a value of the maximum strength of the phase-encoding gradient and the value of the self-diffusion coefficient, one can find an optimum value of the number of phase-encoding steps that maximize the spatial resolution, i.e., minimize the FWHH of the PSF.

The single k-space point mapping (SPI) was originally proposed by Emid and Creyghton[127] and has been used for imaging semisolid materials with short T_2. An extension of this technique, known as the multipoint (MP) k-space mapping,[157] can reduce the imaging time compared to that using SPI. However, depending upon the details of the k-space sampling procedure, artifacts in the MP image can arise from relaxation-induced k-space modulation. In their work on imaging with the MP method, Fernandez-Seara *et al.*[158] were able to obtain the PSF from the k-space sampling function. Using the PSF deconvolution procedure, they were able to reduce the intensity of the ghost image artifact in the image of a Lego piece.

In standard echo planar imaging (EPI) schemes the k-space center is sampled in the middle of the acquisition train. Using the PSF approach, Windischberger and Moser[159] have shown that shifting the acquisition window in k-space can result in loss of resolution under poor SNR conditions in comparison to the standard schemes. It is interesting to note that one of the earliest applications of PSF in MR imaging was to EPI by Tropper[160] who examined the effect of different kinds of gradient modulation on resolution. Improving the design of pulse sequences, choice of optimum k-space sampling schemes, removal/suppression of image artifacts – all these tasks can benefit greatly from PSF analysis. Above all, since the PSF provides a quantitative measure of the factors that affect spatial resolution, PSF analysis is a valuable tool for MR microscopists.

5. OTHER IMAGING METHODS

5.1. *q*-Space and displacement imaging

There is an implicit assumption of a single T_2 and thus single D in Eq. (5), i.e., monoexponential behavior of signal decay in the diffusion experiment. If this is not true, q-space analysis is an efficient and useful method of data interpretation. This technique takes advantage of the Fourier relationship between the signal decay and the displacement probability function, $\bar{P}_s(\vec{R}, t)$, which gives the average probability of a particle having a dynamic displacement $\vec{R}$ over a time t. The echo amplitude, $E_\Delta(\vec{q})$, takes the form:

$$E_\Delta(\vec{q}) = \int \bar{P}_s(\vec{R}, \Delta) e^{i2\pi \vec{q} \cdot \vec{R}} \, d\vec{R} \tag{8}$$

where $\vec{q}$ is defined as $\gamma \delta \vec{g}/2\pi$ (γ is the gyromagnetic ratio, δ is the gradient duration, and $\vec{g}$ represents the pulsed gradient amplitude and direction).

Displacements of spins of the order of a few microns can be measured by means of q-space imaging techniques.[5] The PGSE method[78] forms the basis for the q-space measurements. The gradient pulses used for q-space imaging are much larger and

narrower and the gradient pair has to be well matched. The PGSE-MASSEY pulse sequence of Callaghan[161] gives good compensation for any mismatch in the gradient pair. Both spin-echo and stimulated echo versions[162,163] of the pulse sequence have been proposed for q-space imaging. Comparison of ADC data obtained from diffusion-weighted imaging using lower pulsed gradient strengths with displacement profile data obtained with high pulsed gradient strengths can be useful. Several studies have been carried out for obtaining water displacement profile data on porous materials (e.g., Magnetic Resonance Imaging, Vol. 19, April/May 2001) and biological materials.[164–167] Displacement profiles can be obtained on a pixel-by-pixel basis but the time required for spatial resolution may be prohibitive. Scheenen *et al.*[168,169] adapted the turbo spin echo (RARE) methodology for q-space imaging and were able to get detailed information on diffusion and slow flow in plants. The ability to traverse the k-space faster and the use of spin echoes that avoided the problem of susceptibility artifacts were the key to success in their experiments with plants.

5.2. Multimodal imaging

The value of the MRM image of an object can often be enhanced considerably by having a complementary image obtained from another imaging modality such as optical microscopy. Although MR can provide images of objects that are not optically transparent, optical microscopic images of such objects may be available for thin slices. It would be ideal if one could compare the MRM images of thin slices in the two cases. The optical microscopy images are generally of much higher resolution. However, the ability to impart contrast to the MRM image by a variety of methods (see Section 3) can compensate for the reduced resolution and make the comparison of the two images highly meaningful. Glover *et al.*[170] have constructed a probe consisting of a surface coil integrated into a standard microscope slide for MR imaging at 11.7 T. This arrangement enabled them to view the same sample with the aid of an optical microscope. Direct electrical connection to the surface coil was avoided by using inductive coupling. An in-plane resolution of $\sim 5\,\mu m$ could be routinely obtained in the case of plant and animal cells.

With the aim of studying biological cells simultaneously with MR and optical microscopy, Wind and coworkers[171] have designed and built an integrated confocal and MR microscope. It utilizes a bottom loading optical microscope probe and a top loading MR microscope probe configured around a wide bore 11.7 T magnet. Details of the integrated microscope are available.[172,173] Combining MRM with polarized light microscopy (PLM), for example, has yielded quantitative results in the study of articular cartilage.[174]

Jacobs and Cherry[175] have examined the advantages of employing MRM and PET (positron emission tomography) as complementary techniques for imaging. PET has better temporal resolution than MRM. However, MRM can provide better spatial resolution. The experimental design and construction of such a combination instrument is challenging. Amongst the other techniques that can be usefully combined with MRM to provide useful information are high frequency ultrasound, micro-CT, and fluorescence microscopy.

6. APPLICATIONS

6.1. Cellular imaging with MRM using T_2 and T_2^* contrast: magnetic labeling

T_2 and T_2^* contrast arising from the introduction of small paramagnetic particles inside a cell can facilitate visualization and serve as a useful marker in MRM. The magnetic particles give rise to a local field inhomogeneity and cause a reduction in the T_2 of water protons undergoing translational diffusion near these particles. Spin echo (T_2) and gradient echo (T_2^*) based MR imaging sequences can be used to visualize the presence of small quantities of the particles, with gradient echo being the preferred modality on account of the better image contrast.

MR imaging of iron oxide-labeled neural transplants were reported in the early 1990s.[176,177] Due to the recent interest in stem cell research, a number of laboratories are now engaged in the development of MR contrast agents for cell tracking based on small magnetic particles comprising of iron oxide (usually classified as superparamagnetic iron oxide, SPIO) particles.[7,178–181] The smaller sized particles of SPIO are characterized as USPIO (ultrasmall) and nano-sized (4–7 nm) monocrystalline particles of iron oxide go under the name MION. These particles can be suitably coated with the goal of facilitating their entry and retention in the cell without sacrificing biological activity.

T lymphocytes are key players in the body's defense mechanisms. One major aim in immunology has been to understand the relationship between the functional and migratory properties of antigen-specific T cells.[182] Dodd et al.[7] labeled single mammalian cells (T cells) using dextran-coated SPIO for MR contrast. Along with lymphocytes, macrophages are a favorite system for testing magnetic particles due to the macrophages' propensity to indiscriminately engulf foreign particles. Labeled macrophages have been employed to identify, via MRM, sites of inflammatory cellular activity in soft-tissue infection and CNS lesions.[182–185]

A number of different types of progenitor cells have been labeled and tracked *in situ* (at least in a preliminary manner) with magnetic particles. These systems include endothelial precursor cells associated with neovascularization in the ischemic heart[186]; neural progenitors that may prove useful in treating demyelinating disease[178,187]; transplanted cells in rat brain, spinal cord, and kidney[187–190]; and hematopoietic and mesenchymal stem cells to gain insight into homing and engraftment.[191–194] Labeling and imaging to eventually aid in diagnosis and studies of drug efficacy are the goals of numerous studies using magnetic particles in small animal models of cancer.[195–199] Models of diabetes[200] and atherosclerosis have also received attention. The use of magnetic particles in identifying atherosclerotic lesions is especially compelling as animal model studies[201] are directly extendable to the clinic.[202]

It is generally believed that cellular imaging with either coated or uncoated nanoparticles of iron oxide is equivalent since the biology of the cell is assumed to be unperturbed by the introduction of the magnetic label inside the cell. However, the recent report of Berry et al.[203] that uncoated and dextran-coated iron oxide nanoparticles induce different cell response is a cautionary one. Moreover, anionic nanoparticles show a significantly higher affinity for some cells than dextran-coated particles,[204] while van den Bos et al.[205] have investigated the efficacy of cationic liposomes. The transferrin receptor

has been utilized as an efficient intracellular delivery device.[178,192,206–208] It is not surprising that particle surface properties have a notable effect on initial interactions with the biological systems under study. Bulte *et al.*[209] have given details of the preparation of magnetically labeled cells for cell tracking. Nitin *et al.*[210] have reported the development of micelle-coated iron oxide nanoparticles of uniform (∼10 nm) sizes. Interestingly, Hinds *et al.*[193] have shown that larger, micron-scale, iron oxide particle also can be successfully used for visualizing single cells. In our view the area of cellular imaging with superparamagnetic particles will be one of the most fruitful areas of biological applications of MRM, especially in view of the increasing availability of high field MR microscopes.

6.2. Plants

There is a long history in MR imaging of using fruits and vegetables as convenient demonstration and phantom objects with interesting internal configurations and contrast characteristics.[211] There are also ongoing efforts at macroscopic scales from meter (logs) to millimeter (fruit ripening and seed characterization) sized objects. Spectroscopic studies without imaging were reviewed recently by Shachar-Hill,[212] while Kockenberger[213,214] reviews MR imaging investigation of plant cell metabolism. In this section we concentrate on microscopic scale investigations of plant specimens. The principal, although not sole, use of MRI in this context is the nondestructive assessment of internal characteristics (structure; water, oil, or sugar content; texture, etc.). Chemical shift imaging (CSI) was employed by Gersbach and Reddy[215] to localize the site of accumulation of oil in *Carum copticum* (Apiaceae) fruits using the aromatic resonances of thymol, which is a major component of the oil. Zhong *et al.*[216] take advantage of geometrical effects in the compartmentalization of paramagnetic species that produce exaggerated chemical shift effects. Using high concentration Gd-DOTA^{2-} in root tips of maize seedlings, they can differentiate internal from extracellular H_2O, producing images of each at ∼23 μm in-plane resolution. This method should be of interest for studies of water transport in living plants. Ishida *et al.*[217] used MR diffusion measurements to investigate water compartmentalization during kidney bean development. The MR images and derived water diffusion properties provided information about the cellular matrix, the barrier spacing of water compartments and the reduced permeability of membranes surrounding different compartments, which were observed to change with the stages of growth in individual tissues of the bean. The venous structure in a celery leaf is clearly apparent in the high-resolution (32 μm^2) image shown in Fig. 2.

Viability of seeds and bulbs is an issue of crucial commercial interest, especially when they are shipped long distances and stored for extended periods. Micro-MRI is finding increased application in ascertaining viability and examining causes of physiological aberrations leading to lack of viability. The ability to image and access local water characteristics and concentrations within the small barley seed provide a nondestructive means to distinguish viable from nonviable samples nondestructively. Such methodology is especially important for testing after shipment, handling, and long-term storage under unknown or problematical conditions. Gruwel *et al.*[218] observed characteristically
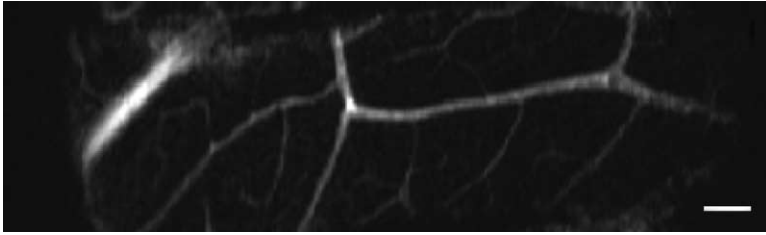
Fig. 2. Celery leaf in air within a 2 mm id D$_2$O matched glass tube in a 3 mm RF shielded microcoil. Conventional spin echo imaging, TR/TE = 1000 ms/7 ms, NA = 32, nonslice selective, scan time = 21 min 20 s, 32 × 32 μm^2, estimated leaf thickness = 100–200 μm. Scale bar = 500 μm (image courtesy: J.M. Tyszka and A. Demyanenko.)

different water uptake (rapid hydration of the scutellum in nonviable seeds) and relaxation properties (shorter T_1 relaxation times) of viable versus nonviable seeds. Two groups centered in the Netherlands have done interesting work on tulip bulb physical, physiological, and morphological changes during storage. Van Kilsdonk *et al.*[219] were particularly interested in determining factors contributing to bud abortion, which increases dramatically after 26 weeks of storage. They measured maps of T_1 and T_2 at 200 MHz as a function of storage time (0–32 weeks), water content, and osmolality of tissue sap. Decreases in T_1 and T_2 relaxation times of stamens in shoots accompanied increases in sap osmolality and decreases in water content. Likely increases in sugar content lead to increased osmolality and concomitant decreased water mobility (translational and rotational), thus causing decreased relaxation times. Although not strictly micro-MRI, Kamenetsky and coworkers[220] have performed a series of low field (20 MHz) studies aimed at characterizing developmental changes and water status in tulip bulbs under different storage conditions. When comparing 4°C (vernalized) and 20°C (nonvernalized) storage conditions, they find that spin density, T_1, T_2, MT and ADC are all significantly different between the two conditions.[220–223] As in the previous study, decreases in relaxation times with storage time were noted. Further, T_2 values in the basal plate were significantly lower in vernalized than nonvernalized bulbs. ADC values remained constant in the vernalized samples, but increased significantly in the nonvernalized samples. It should be noted that intrabulb floral development is similar in both cold stored and room temperature stored bulbs, but stalk elongation and actual bloom occur only in cold stored plants.

Determination of flow and uptake of water, salts, and metabolites are especially appropriate applications of micro-MRI. Pulsed field gradient stimulated echo sequence combined with turbo spin echo imaging has been used to distinguish slow flow from diffusion.[168] In a maize stem vascular bundles were easily distinguished from surrounding parenchymal tissue.[169] Haase and coworkers[224] have imaged slow flowing metabolites and ^{23}Na uptake in living plants. The metabolite imaging is interesting from both technical and biological viewpoints. It combines a flow sensitive magnetization preparation with slice-selective spectroscopy enabling detection of velocities down to 0.1 mm/s and small concentration of metabolites against a large background of stationary and flowing water. In a slice of the hypocotyls of castor bean seedlings

(*Ricinus communis*) metabolite maps show that carbohydrate (resonance at 3.7 ppm) is located exclusively in the phloem region, while an unknown species (resonance at 2.7 ppm) occurs only in the parenchyma. ^{23}Na imaging of the same species was used to map sodium distribution and uptake with remarkable resolution considering the inherent difficulty in imaging this species.[224] Although acquisition times were relatively long (85 min), they appear to be short compared to uptake and accumulation making this methodology potentially useful for studies of salt stress in plants.

6.3. Embryology

The early promise of potential applications of MRM in studies of normal and abnormal development in animal model systems and humans is beginning to be realized.[225–227] MRI observations of different developmental stages (*in vivo* and *ex vivo*) provide three-dimensional images from which quantitative morphometric data about specific changes can be obtained. A wide range of human and animal models have been examined with MRM. We review a sampling of recent work on human, avian, rodent, and amphibian systems. Figures 3 and 4 point out that detailed embryonic anatomy can be identified in MRM images of small animals.

Jeffery[228] imaged 42 fixed human fetuses from museum collections to determine relative rates of growth of the anterior and posterior portions of the skull base. Contrast was significantly better than conventional plain radiography or CT where only completely ossified bone was apparent, allowing landmarks to be readily identified. Descriptive statistics relating age, skull base lengths and the proportions of the posterior cranial fossa provide compelling evidence that the growth rate of the anterior skull base is almost twice that of the posterior skull base and that increases in the width of the posterior cranial fossa exceed those in its length. In a more general vein, Puerta-Fonolla *et al.*[229,230] are compiling 3D MRM images of several fetuses to aid in teaching prenatal human development. Work by Beuls *et al.*[231,232] emphasizes that 3D visualizations of complex structures can provide insights not otherwise attainable. In infants born with spina bifida it is uncertain whether surgical closure of a myelomeningocele at midgestation alters the neurological outcome at birth. The authors recorded *in vitro* high-resolution MR scans of the myelomeningocele of a 20-week fetus and a similar age neurologically intact specimen. Detailed morphology of the fetal cord and associated structures clearly revealed the nonfusion of mesodermal structures and severe distortion of the cord within the myelomeningocele. These or similar high-resolution detailed MRM images may serve as useful references for future clinical intrauterine imaging which in turn would serve to optimize preoperative assessments.

Avian systems have a long history as useful model system with which to explore details of events in early embryogenesis.[233] They offer a self-contained and readily manipulated system. Image resolution down to 25 μm is possible at high field strengths and the use of gadolinium-based contrast agents provides considerable improvement in image quality.[234–236] The transition from precalcified tissue to bone causes dramatic changes in the properties of associated water that can be monitored via changes in MR parameters such as T_2 and magnetization transfer contrast (MTC).[57,237] Morphological
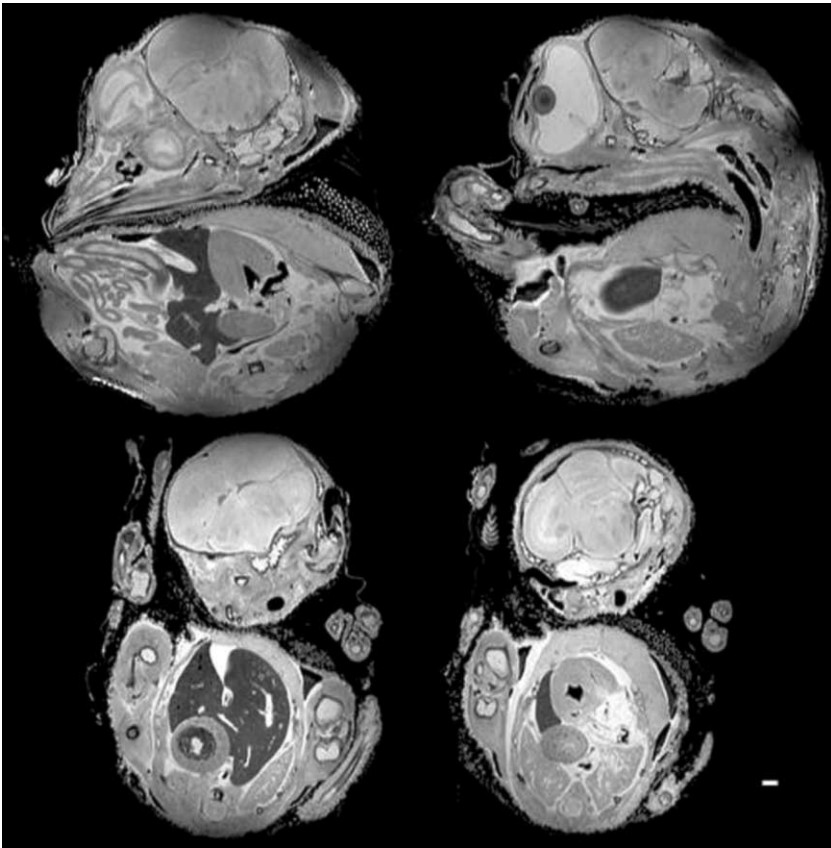
Fig. 3.   Slices through a three-dimensional image of a fixed quail embryo (15 days old). Data were acquired with a UFLARE sequence with four echoes; TR/TE$=1500$ ms/49 ms; resolution$=103$ μm^3. Sagittal (top) and coronal (bottom) slices are shown. B_1 inhomogeneities from the struts in the birdcage RF coil are apparent at the edges of the sagittal images. Scale bar$=1$ mm (image courtesy: R. Jacobs).

and biochemical characterization of bone formation was carried out by Porter *et al.*[238,239] in a chick derived cell culture system and for the growth plate of the embryonic chick femur. Comparison with histological sections indicated that T_2 values varied monotonically with 'tissue cellularity', defined as percent intracellular area on histological section. As might be expected, collagen molecules present in mineralized zones gave rise to a significant MT effect.

Both rats and mice are widely used small animal model systems in the life sciences in general and in developmental biology in particular. Moreover, their relatively small size makes them amenable to study with the narrow bore high field instrumentation typically used in MRM. The ability to alter the genetics of the mouse to produce models of human disease is a boon to the study of these phenomena, but a costly undertaking. MRM is well suited to characterizing anatomical differences between

Fig. 4. Slices through a three-dimensional image of a fixed mouse embryo (14 days post conception). Data were acquired with a UFLARE sequence with eight echoes; TR/TE = 2000 ms/38 ms; resolution 50 µm in the long axis, 80 µm in the other two dimensions. Sagittal (top) and coronal (bottom) slices show a wealth of anatomic detail. Scale bar = 1 mm (image courtesy: B. Boulat and R. Jacobs).

transgenic and normal animals, both *in vitro* and *in vivo*.[240] The obvious disadvantage of MRM over classical histological techniques is the much poorer resolution of MRM; while, some advantages of MRM are that it is nondestructive, noninvasive, and produces true 3D images. *In vitro* scanning of fixed samples at high fields produces images of the highest resolution and SNR. Dhenain *et al.*[241] have acquired high-resolution (20–60 µm isotropic voxels) T_2-weighted 3D images of a series of mouse embryos fixed at different stages of development for use in constructing a digital atlas of mouse development. Although it involves long acquisition times, diffusion tensor images of fixed mouse embryos provide additional contrast not present in T_2-weighted images, which allows unambiguous delineation of many anatomical features.[11] Schneider *et al.*[242] point out that even though MRM scans can take 8–12 h, this

expenditure is still short compared to time needed to section, stain, and process a small sample for histological analysis. Their comparisons of normal mouse embryos and embryos lacking the transcriptional coactivator Cited2 show clear differences in a number of features including the cerebellum, midbrain, and adrenal gland. Using a transgenic mouse model of dilated cardiomyopathy, MRM provided quantitative data about volumes of the atria and ventricles with statistically significant difference between the normal and dilated cardiomyopathy mice.[243] *In vivo in utero* MRM applications are difficult due to sample motion (maternal respiration) and the need for large data matrices (and thus long imaging times) or complicated subvolume imaging sequences to 'isolate' the embryo(s) within the context of the dam. Some recent work at almost microscopic resolution illustrates the power of MRM for *in utero* phenotyping of mice. In a rat model of congenital diaphragmatic hernia (CDH), MRM was used to identify *in utero* those embryos with CDH.[244] Affected embryos were subjected to tracheal ligation at day 19 and followed serially with MRI. Subsequent postmortem MRM and anatomic dissection confirmed that the *in utero* MRI identification of CDH had 97% sensitivity and 100% specificity. The consequences of surgical intervention observed postmortem (lung expansion and flattening of the diaphragm) were also visible in the *in utero* MR images. In producing and phenotyping transgenic mice the simple assessment of number and general anatomy of the embryos during gestation is of crucial importance. Chapon *et al.*[245] have obtained *in utero* time-course images at ∼200 μm resolution in which larger anatomical structures were identifiable. In mice with disruption of one or both osteopotin (OPN) alleles reproductive success is severely compromised. MRM was used to determine embryo number of size and number in gravid wild-type mice and mice with targeted disruption of OPN.[246] With *in vivo in utero* MRM it was determined that OPN−/− embryos were significantly smaller than wild-type at all gestational ages, but no difference was noted in embryo number at any gestational age.

The early development in the amphibian has been studied for well over 100 years.[247] Recent work is being performed almost exclusively on the African clawed frog, *Xenopus laevis*, due to the robustness of the system and ease of obtaining embryos year around. Progress in understanding the developmental mechanisms operating in the *X. laevis* embryo has often been hampered by the inability to visualize cells within the interior of the embryo due to light scattering by the intracellular yolk inclusions. These qualities make it a prime candidate for study with MRM.[46,248,249] Studies on morphogenetic movements and their molecular control are facilitated with high-resolution 3D time-lapse images possible with MRM. Figure 5 shows some recent images of *X. laevis* revealing gastrulation as it progresses *in vivo*.

6.4. Brain

MRM has a long history of rodent brain imaging.[250–252] The resolution of MRM is 1–2 orders of magnitude poorer than optical microscopy used in histopathology or *in vivo* optical studies in neurobiology. Nevertheless, with its nondestructive nature and its ability to acquire three-dimensional images of optically opaque samples, MRI has
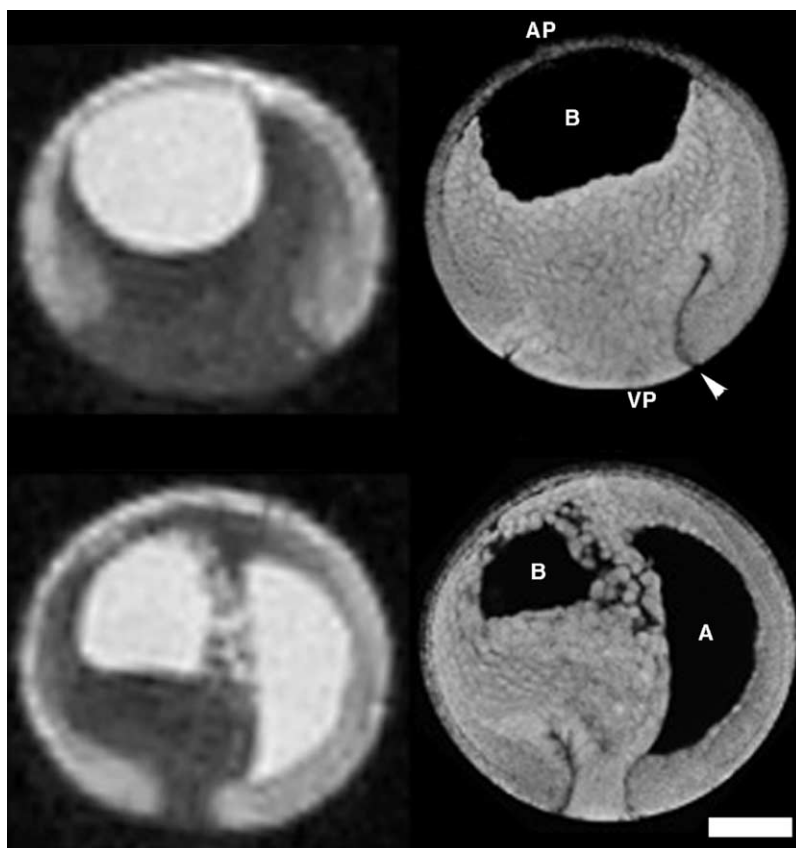
Fig. 5. *Xenopus laevis* gastrulation viewed *in vivo* with MRM. A slice from two *in vivo* 3D MRM images of the same sample recorded several hours apart (left) and histological slices at comparable stages (right). Blastocoel and archenteron are the bright fluid-filled volumes in the MRM images; vegetal fat-filled cells are dark; neural precursor cells are of intermediate intensity. AP, animal pole; VP, vegetal pole; B, blastocoel; A, archenteron; arrowhead, blastopore grove. Scale bar = 200 μm (image courtesy: C. Papan and B. Boulat).

established a firm presence in the arsenal of the forward-looking neurobiologist. Anatomical atlases are a prime example of MRM applications. The 3D digital nature of MRM images allows complex spatial relationships to be viewed directly. Benveniste *et al.*[253] applied T_2^* and contrast agent enhanced MRM to obtain high-resolution MRM images of the C57BL/6J mouse brain and identify many anatomical features. Lower field (2.35 T) *in vivo* mouse brain images offer different contrast and somewhat lower resolution.[254] Multimodal imaging work in which several imaging technologies are applied to the same sample seeks to take advantage of the best features of each.[255] This work and related work on mouse embryos[241] seek to implement 3D digital atlases as frameworks to allow facile management of the increasingly complex and voluminous amounts of data about the mammalian brain. Whole mouse embryo images in Fig. 4

and neonate mouse brain images in Fig. 6 show detail and contrast obtainable at high magnetic fields using a relatively small sample.

Both *in vitro* single time point images and *in vivo* longitudinal imaging studies of the brain's response to a specific insult or the effect of genotypic manipulation offer are beginning to offer much needed insight into complex phenomena. Redwine *et al.*[256] showed that quantitative morphology of anatomic changes in an Alzheimer's disease mouse model system was comparable in accuracy to classical histological determinations. Diffusion weighted and tensor imaging[257,258] have unique abilities to emphasize differences due to the presence or absence of anisotropic features (e.g., neuronal tracts) that influence local water diffusion characteristics. Transgenic mice with subtle brain phenotypes,[11] mice and rats with induced ischemia,[259,260] and mice with induced demyelination[261] all show significant changes in local water diffusional properties that provide important clues about underlying structural and functional changes. Longitudinal brain studies with MRM are of special interest because they obviate the need to examine large populations of animals. Instead, a small number of specimens are examined many times. Thomas *et al.*[262] looked at difference in the effects of herpes simplex virus serotypes 1 and 2 in the mouse by daily MRM imaging and clinical disease scoring. Lesion induced by HSV infection was detected with MRM, sometimes with the use of vascular contrast agent. The correlation between the MRM and endpoint histopathology was excellent, leading the authors to conclude that longitudinal *in vivo* MRM is a useful way to evaluate HSV pathology in the mouse and potentially useful in monitoring the efficacy of anti-infective therapy. In an elegant quantitative multiparametric study combining MRI, EEG, and histopathology, Nairismagi *et al.*[263] observed rats periodically for 260 days after induction of status epilepticus. MR imaging revealed increased T_2, rotating frame T_1 ($T_{1\rho}$), and diffusion values in the primary focal area (amygdala) at 2 days after induction and secondarily connected areas had pathological values of T_2 and $T_{1\rho}$. Acute effects were mostly reversed at 9 days, but at times greater than 20 days $T_{1\rho}$ and diffusion values revealed secondarily affected areas in the amygdala and hippocampus. Initial pathologies noted in both the MR images and histological studies had low predictive value for subsequent severity of seizure and tissue damage, temporal patterns of long-lasting abnormalities. It is hoped that temporal patterns of long-lasting abnormalities seen with MRI will lead to insights about the mechanisms underlying this debilitating disorder.

6.5. Bone

Bone is a dense specialized form of connective tissue with mechanical (skeleton provides rigidity functioning as attachment and lever for ligaments and musculature), chemical (calcium homoeostasis and metabolism), and hematological functions. Cortical (also called compact bone) and trabecular (also known as spongy or cancellous bone) are the two main types of bone. Cortical bone is denser, less porous, and less studied with MR than trabecular bone. Cortical bone forms the shaft of long bones and the covering around trabecular bone at the end of joints and the vertebrae. Trabecular bone is made up of an intricate porous network of tiny strands and thin plates of bone called trabeculae. It
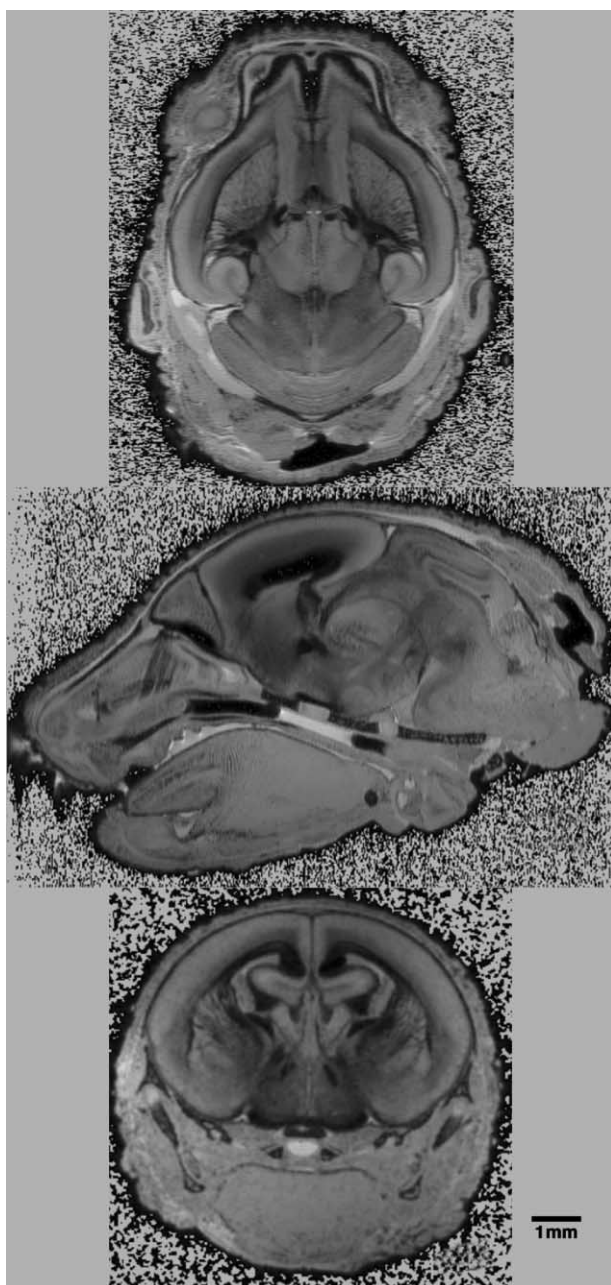
Fig. 6. Orthogonal slices through a three-dimensional image of a fixed mouse neonate (day 0) head. Data were acquired with a GEFI sequence; TR/TE=35 ms/4 ms; isotropic resolution= 33 μm. Note anatomic detail in the not yet fully formed brain (image courtesy: R. Jacobs).

has received a considerable amount of attention with MRM in two main areas: characterization of abnormalities[264–266] and devising models for radiotherapy planning.[267–269] It is important to compare MR imaging of bone morphometry to the established techniques of micro-X-ray and histology analysis. Weber *et al.* characterized mouse femurs (measuring cortical bone thickness, percent marrow area, and trabecular bone area) with all three techniques.[270] Histology and MRM data present as thick slices where analysis is straightforward; in contrast, micro-X-ray data consist of 2D projections of 3D volumes of interest, making quantification difficult. A strong correlation was found between the morphometry derived through MRM and histology. Gradient echo images were found to give better contrast for these measurements than spin-echo images at comparable resolution ($\sim$40 μm in-plane with 200 μm thickness).

The effect of microgravity on bone structure and function is a major concern for long-term space flight. Following 28 days of hindlimb suspension simulating microgravity, tibial trabecular bone structure in the mouse was found to be significantly affected by several measures.[271] 3D MRM images showed bone volume fraction (BVF), trabecular number and thickness decreased along with an increase in trabecular spacing. Toffanin *et al.*[126,272] note that projection reconstruction imaging[273,274] may be more appropriate, in this context, than the more common SE or GE imaging acquisition methods based on Fourier imaging. There are also changes in cartilage in 'loaded' versus 'unloaded' situations that are thought to involve collagen fiber rearrangement. In a study using pig articular cartilage, Gomez *et al.*[275] recorded T_2-weighted MRM images showing several different zones of collagen which subsequent light microscopy and X-ray diffraction patterns revealed differed in fibril diameter and density.

Steroids are known to affect bone properties. Using rat and rabbit model systems, Wehrli and coworkers have applied MRM to characterize trabecular bone structure *in vitro* and longitudinally *in vivo*. In an ovariectomized rat model (OVX), treatments with prostaglandin E-2 (PGE-2) or alendronate (a specific inhibitor of osteoclast-mediated bone resorption used to treat osteoporosis in women after menopause) were evaluated with MRM using extracted tibiae.[276] 3D images at 46 μm^3 resolution were used to calculate mean trabecular plate thickness and separation, BVF, tubularity, and contiguity. All measures showed qualitatively similar responses, but BVF was the strongest discriminator. PGE-2 returned BVF to intact levels, while alendronate kept BVF approximately midway between OVX and intact levels. The same OVX system was also evaluated with an intriguing phase difference map approach generated using a 3D rapid SE pulse sequence.[277] The standard deviation of the phase difference ($\sigma(\Delta\phi)$) and a fictitious rate constant R_2' (slope of the exponential portion of the Fourier transform of the phase difference histogram) were strongly correlated with BVF, suggesting that these may be good surrogate measure of BVF. *In vivo* longitudinal imaging is a principal characteristic of MRI that has been used to good advantage in a serial assessment of adverse side effects on trabecular bone from corticosteroid exposure. Relatively high-resolution MR scans ($98\times98\times300$ μm^3) showed that 2 weeks of dexamethasone exposure at a dose of 0.4 mg/kg caused substantial reduction in trabecular bone volume that occurred by uniform thinning rather than fenestration of trabecular plates. Single voxel proton spectra from bone marrow of the distal femoral metaphysis of treated animals

indicated a conversion of hematopoietic to fatty marrow as evidenced by the reduction in water peak intensity. These studies (performed on a 1.5 T clinical scanner using a custom-built Helmholtz coil) are clearly applicable to patient monitoring and point out that quantitative morphometric and physiological information can be obtained at multiple skeletal locations noninvasively. Lack of estrogen also has significant negative impact on bone growth and metabolism, which has been monitored with both MRM and micro-CT. Ozeki et al.[278] examined the skeletal phenotype of aromatase (ArKO) deficient mice in which newborns had essential normal skeletal system but imaging revealed that adult females had decreased trabecular connectivity, BVF, and bone mineral density. Longitudinal studies of this knockout mouse are expected to be quite revealing.

In radionuclide therapy planning knowing the actual dose of radiation to active bone marrow is critical to planning effective treatment. This requires accurate information about bone geometry and internal constituents, which MR imaging is ideally suited to supply. In a rabbit model with MR imaging somewhat coarser than 'microscopic', Daldrup et al.[267] monitored radiation-induced alterations to the blood–bone marrow barrier (BMB). Using ultrasmall superparamagnetic iron oxide (USPIO) particles, in vivo T_1 and T_2 weighted clearly revealed USPIO leakage into the bone marrow interstitium following radiation treatment that was confirmed by subsequent histopathology. In a series of experiments aimed specifically at using MRM images of trabecular bone to define 3D dosimetric models, Bolch and coworkers present a coherent blend of MRM and mathematical modeling. Trabecular bone sample from the femoral heads and humeral epiphyses of a cadaver were imaged intact and after replacement of the marrow with Gd-doped water.[269,279] Output of standard and customized skeletal dosimetry models using MRM image data was compared with that using current chord-length distribution methods.[280] The authors find that the better definition of input parameters provided by high-resolution MRM reduces errors associated with both geometrical effects (e.g., cellularity) and physiological effects (e.g., fraction of marrow to adipose tissue). Thus, they suggest that patient-specific skeletal dosimetry models derived from MR image data might significantly improve radiotherapy planning.

6.6. Cartilage

Hyaline (articular) cartilage reduces friction and acts as shock-absorbing tissue on the articular surface of bones. It consists of chondrocytes and a matrix composed of water, proteoglycans, and a collagen fiber latticework. The specific organization of the latticework components allows the tissue to undergo the reversible deformations crucial to its shock-absorbing functions. Clinical MRI plays an increasingly important role in the diagnosis of cartilage malfunction[281,282] and MRM provides insights into the structure and function of normal and abnormal cartilage. For an overview of the status of MRM work on cartilage as of 2002, we recommend the review by Cova and Toffanin.[283] The abundance of water and structured environment of hyaline cartilage make it an especially interesting tissue to examine with MRM. Double quantum filtered ^1H and ^2H spectroscopic imaging have been used to examine the anisotropy of water environment and the effects of loading on the orientation of the collagen fiber network and thickness

of different zones within the tissue.[284,285] The orientation dependence of T_2 relaxation was measured at 14 μm resolution by Xia *et al.*[286] and, more recently, $T_{1\rho}$ measurements[287] have been carried out as well. As expected, the relaxation times follow the angular dependence of nuclear dipole–dipole interaction, while the amplitudes of the maxima in the angular dependence vary with tissue depth mapping out the classic three histological subzones (tangential, transitional, and radial). Combined MRM and PLM on specimens from younger animals confirmed these observations and provided comparisons between fiber orientation (determined by PLM) and T_2 relaxation times.

Osteoarthritis is a common and debilitating degenerative disease of cartilage that has several animal models under study with MRM. In a meniscectomized rat knee model, cartilage showed significant increases in T_2 and M_0 but no change in T_1 21 days after the operation. In a rat model using inoculation with heat-killed, dried *Mycobacterium tuberculosis* H37RA, Faure *et al.*[288] conducted an *in vivo* longitudinal MRM examination of the early stages of cartilage degradation. Joint degeneration, such as bone erosion and apparent loss of cartilage thickness, was observable with MRM within 8 days of induction. Although not strictly microscopic scale, two studies on the human wrist point out that improved software (pulse sequences) and hardware (high field magnets) can vastly improve image resolution and quality. New steady-state sequences at 1.5 T can increase SNR-efficiency by as much as 30% and cartilage-synovial fluid contrast by a factor of 3[289] while offering in-plane resolution of 250 μm. The use of smaller surface coils to examine specific cartilaginous regions can improve local SNR and CNR.[290] The simple, but expensive, expediency of working at 8 T with a custom-built wrist coil provides high contrast images at 200 μm resolution.[291]

7. PROSPECTS FOR HIGHER RESOLUTION

The availability of higher field MRI magnets, improved receiver coil and gradient coil design and hardware are some of the factors that have led, in recent years, to an increase in sensitivity. This has naturally led to attempts by several investigators to obtain MRM images with increased resolution in reasonable times especially with a view to extend MRM to biology and in particular to image single cells. The earliest successful attempt in this direction was made by Aguayo *et al.*[248] who obtained an in-plane resolution of 10×13 μm^2 with a slice thickness of 250 μm in their image of an ovum of *X. laevis*. The imaging sequence employed was based on 2D Fourier imaging (2DFT) at 400 MHz. It should be pointed that the in-plane (*X–Y*) resolution alone is not a true measure of resolution since one can compromise the slice (*Z*) direction and compensate for the signal reduction that will otherwise result with an isotropic voxel of smaller dimensions. Thus, by increasing the *Z* dimension the total number of spins in the voxel can be increased to offset the reduction in SNR. The true measure of resolution should therefore be based not on the in-plane (pixel) resolution alone but on the isotropic voxel dimension, its volume and preferably the number of spins in the voxel. Isotropic voxels are preferable from a morphometry point of view since partial volume effects in anisotropic voxels can lead to misinterpretations. Remembering the fact that we are dealing with MRM, we turn our

attention to results of imaging that have yielded isotropic voxels with dimensions well below 100 μm.

As early as 1989 Zhou and Lauterbur[274] were able to achieve an isotropic voxel resolution of 6.37 μm^3 using the 3D projection reconstruction (3DPR) method at 200 MHz with phantoms and fixed tissues. Around this period several workers using the 3DFT method were able to obtain isotropic voxel resolutions in the range of only 15–20 μm. While in-plane resolution of 4–6 μm could be demonstrated with the FT method,[28,292] the goal of realizing still smaller isotropic voxel dimensions remained elusive for almost a decade. Only recently, Lee *et al.*[41] using a specially designed probe with RF microcoil and gradient coils capable of delivering large gradients (>1000 G/cm) were able to obtain an in-plane resolution of 1 μm at 14.1 T (600 MHz). These authors, however, used an oil phantom with a self-diffusion coefficient two orders of magnitude smaller than that of water. The slice thickness was 75 μm. The 2DFT pulse sequence and the imaging parameters were optimized for as high a SNR as possible, taking into account the attenuation effects of diffusion and relaxation. Lee *et al.* have imaged geranium leaf stem cells with voxel dimensions $2\times2\times50$ μm^3. Although the voxels in this work were not isotropic, the in-plane resolution is impressive. The imaging time was also reasonable (~1 h) and hence encouraging. By using strong gradients, one is able to reduce significantly the phase encoding time and thus minimize diffusion problems.[50] In principle, a full 3D phase encoding pulse sequence would be advantageous. On the other hand, since only one point in k-space is acquired in one scan, phase encoding in all three dimensions with the 3DFT scheme carries a severe time penalty. An approximate expression for the imaging time t_i for the isotropic 3D case is available from the work of Mansfield and Morris,[15] namely,

$$t_i \propto (SNR)^2 r^2 \left(\frac{T_1}{T_2^*}\right) \frac{1}{f^{7/2}} \left(\frac{1}{\Delta x}\right)^6 \qquad (9)$$

This expression is applicable for a solenoidal receiver coil of radius r and isotropic voxel of dimension x. f is the spectrometer frequency and T_1 and T_2^* are the longitudinal and inhomogeneously broadened effective transverse relaxation times. We note the dependence of t_i on the inverse sixth power of the voxel size. A reduction in x by one-half increases t_i by a factor of 64 for a given SNR. In order to reduce the imaging time, one therefore chooses receiver coils of smaller radius (microcoils) and images at higher frequencies. In a recent work, Ciobanu *et al.*[42] obtained MRM images at 9 T (383 MHz) with nearly isotropic voxel dimensions of $3.7\times3.3\times3.3$ μm^3 using a microcoil and gradients as high as 5800 G/cm. The pulse sequence employed by these authors is the 'constant time imaging method' based on the work of Emid and Creyghton[127] and further developed by Cory and coworkers[128,129] and is a full 3D phase encode method incorporating the spin echo method (CP and CPMG) to enhance SNR. The effective bandwidth was reduced by acquiring the echoes in the absence of gradients. The price paid for the increased resolution was the prolonged imaging time (~30 h). Any imaging procedure involving micrometer-scale resolution has to be evaluated in terms of the SNR and imaging time in addition to the resolution achieved.

If one is interested in studying fast dynamic processes at high temporal, as well as spatial, resolution, then the method that is favored is the EPI method or modifications of it. Fast traversal of the k-space enables 3D EPI images to be obtained in a matter of minutes. Considering a gradient echo-based EPI method (MBEST) and a spin-echo version (PEPI), Peters and Bowtell[138] have calculated the PSF for diffusion and conclude that resolution consistent with the diffusion limit (~ 28 μm) can be achieved with reasonable imaging parameter values with a water sample. Since MR imagers with wide bore magnets and fields of 17.5 T (750 MHz) are now commercially available, we anticipate that scanners capable of micrometer resolution will become more commonplace.

ACKNOWLEDGEMENTS

REFERENCES

1. P. C. Lauterbur, *Nature*, 1973, **242**, 190.
2. P. Mansfield and P. K. Grannell, *Phys. Rev. B*, 1975, **12** (9), 3618.
3. W. V. House, *IEEE Trans. Nucl. Sci.*, 1984, **NS-31**, 570.
4. Z. H. Cho, C. B. Ahn, S. C. Juh, H. K. Lee, R. E. Jacobs, S. Lee, J. H. Yi and J. M. Jo, *Med. Phys.*, 1988, **15** (6), 815.
5. P. T. Callaghan, *Principles of Nuclear Magnetic Resonance Microscopy*, Oxford University Press, New York, 1991.
6. S. J. Blackband, D. L. Buckley, J. D. Bui and M. I. Phillips, *Magma*, 1999, **9** (3), 112.
7. S. J. Dodd, M. Williams, J. P. Suhan, D. S. Williams, A. P. Koretsky and C. Ho, *Biophys. J.*, 1999, **76** (1), 103.
8. H. Benveniste and S. Blackband, *Prog. Neurobiol.*, 2002, **67** (5), 393.
9. G. A. Johnson, G. P. Cofer, S. L. Gewalt and L. W. Hedlund, *Radiology*, 2002, **222** (3), 789.
10. P. T. Narasimhan and R. E. Jacobs, Neuroanatomical micromagnetic resonance imaging, in *Brain Mapping: The Methods* A. W. Toga and J. C. Mazziotta, eds., Academic Press, New York, 2002, 399.
11. J. Y. Zhang, L. J. Richards, P. Yarowsky, H. Huang, P. C. M. van Zijl and S. Mori, *Neuroimage*, 2003, **20** (3), 1639.
12. P. Blumler, B. Blumich, R. E. Botto and E. Fukushima, *Spatially Resolved Magnetic Resonance: Methods, Materials, Medicine, Biology, Rheology, Geology, Ecology, Hardware*, Wiley-Interscience, New York, 1998, 774.
13. E. T. Ahrens, P. T. Narasimhan, T. Nakada and R. E. Jacobs, *Prog. NMR Spectrosc.*, 2002, **40** (4), 275.
14. J. E. Andaur, A. R. Guesalaga, E. E. Agosin, M. W. Guarini and P. Irarrazaval, *J. Agric. Food Chem.*, 2004, **52** (2), 165.
15. P. Mansfield and P. G. Morris, *NMR Imaging in Biomedicine*, Academic Press, New York, 1982.
16. P. G. Morris, *Nuclear Magnetic Resonance Imaging in Biology and Medicine*, Oxford University Press, New York, 1986.
17. M. Vlaardingerbroek and J. den Boer, *Magnetic Resonance Imaging: Theory and Practice*, Springer, Berlin, 1996.
18. E. Haacke, R. Brown, M. Thompson and R. Venkatesan, *Magnetic Resonance Imaging: Physical Principles and Sequence Design*, Wiley, New York, 1999.
19. B. Blumich and W. Kuhn, *Magnetic Resonance Microscopy*, VCH Publishers, New York, 1992.
20. R. S. Balaban and V. A. Hampshire, *ILAR J.*, 2001, **42** (3), 248.

21. K. K. Bhakoo, J. D. Bell, I. J. Cox and S. D. Taylor-Robinson, The application of magnetic resonance imaging and spectroscopy to gene therapy, in *Methods in Enzymology,* P. M. Conn, ed., Vol. 386, Academic Press, New York, 2004, 303.

22. P. Glover and P. Mansfield, *Rep. Prog. Phys.*, 2002, **65** (10), 1489.

23. B. Blumich, *NMR Imaging of Materials*, Oxford University Press, Oxford, 2000, 568.

24. A. Abragam, *The Principles of Nuclear Magnetism*, Oxford University Press, Oxford, 1973.

25. R. T. Constable, R. C. Smith and J. C. Gore, *J. Comput. Assist. Tomogr.*, 1992, **16**, 41.

26. P. Styles, N. F. Soffe, C. A. Scott, D. A. Cragg, F. Row, D. J. White and P. C. J. White, *J. Magn. Reson.*, 1984, **60** (3), 397.

27. P. Styles, N. F. Soffe and C. A. Scott, *J. Magn. Reson.*, 1989, **84** (2), 376.

28. E. W. McFarland and A. Mortara, *Magn. Reson. Imaging*, 1992, **10** (2), 279.

29. A. C. Wright, H. K. Song and F. W. Wehrli, *Magn. Reson. Med.*, 2000, **43** (2), 163.

30. J. C. Smith and R. L. Nunnally, *Proc. Int. Soc. Magn. Reson. Med.*, 2004, **11**, 42.

31. R. D. Black, P. B. Roemer, A. Mogrocampero, L. G. Turner and K. W. Rohling, *Appl. Phys. Lett.*, 1993, **62** (7), 771.

32. J. G. van Heteren, T. W. James and L. C. Bourne, *Magn. Reson. Med.*, 1994, **32**, 396.

33. R. D. Black, T. A. Early and G. A. Johnson, *J. Magn. Reson. Ser. A*, 1995, **113**, 74.

34. F. Odoj, E. Rommel, M. von Kienlin and A. Haase, *Rev. Sci. Instrum.*, 1998, **69** (7), 2708.

35. S. E. Hurlston, W. W. Brey, S. A. Suddarth and G. A. Johnson, *Magn. Reson. Med.*, 1999, **41** (5), 1032.

36. J. R. Miller, S. E. Hurlston, Q. Y. Ma, D. W. Face, D. J. Kountz, J. R. MacFall, L. W. Hedlund and G. A. Johnson, *Magn. Reson. Med.*, 1999, **41** (1), 72.

37. J. C. Ginefri, L. Darrasse and P. Crozat, *Magn. Reson. Med.*, 2001, **45** (3), 376.

38. T. L. Peck, R. L. Magin and P. C. Lauterbur, *J. Magn. Reson. Ser. B*, 1995, **108** (2), 114.

39. J. E. Stocker, T. L. Peck, A. G. Webb, M. Feng and R. L. Magin, *IEEE Trans. Biomed. Eng.*, 1997, **44** (11), 1122.

40. S. C. Grant, D. L. Buckley, S. Gibb, A. G. Webb and S. J. Blackband, *Magn. Reson. Med.*, 2001, **46** (6), 1107.

41. S. C. Lee, K. Kim, J. Kim, S. Lee, J. H. Yi, S. W. Kim, K. S. Ha and C. Cheong, *J. Magn. Reson.*, 2001, **150** (2), 207.

42. L. Ciobanu, D. A. Seeber and C. H. Pennington, *J. Magn. Reson.*, 2002, **158** (1–2), 178.

43. K. R. Minard and R. A. Wind, *Concepts Magn. Reson.*, 2001, **13**, 128.

44. K. R. Minard and R. A. Wind, *Concepts Magn. Reson.*, 2001, **13**, 190.

45. D. A. Seeber, R. L. Cooper, L. Ciobanu and C. H. Pennington, *Rev. Sci. Instrum.*, 2001, **72**, 2171.

46. K. R. Minard and R. A. Wind, *J. Magn. Reson.*, 2002, **154** (2), 336.

47. Y. Matsuda, S. Utsuzawa, T. Kurimoto, T. Haishi, Y. Yamazaki, K. Kose, I. Anno and M. Marutani, *Magn. Reson. Med.*, 2003, **50** (1), 183.

48. J. Dazai, N. A. Bock, B. J. Nieman, L. M. Davidson, R. M. Henkelman and X. J. Chen, *Magn. Reson. Med.*, 2004, **52** (4), 709.

49. J. S. Schoeniger and S. J. Blackband, *J. Magn. Reson. Ser. B*, 1994, **104**, 127.

50. C. J. Rofe, J. Vannoort, P. J. Back and P. T. Callaghan, *J. Magn. Reson. Ser. B*, 1995, **108**, 125.

51. R. Bowtell and P. Robyr, *J. Magn. Reson.*, 1998, **131** (2), 286.

52. J. E. M. Snaar, P. Robyr and R. Bowtell, *Magn. Reson. Imaging*, 1998, **16** (5–6), 587.

53. J. Leggett, S. Crozier and R. W. Bowtell, *J. Magn. Reson.*, 2003, **165** (2), 196.

54. S. C. Lee, K. Kim, J. Kim, S. Lee, J. Han Yi, S. W. Kim, K. S. Ha and C. Cheong, *J. Magn. Reson.*, 2001, **150** (2), 207.

55. D. A. Seeber, J. H. Hoftiezer, W. B. Daniel, M. A. Rutgers and C. H. Pennington, *Rev. Sci. Instrum.*, 2000, **71** (11), 4263.

56. D. A. Seeber, J. H. Hoftiezer and C. H. Pennington, *Concepts Magn. Reson.*, 2002, **15** (3), 189.

57. R. M. Henkelman, G. J. Stanisz and S. J. Graham, *NMR Biomed.*, 2001, **14** (2), 57.

58. R. E. Hendrick, *Magn. Reson. Imaging*, 1987, **5**, 31.

59. E. M. Haacke, *Magn. Reson. Med.*, 1987, **4**, 407.

60. S. Vinitski, R. Griffey, M. Fuka, N. Matwiyoff and R. Prost, *Magn. Reson. Med.*, 1987, **5**, 278.

61. P. T. Callaghan, *J. Magn. Reson.*, 1990, **87** (2), 304.

62. J. Link and J. Seelig, *J. Magn. Reson.*, 1990, **89**, 310.
63. P. Hjelmström, A. E. Juedes, J. Fjell and N. H. Ruddle, *J. Immunol.*, 1998, **161** (9), 4480.
64. S. C. Jackels, *Pharm. Med. Imag.*, 1990, 645 [Section III, Chapter 20].
65. M. K. Moi and C. F. Meares, *J. Am. Chem. Soc.*, 1988, **110**, 6266.
66. E. J. Russell, T. F. Schaible and W. Dillon, *AJR*, 1989, **152**, 813.
67. D. Meyer, M. Schaefer and D. Doucet, *Invest. Radiol.*, 1990, **25** (Suppl. 1), S53.
68. V. M. Runge and D. Y. Gelblumm, *Top. Magn. Reson. Imaging*, 1991, **3**, 85.
69. L. Pauling and C. D. Coryell, *Proc. Natl Acad. Sci. USA*, 1936, **22**, 210.
70. S. Ogawa, T. M. Lee, A. R. Kay and D. W. Tank, *Proc. Natl Acad. Sci. USA*, 1990, **87** (24), 9868.
71. S. Ogawa, R. S. Menon, S. G. Kim and K. Ugurbil, *Annu. Rev. Biophys. Biomol. Struct.*, 1998, **27**, 447.
72. J. W. Belliveau, D. N. Kennedy, R. C. McKinstry, B. R. Buchbinder, R. M. Weisskoff, M. S. Cohen, J. M. Vevea, T. J. Brady and B. R. Rosen, *Science*, 1991, **254**, 716.
73. J. Frahm, K. D. Merboldt and W. Hanicke, *Magn. Reson. Med.*, 1993, **29** (1), 139.
74. R. Turner, P. Jezzard, H. Wan, K. K. Kwong, D. LeBihan, T. Zeffiro and R. S. Ballaban, *Magn. Reson. Med.*, 1993, **29**, 277.
75. X. Hu and T. H. Le, *Magn. Reson. Med.*, 1996, **36** (1), 166.
76. H. Y. Carr and E. M. Purcell, *Phys. Rev.*, 1954, **94**, 630.
77. E. O. Stejskal, *J. Phys. Chem.*, 1965, **43**, 3597.
78. E. O. Stejskal and J. E. Tanner, *J. Chem. Phys.*, 1965, **42**, 288.
79. W. B. Hyslop and P. C. Lauterbur, *J. Magn. Reson.*, 1991, **94**, 501.
80. B. Putz, D. Barsky and K. Schulten, *J. Magn. Reson.*, 1992, **97**, 27.
81. P. T. Callaghan, A. Coy, L. C. Forde and C. J. Rofe, *J. Magn. Reson. A*, 1993, **101**, 347.
82. H. R. Weiss, E. Buchweitz, T. J. Murtha and M. Auletta, *Circ. Res.*, 1982, **51**, 494.
83. D. Le Bihan, E. Breton, D. Lallemand, M. L. Aubon, J. Vignaud and M. Laval-Jeantet, *Radiology*, 1988, **168**, 497.
84. R. Turner, D. Le Bihan, J. Maier, R. Vavrek, L. K. Hedges and J. Pekar, *Radiology*, 1990, **177**, 407.
85. R. J. Ordidge, J. A. Helpern, Z. X. Qing, R. A. Knight and V. Nagash, *Magn. Reson. Imaging*, 1994, **12**, 455.
86. W. Richter, S. Lee, W. S. Warren and Q. He, *Science*, 1995, **267** (5198), 654.
87. S. Mori, R. E. Hurd and P. C. van Zijl, *Magn. Reson. Med.*, 1997, **37** (3), 336.
88. W. S. Warren, S. Ahn, M. Mescher, M. Garwood, K. Ugurbil, W. Richter, R. R. Rizi, J. Hopkins and J. S. Leigh, *Science*, 1998, **281** (5374), 247.
89. P. T. Narasimhan, S. Velan and R. Jacobs, *Proc. Int. Soc. Magn. Reson. Med.*, 2000, **8**, 2074.
90. W. Richter, M. Richter, W. S. Warren, H. Merkle, P. Andersen, G. Adriany and K. Ugurbil, *Magn. Reson. Imaging*, 2000, **18** (5), 489.
91. R. R. Rizi, S. Ahn, D. C. Alsop, S. Garrett-Roe, M. Mescher, W. Richter, M. D. Schnall, J. S. Leigh and W. S. Warren, *Magn. Reson. Med.*, 2000, **43** (5), 627.
92. J. Zhong, Z. Chen and E. Kwok, *J. Magn. Reson. Imaging*, 2000, **12** (2), 311.
93. J. H. Zhong, Z. Chen and E. Kwok, *Magn. Reson. Med.*, 2000, **43** (3), 335.
94. C. L. Chin, X. Tang, L. S. Bouchard, P. K. Saha, W. S. Warren and F. W. Wehrli, *J. Magn. Reson.*, 2003, **165** (2), 309.
95. R. Bowtell, R. M. Bowley and P. Glover, *J. Magn. Reson.*, 1990, **88** (3), 643.
96. S. Lee, W. Richter, S. Vathyam and W. S. Warren, *J. Chem. Phys.*, 1996, **105** (3), 874.
97. J. P. Marques and R. Bowtell, *Magn. Reson. Med.*, 2004, **51** (1), 148.
98. J. H. Zhong, Z. Chen, E. Kwok and S. Kennedy, *Magn. Reson. Imaging*, 2001, **19** (1), 33.
99. P. T. Narasimhan, S. Velan and R. E. Jacobs, *Proc. Int. Soc. Magn. Reson. Med.*, 2000, **8**, 2074.
100. S. S. Velan, P. T. Narasimhan and R. E. Jacobs, *J. Magn. Reson.*, 2001, **152** (1), 189.
101. N. M. Szeverenyi and E. M. Haacke, *J. Comput. Assist. Tomogr.*, 1986, **10** (3), 484.
102. N. Chandrakumar and S. S. Velan, *J. Magn. Reson. Ser. A*, 1993, **104** (1), 115.
103. J. M. Bohlen, M. Izquierdo and M. Decorps, *J. Magn. Reson. Ser. A*, 1994, **110** (1), 106.
104. L. S. Bouchard, R. R. Rizi and W. S. Warren, *Magn. Reson. Med.*, 2002, **48** (6), 973.
105. S. Capuani, M. Alesiani, R. T. Branca and B. Maraviglia, *Solid State Nucl. Magn. Reson.*, 2004, **25** (1–3), 153.

106. G. D. Charles-Edwards, G. S. Payne, M. O. Leach and A. Bifone, *J. Magn. Reson.*, 2004, **166** (2), 215.
107. P. T. Narasimhan, B. Boulat and R. E. Jacobs, *45th ENC*, Asilomar, CA, 2004.
108. A. Kastler, *J. Opt. Soc. Am.*, 1957, **47** (6), 460.
109. B. M. Goodson, *J. Magn. Reson.*, 2002, **155** (2), 157.
110. A. Cherubini and A. Bifone, *Prog. NMR Spectrosc.*, 2003, **42** (1–2), 1.
111. W. Happer, E. Miron, R. Knize and J. Cecchi, *AIP Conf. Proc.*, 1984, **117**, 114.
112. W. Happer, E. Miron, S. Schaefer, D. Schreiber, W. A. van Wijngaarden and X. Zeng, *Phys. Rev. A*, 1984, **29**, 3092.
113. T. G. Walker and W. Happer, *Rev. Mod. Phys.*, 1997, **69** (2), 629.
114. L. Zhao, A. K. Venkatesh, M. S. Albert and L. P. Panych, *J. Magn. Reson.*, 2001, **148** (2), 314.
115. H. E. Moller, X. J. Chen, M. S. Chawla, G. P. Cofer, B. Driehuys, L. W. Hedlund, S. A. Suddarth and G. A. Johnson, *Magn. Reson. Med.*, 1999, **41** (4), 800.
116. Y. Q. Song, H. C. Gaede, T. Pietrass, G. A. Barrall, G. C. Chingas, M. R. Ayers and A. Pines, *J. Magn. Reson. Ser. A*, 1995, **115** (1), 127.
117. G. A. Johnson, G. P. Cofer, L. W. Hedlund, R. R. Maronpot and S. A. Suddarth, *Magn. Reson. Med.*, 2001, **45** (3), 365.
118. G. Duhamel, P. Choquet, J. L. Leviel, J. Steibel, L. Lamalle, C. Julien, F. Kober, E. Grillon, J. Derouard, M. Decorps, A. Ziegler and A. Constantinesco, *CR Acad. Sci. Ser. III – Sci. Vie/Life Sci.*, 2000, **323** (6), 529.
119. G. Duhamel, P. Choquet, E. Grillon, J. L. Leviel, A. Ziegler and A. Constantinesco, *CR Acad. Sci. Ser. II Fascicule C – Chimie*, 2001, **4** (10), 789.
120. P. Choquet, J. N. Hyacinthe, G. Duhamel, E. Grillon, J. L. Leviel, A. Constantinesco and A. Ziegler, *Magn. Reson. Med.*, 2003, **49** (6), 1014.
121. A. Ziegler, J. N. Hyacinthe, P. Choquet, G. Duhamel, E. Grillon, J. L. Leviel and A. Constantinesco, *Laser-polarized xenon nuclear magnetic resonance, a potential tool for brain perfusion imaging: measurement of the xenon T-1 in vivo. Imaging in Biological Research, Pt A*, Academic Press, San Diego, CA, 2004, 149.
122. G. Navon, Y. Q. Song, T. Room, S. Appelt, R. E. Taylor and A. Pines, *Science*, 1996, **271** (5257), 1848.
123. C. P. Slichter, *Principles of Magnetic Resonance*, 3rd ed, Harper, New York, 1992.
124. R. A. Wind and J. H. Ardenkjaer-Larsen, *J. Magn. Reson.*, 1999, **141** (2), 347.
125. E. Johansson, S. Mansson, R. Wirestam, J. Svesson, S. Petersson, K. Golman and F. Stahlberg, *Magn. Reson. Med.*, 2004, **51** (3), 464.
126. R. Toffanin, V. Jellus, P. Szomolanyi and F. Vittur, *Magn. Reson. Imaging*, 2001, **19** (3–4), 485.
127. S. Emid and J. H. N. Creyghton, *Physica B & C*, 1985, **128** (1), 81.
128. S. Gravina and D. G. Cory, *J. Magn. Reson. Ser. B*, 1994, **104** (1), 53.
129. S. M. Choi, X. W. Tang and D. G. Cory, *Int. J. Imaging Syst. Technol.*, 1997, **8** (3), 263.
130. B. J. Balcom, M. Bogdan and R. L. Armstrong, *J. Magn. Reson. Ser. A*, 1996, **118**, 122.
131. J. Hennig, A. Nauerth and H. Friedburg, *Magn. Reson. Med.*, 1986, **3** (6), 823.
132. J. Hennig, *J. Magn. Reson.*, 1988, **78** (3), 397.
133. A. Haase, J. Frahm and D. Matthaei, *J. Magn. Reson.*, 1986, **67**, 258.
134. S. D. Beyea, B. J. Balcom, I. V. Mastikhin, T. W. Bremner, R. L. Armstrong and P. E. Grattan-Bellew, *J. Magn. Reson.*, 2000, **144** (2), 255.
135. M. Garwood and L. DelaBarre, *J. Magn. Reson.*, 2001, **153** (2), 155.
136. E. W. Hsu, J. S. Schoeniger, R. Bowtell, N. R. Aiken, A. Horsman, S. J. Blackband, S. Crozier, K. Luescher, L. K. Forbes and D. M. Doddrell, *J. Magn. Reson. Ser. B*, 1995, **109**, 66.
137. J. C. Sharp, R. W. Bowtell and P. Mansfield, *Magn. Reson. Med.*, 1993, **29** (3), 407.
138. A. M. Peters and R. Bowtell, *J. Magn. Reson.*, 1999, **137** (1), 196.
139. A. Haase, M. Brandl, E. Kuchenbrod and A. Link, *J. Magn. Reson.*, 1993, **A105**, 230.
140. D. C. Alsop, *Magn. Reson. Med.*, 1997, **38** (4), 527.
141. F. Schick, *Magn. Reson. Med.*, 1997, **38** (4), 638.
142. P. Le Roux, R. J. Gilles, G. C. McKinnon and P. G. Carlier, *J. Magn. Reson. Imaging*, 1998, **8** (5), 1022.
143. X. Zhou, G. P. Cofer, S. A. Suddarth and G. A. Johnson, *Magn. Reson. Med.*, 1993, **30** (1), 60.
144. T. J. Gullion, *Magn. Reson.*, 1993, **A101**, 320.

145. J. Hennig and K. Scheffler, *Magn. Reson. Med.*, 2000, **44** (6), 983.

146. J. Hennig and K. Scheffler, *Magn. Reson. Med.*, 2001, **46** (1), 6.

147. J. Ma, F. W. Wehrli and H. K. Song, *Magn. Reson. Med.*, 1996, **35**, 903.

148. J. H. Lee, M. Garwood, R. Menon, G. Adriany, P. Andersen, C. L. Truwit and K. Ugurbil, *Magn. Reson. Med.*, 1995, **34** (3), 308.

149. S. Kohler, K.-H. Hiller, M. Griswold, W. R. Bauer, A. Haase and P. M. Jakob, *J. Magn. Reson.*, 2003, **161** (2), 252.

150. E. W. McFarland, *Magn. Reson. Imaging*, 1992, **10** (2), 269.

151. P. T. Callaghan, L. C. Forde and C. J. Rofe, *J. Magn. Reson.*, 1994, **B104**, 34.

152. R. T. Constable and J. C. Gore, *Magn. Reson. Med.*, 1992, **28** (1), 9.

153. H. K. Song and F. W. Wehrli, *Magn. Reson. Med.*, 1998, **39** (2), 251.

154. M. D. Robson, J. C. Gore and R. T. Constable, *Magn. Reson. Med.*, 1997, **38** (5), 733.

155. X. H. Zhou, G. P. Cofer, S. A. Suddarth and G. A. Johnson, *Magn. Reson. Med.*, 1993, **30** (1), 60.

156. A. G. Webb, *Concepts Magn. Reson. Part A*, 2004, **22A** (1), 25.

157. Z. H. Cho and Y. M. Ro, *Magn. Reson. Med.*, 1994, **32** (2), 258.

158. M. A. Fernandez-Seara, S. L. Wehrli and F. W. Wehrli, *J. Magn. Reson.*, 2003, **160** (2), 144.

159. C. Windischberger and E. Moser, *Magn. Reson. Imaging*, 2000, **18** (7), 825.

160. M. M. Tropper, *J. Magn. Reson.*, 1981, **42** (2), 193.

161. P. T. Callaghan, *J. Magn. Reson.*, 1990, **88** (3), 493.

162. J. E. Tanner, *J. Chem. Phys.*, 1970, **52**, 2523.

163. D. G. Cory and A. N. Garroway, *Magn. Reson. Med.*, 1990, **14** (3), 435.

164. M. D. King, J. Houseman, D. G. Gadian and A. Connelly, *Magn. Reson. Med.*, 1997, **38** (6), 930.

165. Y. Assaf and Y. Cohen, *Magn. Reson. Med.*, 2000, **43** (2), 191.

166. Y. Assaf, D. Ben-Bashat, J. Chapman, S. Peled, I. E. Biton, M. Kafri, Y. Segev, T. Hendler, A. D. Korczyn, M. Graif and Y. Cohen, *Magn. Reson. Med.*, 2002, **47** (1), 115.

167. Y. Assaf, M. Kafri, H. Shinar, J. Chapman, A. D. Korczyn, G. Navon and Y. Cohen, *Magn. Reson. Med.*, 2002, **48** (1), 71.

168. T. W. Scheenen, D. van Dusschoten, P. A. de Jager and H. Van As, *J. Magn. Reson.*, 2000, **142** (2), 207.

169. T. W. Scheenen, F. J. Vergeldt, C. W. Windt, P. A. de Jager and H. Van As, *J. Magn. Reson.*, 2001, **151** (1), 94.

170. P. M. Glover, R. W. Bowtell, G. D. Brown and P. Mansfield, *Magn. Reson. Med.*, 1994, **31**, 423.

171. R. A. Wind, K. R. Minard, G. R. Holtom, P. D. Majors, E. J. Ackerman, S. D. Colson, D. G. Cory, D. S. Daly, P. D. Ellis, N. F. Metting, C. I. Parkinson, J. M. Price and X. W. Tang, *J. Magn. Reson.*, 2000, **147** (2), 371.

172. P. D. Majors, K. R. Minard, E. J. Ackerman, G. R. Holtom, D. F. Hopkins, C. I. Parkinson, T. J. Weber and R. A. Wind, *Rev. Sci. Instrum.*, 2002, **73** (12), 4329.

173. R. A. Wind, P. D. Majors, K. R. Minard, E. J. Ackerman, D. S. Daly, G. R. Holtom, B. D. Thrall and T. J. Weber, *Appl. Magn. Reson.*, 2002, **22** (2), 145.

174. Y. Xia, J. B. Moody, N. Burton-Wurster and G. Lust, *Osteoarthritis Cartilage*, 2001, **9** (5), 393.

175. R. E. Jacobs and S. R. Cherry, *Curr. Opin. Neurobiol.*, 2001, **11** (5), 621.

176. N. Hawrylak, P. Ghosh, J. Broadus, C. Schlueter, W. T. Greenough and P. C. Lauterbur, *Exp. Neurol.*, 1993, **21** (2), 181.

177. A. B. Norman, S. R. Thomas, R. G. Pratt, S. Y. Lu and R. B. Norgren, *Brain Res.*, 1992, **594** (2), 279.

178. J. W. Bulte, S. Zhang, P. van Gelderen, V. Herynek, E. K. Jordan, I. D. Duncan and J. A. Frank, *Proc. Natl Acad. Sci. USA*, 1999, **96** (26), 15256.

179. L. Josephson, C. H. Tung, A. Moore and R. Weissleder, *Bioconjug. Chem.*, 1999, **10** (2), 186.

180. R. Weissleder, *Radiology*, 1999, **212** (3), 609.

181. J. W. Bulte and M. De Cuyper, *Methods Enzymol.*, 2003, **373**, 175.

182. A. Iparraguirre and W. Weninger, *Int. Arch. Allergy Immunol.*, 2003, **132** (4), 277.

183. V. Dousset, C. Delalande, L. Ballarino, B. Quesson, D. Seilhan, M. Coussemacq, E. Thiaudiere, B. Brochet, P. Canioni and J. M. Caille, *Magn. Reson. Med.*, 1999, **41** (2), 329.

184. A. H. Kaim, T. Wischer, T. O'Reilly, G. Jundt, J. Frohlich, G. K. von Schulthess and P. R. Allegrini, *Radiology*, 2002, **225** (3), 808.

185. C. Billotey, C. Wilhelm, M. Devaud, J. C. Bacri, J. Bittoun and F. Gazeau, *Magn. Reson. Med.*, 2003, **49** (4), 646.

186. A. Weber, I. Pedrosa, A. Kawamoto, N. Himes, J. Munasinghe, T. Asahara, N. M. Rofsky and D. W. Losordo, *Eur. J. Cardiothorac. Surg.*, 2004, **26** (1), 137.

187. J. W. Bulte, T. Ben-Hur, B. R. Miller, R. Mizrachi-Kol, O. Einstein, E. Reinhartz, H. A. Zywicke, T. Douglas and J. A. Frank, *Magn. Reson. Med.*, 2003, **50** (1), 201.

188. Y. Zhang, S. J. Dodd, K. S. Hendrich, M. Williams and C. Ho, *Kidney Int.*, 2000, **58** (3), 1300.

189. P. Jendelova, V. Herynek, J. DeCroos, K. Glogarova, B. Andersson, M. Hajek and E. Sykova, *Magn. Reson. Med.*, 2003, **50** (4), 767.

190. P. Jendelova, V. Herynek, L. Urdzikova, K. Glogarova, J. Kroupova, B. Andersson, V. Bryja, M. Burian, M. Hajek and E. Sykova, *J. Neurosci. Res.*, 2004, **76** (2), 232.

191. B. D. de Laquintane, V. Dousset, A. Solanilla, K. G. Petry and J. Ripoche, *Biosci. Rep.*, 2002, **22** (5–6), 549.

192. H. E. Daldrup-Link, M. Rudelius, R. A. Oostendorp, M. Settles, G. Piontek, S. Metz, H. Rosenbrock, U. Keller, U. Heinzmann, E. J. Rummeny, J. Schlegel and T. M. Link, *Radiology*, 2003, **228** (3), 760.

193. K. A. Hinds, J. M. Hill, E. M. Shapiro, M. O. Laukkanen, A. C. Silva, C. A. Combs, T. R. Varney, R. S. Balaban, A. P. Koretsky and C. E. Dunbar, *Blood*, 2003, **102** (3), 867.

194. H. E. Daldrup-Link, M. Rudelius, S. Metz, G. Piontek, B. Pichler, M. Settles, U. Heinzmann, J. Schlegel, R. A. Oostendorp and E. J. Rummeny, *Eur. J. Nucl. Med. Mol. Imaging* ,2004.

195. D. Artemov, U. Pilatus, S. Chu, N. Mori, J. B. Nelson and Z. M. Bhujwalla, *Magn. Reson. Med.*, 1999, **42** (2), 277.

196. A. Moore, E. Marecos, A. Bogdanov Jr.. and R. Weissleder, *Radiology*, 2000, **214** (2), 568.

197. G. Fleige, C. Nolte, M. Synowitz, F. Seeberger, H. Kettenmann and C. Zimmer, *Neoplasia*, 2001, **3** (6), 489.

198. R. Weissleder, *Nat. Rev. Cancer*, 2002, **2** (1), 11.

199. D. Artemov, N. Mori, B. Okollie and Z. M. Bhujwalla, *Magn. Reson. Med.*, 2003, **49** (3), 403.

200. A. Moore, P. Z. Sun, D. Cory, D. Hogemann, R. Weissleder and M. A. Lipes, *Magn. Reson. Med.*, 2002, **47** (4), 751.

201. S. A. Schmitz, S. E. Coupland, R. Gust, S. Winterhalter, S. Wagner, M. Kresse, W. Semmler and K. J. Wolf, *Invest. Radiol.*, 2000, **35** (8), 460.

202. M. E. Kooi, V. C. Cappendijk, K. B. Cleutjens, A. G. Kessels, P. J. Kitslaar, M. Borgers, P. M. Frederik, M. J. Daemen and J. M. van Engelshoven, *Circulation*, 2003, **107** (19), 2453.

203. C. C. Berry, S. Wells, S. Charles, G. Aitchison and A. S. Curtis, *Biomaterials*, 2004, **25** (23), 5405.

204. C. Wilhelm, C. Billotey, J. Roger, J. N. Pons, J. C. Bacri and F. Gazeau, *Biomaterials*, 2003, **24** (6), 1001.

205. E. J. van den Bos, A. Wagner, H. Mahrholdt, R. B. Thompson, Y. Morimoto, B. S. Sutton, R. M. Judd and D. A. Taylor, *Cell Transplant.*, 2003, **12** (7), 743.

206. D. Hogemann and J. P. Basilion, *Eur. J. Nucl. Med. Mol. Imaging*, 2002, **29** (3), 400.

207. D. Hogemann-Savellano, E. Bos, C. Blondet, F. Sato, T. Abe, L. Josephson, R. Weissleder, J. Gaudet, D. Sgroi, P. J. Peters and J. P. Basilion, *Neoplasia*, 2003, **5** (6), 495.

208. G. Vassaux and T. Groot-Wassink, *J. Biomed. Biotechnol.*, 2003, **2003** (2), 92.

209. J. W. M. Bulte, A. S. Arbab, T. Douglas and J. A. Frank, Preparation of magnetically labeled cells for cell tracking by magnetic resonance imaging, in *Methods in Enzymology,* P. M. Conn, ed., Vol. 386, Academic Press, New York, 2004, 275.

210. N. Nitin, L. E. W. LaConte, O. Zurkiya, X. Hu and G. Bao, *J. Biol. Inorg. Chem.*, 2004, 1432 [online first].

211. S. Kohler, K. H. Hiller, M. Griswold, W. R. Bauer, A. Haase and P. M. Jakob, *J. Magn. Reson.*, 2003, **161** (2), 252.

212. Y. Shachar-Hill, *Metab. Eng.*, 2002, **4** (1), 90.

213. W. Kockenberger, *J. Exp. Bot.*, 2001, **52** (356), 641.

214. W. Kockenberger, C. De Panfilis, D. Santoro, P. Dahiya and S. Rawsthorne, *J. Microsc.*, 2004, **214** (Pt 2), 182.

215. P. V. Gersbach and N. Reddy, *Ann. Bot. (Lond.)*, 2002, **90** (2), 253.

216. K. Zhong, X. Li, Y. Shachar-Hill, F. Picart, A. Wishnia and C. S. Springer Jr., *NMR Biomed.*, 2000, **13** (7), 392.

217. N. Ishida, S. Isobe, H. Ogawa, M. Koizumi, H. Kano and C. F. Hazlewood, *Cell. Mol. Biol. (Noisy-le-grand)*, 2001, **47** (5), 935.

218. M. L. Gruwel, X. S. Yin, M. J. Edney, S. W. Schroeder, A. W. MacGregor and S. Abrams, *J. Agric. Food Chem.*, 2002, **50** (4), 667.

219. M. G. Van Kilsdonk, K. Nicolay, J. M. Franssen and C. Kolloffel, *J. Exp. Bot.*, 2002, **53** (374), 1603.

220. R. Kamenetsky, H. Zemah, A. P. Ranwala, F. Vergeldt, N. K. Ranwala, W. B. Miller, H. Van As and P. Bendel, *New Phytologist*, 2003, **158** (1), 109.

221. H. Zemah, P. Bendel, H. D. Rabinowitch and R. Kamenetsky, *Plant Sci.*, 1999, **147** (1), 65.

222. A. Van der Toorn, H. Zemah, H. Van As, P. Bendel and R. Kamenetsky, *J. Exp. Bot.*, 2000, **51** (348), 1277.

223. P. Bendel, H. Zemah, R. Kamenetsky, F. Vergeldt and H. van As, *Magn. Reson. Imaging*, 2001, **19** (6), 857.

224. S. Olt, E. Krotz, E. Komor, M. Rokitta and A. Haase, *J. Magn. Reson.*, 2000, **144** (2), 297.

225. E. L. Effmann, G. A. Johnson, B. R. Smith, G. A. Talbott and G. Cofer, *Teratology*, 1988, **38** (1), 59.

226. R. E. Jacobs and S. E. Fraser, *J. Neurosci. Methods*, 1994, **54** (2), 189.

227. B. R. Smith, *FASEB J.*, 1999, **13** (5), A1029.

228. N. Jeffery, *Neuroradiology*, 2002, **44** (4), 358.

229. J. Puerta-Fonolla, J. Ruiz-Cabello, T. Vazquez-Osorio, J. Murillo-Gonzalez and A. Pena-Melian, *Ital. J. Anat. Embryol.*, 2001, **106** (2 Suppl. 2), 155.

230. J. Puerta-Fonolla, T. Vazquez-Osorio, J. Ruiz-Cabello, J. Murillo-Gonzalez and A. Pena-Melian, *Clin. Anat.*, 2004, **17** (5), 429.

231. E. Beuls, L. Vanormelingen, J. van Aalst, M. Vandersteen, P. Adriaensen, E. Cornips, H. Vles, Y. Temel and J. Gelan, *Pediatr. Neurosurg.*, 2003, **39** (3), 149.

232. E. A. Beuls, L. Vanormelingen, J. van Aalst, M. Vandersteen, P. Adriaensen, E. M. Cornips, H. J. Vles and J. Gelan, *J. Neurosurg.*, 2003, **98** (2 Suppl.), 210.

233. V. Hamburger and H. L. Hamilton, *J. Morphol.*, 1951, **88**, 49.

234. B. Hogers, D. Gross, V. Lehmann, H. J. de Groot, A. de Roos, A. C. Gittenberger-de Groot and R. E. Poelmann, *J. Magn. Reson. Imaging*, 2001, **14** (1), 83.

235. T. M. Yelbuz, X. Zhang, M. A. Choma, H. A. Stadt, M. Zdanowicz, G. A. Johnson and M. L. Kirby, *Circulation*, 2003, **108** (22), e154.

236. X. W. Zhang, T. M. Yelbuz, G. P. Cofer, M. A. Choma, M. L. Kirby and G. A. Johnson, *Magn. Reson. Med.*, 2003, **49** (6), 1192.

237. R. S. Balaban and T. L. Ceckler, *Magn. Reson. Q.*, 1992, **8** (2), 116.

238. K. Potter, W. J. Landis and R. G. Spencer, *J. Bone Miner. Res.*, 2001, **16** (6), 1092.

239. K. Potter, R. D. Leapman, P. J. Basser and W. J. Landis, *J. Bone Miner. Res.*, 2002, **17** (4), 652.

240. B. R. Smith, *Microsc. Res. Tech.*, 2001, **52** (3), 323.

241. M. Dhenain, S. W. Ruffins and R. E. Jacobs, *Dev. Biol.*, 2001, **232** (2), 458.

242. J. E. Schneider, S. D. Bamforth, C. R. Farthing, K. Clarke, S. Neubauer and S. Bhattacharya, *J. Anat.*, 2003, **202** (2), 239.

243. R. W. Sze, C. B. Chan, B. J. Dardzinski, S. Dunn, A. Sanbe, V. Schmithorst, J. Robbins, S. K. Holland and J. L. Strife, *Pediatr. Radiol.*, 2001, **31** (2), 55.

244. A. K. Hoydu, Y. Kitano, A. Kriss, H. Hensley, P. Bergey, A. Flake, A. Hubbard and J. S. Leigh, *Magn. Reson. Med.*, 2000, **44** (2), 331.

245. C. Chapon, F. Franconi, J. Roux, L. Marescaux, J. J. Le Jeune and L. Lemaire, *Anat. Embryol. (Berl.)*, 2002, **206** (1–2), 131.

246. A. S. Weintraub, X. J. Lin, V. V. Itskovich, J. G. S. Aguinaldo, W. F. Chaplin, D. T. Denhardt and Z. A. Fayad, *Pediatr. Res.*, 2004, **55** (3), 419.

247. J. C. Beetschen, *Int. J. Dev. Biol.*, 2001, **45**, 771.

248. J. B. Aguayo, S. J. Blackband, J. Schoeniger, M. A. Mattingly and M. Hintermann, *Nature (Lond.)*, 1986, **322** (6075), 190.

249. R. E. Jacobs and S. E. Fraser, *Science*, 1994, **263**, 681.

250. B. Blumich and W. Kuhn, eds., *Magnetic Resonance Microscopy*, VCH Publishers, New York, 1992, 604.

251. P. T. Narasimhan and R. E. Jacobs, Neuroanatomical micromagnetic resonance imaging, in *Brain Mapping: The Methods* A. W. Toga and J. C. Mazziotta, eds., Academic Press, New York, 1996, 147.

252. L. van der Weerd, D. L. Thomas, J. S. Thornton and M. F. Lythgoe, MRI of animal models of brain disease, in *Methods in Enzymology,* P. M. Conn, ed., Vol. 386, Academic Press, New York, 2004, 149.
253. H. Benveniste, K. Kim, L. Zhang and G. A. Johnson, *Neuroimage*, 2000, **11** (6 Pt 1), 601.
254. O. Natt, T. Watanabe, S. Boretius, J. Radulovic, J. Frahm and T. Michaelis, *J. Neurosci. Methods*, 2002, **120** (2), 203.
255. A. MacKenzie-Graham, E. F. Lee, I. D. Dinov, M. Bota, D. W. Shattuck, S. Ruffins, H. Yuan, F. Konstantinidis, A. Pitiot, Y. Ding, G. Hu, R. E. Jacobs and A. W. Toga, *J. Anat.*, 2004, **204** (2), 93.
256. J. M. Redwine, B. Kosofsky, R. E. Jacobs, D. Games, J. F. Reilly, J. H. Morrison, W. G. Young and F. E. Bloom, *Proc. Natl Acad. Sci. USA*, 2003, **100** (3), 1381.
257. P. J. Basser, J. Mattiello and D. LeBihan, *J. Magn. Reson. B*, 1994, **103** (3), 247.
258. P. J. Basser, *NMR Biomed.*, 1995, **8** (7–8), 333.
259. K. F. Liu, F. Li, T. Tatlisumak, J. H. Garcia, C. H. Sotak, M. Fisher and J. D. Fenstermacher, *Stroke*, 2001, **32** (8), 1897.
260. B. McDaniel, H. Sheng, D. S. Warner, L. W. Hedlund and H. Benveniste, *Neuroimage*, 2001, **14** (6), 1244.
261. S. K. Song, S. W. Sun, M. J. Ramsbottom, C. Chang, J. Russell and A. H. Cross, *Neuroimage*, 2002, **17** (3), 1429.
262. H. C. Thomas, R. D. Kapadia, G. I. Wells, A. M. Gresham, D. Sutton, H. A. Solleveld, S. K. Sarkar, S. B. Dillon and R. Tal-Singer, *J. Neurovirol.*, 2001, **7** (2), 105.
263. J. Nairismagi, O. H. J. Grohn, M. I. Kettunen, J. Nissinen, R. A. Kauppinen and A. Pitkanen, *Epilepsia*, 2004, **45** (9), 1024.
264. F. W. Wehrli, S. N. Hwang, J. F. Ma, H. K. Song, J. C. Ford and J. G. Haddad, *Radiology*, 1998, **206** (2), 347.
265. B. R. Gomberg, P. K. Saha, H. K. Song, S. N. Hwang and F. W. Wehrli, *IEEE Trans. Med. Imaging*, 2000, **19** (3), 166.
266. F. W. Wehrli, P. K. Saha, B. R. Gomberg and H. K. Song, *Proc. IEEE*, 2003, **91** (10), 1520.
267. H. E. Daldrup, T. M. Link, S. Blasius, A. Strozyk, S. Konemann, H. Jurgens and E. J. Rummeny, *J. Magn. Reson. Imaging*, 1999, **9** (5), 643.
268. D. A. Rajon, D. W. Jokisch, P. W. Patton, A. P. Shah and W. E. Bolch, *Med. Phys.*, 2000, **27** (11), 2624.
269. P. W. Patton, D. W. Jokisch, D. A. Rajon, A. P. Shah, S. L. Myers, B. A. Inglis and W. E. Bolch, *Health Phys.*, 2002, **82** (3), 316.
270. M. H. Weber, J. C. Sharp, T. H. Hassard and F. W. Orr, *Skeletal Radiol.*, 2002, **31** (5), 282.
271. J. R. Gardner, C. P. Hess, A. G. Webb, R. W. Tsika, M. J. Dawson and V. Gulani, *Magn. Reson. Med.*, 2001, **45** (6), 1122.
272. R. Toffanin, A. Accardo and F. Vittur, *J. Gravit. Physiol.*, 2002, **9** (1), P173.
273. G. H. Glover and D. C. Noll, *Magn. Reson. Med.*, 1991, **29** (3), 345.
274. X. Zhou and P. C. Lauterbur, NMR microscopy using projection reconstruction, in *Magnetic Resonance Microscopy* B. Blumich and W. Kuhn, eds., VCH Publishers, New York, 1992, 3.
275. S. Gomez, R. Toffanin, S. Bernstorff, M. Romanello, H. Amenitsch, M. Rappolt, R. Rizzo and F. Vittur, *J. Exp. Zool.*, 2000, **287** (5), 346.
276. M. Takahashi, F. W. Wehrli, S. L. Wehrli, S. N. Hwang, M. W. Lundy, J. Hartke and B. Borah, *J. Bone Miner. Res.*, 1999, **14** (5), 680.
277. M. Takahashi, F. W. Wehrli, S. N. Hwang and S. L. Wehrli, *Magn. Reson. Imaging*, 2000, **18** (1), 33.
278. T. Ozeki, K. Kose, T. Haishi, S. Hashimoto, S. Nakatsubo and K. Nishimura, *Magn. Reson. Imaging*, 2003, **21** (3–4), 351.
279. W. E. Bolch, P. W. Patton, D. A. Rajon, A. P. Shah, D. W. Jokisch and B. A. Inglis, *J. Nucl. Med.*, 2002, **43** (1), 97.
280. D. A. Rajon, A. P. Shah, C. J. Watchman, J. M. Brindle and W. E. Bolch, *Phys. Med. Biol.*, 2003, **48** (12), 1721.
281. P. Renton and A. Veronika, *Orthopaedic Radiology: Pattern Recognition and Differential Diagnosis*, Taylor & Francis, London, 1998, 474.
282. R. Allum and N. Thomas, *Clinical Challenges in Orthopaedics: The Knee*, Taylor & Francis, London, 2000, 206.
283. M. Cova and R. Toffanin, *Eur. Radiol.*, 2002, **12** (4), 814.

284. K. Ikoma, H. Takamiya, Y. Kusaka and Y. Seo, *Magn. Reson. Imaging*, 2001, **19** (10), 1287.

285. H. Shinar, Y. Seo, K. Ikoma, Y. Kusaka, U. Eliav and G. Navon, *Magn. Reson. Med.*, 2002, **48** (2), 322.

286. Y. Xia, J. B. Moody and H. Alhadlaq, *Magn. Reson. Med.*, 2002, **48** (3), 460.

287. V. Mlynarik, P. Szomolanyi, R. Toffanin, F. Vittur and S. Trattnig, *J. Magn. Reson.*, 2004, **169** (2), 300.

288. P. Faure, B. T. Doan and J. C. Beloeil, *NMR Biomed.*, 2003, **16** (8), 484.

289. B. A. Hargreaves, G. E. Gold, C. F. Beaulieu, S. S. Vasanawala, D. G. Nishimura and J. M. Pauly, *Magn. Reson. Med.*, 2003, **49** (4), 700.

290. H. Yoshioka, T. Ueno, T. Tanaka, M. Shindo and Y. Itai, *Skeletal Radiol.*, 2003, **32** (10), 575.

291. S. Farooki, C. J. Ashman, J. S. Yu, A. Abduljalil and D. Chakeres, *Skeletal Radiol.*, 2002, **31** (8), 445.

292. Z. H. Cho, C. B. Ahn, S. C. Juh, H. K. Lee, R. E. Jacobs, S. Lee, J. H. Yi and J. M. Jo, *Med. Phys.*, 1988, **15** (6), 815.

Applications of Optical Pumping and Polarization Techniques in NMR: I. Optical Nuclear Polarization in Molecular Crystals

BOYD M. GOODSON

Department of Chemistry and Biochemistry, Southern Illinois University,
113 Neckers Hall, Carbondale, IL 62901, USA
E-mail: bgoodson@chem.siu.edu

In certain systems, the application of resonant optical fields may be used to enhance the nuclear spin polarization by several orders of magnitude. Such large, non-equilibrium enhancements can translate directly into dramatic improvements in NMR detection sensitivity, and thus offer a variety of novel experimental possibilities. This multi-installment report concerns the development of optically enhanced NMR and MRI, spanning applicable systems that include noble gases, semiconductors, and molecular and ionic crystals, as well as the exploitation of photo-initiated radical pairs in solution and biological solids. Realized and potential NMR applications include void-space imaging of materials and living organisms; probing structure and dynamics in proteins and inclusion complexes; enhanced NMR of bulk and nanostructured materials; quantum computing; fundamental studies of various photophysical and photochemical processes; and low-field and remotely-detected NMR and MRI. Moreover, in some circumstances the presence of gated optical fields can permit novel time-resolved studies as well. Following a brief introduction for the entire review, this installment concerns the principles and practice of optical nuclear polarization (ONP) in organic molecular crystals. Work over the >35-year history of ONP-enhanced NMR is reviewed, with particular emphasis placed upon recent developments including the use of sample-shuttling and field-ramping in ONP experiments; microwave- and radio frequency-driven ONP; enhanced high-resolution NMR of single crystals; the observation of high (order unity) ^1H polarization; and ONP in polycrystalline substances. This installment concludes with a brief discussion of future possibilities concerning ONP, including the expansion of such approaches to other (e.g., biological) systems.

1. INTRODUCTION

The detailed characterization of molecular structure and dynamics is critically important to understanding chemical reactivity, biological function, and disease pathology. Moreover, such fundamental studies provide key insights into how the observed properties of bulk and nanoscale materials are derived from the molecular building blocks that comprise them. As a consequence, spectroscopic methods exploiting nuclear magnetic resonance (NMR)[1] have become extremely popular because the corresponding spectra are remarkably sensitive to structure, dynamics, and sample morphology; moreover, such spectra can be obtained non-invasively *in situ*. Indeed, magnetic resonance imaging (MRI)[2–4] has become a routine way to image various materials and biological systems without sample destruction or ionizing radiation – permitting functional imaging of living tissues, and aiding in the diagnoses and treatment of disease.

However, despite their exquisite *spectral sensitivity* to structure, dynamics, and morphology, conventional NMR methods suffer from a common drawback that in many circumstances, can limit their power and applicability – a notoriously low *detection sensitivity* (especially compared to optical methods). This fundamental insensitivity originates from the miniscule size of nuclear magnetic moments, which results in an exceedingly small (Boltzmann) equilibrium nuclear spin polarization, P, generally given by

$$P = \frac{N_\alpha - N_\beta}{N_\alpha + N_\beta},\tag{1}$$

where N_α and N_β are, respectively, the numbers of 'spin up' ($m_I = +1/2$) and 'spin down' ($m_I = -1/2$) nuclei within the sample (for an ensemble of $I = 1/2$ spins). At thermal equilibrium, P_0 is given by

$$P_0 = \tanh\left(\frac{\gamma\hbar B_0}{2k_B T}\right) \approx \frac{\gamma\hbar B_0}{2k_B T},\tag{2}$$

where γ is the gyromagnetic ratio, B_0 is the strength of the external magnetic field, T is the temperature, $\hbar$ is Planck's constant divided by 2π, and k_B is Boltzmann's constant. Under conditions typically encountered in the laboratory for an ensemble of ^{1}H spins (at room temperature, inside a 400 MHz NMR magnet at 9.39 T), the value for P_0 achieved is only $\sim 3.2 \times 10^{-5}$. This weak thermal spin polarization (Fig. 1(top)) would be even lower in the fields typically employed in MRI, and for virtually all other nuclei. Naturally, the polarization can be improved somewhat by going to higher fields and/or lower temperatures, but such approaches are often of limited feasibility for obvious reasons. In any case, the low spin polarization is a fundamental source of the poor detection sensitivity of NMR – leading to a variety of critical limitations, including: the attainable spatial and temporal resolution; the available information content in structure determination; the minimum amounts of substances and time required to obtain adequate spectra; and ultimately, the overall feasibility of a wide range of potential experiments.

To combat this problem, a variety of related approaches have been developed that combine the high *detection sensitivity* of optical methods with the well-resolved *spectral*
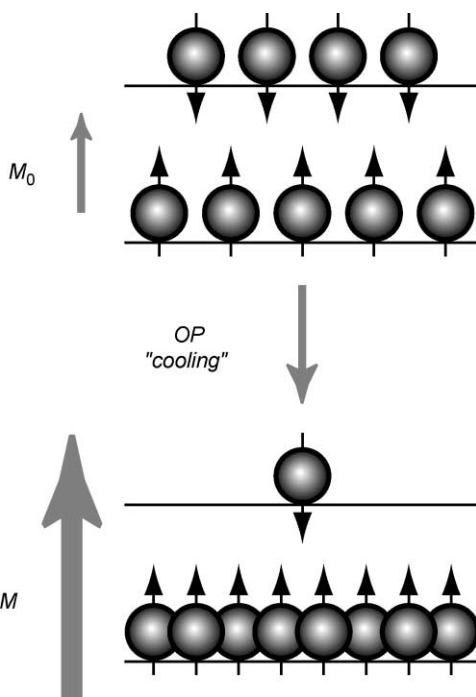
Fig. 1. Cartoon depicting the 'spin-cooling' effect of optical polarization on an ensemble of nuclear spins (assuming $I = 1/2$ and positive gyromagnetic ratio). Normally (at thermal equilibrium), the numbers of spins aligned parallel and antiparallel to the magnetic field (B_0) are nearly equal, yielding a low net spin polarization – and consequently, a tiny detectable magnetization, M_0. However, optical polarization can provide the means to drive the population distribution far away from equilibrium, thereby increasing M by several orders of magnitude. In the spin-temperature model,[42] such polarization can often result in nuclear spin ensembles with milli-Kelvin effective temperatures. (After Ref. [110].)

sensitivity of NMR. In such approaches, optical fields are exploited to increase the nuclear polarization of applicable systems *by 4–5 orders of magnitude* (Fig. 1(bottom)). While such 'applicable systems' (i.e., those for which light can be used to *directly* increase P) are limited in nature – perhaps even exotic by some standards – recent work has been directed towards applying these methods towards a variety of problems of interest in NMR and MRI across many disciplines. It is the development of these optical polarization approaches – and their (realized and potential) NMR applications – that are the subjects of this review.

The possibility of using light to drive *electronic* spin populations out of thermal equilibrium was first demonstrated by the optical pumping experiments of Kastler,[5–8] who also considered the possibility of transferring this spin polarization to nuclei. This prediction was soon realized in the gas phase in heavy metal (e.g., Hg and Cd) vapors[9–11] and noble gases.[12–14] Later work demonstrated optical polarization of nuclei in solid-state samples, including molecular crystals,[15] inorganic ionic solids,[16,17] and

semiconductors.[18,19] Lastly, chemically-induced dynamic nuclear polarization (CIDNP) in solution, initiated by light or by other means (and typically involving organic molecules), was also introduced during this time period[20–22] (later we will be concerned with the photochemical variety of this phenomenon).

Taken as a whole, these systems could not be more different from each other; yet, the various underlying mechanisms for achieving optically enhanced nuclear spin polarization share some common features (Fig. 2). To be clear, it should be obvious that light cannot generally be used to polarize nuclear spins *directly*, simply because the energies of optical transitions are several orders of magnitude greater than the energies of nuclear spin transitions – even in the strongest available magnetic fields (Fig. 2(a)). Instead, all of the optical polarization methods discussed in this review utilize nearby electrons as 'middle men' in order to achieve nuclear spin polarization, via either (a) the polarization of electron spins in species that *already* possess open-shell configurations; or (b) the generation of *transient* excited states with unpaired (and highly polarized) electron spins. Once the electronic populations have been driven significantly away from equilibrium by the incident light, the high electron spin polarization may be transferred to
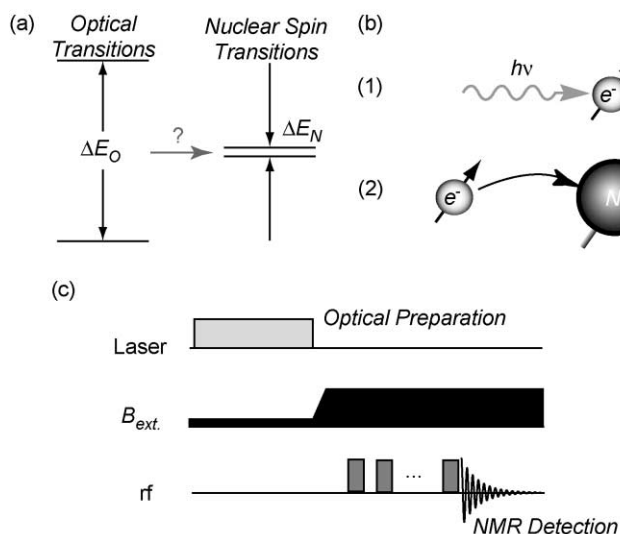
Fig. 2. Cartoons showing generalized aspects of the optical polarization of nuclear spins for NMR enhancement. Because the energies of optical transitions are several orders of magnitude greater than the energies of nuclear spin transitions, the nuclear spins are not polarized directly by the light (a). Instead, all optical polarization methods utilize electrons as intermediating species (b). The incident light drives electronic transitions in such a way that electron spin populations diverge significantly from thermal equilibrium. In a second step, this enhanced electronic spin polarization is transferred to the nuclear spins by one of a variety of possible methods. (c) A generalized pulse sequence for essentially all of the optically enhanced NMR experiments discussed in this review: *optical preparation* of the sample (often performed at low field to increase efficiency), followed by *field ramping* (or *sample transfer*) to high field to permit the application of rf pulse sequences and the subsequent *detection of enhanced, well-resolved NMR signals*. In some circumstances, it may be possible to repeat these steps as desired for a given experiment.

the nuclei (Fig. 2(b)) by hyperfine (e.g., dipolar or Fermi-contact) interactions, or cross-relaxation. It should be noted that the electrons involved in optical polarization need *not* be a part of the same chemical species as the target nuclei – indeed many such processes are inherently intermolecular by nature. Nevertheless, if such optical enhancement of bulk nuclear spin polarization is to occur in a given system, a number of features are thus required, including: optically polarizable electron spins; efficient transfer of enhanced spin polarization to the nuclei; and sufficiently long spin-relaxation times (T_{1e} and T_{1n}) to allow high polarizations to be prepared and accumulated over time. It is primarily these requirements that limit *direct* optical polarization to the 'applicable systems' described in this review. Finally, a generalized outline (shown in the form of a pulse sequence) for many of the experiments described in this review is shown in Fig. 2(c).

The enormous improvement in the nuclear spin polarization achievable by these optical approaches has great potential to impact conventional NMR studies in a variety of ways. Besides simply increasing the detection sensitivity of NMR, the enhanced nuclear spin polarization may be useful for obtaining enhanced spectral *selectivity* (e.g., for some spatial, structural, or dynamical feature of a sample); enhanced contrast and resolution in MRI; and improved density matrix purity (e.g., for NMR quantum computation). Finally, it is worth noting that the optical fields used in some of these methods can be gated, thereby permitting *time-resolved* studies that would not be possible with conventional NMR approaches.

The goal of this review is to be comprehensive (but not exhaustive), and by design 'disproportionately' concentrates on selected recent developments in optically enhanced NMR; in doing so, it is hoped that this work will provide the reader with an overall impression of the current state of the art in this highly interdisciplinary field – as well as an indication of what may be possible in the future. This report is organized as follows. Section 2 is devoted to the development of *optical nuclear polarization (ONP) in organic molecular crystals*. Other sections of this review (to be published in a later volume) will concern: optical pumping in semiconductors; optical polarization in ionic solids; NMR and MRI of laser-polarized noble gases; and photo-CIDNP studies of organics, polymers, and proteins.

2. ONP IN MOLECULAR CRYSTALS

2.1. Introduction

ONP may be used to enhance the nuclear spin polarization of bulk organic crystals by several orders of magnitude. While ONP has been performed in such materials utilizing a variety of related approaches, to date its application has been limited to fundamental investigations of the structure, dynamics, photochemistry, and photophysics of the organic crystalline substances themselves. However, recent results – including the demonstrations of very high polarizations in proton spins under relatively mild conditions, as well as the observation of ONP in polycrystalline materials – bodes well for expansion of the application of these approaches to other fields.

ONP in organic crystals was first reported by Wolf and co-workers in 1967[15]; indeed (to this reviewer's knowledge), these experiments mark the first report of optical enhancement of nuclear spin magnetization in the solid state in any system (see also Refs. [16–19]). In these first ONP experiments, it was shown that exposure of anthracene single crystals to unpolarized light (resonant with singlet–singlet transitions), at low magnetic field and room temperature, resulted in the enhancement of the ^{1}H nuclear spin polarization. Work investigating ONP in other organic crystalline systems was reported soon thereafter in a variety of molecular crystals, including fluorene, naphthalene, and phenazine – pure, or doped with other aromatic molecules serving as chromophores[23–27] – with polarizations reaching as high as 0.1% at room temperature.[27] Such polarizations represented a record enhancement at the time ($\sim$37,000-fold at 80 G).

The observed nuclear polarization enhancements were originally rationalized as the result of a two-step process first involving enhancement of electronic spin polarization following optical excitation, and then a simple Overhauser-type[28,29] cross-relaxation to yield enhancement of the nuclear spin magnetization.[24] However, it was soon realized that such ONP enhancements could only be explained by other, more complex arguments (described below).[25] Extensive reviews of such earlier ONP work can be found in Refs. [30–32]; the last of these pays particular attention to the optical enhancement (and detection) of NQR signals; see also Refs. [26,33,34]. Since the description of these early results, considerable work has involved the development of both the theoretical understanding of ONP observations, as well as experimental work to increase the efficiency of ONP under various conditions (and sample choices). Such work is described in greater detail in the sections below.

2.2. Theory/Principles

ONP (Fig. 3) in organic molecular crystals can be described as a three-step process: (1) optical creation of electronic spin polarization in (transient) excited triplet states; (2) polarization transfer to nearby nuclear spins; and (3) accumulation of bulk nuclear spin magnetization in the (diamagnetic) ground state via spin-diffusion processes. Highly detailed theoretical descriptions and modeling of ONP processes observed in many systems can be found in the reviews mentioned above; thus, only a brief overview is provided here.

2.2.1. Optical electron polarization

The ONP process begins with the generation of optical electron polarization (OEP),[35,36] a phenomenon that is not only useful for ONP – but for optically detected (electron) magnetic resonance (ODMR) as well[30] (outside the scope of this review). First, light is applied directly to the crystal to drive singlet–singlet ($S_0 \rightarrow S_1/S_n$) transitions. Note that because such molecular crystals are held together by weak van der Waals forces, the crystal lattice tends to give only mild perturbations of intramolecular processes like photoexcitations. As a result of spin–orbit coupling (SOC), a small fraction of the excited-state population is transported via inter-system crossing (ISC) into the lowest
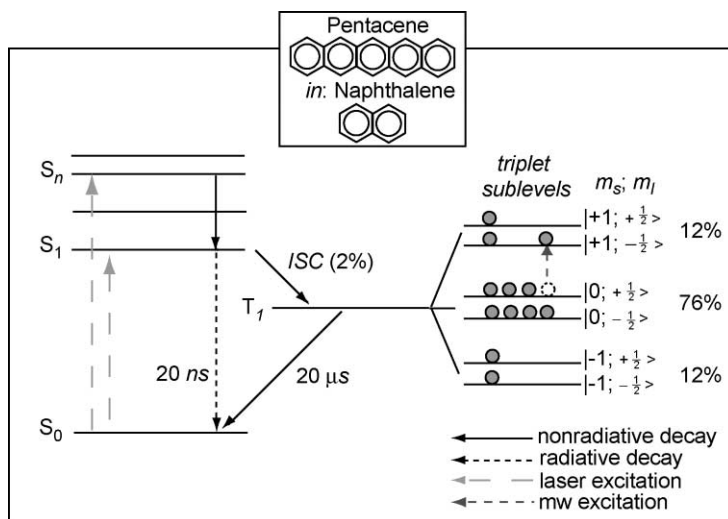
Fig. 3. Jablonski energy-level diagram typical for chromophores involved in ONP processes (specifically for pentacene in naphthalene, after Ref. [39]), showing the respective roles of optical excitation, ISC, OEP, electron-nuclear polarization transfer (here driven by mw radiation), and subsequent decay to the diamagnetic ground state. The relative populations of the triplet magnetic sublevels are given at the far right (assuming the crystal is oriented such that the long molecular axis of pentacene is parallel to the external magnetic field[38]).

triplet state (T_1) (direct excitation to the triplet state ($S_0 \rightarrow T_1$) is also possible because of 'contamination' of triplet states by singlet character, but this pathway is not generally expected to play a major role in the aromatic hydrocarbons typically used in ONP experiments[31]). However, the triplet magnetic sublevels are not degenerate – even at zero field – because of dipolar interactions between the unpaired electrons. The spin Hamiltonian for a system comprised of a triplet electronic state ($S = 1$) and a nucleus in an external magnetic field is given by[37]

$$H = D(S_Z^2 - S^2/3) + E(S_X^2 - S_Y^2) + g\beta\vec{S}\cdot\vec{B}_0 + g_n\beta_n\vec{I}\cdot\vec{B}_0 + \vec{S}\cdot A\cdot\vec{I}, \qquad (3)$$

where D and E are the zero-field splitting (ZFS) parameters (arising from electron dipole–dipole interactions), the third and fourth terms are electron and nuclear Zeeman terms (wherein g (g_n) and β (β_n) are the electron (nuclear) g factor and the Bohr (nuclear) magneton, respectively), and the fifth term governs the electron–nuclear hyperfine interaction, where A is the hyperfine tensor.

Most of the molecules studied via ONP do not possess axes of symmetry greater than twofold; thus, all three electronic spin states are non-degenerate. Typical ZFS magnitudes of are ~ 0.1 cm^{-1} (i.e., generally in the 100s of MHz to GHz range) – about 10^5 times smaller than the optical energy differences among the lowest electronic states. Importantly, the ISC processes can cause selective population and decay of the triplet sublevels as a consequence of symmetry selection rules, which result in unequal spin–orbit matrix elements between coupled singlet and triplet states. Thus, the triplet

sublevels will be populated in a *highly non-Boltzmann* fashion. For example (Fig. 3), the populations of the $m_s = +1, 0$, and -1 triplet sublevels are, respectively, 12, 76, and 12% for pentacene in naphthalene – virtually independent of temperature and external field strength[38,39] – indicating an immense electronic spin polarization. Once the polarized triplet state is created, the time-dependent electronic polarization between two sublevels ($P_e(t)$) can be written as[40]

$$P_e(t) = \frac{Ne^{-kt} - N'e^{-k't}}{Ne^{-kt} + N'e^{-k't}}, \tag{4}$$

where N and N' are the initial populations of the two magnetic sublevels in question, and k and k' are the corresponding decay rates.

2.2.2. Polarization of nuclei

During the excited triplet state lifetime, hyperfine interactions between polarized electrons and neighboring (guest *and* host[41]) nuclei permit polarization transfer via (a) mixing of states, (b) cross-relaxation; or (c) applied electromagnetic fields (nearly) resonant with the electron-spin transitions, i.e., the 'the solid effect'.[42] The relative importance of these mechanisms depends on the system and the experimental conditions; the distinctions can be a bit subtle, and merit some further discussion.

The 'mixing of states' (a) – i.e., polarization transfer via *static* hyperfine interactions – was the dominant polarization transfer pathway in most of the early ONP experiments. The original explanation for the observed enhancements – cross-relaxation (Overhauser[28,29]) transfer of steady-state OEP to nuclei via *dynamic* hyperfine interactions (b) – proved to give an adequate explanation for optical polarization of nuclear spins in semiconductors observed at the time.[18,19] However, most of the ONP experiments in organic crystals showed a surprisingly sensitive (and non-trivial) dependence of both the sign and magnitude of the observed enhancements on the relative orientation of the crystal sample to the external magnetic field, as well as the strength of the magnetic field. These effects could not be explained[24] by a simple Overhauser mechanism, which would exhibit only weak dependence on such factors (that in turn, should have also followed the resulting OEP that had been achieved). Moreover, it was realized[24] that an Overhauser-type mechanism could not account for zero-field 'polarization' (spin alignment),[26] because such hyperfine relaxation should be expected to approach zero with decreasing external field.

Alternatively, it was argued[25,43] that static hyperfine couplings (HFCs) can (slightly) 'mix' the electronic singlet and triplet states; thus, HFCs are subject to symmetry selection rules (like the SOC), and allow nuclear spins to participate in the selective population/decay processes of the electronic sublevels. It should be noted that SOCs exceed HFCs by orders of magnitude (at least in the aromatic hydrocarbons under consideration) – and thus the contribution that HFCs actually have on the electronic *singlet–triplet mixing* is negligible.[31] Nevertheless, the static HFCs *do* cause significant mixing within the electronic spin sublevels of the excited T_1 state. Because of this mixing within the triplet manifold, the respective population/decay rates of the combined

(hyperfine) electron and nuclear spin states may be different, thereby permitting the accumulation of non-Boltzmann polarization within nearby nuclear spins. In short: as a result of the static hyperfine mixing within the triplet manifold, the behavior of nearby *nuclear* spins is (weakly) governed by *electronic* selection rules, even though the optical transitions *into* (and *out of*) the triplet states essentially involve only purely *electronic* processes.[25,31,43,44] It was also shown that this static HFC mixing mechanism could account for the observed nuclear spin alignment in zero field.[31,43]

But why would ONP via a static HFC mechanism be so sensitive to the magnitude and relative direction of the applied magnetic field? The energy spacings between the electronic spin sublevels of the excited triplet states depend on *both* the ZFSs and the Zeeman interaction. Correspondingly, the energy spacing between any two sublevels will be dictated by the interplay between these two contributions. Now, under conditions where electronic spin levels are energetically very close together (so-called level-anticrossing or LAC regions[31] – dictated in a given sample by the strength of the magnetic field and its relative orientation to the molecular axes), the mixing of spin levels by HFCs becomes highly efficient. This effect can be rationalized by considering a perturbation theory treatment; the terms corresponding to the states mixing grow as the denominator – a function of the energy *difference* between the two states – tends to zero. Thus, ONP polarization rates can be expected to be relatively large near such LAC regions (LAC-ONP); indeed, large enhancements observed in such regions were considered as proof that the ONP depended upon 'states-mixing' by static HFCs.[31] To be certain, ONP can still be observed in regions well outside of LAC regions,[45] but large mixing coefficients (and hence, large ONP enhancements) can be most expected in regions with large HFCs and/or small electronic energy differences (i.e., at LAC regions).

Under the right circumstances, ONP can still be mediated by *dynamic* hyperfine interactions (*b*), which can be thought of as a 'polarization-induced' Overhauser effect. For example, in certain types of crystals where the host molecules participate in electronic excitation, the excitation energy may be easily transferred among neighboring molecules, causing a delocalization of this excitation energy. In such cases, the excited states can be effectively described as excitons, which are characterized by motion (mediated by intermolecular spin exchange, which at room temperature is well described as an incoherent, diffusional 'hopping' process). At a given instant, the triplet exciton is localized at a given site, but the average residence time is too short to allow significant ONP via static HFCs. The HF interaction thus becomes highly time dependent, but still allows ONP enhancement during optical excitation – as observed in the charge-transfer crystal of anthracene:tetracyanobenzene.[46]

Finally, ONP may be achieved with the aid of applied electromagnetic (i.e., radio-frequency, rf or microwave, mw) fields (*c*), and thus can most simply be considered as extensions of conventional DNP methods[47]; these approaches are referred to as radio-frequency induced ONP (RFONP)[46,48–55] and microwave-induced ONP (MIONP),[39–41,56–73] respectively. In conventional DNP, magnetization from *thermally* polarized electron spins (residing, for example, in permanent paramagnetic centers) is driven via hyperfine interactions to surrounding nuclei using resonant or near-resonant AC fields. More specifically, this process is governed by the conventional *Overhauser effect* in the case of *dynamic* hyperfine interactions (e.g., in metals or semiconductors),

or the *solid effect* (or *thermal mixing*) in the case of *static* hyperfine interactions; field-driven ONP experiments typically exploit the solid effect.

The solid effect is a two-spin phenomenon observed when AC fields (with $\omega = \omega_e \pm \omega_n$) are applied that induce (formally forbidden) electron-nuclear 'flip-flop' transitions that have become partially allowed due to hyperfine mixing of the spin states,[74] thereby driving electronic spin magnetization to coupled nuclei. Thermal mixing,[75] on the other hand, is typically considered a three-spin effect: this process requires the 'flip-flop' of two electron spins, with the residual energy difference providing the energy ($\hbar\omega_n$) needed to flip one nuclear spin.[74] The thermal mixing mechanism is thus typically considered to involve strong dipolar interactions among participating electrons.[57] Generally, the dominance of a given process (solid effect vs. thermal mixing) depends on experimental parameters (e.g., the EPR linewidth, nuclear Zeeman splitting, etc.); the reader is directed to Refs. [74–78] for enlightening discussions of these concepts.

Regardless of the actual physical method of polarization transfer, the key difference between such 'field-driven' ONP experiments and conventional DNP is that in ONP, the paramagnetic species are optically created – meaning that the species are generally (1) short-lived; and (2) highly spin polarized (i.e., to a much greater value than the Boltzmann electronic spin polarization). Correspondingly, these advantageous properties ensure that (1) the NMR signals should not suffer from the presence of nearby (permanent) paramagnetic centers; and (2) if the electron spin relaxation time, T_{1e}, is long (with respect to the triplet state lifetime, τ), then the NMR enhancements obtained can greatly exceed the typical DNP enhancement 'ceiling' of γ_e/γ_N (≈ 658 for ^{1}H spins).

2.2.3. Accumulation of bulk nuclear spin magnetization

Once $T_1 \rightarrow S_0$ relaxation occurs, the chromophores become diamagnetic, helping to insure long nuclear spin T_1's for the crystal. The fact that enhanced nuclear spin polarization can be obtained via ONP without the presence of permanent paramagnetic centers is a key advantage over conventional DNP studies. The nuclear spins that are initially polarized by the ONP process are nearby the sites of optical excitation. However, the nuclear polarization can spread to other spins within the lattice via efficient spin-diffusion processes (particularly among the abundant ^{1}H spins). The ONP cycle is rapidly repeated over the course of the experiment, permitting the nuclear spin polarization to accumulate and spread throughout the crystal via spin diffusion – thereby endowing the material with a large bulk nuclear spin magnetization.

2.3. Some experimental considerations

Generally speaking, in order to achieve efficient ONP (and correspondingly, high bulk nuclear spin magnetization), a number of experimental factors must be collectively optimized (see, e.g., Ref. [79]), including: high chromophore density; high resonant photon flux (with minimal sample heating/damage); high triplet yield (via ISC); high electronic spin polarization in the triplet state; efficient polarization transfer to nuclei; fast triplet decay to avoid optical saturation (bleaching); efficient nuclear spin diffusion

in the ground state; and slow nuclear spin T_1 relaxation in the ground state. Experimental aspects concerning the target *materials* and the *light sources* employed are discussed immediately below; other experimental aspects, including those concerning applied (static and AC) fields are described in the following sections.

2.3.1. Materials

To date, the organic substances studied via ONP have typically been planar, aromatic molecules in pure or mixed crystalline form. While ONP was first demonstrated in pure anthracene,[15] the most commonly-studied systems for ONP (and related OEP) experiments over the years have been fluorene doped with acridine,[48,49,53–55,69,79–82] phenanthrene,[58–60,68] phenazine,[57,80] and anthracene,[49,50] as well as naphthalene and *p*-terphenyl doped with pentacene.[37–40,55,63,65–67,70–73,83–85] Other investigations of ONP have included studies of anthracene doped with phenazine,[52,86] tetracyanobenzene,[46,79,87,88] and tetracene,[23] as well as acridine,[50] dibromodiphenylether with benzophenone[41] and dichlorobenzophenone,[62,64] and various halogenated benzenes.[26,56]

Naturally, the specific ONP mechanisms involved in a given experiment are dictated primarily by the choice of material under study. For example, ONP in anthracene:tetracyanobenzene 1:1 mixed crystals involves (mobile) triplet *excitons*,[79] whereas ONP in pentacene-doped crystals involves highly *localized* triplet states. Furthermore, choice of materials (particularly the chromophore) also dictates whether T_{1e} or τ determines the limiting behavior of the ONP process.[61] In systems where $T_{1e} \ll \tau$, (e.g., fluorene doped with phenanthrene) the electron spin polarization can thermalize prior to transfer to the nuclei. Such cases have the disadvantage of requiring strong magnetic fields and very low temperatures to achieve significant nuclear spin polarization values (limited by the Boltzmann polarization of the electron spins); however, because each chromophore can be 'used' to polarize neighboring spins several times in a given optical-excitation cycle, the (MI)ONP rate can be quite rapid. On the other hand, in systems where $T_{1e} \gg \tau$, (e.g., naphthalene doped with pentacene), the electron spin polarization can be highly non-Boltzmann during polarization transfer to the nuclei. While the ONP rate will tend to be much slower in such cases, the experiments can be performed over a much wider range of applied fields and temperatures.

With the exception of the recent demonstrations of ONP in polycrystalline samples (see below), ONP experiments have generally been performed using large, carefully grown single crystals. The optical quality of the crystal is important to allow sufficient light penetration into the material to drive ONP. Even so, the primary reason for utilizing single crystals is to obtain a uniform alignment of the chromophore molecules. Indeed, crystal alignment (with respect to the external magnetic field) can be extremely important for ONP, not only because of the sensitive orientation dependence of the LAC-ONP mechanism, but also because it will determine the proper ESR frequencies for field-driven ONP experiments. Moreover, controlling the relative orientations of the molecular axes and the polarizations of the applied (e.g., optical and mw) fields is often needed for achieving high ONP efficiencies and/or desired excitation geometries.

While solvent re-crystallization may suffice in some circumstances, ONP crystal samples are often grown using the standard Bridgman technique;[89,90] this approach may

be used to grow high-quality organic crystals several mm in length. Briefly, the Bridgman method involves the slow, continuous 'pulling' of the (melted) material to be crystallized through a temperature gradient that ends below the liquid–solid phase transition for that material. Generally, the slower the temperature change over the gradient, the better the quality of the crystal. This approach is often combined with zone-refinement[89] to further improve the crystal quality. Once the crystallographic axes are identified (e.g., with a polarizing microscope[38]), the crystal can be attached to a transparent support and mounted on a goniometer prior to the experiment (orientation can also be determined from the enhanced NMR spectra[38,82]).

2.3.2. Light sources

Once the target material has been selected for ONP, a light source must be chosen that best matches the sample's photophysical properties. The original light sources used in ONP were arc lamps, optically filtered to remove unwanted (IR and/or UV) spectral components; these effective and readily available light sources have seen continuous use throughout the development of ONP.[31,41,56,58,68,82,91] More recently – as with other fields described in this review – laboratories exploring ONP adopted various laser technologies as they became available, including N_2 lasers,[39,63,66,70,92] excimer lasers,[53] Ar+ lasers,[41,52] solid-state lasers,[70] and laser-pumped[52,53,62,88,93] and flashlamp-pumped dye lasers.[39,40,71–73] Many of these lasers exhibit pulsed output, allowing the corresponding ONP experiments to exploit the high peak power, gated emission, and defined time resolution provided by such light sources.

Naturally, the first requirement for a light source to be used for ONP is high photon flux at a resonant ($S_0 \rightarrow S_1$ or $S_0 \rightarrow S_n$) transition. Luckily, the chromophores under study exhibit multiple absorption maxima and broad lines in the solid state, often making it possible to utilize a number of different light sources. Generally speaking, the higher the (resonant) light power, the faster the ONP rate[31]; nevertheless, the total amount of power deposited into the sample is naturally limited by the potential of heating or damaging the sample (and peak powers that significantly drive stimulated emission should be avoided, as this decreases the ISC quantum yield[40]). Targeting the $S_0 \rightarrow S_1$ absorption maximum generally provides the most efficient use of the incident light. For example, UV light is often employed in ONP to drive higher energy ($S_0 \rightarrow S_n$) transitions; while the same triplet state is ultimately populated by this process, considerable excess energy is deposited into the crystal as heat.[39] Additionally, when using crystals doped with chromophores, wavelengths at strong absorption maxima for the host should naturally be avoided.

Next, for applications where the ONP process is 'cycled' with the repetition rate of a pulsed laser, other aspects should be considered. One advantage of pulsed laser output is that (in systems with short τ values) there is a low 'steady-state' triplet chromophore population on long-time average during ONP, giving longer nuclear spin T_1's due to the effectively diamagnetic state of the crystal. Often, the overall ONP rate can be limited by the laser pulse repetition rate (typically 1–100 Hz in the lasers utilized thus far, with the notable exceptions of the 1 kHz solid-state laser tested in Ref. [70] and the 1–10 kHz system involved in ongoing work at SIUC[93]). Additionally, using lasers with relatively

long pulses (i.e., with durations much greater than the singlet state lifetime, but shorter than the triplet state lifetime) can be used to combat low triplet-state quantum yields by providing multiple excitation cycles per pulse – thereby generating higher fractions of chromophores participating in each polarization-transfer cycle.[39] As an example, Terao and co-workers determined via simulations that with a laser wavelength of 590 nm and a ∼2 mm thick crystal of pentacene-doped naphthalene (0.018 mol%), an intensity of ∼10^9 W/m^2 should be sufficient to effectively drive 'all' of the pentacene chromophores into the triplet state.[40]

2.4. ONP experiments

Early ONP experiments (i.e., LAC-ONP[15,23–27,43–45,50,80,81,86,87,92,94]) have been extensively reviewed in previous work[30–32]; thus for space reasons we will concentrate on examples from more recent experiments, including: ONP with sample-shuttling; 'field-driven' (rf/mw) ONP; and ONP in polycrystalline samples.

2.4.1. ONP with sample shuttling

Previous ONP experiments performed at low field succeeded in generating relatively high nuclear spin polarizations. However, detection of NMR signals at *high* field is often desirable in order to obtain adequate spectral dispersion (chemical shifts). One early demonstration of ONP with field switching[92] first utilized pulsed UV laser excitation – combined with gated field cycling into (and out of) the LAC regime – to perform ONP at low field (∼400 G) in a crystal of fluorene-d_8h_2 doped with 1000 ppm acridine (at room temperature). Following a short polarization build-up time (15–60 s), the sample was then manually transferred to high field (4.35 T) where the enhanced NMR signals were detected. By carefully controlling both the time delay (t) between the laser and field pulses, as well as the field pulse duration (t'), it was possible to observe the kinetics of the ONP processes. Time constants of ∼14 and ∼125 μs were determined for the hyperfine-mediated nuclear spin relaxation time in the excited triplet state, and the apparent lifetime of the triplet state, respectively. Moreover, the LAC-ONP enhancement was significantly greater when t was short and t' was long. These experiments demonstrated the utility of pulsed/gated approaches to perform time-resolved studies of ONP, as well as the potential importance of sample transport to high field for NMR study.

More recently, Vieth, Buntkowsky, and co-workers constructed an ONP apparatus that utilizes *automated sample shuttling* between low and high magnetic field.[79,82,88,91] In this approach, ONP is performed in a low, variable field (0–160 mT, produced by a Helmholtz coil pair) in order to take advantage of the increased efficiencies of ONP in such weaker fields. Optical excitation is typically performed using an IR/UV-filtered Hg lamp or a pulsed UV laser; for the samples studied, irradiation was typically performed for 10s of seconds. Immediately following optical excitation, the *entire probe head* (including the sample and the crystal goniometer) is pneumatically shuttled up the bore of a high field (7 T) superconducting magnet (in tandem with the HC pair), thereby permitting acquisition of well-resolved, optically enhanced NMR spectra. Because
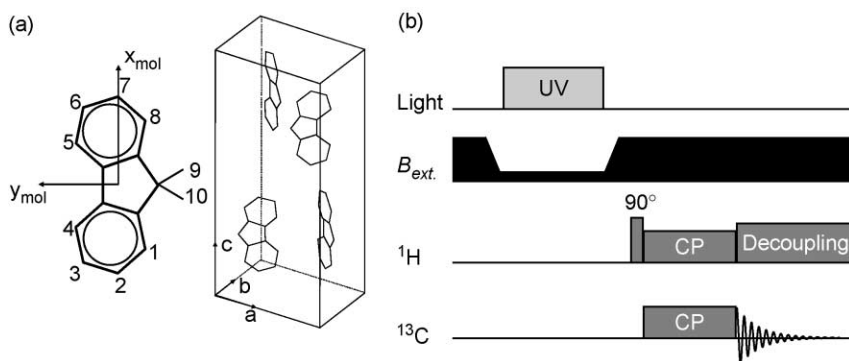
Fig. 4. (a) Structural diagrams of the fluorene molecule and the crystallographic unit cell, with definitions of the molecular and crystal axes. Figure courtesy of G. Buntkowsky, reprinted with permission from Ref. [82], copyright 1998 American Chemical Society. (b) Pulse sequence diagram showing the timing scheme of the applied (static, optical, and rf) fields used to obtain the data shown in Figs. 5 and 6. (After Ref. [82].)

the sample shuttling is automated, rapid ($\sim$3 s), and precise, the entire low-field/high-field process can be repeated as desired over the course of a given experiment.

The first work published involving this apparatus investigated ONP processes in tetracyanobenzene-doped anthracene, as well as fluorene crystals (Fig. 4(a)) doped with a variety of other molecules.[88] 2000-fold signal enhancements were observed for rare (e.g., ^{13}C) nuclei, corresponding to six orders of magnitude reduction in signal acquisition time compared to the corresponding conventional NMR experiment with thermally polarized spins. Studies of enhanced spectra (specifically, the ^{13}C CSA pattern and ^{2}H quadrupolar coupling as a function of orientation) from a crystal of anthracene:tetracyanobenzene (a charge-transfer system where ONP is mediated by mobile excitons) indicated that disorder within the crystal was dynamic in origin. Other experiments investigated fluorene crystals doped with anthracene, acridine, and phenazine, where photoexcitation of the guests leads to abstraction of an H atom from the host CH_2 group, and its subsequent transfer to the guest (resulting in the production of a radical pair). This fully reversible reaction provides a good model for study of chemical reactions under fixed-geometry conditions.[88] In these experiments, the time delay between the ns UV laser pulse (used to generate OEP) and an rf pulse (used to drive OEP to the surrounding nuclei – see the following section) was varied in order to study the time dependencies of the triplet spin order, as well as the radical pair production and decay rates. This work showed that while the forward reaction is determined by a thermally activated quantum tunneling process, the temperature independence and lack of isotope effect observed for the (considerably faster) back reaction – radical decay – indicated that it initially proceeds via intersystem crossing to a singlet radical pair state.

More recent work utilized the shuttling ONP apparatus to perform enhanced, high-resolution ^{13}C NMR studies of the acridine-doped fluorene system.[82] The pulse sequence detailing the relative timing of the various (optical, rf, and static) applied fields is shown in Fig. 4(b). As before, ONP was performed at low field (but without an rf driving field)
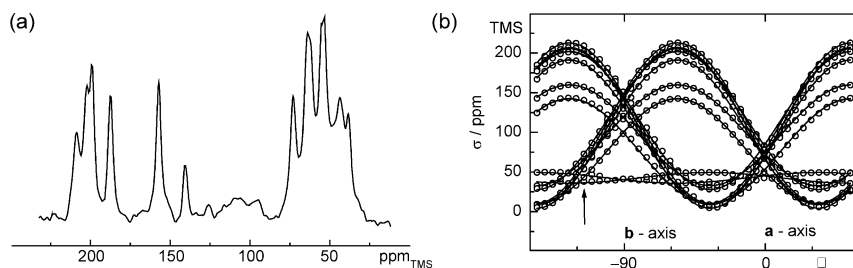
Fig. 5. (a) A selected ^{13}C ONP-CP spectrum from a single crystal of acridine-doped fluorene; the spectrum was obtained in the crystal *ab*-plane at an angle of $-105°$ with respect to the crystallographic *a* direction. (b) Rotation pattern of the primary ^{13}C ONP-CP spectral lines in the crystal *ab*-plane (with $a=0°$). The arrow marks the angle at which the spectrum shown in (a) was obtained. The two sets of lines varying between 10 and 220 ppm are attributed to aromatic protons from two magnetically inequivalent fluorene molecules, whereas the pair of lines varying between 30 and 50 ppm are assigned to the methylene groups (C7).[82] (Figures courtesy of G. Buntkowsky, reprinted with permission from Ref. [82], copyright 1998 American Chemical Society.)

to achieve efficient optical polarization. However, bulk enhancement of ^{13}C spins is normally inefficient because the spin diffusion of (rare) ^{13}C spins is exceedingly slow. For this reason, ONP was used primarily to enhance the lattice ^{1}H spins; then, following rapid sample transfer to high field, the optically enhanced ^{1}H spin magnetization was transferred via 'conventional' cross-polarization (CP[95,96]) to the ^{13}C spins. A typical high-resolution ^{13}C ONP-CP spectrum of fluorene is shown in Fig. 5(a); a corresponding plot of the ^{13}C spectral line positions as a function of crystal rotation (in the *ab* plane) is shown in Fig. 5(b). A number of lines from inequivalent ^{13}C positions are resolved, well enough to determine their positions with an accuracy of ~ 0.2 ppm. These measurements (along with comparisons with quantum chemical calculations) enabled the determination of the ^{13}C chemical shielding tensors of all fluorene carbon positions, as well as the verification of the planar structure of fluorene in the single crystal (within $0.4°$ – an accuracy comparable to X-ray studies). Similar experiments have focused on optically enhanced deuterium NMR studies.[79,91] Figure 6(a) and (b), respectively, shows a typical ^{2}H NMR spectrum from a single crystal sample of deuterated fluorene (doped with acridine), and the corresponding rotational pattern of the spectral lines.[91] These experiments provided values for the full ^{2}H quadrupolar tensors of all fluorene deuterium positions, and manifest an alternative approach for probing molecular structure (and dynamics) in the single crystal.

2.4.2. Field-driven ONP

Considerable efforts over the years have been directed towards enhancing the ONP process by 'driving' the electron-nuclear polarization transfer via resonant or near-resonant (rf/mw) AC fields. This practice can not only improve the efficiency of the ONP process (particularly in systems or experimental regimes where LAC-ONP is not possible), but – with implementation of pulsed optical and AC fields – can permit time-resolved studies as well.
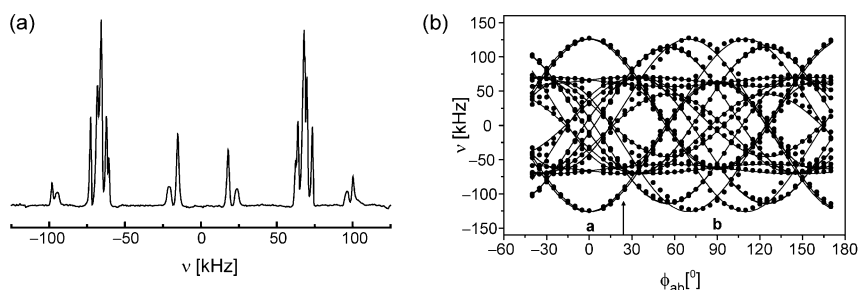
Fig. 6. (a) A selected ^{2}H ONP spectrum from a single crystal of deuterated fluorene doped with acridine; the spectrum was obtained in the crystal *ab*-plane at an angle of 24.8° with respect to the crystallographic *a* direction. (b) Rotation pattern of the primary ^{2}H ONP spectral lines in the crystal *ab*-plane, showing the dependence of the ^{2}H quadrupolar splittings on the crystal orientation. The arrow marks the angle at which the spectrum shown in (a) was obtained.[91] (Figures courtesy of G. Buntkowsky.)

Field-driven ONP was first demonstrated by Vieth *et al.*[48,49] who reported the use of rf to saturate ESR transitions (performed in weak external fields, not too distant from the LAC regime) during the application of light to drive ONP in crystals of fluorene doped with acridine or anthracene. Maximum ^{1}H polarization enhancements were ∼100-fold at room temperature (in an observation field raised to 7 kG); the resulting positive and negative ONP enhancements were qualitatively similar to those observed in the solid effect. However, in the case of RFONP, the transitions that are saturated are partially allowed. These experiments also showed that the additional degree of control provided by the rf (in conjunction with the variable external field) can be used to help determine the polarization transfer mechanisms and pathways underlying observed ONP effects, aiding in the characterization of the corresponding photochemical processes (here, the reversible, light-induced abstraction and transfer of hydrogen from host to guest[48,49]). Later work also showed that RFONP could be used to help distinguish the relative roles of static vs. dynamic HFCs, thereby determining whether the observed ONP processes involve localized or mobile triplet states.[46,52] Additionally, utilization of pulsed rf and optical excitation (with variable interpulse delays) permitted *direct time-resolved studies* (on μs to ns time scales) of various fundamental ONP processes, including polarization transfer, spin de-coherence, relaxation, and photochemical reactions[51–55,88] (as described in the previous section's example[88]).

In many circumstances, it can be advantageous to perform ONP at higher magnetic fields, placing the corresponding ESR frequencies well into the mw regime. Such mw-induced ONP (MIONP) was first demonstrated in crystals of *p*-dibromobenzene doped with dichlorobenzene.[56] In these experiments, continuous, simultaneous irradiation of the sample with light and microwaves (∼9 GHz) resulted in a modest (∼10-fold) enhancement in the ^{1}H nuclear spin polarization over the thermal equilibrium value at 77 K. This effect was observed at fields well outside the LAC regime for this sample

(i.e., under conditions where ONP by light alone does not occur), and followed the field dependence expected for an enhancement originating from the driving of *forbidden* ($\Delta m_s = \pm 1$, $\Delta m_n = \pm 1$) transitions – the classic solid effect – in contrast to the experiments using RFONP.[56]

This work was soon followed by other demonstrations of MIONP, with steadily improving ^{1}H polarizations and enhancements.[41,57–61] Indeed, in one study involving a single crystal sample of fluorene doped with perdeuterated phenanthrene (at 1.6%), a ^{1}H polarization of 42% was achieved.[58] This enormous polarization was achieved by performing MIONP with cw light and mw irradiation at low temperature (1.4 K) and high field (~ 2.7 T, necessitating a mw frequency of ~ 75 GHz), with an accumulation time of 40 min; as with other MIONP experiments, a clear signature of the solid effect was observed for the field dependence of the polarization rate. These results were important for the potential application of ONP for generating polarized targets because the ^{1}H polarization (P_H) values achieved were finally approaching the best values obtained with conventional DNP (see, for example Refs. [97,98]) – but without using permanent paramagnetic centers (which would otherwise cause significantly reduced ^{1}H T_1 values). Details of MIONP in this system (in which $T_{1e} \ll \tau$) were further examined in Ref. [68], including the relative importance of different relaxation pathways, lifetimes, and spin diffusion phenomena on the observed behavior.

One approach to improve the electron-nuclear polarization transfer rate in ONP experiments is to adapt time-tested Hartmann–Hahn-type approaches.[95] Groups at Heidelberg and Leiden separately developed similar approaches (respectively dubbed Hartmann–Hahn ONP (HHONP)[62,64] and nuclear orientation via electron spin locking (NOVEL)[66,67,69,76,99]) whereby a spin-lock mw pulse sequence is applied to the electrons such that their frequency in the rotating frame matches the Larmor frequency of the ^{1}H nuclei in the lab frame. Thus, the formerly 'forbidden' electron/nuclear flip-flop transitions effectively become thermodynamically 'allowed', improving the efficiency of the polarization transfer compared to MIONP experiments performed outside this Hartmann–Hahn condition. The polarization transfer typically occurs on the µs time scale, generally faster than both the electronic T_1 and the triplet lifetime.[63]

However, these approaches still suffered from the general limitation that in cases where the ESR line suffers from significant inhomogeneous broadening, only a fraction of the electron spins may participate.[67] Indeed, it has long been known that in situations where the ESR linewidth exceeds the nuclear Larmor frequency (e.g., at relatively low external magnetic fields), the efficiency of the solid effect in conventional DNP can be significantly reduced.[42] This problem results from the fact that mw irradiation of the ESR line can simultaneously drive *both* forbidden electron/nuclear transitions (at $\omega = \omega_e + \omega_n$ and $\omega = \omega_e - \omega_n$) – respectively, leading to 'positive' and 'negative' contributions to the nuclear spin polarization. Thus, the magnitude (and sign) of the nuclear polarization rate obtained in such cases – as well as the polarization achieved – is determined by the net population *difference* between the involved electron spin packets (characteristics of the differential solid effect, or DSE).[100]

In order to combat this problem, Wenckebach and co-workers devised an approach whereby the external magnetic field is rapidly swept through the entire ESR line during the application of mw fields for DNP.[100] This rapid field sweep is typically performed

with a separate set of coils (see for example, Ref. [85]). With sufficient mw power, the electron spin polarization in each 'spin packet' in the ESR line is inverted via adiabatic rapid passage, such that the $\omega = \omega_e + \omega_n$ transitions are completed prior to inversion, whereas the $\omega = \omega_e - \omega_n$ transitions are completed *after* inversion. Thus, the contributions to the nuclear spin polarization become *additive*, yielding a dramatic improvement in the nuclear polarization rate. This technique was dubbed the *integrated solid effect (ISE)*.

The implementation of the ISE – combined with the utilization of molecular systems where the electronic T_1 greatly exceeds the triplet lifetime – has permitted the demonstration of high nuclear spin polarization enhancements under relatively mild experimental conditions (temperature and external field strength) compared to those needed to achieve the high spin polarizations reported in Ref. [58]. Soon after the demonstration of the ISE to obtain enhanced DNP in an inorganic crystal (boron-doped silicon),[100] MIONP experiments were performed using ISE in crystals of pentacene-doped naphthalene.[63] In these experiments, it was shown that the efficiency of the ISE was significantly greater than the DSE, and that the ISE efficiency is greatest when the power of the mw pulses is set to achieve a Hartmann–Hahn matching condition similar to that utilized in HHONP/NOVEL experiments. With this approach, an enhancement of 5500 was achieved for the bulk ^{1}H spin polarization *at room temperature* in a field of only 0.35 T. Soon after, these authors reported a comparison of the ISE and the NOVEL approaches in the same system. The ISE was found to be superior to the NOVEL approach, yielding a 10-fold improvement in the ^{1}H polarization enhancement under their experimental conditions. Indeed, a maximum P_H enhancement of 15,000 was reported at room temperature and 0.35 T using a 50 Hz N$_2$ laser (with a total polarization accumulation time of $\sim$1 h.[67]).

More recently, Yabuzaki and co-workers have utilized MIONP with ISE to obtain large P_H enhancements in crystals of pentacene-doped naphthalene and *p*-terphenyl at 0.3 T under relatively mild conditions.[39,70] In one set of experiments performed at 77 K with a 1000 min ONP accumulation time, the authors reported P_H values for pentacene-doped naphthalene of 13 and 9%, respectively, obtained using an N$_2$ laser (280 mW, 337 nm; 70 Hz repetition rate; 4 ns) and a solid state 'TFR' laser (200 mW, 523 nm; 1000 Hz repetition rate; 7 ns) as the light source; a ^{1}H polarization of 13% at 0.3 T and 77 K corresponds to an enhancement of over 43,000 compared to the Boltzmann value at thermal equilibrium. Moreover, at 280 K (approaching room temperature), they reported P_H values of 0.08 and 0.13% using a 40 min ONP accumulation time. The reduced P_H values achieved at higher temperatures were the result of accelerated ^{1}H naphthalene T_1 processes (exacerbated by crystal heating accompanying laser excitation).

While these results were impressive, it was clear from the experiments that improved laser characteristics could result in higher polarization enhancements. In particular, the authors noted the possible utility of increased pulse duration for improving the fractional population of chromophores in the triplet state during each ONP cycle (in addition to high power, high repetition rate, and $\sim$600 nm light). This possibility was realized in later work from this group[39] (discussed further in Ref. [103]) in which a flash-pumped dye laser (350 mW; 600 nm; 100 Hz repetition rate; 800 ns) was used to achieve a P_H value of $\sim$32% in pentacene-doped naphthalene – corresponding to an enhancement factor
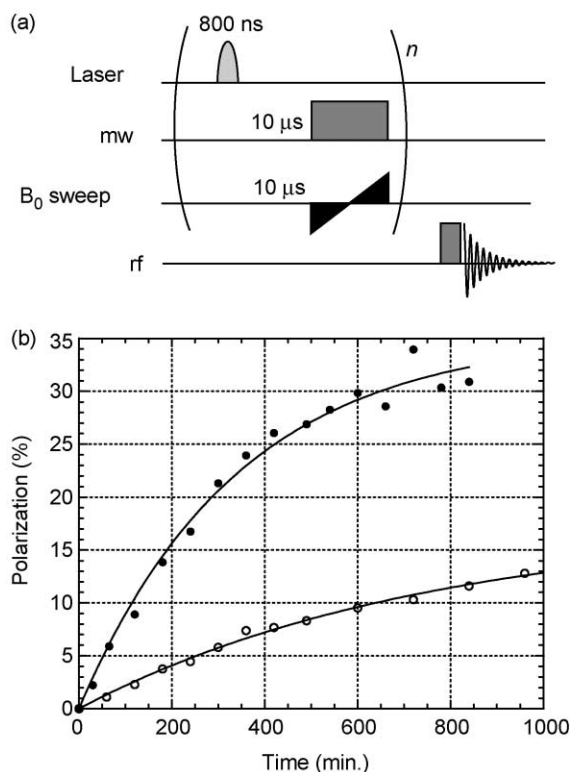
Fig. 7. (a) Pulse sequence diagram showing the timing scheme of the applied (static, optical, mw, and rf) fields used to obtain the data summarized in Fig. 7(b), based upon the experimental description in Ref. [39]. (b) Accumulation of ^{1}H spin polarization at 0.3 T and 77 K in single crystal samples of naphthalene doped with pentacene at $\sim$0.001 mol % (filled circles) and $\sim$0.01 mol % (open circles), respectively, polarized with a 600 nm 350 mW dye laser and a 150 mW N_2 laser. The time constant for the accumulation of polarization for the top curve was 343 min. The greater polarization rate and peak P_H value achieved in the top curve (despite the lower chromophore concentration) indicates the greatly improved ONP efficiency obtained with the dye laser. (Figure courtesy of M. Iinuma, reprinted with permission from Ref. [39]. Copyright 2000 by the American Physical Society.)

of $\sim$80,000 over the Boltzmann value at 77 K and 0.3 T (an enhancement record for ^{1}H spins at the time[39]). This high polarization was achieved by rapidly repeating the application of an ONP pulse sequence (Fig. 7(a)) over several hours, allowing bulk spin magnetization to accumulate and spread throughout the crystal (Fig. 7(b)). The approach was also demonstrated with a crystal of p-terphenyl; this material can generally be doped with a higher concentration of pentacene chromophores (up to 0.1%, allowing a bulk P_H value of $\sim$18% to be achieved in only $\sim$1 h), but suffers from a significantly faster ^{1}H T_1 (33 min at 77 K and 0.3 T, compared with $\sim$15 h for naphthalene).[39] Indeed, the naphthalene T_1 was even shown to be $\sim$2 h at 77 K in a field of only 7 G. Potential applications for their approach were discussed, including NMR quantum

computation[102–104] (where any future viability may depend on the capacity to prepare systems with P_H values approaching unity[105]), as well as polarized targets for particle physics experiments.

As this report was being finished, fresh results were reported by Terao and co-workers claiming the largest P_H values achieved thus far for optically enhanced NMR (and indeed, the largest ${}^1H$ polarization enhancement achieved by *any* method, to this reviewer's knowledge).[40,73] By carefully controlling the experimental parameters for performing MIONP-ISE in the pentacene/naphthalene system (e.g., chromophore doping level, mw power, ISE sweep rate, laser power density, temperature, etc.), a P_H value of $70\pm7\%$ was achieved at 105 K and 3187 G, *indicating an enhancement over the thermal equilibrium polarization by $\sim$210,000-fold*. The time constant for the accumulation of the ${}^1H$ spin polarization was 7890 s. This P_H value represents a $\sim$2-fold improvement over the previous result,[39] but required only about one-third the experimental accumulation time. Because ${}^1H$ polarization is ultimately limited by the electronic spin polarization attained in the triplet state via OEP (expected to average $\sim$0.63 according to their analysis), this new result indicates that the maximum possible enhancement of the ${}^1H$ spin polarization has now been achieved for this system. A similar P_H value was also achieved in a single crystal of perdeuterated naphthalene doped with pentacene.[73] However, because this sample had an extremely low ${}^1H$ spin density (99.21% of the hydrogen nuclei were deuterons), the heat capacity for the ${}^1H$ spin reservoir was greatly reduced – allowing the ${}^1H$ spins to be 'cooled down' much more rapidly by MIONP. The time constant for the polarization accumulation was only 357 s for this sample (a $>$20-fold improvement over the result from the protonated crystal).

2.4.3. ONP in polycrystalline samples

The MIONP approach has recently been extended to polycrystalline samples.[71–73] Interestingly, the possibility of performing ONP in such disordered materials was considered decades ago (see Refs. [31,106]). At first glance, one might expect that ONP signals from samples possessing isotropic distributions of chromophore orientations would be averaged away (because positive and negative enhancements of similar magnitude would be obtained). However, it was predicted that if such a sample were placed in a weak magnetic field (near the LAC region), those chromophores with optimal orientations would undergo more efficient polarization transfer – disproportionately contributing to the LAC-ONP effect (and allowing a net enhancement to be observed). Moreover, it was predicted that particular chromophore orientations could be further selected using polarized light.

However, the recent experiments demonstrating (MI)ONP in polycrystalline samples were actually achieved by selective implementation of the ISE.[71] In this work, an enhancement factor of 3160 was achieved in a polycrystalline (ground and pressed) sample of pentacene-doped naphthalene at 100 K in a field of $\sim$0.32 T (Fig. 8). However, instead of sweeping over the entire triplet ESR line (as is normally done with the ISE), the field sweep was designed to cover only a partial area of the ESR spectrum. With this approach (as implemented), only those crystallites with the long axis of the pentacene chromophores
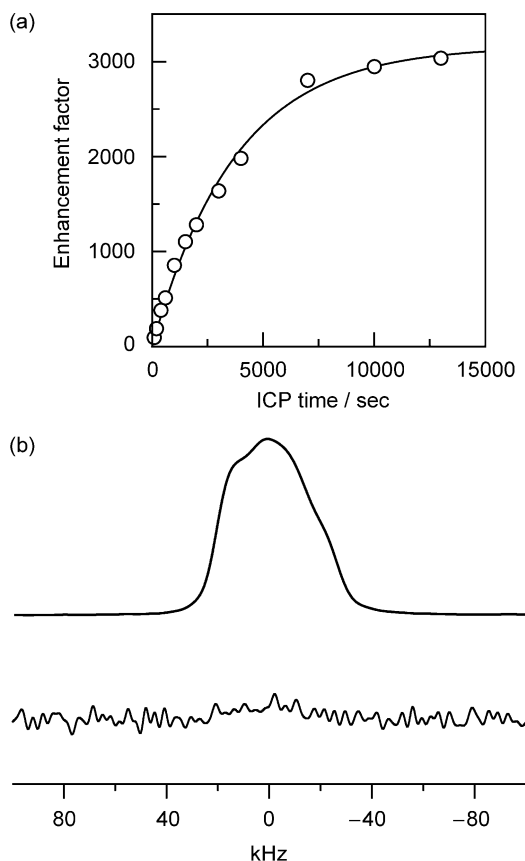
Fig. 8. MIONP enhancement of ^{1}H nuclear spin polarization in a polycrystalline sample of pentacene doped naphthalene.[71] (a) Build-up curve for the enhanced ^{1}H spin polarization, with an MIONP repetition rate of 50 Hz (determined by the laser); the time constant for the build-up was 3730 s. 'ICP' is an acronym for *integrated cross-polarization* – the authors' term for their variant of the ISE. (b) 13.6 MHz single-shot ^{1}H NMR spectra, taken with (*top*) and without (*bottom*) MIONP enhancement (respectively, acquired at 100 K and room temperature). The top spectrum was obtained with a 10,000 s MIONP build-up time. The enormous sensitivity enhancement obtained with ONP is clear from comparing the two spectra. (Figures courtesy of K. Takeda and T. Terao, reprinted from Ref. [71], copyright 2001, with permission from Elsevier.)

nearly parallel with the external magnetic field significantly contribute to the MIONP process. The limiting factor for the P_H values achieved was primarily determined to result from the polycrystalline nature of the sample, as the ^{1}H T_1 was significantly shorter than the corresponding value obtained from a single crystal (4000 s vs. 29,100 s – which in turn, might have resulted from the presence of permanent paramagnetic centers introduced during the sample's creation). Additionally, the respective roles of light penetration, scattering, (poly)crystallinity, and other parameters in determining ONP efficiency were further investigated in separate theoretical work.[72] Finally, this approach was recently

extended to the perdeuterated pentacene/naphthalene samples described above,[40,73] where a P_H value of 3.3% was reached for a ground and pressed polycrystalline sample of this material – a >3-fold improvement over their previous result.[71] As the authors point out, these results could lead the way towards an expansion of ONP methodology to samples beyond organic molecular crystals, including peptides and proteins.

2.5. Summary and future outlook for ONP in molecular crystals

Over its nearly 40-year history, ONP has permitted a wide range of novel photochemical and photophysical experiments in various aromatic molecular crystals; unfortunately, this approach has not yet seen significant application beyond such fundamental studies in these systems. However, tantalizing recent results – particularly (1) the observation of extremely high ^1H polarization values under modest experimental conditions; (2) the transfer of high ^1H polarization to rare nuclei for enhanced, high-resolution NMR studies; and (3) the observation of ONP in polycrystalline samples – bode well for a number of future NMR applications. Arguably, the key to realizing many of the possible applications will be achieving efficient transfer of the enhanced polarization to other molecular systems of interest. One possibility advocated by the reviewer[93,107] (and also suggested in Ref. [40]) would be to use ONP-enhanced single crystals as 'polarizing substrates' for biomolecular or polymer thin films – an idea originally proposed for optically-pumped semiconductors.[108,109] In such an approach, the material to be polarized would be deposited as a thin film onto the surface of the crystal. Following ONP-enhancement of the bulk nuclear spin polarization in the crystal substrate, the sample would be transferred to high field, and the high nuclear spin magnetization would be transferred to the overlayer (by spin diffusion and/or CP) – permitting enhanced NMR spectra to be obtained from the target material. Other possible approaches might involve liquefying/dissolving the polarized crystals – or, in light of the polycrystalline results described above – the preparation of solid-state mixtures of ONP chromophores and target (biological) molecules.[40] In any case – given the exciting and promising results reviewed above, there is good reason to believe that the realization of wider NMR application of ONP is now only a matter of time.

REFERENCES

1. R. R. Ernst, G. Bodenhausen and A. Wokaun, *Principles of Nuclear Magnetic Resonance in One and Two Dimensions*, Oxford University Press, Oxford, 1990.
2. P. T. Callaghan, *Principles of Nuclear Magnetic Resonance Microscopy*, Oxford University Press, 1993.
3. F. W. Wehrli, *Prog. Nucl. Magn. Reson. Spectrosc.*, 1995, **28**, 87.
4. W. S. Price, *Annu. Rep. NMR Spectrosc.*, 1998, **35**, 140.
5. J. Brossel and A. Kastler, *Compt. Rend. Acad. Sci. (Paris)*, 1949, **229**, 1213.
6. A. Kastler, *J. Phys. Radium*, 1950, **11**, 255.
7. J. Brossler, A. Kastler and J. Winter, *J. Phys. Radium*, 1952, **13**, 668.
8. A. Kastler, *J. Opt. Soc. Am.*, 1957, **47**, 460.
9. B. Cagnac and J. Brossel, *Compt. Rend. Acad. Sci. (Paris)*, 1958, **246**, 1827.
10. B. Cagnac, *Ann. Phys. (Paris)*, 1961, **6**, 467.
11. J. C. Lehmann, *J. Phys. (Paris)*, 1964, **25**, 809.
12. M. R. Bouchiat, T. R. Carver and C. M. Varnum, *Phys. Rev. Lett.*, 1960, **5**, 373.
13. F. D. Colegrove, L. D. Schearer and G. K. Walters, *Phys. Rev.*, 1963, **132**, 2561.
14. B. C. Grover, *Phys. Rev. Lett.*, 1978, **40**, 391.
15. G. Maier, U. Haeberlen, H. C. Wolf and K. H. Hausser, *Phys. Lett. A*, 1967, **25**, 384.
16. C. D. Jeffries, *Phys. Rev. Lett.*, 1967, **19**, 1221.
17. L. F. Mollenauer, W. B. Grant and C. D. Jeffries, *Phys. Rev. Lett.*, 1968, **20**, 488.
18. G. Lampel, *Phys. Rev. Lett.*, 1968, **20**, 491.
19. A. L. Ekimov and V. I. Safarov, *Proc. Int. Conf. Phys. Semicond.*, 1972, **11**, 1351.
20. J. Bargon and H. Z. Fischer, *Naturforsch. Teil A*, 1967, **22**, 1556.
21. H. R. Ward and R. G. Lawler, *J. Am. Chem. Soc.*, 1967, **89**, 5518.
22. R. Kaptein, K. Dijkstra and K. Nikolay, *Nature*, 1978, **274**, 233.
23. G. Maier and H. C. Wolf, *Z. Naturforsch. Teil A*, 1968, **23a**, 1068.
24. H. Schuch, D. Stehlik and K. H. Hausser, *Z. Naturforsch. Teil A*, 1971, **26**, 1944.
25. J. P. Colpa, K. H. Hausser and D. Stehlik, *Z. Naturforsch. Teil A*, 1971, **26a**, 1792.
26. A. H. Maki and J. U. v. Schutz, *Chem. Phys. Lett.*, 1971, **11**, 93.
27. P. Lau, D. Stehlik and K. H. Hausser, *J. Magn. Reson.*, 1974, **15**, 270.
28. A. W. Overhauser, *Phys. Rev.*, 1953, **92**, 411.
29. T. R. Carver and C. P. Slichter, *Phys. Rev.*, 1953, **93**, 212.
30. K. H. Hausser and M. Wolf, eds., *Optical Spin Polarization in Molecular Crystals*, 1976.
31. D. Stehlik, ed., *The Mechanism of Optical Nuclear Polarization in Molecular Crystals*, Academic Press, New York, 1977.
32. C.v. Borczyskowski, ed., *Optical Detection of Nuclear Spin Alignment and Quadrupole Resonance in Organic Molecular Crystals*, 1988.
33. C. v. Borczyskowski and E. Boroske, *Chem. Phys.*, 1978, **35**, 367.
34. K. P. Dinse and C. v. Borczyskowski, *Chem. Phys.*, 1979, **44**, 93.
35. D. H. Tanimoto, W. M. Ziniker and J. O. Kemp, *Phys. Rev. Lett.*, 1965, **14**, 645.
36. M. Schwoerer and H. C. Wolf, *Mol. Cryst.*, 1967, **3**, 177.
37. T. Yang, D. J. Sloop, S. I. Weissman and T.-S. Lin, *J. Chem. Phys.*, 2000, **113**, 11194.
38. D. J. Sloop, H.-L. Yu, T.-S. Lin and S. I. Weissman, *J. Chem. Phys.*, 1981, **75**, 3746.
39. M. Iinuma, Y. Takahashi, I. Shake, M. Oda, A. Masaike and T. Yabuzaki, *Phys. Rev. Lett.*, 2000, **84**, 171.
40. K. Takeda, K. Takegoshi and T. Terao, *J. Phys. Soc. Jpn.*, 2004, **73**, 2313.
41. P. Bachert, H. Brunner, K. H. Hausser and J. P. Colpa, *Chem. Phys.*, 1984, **91**, 435.
42. A. Abragam and M. Goldman, *Nuclear Magnetism: Order and Disorder*, Clarendon Press, Oxford, 1982.
43. J. P. Colpa and D. Stehlik, *Z. Naturforsch. Teil A*, 1972, **27a**, 1695.
44. D. Stehlik, A. Doehring, J. P. Colpa, E. Callaghan and S. Kesmarky, *Chem. Phys.*, 1975, **7**, 165.
45. J. P. Colpa and D. Stehlik, *Chem. Phys.*, 1977, **21**, 273.
46. J. Allgeier, V. Macho, D. Stehlik, H. M. Vieth, W. Auch and J. U. v. Schutz, *Chem. Phys. Lett*, 1982, **186**, 522.
47. A. Abragam, *Principles of Nuclear Magnetism*, Oxford University Press, Oxford, 1961.

48. H. M. Vieth, V. Macho and D. Stehlik, *Chem. Phys. Lett.*, 1979, **60**, 368.

49. H. M. Vieth, V. Macho and D. Stehlik, *J. Phys. Chem.*, 1979, **83**, 3435.

50. D. Stehlik, R. Furrer and V. Macho, *J. Phys. Chem.*, 1979, **83**, 3440.

51. H. M. Vieth, *Chem. Phys. Lett.*, 1983, **103**, 124.

52. G. Buntkowsky, M. Nack, D. Stehlik and H. M. Vieth, *Isr. J. Chem.*, 1989, **29**, 109.

53. G. Buntkowsky, D. Stehlik, H. M. Vieth and K. M. Salikhov, *J. Phys.: Condens. Matter*, 1991, **3**, 6093.

54. V. Macho, D. Stehlik and H. M. Vieth, *Chem. Phys. Lett.*, 1991, **180**, 398.

55. M. Benkert and H. M. Vieth, *Chem. Phys. Lett.*, 1994, **230**, 153.

56. M. Deimling, H. Brunner, K. P. Dinse, K. H. Hausser and J. P. Colpa, *J. Magn. Reson.*, 1980, **39**, 185.

57. H. W. v. Kesteren, W. T. Wenckebach, J. Schmidt and N. J. Poulis, *Chem. Phys. Lett.*, 1982, **89**, 66.

58. H. W. v. Kesteren, W. T. Wenckebach and J. Schmidt, *Phys. Rev. Lett.*, 1985, **55**, 1642.

59. H. W. v. Kesteren, W. T. Wenckebach and J. Schmidt, *Chem. Phys. Lett.*, 1985, **121**, 440.

60. H. W. v. Kesteren, W. T. Wenckebach and J. Schmidt, *Mol. Phys.*, 1986, **58**, 263.

61. W. T. Wenckebach, *Helv. Phys. Acta*, 1986, **59**, 737.

62. H. Brunner, R. H. Fritsch and K. H. Hausser, *Z. Naturforsch. Teil A*, 1987, **42a**, 1456.

63. A. Henstra, T.-S. Lin, J. Schmidt and W. T. Wenckebach, *Chem. Phys. Lett.*, 1990, **165**, 4.

64. R. H. Fritsch, H. Brunner and K. H. Hausser, *Chem. Phys.*, 1991, **151**, 261.

65. J. Schmidt, D. J. van den Heuvel, A. Henstra, T.-S. Lin and W. T. Wenckebach, *Pure Appl. Chem.*, 1992, **64**, 859.

66. D. J. van den Heuvel, A. Henstra, T.-S. Lin, J. Schmidt and W. T. Wenckebach, *Chem. Phys. Lett.*, 1992, **188**, 194.

67. J. Schmidt, D. J. van den Heuvel, A. Henstra, T.-S. Lin and W. T. Wenckebach, *Isr. J. Chem.*, 1992, **32**, 165.

68. P. F. A. Verheij, W. T. Wenckebach and J. Schmidt, *Appl. Magn. Reson.*, 1993, **5**, 187.

69. D. J. van den Heuvel, J. Schmidt and W. T. Wenchebach, *Chem. Phys.*, 1994, **187**, 365.

70. M. Iinuma, I. Shake, R. Takizawa, M. Daigo, H. M. Shimizu, M. Takahashi, A. Masaike and T. Yabuzaki, *Phys. Lett. A*, 1995, **208**, 251.

71. K. Takeda, K. Takegoshi and T. Terao, *Chem. Phys. Lett.*, 2001, **345**, 166.

72. K. Takeda, K. Takegoshi and T. Terao, *J. Chem. Phys.*, 2002, **117**, 4940.

73. K. Takeda, K. Takegoshi and T. Terao, *J. Phys. Soc. Jpn.*, 2004, **73**, 2319.

74. E. C. Reynhardt, *Concepts Magn. Reson.*, 2003, **19A**, 36.

75. M. Goldman, *Spin Temperature and Nuclear Magnetic Resonance in Solids*, Oxford, London, 1970.

76. E. C. Reynhardt, *Concepts Magn. Reson.*, 2003, **19A**, 44.

77. V. Weis, M. Bennati, M. Rosay and R. G. Griffin, *J. Chem. Phys.*, 2000, **113**, 6795.

78. C. T. Farrar, D. A. Hall, G. J. Gerfen, S. J. Inati and R. G. Griffin, *J. Chem. Phys.*, 2001, **114**, 4922.

79. J. Allgeier, G. Buntkowsky, S. Hentrich, W. Hoffmann and H. M. Vieth, *Isr. J. Chem.*, 1992, **32**, 205.

80. D. Stehlik, P. Rosch, P. Lau, H. Zimmermann and K. H. Hausser, *Chem. Phys.*, 1977, **21**, 301.

81. V. Macho, J. P. Colpa and D. Stehlik, *Chem. Phys.*, 1979, **44**, 113.

82. G. Buntkowsky, W. Hoffmann, T. Kupka, G. Pasterna, M. Jaworska and H.-M. Veith, *J. Phys. Chem. A*, 1998, **102**, 5794.

83. A. J. v. Strien and J. Schmidt, *Chem. Phys. Lett.*, 1980, **70**, 513.

84. T. Yang, D. J. Sloop, S. I. Weissman and T.-S. Lin, *Chem. Phys. Lett.*, 2000, **331**, 489.

85. T. Yang, D. J. Sloop, S. I. Weissman and T.-S. Lin, *Mol. Phys.*, 2002, **100**, 1333.

86. G. Dittrich, D. Stehlik and K. H. Hausser, *Z. Naturforsch. Teil A*, 1977, **32a**, 652.

87. W. Auch and J. U. v. Schutz, *Phys. Stat. Sol.*, 1980, **101b**, 287.

88. J. Allgeier, G. Buntkowsky, S. Hentrich, M. Nack and H. M. Vieth, *Ber. Bunsenges. Phys. Chem.*, 1989, **93**, 1281.

89. H. E. Buckley, *Crystal Growth*, Wiley, New York, 1951.

90. E. Monberg, ed., *Handbook of Crystal Growth*, North-Holland, Amsterdam, 1994.

91. G. Buntkowsky, W. Hoffmann and H.-M. Veith, *Appl. Magn. Reson.*, 1999, **17**, 489.

92. R. Tycko, A. Pines and D. Stehlik, *Chem. Phys. Lett.*, 1982, **93**, 392.

93. J. L. Shapiro, P. Nikolaou and B. M. Goodson, *Midwest Organic Solid State Chemistry Symposium (MOSSCS) XV*, Carbondale, IL, 2004.

94. D. Stehlik and J. P. Colpa, *Chem. Phys.*, 1977, **21**, 289.
95. S. R. Hartmann and E. L. Hahn, *Phys. Rev.*, 1962, **128**, 2042.
96. A. Pines, M. G. Gibby and J. S. Waugh, *J. Chem. Phys.*, 1972, **56**, 1776.
97. D. G. Crabb, C. B. Higley, A. D. Krisch, R. S. Raymond, J. A. Stewart and G. R. Court, *Phys. Rev. Lett.*, 1990, **64**, 2627.
98. W. de Boer, M. Borghini, K. Morimoto, T. O. Niinikoski and F. Udo, *J. Low Temp. Phys.*, 1974, **15**, 249.
99. A. Henstra, P. Dirksen, D. M. Schmidt and W. T. Wenckebach, *J. Magn. Reson.*, 1988, **77**, 389.
100. A. Henstra, P. Dirksen and W. T. Wenckebach, *Phys. Lett. A*, 1988, **134**, 134.
101. M. Iinuma, Y. Takahashi, I. Shake, M. Oda, A. Masaike, T. Yabuzaki and H. M. Shimizu, *Nucl. Instrum. Meth. Phys. Res. A*, 2004, **529**, 199.
102. N. A. Gershenfeld and I. L. Chuang, *Science*, 1997, **275**, 350.
103. D. G. Cory, A. F. Fahmy and T. F. Havel, *Proc. Natl Acad. Sci. USA*, 1997, **94**, 1634.
104. J. A. Jones, *Prog. NMR Spectrosc.*, 2001, **38**, 325.
105. W. S. Warren, *Science*, 1997, **277**, 1688.
106. S. Sukhenko and K. M. Salikhov, *Chem. Phys.*, 1985, **98**, 431.
107. B. M. Goodson, *SLNMR Seminar*, Washington University, St. Louis, 2002.
108. R. Tycko, *Solid State Nucl. Magn. Reson.*, 1998, **11**, 1.
109. L. Goehring and C. Michal, *J. Chem. Phys.*, 2003, **119**, 10325.
110. B. M. Goodson, *Concepts Magn. Reson.*, 1999, **11**, 203.

Index